The Dissertation Committee for Will Zhang
certifies that this is the approved version of the following dissertation:

Modeling and simulating time-dependent changes in soft-tissue derived bioprosthetic heart valve biomaterial in response to cyclic loading

Committee:

Michael S. Sacks, Supervisor

Aaron Baker

Christopher G. Rylander

Krishnaswamy Ravi-Chandar

Naren Vyavahare

Modeling and simulating time-dependent changes in soft-tissue derived bioprosthetic heart valve biomaterial in response to cyclic loading

by

Will Zhang

DISSERTATION

Presented to the Faculty of the Graduate School of

The University of Texas at Austin

in Partial Fulfillment

of the Requirements

for the Degree of

DOCTOR OF PHILOSOPHY

THE UNIVERSITY OF TEXAS AT AUSTIN

December 2018

Acknowledgments

Firstly, I would like to thank my advisor, Dr. Michael Sacks, for introducing to me to the world of biomechanics, the opportunity to work with his research group, and his patience and guidance over the years to prepare me for an academic career. Also, thank you to my committee members and the Department of Biomedical Engineering at the University of Texas at Austin for their support throughout this process. It has been an honor to represent the Willerson Center for Cardiovascular Modeling and Simulation, the Department of Biomedical Engineering and the Institute for Computational Engineering and Sciences during my time here.

I would like to thank my wonderful lab mates for giving me strength and support throughout this long process, lifting me up when I needed it the most. I also like to thank the post-doctoral fellows in our lab in particular, specifically Rong Fan, Chung-Hao Lee, Ankush Aggarwal and Joao Soares for their mentorship and guidance both in research and academically.

Lastly, and most importantly I would like to thank my family, my parents, for raising me to the way I am, and all of the support they have given me throughout my life. I love you all.

Modeling and simulating time-dependent changes in soft-tissue derived bioprosthetic heart valve biomaterial in response to cyclic loading

Publication No. _____

Will Zhang, Ph.D.
The University of Texas at Austin, 2018

Supervisor: Michael S. Sacks

Soft tissue-derived exogenously cross-linked (EXL) biomaterials continue to be the best choice for the fabrication of bioprosthetic heart valves (BHV). Despite years of use, our understanding of these biomaterials and of the mechanisms leading to their failure remain at an empirical level. The need for advancements in modeling their behavior is further underscored by the development of percutaneously delivered BHV devices. While these devices offer reduced surgical risk, they also present additional challenges for the design of the leaflets due to limitations in thickness and folding during delivery, resulting in a 2-year mortality rate of 33.9% in general. Thus, we seek to develop a framework for modeling and simulating soft-tissue-derived EXL biomaterials, accounting for the effects of exogenous cross-linking in permanent set and mechanical fatigue. Such approaches can significantly improve the accuracy and reliability of long-term predictions of durability and mechanical function. Firstly, we will establish the form of a nonlinear hyperelastic meso-scale structural constitutive model (MSSCM) for fibrous soft tissues, that can accurately capture the mechanical response of common soft tissues used as a basis for EXL biomaterial. Second, we

will study the effect of exogenous crosslinks on these tissues using glutaraldehyde (GLUT) EXL bovine pericardium. GLUT-EXLs form polymeric chains through the cross-linking process which more tightly bonds the fibers to the matrix, increasing the non-fibrous matrix stiffness and fiber-fiber interactions. However, GLUT EXLs undergo Schiff-base reactions that lead to scission-healing behaviors that change the geometry of BHVs. We model this effect based on the first-order kinetics of the scission healing reaction and validate it using static strain, cyclic strain, and stress control experiments. Next, we will develop a full 3D finite element implementation of the MSSCM with the modifications for EXL for real device applications. We then parametrically examine the changes in geometry and stress distribution of BHVs overtime, exploring initial geometries and material properties which may minimize the risks of the former effects. With this, we aim to develop a better understanding of the underlying process that occurs during long-term cyclic loading through our constitutive modeling approach and device level applications and translate the insights gained to improve BHV design and durability.

Table of Contents

List of Tables

List of Figures

Chapter 1

Introduction

Preface

Heart valves play a critical role in preventing backflow during cardiac operations. They are designed to withstand the demanding mechanical environment of the heart while maintaining an optimal state for over 3 billion cycles. When they can no longer function properly due to fatigue, diseases or trauma, and when surgical repair is not an option, surgical replacement using bioprosthetic heart valves is often the best choice. This introductory chapter focus on the current state of heart valve replacements and design, and methods for improving the durability of these devices. First, an overview of the structure and functions of heart valves is provided. Then the current state of heart valve repair and replacement is summarized, followed by the current state of bioprosthetic valve design and fabrication as well as their durability and limitations. Finally, the causes and mechanisms of bioprosthetic heart valve failure are discussed, and we outline the motivation, rationale, and aims of this dissertation, on how constitutive modeling and simulations can be used to better understand bioprosthetic heart valve failure and facilitate the improvement of bioprosthetic heart valve design.

1.1 Introduction and Background

Cardiovascular diseases remain the leading cause of death (31.8% of all deaths) in the U.S., costing 320.1 billion each year [39]. One significant area that needs improvements is heart valve replacement and repair procedures such as aortic valve repair using bioprosthetic heart valves (BHVs), where the mortality has not seen any major improvements since 1985 – the rate of survival after 10 years still remains only 29.7%. Soft-tissue-derived exogenously cross-linked (EXL) biomaterials, which has only existed since the beginning of the 1970s, is the dominant choice due to advantages in immunogenicity and flow dynamics over their mechanical counterparts [65]. However, our understanding of these materials and of the mechanisms of their failure is still incomplete. As such, current design and development are very empirical in nature – depending on trial and error, extrapolation from accelerated wear test and long periods of clinical testing. The need for better BHV designs is further accelerated by the emergence of percutaneous devices such as the transcatheter aortic valve replacement (TAVR) [10][23]. TAVRs are an attractive alternative to open-heart surgeries, especially for people at high surgical risk, as well as youths who may require multiple surgical replacements over their lifetime. However, they are more often associated with peri-valvular regurgitation and is currently lacking in long-term data pertaining to their durability [23]. Existing TAVR data suggest only 2-year mortality rate of 33.9% [32] in general and 68% for aortic valve stenosis [35]. Much of the existing challenges are associated with the necessary compact folded delivery system, which places additional constraints on their geometrical design and mechanical properties. It is clear that there is a strong need for a better understanding of the mechanism associated with their failure and frameworks for predicting the long-term failure of these devices.

1.2 Structure and function of heart valves

Heart valves are complex multi-layered structures that prevent backflow by opening and closing depending on the direction of flow. There are four valves in the heart, consisting of two atrioventricular preventing backflow between the atriums and ventricles, the mitral (MV) and tricuspid valves (TV), and two semilunar preventing backflows from the aorta and to the vena cava, the aortic (AV) and pulmonary valves (PV) (Fig. 1.1). The coordinated movement of the four heart valves enables them to maintain unidirectional blood flow during the cardiac cycle. When healthy, heart valves are incredibly resilient, opening and closing approximately 3 - 4 billion times throughout an average life-span [54]. The pressure changes during the cardiac cycle expose the heart valves to constant changes in forces and hemodynamics. This physiological demand is especially harsh on the mitral and aortic valves, needing to withstand average pressures of 80mmHg for the aortic and 120mmHg for the mitral valve to sustain circulation throughout the rest of the body. The biomechanical properties of heart valves must be able to withstand and function efficiently in this complex mechanical environment. Thus, the heart valve leaflets develop and maintain an intricate, highly organized, and multi-scale connective tissue system that allows them to do so [72].

1.2.1 Multi-scale structure of heart valves

To fully understand the functional properties of heart valves, multi-scale approaches are needed (Fig. 1.2) [3]. This complex hierarchical structure is what lends to seamless heart valve performance under highly dynamic loading conditions. Heart valves have evolved to have multi-layered leaflet structures. The aortic valve, for example, consists of three histologically distinct layers, whereas the mitral valve has four

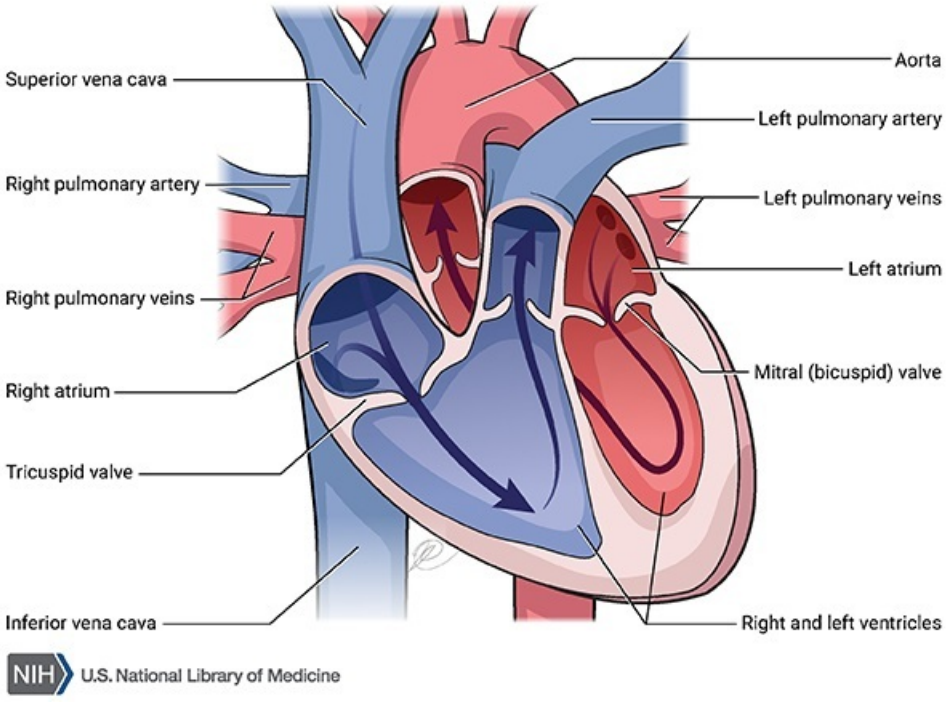

Figure 1.1: Artist rendition of the human heart depicting the location of the four heart valves and major vessels (obtained from U.S. National Library of Science website)

(Fig. 1.3). The fibrosa layer, which is located on the ventricular side of atrioventricular valves and the atrial side of semilunar valves, is composed of circumferentially aligned collagen fibers that provide the leaflets with the necessary tensile strength to open and transmit forces during coaptation while closed. The spongiosa layer is situated adjacent to the fibrosa and though it contains some collagen, its main constituents are the hydrophilic glycosaminoglycans and proteoglycans, which give the valve its compressive properties and allow it to absorb high forces during coaptation. The ventricularis and atrialis are the layers that are adjacent to blood flow in atrioventricular valves and semilunar valves, respectively. These layers are rich in radially oriented elastin fibers and facilitate the closure movement by extending the valve leaflet as it opens and recoils when it closes. The annulus and chordae tendineae of the atrioventricular valves and the connection between the leaflets and the surrounding myocardium in the semilunar valves provide additional support.

The collagen-dense fibrosa layer is the predominant stress-bearing layer. Collagen fibers have low torsional and flexural stiffness but can withstand high tensile forces. As such, fiber orientation can be used as an identifier for the material axes of the tissue, or in other words the directions in which the tissue is able to withstand the greatest tensile stresses. To measure the orientation distribution of the collagen fibers, small angle light scattering (SALS) is a popular choice [52]. In this technique, a laser beam, 500-600 nm in wavelength, is passed through a tissue specimen and is then scattered. The spatial intensity distribution of the resulting scattered light depends on the orientation of the collagen fibers (which is at a similar length scale as the light particles), which can be used to obtain structural information of the tissue. As an example, Sacks et al. used SALS to quantify the changes that occur in the AV leaflet structure with increasing transvalvular pressure (TVP) [53]. Fresh porcine

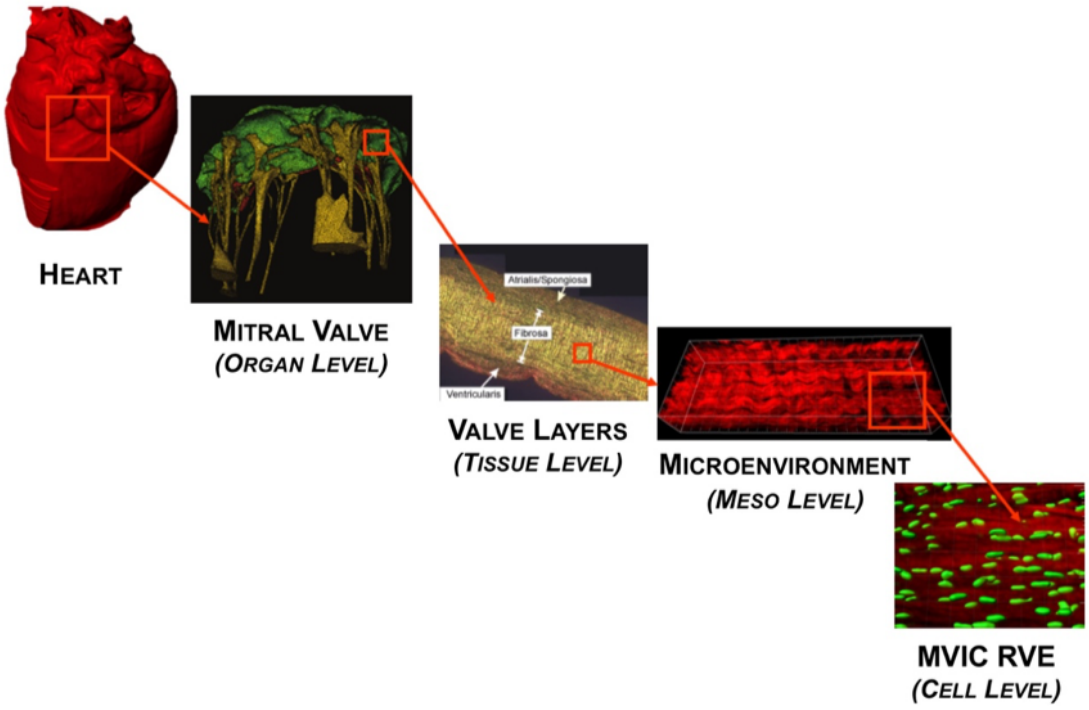

Figure 1.2: The multiscale nature of heart valve biomechanics: a representation of the mitral valve at the organ, tissue, and cell levels. At the tissue-level: a circumferentially oriented cross-section of the mitral valve anterior leaflet stained with Movat pentachrome, which colors collagen yellow, elastic fibers black, and hydrated PGs and GAGs blue. At the cell-level: a transmission electron micrograph of a mitral VIC from the fibrosa layer. (Adapted from [3])

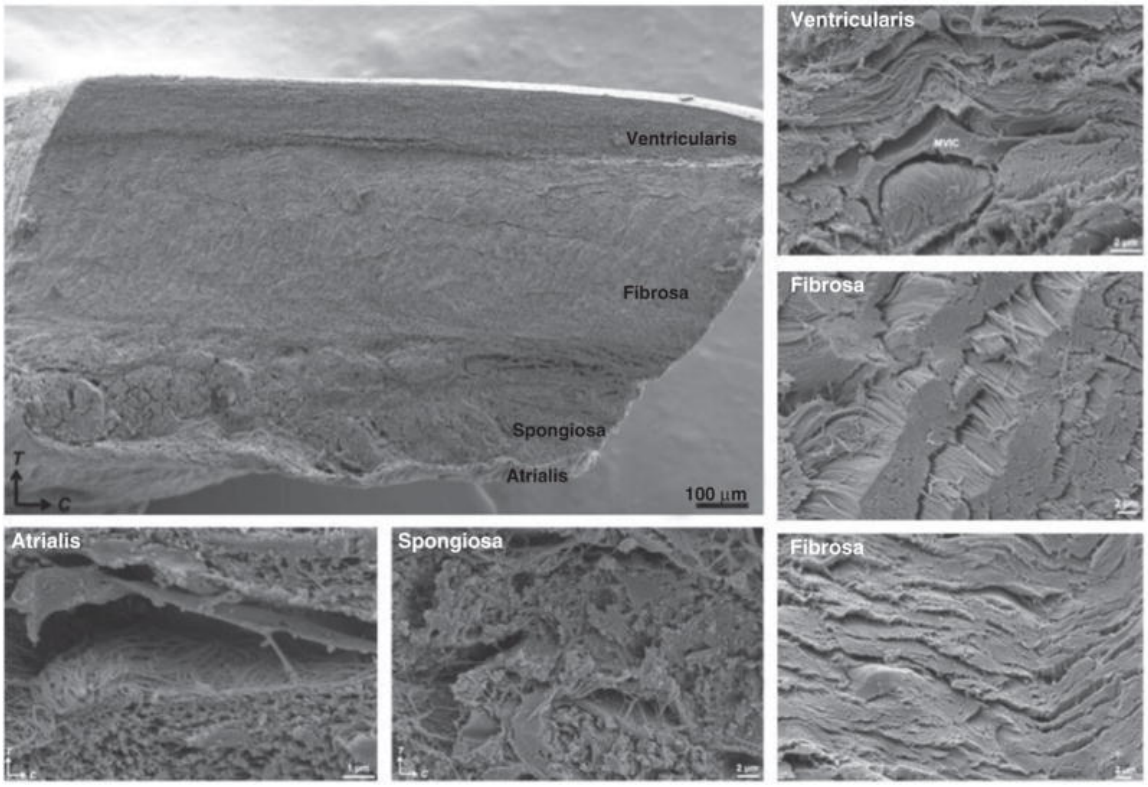

Figure 1.3: Scanning electron micrograph of the multilayered microenvironment of the MV anterior leaflet. Individual micrographs of each layer are also presented: elastin-rich ventricularis and atrialis, highly collagenous fibrosa, and proteoglycan-rich spongiosa. The collagen fibrils and elastic fibers closely surround the interstitial cells and highlight the long cellular extensions. In the fibrosa, collagen fibrils are aligned in the circumferential direction of the leaflet, which is responsible for the observed anisotropy in leaflet mechanical behavior. (T: transmural, C: circumferential). (Adapted from [3].)

AVs were fixed at TVPs ranging from 0 to 90 mmHg and imaged using small angle light scattering (SALS). Overall, increasing TVP induced the greatest changes in fiber alignment between 0 and 1 mmHg, and past 4 mmHg there was no detectable improvement in fiber alignment (Fig. 1.4b-d).

The other most important structural information about collagen fibers is the amount to which the collagen fibers are crimped. As collagen fibers have low torsional and flexural stiffness, they bear minimal stresses before they are fully straightened. Thus, the stretch needed to straighten these collagen fibers will determine the compliance or extensibility at the tissue level. One example of the attempt to quantification of collagen fiber crimp is the methods of Hilbert et al. [24, 25]. They quantified the amount of collagen fiber crimp in the native pulmonary and aortic HVs by identifying the cross-sectional regions that displayed observable crimp [29]. It was found that at 0 mmHg, approximately 60% of the AV transverse cross-sectional area was occupied by crimp structure (Fig. 1.4e). As the TVP increased, the percent crimp decreased rapidly until 20 mmHg, with minimal decreases in percent crimp thereafter. For the AV, much of the observed change in collagen structure is due to the finely tuned straightening of the collagen fibers, which must occur at the right strain level and at the right rate to facilitate coaptation without allowing excessive tissue deformations that could lead to regurgitation. The unique structure of the commissure region, which approximately corresponds to the coaptation region, highlights the adaptive structure of HVs. Instead of undergoing TVP differences, the coaptation region is loaded in a uniaxial-like manner due to tethering forces generated at the attachment of the commissures to the aortic root. Unlike the biaxially loaded belly regions of the valve, the uniaxial loading of the commissures makes them more highly aligned, similar to in tendons. Fiber uncrimping with stress occurs very rapidly for this highly

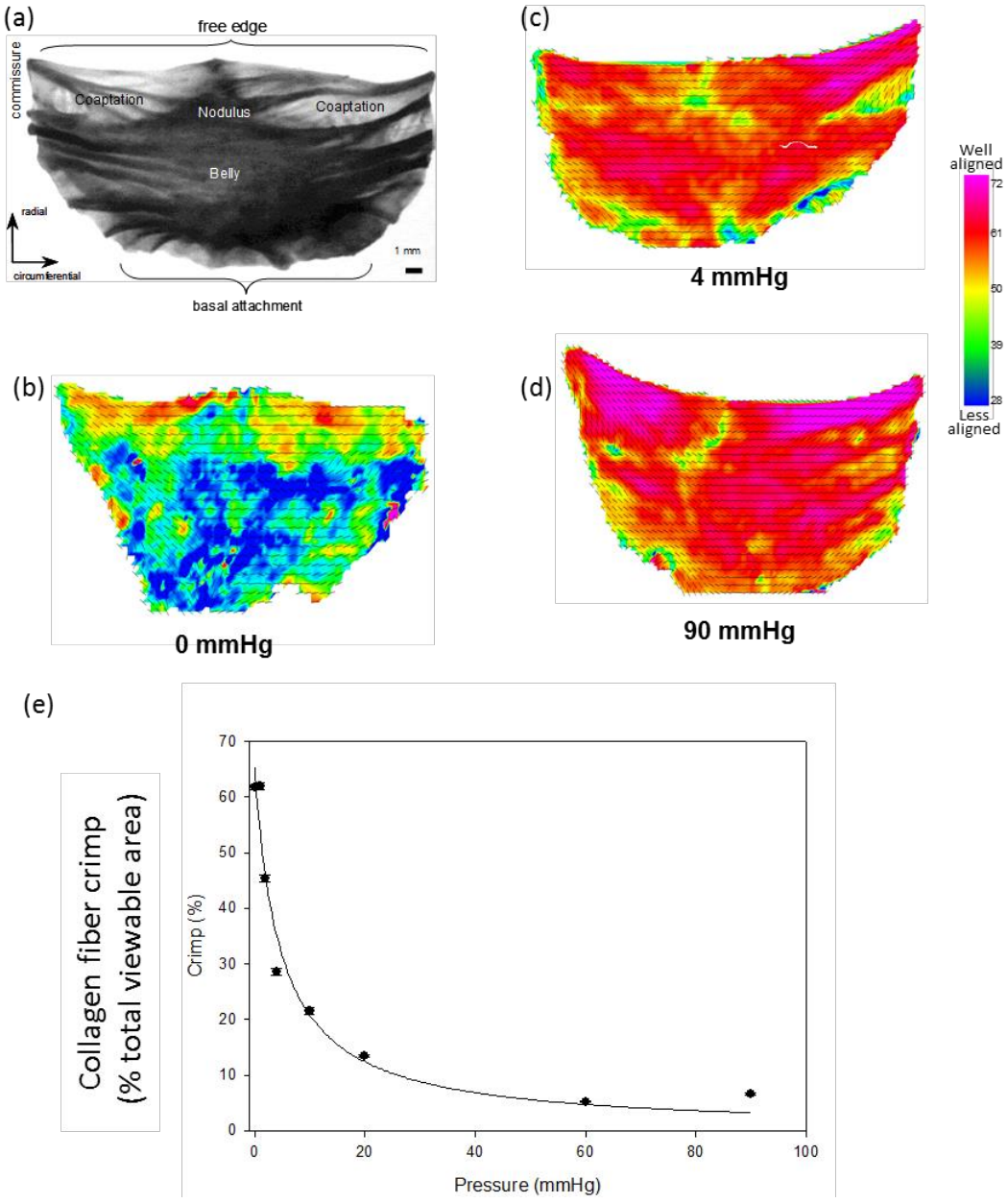

Figure 1.4: (a) Diagram of the AV cusp highlighting the belly, commissures, nodulus, and regions of coaptation. Small angle light scattering results with the orientation index at (b) 0mmHg, (c) 4mmHg, and (d) 90mmHg transvalvular pressure. No further changes in fiber alignment were observed past 4mmHg. These results are consistent with histological-based data that quantifies the percent area of tissue displaying collagen fiber crimp (e). (Adapted from Sacks et al. [53])

aligned fiber network, as demonstrated by the short transition region from low to high stiffness. The highly aligned nature of the commissure region in the unloaded state and more rapid realignment with TVP in the 10 commissure regions are consistent with the pre-transition strain level behavior of tendon-like materials.

1.3 Valvular diseases and prevalence

Cardiovascular diseases are the number one killer in the United States and around the world. Heart valve treatment is a common cardiovascular surgical procedure with over 100,800 done annually in the U.S. alone [39] and 275,000 to 370,000 in developed nations [36]. Calcification is the primary cause of AV failure and no proven therapy currently exists for halting this progression. Calcified aortic valve disease is a slow, progressive, multi-factorial disorder that is more common with age, without being an inevitable consequence of aging [74, 16, 15, 33, 4]. The disease is characterized by a thickening and calcification of the leaflets and is diagnosed in two stages: aortic sclerosis and aortic stenosis. aortic sclerosis, present in more than 25% of patients over the age of 65 [40], represents the early onset of calcified aortic valve disease absent of physical obstruction to the left ventricular outflow. Aortic stenosis exists in 2-5% of the elderly population [40], which is characterized by late-stage obstruction, impaired leaflet motion, valve tissue adaptation, and resistance to blood flow [45, 22, 18, 44]. Although aortic sclerosis causes significant thickening of the AV leaflets, there is little to no change in the mechanical properties of the valve, making the disease relatively asymptomatic. Recent statistics have shown that within 10 years of their initial diagnosis, 10% of aortic sclerotic patients reach a state of severe calcified aortic valve disease that requires immediate AV replacement once symptoms emerge [18].

Aortic stenosis has been identified as the end-stage of calcified aortic valve disease that progresses from the microscopic early changes of aortic sclerosis to, in a subset of patients, asymptomatic and then symptomatic Aortic stenosis [33, 41, 2]. Once aortic sclerosis is detected, there is an increased risk of cardiovascular events. In early Aortic stenosis, when mild symptoms begin to present, survival rates deviate much more than expected and decline dramatically with the onset of severe symptomatic Aortic stenosis. Over the last decade, several clinical trials, mostly extensions of atherosclerosis-related studies, have been performed to halt the progression of calcified aortic valve disease with randomized studies showing substantial equivalence between treatments and placebo [42, 38, 13, 5, 47]. However, there are currently no pharmacological therapies available to treat calcified aortic valve disease symptomatic patients that are considered superior to full valve replacement surgery.

1.3.1 Bioprosthetic heart valve replacements

Since initially introduced in 1960, valve replacement surgery has significantly reduced the mortality of patients with heart valve diseases [11, 56, 46]. As reported by The Society of Thoracic Surgeons 59,555 Americans underwent valve replacement surgery in 2014 (48,060 AV replacement, 9595 MV replacement, 1900 replacing both the AV and MV). Of the four heart valves, the AV has been studied most, followed next by the MV, whereas fewer studies have been performed. This is primarily due to the fact that the AV [12, 37, 1, 53, 6, 8, 75, 77, 76] and MV [66, 49, 20, 21] are more susceptible to diseases and more frequently warrant replacement surgery. While important differences exist in valve geometries and function, the mechanics of the AV are primarily used as a baseline for the development of models of heart valve function. Thus, this dissertation will focus on the aortic valve as an example as it is one of the most common valves for heart valve replacement surgeries. The same framework

proposed in this dissertation is otherwise applicable to the mitral and other valves.

Current clinically surgical valve replacement utilize either mechanical valves (usually made of pyrolytic carbon or titanium) or valves constructed from biologically-derived soft tissues. Mechanical valves have evolved significantly since the first ball and cage design, spanning a variety of shapes sizes and materials and rarely experiencing mechanical failure. However, they non-physiologic blood flow patterns and results in a substantial thrombogenic response, requiring lifelong postoperative anticoagulation therapy and its inherent risks [56].

On the other hand, bioprosthetic heart valves (BHVs) are comprised of decellularized bovine pericardium or porcine aortic valve tissues (most commonly the pericardium) and offer a higher degree of functionality including improved hemodynamics and a higher resistance to thrombosis. Although they are chemically fixed, these tissues are still prone to valve calcification, structural deterioration, and eventual failure [48, 79]. Durability is the major limitation of current BHV technology—the 15-year durability of heterograft BHVs in the aortic position is less than 50% for middle-aged patients and slightly better for older patients, however, BHVs continue to be the preferred replacement valve [61]. Regardless of its shortcomings, heart valve replacement has had a substantial impact on cardiac surgery with a consistently increasing number of surgeries per year [65].

Currently, bovine pericardium (BP) and porcine AV tissues are still the only clinically approved xenograft biomaterial for BHVs. Other tissue sources have been pursued, but none has reached a clinical widespread application. Collagenous soft tissues used for bioprosthetic devices are EXL, often using glutaraldehyde (GLUT), to suppress antigenic properties of the tissue and to stabilize the CFA [31]. GLUT is popular due to its affordability and solubility in an aqueous solution [28]. However,

GLUT is also implicated in the calcification of BHVs [19], which is further accelerated by mechanical stress [60]. There exist some alcohol based pretreatments for GLUT EXL BHV to reduce calcification [78], but there is little that we understand about the mechanical properties of EXL tissue. Specifically, there has been no attempt to constitutively model exogenous cross-linking and how it modulates the stresses.

GLUT is observed to significantly stiffen the ECM but not that of the collagen fibers [17, 82, 81]. It is also a Schiff-base, which means it reversibly reacts with aldehydes. Over time, this scission-healing behavior allows for a gradual change in the reference state, resulting in PS. This has yet to be properly modeled in biological tissues. Although there have not been any introduction of new cross-linking methods from an industrial standpoint, research in alternative technologies such as carbodiimide is ongoing [70, 7, 30], including a new method developed by our collaborator to stabilize elastin and GAGs in addition to collagen [71]. As GLUT and these other exogenous cross-linking methods remain necessary, it is important that we understand their role in predicting the fatigue and durability of bioprosthetic devices.

The most recent development in BHV technology is the percutaneous (or transcatheter) valve replacement. This technology is a minimally invasive procedure which delivers the replacement valves with catheterization from a large blood vessel, most commonly the femoral artery. This procedure makes valve replacement more feasible for those who cannot tolerate full surgical interventions. However, this new technology also presents additional design challenges, including complex folding and compression during delivery. As a result, the leaflets are required to be significantly thinner than in traditional BHVs, which increases the leaflet stress and potentially the rate of failure. Existing data on transcatheter aortic valve interventions suggest a 2-year mortality rate of 33.9% overall [39] and over 68% when specifically replacing

stenotic aortic valves [35]. As such, this further accentuates the need to develop an approach to improve BHV durability.

BHVs have become the preferred replacement valve. The sustained growth of AV and MV replacement surgeries, the lack of substantial technological breakthroughs in the field over the last decades [64], and the continuous need to improve BHV durability, promote a strong necessity to develop a higher understanding of the mechanisms involved in BHV function and failure. Critical BHV engineering aims to ensure valve functionality for its clinical performance with a combination of hemodynamic, biomechanical and biological aspects, and to predict and extend as much as possible valve durability. The major hurdle of the technology remains the lifespan of the BHV implant. Improvements to BHV design and durability have substantial impact clinically, even if these improvements are marginal (i.e. 3–5 years) [27].

1.4 Mechanisms of Bioprosthetic heart valve fatigue and failure

The mechanisms of limiting the durability of BHV can be divided into two categories: mineralization and Mechanical fatigue [59, 55, 60]. Tissue calcification primarily initiates from devitalized residual cells, usually from glutaraldehyde pretreatment [60]. Mineralization occurs due to interactions between the cell membrane phosphates and the calcium within the extracellular fluids. Mechanical stress appears to accelerate calcification, but mineralization and also occur in the absence of mechanical stress. To some extent, mineralization and calcification are interdependent processes [48]. Evidence suggests that mechanical deformation, either dynamic or static, potentiates mineralization but the mechanisms are unclear [59]. High levels of calcification have been generally reported to coincide with regions of high flexure,

especially the commissures and basal attachment margin [73, 55]. It is postulated that disruption of the collagen structure may produce new nucleation sites for calcific crystals, promoting mineral growth, or simply allow fluid insudation leading to exposure to greater amounts of calcium and phosphorus ions [59]. Conversely, mechanical damage could result from direct fatigue effects, stress concentrations within the cusp induced by calcification or direct structural damage induced by calcification [60]. Many BHVs fail with little or no calcification [59, 58, 55]. In the study by Sacks and Schoen, it was observed that regions with disruptions in collagen fiber architecture did not necessarily correspond with regions with high calcification (Fig. 1.5) [48]. Thus, calcification independent could be equally important mechanisms for BHV failure.

Damage initially accumulates in the collagen fiber architecture (CFA) (Fig. 1.6) which in turn lead to tearing and delamination [79]. Predicting tearing and delamination (fracturing) is an extremely complex process even for solid materials without biological factors. Before tackling this, a solid groundwork for the processes that lead to this failure is needed. For BHVs this can be done by predicting the accumulation of collagen fiber damage, which leads to the development of microtears in the extracellular matrix (ECM) before propagating to full tissue-scale tearing. Thus, simulating fiber-level damage can be used to form preliminary estimation of BHV durability.

The most significant change in response to cyclic loading is the change in geometry of the BHV leaflets. In a study on the porcine aortic BHVs [62], Smith *et al.* found significant changes in the unloaded geometry of BHVs after AWT, especially in the belly region of the leaflets (Fig. 1.7A). By changing the unloaded reference configuration, the shape of the leaflets and their mechanical response will change as

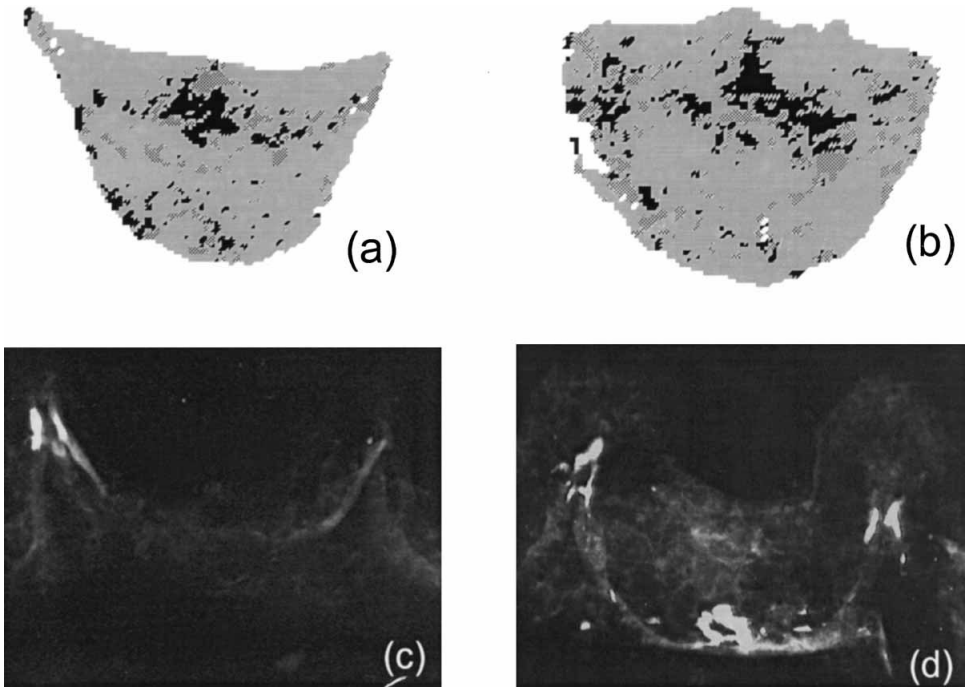

Figure 1.5: (a,b) Regions of collagen fiber damage derived from SALS data by plotting regions with large distruptions in collagen fiber structure in black. (c,d) Corresponding X-ray photos showing pronounced calcification along the commissure and basal attachment. In both cusps regions of structural damage did not spatially correlate with regions of calcification. As shown in (e), this lack of correlation was consistent in all explanted cusps. (Adapted from [48])

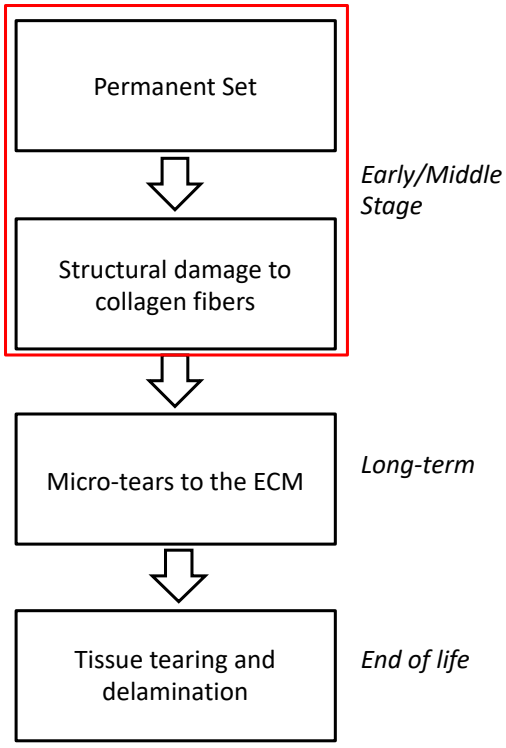

Figure 1.6: Stages of fatigue and failure. We will focus on the early and mid-term (Red).

well. The further analysis has shown that significant structural damage occurred within the belly region as compared to other regions of the leaflet, where the stress significantly increased [63]. Interestingly, Smith et al. also found most the most significant changes in BHV leaflet geometry to occur within first 50 million cycles [62]. Moreover, Sacks and Smith [51] also found that there was minimal structural damage in this early stage (Fig. 1.7B). This is further supported by another study by Wells *et al* [80], where they found minimal structural changes during the first 50 million cycles for the pressure fixed BHVs, with most significant change observed in the first million cycles. Clearly, there is a non-damage based mechanism at play that changes the geometry of the material, with significant impact on the early stage of cycling and the rate of fatigue in later stages.

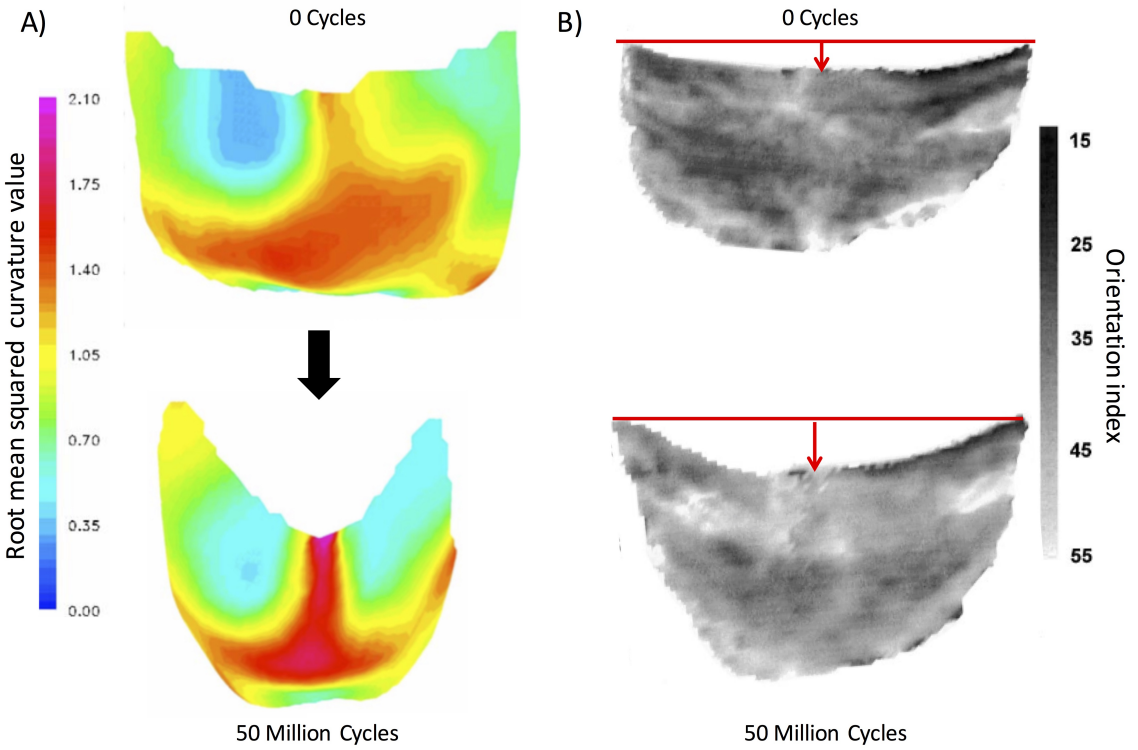

Figure 1.7: A) The 3D unloaded geometry a BHV leaflet before and after cyclic loading, with the color indicating the local root mean squared curvature. The most significant change in geometry is in the belly region. B) BHV leaflet collagen fiber architecture, showing that the collagen fiber architecture is convected by the dimensional changes. The grayscale scale bar shows the orientation index (OI), which is angle containing 50 % of fibers. The lack of changes in the OI suggests that minimal damage to the collagen fiber architecture has occurred.

1.5 Computational approach to studying bioprosthetic heart valve failure

Computational modeling is a valuable tool for studying the mechanisms underlying the heart valves functions [64]. Due to complex valve anatomy and dynamic environment, there is no in vitro system that can truly completely replicate and controllably perturb the complex in vivo environment. Computational simulations have been used for determining the stress distribution on the leaflets, correlate regions of

stress concentration with regions of leaflet calcification and/or leaflet tear in implanted valves, and guide the design of biomedical device using this information. For example, Sun et al. [67] presented a study of prosthetic valve deformation under quasi-static loading. In this study, quasi-static leaflet deformations under 40, 80, and 120 mmHg transvalvular pressures were simulated in a pericardial BHV. A Fung-elastic material model utilizing material parameters derived from actual leaflet biaxial tests and measured leaflet collagen fiber structure axes obtained from physical leaflets were used [68, 69]. However, central to any predictive simulation is a predictive and mechanism-based constitutive model. There have been no true mechanism-based models for predicting the evolution of material properties, geometry, and microstructure for soft tissue or soft tissue-derived material. Thus, the goal of this current dissertation is the constitutive modeling and simulation of evolving properties of BHVs under long-term cyclic loading, utilizing the underlying mechanisms of soft tissue biomechanics and scission-healing of glutaraldehyde to predict geometrical and mechanical properties.

1.6 Motivation, innovation, and specific aims

1.6.1 Motivation

The basis of this proposal is fulfilling the lack of knowledge on the underlying mechanism driving the fatigue and failure of BHV devices, which is the major hurdle impede the development of new BHV technologies. Traditionally, the development of BHV starts with simple mechanical characterization for their ability to handle their mechanical demands, and accelerated wear testing (AWT) at 10-15 time normal physiological rate to evaluate durability. Successful designs are then put through animal models and clinical testing. The first stage only offers a simple understanding of the functional properties and durability of these devices while the latter is a complex

and unpredictable system and the ultimate cause of failure is difficult to be understood. Thus the crux of this proposal is the lack of a more rigorous approach that better utilities in vitro experimental measurements and fundamental understanding of structure-functional relationship to predict the performance of BHVs.

1.6.2 Innovations

1.6.2.1 The Lack of Established Constitutive Models for Planar Soft Tissues

Although finite element analysis is an effective method for stress analysis, truly predictable computational simulations cannot be done without an accurate constitutive model for the underlying biomechanical response. There is currently a lack of a well established constitutive model for collagenous soft tissues. Currently, each research group uses their own model, often simple forms of the Fung model or linear functions of the invariants. These models are often not informative, offering no insights into the structural-functional relationship. Unfortunately, this also means these models also lack predictive capabilities as a result, and can only interpolate the experimental data. This is a problem for simulating the effect of fatigue in which the geometry and the mechanical properties of BHVs can change significantly, necessitating extrapolation of the data into the unmeasured regime. Structural models theories exists [50, 34, 14] but is underutilized and not well validated for the wide range of tissue that may be applicable for BHV devices. Thus, the establishment of a generalized and well-validated constitutive model is a critical step the in process of developing accurate simulations of BHV devices.

1.6.2.2 The Lack of Fundamental Modeling Approach for EXLs, PS, and Collagen Fiber-Level Damage in Soft Tissue-Derived Biomaterials

There is no accepted constitutive model for the effect of EXLs on the mechanical properties of soft tissues. Without understanding the mechanical properties of the subcomponents of the bioprosthetic biomaterial, we cannot properly predict how they will change over time. Although calcification plays an important role in the failure of BHVs, addressing this concern alone will not alleviate the loss of function due to mechanical fatigue. Although this proposal will not simulate the full process of failure, as previously indicated (1.B), we will for the first time examine the early stages of fatigue in PS and collagen fiber-level damage. This will nevertheless give us a firsthand estimate of BHV durability and design, as well as build the foundation for future extensions of the model.

1.6.2.3 The Lack of A Framework for Simulating The Response of BHV Devices in Response to Cyclic Loading

Our ability to evaluate the design of BHVs devices are directly linked to our ability to understand and rigorously experiment on the in vivo durability of these devices. However, clinical and large anime testing remains costly and reserved for later stages of the design analysis. Furthermore, it is difficult for such studies to paint a complete picture of the underlying mechanisms due bio-variability and direct ways of controlling the biological system. This has led to a stagnation of BHV device development [57]. Computational simulations can be an exceptional complement to in vitro and animal experiment in understanding how biomechanical properties evolve and drive mechanical function and performance. Indeed, the consensus in the field is the increasing role of computational simulation in the development of cardiovascular devices. Finite element analysis is unknown for its ability to determine the stress

at a device-level and can be used to reiterate on conceptual designs to optimize the functional properties of prototypes [43, 26, 9]. Thus, computational implementation of the tissue structural PS-fatigue model is the best way to guide our understanding of BHV device performance.

1.6.3 Specific aims

Soft-tissue-derived exogenously cross-linked (EXL) biomaterials continue to play an important role in surgical repair and medical devices. This is especially true for bioprosthetic heart valves (BHV), by having advantages in immunogenic and mechanical behaviors [65]. Despite ongoing research, our understanding of these materials and of the mechanisms leading to their failure remains at an empirical level. The need for advancements in predicting the material behavior is further underscored by the development of percutaneously-delivered BHV devices. While these devices reduce surgical risk, they also present additional challenges for the design of the BHVs due to limitations in thickness, and folding and compression during delivery. A significant challenge prohibiting accurate and predictive simulations of BHVs is a lack of understanding of the effect of exogenous cross-linkers, such as glutaraldehyde (GLUT), and an associated predictive material model in response to cyclic loading. GLUT EXLs form polymeric chains through the cross-linking process which more tightly bond the collagen fibers to the non-fibrous matrix, increasing the non-fibrous matrix stiffness and fiber-fiber interactions. However, GLUT EXLs also undergo Schiff-base reactions that are hypothesized to lead to scission-healing behaviors that result in the permanent set (PS) phenomena. PS continuously changes in the reference geometry of the BHV and can induce extra-physiological stress concentrations in the BHV leaflets. Microstructural-based constitutive models for tissues and their use in valve-level simulations can lead to insights into the underlying mechanisms and

more accurate prediction of their long-term performance. Thus, we seek to develop a framework for modeling and simulating biologically-derived EXL soft collagenous tissues for BHV, accounting for the effects of EXL, PS, and collagen fiber-level damage, taking the following approach:

Specific Aim 1: Establish and validate a generalized nonlinear hyperelastic meso-scale structural constitutive model (MSSCM) for native collagenous soft tissues.

As a first step towards modeling EXL biomaterials, we will take a generalized meso-scale (at the level of the constituent fibers) structural modeling approach to accurately model the mechanical response of soft tissues. Firstly, we will develop an improved analytical method for processing extant mechanical data under generalized 2D deformations, to more accurately characterize the tissue. Next, after posing the model form, we will extensively validate critical assumptions such as affine fiber deformation, the mechanical response of the constituent fibers, and direct integration of physical measurements of the fiber microstructure. The validation will be done through extensive mechanical characterization through different testing methods and microstructural characterization at the 1) micro-scale (fibril) and 2) meso-scale using optical techniques such as multiphoton microscopy and x-ray scattering. The two soft tissues we will examine for application and validation of the model are the ovine pulmonary artery and the porcine mitral valve leaflets, which offer a diverse selection of structural compositions to span applicable realms.

Specific Aim 2: Extend the MSSCM to account for of the presence of EXLs and subsequent response to continuous cyclic loading.

Using GLUT treated bovine pericardium, we aim to separately model the mechanical response of the collagen fibers, matrix, and fiber-fiber interactions due to

cross-linking. For this, we will develop a method to map the collagen fiber architecture characterized from the native state to the EXL state. Next, we will develop a PS model based on a constantly evolving referential configuration that occurs due to scission-healing when the tissue is held in an extended state. We will validate the model for orientation and strain level dependence. The model will be tested and validated using constant cyclic strain, as well as stress control experimental data. Finally, we will extend the model for collagen fiber-level damage that may occur during cyclic loading.

Specific Aim 3: Application to organ/device level.

In this final aim, we will develop a full 3D finite element framework for the simulation of permanent set utilizing an effective model approach, acting as an intermediate between the predictive constitutive model and the numerical implementation. This approach has great potential to improve the computational efficiency of numerical simulations using multi-scale or structural modeling approaches. We will parametrically explore initial geometries and material properties which may minimize the risks of these effects. With this, we aim to develop a better understanding of the underlying process that occurs during long-term cyclic loading using our constitutive modeling approach and device level applications and translate the insights gained to improving BHV design and durability.

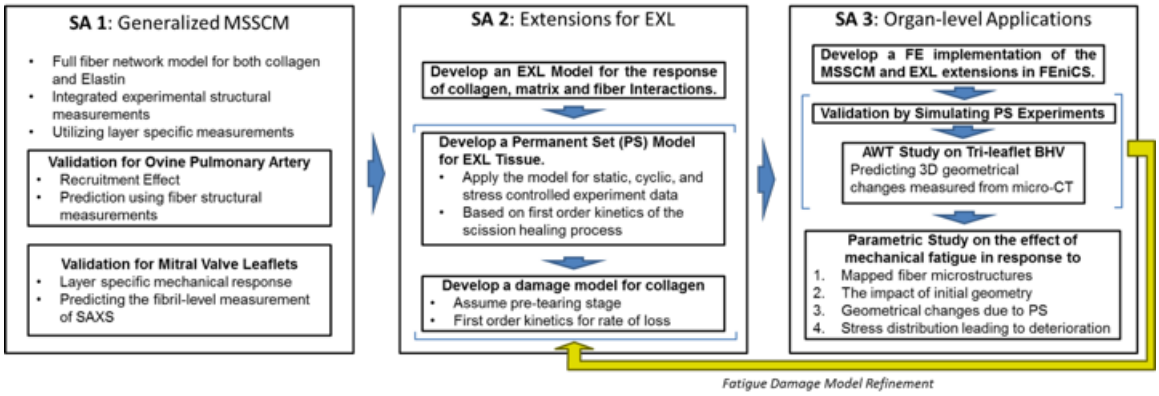

Figure 1.8: Overview of the entire project, showing how we will develop a FDM model for a BHV starting from with a generalized model of its mechanical response (SA 1) and extended for cross-linking effects including the stiffening of the matrix, increasing of collagen fiber-fiber interactions and PS (SA 2) and finally applied at the organ-level using a finite element framework (SA 3).

Chapter Bibliography

[1] Margaret M. Adamczyk and Ivan Vesely. Characteristics of compressive strains in porcine aortic valves cusps. *The Journal of heart valve disease*, 11(1):75–83, January 2002. ISSN 0966-8519. URL `http://www.ncbi.nlm.nih.gov/entrez/query.fcgi?cmd=Retrieve&db=PubMed&dopt=Citation&list_uids=11843509`.

[2] E. Aikawa and C. M. Otto. Look more closely at the valve: imaging calcific aortic valve disease. *Circulation*, 125(1):9–11, nov 2011. ISSN 0009-7322. doi: 10.1161/circulationaha.111.073452. URL `http://circ.ahajournals.org/content/125/1/9.full.pdf`.

[3] Salma Ayoub, Giovanni Ferrari, Robert C. Gorman, Joseph H. Gorman, Frederick J. Schoen, and Michael S. Sacks. *Heart Valve Biomechanics and Underlying Mechanobiology*, pages 1743–1780. American Cancer Society, 2016. ISBN

9780470650714. doi: 10.1002/cphy.c150048. URL https://onlinelibrary.wiley.com/doi/abs/10.1002/cphy.c150048.

[4] Erik Beckmann, Juan B Grau, Rachana Sainger, Paolo Poggio, and Giovanni Ferrari. Insights into the use of biomarkers in calcific aortic valve disease. *The Journal of heart valve disease*, 19(4):441–452, July 2010. ISSN 0966-8519. URL http://www.ncbi.nlm.nih.gov/pmc/articles/PMC2941903/pdf/nihms214883.pdf.

[5] J. A. Benton, H. B. Kern, L. A. Leinwand, P. D. Mariner, and K. S. Anseth. Statins block calcific nodule formation of valvular interstitial cells by inhibiting smooth muscle actin expression. *Arteriosclerosis, Thrombosis, and Vascular Biology*, 29(11):1950–1957, aug 2009. ISSN 1079-5642. doi: 10.1161/atvbaha.109.195271. URL http://atvb.ahajournals.org/content/29/11/1950.full.pdf.

[6] K. L. Billiar and M. S. Sacks. Biaxial mechanical properties of the natural and glutaraldehyde treated aortic valve cusp: part I experimental results. *Journal of Biomechanical Engineering*, 122(1):23–30, February 2000. ISSN 0148-0731 (Print) 0148-0731 (Linking). doi: 10.1115/1.429624. URL http://www.ncbi.nlm.nih.gov/pubmed/10790826.

[7] Kristen Billiar, Jim Murray, Damien Laude, Ginger Abraham, and Nathaniel Bachrach. Effects of carbodiimide crosslinking conditions on the physical properties of laminated intestinal submucosa. *Journal of Biomedical Materials Research*, 56(1):101–108, July 2001. doi: 10.1002/1097-4636(200107)56:1⟨101::aid-jbm1074⟩3.0.co;2-6. URL http://www.ncbi.nlm.nih.gov/entrez/query.fcgi?cmd=Retrieve&db=PubMed&dopt=Citation&list_uids=11309796.

[8] Kristen L. Billiar and Michael S. Sacks. Biaxial mechanical properties of the native and glutaraldehyde-treated aortic valve cusp: part II a structural constitutive model. *Journal of Biomechanical Engineering*, 122(4):327–35, August 2000. ISSN 0148-0731 (Print) 0148-0731 (Linking). doi: 10.1115/1.1287158. URL `http://www.ncbi.nlm.nih.gov/pubmed/11036555`.

[9] M.M. Black, I.C. Howard, X. Huang, and E.A. Patterson. A three-dimensional analysis of a bioprosthetic heart valve. *Journal of Biomechanics*, 24(9):793–801, jan 1991. ISSN 0021-9290 (Print) 0021-9290 (Linking). doi: 10.1016/0021-9290(91)90304-6. URL `http://www.ncbi.nlm.nih.gov/pubmed/1752863`.

[10] Robert O. Bonow, Blase A. Carabello, Kanu Chatterjee, Antonio C. de Leon, David P. Faxon, Michael D. Freed, William H. Gaasch, Bruce Whitney Lytle, Rick A. Nishimura, Patrick T. O'Gara, Robert A. O'Rourke, Catherine M. Otto, Pravin M. Shah, Jack S. Shanewise, Sidney C. Smith, Alice K. Jacobs, Cynthia D. Adams, Jeffrey L. Anderson, Elliott M. Antman, David P. Faxon, Valentin Fuster, Jonathan L. Halperin, Loren F. Hiratzka, Sharon A. Hunt, Bruce W. Lytle, Rick Nishimura, Richard L. Page, and Barbara Riegel. ACC/AHA 2006 guidelines for the management of patients with valvular heart disease. *Journal of the American College of Cardiology*, 48(3):e1–e148, aug 2006. ISSN 1558-3597 (Electronic) 0735-1097 (Linking). doi: 10.1016/j.jacc.2006.05.021. URL `http://www.ncbi.nlm.nih.gov/entrez/query.fcgi?cmd=Retrieve&db=PubMed&dopt=Citation&list_uids=16875962`.

[11] N. S. Braunwald, T. Cooper, and A. G. Morrow. Complete replacement of the mitral valve. Successful clinical application of a flexible polyurethane prosthesis. *The Journal of thoracic and cardiovascular surgery*, 40:1–11, July 1960. ISSN 0022-5223.

[12] Grant W. Christie and Brian G. Barratt-Boyes. Age-dependent changes in the radial stretch of human aortic valve leaflets determined by biaxial testing. *The Annals of Thoracic Surgery*, 60(2 Suppl):S156–S159, aug 1995. doi: 10.1016/0003-4975(95)00219-b.

[13] S. Joanna Cowell, David E. Newby, Robin J. Prescott, Peter Bloomfield, John Reid, David B. Northridge, and Nicholas A. Boon. A randomized trial of intensive lipid-lowering therapy in calcific aortic stenosis. *New England Journal of Medicine*, 352(23):2389–2397, jun 2005. ISSN 0028-4793. doi: 10.1056/nejmoa043876. URL `http://www.nejm.org/doi/pdf/10.1056/NEJMoa043876`.

[14] Niels J. B. Driessen, Carlijn V. C. Bouten, and Frank P. T. Baaijens. A structural constitutive model for collagenous cardiovascular tissues incorporating the angular fiber distribution. *Journal of Biomechanical Engineering*, 127(3):494–503, June 2005. ISSN 0148-0731 (Print). doi: 10.1115/1.1894373. URL `http://www.ncbi.nlm.nih.gov/entrez/query.fcgi?cmd=Retrieve&db=PubMed&dopt=Citation&list_uids=16060356`.

[15] R. V. Freeman. Spectrum of calcific aortic valve disease: pathogenesis, disease progression, and treatment strategies. *Circulation*, 111(24):3316–3326, jun 2005. ISSN 0009-7322. doi: 10.1161/circulationaha.104.486738. URL `http://circ.ahajournals.org/content/111/24/3316.full.pdf`.

[16] R. V. Freeman and C. M. Otto. Management of asymptomatic valvular aortic stenosis. *Indian Heart Journal*, 54(1):31–8, January 2002. ISSN 0019-4832 (Print) 0019-4832.

[17] Eileen Gentleman, Andrea N. Lay, Darryl A. Dickerson, Eric A. Nauman, Glen A. Livesay, and Kay C. Dee. Mechanical characterization of collagen

fibers and scaffolds for tissue engineering. *Biomaterials*, 24(21):3805–3813, sep 2003. ISSN 0142-9612. doi: 10.1016/s0142-9612(03)00206-0. URL http://www.sciencedirect.com/science/article/pii/S0142961203002060.

[18] S. Michael Gharacholou, Barry L. Karon, Clarence Shub, and Patricia A. Pellikka. Aortic valve sclerosis and clinical outcomes: moving toward a definition. *The American Journal of Medicine*, 124(2):103–110, feb 2011. ISSN 0002-9343. doi: 10.1016/j.amjmed.2010.10.012. URL http://www.amjmed.com/article/S0002-9343(10)00913-7/abstract.

[19] G. Golomb, F. J. Schoen, M. S. Smith, J. Linden, M. Dixon, and R. J. Levy. The role of glutaraldehyde-induced cross-links in calcification of bovine pericardium used in cardiac valve bioprostheses. *The American journal of pathology*, 127(1): 122–130, April 1987. ISSN 0002-9440. URL http://www.ncbi.nlm.nih.gov/htbin-post/Entrez/query?db=m&form=6&dopt=r&uid=0003105321.

[20] Joseph H. Gorman, Krishanu B. Gupta, James T. Streicher, Robert C. Gorman, Benjamin M. Jackson, Mark B. Ratcliffe, Daniel K. Bogen, and L.Henry Edmunds. Dynamic three-dimensional imaging of the mitral valve and left ventricle by rapid sonomicrometry array localization. *The Journal of Thoracic and Cardiovascular Surgery*, 112(3):712–724, sep 1996. doi: 10.1016/s0022-5223(96)70056-9. URL http://www.ncbi.nlm.nih.gov/entrez/query.fcgi?cmd=Retrieve&db=PubMed&dopt=Citation&list_uids=8800160.

[21] Joseph H Gorman, Benjamin M Jackson, Yoshiharu Enomoto, and Robert C Gorman. The effect of regional ischemia on mitral valve annular saddle shape. *The Annals of Thoracic Surgery*, 77(2):544–548, feb 2004. doi: 10.1016/

s0003-4975(03)01354-7. URL http://www.ncbi.nlm.nih.gov/entrez/query.fcgi?cmd=Retrieve&db=PubMed&dopt=Citation&list_uids=14759435.

[22] Juan B. Grau, Paolo Poggio, Rachana Sainger, William J. Vernick, William F. Seefried, Emanuela Branchetti, Benjamin C. Field, Joseph E. Bavaria, Michael A. Acker, and Giovanni Ferrari. Analysis of osteopontin levels for the identification of asymptomatic patients with calcific aortic valve disease. *The Annals of Thoracic Surgery*, 93(1):79–86, January 2012. ISSN 0003-4975. doi: 10.1016/j.athoracsur.2011.08.036. URL http://www.annalsthoracicsurgery.org/article/S0003-4975(11)02049-2/pdf.

[23] Robert Guidoin, Yvan Douville, Marie-Annick Clavel, Ze Zhang, Mark Nutley, Philippe Pîbarot, and Guy Dionne. The marvel of percutaneous cardiovascular devices in the elderly. *Annals of the New York Academy of Sciences*, 1197(1):188–199, June 2010. ISSN 1749-6632 (Electronic) 0077-8923 (Linking). doi: 10.1111/j.1749-6632.2010.05517.x. URL http://www.ncbi.nlm.nih.gov/entrez/query.fcgi?cmd=Retrieve&db=PubMed&dopt=Citation&list_uids=20536849.

[24] Stephen L. Hilbert, Victor J. Ferrans, and W. Milton Swanson. Optical methods for the nondestructive evaluation of collagen morphology in bioprosthetic heart valves. *Journal of Biomedical Materials Research*, 20(9):1411–1421, nov 1986. doi: 10.1002/jbm.820200914.

[25] Stephen L. Hilbert, Mary K. Barrick, and Victor J. Ferrans. Porcine aortic valve bioprostheses: a morphologic comparison of the effects of fixation pressure. *Journal of Biomedical Materials Research*, 24(6):773–787, jun 1990. doi: 10.1002/jbm.820240611.

[26] X. Huang, M. M. Black, I. C. Howard, and E. A. Patterson. A two-dimensional finite element analysis of a bioprosthetic heart valve. *Journal of Biomechanics*, 23(8):753–762, jan 1990. ISSN 0021-9290 (Print) 0021-9290 (Linking). doi: 10.1016/0021-9290(90)90022-u. URL `http://www.ncbi.nlm.nih.gov/pubmed/2384487`.

[27] W. R. Eric Jamieson, Hilton Ling, Lawrence H Burr, Guy J Fradet, Robert T Miyagishima, Michael T Janusz, and Samuel V. Lichtenstein. Carpentier-Edwards supraannular porcine bioprosthesis evaluation over 15 years. *The Annals of Thoracic Surgery*, 66(6):S49–S52, dec 1998. doi: 10.1016/s0003-4975(98)01127-8.

[28] A. Jayakrishnan and S. R. Jameela. Glutaraldehyde as a fixative in bioprostheses and drug delivery matrices. *Biomaterials*, 17(5):471–484, jan 1996. doi: 10.1016/0142-9612(96)82721-9.

[29] Erinn M. Joyce, Jun Liao, Frederick J. Schoen, John E. Mayer, and Michael S. Sacks. Functional collagen fiber architecture of the pulmonary heart valve cusp. *The Annals of Thoracic Surgery*, 87(4):1240–1249, April 2009. ISSN 1552-6259 (Electronic). doi: 10.1016/j.athoracsur.2008.12.049. URL `http://www.ncbi.nlm.nih.gov/entrez/query.fcgi?cmd=Retrieve&db=PubMed&dopt=Citation&list_uids=19324159`.

[30] Paul D. Kemp, John F. Cavallaro, and Deborah N. Hastings. Effects of carbodiimide crosslinking and load environment on teh remodeling of collagen scaffolds. *Tissue Engineering*, 1(1):71–79, mar 1995. doi: 10.1089/ten.1995.1.71.

[31] Eugene Khor. Methods for the treatment of collagenous tissues for bioprostheses. *Biomaterials*, 18(2):95–105, January 1997. doi: 10.1016/

s0142-9612(96)00106-8. URL http://www.ncbi.nlm.nih.gov/entrez/query.fcgi?cmd=Retrieve&db=PubMed&dopt=Citation&list_uids=9022956.

[32] Susheel K. Kodali, Mathew R. Williams, Craig R. Smith, Lars G. Svensson, John G. Webb, Raj R. Makkar, Gregory P. Fontana, Todd M. Dewey, Vinod H. Thourani, Augusto D. Pichard, Michael Fischbein, Wilson Y. Szeto, Scott Lim, Kevin L. Greason, Paul S. Teirstein, S. Chris Malaisrie, Pamela S. Douglas, Rebecca T. Hahn, Brian Whisenant, Alan Zajarias, Duolao Wang, Jodi J. Akin, William N. Anderson, and Martin B. Leon. Two-year outcomes after transcatheter or surgical aortic-valve replacement. *New England Journal of Medicine*, 366(18):1686–1695, may 2012. doi: 10.1056/nejmoa1200384. URL http://www.nejm.org/doi/full/10.1056/NEJMoa1200384.

[33] Christopher E. Kurtz and Catherine M. Otto. Aortic stenosis: clinical aspects of diagnosis and management, with 10 illustrative case reports from a 25-year experience. *Medicine*, 89(6):349–379, November 2010. ISSN 0025-7974. doi: 10.1097/md.0b013e3181fe5648.

[34] Y. Lanir. A structural theory for the homogeneous biaxial stress-strain relationships in flat collagenous tissues. *Journal of Biomechanics*, 12(6):423–436, jan 1979. doi: 10.1016/0021-9290(79)90027-7.

[35] Raj R. Makkar, Gregory P. Fontana, Hasan Jilaihawi, Samir Kapadia, Augusto D. Pichard, Pamela S. Douglas, Vinod H. Thourani, Vasilis C. Babaliaros, John G. Webb, Howard C. Herrmann, Joseph E. Bavaria, Susheel Kodali, David L. Brown, Bruce Bowers, Todd M. Dewey, Lars G. Svensson, Murat Tuzcu, Jeffrey W. Moses, Matthew R. Williams, Robert J. Siegel,

Jodi J. Akin, William N. Anderson, Stuart Pocock, Craig R. Smith, and Martin B. Leon. Transcatheter aortic-valve replacement for inoperable severe aortic stenosis. *New England Journal of Medicine*, 366(18):1696–1704, may 2012. doi: 10.1056/nejmoa1202277. URL http://www.nejm.org/doi/full/10.1056/NEJMoa1202277.

[36] Rizwan A Manji, Alan H Menkis, Burcin Ekser, and David KC Cooper. The future of bioprosthetic heart valves. *The Indian journal of medical research*, 135 (2):150, 2012. ISSN 0971-5916.

[37] W. David Merryman, Inchan Youn, Howard D. Lukoff, Paula M. Krueger, Farshid Guilak, Richard A. Hopkins, and Michael S. Sacks. Correlation between heart valve interstitial cell stiffness and transvalvular pressure: implications for collagen biosynthesis. *American Journal of Physiology-Heart and Circulatory Physiology*, 290(1):H224–H231, January 2006. doi: 10.1152/ajpheart.00521.2005. URL http://www.ncbi.nlm.nih.gov/entrez/query.fcgi?cmd=Retrieve&db=PubMed&dopt=Citation&list_uids=16126816.

[38] Luis M. Moura, Sandra F. Ramos, José L. Zamorano, Isabel M. Barros, Luis F. Azevedo, Francisco Rocha-Gonçalves, and Nalini M. Rajamannan. Rosuvastatin affecting aortic valve endothelium to slow the progression of aortic stenosis. *Journal of the American College of Cardiology*, 49(5):554–561, February 2007. ISSN 0735-1097. doi: 10.1016/j.jacc.2006.07.072. URL http://ac.els-cdn.com/S0735109706028579/1-s2.0-S0735109706028579-main.pdf?_tid=05961d66-3e08-11e4-b55e-00000aab0f26&acdnat=1410916670_d5494ce195923cac55e850293f0e130a.

[39] Dariush Mozaffarian, Emelia J. Benjamin, Alan S. Go, Donna K. Arnett,

Michael J. Blaha, Mary Cushman, Sandeep R. Das, Sarah de Ferranti, Jean-Pierre Després, Heather J. Fullerton, Virginia J. Howard, Mark D. Huffman, Carmen R. Isasi, Monik C. Jiménez, Suzanne E. Judd, Brett M. Kissela, Judith H. Lichtman, Lynda D. Lisabeth, Simin Liu, Rachel H. Mackey, David J. Magid, Darren K. McGuire, Emile R. Mohler, Claudia S. Moy, Paul Muntner, Michael E. Mussolino, Khurram Nasir, Robert W. Neumar, Graham Nichol, Latha Palaniappan, Dilip K. Pandey, Mathew J. Reeves, Carlos J. Rodriguez, Wayne Rosamond, Paul D. Sorlie, Joel Stein, Amytis Towfighi, Tanya N. Turan, Salim S. Virani, Daniel Woo, Robert W. Yeh, and Melanie B. Turner. Heart disease and stroke statistics-2016 update: a report from the american heart association. *Circulation*, 133(4):e38–e360, dec 2015. ISSN 1524-4539 (Electronic) 0009-7322 (Linking). doi: 10.1161/cir.0000000000000350. URL `http://www.ncbi.nlm.nih.gov/pubmed/26673558`.

[40] K. D. O'Brien. Pathogenesis of calcific aortic valve disease: a disease process comes of age (and a good deal more). *Arteriosclerosis, Thrombosis, and Vascular Biology*, 26(8):1721–1728, aug 2006. doi: 10.1161/01.atv.0000227513.13697.ac.

[41] Catherine M. Otto. Calcific aortic valve disease: new concepts. *Seminars in Thoracic and Cardiovascular Surgery*, 22(4):276–284, dec 2010. ISSN 1043-0679. doi: 10.1053/j.semtcvs.2011.01.009.

[42] A. Parolari, E. Tremoli, L. Cavallotti, M. Trezzi, S. Kassem, C. Loardi, F. Veglia, G. Ferrari, D. Pacini, and F. Alamanni. Do statins improve outcomes and delay the progression of non-rheumatic calcific aortic stenosis? *Heart*, 97(7):523–529, jan 2011. ISSN 1355-6037. doi: 10.1136/hrt.2010.215046. URL `http://heart.bmj.com/content/97/7/523.full.pdf`.

[43] E. A. Patterson, I. C. Howard, and M. A. Thornton. A comparative study of linear and nonlinear simulations of the leaflets in a bioprosthetic heart valve during the cardiac cycle. *Journal of Medical Engineering & Technology*, 20(3):95–108, jan 1996. doi: 10.3109/03091909609008387. URL http://www.ncbi.nlm.nih.gov/htbin-post/Entrez/query?db=m&form=6&dopt=r&uid=0008877750.

[44] Tobias Pflederer and Stephan Achenbach. Aortic valve stenosis: CT contributions to diagnosis and therapy. *Journal of Cardiovascular Computed Tomography*, 4(6):355–364, November 2010. ISSN 1876-861x. doi: 10.1016/j.jcct.2010.09.008. URL http://www.journalofcardiovasculartct.com/article/S1934-5925(10)00542-3/abstract.

[45] Paolo Poggio, Rachana Sainger, Emanuela Branchetti, Juan B. Grau, Eric K. Lai, Robert C. Gorman, Michael S. Sacks, Alessandro Parolari, Joseph E. Bavaria, and Giovanni Ferrari. Noggin attenuates the osteogenic activation of human valve interstitial cells in aortic valve sclerosis. *Cardiovascular Research*, 98(3):402–410, mar 2013. ISSN 1755-3245 (Electronic) 0008-6363 (Linking). doi: 10.1093/cvr/cvt055. URL http://www.ncbi.nlm.nih.gov/pubmed/23483047.

[46] DonaldN. Ross. Replacement of aortic and mitral valves with a pulmonary autograft. *The Lancet*, 290(7523):956–958, November 1967. doi: 10.1016/s0140-6736(67)90794-5. URL http://www.ncbi.nlm.nih.gov/entrez/query.fcgi?cmd=Retrieve&db=PubMed&dopt=Citation&list_uids=4167516.

[47] Anne B. Rossebø, Terje R. Pedersen, Kurt Boman, Philippe Brudi, John B. Chambers, Kenneth Egstrup, Eva Gerdts, Christa Gohlke-Bärwolf, Ingar Holme, Y. Antero Kesäniemi, William Malbecq, Christoph A. Nienaber, Simon Ray, Terje Skjærpe, Kristian Wachtell, and Ronnie Willenheimer. Intensive lipid

lowering with simvastatin and ezetimibe in aortic stenosis. *New England Journal of Medicine*, 359(13):1343–1356, September 2008. ISSN 0028-4793. doi: 10.1056/nejmoa0804602. URL http://www.nejm.org/doi/pdf/10.1056/NEJMoa0804602.

[48] M. S. Sacks and F. J. Schoen. Collagen fiber disruption occurs independent of calcification in clinically explanted bioprosthetic heart valves. *J Biomed Mater Res*, 62(3):359–71, December 2002. doi: 10.1002/jbm.10293. URL http://www.ncbi.nlm.nih.gov/entrez/query.fcgi?cmd=Retrieve&db=PubMed&dopt=Citation&list_uids=12209921.

[49] M. S. Sacks, Z. He, L. Baijens, S. Wanant, P. Shah, H. Sugimoto, and A. P. Yoganathan. Surface strains in the anterior leaflet of the functioning mitral valve. *Annals of Biomedical Engineering*, 30(10):1281–1290, November 2002. doi: 10.1114/1.1529194. URL http://www.ncbi.nlm.nih.gov/entrez/query.fcgi?cmd=Retrieve&db=PubMed&dopt=Citation&list_uids=12540204.

[50] Michael S. Sacks. Incorporation of experimentally-derived fiber orientation into a structural constitutive model for planar collagenous tissues. *Journal of Biomechanical Engineering*, 125(2):280–7, April 2003. doi: 10.1115/1.1544508. URL http://www.ncbi.nlm.nih.gov/entrez/query.fcgi?cmd=Retrieve&db=PubMed&dopt=Citation&list_uids=12751291.

[51] Michael S. Sacks and David B. Smith. Effects of accelerated testing on porcine bioprosthetic heart valve fiber architecture. *Biomaterials*, 19(11-12):1027–1036, jun 1998. doi: 10.1016/s0142-9612(98)00002-7.

[52] Michael S. Sacks, David B. Smith, and Erik D. Hiester. A small angle light scattering device for planar connective tissue microstructural analysis. *Annals*

of Biomedical Engineering, 25(4):678–689, jul 1997. ISSN 1573-9686. doi: 10.1007/bf02684845. URL https://doi.org/10.1007/BF02684845.

[53] Michael S. Sacks, David B. Smith, and Erik D. Hiester. The aortic valve microstructure: effects of transvalvular pressure. *Journal of Biomedical Materials Research*, 41(1):131–141, jul 1998. doi: 10.1002/(sici)1097-4636(199807)41:1⟨131::aid-jbm16⟩3.0.co;2-q.

[54] Michael S. Sacks, W. David Merryman, and David E. Schmidt. On the biomechanics of heart valve function. *Journal of Biomechanics*, 42(12):1804–1824, aug 2009. ISSN 1873-2380 (Electronic). doi: 10.1016/j.jbiomech.2009.05.015. URL http://www.ncbi.nlm.nih.gov/entrez/query.fcgi?cmd=Retrieve&db=PubMed&dopt=Citation&list_uids=19540499.

[55] F. J. Schoen. Pathology of heart valve substitution with mechanical and tissue prostheses. In M.D. Silver, A.I. Gotlieb, and F. J. Schoen, editors, *Cardiovascular Pathology*, volume 3. Livingstone, New York, 2001.

[56] F. J. Schoen. Valvular heart disease: changing concepts in disease management. *Circulation*, 118(18):1864–1880, oct 2008. doi: 10.1161/circulationaha.108.805911.

[57] Frederick J. Schoen. Cardiac valves and valvular pathology: update on function, disease, repair, and replacement. *Cardiovascular Pathology*, 14(4):189–194, July 2005. ISSN 1054-8807 (Print). doi: 10.1016/j.carpath.2005.03.005. URL http://www.ncbi.nlm.nih.gov/entrez/query.fcgi?cmd=Retrieve&db=PubMed&dopt=Citation&list_uids=16009317.

[58] Frederick J. Schoen and Charles E. Hobson. Anatomic analysis of removed prosthetic heart valves: causes of failure of 33 mechanical valves and 58 bioprostheses, 1980 to 1983. *Human Pathology*, 16(6):549–559, jun 1985. doi: 10.1016/s0046-8177(85)80103-9.

[59] Frederick J. Schoen and Robert J. Levy. Tissue heart valves: current challenges and future research perspectives. *Journal of Biomedical Materials Research*, 47(4):439–465, dec 1999. doi: 10.1002/(sici)1097-4636(19991215)47:4⟨439::aid-jbm1⟩3.0.co;2-o.

[60] Frederick J. Schoen and Robert J. Levy. Calcification of tissue heart valve substitutes: progress toward understanding and prevention. *The Annals of Thoracic Surgery*, 79(3):1072–1080, March 2005. doi: 10.1016/j.athoracsur.2004.06.033. URL `http://www.ncbi.nlm.nih.gov/entrez/query.fcgi?cmd=Retrieve&db=PubMed&dopt=Citation&list_uids=15734452`.

[61] Raheela Fareed Siddiqui, Johnathan Rajiv Abraham, and Jagdish Butany. Bioprosthetic heart valves: modes of failure. *Histopathology*, 55(2):135–144, aug 2009. doi: 10.1111/j.1365-2559.2008.03190.x.

[62] D. B. Smith, M. S. Sacks, P. M. Pattany, and R. Schroeder. High-resolution magnetic resonance imaging to characterize the geometry of fatigued porcine bioprosthetic heart valves. *The Journal of heart valve disease*, 6(4):424–432, July 1997. ISSN 0966-8519.

[63] D. B. Smith, M. S. Sacks, P. M. Pattany, and R. Schroeder. Fatigue-induced changes in bioprosthetic heart valve three-dimensional geometry and the relation to tissue damage. *The Journal of heart valve disease*, 8(1):25–33, January 1999. ISSN 0966-8519.

[64] Joao S. Soares, Kristen R. Feaver, Will Zhang, David Kamensky, Ankush Aggarwal, and Michael S. Sacks. Biomechanical behavior of bioprosthetic heart valve heterograft tissues: characterization, simulation, and performance. *Cardiovascular Engineering and Technology*, 7(4):309–351, aug 2016. ISSN 1869-4098. doi: 10.1007/s13239-016-0276-8. URL `http://dx.doi.org/10.1007/s13239-016-0276-8`.

[65] Albert Starr. The artificial heart valve. *Nature Medicine*, 13(10):1160–1164, oct 2007. doi: 10.1038/nm1644.

[66] John A. Stella and Michael S. Sacks. On the biaxial mechanical properties of the layers of the aortic valve leaflet. *Journal of Biomechanical Engineering*, 129(5):757–66, 2007. ISSN 0148-0731 (Print) 0148-0731 (Linking). doi: 10.1115/1.2768111. URL `http://www.ncbi.nlm.nih.gov/entrez/query.fcgi?cmd=Retrieve&db=PubMed&dopt=Citation&list_uids=17887902`.

[67] W. Sun, A. Abad, and M.S. Sacks. Simulated bioprosthetic heart valve deformation under quasi-static loading. *Journal of Biomechanical Engineering*, 127(6): 905–914, jul 2005. doi: 10.1115/1.2049337.

[68] Wei Sun and Michael S. Sacks. Finite element implementation of a generalized Fung-elastic constitutive model for planar soft tissues. *Biomechanics and Modeling in Mechanobiology*, 4(2-3):190–199, August 2005. doi: 10.1007/s10237-005-0075-x. URL `http://www.ncbi.nlm.nih.gov/entrez/query.fcgi?cmd=Retrieve&db=PubMed&dopt=Citation&list_uids=16075264`.

[69] Wei Sun, Michael S. Sacks, and Michael J. Scott. Effects of boundry conditions on the estimation of the planar biaxial mechanical properties of soft tissues. *Journal*

of Biomechanical Engineering, 127(4):709–715, August 2005. ISSN 0148-0731. doi: 10.1115/1.1933931. URL ://WOS:000231034400019.

[70] Hsing-Wen Sung, Wen-Hisang Chang, Chiun-Yuang Ma, and Meng-Horng Lee. Crosslinking of biological tissues using genipin and/or carbodiimide. *Journal of Biomedical Materials Research*, 64A(3):427–438, feb 2003. doi: 10.1002/jbm.a.10346.

[71] Hobey Tam, Will Zhang, Kristen R. Feaver, Nathaniel Parchment, Michael S. Sacks, and Naren Vyavahare. A novel crosslinking method for improved tear resistance and biocompatibility of tissue based biomaterials. *Biomaterials*, 66:83–91, October 2015. ISSN 1878-5905 (Electronic) 0142-9612 (Linking). doi: 10.1016/j.biomaterials.2015.07.011. URL http://www.ncbi.nlm.nih.gov/pubmed/26196535.

[72] Ge Tao, James D. Kotick, and Joy Lincoln. Heart valve development, maintenance, and disease. In *Current Topics in Developmental Biology*, pages 203–232. Elsevier, 2012. doi: 10.1016/b978-0-12-387786-4.00006-3.

[73] M Thubrikar. *The aortic valve*. CRC, Boca Raton, 1990.

[74] D. A. Towler. Molecular and cellular aspects of calcific aortic valve disease. *Circulation Research*, 113(2):198–208, July 2013. ISSN 0009-7330. doi: 10.1161/circresaha.113.300155. URL http://circres.ahajournals.org/content/113/2/198.full.pdf.

[75] I. Vesely and W. J. Mako. Comparison of the compressive buckling of porcine aortic valve cusps and bovine pericardium. *The Journal of heart valve disease*, 7(1):34–39, January 1998. ISSN 0966-8519. URL

http://www.ncbi.nlm.nih.gov/entrez/query.fcgi?cmd=Retrieve&db=PubMed&dopt=Citation&list_uids=9502137.

[76] Ivan Vesely. The role of elastin in aortic valve mechanics. *Journal of Biomechanics*, 31(2):115–123, may 1997. doi: 10.1016/s0021-9290(97)00122-x.

[77] Ivan Vesely and Ronald Noseworthy. Micromechanics of the fibrosa and the ventricularis in aortic valve leaflets. *Journal of Biomechanics*, 25(1):101–113, jan 1992. doi: 10.1016/0021-9290(92)90249-z.

[78] N. Vyavahare, D. Hirsch, E. Lerner, J. Z. Baskin, F. J. Schoen, R. Bianco, H. S. Kruth, R. Zand, and R. J. Levy. Prevention of bioprosthetic heart valve calcification by ethanol preincubation. Efficacy and mechanisms. *Circulation*, 95(2): 479–488, jan 1997. doi: 10.1161/01.cir.95.2.479. URL http://www.ncbi.nlm.nih.gov/htbin-post/Entrez/query?db=m&form=6&dopt=r&uid=0009008467.

[79] Narendra Vyavahare, Matthew Ogle, Frederick J. Schoen, Robert Zand, D. Claire Gloeckner, Michael Sacks, and Robert J. Levy. Mechanisms of bioprosthetic heart valve failure: fatigue causes collagen denaturation and glycosaminoglycan loss. *Journal of Biomedical Materials Research*, 46(1):44–50, July 1999. ISSN 0021-9304 (Print) 0021-9304 (Linking). doi: 10.1002/(sici)1097-4636(199907)46:1⟨44::aid-jbm5⟩3.0.co;2-d. URL http://www.ncbi.nlm.nih.gov/pubmed/10357134.

[80] Sarah M. Wells, Tiffany Sellaro, and Michael S. Sacks. Cyclic loading response of bioprosthetic heart valves: effects of fixation stress state on the collagen fiber architecture. *Biomaterials*, 26(15):2611–2619, May 2005. doi: 10.1016/j.biomaterials.2004.06.046. URL http://www.ncbi.nlm.nih.gov/entrez/query.fcgi?cmd=Retrieve&db=PubMed&dopt=Citation&list_uids=15585264.

[81] Lanti Yang, Kees O. van der Werf, Bart F.J.M. Koopman, Vinod Subramaniam, Martin L. Bennink, Pieter J. Dijkstra, and Jan Feijen. Micromechanical bending of single collagen fibrils using atomic force microscopy. *Journal of Biomedical Materials Research Part A*, 82A(1):160–168, 2007. ISSN 1552-4965. doi: 10.1002/jbm.a.31127. URL `http://dx.doi.org/10.1002/jbm.a.31127http://onlinelibrary.wiley.com/doi/10.1002/jbm.a.31127/abstract`.

[82] Lanti Yang, Carel F.C. Fitié, Kees O. van der Werf, Martin L. Bennink, Pieter J. Dijkstra, and Jan Feijen. Mechanical properties of single electrospun collagen type i fibers. *Biomaterials*, 29(8):955–962, mar 2008. doi: 10.1016/j.biomaterials.2007.10.058.

Chapter 2

Structural constitutive models for planar collagenous soft tissues[1]

Preface

Fundamental to developing a deeper understanding of soft tissue function and pathology is the development of an accurate tissue-level constitutive model. In the present work, we developed a novel meso-scale (i.e. at the level of the fiber, 10-100 μm in length scale) structural constitutive model (MSSCM) with application to MV leaflet. This model takes into account the layered structure of these tissues and the contributions from the distinct collagen and elastin fiber networks within each tissue layer. The requisite collagen and elastin fibrous structural information for each layer was quantified using second harmonic generation microscopy and conventional histology. A comprehensive mechanical data set was also used to guide the model formulation and parameter estimation. Furthermore, novel to tissue-level structural constitutive modeling approaches, we allowed the collagen fiber recruitment function to vary with orientation. Finally, a novel fibril-level (0.1 to 1 μm) validation approach was used to compare the predicted collagen fiber/fibril mechanical behavior with extant MV small angle X-ray scattering data. Results demonstrated excellent

[1]**The work contained in this chapter was published as**:
Zhang, W.; Ayoub, S.; Liao, J. & Sacks, M. S. A meso-scale layer-specific structural constitutive model of the mitral heart valve leaflets Acta Biomater, 2016, 32, 238-55
The author contributed to: performing the research, model development, data analysis, coding development, and writing the corresponding manuscript.

agreement, indicating that the MSSCM fully captures the tissue-level function. Future utilization of the MSSCM in computational models of the MV will aid in producing highly accurate simulations in non-physiological loading states that can occur in repair situations, as well as guide the form of simplified models for real-time simulation tools.

2.1 Introduction

The mitral valve (MV) is the most structurally complex and physically demanded valve within the heart. It is one of the most suitable choices for the development and validation of a generalized meso-scale structural constitutive model (MSSCM). According to the American Heart Association in 2013, it is estimated that MV disease is present in over 4 million adults [21]. MV regurgitation is the most common pathology resulting from myocardial infarction (ischemic mitral regurgitation or IMR). The most frequent corrective approach used to restore leaflet function is MV annuloplasty [31, 1], wherein an annuloplasty ring is used to induce MV leaflet closure during systole. However, such procedures alter the distribution of stress within the leaflet [1, 56, 45, 30, 47, 53, 12, 49], which may influence the long-term durability of the repair procedure. Long-term studies suggest that 60% of patients who underwent MV repair show recurrence of MV regurgitation within 3–5 years, and 10–15% of patients require re-operation within the following 10 years [17, 18]. The need for computational models based on the understanding of the underlying mechanobiological processes is self-evident for predicting the outcome of surgically repaired MVs and driving the development of improved patient-specific surgical techniques.

While MV leaflets may first appear essentially to be membranous flaps, they are in actuality complex multilayered structures that undergo large anisotropic deformations in vivo [53]. Specifically, there are four morphologically distinct layers of the MV: the ventricularis, fibrosa, spongiosa, and atrialis [6]. All layers are composed of various amounts of dense networks of collagen (mostly type I) and elastin fibers, as well as non-fibrous proteoglycans (PG) and glycosaminoglycans (GAG). In a recent study [38], we demonstrated that the layer-specific deformations of the MV interstitial cells (MVIC) are a direct result of the layer-specific architectures. This suggests

that layer-specific adaptations are possible, as observed in Wells et al.[64]. Yet, it remains unclear as to (1) why the MV has this distinct pattern of layers, (2) what the respective mechanical roles of each layer are, and (3) how do these patterns relate to the bulk macro-scale responses.

The underlying layer-specific differences in mechanical properties are a result of the constituent fiber populations. Type I collagen is the most abundant protein found in MV tissue, and it is the major determinant of its mechanical behavior [48, 19]. The functional subunit of collagen is the collagen fibril, which composed of tropocollagen molecules that arrange themselves into a quarter stacking array [48, 19]. It is this structure that allows small angle X-ray scattering (SAXS) studies to measure the underlying fibril deformations for tendon [57, 58] and MV leaflet tissues [42]. At the next structural level, the collagen fibrils group to form collagen fibers. There is an incomplete understanding regarding the functional relationship between collagen fibers and the fibrils. In fact, the exact definition of collagen fibers in relation to fibrils is usually tissue-specific. Like the fibrils from which their functional properties are derived, collagen fibers exhibit tensile strength of up to 1 GPa [60, 20, 14, 67, 54] with low flexural stiffness [54]. As a result, collagen fibers typically extend by no more than a 4–5%. To increase the tissue-level compliance, collagen fibers at the macroscopic scale become sinusoidally crimped [48] and does not contribute mechanically until fully straightened. Moreover, the distribution of collagen fiber-level straightening strains is the mechanism for tissue-level non-linearity [35, 51].

In contrast to collagen, elastin forms complex cross-linked fibrous networks with comparatively low modulus that are thought to assist in tissue recoil [10, 11] and maintaining collagen fiber crimp [63, 59]. Unlike large arteries, elastin is present in much lower quantities in valvular tissues compared to collagen [54, 63, 43, 61] and

its role in valve mechanics is not well understood. Finally, we note that glycosaminoglycans (GAGs) are known to affect water retention and hysteresis in valvular tissues [44, 13], with the loss of GAGs known to reduce the cuspal thickness and diminish rehydration capacity. However, GAGs are not a primary load bearing component, but appear act as a dampening mechanism to smooth rapid bending motions of the leaflet during valve function [13].

Thus, a more complete understanding of MV function and failure must involve an improved understanding of how the above MV leaflet structures mechanically interact. This is best done through the mathematical development of constitutive models that incorporate these features, which can aid both in providing insight and in forming a predictive modeling framework for their remodeling and failure. In the present, work we developed a novel comprehensive meso-scale (i.e. at the level of the fiber) structural constitutive model (MSSCM) for MV leaflets, focusing on the specific collagen and elastin fiber networks within each of its four distinct layers. We used a comprehensive set of structural and mechanical studies (Table 2.1) and a rigorous experimentally guided approach to tackle model formulation, parameter optimization and model validation (Fig. 2.1). The results were then validated at both the micro (fibril) and tissue-level using a novel approach based on a previous SAXS study on the mitral valve [42], and again at the meso-scale using measured fiber structures. We also explored a novel extension to previous structural constitutive model approaches [28, 8, 16, 50] to allow for angular dependency of collagen fiber recruitment (orientation-variant) and assessed the model predictive capabilities under extra physiological loading that could occur in post-surgical scenarios.

Table 2.1: Experimental Techniques and Deliverables

	Study	**Description**	**Purpose**	**Description**
Structure	SHG	Image of fluorescently labeled collagen and elastin	Image processing is done to quantify the fiber orientation distribution function of collagen and elastin within each layer.	ODF (used for validation)
	Histology	Collagen, elastin, and Proteoglycans are stained in a transmural slice.	The image is separated into channels and is used to quantify the mass fractions and relative fraction of collagen and elastin of each layer. This is used directly in the model.	Mass fractions
Mechanical	SAXS	X-ray scattering at a length comparable to D-period of the fiber	The SAXS scatter pattern have periods related to the D-period of the collagen fibers. The D-period can be used to quantify the fiber-level strain and the fiber stiffness	Collagen Fiber Modulus, (for validation)
	Planar Biax (EB)	Biax with equal strain along both axes	Under equibiaxial strain, we can recover the ensemble stress from the sum of the axial stresses. This allows us to model the ensemble stress directly to determine the fiber modulus and fiber recruitment.	Collagen Fiber Modulus, Recruitment Parameters (For validation)
	Uniaxial	Tissue is deformed along the preferred direction of the fibers	With the tight splay, under uniaxial extension all fibers become nearly aligned to the test axis, allowing us to use a simplified model rather like using the ensemble stress to recover the fiber modulus and recruitment.	
	Planar Biax (Multi-prot)	Data is taken over the physiological and extra-physiological range.	This with us the data to performed parameter estimation to determine the properties of the MV. The outer extra-physiological protocols can be used to check the predictive ability of the model.	Layer dependent material properties.

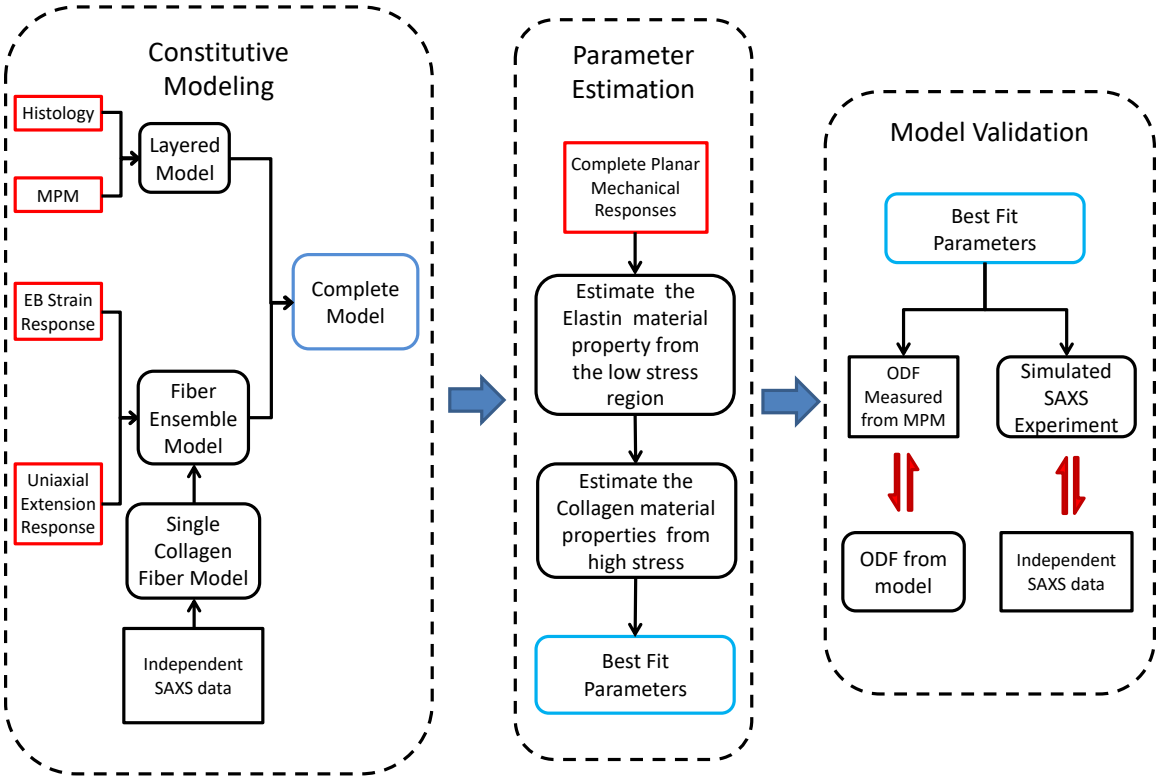

Figure 2.1: Our modeling approach can be divided into 3 parts: (1) constitutive modeling, where we use both structural and mechanical data to guide model formulation. (2) Parameter estimation, where we used a detailed sequential approach to narrow down the optimal parameters. (3) Model validation, where we used SAXS and MPM to validate the model at both the micro- and meso-scale.

2.2 Methods

2.2.1 General consideration and assumptions

2.2.1.1 Collagen fibrils and fibers

In the present work, we assumed that the collagen fibrils were contiguous subunits of the collagen fibers so that there was negligible slippage between fibrils. To characterize the straightening behavior of the fiber-level crimped structure [35, 16, 50, 34, 32, 25, 5, 24], we use only the fiber axial stretch needed to fully straighten the fiber, slack stretch, rather than the period and amplitude of the collagen fibers. This avoids the necessity of incorporating detailed unloaded geometry for the collagen fibers.

In most structural models, the distribution of collagen slack strains (the recruitment distribution) is assumed to be independent of the orientation. This approach has the advantage of allowing collagen fiber recruitment model parameters to be determined directly from a single planar equibiaxial strain (EB) tests, where the deformation gradient tensor is $F = \mathrm{diag}[\lambda, \lambda, 1/\lambda^2]$ and no fiber rotations occur (e.g. [16]). For bovine pericardium, we have shown that when the collagen fiber orientation distribution function (ODF) is obtained independently, the complete in-plane response can be predicted [50]. However, some angular dependence may be physiologically relevant for general tissues. For example, collagen fibers are constantly produced and degraded under physiological stresses and prefer to function within homeostatic stress levels [29]. Moreover, MV leaflets experience large and highly anisotropic deformations in vivo, which would induce substantially higher fiber ensemble stresses in the larger strain direction [1, 53]. We thus speculate that collagen fibers may exhibit larger undulations in the directions of larger physiological strain to maintain a constant fiber ensemble stress. However, the exact dependence of collagen

recruitment on fiber orientation remains unknown and has yet to be explored in the literature.

For the collagen fiber material model, a stress-strain relation that is linear in 2nd Piola Kirchhoff stress and Green Lagrange strain is the predominant fiber model of choice [50, 34, 15]. However, SAXS studies of intact tissue shows that the fibril strain varies linearly with applied forces in tendon [57, 58] and MV leaflet tissues [42]. Furthermore, the results are corroborated by the atomistic modeling results by Buehler [4], where the force-displacement relation is essentially linear at strains lower than 0.35.

2.2.1.2 Elastin fiber network

Elastin fibers function through an entropy-driven process wherein the decrease in entropy drives the increase in fiber stress as the fiber is elongated. As of yet, there is no first-principle form for elastin when modeled either as a continuous phase or a discrete fibrous network. Typical MV models are either purely phenomenological or ignore the elastin component entirely. In a previous study on ovine pulmonary artery [16], we found the elastin fibers to behave linearly in second Piola–Kirchhoff stress and Green Lagrange strain. However, the specific form of the elastin likely depends on a variety of factors including cross-linking and residual strain. Moreover, it is not clear if there are layer-specific differences, and thus a more general material model for the MV elastin fiber network is needed.

2.2.1.3 Affine kinematics and layer averaged responses

As in previous structural approaches, we assume affine fiber kinematics. This assumption is supported by a recent study wherein we demonstrated that the MV an-

terior leaflet collagen and elastin fibers all deformed in a manner consistent with affine deformation kinematics [40]. We further assume each layer is structurally homogeneous (i.e. ignore intra-layer structural variations). Thus, and in order to derive the total individual layer response as a function of its collagen and elastin components, the following information was used (Table 2.1):

1. The mass composition of each layer, including the quantities of collagen and elastin.

2. The ODF for the collagen and elastin fibers within each layer.

3. The recruitment behaviors of the collagen fiber network for each layer.

Finally, the following assumptions were made according to the current understanding of heart valve leaflet tissues:

1. All layers are tightly bonded with no slippage, similar to what is observed in the aortic valve leaflet [3].

2. There are no mechanical interactions between layers and that they deform with the bulk tissue.

3. The collagen fiber modulus is the same for all layers and that the differences in collagen mechanical contribution response are due to variations in structural organization.

4. Fiber–fiber interactions are negligible.

5. Fiber–matrix interactions are negligible.

2.2.2 Constitutive model formulation

2.2.2.1 Single fiber models

Based on the above considerations (Section 2.2.1.1), the following linear force-displacement relation for the collagen fibrils and fibers was used

$$\begin{aligned} P_f =& \eta_C \left(\lambda_t - 1\right) \frac{1}{\lambda_s} = \frac{\eta_C}{\lambda_s} \left(\frac{\lambda_f}{\lambda_s} - 1\right) \\ S_f =& \frac{1}{\sqrt{2E_s + 1}} \left(\frac{1}{\sqrt{2E_s + 1}} - \frac{1}{\sqrt{\sqrt{2E_f + 1}}}\right) \end{aligned} \tag{2.1}$$

where P_f and S_f are the 1st and 2nd Piola Kirchhoff fibers stresses, η_C is the collagen fiber modulus, λ_f and E_f are the fiber stretch and Green's strain, λ_t and E_t are the true fiber stretches and Green's strains, and λ_s and E_s are the slack fiber stretches and Green's strains. For the elastin fibers, based on Section 2.2.1.2 and our previous work on the pulmonary artery [16], we use the following generalized form,

$$S_f^e = \eta_e \left(E_f^e\right)^d \tag{2.2}$$

Here η_e is the elastin fiber modulus and d is the exponent that determines the degree of non-linearity of the fiber. This allows us to alter the stress strain relationship of the fiber based on the mechanical and structural data acquired.

2.2.2.2 Fiber ensemble models

As in previous works [35, 50, 15], we scale up to the tissue-level by first considering an ensemble of collagen fibers, which is defined as a sub-group of fibers that share a common initial orientation n_0. Collagen fiber recruitment is commonly assumed to be independent of n_0, i.e. is orientation-invariant [16, 50, 34, 15]. To evaluate the hypothesis that there may be angular variations is due to homeostasis

(Section 2.2.1.1), we developed the following generalized framework for orientation-variant fiber recruitment. The fiber recruitment distribution function $D\left[E_s(n_0)\right]$ is a function of the fiber slack strain E_s and orientation n_0, and is represented by a beta distribution function. $D\left[E_s(n_0)\right]$ was parametrized by a mean μ_r, a standard deviation σ_r, and was defined over a strain range bounded by the lower- and upper-bounds E_{lb} and E_{ub}. The general form given by,

$$D(\xi, E_s) = \frac{(y)^{\alpha-1}(1-y)^{\beta-1}}{B(\alpha,\beta)(E_{ub}-E_{lb})}, \quad y = \frac{E_s - E_{lb}}{E_{ub}-E_{lb}}, \quad y \in (0,1) \tag{2.3}$$

where the parameter vector is $\xi = \{\mu, \sigma, E_{lb}, E_{ub}\}$. Here, $B(\alpha,\beta)$ is the Beta distribution function with shape parameters α, β. The interrelationships between the two are

$$\begin{gathered} \hat{\mu}_r = (\mu_r - E_{lb})/(E_{ub}-E_{lb}), \quad \hat{\sigma}_r = \sigma_r/(E_{ub}-E_{lb}), \\ \alpha = \frac{-\hat{\mu}_r(\hat{\sigma}_r^2 + \hat{\mu}_r^2 - \hat{\mu}_r)}{\hat{\sigma}_r^2}, \quad \beta = \frac{(\hat{\mu}_r - 1)(\hat{\sigma}_r^2 + \hat{\mu}_r^2 - \hat{\mu}_r)}{\hat{\sigma}_r^2}, \\ \mu_r \in (E_{lb}, E_{ub}), \quad \hat{\mu}_r \in (0,1) \end{gathered} \tag{2.4}$$

It should be noted that the parameters in Eqns 2.3, 2.4 are functions of the initial fiber ensemble orientation n_0, so that $\xi(n0)$.

While comprehensive, equations 2.3, 2.4 present difficulties in actual implementation by either direct experimental measurement or parameter estimation [26]. However, the equations can be reduced using the assumption that the ensemble stresses are constant with orientation. Here the ensemble strain Es is scaled by the maximum ensemble strain $E_{max}(\mathbf{n}_0)$ in the fully loaded state.

$$D(\xi, E_s) = \bar{D}\left(\bar{\xi}, \frac{E_s}{E_max(\mathbf{n}_0)}\right) \tag{2.5}$$

where the parameter vector is now $\bar{\xi} = \bar{\xi}(\mathbf{n}_0) = (\bar{\mu}, \bar{\sigma}, \bar{E}_{lb}, \bar{E}_{ub})$, which is non-dimensionalized as indicated by the overbar. Using this form, the same fraction of fibers is recruited for each fiber ensemble at the maximum strain and the ensemble

stresses becomes approximately constant with orientation. This form also requires no additional parameters. In addition to the above analysis, we utilized the standard orientation-invariant approach [16] defined as

$$D(\xi, E_s) = D(\{\mu_r, \sigma_r, E_{lb}, E_{ub}\}, E_s(\mathbf{n}_0)) \tag{2.6}$$

For both forms, the resulting ensemble stress is given by

$$\begin{aligned} S_e^{ens}\left[\xi, E_{ens}(\mathbf{n}_0)\right] &= \eta_C \int_0^{E_{ens}(\mathbf{n}_0)} \frac{D(\xi, x)}{\sqrt{2x+1}} \left(\frac{1}{\sqrt{2x+1}} - \frac{1}{\sqrt{2E_{ens}(\mathbf{n}_0)+1}} \right) \\ \text{where} \quad D(\xi, x) &= \begin{cases} \bar{D}(\bar{\xi}, x, \mathbf{n}_0) & \text{orientation variant} \\ D(\xi, x) & \text{orientation invariant} \end{cases} \end{aligned} \tag{2.7}$$

Finally, since elastin fibers are straight (i.e. not undulated like collagen fibers), the elastin ensemble stress is simply $S_e^{ens} = \eta_e (E_{ens})^d$.

2.2.2.3 Complete layer and full tissue forms

The strain energy of collagen and elastin fibers for each layer is given by the sum of the fiber ensembles weighted by the fiber ODF $\Gamma(\theta)$ and mass fraction with respect to each layer ϕ. $\Gamma(\theta)$ is approximated using another beta distribution function with a mean μ and standard deviation σ [16]. Since $\Gamma(\theta)$ is nearly symmetric, the shape parameters α and β are forced to be equal (Eqn. 2.4), thus $\bar{\mu} = 0.5$ at all points. A remainder function is then used to ensure $\theta \in \left[\mu - \pi/2, \mu + \pi/2\right]$, before normalizing it to the domain of the beta function $y \in [0, 1]$, yielding

$$\begin{aligned} \Gamma(\theta) = \frac{B(\alpha, \alpha, y)}{\pi}, \quad y = \frac{\text{Mod}(\theta - (\mu - \pi/2), \pi)}{\pi}, \\ \alpha = -0.5\left(\bar{\sigma}^2 + 0.25 - 0.5\right)/\bar{\sigma}^2, \quad \bar{\sigma} = \sigma/\sigma\pi \end{aligned} \tag{2.8}$$

where B is the Beta function.

Next, we define the tissue "matrix" as PG, GAGs, and water into a homogenized single phase and represented using an incompressible Neo–Hookean model. The

resulting matrix stress tensor, assuming a planar configuration and no distinctions between layers, is $S_m = \mu_m(\mathbf{I} - C_{33}\mathbf{C}^{-1})$. This phase is necessary to enforce incompressibility and to obtain accurate results in computational simulations [15]. The resulting total tissue stress, weighted by the mass fractions ϕ, is given by

$$\mathbf{S} = \sum_{L=1}^{\text{nlayers}} \left\{ \begin{array}{l} \phi_c^L \eta_c \int_{-\pi/2}^{\pi/2} \Gamma_c^L(\theta) \int_0^{E_{ens}(\theta)} \frac{D_L(x,\theta)}{\sqrt{2x+1}} \left(\frac{1}{\sqrt{2x+1}} - \frac{1}{\sqrt{2E_{ens}(\theta)+1}} \right) \mathbf{n}_0 \otimes \mathbf{n}_0 \, \mathrm{d}x \, \mathrm{d}\theta \\ + \phi_e^L \eta_e^L \int_{-\pi/2}^{\pi/2} \Gamma_e^L(\theta) (E_{ens})^{d_L} \mathbf{n}_0 \otimes \mathbf{n}_0 \, \mathrm{d}\theta \end{array} \right\} + \phi_m \eta_m \left(\mathbf{I} - C_{33}\mathbf{C}^{-1} \right) \tag{2.9}$$

where the superscript L indicates the layer and the parameter list for Eqn. 2.9 is given in Table 2.2.

2.2.3 Structural characterization

To obtain the mass fractions of the major ECM components for each layer, additional porcine MV leaflets (n = 3) were harvested from a local slaughterhouse and immediately transported for sectioning. Transverse sections from the central region of each leaflet were stained using Movat's Pentachrome stain (Fig. 2.2) and then imaged using light microscopy to determine the relative thickness of each layer. Color deconvolution was then used to separate the collagen (yellow), elastin (Black), and PGs (Blue). The relative area fraction in each layer was determined using the total color intensity (Table 2.3). ODFs for both collagen and elastin fiber networks were quantified by SHG imaging using methods described by Carruthers et al. [6] (Fig. 2.2). The resulting orientation distribution functions (ODF) for collagen and elastin were obtained using the methods of Courtney et al. [9].

Table 2.2: Parameter of the meso-scale structural constitutive model.

	Parameter		Description	Layer
Collagen	1	η_c	Mean collagen fiber modulus	
	2	σ_c^f	Standard Deviation of the collagen fiber ODF	Fibrosa
	3	σ_c^a		Atrialis
	4	μ_c^f	Mean of the collagen fiber recruitment distribution	Fibrosa
	5	μ_c^a		Atrialis
	6	μ_c^s		Spongiosa
	7	σ_r^f	Standard deviation of the collagen fiber recruitment distribution	Fibrosa
	8	σ_r^a		Atrialis
	9	σ_r^s		Spongiosa
	10	E_{ub}^f	The upper-bound of the collagen fiber recruitment distribution	Fibrosa
	11	E_{ub}^a		Atrialis
	12	E_{ub}^s		Spongiosa
Elastin	13	σ_e^v	Standard deviation of the elastin fiber ODF	Ventricularis
	14	σ_e^a		Atrialis
	15	η_e^f	Mean elastin ensemble modulus	Ventricularis
	16	η_e^a		Atrialis
	17	η_e^s		Spongiosa
	18	d_e^f	Mean elastin ensemble exponent	Ventricularis
	19	d_e^a		Atrialis
	20	d_e^s		Spongiosa
Matr.	21	η_m	Mean matrix shear modulus homogenized over all four layers	
	22	μ_θ	Preferred direction of the mitral valve leaflet relative to the testing axes	

Table 2.3: Volume fractions of ECM components in MV (unitless)

Leaflet	**ECM**	**Ventricularis**	**Fibrosa**	**Spongiosa**	**Atrialis**
Anterior	Collagen	0.078 ± 0.018	0.839±0.021	0.036±0.015	0.047±0.007
	Elastin	0.487 ± 0.039	0.066±0.030	0.067±0.000	0.380±0.036
Posterior	Collagen	0.068 ± 0.008	0.778±0.052	0.043±0.018	0.110±0.044
	Elastin	0.104 ± 0.021	0.067±0.017	0.118±0.036	0.711±0.035

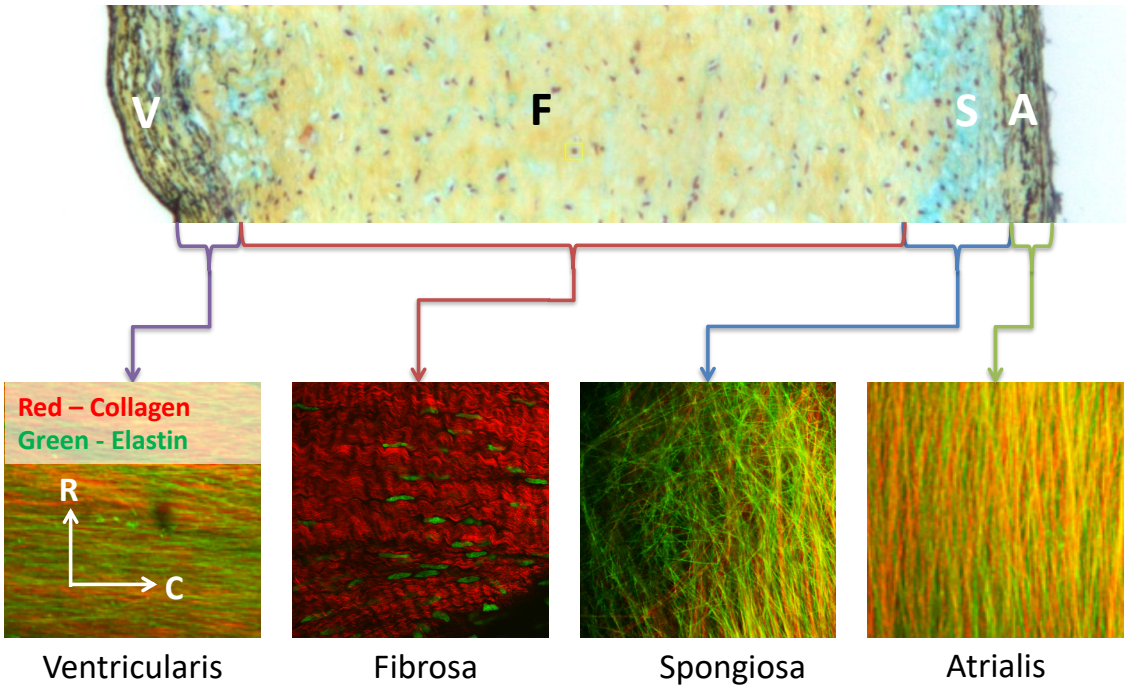

Figure 2.2: Microstructural analysis was done using Movat pentachrome stain of the transverse-radial section of the center region of the MV anterior leaflet (Top), and multiphoton microscopy (MPM) of the ventricularis (V), fibrosa (F), spongiosa (S) and atrialis (A) layer of the anterior leaflet (Bottom). The histological section shows the relative thickness of each layer, and the MPM shows the orientation or collagen (red) and elastin (green) fibers in each layer.

2.2.4 Experimental mechanical studies

In order to develop a comprehensive model to simulate the leaflets in both physiological and surgically altered/pathological conditions, it is necessary to explore the MV properties beyond the physiological range. Moreover, no single deformation mode can provide all the data needed for parameter optimization. Thus, the following deformation modes were utilized.

2.2.4.1 Uniaxial loading

Under uniaxial loading along the circumferential direction, only the highly circumferentially aligned collagen in the fibrosa and ventricularis layers, which constitute the bulk of the MV, is loaded. This aided the preliminary examination of the collagen fibers mechanics, as the contribution of elastin becomes negligible at high stress. To perform these tests, specimens from four anterior MV leaflets were tested under uniaxial strain until failure. Each specimen was cut into 5 by 20 mm stripes with the long axis oriented along the preferred direction (circumferential) of the leaflet. The specimens were clamped at both ends of the long axis with a separation of 13.5 mm to serve as the gauge length. The transverse direction was unconfined and allowed to contract laterally. One end of the clamps was then displaced at a rate of 0.1 mm/s. The tests were manually aborted after the tissue tears. No preconditioning was done and the tissue was not preloaded. To measure the internal strains more accurately, an optical marker tracking method was used [2]. All testing was done at room temperature in phosphate buffered saline (PBS).

2.2.4.2 Equibiaxial planar strain tests

EB planar strain kinematics has several important advantages for examining the effective stress-strain relations in MV leaflet tissues. Firstly, like uniaxial testing, the test can be carried out into the MPa range, exceeding physiological stress levels to ensure all collagen fibers are fully recruited. Secondly, as there are no fiber rotations, one can obtain the fiber ensemble response under the assumption of orientation-invariant fiber recruitment [16, 50, 15]. This allows direct estimation of the orientation-invariant fiber recruitment function and effective fiber modulus.

To obtain the requisite EB strain data, porcine MV specimens were harvested from a local slaughterhouse and immediately transported for testing. 10 mm by 10 mm sections were taken from the center region of each leaflet and mounted to a custom-built biaxial device [23, 22] with the circumferential and radial directions aligned to the device axes. The specimens were immersed in PBS and tested at room temperature. The strain was determined via four fiducial markers glued to the central region of the specimen [2]. The free-floating state was used as the stress-free reference state, while a preload of 1 g was applied for testing purposes. Starting at 10% strain, each specimen was tested for ten 30 s cycles with the tenth cycle taken as representative. The maximum strain was then systematically increased until a linear stress-strain region was observed. A total of 7 anterior and 7 posterior porcine MV leaflets were tested.

2.2.4.3 Full in-plane responses

To obtain the necessary mechanical data for full parameter estimation, a comprehensive set of planar biaxial mechanical data was obtained that encompassed the extra-physiological range. Porcine MV specimens were harvested using a protocol

similar to the EB strain testing above. Following mounting, these specimens were first preconditioning for 10 cycles at 90 N/m. The specimens were then unloaded, and the post-preconditioned free-floating state was used as the stress-free references state. Similar to the above, a preload of 1 g was applied for testing purposes. For each loading path, the specimens were loaded to a maximum membrane tension of 90 N/m for ten 30 s cycles with the last cycle taken as representative [23, 22]. Circumferential (x_1) to radial (x_2) ratios of $P_{11} : P_{22}$ = 1:2, 3:4, 1:1, 4:3, and 2:1 were used, with two additional extreme loading protocols that represented extra-physiological ranges of 1:10 and 10:1 to evaluate the MSSCM predictive capabilities.

2.2.4.4 Collagen fiber ensemble analysis using SAXS

One way we can assess the intrinsic mechanical properties of collagen fibers, dissociated from the effects of crimping, is using fibril-level measurements from SAXS. We thus utilized extant data from a porcine MV study by Liao et al. [42] to validate the collagen modulus and recruitment. The experiment was performed on MV anterior leaflets specimens, which were loaded under EB stress. SAXS was used at each load step to measure the fibril strain. Experimental details have been provided in [42].

2.2.5 Parameter estimation

2.2.5.1 General considerations

Obtaining the true global cost-function minimum can become exceptionally difficult for highly nonlinear models with a large number of parameters, such as equation 2.9. This will often include issues such as parameter covariance and the presence of local minima. We thus developed the following detailed sequential procedure for parameter estimation using observations from the structure of the MV leaflet (Section

2.2.3).

Firstly, the ventricularis is rich in both elastin and collagen, with a relatively narrow ODF and a preferential orientation in the circumferential direction for both fiber types (Fig. 2.2). Secondly, the fibrosa, comprising the bulk of the MV leaflet, contains mainly collagen fibers highly aligned to the circumferential direction with almost no elastin except for trace amounts near the spongiosa. Thirdly, the spongiosa contains relatively small amounts of elastin and collagen, both of which are randomly oriented, and is predominately composed of PGs and GAGs. Fourthly, the atrialis contains the largest population of elastin and some collagen, both of which has a narrow ODF and oriented along the radial direction. Fifthly, since the collagen and elastin fibers in the ventricularis and fibrosa were observed to have very similar ODFs, they cannot be separated reliably from a parameter optimization standpoint. Thus, the small amount of elastin in the fibrosa was considered part of the ventricularis elastin, and the collagen in the ventricularis was considered part of the fibrosa collagen. Also, since the collagen and elastin fibers in the ventricularis and fibrosa were found to be identically aligned and orthogonal to the atrialis, their respective preferred directions were fixed during parameter estimation.

2.2.5.2 Modifications for collagen fiber recruitment bounds

As observed in both uniaxial and EB strain data (Fig. 2.3), a gradual increase in collagen fiber recruitment and a transition to a linear stress-strain response were clearly visible. In preliminary studies of the collagen fiber recruitment probability function $D(E_s)$, we observed that when the lower-bound E_{lb} was sufficiently distant from the mean μ_r, the overall shape of $D(E_s)$ did not change significantly with further decreases in E_{lb}. Thus, to reduce the number of parameters, the lower-bound of the

distribution was set to $E_{lb} = 0$.

2.2.5.3 Elastin fiber model

To determine the elastin fiber model (Sections 2.2.1.2 Elastin fiber network, 2.2.1.1 Single fiber models), we utilized the low stress region of the mechanical response. Due to the collagen fiber recruitment, we can retroactively determine the Elb of the recruitment distribution as the point when the cumulative distribution is less than 1% (typically less than 3–8 kPa). Since collagen does not contribute significantly to this region, the response in this region can be considered entirely due to elastin (Fig. 2.4a). In pilot studies, we found that $d > 1$ in equation 2.2. In fact, the exponent for the ventricularis and atrialis layer appeared to be different. Thus, we allowed d to vary during parameter estimation rather than being a set to a constant value.

2.2.5.4 Parameter estimation part 1 – collagen fiber recruitment

From the above analysis, the number of parameters was reduced to 22 (Table 2.2). To start with the parameter estimation, we took advantage of the simplified kinematics of the uniaxial and EB test data to isolate the effects of collagen fiber recruitment in a simplified fiber recruitment model. For both datasets, the collagen fiber network in the fibrosa and ventricularis were idealized as a family of uni-directionally aligned fibers, with the elastin fibers neglected as their contributions to the total stress were insignificant in this loading state. Also, note that for the EB tests the fiber ensemble stress can be determined directly by [55].

$$S_{ens} = S_{11} + S_{22} \quad \text{for} \quad E_{11} = E_{22}, E_{12} = 0 \tag{2.10}$$

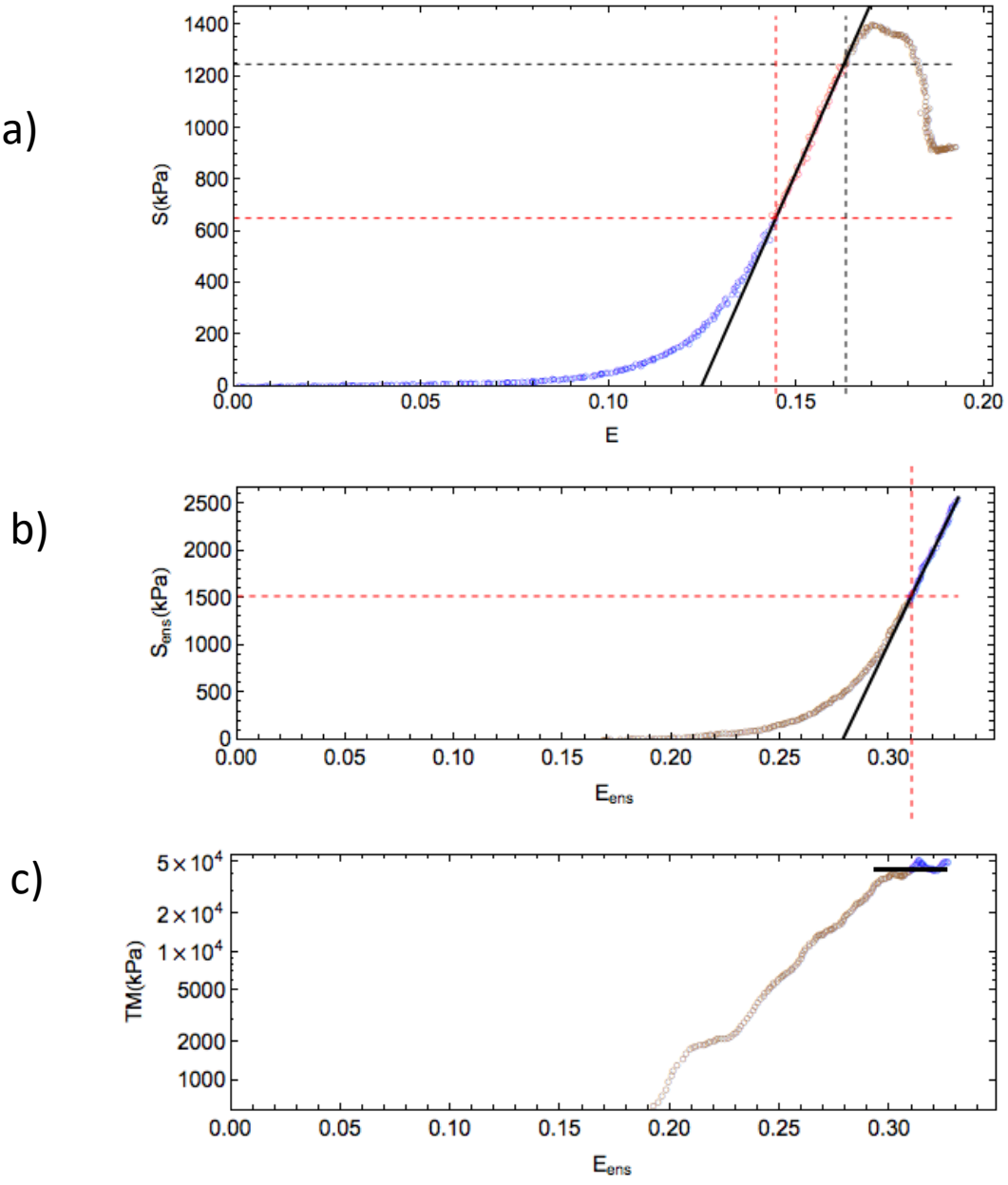

Figure 2.3: Example mechanical testing result of (a) uniaxial and (b) and (c) equibiaxial strain test data from an anterior leaflet. The linear post recruitment region is shown by the black line, which indicates full collagen fiber recruitment. The (c) tangent modulus curve in equibiaxial strain test shows a clear flattened section in the post-transition region. Tangent modulus curve for uniaxial extension is not shown due to similarities.

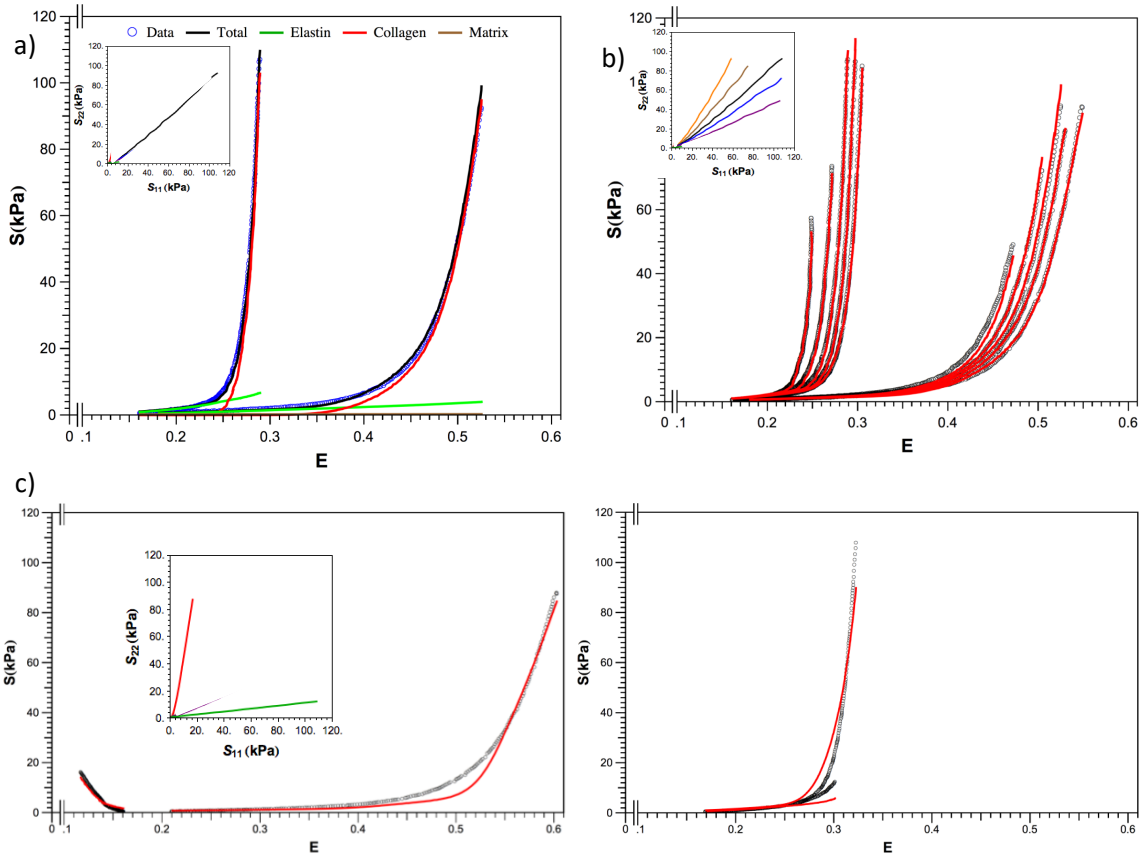

Figure 2.4: Example of the best fit from an anterior leaflet. The (a) equibiaxial stress protocol was fit with only the elastin (green) first, followed by fitting the collagen only while keeping the elastin fixed. (b) The final fit of all "physiological" protocols are shown. (c) The two extra-physiological protocols, which were not fit, is shown. This suggests that the model have good predictive capability.

We assumed in this first step that the recruitment distribution is orientation invariant, so that the collagen recruitment function $D(\xi, E_s) = D(\{\mu_r, \sigma_r, E_{lb}, E_{ub}\})$. E_{ub} was determined by the transition point to the linear region (Fig. 2.3), leaving only μr, σr to be fit in this part of the parameter estimation.

2.2.5.5 Parameter estimation part 2 - full planar biaxial mechanical data set

Ideally, the measured ODFs $\Gamma(\theta)$ from the same specimen should be directly inserted into Eqn. 2.9. However, in practice, we found that the ODFs had to be fitted to adjust for the specimen to specimen variability. Nevertheless, the mean best-fitted ODFs can be compared to the mean measured ODFs to ensure that the estimated parameters are reasonable comparing to the true value. We expedited the process by assuming that the ODFs for each specimen is not significantly different from the true measured mean ODFs. Thus, the mean ODFs can be used as an initial guess and speed up the convergence to the optimal value. The use of a global algorithm will also ensure the optimized parameters do not become trapped at the mean value. Similarly, the estimated recruitment distribution $D(\xi, x)$ is also obtain from independent specimens. The recruitment distribution parameters ξ are again used only as initial guesses and parameter validation.

Taking a similar approach to Fata et al. [16], we first examined the equibiaxial stress protocol ($P_{11} : P_{22} = 1{:}1$), which is the best approximation of the in vivo loading state of the MV. The low stress region as defined in section 2.2.5.3 was used to fit the elastin (Fig. 2.4a). This is easily identified as the nearly linear response before the exponential-like collagen response. Furthermore, due to limitations concerning the elastin model form, where the elastin response can increase exponentially to unrealistically surpass the response of the collagen, the exponent parameter d for the elastin

(Table 2.2) was constrained to be less than 3.5. Next, the remaining high-stress region was used to fit the collagen fiber response independently. Using this coupled approach, we were able to minimize the search space to the 12 parameters associated with collagen (Table 2.2). Once a reliable estimate of the parameters was obtained for this protocol, the inner 3 protocols (3:4, 1:1, 4:3) were fit using the existing parameters as the initial guess. We then progressed to the remaining "physiological" protocols (1:2, 3:4, 1:1, 4:3, 2:1) once again keeping the previous parameters as the initial guess to obtain better-estimated parameters.

Preliminary attempts demonstrated that gradient algorithms were unable to converge to the proper solution and tended to become unable to handle local minima. As a result, we employed the genetics-based differential evolution algorithm to perform the optimization, similar to Fata et al. [16]. To narrow down the search space and guide the optimization, initial guess was derived from the above mechanical studies (Section 2.2.4). Parameter estimation was performed using a custom program written in Mathematica (Wolfram Research Corp.).

2.2.6 Model validation

The mean fitted fiber ODFs $\Gamma(\theta)$ from each layer of the MV anterior leaflet were compared to the measured ODFs obtained from SHG imaging (section 2.2.3). Since the orientation of the fibers is referenced to the laboratory testing or imaging configurations for the mechanical and imaging data respectively, which may be different, the preferred direction of the $\Gamma(\theta)$ was rotated to $\mu_\theta = 0^\circ$ to give the appropriate comparison. Next, in the SAXS study [42], the average fibril strain for all fibrils in the leaflet, $\bar{\epsilon}_{\text{fibril}} = \bar{\lambda}_t - 1$, where is the mean true stretch of the fibrils, was measured. Since the loading protocol was equibiaxial stress (P_{11}:P_{22} = 1:1), the tissue was in an

anisotropic strain state, with each fiber ensemble experience different ensemble strain. Additionally, the fiber slack strain reduces the effective stiffness of the fibrils at the tissue-level (Eqn. 2.1). Hence we needed to incorporate the $\Gamma_c(\theta)$ as well as collagen fiber recruitment distribution ($D(\xi, x)$) in the SAXS simulations. The correct fiber modulus (η) is also necessary to determine the tissue-level stress. Therefore, SAXS gives us an independent method to validate the collagen network model used in this study.

To simulate the full SAXS response, as compared to those measured by Liao et al. [42], we assume standard affine kinematics (section 2.2.1) [40]. Thus the fibril stretch is equal to the true stretch of the collagen fibers. Using structural parameters determined from parameter estimation, we simulated a population of fibers based on the fiber ODF and collagen recruitment distributions. The fibers were then deformed based on the EB tension protocol. This corresponds to a mean true fiber stretch given by

$$\bar{\lambda}_t = \int_\theta \Gamma(\theta) \left[\int_1^{\lambda_{ens}(\theta)} D(\xi, x) \frac{\lambda_{ens}(\theta)}{x} \, \mathrm{d}x \right] \mathrm{d}\theta \tag{2.11}$$

The resulting mean fibril strains $\bar{\epsilon}_{\text{fibril}} = \bar{\lambda}_t - 1$ were plotted against the measured tissue-level stresses and compared to the SAXS ϵ_{fibril} [42].

2.2.7 Statistical testing

Standard independent two-sample t-tests were used to determine the statistical significance of the results.

2.3 Results

2.3.1 Uniaxial and EB strain analysis

It was observed under these tests that the resulting stress-strain responses transitioned to a linear region prior to failure (Fig. 2.3). This observation supported the use of a collagen fiber recruitment model for MV tissue (Section 2.2.1). Under EB strain testing kinematics, full recruitment was reached on average at a mean and standard deviation value of 0.284 ± 0.047 in Green's strain and 782.1 ± 121.5 kPa in ensemble stress for the anterior leaflet. For the posterior leaflet, full recruitment strain was achieved at 0.2730 ± 0.0156 in Green strain and 1434.0 ± 165.4 kPa in ensemble stress. The posterior leaflet appeared to recruit more gradually than that of the anterior leaflet, with an average σ_r (the standard deviation of the collagen fiber recruitment function) of 0.0231 ± 0.001 in Green strain compared to 0.015 ± 0.003 for the anterior leaflet. In comparison, the average maximum tensile strength under uniaxial loading along the circumferential direction for the anterior leaflet was $2,\ 220.1 \pm 794.5$ kPa. This suggests that the stress required to tear the tissue is approximately three times higher than the stress required to reach full recruitment on average.

2.3.2 Parameter estimation

For the fitted parameters obtained from uniaxial extension and EB strain datasets (Section 2.2.5.4, Table 2.4, Table 2.5), we observed similar collagen modulus η_c for both tests. There appeared to be a shift in strain for the recruitment parameters values due to the differences in testing methodology. For all specimens tested under the full planar tension test protocols, they demonstrated a clear toe region at stresses below 7 kPa. This gave us a good initial estimate of the elastin response in comparison

Table 2.4: Uniaxial extension testing results for the MV anterior leaflet.

	η_c(MPa)	μ_r^f	σ_r^f	E_{ub}^f
1	68.2420	0.12543	0.01602	0.1434
2	345.6285	0.23445	0.02099	0.2558
3	114.5181	0.13822	0.02682	0.1592
4	25.7835	0.11667	0.02545	0.1592
Mean	138.5431	0.15369	0.02232	0.1794
SEM	71.3667	0.02728	0.00244	0.0257

Table 2.5: Equibiaxial strain testing results.

	Anterior				**Posterior**			
	η_c	μ_r^f	σ_r^f	E_{ub}^f	η_c	μ_r^f	σ_r^f	E_{ub}^f
1	83.93	0.270	0.023	0.298	151.06	0.200	0.022	0.224
2	146.67	0.187	0.009	0.194	118.51	0.272	0.023	0.293
3	218.24	0.178	0.008	0.184	149.48	0.260	0.024	0.287
4	143.29	0.280	0.023	0.302	155.48	0.222	0.021	0.250
5	188.67	0.427	0.013	0.442	127.20	0.283	0.026	0.311
Mean	156.16	0.268	0.015	0.284	140.34	0.247	0.023	0.273
SEM	22.78	0.045	0.003	0.047	7.338	0.016	0.0008	0.0156

to the final fitted values, while fitting the high stress region resulted in recruitment parameter values that were consistent with EB strain testing (Fig. 2.4a). The fit of the full model (Eqn. 2.9) (Fig. 2.4b) had a very good mean R-squared value of 0.964 for the anterior leaflet and 0.951 for the posterior leaflet (Table 2.6, Table 2.7). The full model (Eqn. 2.9) was used to predict the stress of the extra-physiological protocols and obtained similar results (Fig. 2.4c and d). The modulus of the collagen fibers was found to be 164.0 ± 16.4 MPa for the anterior and posterior leaflets under planar tension, which is comparable for all mechanical data (Fig. 2.5a, Table 2.4, 2.5, 2.6, 2.7).

Next, we compared the result for the two collagen fiber recruitment models: orientation-invariant (Eqn. 2.6) and orientation-variant (Eqn. 2.5). Interestingly, we found no major difference between these modeling approaches (Fig. 2.6). The

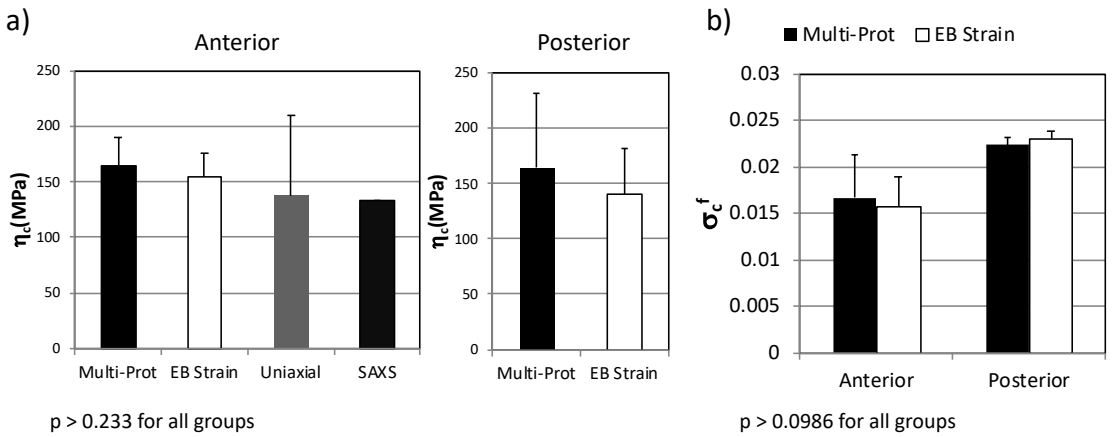

Figure 2.5: (a) The mean and standard deviation of the collagen fiber modulus as determined from uniaxial, equibiaxial strain, and planar biaxial stress testing for both the anterior and posterior leaflets is shown. No statistical significance was found from ANOVA and student-t tests. (b) The mean and standard deviation of σ_r, which is the standard deviation of the recruitment distribution of collagen fibers, in the fibrosa layer for both the anterior and posterior leaflet is shown. Again, no statistical significance was found, but the posterior leaflet appears to have larger σ_r based on the trend.

Table 2.6: Parameter estimation results from the MV anterior leaflet.

	Collagen											
	Modu.	**Fibrosa + Ventricularis**				**Atrialis**				**Spongiosa**		
ID	η_c	σ_c^f	μ_r^f	σ_r^f	E_{ub}^f	σ_c^a	μ_r^a	σ_r^a	E_{ub}^a	μ_r^s	σ_r^s	E_{ub}^s
1	144.92	0.163	0.210	0.010	0.223	0.465	0.864	0.042	0.989	0.790	0.015	0.835
2	86.23	0.140	0.522	0.010	0.537	0.077	1.172	0.019	1.204	1.177	0.038	1.256
3	235.26	0.075	0.425	0.041	0.494	0.075	0.613	0.028	0.653	0.676	0.015	0.720
4	199.33	0.136	0.293	0.011	0.307	0.075	0.914	0.010	0.927	0.890	0.010	0.902
5	207.55	0.149	0.391	0.006	0.397	0.400	1.791	0.154	2.099	1.798	0.006	1.810
6	196.41	0.180	0.286	0.015	0.307	0.250	0.520	0.019	0.545	0.525	0.015	0.559
7	69.35	0.222	0.275	0.024	0.300	0.075	0.472	0.015	0.517	0.540	0.026	0.617
Mean	162.72	0.153	0.335	0.017	0.361	0.170	0.759	0.022	0.806	0.766	0.020	0.815
SEM	26.16	0.020	0.047	0.005	0.051	0.066	0.111	0.005	0.113	0.100	0.004	0.103

	Elastin								**Mat.**	**Ori.**	R^2
	Ventricularis			**Atrialis**			**Spongiosa**				
ID	η_e^v	d^v	σ_e^v	η_e^v	d^v	σ_e^v	η_e^v	d^v	η_m	μ_θ	
1	53.91	2.878	0.077	125.0	1.732	0.078	54.67	2.747	0.000	0.304	0.980
2	0.07	3.416	0.079	0.12	2.982	0.082	0.04	1.742	0.010	0.350	0.893
3	12.25	3.500	0.077	27.21	3.000	0.079	0.06	2.986	0.000	0.622	0.957
4	14.52	3.000	0.076	67.28	1.000	0.151	0.00	2.048	0.000	0.384	0.986
5	2.08	2.980	0.106	0.05	1.681	0.340	0.00	1.553	0.911	-0.05	0.970
6	13.71	3.443	0.081	287.3	2.132	0.097	0.00	2.824	0.281	0.449	0.996
7	2.33	1.886	0.199	0.34	2.704	0.341	0.00	3.000	0.000	-0.20	0.970
Mean	16.13	3.021	0.098	84.55	2.258	0.138	9.13	2.558	0.049	0.274	0.964
SEM	7.9	0.250	0.020	44.94	0.324	0.042	9.13	0.217	0.047	0.102	0.015

Table 2.7: Parameter estimation results from the MV Posterior leaflet.

	Collagen											
	Modu.	**Fibrosa + Ventricularis**				**Atrialis**				**Spongiosa**		
ID	η_c	σ_c^f	μ_r^f	σ_r^f	E_{ub}^f	σ_c^a	μ_r^a	σ_r^a	E_{ub}^a	μ_r^s	σ_r^s	E_{ub}^s
1	200.000	0.352	0.300	0.011	0.314	0.400	0.487	0.033	0.539	1.554	0.168	2.020
2	197.276	0.247	0.393	0.010	0.411	0.400	0.840	0.051	0.966	1.911	0.157	2.218
3	96.535	0.422	0.715	0.044	0.760	0.427	2.500	0.158	2.966	1.329	0.020	1.369
4	160.354	0.216	0.543	0.010	0.558	0.400	1.323	0.052	1.436	2.028	0.018	2.079
5	200.000	0.370	0.454	0.033	0.501	0.104	1.366	0.048	1.480	0.780	0.037	0.824
6	181.100	0.292	0.608	0.017	0.639	0.400	1.380	0.079	1.563	1.079	0.039	1.196
7	112.588	0.325	0.392	0.032	0.428	0.400	0.699	0.064	0.890	1.668	0.107	1.811
Mean	163.979	0.318	0.486	0.022	0.516	0.362	1.228	0.069	1.406	1.478	0.078	1.645
SEM	16.330	0.027	0.054	0.005	0.057	0.043	0.251	0.016	0.296	0.169	0.025	0.197

	Elastin								**Mat.**	**Ori.**	R^2
	Ventricularis			**Atrialis**			**Spongiosa**				
ID	η_e^v	d^v	σ_e^v	η_e^v	d^v	σ_e^v	η_e^v	d^v	η_m	μ_θ	
1	83.48	2.866	0.129	789.7	1.686	0.400	234.7	2.610	0.001	-0.60	0.993
2	1.537	2.705	0.082	0.029	3.000	0.085	0.011	1.000	0.000	-0.04	0.967
3	0.743	2.918	0.349	0.000	2.999	0.400	0.000	2.549	0.000	-0.31	0.864
4	0.685	2.884	0.078	1.223	1.006	0.092	0.041	2.874	0.000	1.425	0.930
5	0.198	1.044	0.285	2.993	2.116	0.393	0.778	3.000	0.426	-0.39	0.972
6	0.103	1.001	0.075	0.000	2.731	0.311	0.000	1.774	0.253	-0.23	0.984
7	1.789	2.050	0.285	239.3	3.000	0.400	119.7	3.000	0.333	-0.16	0.985
Mean	12.65	2.210	0.183	147.6	2.363	0.297	50.74	2.401	0.145	-0.32	0.956
SEM	11.81	0.326	0.045	112.2	0.297	0.055	34.98	0.283	0.071	0.170	0.017

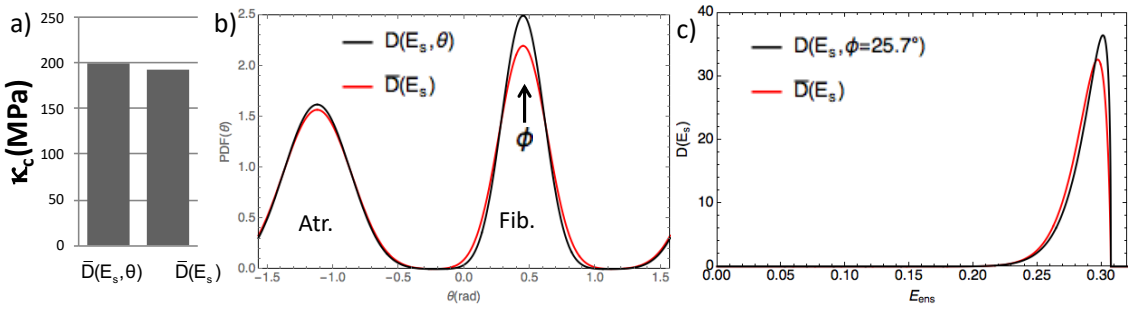

Figure 2.6: The specimen was fit using both the comparisons for the orientation-variant $\bar{D}(\bar{\xi}, x)$ (Black) and orientation invariant $D(\xi, x, \mathbf{n}_0)$ (Red) modeling approaches for the recruitment functions. Both methods produce (a) nearly the same collagen fiber modulus. (b) The fiber ODFs also appears to the equivalent width (σ_c^f). (c) The recruitment distribution also appears to be similar.

R-squared value of fit was very good for both models ($R^2 = 0.996$ vs 0.988 for Eqns. 2.6, 2.5 respectively). There were no significant difference in the predicted collagen fiber modulus η_c (Fig. 2.6a) and the collagen fiber $\Gamma(\theta)$ shows only a difference of 0.44° in η_c for the atrialis and 1.21° in for the fibrosa (Fig. 2.6b). Furthermore, the collagen fiber recruitment distribution $D(\xi, x)$ when scaled to the same range [0,1] by their upper-bound value (Fig. 2.6c) were similar for either case.

The optimal recruitment parameters for both the multi-protocol data and the EB strain data were very similar (Table 2.5, 2.6, 2.7). We found no significant differences in the averaged standard deviation of recruitment, σ_r, between the anterior and posterior leaflets for either test (Fig. 2.5b). There were minor differences in the distributions due to the way the upper-bound parameter was determined. The analysis of the EB strain kinematic state was done visually, where the upper-bound may have been underestimated. For analysis of the stress-controlled planar biaxial tests, which does not reach full recruitment, the upper-bound was predicted by the parameter estimation algorithm and tended to be slightly overestimated. Uniaxial testing instead shows a very different recruitment response (Table 2.4). This is most likely due to

the vastly different testing modes, where the differences in preconditioning and gauge length result in a drastically different reference state for the fibers. Additionally, fiber rotation effects in the uniaxial testing slow the recruitment of fibers away from the test axis and produce a greater standard deviation for the recruitment distribution. However, we observe a trend that the posterior leaflet recruits slower than the anterior leaflet (Fig. 2.5b), possibly due to differences in their role mechanically during valve closure.

2.3.3 Parameter validation

Perhaps the most important validation finding was that the simulated SAXS response (Eqn. 2.11), using the best fit parameters, matched very well to the MV SAXS data from Liao et al. [42] (Fig. 2.7). The squared correlation coefficient was computed ($r^2 = 0.971$), and we found no statistical significance ($p = 0.285$) between the two curves. To assess the sensitivity of the SAXS simulation (Eqn. 2.11), the origin recruitment distribution parameters $\mu_r^f = 0.286$ and $E_{ub}^f = 0.307$ were shifted by ± 0.01 in Green Lagrange strain, and the standard deviation of the collagen fiber ODF $\sigma_r^f = 10.3^\circ(\Gamma_c(\theta))$ was adjusted by $\pm 1^\circ$ (Fig. 2.7). Despite the perturbation being so small, there was a 54% increase in the slope of the simulated SAXS response when the mean and upper-bound of the recruitment was increased by 0.01, and a 38% decrease in slope when the parameters were decreased by 0.01. Similarly, the slope decreased by 17% when was increased by 1°, and increased by 20% when decreased by 1°. An estimate of the fiber modulus for the MV SAXS data was made by comparing against the simulated data. No statistical significance for the collagen fiber modulus between any mechanical tests or between either leaflet was found. In addition, the predicted ODFs $\Gamma_c(\theta)$ and $\Gamma_e(\theta)$ compared very well with the SHG measurements, with standard deviations differing by no more than 3 degrees

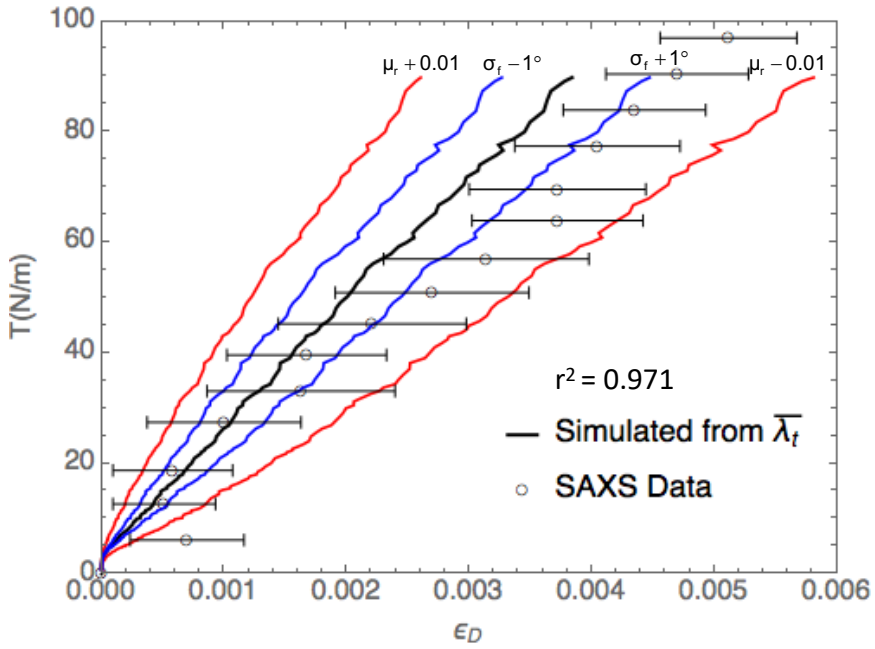

Figure 2.7: Collagen fibril stress–strain data from SAXS studies from Liao et al. [42] (circles) along with the simulated result based on the current model parameters (Black) showing very good agreement. This approach is very sensitive. Perturbing the ODF (σ_c^f) by 1° (Blue) and shifting the recruitment distribution by 0.01 in Green strain (Red) significantly changed the slop of the curve.

(Fig. 2.8). Thus, despite the model complexity, these validation results suggest that the parameters were sufficiently independent and each can be accurately determined as a representation of the mechanical behavior of the MV.

2.3.4 Differences between layers and leaflets

All ODFs $\Gamma(\theta)$ of the ventricularis, fibrosa and atrialis were much narrower in the anterior leaflets than the posterior leaflets (Fig. 2.9). To estimate the mean ensemble elastin response, each elastin ensemble was scaled by the principle strain at maximum loading under EB stress and then averaged. Like the structural differences between the anterior and posterior leaflets, the mechanical response of ventricularis was much stiffer in the anterior leaflets comparing to the posterior leaflet (Fig. 2.10).

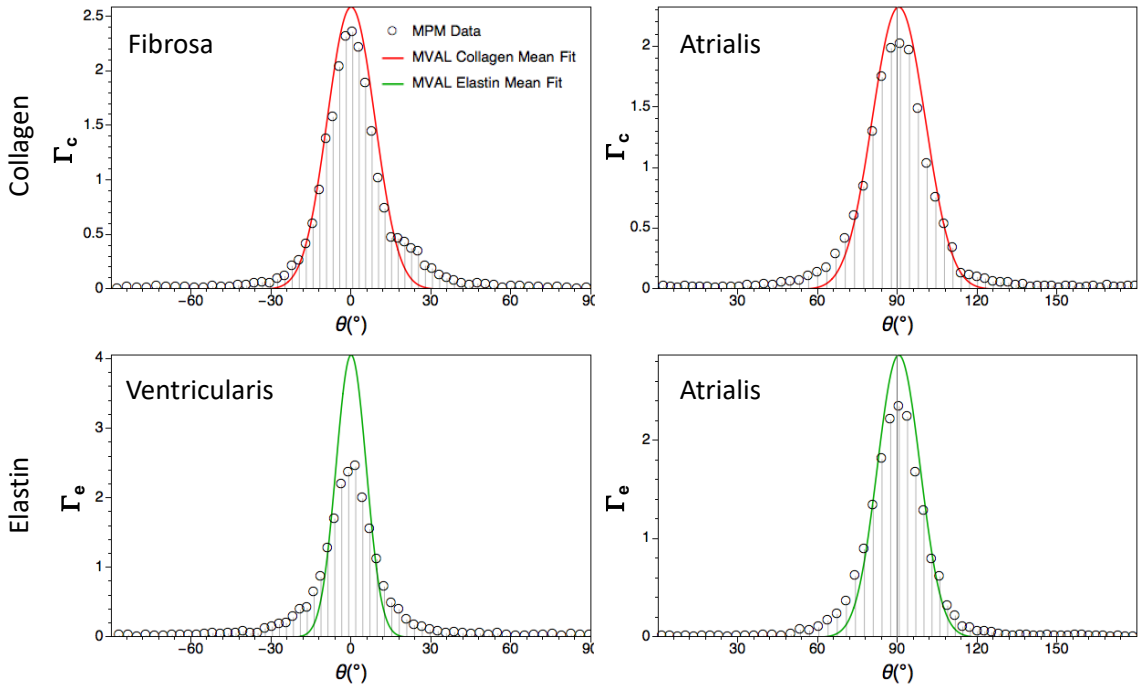

Figure 2.8: The fitted orientation distribution functions of the collagen (Red) and elastin (Green) for the anterior leaflet are shown in comparison to the measured distribution from SHG (circle). The results are shown for the ventricularis, fibrosa and atrialis. The fitted and measured ODF appears to show good agreement.

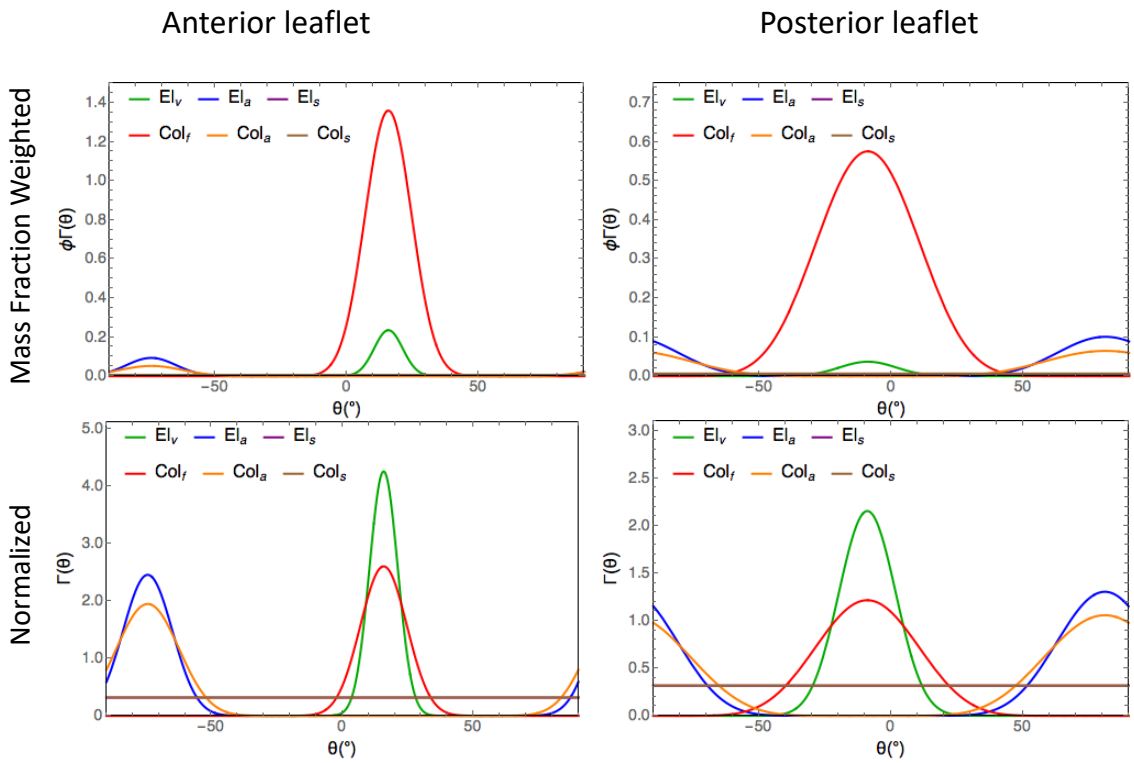

Figure 2.9: The predicted fiber orientation distributions from the anterior (Left) and posterior leaflets (Right) for collagen and elastin from all layers as an average (n = 7 for both leaflets). Both the mass fraction scaled (Top) and normalized (Both) ODFs are shown. In both leaflets, the collagen of the fibrosa layer is clearly the most dominant but is more broadly distributed in the posterior leaflet. Elastin also showed similar trends but is more evenly distributed in the anterior leaflet, while favoring the atrialis in the posterior leaflet.

On the other hand, the atrialis was stiffer in the posterior leaflet (Fig. 2.10). For the overall layer contributions, the mechanical response of the circumferential direction is mainly due to the elastin in the ventricularis at lower stress and the collagen within the fibrosa at high stress, whereas the radial direction is a combination of collagen fibers in the fibrosa as they extend and rotate under physiological loading and collagen in the atrialis at higher strains (Fig. 2.11). The mechanical contribution from the spongiosa was, as anticipated, negligible for both leaflets.

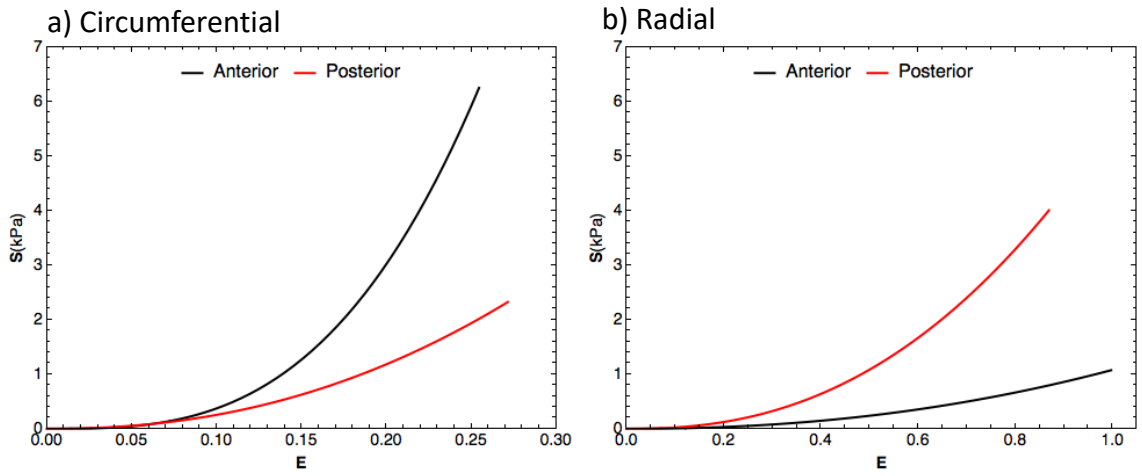

Figure 2.10: The mean elastin response in the physiological range from both anterior (Black) and posterior (Red) leaflets in the circumferential (a) and radial (b) directions. n = 7 for both leaflets. The elastin in the anterior leaflet is heavily anisotropy and favoring the circumferential direction, which the elastin in the posterior leaflet is more isotropic and only slightly favoring the radial direction.

2.4 Discussion

2.4.1 Modeling approach and major findings

In the present study, we developed a novel layer-specific meso-scale structural model of the MV leaflets starting from the fiber-level. The mechanical response at the layer- and tissue-level is driven by structural measurements and observations obtained from SHG and histology. We then utilized an extensive experimental mechanical database that included uniaxial, planar EB strain, and a comprehensive set of planar biaxial stress test protocols. This approach allowed us to properly evaluate the mechanical properties of MV tissues and to form a complete dataset for parameter estimation. All information was then integrated to form a predictive model for the MV leaflet tissues.

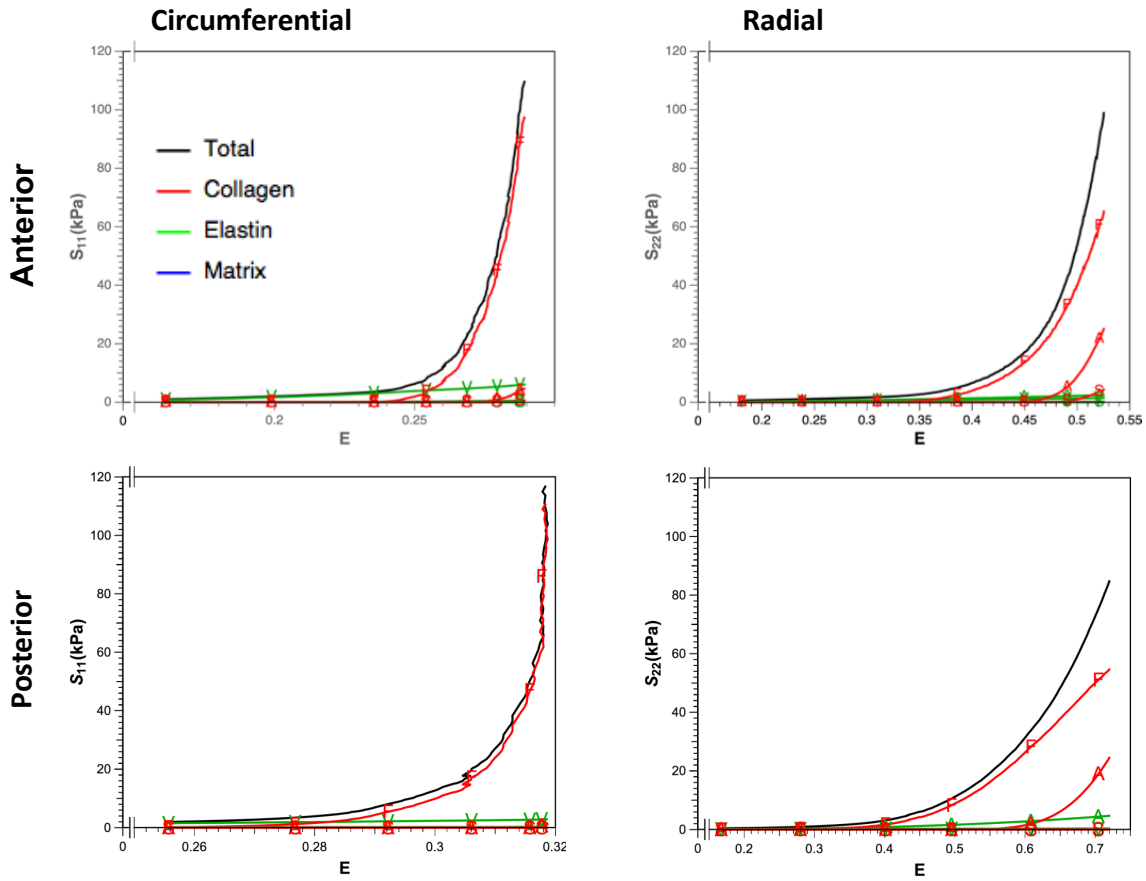

Figure 2.11: The net stress contribution from each ECM component from each layer for the equibiaxial stress protocol is shown for the circumferential (Left) and radial (Right) direction of the anterior (Top) and posterior (Bottom) leaflets. Here, the contributions from the layers are ventricularis (V), fibrosa (F), spongiosa (S), and atrialis (A). Interestingly, while the fibrosa layer is dominant circumferential directions in both leaflets, the atrialis also contributes substantially in the radial direction. Elastin clearly contributes minimal stress comparing to collagen, but it forms the bulk of the response in the toe region.

2.4.2 Model validation

Novel to this study was the use of the MV SAXS data [42] to validate the predicted collagen fiber modulus and fiber recruitment (Section 2.2.6). SALS techniques have been previously used to obtain the orientation of fibrous structures in biological tissues [52]. However, the wavelength of light (in the hundreds of nm) is much too large in comparison the size of the fibrils, which have a D-period of approximately 64 nm [32, 27, 7]. SAXS, on the other hand, utilizes a wavelength of 0.1–0.2 nm and provides a direct way of measuring the collagen fibril D-period, and thus the fibril strains [57, 58, 42]. In response to tissue-level deformation, the fibril strain depends on both its orientation and slack strain (Section 2.2.6). Therefore, the MV SAXS simulation can provide an independent way of validating the MSSCM collagen model component. Both the good agreement and sensitivity to accurate measures (Section 2.3.3, Fig. 2.7) provide additional confidence in our approach beyond basic measures such as goodness of fit. In particular, this lends confidence to the fiber/fibril kinematics used in the present form of the MSSCM and suggests that the fibrils do indeed form contiguous, tightly bounded fibers and undergo minimal slipping.

It is also important to note that it is difficult to directly combine measurements at multiple scales, such as fibril strain as measured by SAXS and the applied tissue-level membrane stress, and interpret them directly. In this case, we cannot approximate the modulus of collagen fibrils using the slope of the tissue-level stress–fibril strain curve. Although we assume every fibril has a similar modulus, the apparent modulus of collagen fibrils at the tissue-level decreases in response to an increase in the slack stretch (Eqn. 2.1). Thus the interpretation of such results requires careful analysis of the structure and kinematically related mechanisms of the tissue. Finally, we also validated the fiber $\Gamma(\theta)$ against optical SHG measurements, which demon-

strated very good agreement (Fig. 2.8). To the authors' knowledge, this is the first time macro/micro validations of this kind have been performed for any soft tissue

2.4.3 Collagen fiber modulus

As the most important load-bearing component of soft tissues, the structure, and properties of collagen is of major interest. One specific property is the modulus of the collagen fiber, which when combined with the level of fiber undulation, determines the macroscopic behavior of the collagen network at the tissue level. Given that type I collagen fibers forms the common building blocks for the bulk of the MV tissue (Fig. 2.2), the modulus serves both as an important validation for the results of the model and predicting the correct behavior of the tissue under complex loading conditions. There have been many attempts to measure the stiffness of collagen fibers in the literature [60, 20, 14, 67, 66, 65]. These measurements come in two forms: (1) models at the tissue-level and (2) direct measurements at the fibril-level. Measurements at the tissue-level can be inaccurate, as they demand an extensive understanding of the biomechanics of the tissue, physically accurate models of the mechanical behavior and detailed measurements of the structure and composition. On the other hand, there is currently no method for the real-time estimation of the instantaneous cross-sectional area of collagen fiber or fibrils. Current measurements are typically done a priori [20] or a posteriori [14], and can have significant impact on the results. These measurements also require highly accurate and noise insensitive instruments operating at the micrometer and nanometer scale. As such, these experiments are typically done using techniques such as atomic force microscopy (AFM) and have a large variability for the resulting numbers. Nonetheless, these measurements serve as an important reference for any results measure at the tissue-level, and the current literature paints a distinct picture.

For the most part, these findings fall into two distinct categories: (1) the dried properties at the 2–10 GPa range and (2) hydrated properties at the 200–900 MPa range. This difference in stiffness is due to water acting as a plasticizer in collagen fibrils [62]. Using AFM, Yang et al. [66] found a stiffness of 1.4 GPa for non-cross linked fibrils and 3.4 GPa for cross-linked collagen fibrils in the bovine Achilles tendon. Similarly, Wenger et al. [65] found collagen fibril stiffness of 5–11.5 GPa in rat tail tendon. However, in both papers, the fibrils were dried under ambient conditions and nitrogen, respectively. On the other side, Shen et al. [60] found a modulus of 860 ± 450 MPa for collagen fibrils obtained from sea cucumber dermis. In the study by Gentleman et al. [20], they found a modulus of 269.7 ± 11.9 to 484.7 ± 76.3 MPa for collagen fibers in the bovine Achilles tendon, varying with the fiber diameter, but only for the cross-linked fibers. Eppell et al. [14], found a modulus of 0.5–0.4 GPa at low strain (0.05–0.30) but can increase to up to 12 GPa at high strain. In these cases, the fibrils were hydrated before testing. This effect has also been studied using electrospun collagen scaffolds, where Yang et al. found that the fibril modulus decrease from 1.3–7.8 GPa to 0.07–0.26 GPa when hydrated[67].

In the present study, we found the collagen fiber modulus to be between 132.5 and 167.3 MPa. In our estimation of the collagen volume fraction, we assumed the tissue is entirely composed of collagen, elastin, and proteoglycans. While this serves as a good estimation of the relative composition of the MV, fluid constitutes 81.8% of the total mass of the MV anterior leaflet [43]. Additionally, using the dry mass is not a viable alternative as the fibers may have shrunk when they are dried [41]. As such, we chose the current approach to provide an unbiased effective collagen modulus for the MV. This value is not applicable to other tissues with significantly different structural composition and may explain minor differences in the modulus estimate for

the anterior and posterior leaflet. When the residual volume is taken into account, it is not difficult to imagine the estimated modulus to be 2–4 times higher than the value reported, allowing it to fall in line with the modulus of the hydrated collagen fibrils in other studies. This suggests that the model is reasonably accurate in estimating the mechanical properties of the collagen fibers. Furthermore, there was no statistical significance between the fiber modulus for either leaflet, which is reasonable given that the majority of collagen fibers are type I. Finally, that the assumption of minimal fiber–fiber and fiber–matrix interaction appears to be essentially correct. This is consistent with the ability for the fibers to rotate and extend freely with applied forces, keeping the effective tissue modulus low so the leaflets can coapt as necessary for valve function.

2.4.4 Collagen fiber recruitment

While type I collagen naturally occurs in a crimped state, the bending stiffness as the collagen fiber unravels is typically small enough to allow us to use the recruitment approach [35, 16, 50, 34, 32, 25, 5, 24]. Novel to recruitment approach, we propose an angle variant recruitment distribution based on the hypothesis that the ensemble stress will be limited to a small range due to homeostasis. Current experimental techniques do not easily allow for direct measurement, and distinguishing individual fibers is difficult and sometimes required to be specified manually [26]. Determining whether a fiber is straightened is also problematic. For best accuracy, the fiber must lay in the plane of the image. The planar projection of a fiber at an angle with the plane of the image creates a misrepresentation of the tortuosity of the fiber. Additionally, the tissue must be loaded under EB strain with no shearing. Failure to do so will result in different strain for each fiber ensemble, thus the tortuosity of fibers at different angles cannot be referenced to the same strain. These issues are fur-

ther magnified when quantifying angular variations. In the end, direct measurement methods are best served as a preliminary estimate for modeling purposes.

Assuming that the ensemble stress of collagen fibers is constant with orientation due to homeostasis, both the current model (Eqn. 2.5) and the orientation-variant model (Eqn. 2.6) produce similar results for the MV leaflets; the quality of the best fits ($R^2 = 0.988$ vs 0.996) are very comparable for both models. We hypothesize that this is due to the narrow splay of the collagen fiber ODF in the MV and thus the ensemble stress was effectively constant over this range for both models. This simplifies the recruitment distribution function for implementation in MV simulation and measurement via experimental means. Also, by assuming orientation-variance in Eqn. 2.5, the parameters are expressed as a percentage of the maximum ensemble strain, which is not an intuitive quantity. Thus, the parameters determined from Eqn. 2.5 best serve as an approximation, rather than any physically accurate quantity. Therefore, we refocused the results as if the recruitment strains are invariant with angle (Eqn. 2.6), which has a more interpretive physical meaning. In either case, the theory then dictates that the tissue should exhibit a linear response once all fibers are straightened under EB strain loading. Indeed, this is observed in the MV for both the anterior (Fig. 2.3) and the posterior leaflet.

For each leaflet tested under EB strain and uniaxial extension, the stress-strain curve transitions to linear in P–F [57, 58, 42]. For the anterior leaflet, this transition point occurs at 782.1 ± 121.5 kPa in 2nd Piola Kirchhoff or 1243.8 ± 220.8 kPa in Cauchy stress. Our inverse model using a full collagen mapped transverse model shows that the peak circumferential stress is at 241.4 ± 40.5 kPa and the peak radial stress is at 432.6 ± 46.5 kPa [36]. While it is not possible to produce the equivalent ensemble stress for the in vivo data, it is estimated that only 20–40% of fibers are recruited

under physiological stress. This substantial structural reserve is likely an adaption to maintain structural integrity for when the body is under extraneous physiological stress or attempt to maintain basic function in cases of heart diseases.

2.4.5 Elastin fiber network response

There is no established constitutive model form for individual elastin fibers in valvular tissue. We have taken a similar approach to model the fiber ensembles in the ovine pulmonary arteries [16]. However, in the MV, we noticed a slight nonlinearity in the pre collagen fiber recruitment response contrary to that of the pulmonary arteries [16]. It is not clear what the reason behind this is. Likely the cross-linking, both between and within a fiber in the elastin network, is different in order to fulfill the different functions for each tissue. To fit the low-stress region, an exponential or power law is necessary. We chose the power law so we can constrain the order of the nonlinearity. This may result in some error when predicting and extrapolating past the range of the data. However, the stress contribution of elastin peaks at around 5–15 kPa at maximum stretch, which is much less that of the collagen (Fig. 2.4a), so this should not be a significant effect. The collagen also essentially functions as a stopper, putting a constraint on the maximum extension of the leaflets (especially in the circumferential direction). For this reason, the material model of the elastin this should not be a problem for the predictive capabilities of the model in most applications.

Another interesting result is that the exponents of the elastin model differed between the layers and between the leaflets. This may be evidence of residual stress or strain between the layers. For the aortic valve, Stella and Sacks [61] noted that the elastin dominant ventricularis of the leaflet contracted by 10.9% and 8.2% in the radial

and circumferential direction while the collagen dominant fibrosa elongated by 28.2% and 4.8% in the radial and circumferential direction after layer separation. Similar effect likely exists in the MV and the additional strain will result in a higher apparent stiffness due to the nonlinearity in the stress-strain response. Thus the difference in the atrialis and ventricular of each leaflet may, at least in part, be due to this reason. It is interesting that the elastin in the anterior leaflet is significantly stiffer in the circumferential direction compared to that of the posterior leaflet, while in the radial direction it was the opposite. This corroborates with physical observations where the ventricularis in the posterior leaflet was much smaller compared to the anterior leaflet; sometimes nearly nonexistent. Again, this may be a product of the motion of the leaflets when closing.

2.4.6 Layer structure and function

In the MV, the anterior leaflet extends to meet the posterior leaflet, while the posterior expands much less in comparison [1, 49]. In order to accomplish this, the radial direction of the anterior leaflet needs to be able to extend significantly, while the circumferential direction needs to be able to maintain its integrity as it meets the posterior leaflet. There are a number of ways in which collagenous tissue have adapted to increase extensibility. The most common way is through adjustment in the crimping of the collagen fibers. However, once fiber recruitment is initiated, the tangent modulus increases rapidly, limiting further extension. A second method is through the rotation of fiber ensembles. As the ratio of radial to circumferential stretch increases, this induces a rotation of all fibers toward the radial direction. The overall effect is similar to recruitment due to crimping, but the tangent modulus increases more gradually in comparison. Intriguingly, this adaptation is seen in the MV leaflets. For both leaflets, collagen is mostly present in the fibrosa (Fig. 2.2).

This results in the majority of collagen fibers being circumferentially aligned. Rather than having independent families of fibers each dictating the mechanical response of each direction, this is highly coupled (Fig. 2.11), with the bulk of the stress in the radial direction coming from the circumferential splay. However, the collagen fibers in atrialis are still needed for additional support. This makes the width of the fibers splay dictate the resulting response. In the anterior leaflet, the elastin and collagen fiber splays are narrower (Fig. 2.9), thus increasing the radial extensibility. Comparatively, the wider splay in the posterior leaflet produces a slightly more isotropic response resulting in smaller radial extension. Additionally, collagen fibers are also recruited faster in the anterior leaflet to further constrain the circumferential extension. Overall, collagen primarily functions to limit extension, whereas elastin determines the motion of the valve in the low-stress region. This is perhaps why the radial direction of the anterior leaflet has the lowest stiffness, which allows for the fastest rate of extension. Interestingly, elastin is also the stiffest in the circumferential direction of the anterior leaflet, following a similar trend to the collagen. The elastin in the posterior leaflet is likewise more isotropic than that of the anterior.

2.4.7 Model predictive capabilities

Overall the model demonstrated a very good ability to predict the extra physiological protocols (Fig. 2.4c & d). Using the correct mass fractions, for the ratio of collagen in the fibrosa vs the atrialis in particular, was especially important for accurately predicting these extra-physiological protocols. For predictive purposes, more leeway can be given for the mass fraction of elastin. Since the layers are treated completely independent of each other (not sharing a single modulus), errors in the mass fraction are absorbed by the modulus.

2.4.8 Limitations

While every effort was made to ensure tissue viability, all studies were performed under in vitro conditions. While there appear to be differences between the in vivo properties of MV anterior leaflet [33] and the passive properties measured in an in vitro setting [22, 46]. The mechanism behind these estimated differences remains unknown. It is unlikely to be due to the contractile forces exerted by the MV interstitial cells on the surrounding ECM, which appears to be small [3]. Residual stress may be involved, as studies have shown that the MV leaflets are also under significant residual strain [1]. Additionally, the viscoelastic properties of the MV were not considered in this model. However, we have found that the leaflet tissues are essentially functionally elastic [23, 22]. Direct validation of the individual layer stress contributions is not currently available, as it requires the separation of the individual layers, which in itself is a complex task. Additionally, a more sophisticated model is also necessary to take into account the effect of residual strain on the mechanical response. Nevertheless, we have shown that our models have good predictive capabilities for the mechanical response and fiber orientations distributions, and are validated using SAXS studies. Overall, this model is a faithful representation of the structural function relationship of MV tissues.

2.5 Conclusions and future directions

In this study, we developed a novel fiber- and layer-specific structurally-driven constitutive model of the MV leaflets. The model incorporated fiber ODFs for collagen and elastin, collagen fiber recruitment, and related fiber-level mechanical phenomena. The model was validated by simulating the SAXS experiments and compared against the measured response. The results were consistent and show that the model correctly

predicted the collagen fibril deformations measured by SAXS. Furthermore, the material parameters estimated were also consistent under EB strain testing and uniaxial testing. Thus the model is validated both via microscopic and meso-scale measurement. For the MV leaflets, we determined an effective modulus of 132.5–167.3 MPa for the collagen fibers which matches well with existing literature. This result suggests the tissue structure is an important predictor of leaflet function, where the fiber ODF and recruitment couples to determine the mechanical response of each leaflet. Moreover, fiber ODF tends to be narrower and the recruitment tends to happen over a smaller strain range to allow for a larger extension of the anterior leaflets while maintaining tensile strength. Overall, the model shows very good predictive ability and hopes to help in producing more accurate simulations of MV behavior in vivo, with the ultimate goal in improving long-term durability of MV repair.

This model may also serve as a baseline for the study of disease and aging valvular tissues. Pathological change to biological tissue is a very complex topic. In addition to the variety of pathological conditions, the changes due to a common disorder will be different among individuals. There is not yet sufficient data to fully understand and predict the mechanical changes. However, this model can serve as a starting point for analyzing the underlying changes due to pathological conditions, when the requisite data become available.

We should note that the utility of the present model lies in the accuracy and details of how the various aspects of the MV tissue coordinate to produce the bulk-level response. This is not only important to ECM mechanics but also coupling to the interstitial cell (MVIC) population. We have recently shown that simulated MVIC moduli for the four layers were found to be all within a narrow range of 4.71–5.35 kPa, suggesting that MVIC deformation is primarily controlled by each tissue layer's

respective structure and mechanical behavior rather than the intrinsic MVIC stiffness [39]. This novel result further suggests that while the MVICs may be phenotypically similar throughout the leaflet, they experience layer-specific mechanical stimulatory inputs due to distinct extracellular matrix architecture and mechanical behaviors of the four MV leaflet tissue layers. This also suggests that MVICs may behave in a layer-specific manner in response to mechanical stimuli in both normal and surgically modified MVs. Development of detailed layer-specific models, such as the one presented herein, will clearly aid in further our understanding of these phenomena. However, for computational implementation, a multi-scale approach [37] will likely be needed to make the current implementation computationally tractable.

Nomenclature

Key Terms

MV	Mitral valve
PG	Proteoglycan
GAG	Glycosaminoglycans
$SAXS$	Small angle X-ray scattering
SHG	Second harmonic generation
EB	Equibiaxial
ODF	Orientation distribution function
ens	Ensemble

Symbols

$\mathbf{F}$	Deformation gradient tensor
$\mathbf{E}$	Green-Lagrange strain tensor
$\mathbf{P}$	1st Piola Kirchhoff stress tensor
$\mathbf{S}$	2nd Piola Kirchhoff stress tensor
$\mathbf{C}$	Right Cauchy Green strain tensor
$\mathbf{n}_0$	Orientation vector
λ	Stretch
λ_s	Slack Stretch
λ_t	True fiber stretch
E_s	Slack stretch
ϵ_D	D-period strain of the collagen fiber
Ψ	Strain energy density
ϕ	Mass fraction
D	Distribution of slack strains for fiber recruitment

Γ	Fiber orientation distribution
η	Modulus, subscript for elastin, collagen and matrix
μ_θ	Mean circumferential orientation
σ_θ	Standard deviation of the orienation distribution function
μ_r	Mean of the recruitment distribution function
σ_r	Standard deviation of the recruitment distribution function
E_{lb}	Lower bound of the recruitment distribution function
E_{ub}	Upper bound of the recruitment distribution function
d	Exponent parameter for the elastin ensemble

Chapter Bibliography

[1] Rouzbeh Amini, Chad E. Eckert, Kevin Koomalsingh, Jeremy McGarvey, Masahito Minakawa, Joseph H. Gorman, Robert C. Gorman, and Michael S. Sacks. On the in vivo deformation of the mitral valve anterior leaflet: effects of annular geometry and referential configuration. *Annals of Biomedical Engineering*, 40(7):1455–1467, feb 2012. ISSN 1573-9686 (Electronic) 0090-6964 (Linking). doi: 10.1007/s10439-012-0524-5. URL `http://www.ncbi.nlm.nih.gov/pubmed/22327292`.

[2] K. L. Billiar and M. S. Sacks. Biaxial mechanical properties of the natural and glutaraldehyde treated aortic valve cusp: part I experimental results. *Journal of Biomechanical Engineering*, 122(1):23–30, February 2000. ISSN 0148-0731 (Print) 0148-0731 (Linking). doi: 10.1115/1.429624. URL `http://www.ncbi.nlm.nih.gov/pubmed/10790826`.

[3] Rachel M. Buchanan and Michael S. Sacks. Interlayer micromechanics of the aortic heart valve leaflet. *Biomechanics and Modeling in Mechanobiology*, 13(4):813–826, nov 2013. ISSN 1617-7940 (Electronic) 1617-7940 (Linking). doi: 10.1007/s10237-013-0536-6. URL `http://www.ncbi.nlm.nih.gov/pubmed/24292631`.

[4] Markus J. Buehler. Atomistic and continuum modeling of mechanical properties of collagen: elasticity, fracture, and self-assembly. *Journal of Materials Research*, 21(08):1947–1961, aug 2006. ISSN 2044-5326. doi: 10.1557/jmr.2006.0236. URL `http://dx.doi.org/10.1557/jmr.2006.0236`.

[5] F. Cacho, P.J. Elbischger, J.F. Rodriguez, M. Doblare, and G.A. Holzapfel. A constitutive model for fibrous tissues considering collagen fiber crimp. *International Journal of Non-Linear Mechanics*, 42(2):391–402, mar 2007.

ISSN 0020-7462. doi: 10.1016/j.ijnonlinmec.2007.02.002. URL http://www.sciencedirect.com/science/article/pii/S0020746207000558.

[6] Christopher A. Carruthers, Bryan Good, Antonio D'Amore, Jun Liao, Rouzbeh Amini, Simon C. Watkins, and Michael S. Sacks. Alterations in the microstructure of the anterior mitral valve leaflet under physiological stress. In *ASME 2012 Summer Bioengineering Conference, Parts A and B*, pages 227–228. American Society of Mechanical Engineers, jun 2012. doi: 10.1115/sbc2012-80820.

[7] John A. Chapman and David J. S. Hulmes. Electron microscopy of the collagen fibril. In A. Ruggeri and P. M. Motto, editors, *Ultrastructure of the Connective Tissue Matrix*, pages 1–33. Springer US, Boston, 1984. doi: 10.1007/978-1-4613-2831-5_1.

[8] Huan Chen, Yi Liu, Xuefeng Zhao, Yoram Lanir, and Ghassan S. Kassab. A micromechanics finite-strain constitutive model of fibrous tissue. *Journal of the Mechanics and Physics of Solids*, 59(9):1823–1837, sep 2011. ISSN 0022-5096 (Electronic) 0022-5096 (Linking). doi: 10.1016/j.jmps.2011.05.012. URL http://www.ncbi.nlm.nih.gov/pubmed/21927506.

[9] T. Courtney, M. S. Sacks, J. Stankus, J. Guan, and W. R. Wagner. Design and analysis of tissue engineering scaffolds that mimic soft tissue mechanical anisotropy. *Biomaterials*, 27(19):3631–8, July 2006. ISSN 0142-9612 (Print). URL http://www.ncbi.nlm.nih.gov/entrez/query.fcgi?cmd=Retrieve&db=PubMed&dopt=Citation&list_uids=16545867.

[10] L. Debelle and A.M. Tamburro. Elastin: molecular description and function. *The International Journal of Biochemistry & Cell Biology*, 31(2):261–272, feb

1999. doi: 10.1016/s1357-2725(98)00098-3. URL http://www.ncbi.nlm.nih.gov/htbin-post/Entrez/query?db=m&form=6&dopt=r&uid=10216959.

[11] Laurent Debelle and Alain J.P. Alix. The structures of elastins and their function. *Biochimie*, 81(10):981 – 994, 1999. ISSN 0300-9084. doi: https://doi.org/10.1016/S0300-9084(99)00221-7. URL http://www.sciencedirect.com/science/article/pii/S0300908499002217.

[12] Chad E. Eckert, Brett Zubiate, Mathieu Vergnat, Joseph H. Gorman, Robert C. Gorman, and Michael S. Sacks. In vivo dynamic deformation of the mitral valve annulus. *Annals of Biomedical Engineering*, 37 (9):1757–1771, jul 2009. ISSN 1521-6047 (Electronic). doi: 10.1007/s10439-009-9749-3. URL http://www.ncbi.nlm.nih.gov/entrez/query.fcgi?cmd=Retrieve&db=PubMed&dopt=Citation&list_uids=19585241.

[13] Chad E. Eckert, Rong Fan, Brandon Mikulis, Mathew Barron, Christopher A. Carruthers, Vincent M. Friebe, Naren R. Vyavahare, and Michael S. Sacks. On the biomechanical role of glycosaminoglycans in the aortic heart valve leaflet. *Acta Biomaterialia*, 9(1):4653–4660, jan 2013. ISSN 1878-7568 (Electronic) 1742-7061 (Linking). doi: 10.1016/j.actbio.2012.09.031. URL http://www.ncbi.nlm.nih.gov/pubmed/23036945.

[14] S.J Eppell, B.N Smith, H Kahn, and R Ballarini. Nano measurements with micro-devices: mechanical properties of hydrated collagen fibrils. *Journal of The Royal Society Interface*, 3(6):117–121, feb 2006. doi: 10.1098/rsif.2005.0100. URL http://rsif.royalsocietypublishing.org/content/3/6/117.abstract.

[15] Rong Fan and Michael S. Sacks. Simulation of planar soft tissues using a structural constitutive model: finite element implementation and validation. *Journal*

of Biomechanics, 47(9):2043–2054, jun 2014. doi: 10.1016/j.jbiomech.2014.03.014.

[16] Bahar Fata, Will Zhang, Rouzbeh Amini, and Michael S. Sacks. Insights into regional adaptations in the growing pulmonary artery using a meso-scale structural model: effects of ascending aorta impingement. *Journal of Biomechanical Engineering*, 136(2):021009–021009–13, feb 2014. ISSN 0148-0731. doi: 10.1115/1.4026457. URL `http://dx.doi.org/10.1115/1.4026457`.

[17] W. Flameng, P. Herijgers, and K. Bogaerts. Recurrence of mitral valve regurgitation after mitral valve repair in degenerative valve disease. *ACC Current Journal Review*, 12(4):85, jul 2003. doi: 10.1016/s1062-1458(03)00323-4. URL `http://www.ncbi.nlm.nih.gov/entrez/query.fcgi?cmd=Retrieve&db=PubMed&dopt=Citation&list_uids=12668494`.

[18] Willem Flameng, Bart Meuris, Paul Herijgers, and Marie-Christine Herregods. Durability of mitral valve repair in Barlow disease versus fibroelastic deficiency. *The Journal of Thoracic and Cardiovascular Surgery*, 135(2):274–282, feb 2008. ISSN 0022-5223. doi: 10.1016/j.jtcvs.2007.06.040.

[19] K. Gelse, E. Poschl, and T. Aigner. Collagens–structure, function, and biosynthesis. *Advanced Drug Delivery Reviews*, 55(12):1531–1546, nov 2003. ISSN 0169-409X (Print). doi: 10.1016/j.addr.2003.08.002. URL `http://www.ncbi.nlm.nih.gov/entrez/query.fcgi?cmd=Retrieve&db=PubMed&dopt=Citation&list_uids=14623400`.

[20] Eileen Gentleman, Andrea N. Lay, Darryl A. Dickerson, Eric A. Nauman, Glen A. Livesay, and Kay C. Dee. Mechanical characterization of collagen fibers and scaffolds for tissue engineering. *Biomaterials*, 24(21):3805–3813, sep

2003. ISSN 0142-9612. doi: 10.1016/s0142-9612(03)00206-0. URL http://www.sciencedirect.com/science/article/pii/S0142961203002060.

[21] A. S. Go, D. Mozaffarian, V. L. Roger, E. J. Benjamin, J. D. Berry, M. J. Blaha, S. Dai, E. S. Ford, C. S. Fox, S. Franco, H. J. Fullerton, C. Gillespie, S. M. Hailpern, J. A. Heit, V. J. Howard, M. D. Huffman, S. E. Judd, B. M. Kissela, S. J. Kittner, D. T. Lackland, J. H. Lichtman, L. D. Lisabeth, R. H. Mackey, D. J. Magid, G. M. Marcus, A. Marelli, D. B. Matchar, D. K. McGuire, E. R. Mohler, C. S. Moy, M. E. Mussolino, R. W. Neumar, G. Nichol, D. K. Pandey, N. P. Paynter, M. J. Reeves, P. D. Sorlie, J. Stein, A. Towfighi, T. N. Turan, S. S. Virani, N. D. Wong, D. Woo, and M. B. Turner and. Heart disease and stroke statistics–2014 update: a report from the American Heart Association. *Circulation*, 129 (3):e28–e292, dec 2013. ISSN 0009-7322. doi: 10.1161/01.cir.0000441139.02102.80. URL http://graphics.tx.ovid.com/ovftpdfs/FPDDNCGCFADEAN00/fs046/ovft/live/gv025/00003017/00003017-201401210-00019.pdf.

[22] Jonathan S. Grashow, Michael S. Sacks, Jun Liao, and Ajit P. Yoganathan. Planar biaxial creep and stress relaxation of the mitral valve anterior leaflet. *Annals of Biomedical Engineering*, 34(10): 1509–1518, October 2006. ISSN 0090-6964 (Print). doi: 10.1007/s10439-006-9183-8. URL http://www.ncbi.nlm.nih.gov/entrez/query.fcgi?cmd=Retrieve&db=PubMed&dopt=Citation&list_uids=17016761.

[23] Jonathan S. Grashow, Ajit P. Yoganathan, and Michael S. Sacks. Biaxial stress-stretch behavior of the mitral valve anterior leaflet at physiologic strain rates. *Annals of Biomedical Engineering*, 34(2):315–325, feb 2006. doi: 10.1007/s10439-005-9027-y. URL http://www.ncbi.nlm.nih.gov/entrez/query.fcgi?cmd=Retrieve&db=PubMed&dopt=Citation&list_uids=16450193.

[24] Rafael Grytz and Günther Meschke. Constitutive modeling of crimped collagen fibrils in soft tissues. *Journal of the Mechanical Behavior of Biomedical Materials*, 2(5):522–533, October 2009. ISSN 1751-6161. doi: 10.1016/j.jmbbm.2008.12.009. URL http://www.sciencedirect.com/science/article/pii/S1751616108001227.

[25] Kristi A. Hansen, Jeffrey A. Weiss, and Jennifer K. Barton. Recruitment of tendon crimp with applied tensile strain. *Journal of Biomechanical Engineering*, 124(1):72–7, February 2002. doi: 10.1115/1.1427698. URL http://www.ncbi.nlm.nih.gov/entrez/query.fcgi?cmd=Retrieve&db=PubMed&dopt=Citation&list_uids=11871607.

[26] Michael R. Hill, Xinjie Duan, Gregory A. Gibson, Simon Watkins, and Anne M. Robertson. A theoretical and non-destructive experimental approach for direct inclusion of measured collagen orientation and recruitment into mechanical models of the artery wall. *Journal of Biomechanics*, 45(5):762–771, March 2012. ISSN 1873-2380 (Electronic) 0021-9290 (Linking). doi: 10.1016/j.jbiomech.2011.11.016. URL http://www.ncbi.nlm.nih.gov/pubmed/22305290.

[27] A.J. Hodge and J.A. Petruska. Recent studies with the electron microscope on ordered aggregates of the tropocollagen molecules. *Aspects of protein structure*, pages 289–300, 1963. URL https://ci.nii.ac.jp/naid/10027103318/en/.

[28] Yaniv Hollander, David Durban, Xiao Lu, Ghassan S. Kassab, and Yoram Lanir. Constitutive modeling of coronary arterial media–comparison of three model classes. *Journal of Biomechanical Engineering*, 133(6):061008, June 2011. ISSN 1528-8951 (Electronic) 0148-0731 (Linking). doi: 10.1115/1.4004249. URL http://www.ncbi.nlm.nih.gov/pubmed/21744928.

[29] JD Humphrey and M Epstein. Cardiovascular solid mechanics: cells, tissues, and organs. *Applied Mechanics Reviews*, 55(5):B103, 2002. doi: 10.1115/1.1497492.

[30] Jorge H. Jimenez, Shasan W. Liou, Muralidhar Padala, Zhaoming He, Michael Sacks, Robert C. Gorman, Joseph H. Gorman, and Ajit P. Yoganathan. A saddle-shaped annulus reduces systolic strain on the central region of the mitral valve anterior leaflet. *The Journal of Thoracic and Cardiovascular Surgery*, 134(6):1562–1568, dec 2007. ISSN 1097-685X (Electronic) 0022-5223 (Linking). doi: 10.1016/j.jtcvs.2007.08.037. URL `http://www.ncbi.nlm.nih.gov/pubmed/18023684`.

[31] Tsuyoshi Kaneko and Lawrence H Cohn. Mitral valve repair. *Circulation Journal*, 78(3):560–566, 2014. ISSN 1346-9843. doi: 10.1253/circj.cj-14-0069.

[32] J. Kastelic, I. Palley, and E. Baer. A structural mechanical model for tendon crimping. *Journal of Biomechanics*, 13(10):887–893, jan 1980. ISSN 0021-9290 (Print). doi: 10.1016/0021-9290(80)90177-3. URL `http://www.ncbi.nlm.nih.gov/entrez/query.fcgi?cmd=Retrieve&db=PubMed&dopt=Citation&list_uids=7462263`.

[33] Gaurav Krishnamurthy, Daniel B. Ennis, Akinobu Itoh, Wolfgang Bothe, Julia C. Swanson, Matts Karlsson, Ellen Kuhl, D. Craig Miller, and Neil B. Ingels. Material properties of the ovine mitral valve anterior leaflet in vivo from inverse finite element analysis. *American Journal of Physiology-Heart and Circulatory Physiology*, 295(3):H1141–H1149, September 2008. ISSN 0363-6135 (Print) 0363-6135 (Linking). doi: 10.1152/ajpheart.00284.2008. URL `http://www.ncbi.nlm.nih.gov/pubmed/18621858`.

[34] Y. Lanir. A structural theory for the homogeneous biaxial stress-strain relation-

ships in flat collagenous tissues. *Journal of Biomechanics*, 12(6):423–436, jan 1979. doi: 10.1016/0021-9290(79)90027-7.

[35] Y. Lanir. Constitutive equations for fibrous connective tissues. *Journal of Biomechanics*, 16(1):1–12, jan 1983. doi: 10.1016/0021-9290(83)90041-6.

[36] Chung-Hao Lee, Rouzbeh Amini, Robert C. Gorman, Joseph H. Gorman, and Michael S. Sacks. An inverse modeling approach for stress estimation in mitral valve anterior leaflet valvuloplasty for in-vivo valvular biomaterial assessment. *Journal of Biomechanics*, 47(9):2055–2063, June 2014. ISSN 1873-2380 (Electronic) 0021-9290 (Linking). doi: 10.1016/j.jbiomech.2013.10.058. URL `http://www.ncbi.nlm.nih.gov/pubmed/24275434`.

[37] Chung-Hao Lee, Rouzbeh Amini, Yusuke Sakamoto, Christopher A. Carruthers, Ankush Aggarwal, Robert C. Gorman, Joseph H. Gorman, and Michael S. Sacks. Mitral valves: a computational framework. In *Multiscale Modeling in Biomechanics and Mechanobiology*, pages 223–255. Springer London, oct 2014. ISBN 1-4471-6598-5. doi: 10.1007/978-1-4471-6599-6_10.

[38] Chung-Hao Lee, Christopher A. Carruthers, Salma Ayoub, Robert C. Gorman, Joseph H. Gorman, and Michael S. Sacks. Quantification and simulation of layer-specific mitral valve interstitial cells deformation under physiological loading. *Journal of Theoretical Biology*, 373:26–39, may 2015. doi: 10.1016/j.jtbi.2015.03.004.

[39] Chung-Hao Lee, Jean-Pierre Rabbah, Ajit P. Yoganathan, Robert C. Gorman, Joseph H. Gorman, and Michael S. Sacks. On the effects of leaflet microstructure and constitutive model on the closing behavior of the mitral valve. *Biomechanics and Modeling in Mechanobiology*, 14(6):1281–1302, May 2015. ISSN 1617-7940

(Electronic) 1617-7940 (Linking). doi: 10.1007/s10237-015-0674-0. URL http://www.ncbi.nlm.nih.gov/pubmed/25947879.

[40] Chung-Hao Lee, Will Zhang, Jun Liao, Christopher A. Carruthers, Jacob I. Sacks, and Michael S. Sacks. On the presence of affine fibril and fiber kinematics in the mitral valve anterior leaflet. *Biophysical Journal*, 108(8):2074–2087, April 2015. ISSN 1542-0086 (Electronic) 0006-3495 (Linking). doi: 10.1016/j.bpj.2015.03.019. URL http://www.ncbi.nlm.nih.gov/pubmed/25902446.

[41] S. Leikin, V. A. Parsegian, W.-H. Yang, and G. E. Walrafen. Raman spectral evidence for hydration forces between collagen triple helices. *Proceedings of the National Academy of Sciences*, 94(21):11312–11317, October 1997. doi: 10.1073/pnas.94.21.11312. URL http://www.pnas.org/content/94/21/11312.abstract.

[42] Jun Liao, Lin Yang, Jonathan Grashow, and Michael S. Sacks. The relation between collagen fibril kinematics and mechanical properties in the mitral valve anterior leaflet. *Journal of Biomechanical Engineering*, 129(1):78–87, 2007. ISSN 0148-0731 (Print). doi: 10.1115/1.2401186. URL http://www.ncbi.nlm.nih.gov/entrez/query.fcgi?cmd=Retrieve&db=PubMed&dopt=Citation&list_uids=17227101.

[43] Y. Lis, M. C. Burleigh, D. J. Parker, A. H. Child, J. Hogg, and M. J. Davies. Biochemical characterization of individual normal, floppy and rheumatic human mitral valves. *Biochemical Journal*, 244(3):597–603, jun 1987. doi: 10.1042/bj2440597. URL http://www.ncbi.nlm.nih.gov/entrez/query.fcgi?cmd=Retrieve&db=PubMed&dopt=Citation&list_uids=3446179.

[44] Joshua J. Lovekamp, Dan T. Simionescu, Jeremy J. Mercuri, Brett Zubiate, Michael S. Sacks, and Narendra R. Vyavahare. Stability and function of glycosaminoglycans in porcine bioprosthetic heart valves. *Biomaterials.*, 27(8):1507–1518, March 2006. ISSN 0142-9612. doi: 10.1016/j.biomaterials.2005.08.003. URL http://www.sciencedirect.com/science/article/pii/S0142961205007702.

[45] Feroze Mahmood, Balachundhar Subramaniam, Joseph H. Gorman, Robert M. Levine, Robert C. Gorman, Andrew Maslow, Peter J. Panzica, Robert M. Hagberg, Swaminathan Karthik, and Kamal R. Khabbaz. Three-dimensional echocardiographic assessment of changes in mitral valve geometry after valve repair. *The Annals of Thoracic Surgery*, 88(6):1838–1844, dec 2009. ISSN 1552-6259 (Electronic) 0003-4975 (Linking). doi: 10.1016/j.athoracsur.2009.07.007. URL http://www.ncbi.nlm.nih.gov/pubmed/19932245.

[46] K. May-Newman and F. C. Yin. Biaxial mechanical behavior of excised porcine mitral valve leaflets. *American Journal of Physiology-Heart and Circulatory Physiology*, 269(4):H1319–H1327, oct 1995. doi: 10.1152/ajpheart.1995.269.4.h1319. URL http://www.ncbi.nlm.nih.gov/htbin-post/Entrez/query?db=m&form=6&dopt=r&uid=0007485564.

[47] Muralidhar Padala, Ross A. Hutchison, Laura R. Croft, Jorge H. Jimenez, Robert C. Gorman, Joseph H. Gorman, Michael S. Sacks, and Ajit P. Yoganathan. Saddle shape of the mitral annulus reduces systolic strains on the P2 segment of the posterior mitral leaflet. *The Annals of Thoracic Surgery*, 88(5):1499–1504, nov 2009. ISSN 1552-6259 (Electronic) 0003-4975 (Linking). doi: 10.1016/j.athoracsur.

2009.06.042. URL http://www.ncbi.nlm.nih.gov/entrez/query.fcgi?cmd=Retrieve&db=PubMed&dopt=Citation&list_uids=19853100.

[48] David A.D. Parry. The molecular and fibrillar structure of collagen and its relationship to the mechanical properties of connective tissue. *Biophysical Chemistry*, 29(1-2):195–209, feb 1988. doi: 10.1016/0301-4622(88)87039-x. URL http://www.ncbi.nlm.nih.gov/entrez/query.fcgi?cmd=Retrieve&db=PubMed&dopt=Citation&list_uids=3282560.

[49] Manuel K. Rausch, Wolfgang Bothe, John-Peder Escobar Kvitting, Serdar Göktepe, D. Craig Miller, and Ellen Kuhl. In vivo dynamic strains of the ovine anterior mitral valve leaflet. *Journal of Biomechanics*, 44(6):1149–1157, apr 2011. ISSN 1873-2380 (Electronic) 0021-9290 (Linking). doi: 10.1016/j.jbiomech.2011.01.020. URL http://www.ncbi.nlm.nih.gov/pubmed/21306716.

[50] Michael S. Sacks. Incorporation of experimentally-derived fiber orientation into a structural constitutive model for planar collagenous tissues. *Journal of Biomechanical Engineering*, 125(2):280–7, April 2003. doi: 10.1115/1.1544508. URL http://www.ncbi.nlm.nih.gov/entrez/query.fcgi?cmd=Retrieve&db=PubMed&dopt=Citation&list_uids=12751291.

[51] Michael S. Sacks and Wei Sun. Multiaxial mechanical behavior of biological materials. *Annual Review of Biomedical Engineering*, 5(1):251–284, aug 2003. doi: 10.1146/annurev.bioeng.5.011303.120714. URL http://www.ncbi.nlm.nih.gov/entrez/query.fcgi?cmd=Retrieve&db=PubMed&dopt=Citation&list_uids=12730082.

[52] Michael S. Sacks, David B. Smith, and Erik D. Hiester. A small angle light scattering device for planar connective tissue microstructural analysis. *Annals*

of Biomedical Engineering, 25(4):678–689, jul 1997. ISSN 1573-9686. doi: 10.1007/bf02684845. URL https://doi.org/10.1007/BF02684845.

[53] Michael S. Sacks, Yoshiharu Enomoto, Jeffrey R. Graybill, W. David Merryman, Ahmad Zeeshan, Ajit P. Yoganathan, Robert J. Levy, Robert C. Gorman, and Joseph H. Gorman. In-vivo dynamic deformation of the mitral valve anterior leaflet. *The Annals of Thoracic Surgery*, 82(4):1369–1377, oct 2006. ISSN 1552-6259 (Electronic). doi: 10.1016/j.athoracsur.2006.03.117. URL http://www.ncbi.nlm.nih.gov/entrez/query.fcgi?cmd=Retrieve&db=PubMed&dopt=Citation&list_uids=16996935.

[54] Michael S. Sacks, W. David Merryman, and David E. Schmidt. On the biomechanics of heart valve function. *Journal of Biomechanics*, 42(12):1804–1824, aug 2009. ISSN 1873-2380 (Electronic). doi: 10.1016/j.jbiomech.2009.05.015. URL http://www.ncbi.nlm.nih.gov/entrez/query.fcgi?cmd=Retrieve&db=PubMed&dopt=Citation&list_uids=19540499.

[55] MS Sacks. Biaxial mechanical evaluation of planar biological materials. *J Elasticity*, 61:199–246, 2000.

[56] I. S. Salgo, J. H. Gorman, R. C. Gorman, B. M. Jackson, F. W. Bowen, T. Plappert, M. G. S. J. Sutton, and L. H. Edmunds. Effect of annular shape on leaflet curvature in reducing mitral leaflet stress. *Circulation*, 106(6):711–717, jul 2002. ISSN 0009-7322. doi: 10.1161/01.Cir.0000025426.39426.83. URL ://WOS:000177401700015.

[57] Naoki Sasaki and Shingo Odajima. Elongation mechanism of collagen fibrils and force-strain relations of tendon at each level of structural hierarchy. *Journal of Biomechanics*, 29(9):1131–1136, sep 1996. doi: 10.1016/0021-9290(96)00024-3.

[58] Naoki Sasaki and Singo Odajima. Stress-strain curve and Young's modulus of a collagen molecule as determined by the X-ray diffraction technique. *Journal of Biomechanics*, 29(5):655–658, may 1996. doi: 10.1016/0021-9290(95)00110-7.

[59] Michael Scott and Ivan Vesely. Aortic valve cusp microstructure: the role of elastin. *The Annals of Thoracic Surgery*, 60:S391–S394, aug 1995. doi: 10.1016/0003-4975(95)00263-k.

[60] Zhilei L. Shen, Mohammad Reza Dodge, Harold Kahn, Roberto Ballarini, and Steven J. Eppell. Stress-strain experiments on individual collagen fibrils. *Biophysical Journal*, 95(8):3956–3963, oct 2008. ISSN 0006-3495. doi: 10.1529/biophysj.107.124602. URL `http://www.sciencedirect.com/science/article/pii/S0006349508785345`.

[61] John A. Stella and Michael S. Sacks. On the biaxial mechanical properties of the layers of the aortic valve leaflet. *Journal of Biomechanical Engineering*, 129(5):757–66, 2007. ISSN 0148-0731 (Print) 0148-0731 (Linking). doi: 10.1115/1.2768111. URL `http://www.ncbi.nlm.nih.gov/entrez/query.fcgi?cmd=Retrieve&db=PubMed&dopt=Citation&list_uids=17887902`.

[62] G. I. Tseretely and O. I. Smirnova. DSC study of melting and glass transition in gelatins. *Journal of Thermal Analysis*, 38(5):1189–1201, may 1992. doi: 10.1007/bf01979179. URL `http://dx.doi.org/10.1007/BF01979179`.

[63] I. Vesely and W. J. Mako. Comparison of the compressive buckling of porcine aortic valve cusps and bovine pericardium. *The Journal of heart valve disease*, 7(1):34–39, January 1998. ISSN 0966-8519. URL `http://www.ncbi.nlm.nih.gov/entrez/query.fcgi?cmd=Retrieve&db=PubMed&dopt=Citation&list_uids=9502137`.

[64] Sarah M. Wells, Caitlin M. Pierlot, and Andrew D. Moeller. Physiological remodeling of the mitral valve during pregnancy. *American Journal of Physiology-Heart and Circulatory Physiology*, 303(7):H878–H892, oct 2012. ISSN 1522-1539 (Electronic) 0363-6135 (Linking). doi: 10.1152/ajpheart.00845.2011. URL http://www.ncbi.nlm.nih.gov/pubmed/22886410.

[65] Marco P.E. Wenger, Laurent Bozec, Michael A. Horton, and Patrick Mesquida. Mechanical properties of collagen fibrils. *Biophysical Journal*, 93(4):1255–1263, August 2007. ISSN 0006-3495. doi: 10.1529/biophysj.106.103192. URL http://www.sciencedirect.com/science/article/pii/S0006349507713838http://www.ncbi.nlm.nih.gov/pmc/articles/PMC1929027/pdf/1255.pdf.

[66] Lanti Yang, Kees O. van der Werf, Bart F.J.M. Koopman, Vinod Subramaniam, Martin L. Bennink, Pieter J. Dijkstra, and Jan Feijen. Micromechanical bending of single collagen fibrils using atomic force microscopy. *Journal of Biomedical Materials Research Part A*, 82A(1):160–168, 2007. ISSN 1552-4965. doi: 10.1002/jbm.a.31127. URL http://dx.doi.org/10.1002/jbm.a.31127http://onlinelibrary.wiley.com/doi/10.1002/jbm.a.31127/abstract.

[67] Lanti Yang, Carel F.C. Fitié, Kees O. van der Werf, Martin L. Bennink, Pieter J. Dijkstra, and Jan Feijen. Mechanical properties of single electrospun collagen type i fibers. *Biomaterials*, 29(8):955–962, mar 2008. doi: 10.1016/j.biomaterials.2007.10.058.

Chapter 3

Effect of exogenous cross-linking on the mechanical response of soft tissues[1]

Preface

Exogenous cross-linking of soft collagenous tissues is a common method for biomaterial development and medical therapies. It is an important part of the fabrication process of BHVs and significantly affects their mechanical properties. To enable improved applications through computational methods, physically realistic constitutive models are required. Yet, despite decades of research, development and clinical use, no such model exists. In this study, we develop the first rigorous full structural model (i.e. explicitly incorporating various features of the collagen fiber architecture) for exogenously cross-linked soft tissues. This was made possible, in part, with the use of native to cross-linked matched experimental datasets and an extension to the collagenous structural constitutive model so that the uncross-linked collagen fiber responses could be mapped to the cross-linked configuration. This allowed us to separate the effects of cross-linking from kinematic changes induced in the cross-linking process, which in turn allowed the non-fibrous tissue matrix component and the interaction effects to be identified. It was determined that the matrix

[1]**The work contained in this chapter was published as**: Sacks, M. S.; Zhang, W. & Wognum, S. A novel fiber-ensemble level constitutive model for exogenous cross-linked collagenous tissues Interface Focus, The Royal Society, 2016, 6, 20150090
The author contributed to: performing the research, model development, data analysis, coding development, and writing sections of the methods and results.

could be modeled as an isotropic material using a modified Yeoh model. The most novel findings of this study were that: (i) the effective collagen fiber modulus was unaffected by cross-linking and (ii) fiber-ensemble interactions played a large role in stress development, often dominating the total tissue response (depending on the stress component and loading path considered). An important utility of the present model is its ability to separate the effects of exogenous cross-linking on the fibers from changes due to the matrix. Applications of this approach include the utilization in the design of novel chemical treatments to produce specific mechanical responses and the study of fatigue damage in bioprosthetic heart valve biomaterials.

3.1 Introduction

The application of exogenous-cross-links (EXLs) to native or biologically derived soft collagenous tissues finds its way into a wide range of medical therapies and device applications, such as surgical biomaterials, modification of corneal tissues (using riboflavin/UVA) and vascular grafts. Perhaps the most mechanically demanding application is the so-called bioprosthetic heart valve (BHV), which is fabricated from several types of biologically derived soft collagenous tissue membranes. From a clinical perspective, BHVs have important advantages in that they do not require permanent anticoagulation therapy, operate noiselessly, and have blood flow characteristics similar to the native valve, and thus have become the dominant heart valve therapy worldwide [3, 55, 54]. However, BHV durability continues to remain limited to the range of 10–15 years, resulting from leaflet structural deterioration mediated by fatigue and/or tissue mineralization [64, 43]. In general, structural damage is a critical factor in BHV degeneration, and clearly implicates coupled material and design factors as major limiters to long-term durability [56, 53]. However, a major reason why advances in the use of cross-linked tissues in BHVs and other biomedical applications is a dearth of knowledge on how EXLs affect the underlying tissue structure and macroscopic mechanical behavior. Moreover, the integration of such information into truly predictive modeling cannot proceed without accurate constitutive models of the EXL tissues and the subsequent fatigue processes [45, 62].

The most common medical applications of cross-linked biologically-derived tissues are for dense collagenous tissues. Such tissues are typically composed of a dense, highly-organized network of type I collagen fibers, along with elastin, proteoglycans, glycosaminoglycans, cellular materials and a small amount of other fibrillar proteins. Type I collagen is the major determinant of its mechanical behavior [40, 17] and is

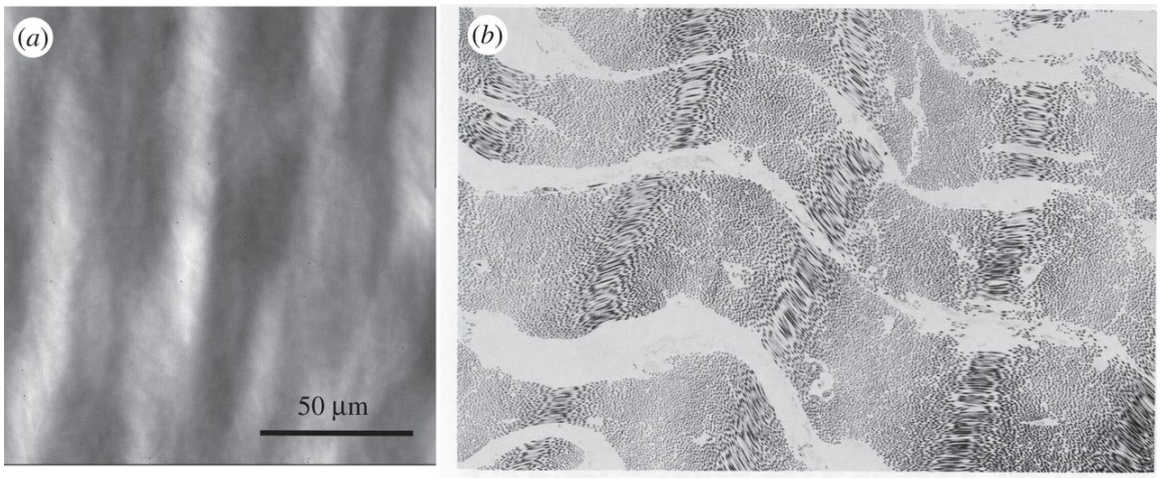

Figure 3.1: (a) Photomicrograph of native bovine pericardium showing the undulated collagen fibres (adapted from [45]). (b) TEM image also of native bovine pericardium clearly showing interrelationships between the undulated collagen fibres and the underlying fibril structures (magnification 4150×; adapted from [39]).

the major tissue component affected by EXLs. At the molecular level, tropocollagen molecules are composed of a triple helix of three alpha chains [40, 17] that arrange themselves into a quarter stacking array to form the collagen fibril [40, 17]. Collagen fibrils form the functional subunits of the collagen fibres, as described by the Hodge–Petruska model [40, 41], and then exhibit distinct large-scale structures (figure 3.1). Like the fibrils from which their functional properties are derived, collagen fibers exhibit high tensile but low flexural stiffness [49]. We note that there is no standard definition for a fiber and its relation to the fibril. They are very dependent on the specific tissues involved, and thus caution should always be exercised in the terminology used. In the mainstream tissue biomechanics literature, the fiber/fibril definition is often taken from the well-known work of Kastelic et al. [39], which focused on tendons. The pericardial tissues considered in this study clearly show fiber and fibril structures, including the fiber undulations commonly observed optically [58] (figure 3.1).

The fiber longitudinal/axial direction is the primary determinant of the stiffness of the tissue composite. Interestingly, collagen fibres typically have a stiffness of 1 GPa [58, 19, 13, 70] and extend by no more than 4–5%. To increase the tissue-level compliance, collagen fibers at the macroscopic scale are sinusoidally crimped [40]. Tissue-level stress will not occur until the fiber-level crimp has been straightened. Moreover, the distribution of fiber straightening strains is the mechanism of tissue nonlinearity at large strains [25, 47]. Thus, as in many other fields, the connection to the underlying structure can greatly inform our understanding of how collagenous tissues work and guide the development of mathematical models of their mechanical function.

While there is a wide range of application-specific chemical agents (e.g. riboflavin/UVA cross-linking for corneas), for mechanically-demanding and blood-contacting applications (e.g. BHVs) using collagenous tissues, an aqueous solution of glutaraldehyde (GLUT) is used. GLUT application is necessary to both biochemically and mechanically stabilize the tissue for in vivo use. During the cross-linking process GLUT rapidly permeates the tissue, with the cross-linking process largely complete within an hour and essentially stabilized by 24 hrs. Much of what we know about how GLUT EXLs alter the structures of collagenous tissues was reported by Nimni, Cheung and co-workers [10, 38, 9, 18, 6, 7, 8]. Briefly, GLUT reacts primarily with e-amino groups of lysyl residues in proteins, with Michael-addition reaction products of Schiff bases usually the final stable products. Based on the spectral characteristics and the molecular weights of the reaction products, it has been predicted that GLUT reacts with free amines to form an intermediate with a molecular weight of about 200 Da. The GLUT–polymer amine complex is self-limiting in size and can undergo internal rearrangement to become chemically inert. An increased

molecular length of GLUT polymers from the initial glutaraldehyde and lysyl-residue reaction is more likely than an increased number of cross-linked sites. Following free GLUT depletion by binding to reactive groups, additional GLUT molecules attached to already reacted molecules can give rise to larger GLUT polymers that are able to generate 'long-range cross-links' between further removed reactive sites (figure 3.2). It is apparent from a mechanical behavior perspective that GLUT-associated chemical cross-linking of the collagen structure and biochemistry can produce complex changes from the native state at the molecular, fibril, fiber and tissue levels.

To enable improved application of the use of EXL tissues in *in situ* treatment and prosthesis design, the development of physically realistic constitutive models is clearly required. In a previous work, a structural approach was used that incorporated experimentally measured angular distribution of collagen fibers and an assumed isotropic form for the EXL matrix [44]. Good agreement with the experimental data was observed, supporting the basic approach. An important utility of that early model was its ability to separate the effects of the fibers and matrix. However, it was only a first step; other factors such as bending rigidity of EXL fibers, fiber-fiber interactions, and fiber-matrix interactions were not considered. Moreover, the experimental data were reduced under the assumption of an isotropic Fung model; no rigorous investigation of the most appropriate form was undertaken.

The focus of the present work is to more fully investigate the underlying characteristics of the effects of EXLs on soft collagenous tissues and to use this information to develop a meso-scale (i.e. at the level of the fiber) structural constitutive model. In particular, we explored the following questions of the effects of EXLs on native collagenous tissues: (i) what are the effects on individual collagen fibres, (ii) what are the effects on single collagen fibre ensembles, (iii) are there interactions between fibre

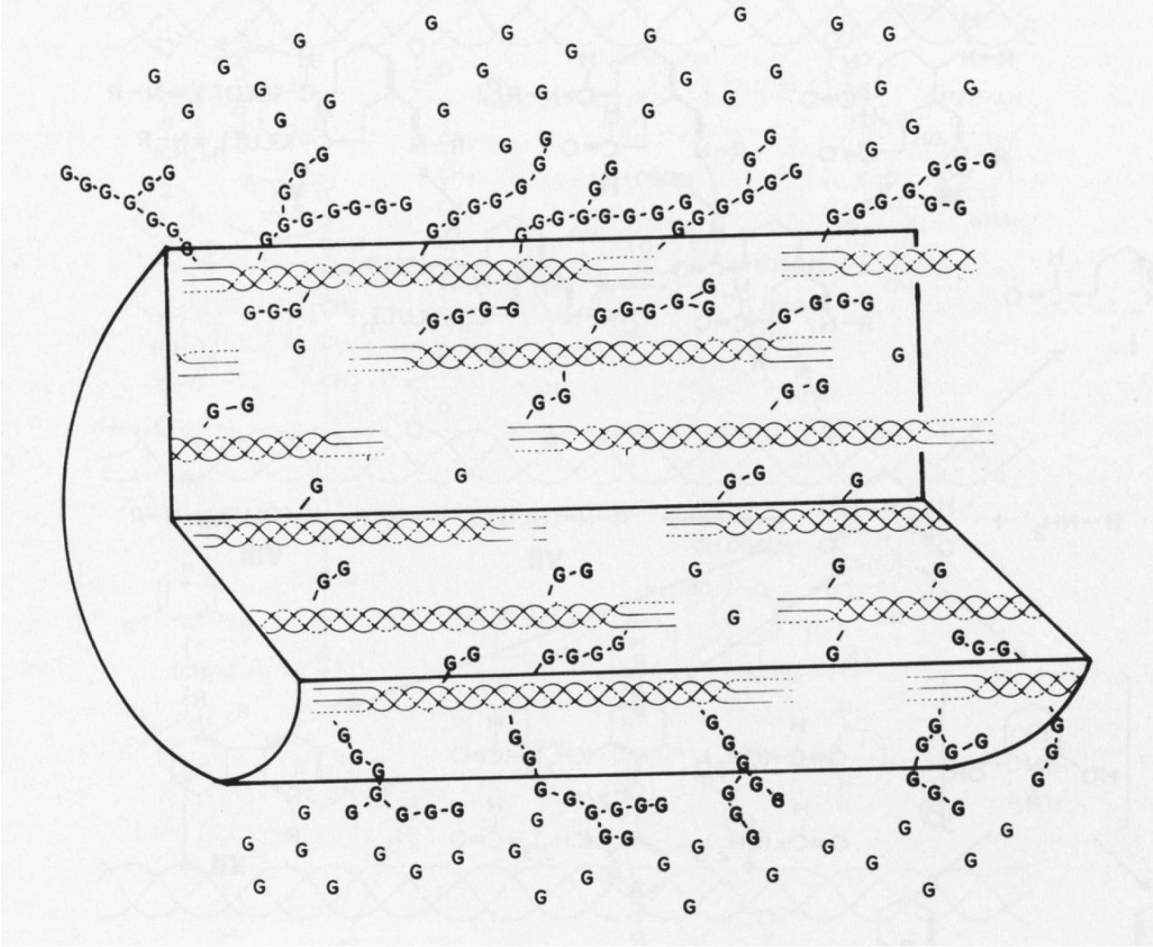

Figure 3.2: A diagram showing the interaction of tropocollagen molecules with glutaraldehyde and how cross-links can form. As the concentration of GLUT increases, the number of activation sites and chain length increases, and a limited number of cross-links will form between such molecules (magnification 4150×; adapted from [39]).

ensembles, and (iv) what is the functional form of the effective matrix response? This was done by exploiting experimental data from [60], wherein structurally controlled pericardial specimens were tested in the native state and then the EXL state. From these results, a comprehensive structural constitutive model was developed for EXL collagenous tissues and its predictive capability was evaluated. We note that, while we ultimately seek the micro-mechanical basis for macro-scale function, the present work is focused on a fiber-ensemble level approach.

3.2 Experimental methods and data post-processing

3.2.1 Tissue sources and experimental methods

Details of the tissue source, preparation, and mechanical evaluation have been previously presented [60]. Briefly, large sections of native bovine pericardium were stored in phosphate-buffered saline (pH 7.4) at $4°C$, then optically cleared using a hyperosmotic solution and the collagen fiber architecture (CFA) quantified. From the resulting CFA information, 25×25 mm test specimens exhibiting a high degree of structural uniformity suitable for biaxial testing were selected. The collagen fibre preferred and cross-preferred directions were aligned to the X_1-X_2 axes (figure 3.3). A total of five specimens were prepared in the native state.

Biaxial mechanical testing methods have been previously described in detail [46, 42]. Briefly, testing was performed with the specimen immersed in phosphate-buffered normal saline (pH 7.4) at room temperature. First, the Piola Kirchhoff stress $\mathbf{P}$ controlled test protocol was used, wherein the ratio of the normal stress components P_{11}:P_{22} was kept constant, with $P_{12} = P_{21} = 0$ and a maximum stress level of 1 MPa was used. Tissue deformations were quantified from the motion of four markers placed in the central third of the specimen, from which the deformation

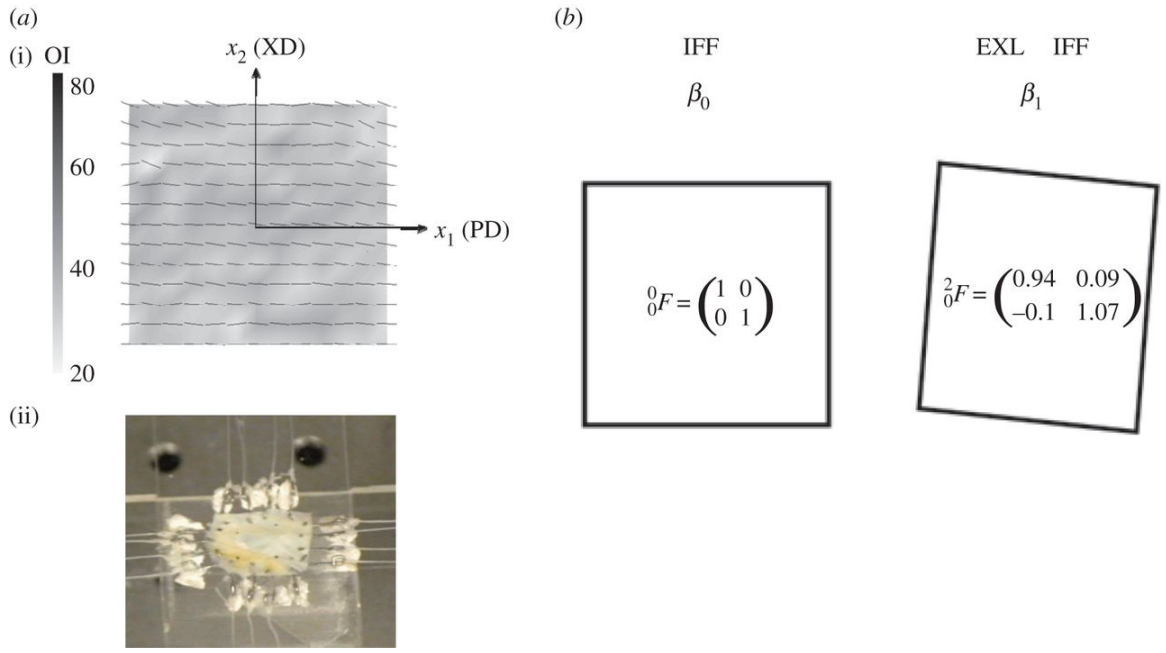

Figure 3.3: a)(i) Pericardial test specimen showing a high degree of fibre orientation and uniformity in preferred fibre directions, with the PD = X_1 and XD = X_2 axes defined, and (ii) a typical biaxial test specimen mounted on the device. (b) A schematic of the biaxial test specimen geometry changes with cross-linking and the corresponding mean deformation gradient tensor components in native state β_0 and EXL state state β_1. Here, cross-linking induced a 6% contraction in the PD and and 7% direction in the XD, with some small shearing.

gradient tensor $\mathbf{F}$ was determined. For the first testing phase, an equibiaxial stress protocol (i.e. P_{11}:$P_{22} = 1 : 1$) was used for both preconditioning and data acquisition. A total of 15 contiguous cycles were run with an approximate strain rate of 0.01 s^{-1}. Next, seven successive protocols were performed using ratios P_{11}:P_{22} = 1 : 0.1, 1 : 0.5, 1 : 0.75, 1 : 1, 0.75 : 1, 0.5 : 1 and 0.1 : 1. This range was chosen for extensive coverage of in-plane strain state. After testing, each native specimen was allowed to mechanically re-equilibrate by storing them in a stress-free state at $4°C$ for 24 h. Next, each specimen was chemically treated with 0.625% GLUT for a minimum of 72 h, with the tissue marker dimensions monitored throughout the cross-linking procedure, and then stored in phosphate-buffered normal saline at $4°C$. As a final step, the above biaxial testing sequence was repeated. Data post-processing included computation of the second Piola-Kirchhof tensor $\mathbf{S}$ and deformation gradient tensor $\mathbf{F}$ using established methods [71]. This test design allowed a comprehensive planar mechanical behavior dataset to be collected on matched native and EXL specimens, compensating for inter-specimen variations.

3.2.2 Kinematic considerations and mechanical data post-processing

As observed in our other studies [50, 71], the chemical fixation process will affect the specimen dimensions, and any analysis must carefully account for these effects on the collagen fiber kinematics. We thus defined the following configurations: β_0-native, β_1-EXL (figure 3.3b), used as the referential configurations for the native and EXL states, respectively. We represented all deformations using the notation for the deformation gradient tensor ${}^{j}_{i}\mathbf{F}$ where i and j represent the initial and final configurations, respectively (Nomenclature). Values for the components of ${}^{j}_{i}\mathbf{F}$ were determined using the same method from section 3.2.1 for the displacements of the four markers pre- and post-cross-linking for each specimen. Next, as first described by

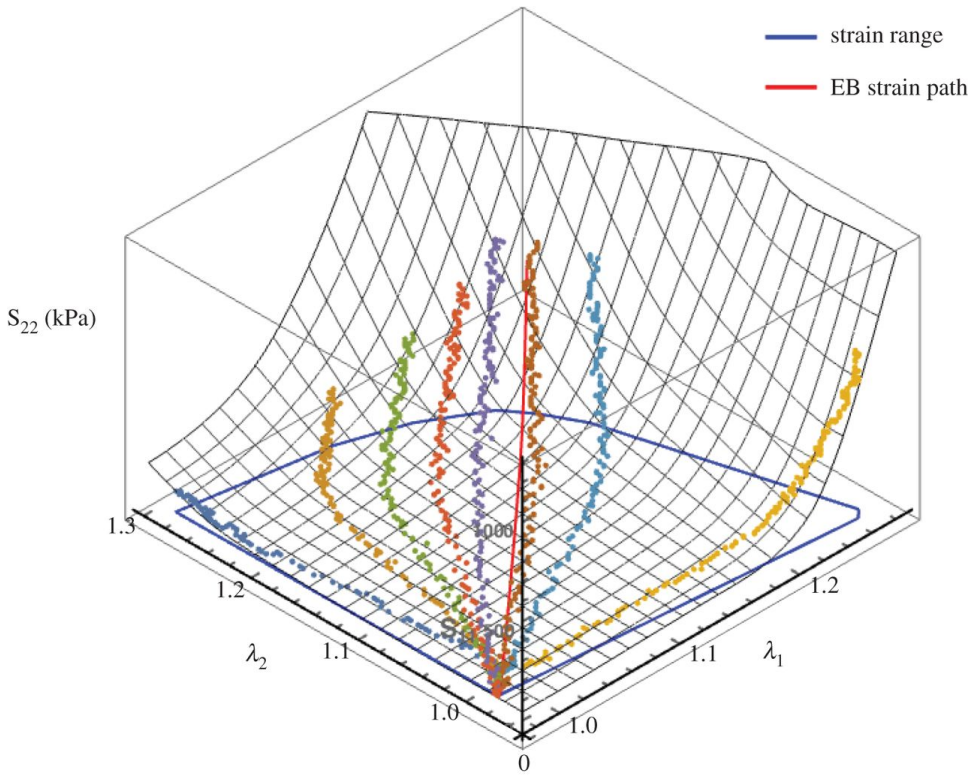

Figure 3.4: An example of the bicubic Hermite surface interpolation of the S_{22} biaxial test responses to allow interpolation of an equibiaxial strain path, shown here in red. The blue path defines the span of the strain.

Lanir [25], we defined a fiber ensemble as a group of fibers with a common orientation. It has been shown that the ensemble stress-strain relation can be obtained from the interpolated equibiaxial strain path, where $\mathbf{F} = \mathrm{diag}[\lambda, \lambda, 1/\lambda^2]$ using $S_{ens} = S_{11} + S_{22}$ [45]. To derive the equibiaxial strain path $\lambda_1 = \lambda_2$ from the stress-controlled experimental data, all mechanical data were combined and interpolated using cubic Hermite patches [15]. A strain path with $\lambda_1 = \lambda_2$ was interpolated within the range of the data as defined by the convex hull of (λ_1, λ_2), and was implemented separately for each stress component (figure 3.4). To reliably overcome regions of sparse data we enforced the surface to be strictly convex everywhere. Finally, since the S_{12} component was negligible in all specimens, it was ignored in the subsequent analyses.

3.2.3 Establishing and modeling the mechanical behavior of the native collagen fiber ensemble

Based on our previous tissue model findings [45, 15, 14, 27], the dominant cause of the nonlinearity of the tissue-level mechanical behaviour of collagenous tissues is the gradual recruitment of collagen fibres [25]. The collagen fibers themselves behave linearly under typical fiber strains experienced under physiological stresses in tissues (2–5%). Once all fibers are fully straightened, the summed response should appear linear in the ensemble response. When applied to the equibiaxial strain derived fiber-ensemble data, the upper bound can be directly determined as the transition point between the nonlinear and linear regions, with the slope of the linear region establishing the maximum tangent modulus (MTM) of the collagen fiber ensemble (e.g. [15]). The matrix response can also be determined from the pre-recruitment region where collagen fibers do not contribute. To determine the recruitment upper bound in the native tissue, we started at the largest measured strain and decreased the strain level until the region above was no longer linear. Linearity was defined from the mean squared error (MSE) of the linear regression to be less than 0.005% of the total MSE of all data, where MSE $= \sum_i^n (\mathrm{S}_{ens}^i - \bar{\mathrm{S}}_{ens})/n$. Similarly, we determined the lower bound by starting at zero strain and increasing the strain until a deviation from linearity was determined.

Next, we note that in some previous structural models a fiber stress-strain relationship that is linear in the second Piola-Kirchhoff stress and Green Lagrange strain has been used [45, 14, 24]. However, SAXS studies have demonstrated a linear force-displacement relation for collagen fibrils in the tendon [51, 52] and MV tissue [34]. This is further corroborated by the atomistic modeling results by Buehler [4], where the force-displacement relation is essentially linear at strains lower than 0.35. We have recently determined that for the mitral valve leaflet the tissue level-derived

collagen fiber mechanical behavior is actually quite linear, with an effective modulus of approximately 160 MPa. Based on these considerations, we assumed that the native collagen fibers

1. exhibit a linear $P - \lambda$ response

2. have collagen fibers slack stretches that do not vary with orientation.

From these two basic considerations, we used the following effective native collagen fibre model [15, 14]. We start by defining the native collagen fiber strain energy as

$$\Psi_f(\lambda_t) = \begin{cases} \frac{\eta_c}{2}\left(\lambda_t - 1\right)^2 & \text{for } \lambda_t > 1 \\ 0 & \text{for } \lambda_t < 1 \end{cases} \tag{3.1}$$

where $\lambda_t = \lambda_f/\lambda_s$ is the true stretch of the fibre. This leads to the following $P - \lambda$ form using $P_f = \partial\Psi_f(\lambda_t)/\partial\lambda_f = \partial\Psi_f(\lambda_t)/\partial\lambda_t \cdot \partial\lambda_t/\partial\lambda_f$

$$P_f = \begin{cases} \frac{\eta_c}{\lambda_s}\left(\lambda_t - 1\right) & \text{for } \lambda_t > 1 \\ 0 & \text{for } \lambda_t < 1 \end{cases} \tag{3.2}$$

where P_f is the first Piola-Kirchhoff stress of the fibre, η_c is the modulus of the fibre, λ_f is the fibre stretch and λ_s is the fibre slack stretch. Next, we use this fibre model in the expression for the native collagen fibre ensemble using

$$\begin{aligned} P_c^{ens} =& \phi_c \eta_c \int_1^{\lambda_\theta} \frac{D(x)}{x}\left(\frac{\lambda_\theta}{x} - 1\right) \mathrm{d}x \\ \text{and} \quad \frac{\partial P_c^{ens}}{\partial \lambda_\theta} =& \mathrm{TM}_c^{ens} = \phi_c \eta_c \int_1^{\lambda_\theta} \frac{D(x)}{x^2}\, \mathrm{d}x, \end{aligned} \tag{3.3}$$

where ϕ_c is the collagen fibre mass fraction, λ_θ is the fibre-ensemble stretch along the direction defined by θ (computed from the tissue-level deformation using $\lambda_\theta = \mathbf{F} \cdot \mathbf{n}(\theta)$), and $D(\lambda_s)$ is the probability distribution function describing the distribution of collagen fibre slack length within the ensemble. We assumed $D(\lambda_s)$ is Beta

distributed, so that

$$
\begin{aligned}
D(\alpha,\beta,\lambda_{lb},\lambda_{ub},\lambda_s) = &\begin{cases} \frac{y^{\alpha-1}(1-y)^{\beta-1}}{B(\alpha,\beta)(\lambda_{ub}-\lambda_{lb})} & \text{for } y \in [0,1] \\ 0 & \text{otherwise} \end{cases} \\
y = &\frac{\lambda_s-\lambda_{lb}}{\lambda_{ub}-\lambda_{lb}}, \quad \bar{\mu} = \frac{\mu-\lambda_{lb}}{\lambda_{ub}-\lambda_{lb}} \\
\textit{and} \quad \bar{\sigma} = &\frac{\sigma}{\lambda_{ub}-\lambda_{lb}}, \quad \alpha = \frac{\bar{\mu}^2-\bar{\mu}^3-\bar{\sigma}^2\bar{\mu}}{\bar{\sigma}^2}, \\
\beta = &\alpha\frac{1-\bar{\mu}}{\bar{\mu}}
\end{aligned}
\tag{3.4}
$$

where λ_{lb} and λ_{ub} are the lower and upper bound stretch of the collagen fibre recruitment, respectively. Note that in preliminary examinations of the data we found that all specimens exhibited distinct pre- and post-transition locations (figure 3.5), allowing λ_{lb} and λ_{ub} to be determined directly from the collagen fibre ensemble data. Thus, the complete initial ensemble model (equation 3.3) has three parameters $\{\eta_c, \alpha, \beta\}$ to fit to the data using standard techniques [15].

3.3 Delineation and modelling of the tissue-level mechanical effects of exogenous cross-links

3.3.1 Rationale

While extensive work has been done on the characterization of the biomechanical effects of EXL formation on soft tissues [60, 48, 61, 57, 1, 67, 65, 68, 66, 31, 37, 32, 2, 36], there has been surprisingly little work done known to the authors on the development of formal constitutive models (other than [44]). Related work on proteoglycan and related collagen fibril sub-forms have revealed complex micromechanical interactions (e.g. [5, 11]), but micromechanical interactions modified by EXLs on the macroscale tissue responses remain largely unknown. Thus, prior to developing the constitutive model form, we first carefully examined the effects of EXL formation on the measured tissue-level biomechanical behaviours in the present data set.

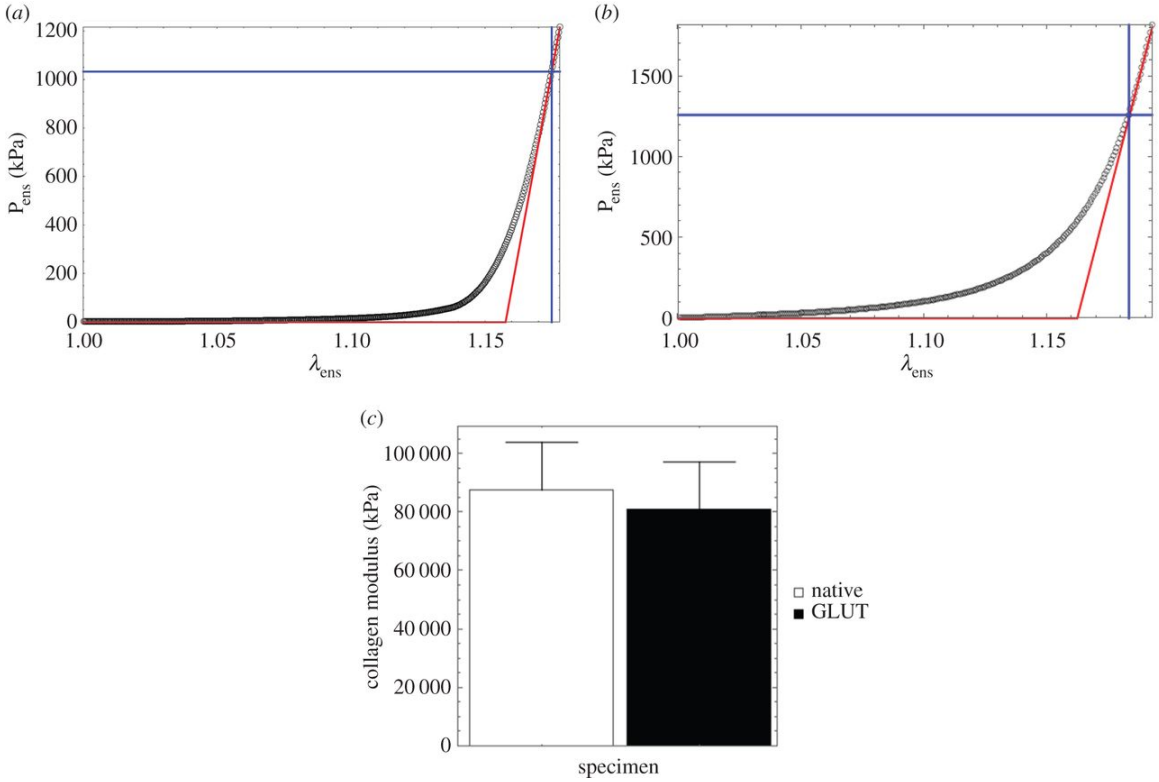

Figure 3.5: A representative fibre-ensemble stress–strain (in $P_{\text{ens}} - \lambda_{\text{ens}}$) response for (a) native and (b) cross-linked bovine pericardium illustrating a well-defined post-transition fibre recruitment point wherein the response becomes linear. While the native pericardium demonstrated a very low initial modulus (approx. 75 kPa; table 3.1), the EXLs demonstrate a significantly stiffer modulus.

Table 3.1: Key collagen fibre-ensemble results for the native and matched GLUT EXL specimens, both reference to β_1.

ID	**12**	**21**	**41**	**61**	**68**	**mean**	**s.e.m.**	**p-value**
initial tangent modulus (kPa)								
native	73.9	65.6	25.5	110.6	107.3	76.6	17.4	
GLUT	1059.3	248.4	152.4	746.0	272.1	495.6	195.2	0.037
MTM (kPa)								
native	54208	49014	53091	72460	77121	61179	6341.3	
GLUT	67771	28615	58025	62319	70718	57490	8433.8	0.567
upper bound stress (kPa)								
native	1164.0	885.4	956.2	1048.4	1289.4	1068.7	80.80	
GLUT	1081.7	925.8	1204.2	1138.2	1353.8	1140.8	78.69	0.245

3.3.2 Effects of exogenous cross-link formation on collagen fibre ensembles

All specimens exhibited anisotropic dimensional changes due to preconditioning and cross-linking (figure 3.3b). Interestingly, we found that about 6% shrinkage occurred in the preferred direction and approximately 7% expansion in the cross-preferred directions. Such changes can alter both the angular dependence on collagen recruitment and the collagen fiber orientation distribution. We determined basic characteristics of the collagen fiber stress-strain relations directly from the data (no modeling), including the lower and upper bound-associated stresses, the initial tangent modulus, and the MTM from a running 15-point window. From this analysis, we were able to determine the number of important mechanical characteristics (table 2 and figure 3.5). These include:

1. All specimens exhibited an approximately 6.5-fold increase in the initial tangent modulus (table 2), very similar to values and native/EXL ratios reported in [36], which were conducted under flex conditions.

2. The upper bound stress and MTM were found to be unaffected by EXL formation (table 2).

3. EXL formation induced a reduction in achieved strain levels compared with the native state (figure 3.5a).

4. The effective collagen modulus was unaffected by EXL formation (figure 3.5c).

Collectively, these results reveal some important features of the effects of EXLs on collagen tissues. First, as noted in our previous studies [44, 36] EXLs produce a substantial increase in the low-strain modulus. Next, equation 3.3 indicates that the

MTM is proportional to the collagen fibre modulus and the recruitment function D. Use of equation 3.3 compensates for the effect of the changes in tissue dimensions due to cross-linking on the fibre recruitment, allowing separation of changes in fibre architecture from the modulus on the ensemble stress-strain curve. Thus, the lack of changes in effective modulus is independent of any effects of changes resulting from tissue dimensions and represent an accurate modulus estimate.

3.4 Initial model formulation

3.4.1 General approach

The above findings provide sufficient information to develop a new model. In the present study, we assume EXLs induce fibre–fibre and fibre–matrix interactions that are mechanically significant. We ignore any time-dependent effects, as we have found that native and cross-linked valvular tissues exhibit minimal time-dependent effects [20, 21, 59, 12]. Next, we assume that the pericardial tissues considered are only composed of collagen fibres and a matrix constituent that represents non-cross-linked and cross-linked components, and water. The contributions from elastin or other tissue components are ignored, because they have either negligible mass or stiffness. In all previous structural models of soft tissues, interactions between components (fibres, matrix) have been ignored. As we cannot assume this in the present investigation, we use the following hyperelastic general form:

$$\Psi(\mathbf{C}) = \phi_c[\Psi_c(\mathbf{C} + \Psi_{\text{int}}(\mathbf{C}] + (1 - \phi_c)\Psi_m(\mathbf{C} + p(J - 1) \tag{3.5}$$

where ϕ_c is the mass fraction of the collagen fibres, ϕ_c, ϕ_m and ϕ_{int} are the strain energy density functions of the collagen, matrix and interaction terms, respectively, $J = \det(\mathbf{F})$, and p is the Lagrange multiplier to enforce incompressibility. The resulting

tissue-level response in terms of the second Piola-Kirchhoff stress tensor $\mathbf{S}$ is given by

$$\begin{aligned}\mathbf{S} =& 2\,\frac{\partial \psi}{\partial \mathbf{C}} - p\mathbf{C}^{-1} \\ =& 2\left[\phi_c\,\frac{\partial \Psi_c}{\partial \mathbf{C}} + (1-\phi_c)\,\frac{\partial \Psi_m}{\partial \mathbf{C}} + \phi_c\,\frac{\partial \Psi_{\text{int}}}{\partial \mathbf{C}}\right] - p\mathbf{C}^{-1}.\end{aligned} \tag{3.6}$$

3.4.2 Accounting for changes in tissue dimensions for the collagen phase

Results from section 3.3 suggest that the native collagen fiber modulus is unaffected by cross-linking. However, the observed changes in tissue dimensions can also induce changes in tissue-level mechanical behavior by altering the structure due to tissue shrinkage. This essentially results in a different reference configuration. There is thus a need to reformulate structural models to account for these effects directly. The formulation described in the following allows handling of changes in tissue reference state geometry. The key assumptions are:

1. Changes are due to alterations in the initial geometric configuration only, so that

   (a) Mass fractions of each phase remain unchanged.

   (b) The internal mechanical energy remains zero. Thus, all changes in internal component configurations are not associated with any change in internal energy (which remains zero)—just initial configuration (e.g. fiber orientation, the degree of undulation, thickness and length).

2. Tissue dimensions and internal architecture change under the *affine* kinematic assumption. Thus, the configuration of all constituent fibers in the altered reference state (after all changes in initial specimen geometry have taken place) can be predicted. Moreover, the configurational change is homogeneous and can be thus described by a deformation gradient tensor with constant components.

3. To be consistent with the fibre recruitment mechanisms (e.g. [45, 15]), all fibres remain undulated in the new reference state.

4. The matrix phase is unaffected by the geometric configuration changes and is referenced to β_1 (figure 3.3b) for all subsequent stress calculations.

As a first step, we recast the recruitment function parameters determined in β_0 but mapped to β_1 using

$$
\begin{aligned}
&D_1(\mu_0, \sigma_0, {}_0\lambda_{lb}, {}_0\lambda_{ub}, {}^1_0\lambda, {}_1\lambda_s) = \begin{cases} \frac{y^{\alpha-1}(1-y)^{\beta-1}}{B(\alpha,\beta)({}_1\lambda_{ub}-{}_1\lambda_{lb})} & \text{for } y \in [0,1] \\ 0 & \text{otherwise} \end{cases} \\
&y = \frac{{}^t_1\lambda_s - {}_1\lambda_{lb}}{{}_1\lambda_{ub} - {}_1\lambda_{lb}}, \quad {}_1\lambda_{ub} = \frac{{}_0\lambda_{ub}}{{}^1_0\lambda}, \quad {}_1\lambda_{lb} = \frac{{}_0\lambda_{lb}}{{}^1_0\lambda} \\
&\bar{\mu} = \frac{\mu - {}_0\lambda_{lb}}{{}_0\lambda_{ub} - {}_0\lambda_{lb}}, \quad \bar{\sigma} = \frac{\sigma}{{}_0\lambda_{ub} - {}_0\lambda_{lb}}, \\
&\alpha = \frac{\bar{\mu}^2 - \bar{\mu}^3 - \bar{\sigma}^2\bar{\mu}}{\bar{\sigma}^2}, \quad \beta = \alpha\frac{1-\bar{\mu}}{\bar{\mu}}
\end{aligned}
\tag{3.7}
$$

where the left subscript denotes the configuration state. Note carefully that ${}^1_0\lambda$ will in general be a function of θ_1, so that even though the collagen fibre recruitment is orientation-independent in β_0, it will have angular dependence in β_1 unless ${}^1_0F_{11} = {}^1_0F_{22}$ and ${}^1_0F_{12} = {}^1_0F_{21} = 0$. The resulting expression for the ensemble stress is

$$
{}^t_1\mathbf{S}^{ens}_c = \phi_c \frac{\eta_c}{{}^t_1\lambda} \int_1^{{}^t_1\lambda} \frac{D_1(x)}{x} \left(\frac{{}^t_1\lambda}{x} - 1 \right) \mathrm{d}x \tag{3.8}
$$

To complete the tissue-level formulation, we use the affine transformation assumption and the formulation described in [14] to obtain the collagen fibre orientation distribution function Γ_0 in the native state to that in β_1 using

$$
\Gamma_1[\mu_\Gamma, \sigma_\Gamma, \theta_1 = \Gamma_0[\mu_\Gamma, \sigma_\Gamma, \theta_0({}^1_0\mathbf{F}, \theta_1) \frac{{}^1_0\lambda^2_{\theta_0}}{{}^1_0J_{2\mathrm{D}}}]. \tag{3.9}
$$

Note that the angle θ_1 of a fibre originally oriented at θ_0 can be determined using

$$
\theta_1({}^1_0\mathbf{F}, \theta_0) = \tan^{-1}\left(\frac{{}^1_0F_{21}\cos\theta_0 + {}^1_0F_{22}\sin\theta_0}{{}^1_0F_{11}\cos\theta_0 + {}^1_0F_{12}\sin\theta_0} \right) \tag{3.10}
$$

The final form of the native collagen fibre phase expressed in the EXL state is thus

$$
\begin{aligned}
{}^{t}_{1}\mathbf{S}(\eta_c, \mu_\Gamma, \sigma_\Gamma, \mu_0, \sigma_0) = \phi_c \frac{\eta_c}{{}^{t}_{1}\lambda} \int_{\theta_1} \Gamma_1(\mu_\Gamma, \sigma_\Gamma, \theta_1)) \\
\left\{ \frac{D_1(\mu_0, \sigma_0, {}_0\lambda_{lb}, {}_0\lambda_{ub}, {}^{1}_{0}\lambda[\theta_0(\theta_1)], x)}{x} \left(\frac{{}^{1}_{0}\lambda}{x} - 1 \right) \mathrm{d}x \right\} \mathbf{n}_1 \otimes \mathbf{n}_1 \, \mathrm{d}\theta
\end{aligned}
\tag{3.11}
$$

The above equation has a total of five fitted model parameters η_c, μ_Γ, σ_Γ, μ_0, and σ_0 (λ_{lb} and λ_{lb} are determined from the experimental data), all with a physical meaning and all referenced to β_0.

3.4.3 The matrix phase

The matrix response can be estimated from the low stress region where collagen does not contribute any stress (figures 3.5 and 3.6). A careful examination revealed that the toe region is a convex curve in $S - \lambda$, which is inconsistent with a neo-Hookean material model which is concave in $S - \lambda$ (figure 3.6). While we have used an exponential isotropic function for the matrix before [44], we considered the Yeoh model but found it unable to fit the data. Therefore, we developed a modified Yeoh model as

$$
\begin{aligned}
\Psi_m(\mathbf{C}) =& \frac{1}{2}\frac{\mu_a}{a}(I_1 - 3)^a + \frac{1}{2}\frac{\mu_b}{b}(I_1 - 3)^b \\
\mathbf{S}_m =& \left(\mu_a (I_1 - 3)^{a-1} + \mu_b (I_1 - 3)^{b-1} \right) (\mathbf{I} - C_{33}\mathbf{C}^{-1}), \\
& \text{with } 1 < a < b, \quad a \times b < 2
\end{aligned}
\tag{3.12}
$$

When applied to all pre-transition mechanical data (i.e. from all protocols and where there is no collagen fibre contribution), this form was found to fit the low-stress data quite well (figure 3.6).

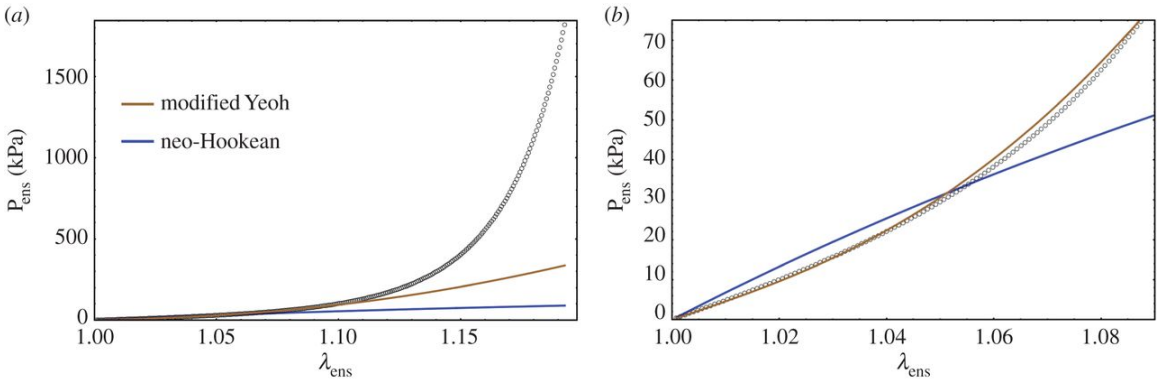

Figure 3.6: A representative fibre-ensemble stress–strain (in $P_{\text{ens}} - \lambda_{\text{ens}}$) for EXL treated bovine periardium, and (b) a close-up of the low stress region. A careful examination revealed that the toe region suggests that a modified Yeoh model was necessary to accurately capture its response (equation 3.12) due to the convexity of the response.

3.4.4 Interactions

Our key working assumption is that all fiber– fiber and fiber-matrix interactions can be represented at the fiber-ensemble level. This is done to simplify the model formulation, and further since the exact micromechanical mechanisms of cross-linking have yet to be determined. Based on the form assumed in equation 3.4.2, we now have the ability to estimate the form and magnitude of the fibre-ensemble interactions from the fibre-ensemble data using $\mathbf{S}_{\text{int}} \approx \mathbf{S}_{\text{ens}} - 1/\phi_c(\phi_c \mathbf{S}_c + (1-\phi_c)\mathbf{S}_m)$, where $\mathbf{S}_{\text{ens}}$ is the ensemble stress (figure 3.5). Note here that the collagen stress Embedded Image and is thus the contribution of the collagen fibers expressed in the EXL configuration β_1 using equation 3.11. This approach allowed us to exploit the matched native–EXL mechanical data by fitting the native responses then mapping them to the EXL state so that they are a known quantity rather than one that required data fitting. Results of this analysis indicated some intriguing results. First, while the collagen phase contributed substantially to the total ensemble stress, it was only about 50%, and the matrix only about 20%. This revealed that the remaining approximately 30% portion

of the total ensemble stress must be a result of the interaction mechanisms.

To model the interactions, we first consider two fibre ensembles with orientation vectors $\mathbf{n}_0(\alpha)$ and $\mathbf{m}_0(\beta)$ in the reference configuration (figure 3.7). These two ensembles can mechanically interact by elongation and relative rotation. Kinematically, these mechanisms can be captured using the pseudo-invariant I_8 [22, 35]

$$\begin{aligned} I_8 &= \mathbf{n}_0 \cdot \mathbf{C}\mathbf{m}_0 = \cos(\theta)\lambda_\alpha\lambda_\beta \\ \cos(\theta) &= \frac{\mathbf{n}_0 \cdot \mathbf{m}_0}{\lambda_\alpha\lambda_\beta}, \quad \lambda_\alpha = \sqrt{\mathbf{n}_0 \cdot \mathbf{C}\mathbf{n}_0}, \quad \lambda_\alpha = \sqrt{\mathbf{m}_0 \cdot \mathbf{C}\mathbf{m}_0} \end{aligned} \tag{3.13}$$

Note that we can also use $I_8' = I_8 - I_8^0$ [35] to account for the relative change in fibre rotations if necessary. Thus, i_8 can be considered the product of an extensional term $\lambda_\alpha\lambda_\beta$ and a rotational term $\cos(\theta)$. We consider two sub-aspects of ensemble-level effects: intra- and inter-ensemble levels. The intra-ensemble incorporates all fibre–fibre interactions that occur within a single ensemble and are limited to extensional effects only. By contrast, inter-ensemble effects can include both extensional and rotational effects.

To best capture these phenomena, we do not use I_8 directly but rather the following forms. The results for the ensemble stress suggest that the interaction terms are exponential in character (figure 3.8). Thus, for the extensional intra-ensemble effects we use

$$\Psi^e_{\text{int}}(\mathbf{C}) = \frac{c_0}{4}\int_\theta \Gamma(\theta)\left[e^{c_1(\lambda-1)^2} - 1\right]\mathrm{d}\theta \tag{3.14}$$

where $\lambda = \sqrt{\mathbf{n}_0 \cdot \mathbf{C}\mathbf{n}_0} = \sqrt{I_4}$ and c_0, c_1 are constants, and the associated single ensemble stress extensional interaction is

$$\mathbf{S}^e_{\text{int}} = 2\frac{\partial\Psi(\mathbf{C})}{\partial\mathbf{C}} = 2\frac{\partial\Psi(\lambda)}{\partial\lambda}\frac{\partial\lambda}{\partial\mathbf{C}} = \int_\theta \Gamma(\theta)\left[\frac{c_0c_1(\lambda-1)e^{c_1(\lambda-1)^2}}{\lambda}\mathbf{n}_0 \otimes \mathbf{n}_0\right]\mathrm{d}\theta \tag{3.15}$$

Next, for the extensional inter-ensemble interactions, we use a similar form

$$\Psi^{ee}_{\text{int}}(\mathbf{C}) = \frac{d_0}{4}\int_\alpha\int_\beta \Gamma(\alpha)\Gamma(\beta)\left[e^{d_1(\lambda_\alpha\lambda_\beta-1)^2} - 1\right]\mathrm{d}\alpha\,\mathrm{d}\beta \tag{3.16}$$

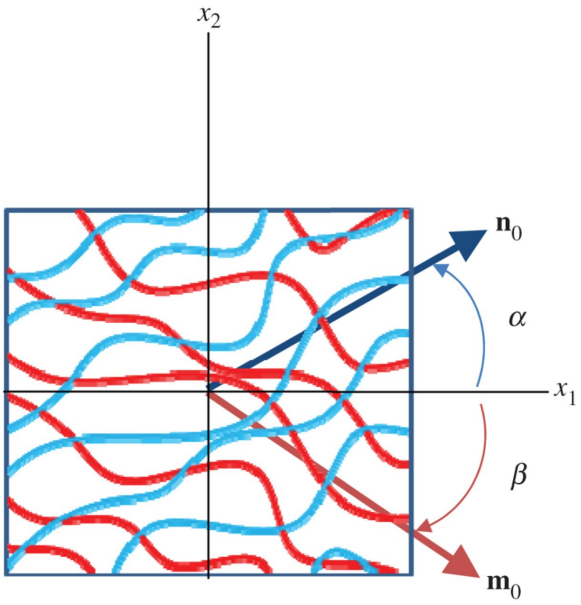

Figure 3.7: A schematic of two collagen fibre ensembles with respective orientations α and β (not restricted to be symmetric about the X_1-axis) with associated orientation vector $\mathbf{n}_0$ and $\mathbf{m}_0$ in the reference configuration.

where d_0 and d_1 are parameters, with associated stresses

$$\mathbf{S}^e_{\text{int}} = \int_\alpha \int_\beta \Gamma(\alpha)\Gamma(\beta) \times \left[d_0 d_1 (\lambda_\alpha \lambda_\beta - 1) e^{d_1(\lambda_\alpha \lambda_\beta - 1)^2} \left(\frac{\lambda_\beta}{\lambda_\alpha} \mathbf{n}_0 \otimes \mathbf{n}_0 + \frac{\lambda_\alpha}{\lambda_\beta} \mathbf{m}_0 \otimes \mathbf{m}_0 \right) \right] \mathrm{d}\alpha \, \mathrm{d}\beta \tag{3.17}$$

Note that the exponential term was set to zero if $\lambda_\alpha \lambda\beta < 1$ In this approach, we integrate over all ensembles, weighted by their respective orientation distribution functions, to obtain the total contribution.

Next, we developed a rotational pseudo-invariant defined as the change in the cosine between the two ensemble fiber directions, which is simply

$$I^r_{\text{int}}(\alpha, \beta) = \frac{I_8}{\lambda_\alpha \lambda\beta} - \mathbf{n}_0 \cdot \mathbf{m}_0 = \cos\theta - \cos\theta_0 \approx \Delta\theta. \tag{3.18}$$

Using $\Psi^r_{\text{int}}(\mathbf{C}) = \frac{\eta^r}{4}(I^r_{\text{int}})^2$ it can be shown that for planar distributed fibre ensembles

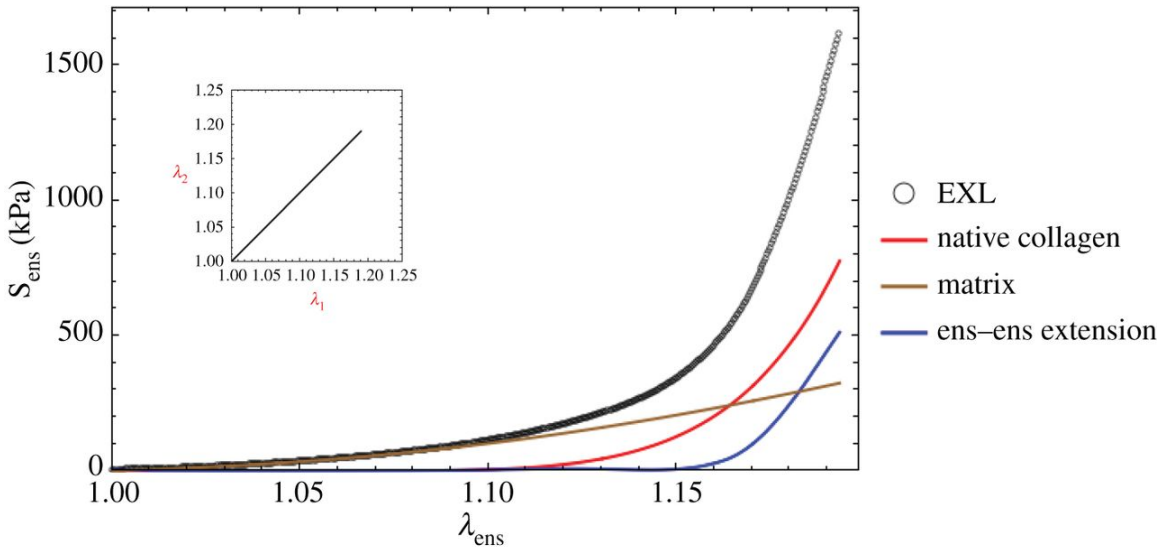

Figure 3.8: Representative final model results (equation 3.23) for a single fibre-ensemble stress–strain (in $S_{\text{ens}} - \lambda_{\text{ens}}$) response for EXL treated bovine pericardium. All model components contributed signficantly to the total stress. Surprisingly, while the collagen phase produced the greatest contribution, the interaction term was of comparable magnitude.

the stress tensor is

$$\begin{aligned}\mathbf{S}^r_{\text{int}} =& \eta^r \int_\alpha \int_\beta \Gamma(\alpha)\Gamma(\beta)\frac{I^r_{\text{int}}(\alpha,\beta)}{\lambda_\alpha \lambda_\beta} \\ & \left[(\mathbf{m}_0 \otimes \mathbf{n}_0 + \mathbf{n}_0 \otimes \mathbf{m}_0) - I_8 \left(\frac{\mathbf{n}_0 \otimes \mathbf{n}_0}{\lambda^2_\alpha} + \frac{\mathbf{m}_0 \otimes \mathbf{m}_0}{\lambda^2_\beta}\right)\right] \mathrm{d}\alpha\, \mathrm{d}\beta\end{aligned} \tag{3.19}$$

Combining equations 3.113.123.153.173.19, we obtain the final form of the full model stress as

$$\begin{aligned}\mathbf{S} =& \phi_c \mathbf{S}_c(\eta_c, \mu_\Gamma, \sigma_\Gamma, \mu_0, \sigma_0) + (1-\phi_c)\mathbf{S}_m(\mu_a, \mu_b, a, b) \\ & + \phi_c[\mathbf{S}^e_{\text{int}}(c_0, c_1) + \mathbf{S}^{ee}_{\text{int}}(d_0, d_1) + \mathbf{S}^r_{\text{int}}(\eta^r)] - p\mathbf{C}^{-1}\end{aligned} \tag{3.20}$$

3.5 Model simplifications and parameter estimation

3.5.1 Final form

While in principle equation 3.20 can be implemented within a robust parameter estimation procedure, simplifications are clearly in order given its complexity (14 parameters). We first consider an equi-biaxial test wherein all fibre rotations are zero, so that $I^r_{\text{int}} = 0$ The total interaction stress is thus given by just the following extensional contributions:

$$\begin{aligned}\mathbf{S}_{\text{int}} = &\int_\theta \Gamma(\theta) \left[\frac{c_0 c_1 (\lambda - 1) e^{c_1(\lambda-1)^2}}{\lambda} \mathbf{n}_0 \otimes \mathbf{n}_0 \right] \mathrm{d}\theta \\ &+ \int_\alpha \int_\beta \Gamma(\alpha)\Gamma(\beta) \left[d_0 d_1 (\lambda^2 - 1) e^{d_1(\lambda^2-1)^2} \left(\mathbf{n}_0 \otimes \mathbf{n}_0 + \mathbf{m}_0 \otimes \mathbf{m}_0 \right) \right] \mathrm{d}\alpha \, \mathrm{d}\beta\end{aligned} \tag{3.21}$$

In practice, we found that while the intra-ensemble form (first r.h.s. term) was used alone it was able to capture the equi-biaxial strain behaviour (figure 3.5), it was unable to capture the response from all test protocols. Moreover, given the similarity in form, the two components on the r.h.s. of equation (5.1) can capture similar responses. We thus chose to ignore the intra-ensemble stress contribution $\mathbf{S}^e_{\text{int}}(c_0, c_1)$ removing two parameters. Next, while it is intuitive that fibre-ensemble rotations produce important contributions to the total tissue stress, closer analysis of equation 3.19 indicated that it will produce compressive stresses in the direction of lesser stretch. These characteristics were not consistent with any of the observed experimental data. Even when choosing various forms of Ψ^r_{int} we could not match the experimentally observed responses. Interestingly, only the S^{ee}_{int} contribution of equation 3.20 was found to model the interaction stresses well.

Thus, we are left with the following interaction stresses:

$$\begin{aligned}\mathbf{S}^{e}_{\text{int}} = &\int_{\alpha}\int_{\beta}\Gamma(\alpha)\Gamma(\beta) \\ &\times\left[d_0 d_1(\lambda_\alpha\lambda_\beta-1)e^{d_1(\lambda_\alpha\lambda_\beta-1)^2}\left(\frac{\lambda_\beta}{\lambda_\alpha}\mathbf{n}_0\otimes\mathbf{n}_0+\frac{\lambda_\alpha}{\lambda_\beta}\mathbf{m}_0\otimes\mathbf{m}_0\right)\right]\mathrm{d}\alpha\,\mathrm{d}\beta\end{aligned} \tag{3.22}$$

leading to the following final form of the constitutive model:

$$\begin{aligned}\mathbf{S} =&\mathbf{S}_c+\mathbf{S}_{int}+\mathbf{S}_m \\ =&\phi_c\frac{\eta_c}{{}^{t}_{1}\lambda}\int_{\theta_1}\Gamma_1(\mu_\Gamma,\sigma_\Gamma,\theta_1))\frac{D_1(x)}{x}\left(\frac{{}^{1}_{0}\lambda}{x}-1\right)\mathbf{n}_1\otimes\mathbf{n}_1\,\mathrm{d}x\,\mathrm{d}\theta \\ &+\phi_c\int_{\alpha}\int_{\beta}\Gamma(\alpha)\Gamma(\beta)d_0d_1(\lambda_\alpha\lambda_\beta-1)e^{d_1(\lambda_\alpha\lambda_\beta-1)^2}\left(\frac{\lambda_\beta}{\lambda_\alpha}\mathbf{n}_0\otimes\mathbf{n}_0+\frac{\lambda_\alpha}{\lambda_\beta}\mathbf{m}_0\otimes\mathbf{m}_0\right)\mathrm{d}\alpha\,\mathrm{d}\beta \\ &+(1-\phi_c)\left(\mu_a(I_1-3)^{a-1}+\mu_b(I_1-3)^{b-1}\right)(\mathbf{I}-C_{33}\mathbf{C}^{-1}),\end{aligned} \tag{3.23}$$

It is understood that $\mathbf{n}_0$ and $\mathbf{m}_0$ are referred to β_1 and that we merged the Lagrange multiplier with the matrix by assuming a planar tissue to simplify the formulation. This final model has 11 independent fitted parameters $\{\eta_c,\ \mu_\Gamma,\ \sigma_\Gamma,\ \mu_0,\ \sigma_0,\ d_0,\ d_1,\ \mu_a,\ \mu_b,\ a,\ b\}$ and three directly determined parameters $\phi_c, {}_0\lambda_{lb}, {}_0\lambda_{ub}$ all with a physical meaning.

3.5.2 Parameter estimation procedures

While at first glance this appears to be a major nonlinear optimization undertaking with all the usual pitfalls, we can use the following sequence to make actual parameter estimation quite tractable:

1. From the native tissue mechanical data, predict the collagen phase parameters $\{\eta_c, \mu_\Gamma, \sigma_\Gamma, \mu_0, \sigma_0\}$ using standard procedures [15, 72].

2. From the pre-transition collagen recruitment portion of all of the EXL tissue mechanical data, determine the matrix parameters $\{\mu_a, \mu_b, a, b\}$.

3. Taking the collagen and matrix responses, determine the interaction stress responses for all test protocols using $\mathbf{S}_{\text{int}} = \mathbf{S} - \frac{1}{\phi_c}\left(\phi_c\, {}^1_0S_c + (1-\phi_c)\mathbf{S}_m\right)$

4. Using the results of step 3, determine the final two parameters (d_0 and d_1) by fitting equation 3.23 but only allowing them to vary while keeping the other terms to their above-fitted values.

We found that this basic sequence ensured a robust parameter is obtained, because the entire model is never fitted at once. Moreover, this approach allowed us to separate the contributions to the stress of each of these mechanisms. As in our previous studies [15, 72], we employed the genetic based Differential Evolution algorithm in Mathematica to perform the optimization. All parameter estimation was performed using a custom program written in Mathematica (Wolfram Research Corp.).

3.6 Primary results

From the five specimens used, the model was able to successfully fit all data quite well (total fit $r^2 > 0.97$). Moreover, the final parameter values were quite consistent, with generally low standard errors (table 3). The mean collagen fiber modulus (approx. 279 MPa) and fiber splay (approx. 38°) were comparable to previous studies [14]. Interestingly, the lower bound stretch was small (1.01 or approx. 1% strain), so it is likely that it could be set to 1 (i.e. zero strain). The native collagen fiber recruitment parameters were also consistent (table 3), and indicated a very rapid recruitment at stretch of approximately 1.18–1.2 (figure 3.9). This is a more complete picture of the entire fiber recruitment than in our previous work [62, 14], and suggests that the collagen fibers are effectively well ordered with a small deviation in crimp amplitude and wavelength.

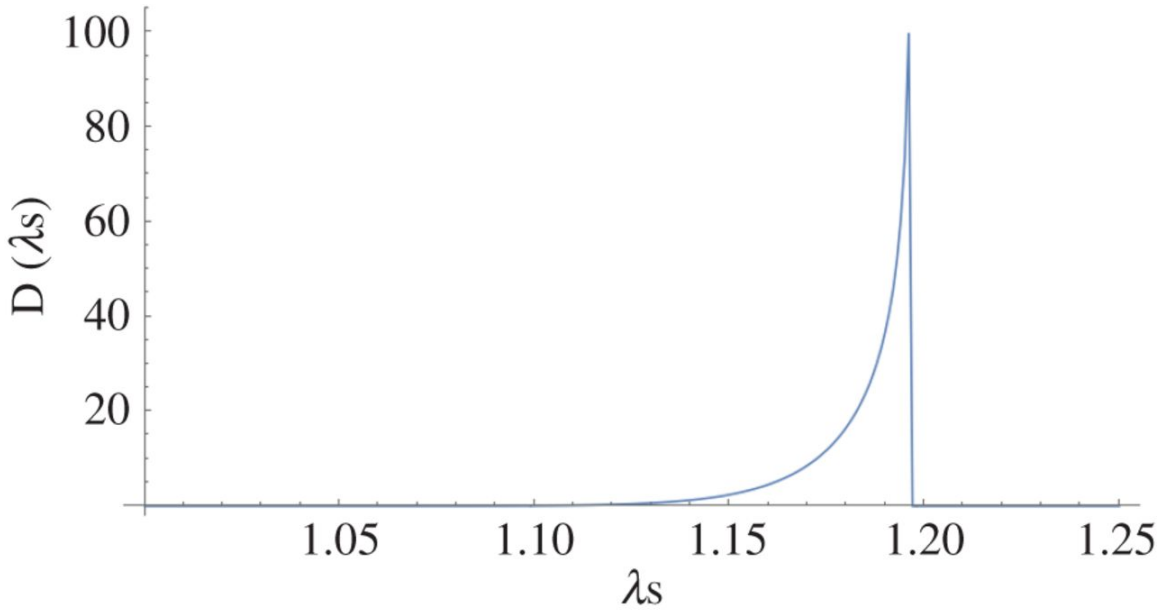

Figure 3.9: Representative complete collagen fibre recruitment for the pericardial tissue, showing a rapid recruitment near the upper bound, suggesting the collagen fibres have similar crimp geometries in the native state.

Table 3.2: Final parameter values for the full model (Eqn. 3.23) for all five specimens.

	modulus	**ODF**		**recruitment**			
	$\eta_c(MPa)$	$\mu_\Gamma(^\circ)$	$\sigma_\Gamma(^\circ)$	μ_0	σ_0	${}_0\lambda_{lb}$	${}_0\lambda_{ub}$
mean	278.94	6.513	38.430	1.185	0.014	1.011	1.197
s.e.m.	22.38	1.645	0.922	0.032	0.001	0.007	0.035
	Interactions			**Matrix**			
	$d_0(kPa)$	d_1		$\mu_a(kPa)$	a	$\mu_b(kPa)$	b
mean	1.040	42.267		56.74	1.068	1294.38	1.873
s.e.m.	0.255	9.772		10.69	0.004	340.71	0.007

One advantage of our approach is that the various contributions to the total stress can be separated (figure 3.8). To better reveal the present findings, it is useful to examine the effects on the individual stress components under various loading paths. Following the trends of the ensemble results (figure 3.9), we noted that the interactions produced substantial contributions to the total stress (figure 3.10). Interestingly, for S_{11} the interactions actually produced the largest contributions, followed by the matrix and collagen fibers. By contrast, for S_{22} the contributions were much more dependent on the particular loading path, with the collagen phase dominating when $\lambda_2 > \lambda_1$. When $\lambda_1 > \lambda_2$, the matrix phase dominated S_22. We further note here that the contribution of the matrix was much less loading path sensitive, due to its near-linear, isotropic behavior.

3.7 Discussion

3.7.1 Major findings

This study represents the first rigorous full structural model (i.e. explicitly incorporating various features of the CFA) for cross-linked soft tissues, and also includes a specific interaction term. An important utility of this model is its ability to separate the effects of EXLs on the fibers and matrix, so that the matrix, collagen and interaction effects could be clearly identified. This was made possible, in part, with the use of the native–EXL matched experimental dataset and a modification to the structural model so that the uncross-linked collagen fiber responses could be mapped to the EXL configuration. As in our previous study, we found that the matrix could be well modeled as an isotropic material. However, we found that a much more linear-like response was necessary. Perhaps the most novel findings of this study were that (i) the effective collagen fiber modulus was unaffected by cross-linking and (ii)

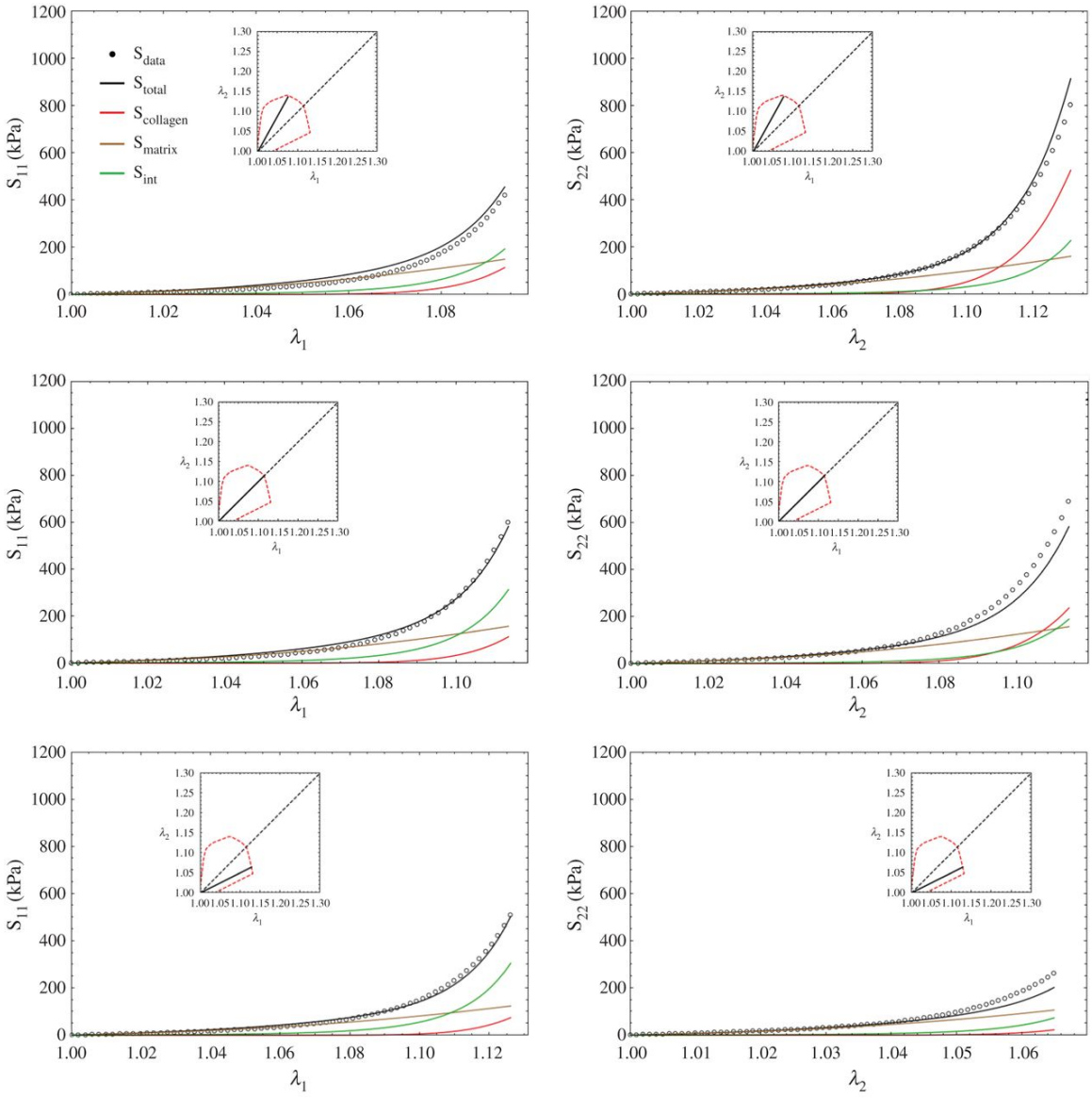

Figure 3.10: Complete model (equation 3.23) results for the S_{11} and S_{22} stress components for three protocols. Interestingly for S_{11} the interactions actually produced the largest contributions, followed by the matrix and collagen fibres. By contrast, for S_{22} the contributions were much more dependent on the particular loading path, with the collagen phase dominating when $\lambda_2 > \lambda_1$. When $\lambda_1 > \lambda_2$ the matrix phase dominated S_{22}. We further note here that the contribution of the matrix was much less loading path sensitive, owing to its near-linear, isotropic behaviour.

the interaction term played such a large role in stress development, often dominating the response (depending on the component and loading path being considered).

The lack of change in the effective collagen fiber modulus has been corroborated by experimental results from Gentleman et al. [19]. In that study, they found a modulus range of 269.7 ± 11.9 to 484.7 ± 76.3 for cross-linked collagen fibers in the bovine Achilles tendon, which corresponds to the same range as another study for native collagen fibers from various sources [13]. Yang et al. [70, 69] determined that for the mechanical properties of hydrated native and cross-linked type I collagen fibrils that cross-linking the collagen fibrils with a water-soluble carbodiimide did not significantly affect the bending modulus. The work by Shen et al. [58] noted a modulus of 0.86 ± 0.45 GPa (range, 0.36–1.60 GPa; n = 13), in reasonable agreement with our results. Further, six of the 13 fibrils showed linear behavior. At the tissue level, our findings are also consistent with the findings of Lee et al. [29, 28, 30], who found no change in MTM in cross-linked pericardial tissues as in our study (table 3.1). It is interesting to note that, when using the native tissue fibre-ensemble model (equation 3.8) on both the native and cross-linked data (figure 3.5), one can increase the fibre modulus determined from the native state to match the post-EXL data (figure 3.11a). However, this will induce a parallel increase in the MTM of approximately 75% (figure 3.11b), which is inconsistent with the experimental findings (table 3.1). This is the case even when compensating for the effects of tissue contraction. This simple simulation lends support to the collagen modulus results (figure 3.5c).

Our model results suggest that the major effect of EXL formation was not the formation of a mechanically substantial matrix or stiffening of the collagen fibers, but rather a dramatically enhanced bonding both within and between fiber ensembles. Note that our specific interaction term (equation 3.17) captured the effects of both

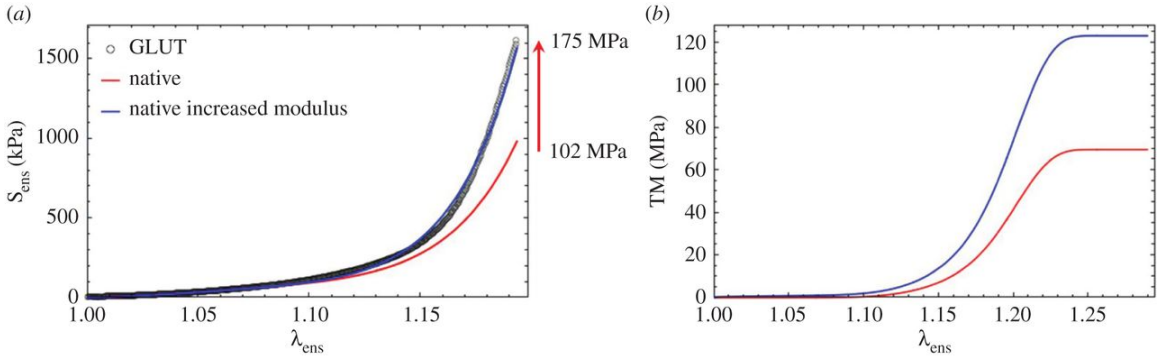

Figure 3.11: Simulation results using the unmodified native tissue fibre-ensemble model (equation 3.8) on both the native and cross-linked data from figure 3.5, showing that one can increase the fibre modulus determined from the native state to match the post-EXL data (a). However, this will induce a parallel increase in the MTM of approximately 75% (b), which is inconsistent with the experimental findings (table 3.1). This is the case even when compensating for the effects of tissue contraction.

individual ensemble stretch and relative stretching between ensembles. This is consistent with what is known about GLUT bond formations (figure 3.1a) [38, 9, 6, 7, 8]. Yet, we found that relative rotations between fibre ensembles as modelled by equation 3.19 could not capture the observed responses. The underlying structural mechanisms for this behavior remain largely uncharacterized. One possibility is that the protein core of the proteoglycans that bind collagen fibrils become strongly cross-linked and are thus substantially stiffened, acting to more cohesively bind the collagen fibers. This is supported by findings of Liao & Vesely [33], who observed substantial deformations of proteoglycans in mitral valve chordae under stretch. Moreover, the present model suggests that such mechanisms are strongly associated with fiber-ensemble orientation distributions. While not the final word, our results suggest that EXLs produce a stiffening effect via an isotropic matrix, with the interaction effects being the dominant effect.

3.7.2 Modelling approach

The present approach was a direct extension of the stochastic, tissue-level meso-structural models first pioneered by Lanir [25] and used in various applications and extensions by our group [45, 15, 72]. By meso-scale, we refer to the fiber-ensemble scale, which is fiber features down to approximately 100 μm. Moreover, recent evidence has demonstrated that the underlying affine kinematic assumption is valid [15, 14] so that the strain energy of each fiber ensemble can be kinematically connected with the macroscopic strain tensor. We took the approach to develop a more general model first, then show what components could be modified or removed entirely. Given the lack of knowledge and modeling efforts in this area, we felt this was appropriate and helped to illustrate what underlying mechanisms should be incorporated. We also considered a more extensive approach based on the elastica-based theory for sinusoidal fibers based on [16] under the assumption that EXL formation dramatically increased the fiber modulus, which ultimately proved to be unnecessary. An inter-fiber sliding model was also developed based on the relative sliding between fibers due to differences between their respective slack lengths, and used as a means to model the intra-ensemble EXL effects. However, this approach was found to be unable to capture the individual fiber-ensemble responses, suggesting that relative sliding between fibers at the ensemble level was not a major mechanism. A final question that may impact physical plausibility of the current model is convexity and physical plausibility. Lanir [26] demonstrated that the native tissue structural model is compatible with a physically plausible response. Based on both this and the experimental observations, we focused on monotonically increasing functions of strain for all model terms to ensure physical plausibility and that convexity was maintained.

3.7.3 Limitations and future directions

The current model is limited in the fact that it is quasi-static and does not account for permanent set phenomena we have observed [63]. The homogenization method used in section 3.3 is fairly standard and has been used by others and the author for some time (e.g. [45, 15, 14]). We have observed that for soft tissues, whose composition is dominated by a dense network of distinct fibers, especially collagen type I and elastin, these structures can be mechanically treated as fiber ensembles; that is, groups of fibers with a common orientation. The scale of the representative volume element is about 100 μm, which is sufficient to capture the salient mechanical features of the fiber ensemble. We emphasize that this is not meant to be a universal model of all types of soft tissue structures, which are very diverse for a single theoretical treatment. Rather, we focus on a sufficiently generalized approach for exogenously cross-linked dense collagenous tissues, such as pericardium, heart valves, and sclera. These structures fit our approach well and also have important biomedical therapeutic applications.

A complete understanding of the current phenomena must be based on well-characterized micro-scale events. For example, Kojic et al. [23] developed a model for fiber– fiber kinetics that uses Coulomb friction, which results in a simple and robust approach for tissue simulations. However, our knowledge of even native tissues at the micro-level remains limited. The situation remains more complicated by the fact that our knowledge of the interrelationships between the physical chemistry of EXLs and the macro-scale mechanics of collagenous tissues remains limited at the present time for more sophisticated models to be reliably attempted. To date, no material model is able to fully account for such complex observed microstructural and biological behavior. The next steps include incorporation of the permanent set effect

commonly observed in cross-linked tissues into the present model and exploration of how alternative cross-linking methods affect macro-scale tissue behaviors.

Nomenclature

int	Interaction term
c	Collagen
m	Matrix
EB	Equibiaxial
ODF	Orientation distribution functio z
$\mathbf{F}$	Deformation gradient tensor
$\mathbf{E}$	Green Lagrange strain
$\mathbf{P}$	First Piola Kirchhoff stress tensor
$\mathbf{S}$	Second Piola Kirchhoff tensor
$\mathbf{C}$	Right Cauchy-Green strain tensor
$\mathbf{m}_0$,$\mathbf{n}_0$	fibre-ensemble orientation vectors
ens	ensemble
λ	Stretch
λ_s	The slack stretch, the stretch needed to straighten the collagen fiber crimp
λ_t	The true stretch after the collagen fibers are straightened
E_s	The slack strain
Ψ	The strain energy
ϕ	The mass fractions
D	Distribution of slack strains for fibre recruitment
Γ	Fiber orientation distribution function
η	modulus, subscript for elastin collagen and matrix
μ_θ	mean circumferential orientation
σ	standard deviation of the fibre splay
μ_r	mean of the recruitment distribution

σ_r	standard deviation of the recruitment distribution
λ_{lb}	lower bound of the recruitment distribution
λ_{ub}	upper bound of the recruitment distribution
c_0, c_1	exponent for intra-fibre-ensemble interaction terms
d_0, d_1	exponent for inter-fibre-ensemble interaction terms

Chapter Bibliography

[1] Ivan Alferiev, Stanley J. Stachelek, Zhibin Lu, Angela L. Fu, Tiffany L. Sellaro, Jeanne M. Connolly, Richard W. Bianco, Michael S. Sacks, and Robert J. Levy. Prevention of polyurethane valve cusp calcification with covalently attached bisphosphonate diethylamino moieties. *Journal of Biomedical Materials Research*, 66A(2):385–395, jul 2003. doi: 10.1002/jbm.a.10896. URL http://www.ncbi.nlm.nih.gov/entrez/query.fcgi?cmd=Retrieve&db=PubMed&dopt=Citation&list_uids=12889009.

[2] J. E. Barber, N. Ratliff, and I. Vesely. Mechanics of explanted bioprosthetic heart valves. *Biomedical Sciences Instrumentation*, 35:29–32, 1999. ISSN 0067-8856. URL http://www.ncbi.nlm.nih.gov/entrez/query.fcgi?cmd=Retrieve&db=PubMed&dopt=Citation&list_uids=11143364.

[3] A. Bini, K. G. Mann, B. J. Kudryk, and F. J. Schoen. Noncollagenous bone matrix proteins, calcification, and thrombosis in carotid artery atherosclerosis. *Arteriosclerosis, Thrombosis, and Vascular Biology*, 19(8):1852–1861, aug 1999. doi: 10.1161/01.atv.19.8.1852. URL http://www.ncbi.nlm.nih.gov/htbin-post/Entrez/query?db=m&form=6&dopt=r&uid=0010446063http://www.atvbaha.org/cgi/content/full/19/8/1852http://www.atvbaha.org/cgi/content/abstract/19/8/1852.

[4] Markus J. Buehler. Atomistic and continuum modeling of mechanical properties of collagen: elasticity, fracture, and self-assembly. *Journal of Materials Research*, 21(08):1947–1961, aug 2006. ISSN 2044-5326. doi: 10.1557/jmr.2006.0236. URL http://dx.doi.org/10.1557/jmr.2006.0236.

[5] Francisco S. A. Cavalcante, Satoru Ito, Kelly Brewer, Hiroaki Sakai, Adriano M. Alencar, Murilo P. Almeida, José S. Andrade, Arnab Majumdar, Edward P. Ingenito, and Béla Suki. Mechanical interactions between collagen and proteoglycans: implications for the stability of lung tissue. *Journal of Applied Physiology*, 98(2):672–679, feb 2005. doi: 10.1152/japplphysiol.00619.2004. URL `http://www.ncbi.nlm.nih.gov/entrez/query.fcgi?cmd=Retrieve&db=PubMed&dopt=Citation&list_uids=15448123`.

[6] D T Cheung, P DiCesare, P D Benya, E Libaw, and M E Nimni. The presence of intermolecular disulfide cross-links in type III collagen. *The Journal of biological chemistry*, 258(12):7774–7778, June 1983. ISSN 0021-9258.

[7] David T. Cheung and Marcel E. Nimni. Mechanism of crosslinking of proteins by glutaraldehyde I: reaction with model compounds. *Connective Tissue Research*, 10(2):187–199, jan 1982. doi: 10.3109/03008208209034418.

[8] David T. Cheung and Marcel E. Nimni. Mechanism of crosslinking of proteins by glutaraldehyde II.: reaction with monomeric and polymeric collagen. *Connective Tissue Research*, 10(2):201–216, jan 1982. doi: 10.3109/03008208209034419.

[9] David T. Cheung, Natasha Perelman, Ellen C. Ko, and Marcel e. Nimni. Mechanism of crosslinking of proteins by glutaraldehyde III: reaction with collagen in tissues. *Connective Tissue Research*, 13(2):109–115, jan 1985. doi: 10.3109/03008208509152389.

[10] David T. Cheung, Deborah Tong, Natasha Perelman, Delia Ertl, and Marcel E. Nimni. Mechanism of crosslinking of proteins by glutaraldehyde IV: in vitro and in vivo stability of a crosslinked collagen matrix. *Connective Tissue Research*, 25(1):27–34, jan 1990. doi: 10.3109/03008209009009810.

[11] M. F. Coughlin, B. Suki, and D. Stamenovic. Dynamic behavior of lung parenchyma in shear. *Journal of Applied Physiology*, 80 (6):1880–1890, jun 1996. doi: 10.1152/jappl.1996.80.6.1880. URL http://www.ncbi.nlm.nih.gov/entrez/query.fcgi?cmd=Retrieve&db=PubMed&dopt=Citation&list_uids=8806890.

[12] Chad E. Eckert, Rong Fan, Brandon Mikulis, Mathew Barron, Christopher A. Carruthers, Vincent M. Friebe, Naren R. Vyavahare, and Michael S. Sacks. On the biomechanical role of glycosaminoglycans in the aortic heart valve leaflet. *Acta Biomaterialia*, 9(1):4653–4660, jan 2013. ISSN 1878-7568 (Electronic) 1742-7061 (Linking). doi: 10.1016/j.actbio.2012.09.031. URL http://www.ncbi.nlm.nih.gov/pubmed/23036945.

[13] S.J Eppell, B.N Smith, H Kahn, and R Ballarini. Nano measurements with micro-devices: mechanical properties of hydrated collagen fibrils. *Journal of The Royal Society Interface*, 3(6):117–121, feb 2006. doi: 10.1098/rsif.2005.0100. URL http://rsif.royalsocietypublishing.org/content/3/6/117.abstract.

[14] Rong Fan and Michael S. Sacks. Simulation of planar soft tissues using a structural constitutive model: finite element implementation and validation. *Journal of Biomechanics*, 47(9):2043–2054, jun 2014. doi: 10.1016/j.jbiomech.2014.03.014.

[15] Bahar Fata, Will Zhang, Rouzbeh Amini, and Michael S. Sacks. Insights into regional adaptations in the growing pulmonary artery using a meso-scale structural model: effects of ascending aorta impingement. *Journal of Biomechanical Engineering*, 136(2):021009–021009–13, feb 2014. ISSN 0148-0731. doi: 10.1115/1.4026457. URL http://dx.doi.org/10.1115/1.4026457.

[16] K. Garikipati, S. Göktepe, and C. Miehe. Elastica-based strain energy functions for soft biological tissue. *Journal of the Mechanics and Physics of Solids*, 56(4):1693–1713, April 2008. ISSN 0022-5096. doi: 10.1016/j.jmps.2007.07.005. URL http://www.sciencedirect.com/science/article/pii/S0022509607001597.

[17] K. Gelse, E. Poschl, and T. Aigner. Collagens–structure, function, and biosynthesis. *Advanced Drug Delivery Reviews*, 55(12):1531–1546, nov 2003. ISSN 0169-409X (Print). doi: 10.1016/j.addr.2003.08.002. URL http://www.ncbi.nlm.nih.gov/entrez/query.fcgi?cmd=Retrieve&db=PubMed&dopt=Citation&list_uids=14623400.

[18] E. Gendler, S. Gendler, and M. E. Nimni. Toxic reactions evoked by glutaraldehyde-fixed pericardium and cardiac valve tissue bioprosthesis. *Journal of Biomedical Materials Research*, 18(7):727–736, sep 1984. ISSN 1097-4636. doi: 10.1002/jbm.820180703. URL http://dx.doi.org/10.1002/jbm.820180703.

[19] Eileen Gentleman, Andrea N. Lay, Darryl A. Dickerson, Eric A. Nauman, Glen A. Livesay, and Kay C. Dee. Mechanical characterization of collagen fibers and scaffolds for tissue engineering. *Biomaterials*, 24(21):3805–3813, sep 2003. ISSN 0142-9612. doi: 10.1016/s0142-9612(03)00206-0. URL http://www.sciencedirect.com/science/article/pii/S0142961203002060.

[20] Jonathan S. Grashow, Michael S. Sacks, Jun Liao, and Ajit P. Yoganathan. Planar biaxial creep and stress relaxation of the mitral valve anterior leaflet. *Annals of Biomedical Engineering*, 34(10):1509–1518, October 2006. ISSN 0090-6964 (Print). doi: 10.1007/

s10439-006-9183-8. URL http://www.ncbi.nlm.nih.gov/entrez/query.fcgi?cmd=Retrieve&db=PubMed&dopt=Citation&list_uids=17016761.

[21] Jonathan S. Grashow, Ajit P. Yoganathan, and Michael S. Sacks. Biaxial stress-stretch behavior of the mitral valve anterior leaflet at physiologic strain rates. *Annals of Biomedical Engineering*, 34(2):315–325, feb 2006. doi: 10.1007/s10439-005-9027-y. URL http://www.ncbi.nlm.nih.gov/entrez/query.fcgi?cmd=Retrieve&db=PubMed&dopt=Citation&list_uids=16450193.

[22] Gerhard A. Holzapfel. *Nonlinear Solid Mechanics: A Continuum Approach for Engineering*. John Wiley & Sons, Ltd., Chichester, 2000. ISBN 0471823198. URL https://www.ebook.de/de/product/3056011/gerhard_a_holzapfel_nonlinear_solid_mechanics.html.

[23] M Kojic, S Mijailovic, and N Zdravkovic. A numerical algorithm for stress integration of a fiber-fiber kinetics model with Coulomb friction for connective tissue. *Computational Mechanics*, 21(2):189–198, mar 1998. doi: 10.1007/s004660050294.

[24] Y. Lanir. A structural theory for the homogeneous biaxial stress-strain relationships in flat collagenous tissues. *Journal of Biomechanics*, 12(6):423–436, jan 1979. doi: 10.1016/0021-9290(79)90027-7.

[25] Y. Lanir. Constitutive equations for fibrous connective tissues. *Journal of Biomechanics*, 16(1):1–12, jan 1983. doi: 10.1016/0021-9290(83)90041-6.

[26] Y. Lanir. Plausibility of structural constitutive equations for isotropic soft tissues in finite static deformations. *Journal of Applied Mechanics*, 61(3):695–702, September 1994. doi: 10.1115/1.2901516.

[27] Chung-Hao Lee, Will Zhang, Jun Liao, Christopher A. Carruthers, Jacob I. Sacks, and Michael S. Sacks. On the presence of affine fibril and fiber kinematics in the mitral valve anterior leaflet. *Biophysical Journal*, 108(8):2074–2087, April 2015. ISSN 1542-0086 (Electronic) 0006-3495 (Linking). doi: 10.1016/j.bpj.2015.03.019. URL `http://www.ncbi.nlm.nih.gov/pubmed/25902446`.

[28] J. Michael Lee, Ralph Corrente, and Sean A. Haberer. The bovine pericardial xenograft: II. Effect of tethering or pressurization during fixation on the tensile viscoelastic properties of bovine pericardium. *Journal of Biomedical Materials Research*, 23(5):477–489, may 1989. doi: 10.1002/jbm.820230503.

[29] J. Michael Lee, Sean A. Haberer, and Derek R. Boughner. The bovine pericardial xenograft: I. Effect of fixation in aldehydes without constraint on the tensile viscoelastic properties of bovine pericardium. *Journal of Biomedical Materials Research*, 23(5):457–475, may 1989. doi: 10.1002/jbm.820230502.

[30] J. Michael Lee, Michael Ku, and Sean A. Haberer. The bovine pericardial xenograft: III. Effect of uniaxial and sequential biaxial stress during fixation on the tensile viscoelastic properties of bovine pericardium. *Journal of Biomedical Materials Research*, 23(5):491–506, may 1989. doi: 10.1002/jbm.820230504.

[31] JM Lee, SA Haberer, CA Pereira, WA Naimark, DW Courtman, and GJ Wilson. High strain rate testing and structural analysis of pericardial bioprosthetic materials. In HE Kambic and AT Yokobori, editors, *Biomaterials' Mechanical Properties*, volume STP 1173, pages 19–19–24. ASTM International, Philadelphia, 1994. doi: 10.1520/stp18091s.

[32] Tse Chung Lee, Ronald J Midura, Vincent C Hascall, and Ivan Vesely. The effect of elastin damage on the mechanics of the aortic valve. *Jour-*

nal of Biomechanics, 34(2):203–210, feb 2001. doi: 10.1016/s0021-9290(00)00187-1. URL http://www.ncbi.nlm.nih.gov/htbin-post/Entrez/query?db=m&form=6&dopt=r&uid=11165284.

[33] Jun Liao and Ivan Vesely. Relationship between collagen fibrils, glycosaminoglycans, and stress relaxation in mitral valve chordae tendineae. *Annals of Biomedical Engineering*, 32(7):977–983, July 2004. doi: 10.1023/b:abme.0000032460.97278.e9. URL http://www.ncbi.nlm.nih.gov/entrez/query.fcgi?cmd=Retrieve&db=PubMed&dopt=Citation&list_uids=15298435.

[34] Jun Liao, Lin Yang, Jonathan Grashow, and Michael S. Sacks. The relation between collagen fibril kinematics and mechanical properties in the mitral valve anterior leaflet. *Journal of Biomechanical Engineering*, 129(1):78–87, 2007. ISSN 0148-0731 (Print). doi: 10.1115/1.2401186. URL http://www.ncbi.nlm.nih.gov/entrez/query.fcgi?cmd=Retrieve&db=PubMed&dopt=Citation&list_uids=17227101.

[35] J. Merodio and R. W. Ogden. The influence of the invariant I-8 on the stress-deformation and ellipticity characteristics of doubly fiber-reinforced non-linearly elastic solids. *International Journal of Non-Linear Mechanics*, 41(4):556–563, May 2006. ISSN 0020-7462. doi: 10.1016/j.ijnonlinmec.2006.02.001. URL ://WOS:000237905700008.

[36] A. Mirnajafi, J. Raymer, M. J. Scott, and M. S. Sacks. The effects of collagen fiber orientation on the flexural properties of pericardial heterograft biomaterials. *Biomaterials*, 26(7):795–804, March 2005. doi: 10.1016/j.biomaterials.2004.03.004. URL http://www.ncbi.nlm.nih.gov/entrez/query.fcgi?cmd=Retrieve&db=PubMed&dopt=Citation&list_uids=15350785.

[37] W.A. Naimark, J.M. Lee, H. Limeback, and D. Cheung. Correlation of structure and viscoelastic properties in the pericardia of four mammalian species. *American Journal of Physiology-Heart and Circulatory Physiology*, 263(4):H1095–H1106, oct 1992. doi: 10.1152/ajpheart.1992.263.4.h1095.

[38] M. E. Nimni, D. Cheung, B. Strates, M. Kodama, and K. Sheikh. Chemically modified collagen : a natural biomaterial for tissue replacement. *Journal of Biomedical Materials Research*, 21(6):741–771, jun 1987. doi: 10.1002/jbm.820210606.

[39] Marcel E Nimni. *Collagen: volume II: biochemistry and biomechanics*. CRC Press, 2018.

[40] David A.D. Parry. The molecular and fibrillar structure of collagen and its relationship to the mechanical properties of connective tissue. *Biophysical Chemistry*, 29(1-2):195–209, feb 1988. doi: 10.1016/0301-4622(88)87039-x. URL `http://www.ncbi.nlm.nih.gov/entrez/query.fcgi?cmd=Retrieve&db=PubMed&dopt=Citation&list_uids=3282560`.

[41] John A. Petruska and Alan J. Hodge. A subunit model for the tropocollagen macromolecule. *Proceedings of the National Academy of Sciences*, 51(5):871–876, May 1964. doi: 10.1073/pnas.51.5.871. URL `http://www.pnas.org/content/51/5/871.short`.

[42] M. S. Sacks. A method for planar biaxial mechanical testing that includes in-plane shear. *Journal of Biomechanical Engineering*, 121(5):551–5, 1999. doi: 10.1115/1.2835086.

[43] M. S. Sacks and F. J. Schoen. Collagen fiber disruption occurs independent of calcification in clinically explanted bioprosthetic heart valves.

J Biomed Mater Res, 62(3):359–71, December 2002. doi: 10.1002/jbm.10293. URL http://www.ncbi.nlm.nih.gov/entrez/query.fcgi?cmd=Retrieve&db=PubMed&dopt=Citation&list_uids=12209921.

[44] Michael S. Sacks. A structural constitutive model for chemically treated planar tissues under biaxial loading. *Computational Mechanics*, 26(3):243–249, sep 2000. doi: 10.1007/s004660000175.

[45] Michael S. Sacks. Incorporation of experimentally-derived fiber orientation into a structural constitutive model for planar collagenous tissues. *Journal of Biomechanical Engineering*, 125(2):280–7, April 2003. doi: 10.1115/1.1544508. URL http://www.ncbi.nlm.nih.gov/entrez/query.fcgi?cmd=Retrieve&db=PubMed&dopt=Citation&list_uids=12751291.

[46] Michael S. Sacks and C. J. Chuong. Orthotropic mechanical properties of chemically treated bovine pericardium. *Annals of Biomedical Engineering*, 26(5):892–902, sep 1998. doi: 10.1114/1.135.

[47] Michael S. Sacks and Wei Sun. Multiaxial mechanical behavior of biological materials. *Annual Review of Biomedical Engineering*, 5(1):251–284, aug 2003. doi: 10.1146/annurev.bioeng.5.011303.120714. URL http://www.ncbi.nlm.nih.gov/entrez/query.fcgi?cmd=Retrieve&db=PubMed&dopt=Citation&list_uids=12730082.

[48] Michael S Sacks, Ali Mirnajafi, Wei Sun, and Paul Schmidt. Bioprosthetic heart valve heterograft biomaterials: structure, mechanical behavior and computational simulation. *Expert Review of Medical Devices*, 3(6):817–834, November 2006. ISSN 1743-4440 (Print). doi: 10.1586/

17434440.3.6.817. URL http://www.ncbi.nlm.nih.gov/entrez/query.fcgi?cmd=Retrieve&db=PubMed&dopt=Citation&list_uids=17280546.

[49] Michael S. Sacks, W. David Merryman, and David E. Schmidt. On the biomechanics of heart valve function. *Journal of Biomechanics*, 42(12):1804–1824, aug 2009. ISSN 1873-2380 (Electronic). doi: 10.1016/j.jbiomech.2009.05.015. URL http://www.ncbi.nlm.nih.gov/entrez/query.fcgi?cmd=Retrieve&db=PubMed&dopt=Citation&list_uids=19540499.

[50] MS Sacks. Biaxial mechanical evaluation of planar biological materials. *J Elasticity*, 61:199–246, 2000.

[51] Naoki Sasaki and Shingo Odajima. Elongation mechanism of collagen fibrils and force-strain relations of tendon at each level of structural hierarchy. *Journal of Biomechanics*, 29(9):1131–1136, sep 1996. doi: 10.1016/0021-9290(96)00024-3.

[52] Naoki Sasaki and Singo Odajima. Stress-strain curve and Young's modulus of a collagen molecule as determined by the X-ray diffraction technique. *Journal of Biomechanics*, 29(5):655–658, may 1996. doi: 10.1016/0021-9290(95)00110-7.

[53] F. J. Schoen. Pathology of heart valve substitution with mechanical and tissue prostheses. In M.D. Silver, A.I. Gotlieb, and F. J. Schoen, editors, *Cardiovascular Pathology*, volume 3. Livingstone, New York, 2001.

[54] F. J. Schoen and R. J. Levy. Founder's award, 25th annual meeting of the society for biomaterials, perspectives. providence, RI, april 28-may 2, 1999. Tissue heart valves: current challenges and future research perspectives. *Journal of biomedical materials research*, 47(4):439–465, December 1999. ISSN 0021-9304. URL http://www.ncbi.nlm.nih.gov/htbin-post/Entrez/query?db=m&form=6&dopt=r&uid=0010497280.

[55] Frederick J. Schoen. Cardiac valves and valvular pathology: update on function, disease, repair, and replacement. *Cardiovascular Pathology*, 14 (4):189–194, July 2005. ISSN 1054-8807 (Print). doi: 10.1016/j.carpath.2005.03.005. URL http://www.ncbi.nlm.nih.gov/entrez/query.fcgi?cmd=Retrieve&db=PubMed&dopt=Citation&list_uids=16009317.

[56] Frederick J. Schoen and Robert J. Levy. Calcification of tissue heart valve substitutes: progress toward understanding and prevention. *The Annals of Thoracic Surgery*, 79(3):1072–1080, March 2005. doi: 10.1016/j.athoracsur.2004.06.033. URL http://www.ncbi.nlm.nih.gov/entrez/query.fcgi?cmd=Retrieve&db=PubMed&dopt=Citation&list_uids=15734452.

[57] Tiffany L. Sellaro, Daniel Hildebrand, Qijin Lu, Naren Vyavahare, Michael Scott, and Michael S. Sacks. Effects of collagen fiber orientation on the response of biologically derived soft tissue biomaterials to cyclic loading. *Journal of Biomedical Materials Research Part A*, 80A(1):194–205, January 2007. ISSN 1549-3296 (Print). doi: 10.1002/jbm.a.30871. URL http://www.ncbi.nlm.nih.gov/entrez/query.fcgi?cmd=Retrieve&db=PubMed&dopt=Citation&list_uids=17041913.

[58] Zhilei L. Shen, Mohammad Reza Dodge, Harold Kahn, Roberto Ballarini, and Steven J. Eppell. Stress-strain experiments on individual collagen fibrils. *Biophysical Journal*, 95(8):3956–3963, oct 2008. ISSN 0006-3495. doi: 10.1529/biophysj.107.124602. URL http://www.sciencedirect.com/science/article/pii/S0006349508785345.

[59] John A. Stella, Jun Liao, and Michael S. Sacks. Time-dependent biaxial mechanical behavior of the aortic heart valve leaflet. *Journal of Biomechanics*, 40(14):

3169–3177, jan 2007. ISSN 0021-9290 (Print) 0021-9290 (Linking). doi: 10.1016/j.jbiomech.2007.04.001. URL http://www.ncbi.nlm.nih.gov/entrez/query.fcgi?cmd=Retrieve&db=PubMed&dopt=Citation&list_uids=17570376.

[60] W. Sun, M.S. Sacks, T.L. Sellaro, W.S. Slaughter, and M.J. Scott. Biaxial mechanical response of bioprosthetic heart valve biomaterials to high in-plane shear. *Journal of Biomechanical Engineering*, 125(3):372–380, jun 2003. doi: 10.1115/1.1572518.

[61] W. Sun, A. Abad, and M.S. Sacks. Simulated bioprosthetic heart valve deformation under quasi-static loading. *Journal of Biomechanical Engineering*, 127(6): 905–914, jul 2005. doi: 10.1115/1.2049337.

[62] Wei Sun and Michael S. Sacks. Finite element implementation of a generalized Fung-elastic constitutive model for planar soft tissues. *Biomechanics and Modeling in Mechanobiology*, 4(2-3):190–199, August 2005. doi: 10.1007/s10237-005-0075-x. URL http://www.ncbi.nlm.nih.gov/entrez/query.fcgi?cmd=Retrieve&db=PubMed&dopt=Citation&list_uids=16075264.

[63] Wei Sun, Michael Sacks, Gregory Fulchiero, Joshua Lovekamp, Naren Vyavahare, and Michael Scott. Response of heterograft heart valve biomaterials to moderate cyclic loading. *Journal of Biomedical Materials Research*, 69A(4):658–669, June 2004. doi: 10.1002/jbm.a.30031. URL http://www.ncbi.nlm.nih.gov/entrez/query.fcgi?cmd=Retrieve&db=PubMed&dopt=Citation&list_uids=15162408.

[64] I. Vesely, J. E. Barber, and N. B. Ratliff. Tissue damage and calcification may be independent mechanisms of bioprosthetic heart valve failure. *The Journal of heart valve disease*, 10(4):471–477, July 2001. ISSN

0966-8519. URL http://www.ncbi.nlm.nih.gov/entrez/query.fcgi?cmd=Retrieve&db=PubMed&dopt=Citation&list_uids=11499593.

[65] S. M. Wells and M. S. Sacks. Effects of fixation pressure on the biaxial mechanical behavior of porcine bioprosthetic heart valves with long-term cyclic loading. *Biomaterials*, 23(11):2389–2399, June 2002. doi: 10.1016/s0142-9612(01)00375-1. URL http://www.ncbi.nlm.nih.gov/entrez/query.fcgi?cmd=Retrieve&db=PubMed&dopt=Citation&list_uids=12013187.

[66] S. M. Wells, S. L. Adamson, B. L. Langille, and J. M. Lee. Thermomechanical analysis of collagen crosslinking in the developing ovine thoracic aorta. *Biorheology*, 35(6):399–414, November 1998. doi: 10.1016/s0006-355x(99)80019-5. URL http://www.ncbi.nlm.nih.gov/entrez/query.fcgi?cmd=Retrieve&db=PubMed&dopt=Citation&list_uids=10656049.

[67] Sarah M. Wells, Tiffany Sellaro, and Michael S. Sacks. Cyclic loading response of bioprosthetic heart valves: effects of fixation stress state on the collagen fiber architecture. *Biomaterials*, 26(15):2611–2619, May 2005. doi: 10.1016/j.biomaterials.2004.06.046. URL http://www.ncbi.nlm.nih.gov/entrez/query.fcgi?cmd=Retrieve&db=PubMed&dopt=Citation&list_uids=15585264.

[68] SM Wells and MS Sacks. Effects of stress-state during fixation on the fatigue properties of bioprosthetic heart valve tissue. In *Transactions of the Sixth World Biomaterials Congress, Kamuela, HI, May*, pages 15–20, 2000.

[69] Lanti Yang, Kees O. van der Werf, Bart F.J.M. Koopman, Vinod Subramaniam, Martin L. Bennink, Pieter J. Dijkstra, and Jan Feijen. Micromechanical bending

of single collagen fibrils using atomic force microscopy. *Journal of Biomedical Materials Research Part A*, 82A(1):160–168, 2007. ISSN 1552-4965. doi: 10.1002/jbm.a.31127. URL http://dx.doi.org/10.1002/jbm.a.31127http://onlinelibrary.wiley.com/doi/10.1002/jbm.a.31127/abstract.

[70] Lanti Yang, Carel F.C. Fitié, Kees O. van der Werf, Martin L. Bennink, Pieter J. Dijkstra, and Jan Feijen. Mechanical properties of single electrospun collagen type i fibers. *Biomaterials*, 29(8):955–962, mar 2008. doi: 10.1016/j.biomaterials.2007.10.058.

[71] Will Zhang, Yuan Feng, Chung-Hao Lee, Kristen L. Billiar, and Michael S. Sacks. A generalized method for the analysis of planar biaxial mechanical data using tethered testing configurations. *Journal of Biomechanical Engineering*, 137(6):064501, apr 2015. ISSN 1528-8951 (Electronic) 0148-0731 (Linking). doi: 10.1115/1.4029266. URL http://www.ncbi.nlm.nih.gov/pubmed/25429606.

[72] Will Zhang, Salma Ayoub, Jun Liao, and Michael S. Sacks. A meso-scale layer-specific structural constitutive model of the mitral heart valve leaflets. *Acta Biomaterialia*, 32:238–255, March 2016. ISSN 1878-7568 (Electronic) 1742-7061 (Linking). doi: 10.1016/j.actbio.2015.12.001. URL http://www.ncbi.nlm.nih.gov/pubmed/26712602.

Chapter 4

Modeling the effects of cyclic loading on exogenously cross-linked tissues[1]

Preface

Bioprosthetic heart valves (BHVs), fabricated from exogenously crosslinked collagenous tissues, remain the most popular heart valve replacement design. However, the lifespan of BHVs remains limited to 10–15 years, in part because the mechanisms that underlie BHV failure remain poorly understood. Experimental evidence indicates that BHVs undergo significant changes in geometry with in vivo operation, which lead to stress concentrations that can have a significant impact on structural damage. These changes do not appear to be due to plastic deformation, as the leaflets only deform in the elastic regime. Moreover, structural damage was not detected by the 65 million cycle time point. Instead, we found that this nonrecoverable deformation is similar to the permanent set effect observed in elastomers, which allows the reference configuration of the material to evolve over time. We hypothesize that the scission-healing reaction of glutaraldehyde is the underlying mechanism responsible for permanent set in exogenously crosslinked soft tissues. The continuous scission-healing process of glutaraldehyde allows a portion of the exogenously crosslinked

[1]**The work contained in this chapter was published as**: Zhang, W. & Sacks, M. S. Modeling the response of exogenously crosslinked tissue to cyclic loading: The effects of permanent set. Journal of the mechanical behavior of biomedical materials, 2017, 75, 336-350
The author contributed to: performing the research, model development, data analysis, coding development, and writing the manuscript.

matrix, which is considered to be the non-fibrous part of the extracellular matrix, to be re-crosslinked in the loaded state. Thus, this mechanism for permanent set can be used to explain the time evolving mechanical response and geometry of BHVs in the early stage. To model the permanent set effect, we assume that the exogenously crosslinked matrix undergoes changes in reference configurations over time. The changes in the collagen fiber architecture due to dimensional changes allow us to predict subsequent changes in mechanical response. Results show that permanent set alone can explain and, more importantly, predict how the mechanical response of the biomaterial change with time. Furthermore, we found is no difference in permanent set rate constants between the strain controlled and the stress-controlled cyclic loading studies. An important finding we have is that the collagen fiber architecture has a limiting effect on the maximum changes in geometry that the permanent set effect can induce. This is due to the recruitment of collagen fibers as the changes in geometry due to permanent set increase. This means we can potentially optimize the BHV geometry based on the predicted the final BHV geometry after permanent set has largely ceased. Thus, we have developed the first structural constitutive model for the permanent set effect in exogenously crosslinked soft tissue, which can help to simulate BHV designs and reduce changes in BHV geometry during cyclic loading and thus potentially increasing BHV durability.

4.1 Introduction

4.1.1 Background and clinical significance

Heart valve treatment is a common cardiovascular surgical procedure with over 100,800 done annually in the U.S. alone [21] and 275,000 to 370,000 in developed nations [17]. Almost all contemporary heart valve replacement designs use exogenously crosslinked (EXL) collagenous soft tissues (e.g. bovine pericardium) to manufacture leaflets for bioprosthetic valves (BHVs) [39, 38]. BHVs have advantages in immunogenicity and hemodynamics over other designs, but also have a limited lifespan of 10-15 years. As a recent development in BHV technology, transcatheter valve interventions [2, 12] reduce surgical risk and make valve replacement more feasible for those who cannot tolerate full surgical interventions. However, this new technology also presents additional design challenges, including complex folding and compression during delivery. As a result, the leaflets are required to be significantly thinner than in traditional BHVs, which increases the leaflet stress and potentially the rate of failure. Existing data on transcatheter aortic valve interventions suggest a 2-year mortality rate of 33.9% overall [21] and over 68% when specifically replacing stenotic aortic valves [16]. As such, this further accentuates the need to develop an approach to improve BHV durability.

4.1.2 Mechanisms of BHV failure

The causes of BHV failure can be divided into two broad categories, mineralization, and structural damage, with both processes occurring in parallel or independently [29]. Mineralization is the accumulation of mineral deposits, mainly calcium phosphate, within the BHV leaflets [34]. This disrupts the underlying microstructure preventing the proper mechanical function of BHVs, increasing the likelihood

of tearing, and reducing flexibility (preventing normal opening and closing motions, and induce valve stenosis). This process is exacerbated by the presence of exogenous crosslinkers, such as glutaraldehyde (GLUT), where the phosphates from the devitalized endothelial cells bind with the calcium in the blood to form deposits. The causes of calcification and associated anti-calcification treatments are extensively studied in literature [23, 13, 43]. On the other hand, structural damage includes the collagen fiber damage and breakdown of the non-fibrous part of the extracellular matrix (ECM), *which we will refer to as simply the matrix*. Fourier transform infrared spectroscopy(FTIR) results have shown changes in the collagen fiber molecular structure after 50 million cycles [40], which suggests that some collagen fiber damage has occurred during this period. However, its effect on the mechanical response of BHVs was not detectable. Nevertheless, it is important to maintain the structural integrity of the BHV, as this will help to improve BHV durability.

4.1.3 Response to long-term cyclic loading

The current process for evaluating BHV designs is an expensive and time-consuming three-stage process: 1) accelerated wear testing(AWT), 2) large animal studies, and 3) clinical trials. AWT is performed by cycling BHVs in sterile saline at 10 to 20 times the normal heart rate. It is currently the only way to evaluate BHV durability in a feasible amount of time (months instead of years). However, the loading conditions and environment during AWT are not physiological and the only durability information currently used is the presence of visible damage. Designs which show promise are then put through costly large animal studies, which still do not fully duplicate the human native environment. The final and most important stage is clinical evaluations. This is the only stage in the evaluation process that can provide true indications of the *in vivo* performance of BHV designs. However, this

is the final, most difficult, most expensive and most time-consuming stage. Clearly, current methods of evaluating BHV designs are not feasible for advancing the BHV technology in a timely manner. Computational simulations have been presented as an effective approach to this problem[38]. To be effective, we need a better understanding of the underlying mechanisms of structural damage.

However, these mechanisms are poorly understood, especially for how they affect the mechanical response of the exogenously crosslinked tissues used to construct the BHV leaflets. The most significant change in response to cyclic loading is the change in geometry of the BHV leaflets. In a study on the porcine aortic BHVs [36], Smith *et al.* found significant changes in the unloaded geometry of BHVs after AWT, especially in the belly region of the leaflets (Fig. 4.1A). By changing the unloaded reference configuration, the shape of the leaflets and their mechanical response will change as well. Further analysis has shown that significant structural damage occurred within the belly region as compared to other regions of the leaflet, where the stress significantly increased [37]. Interestingly, Smith et al. also found most the most significant changes in BHV leaflet geometry to occur within first 50 million cycles [36]. Moreover, Sacks and Smith [31] also found that there was minimal structural damage in this early stage (Fig. 4.1B). This is further supported by another study by Wells *et al* [44], where they found minimal structural changes during the first 50 million cycles for the pressure fixed BHVs, with most significant change observed in the first million cycles. Clearly, there is a non-damage based mechanism at play that changes the geometry of the material, with significant impact on the early stage of cycling and the rate of fatigue in later stages.

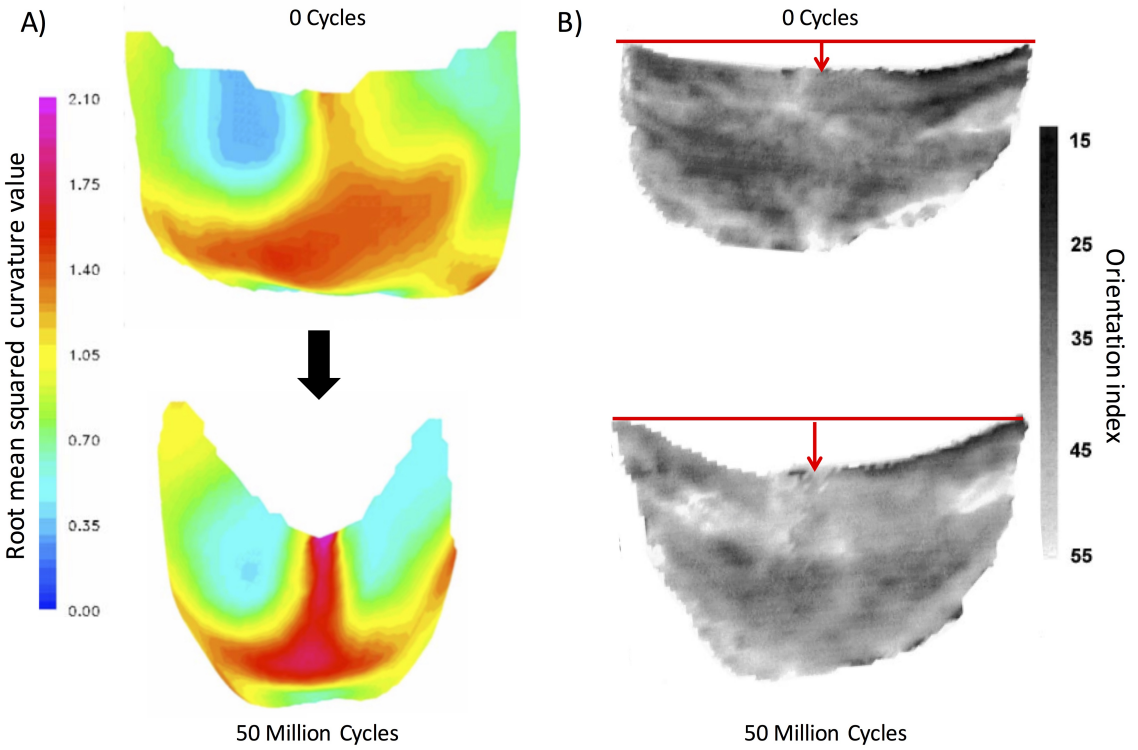

Figure 4.1: A) The 3D unloaded geometry a BHV leaflet before and after cyclic loading, with the color indicating the local root mean squared curvature. The most significant change in geometry is in the belly region. B) BHV leaflet collagen fiber architecture, showing that the collagen fiber architecture was convected by the dimensional changes. The grayscale scale bar shows the orientation index (OI), which is angle containing 50 % of fibers. The lack of changes in the OI suggests that minimal damage to the collagen fiber architecture has occurred.

4.1.4 The effect of exogenous crosslinking

Bovine pericardium (BP) is a dense collagenous tissue composed mostly of collagen type I fibers with some elastin, GAGs, cells, and vasculature. Collagen fibers are complex protein structures at the 2 - 10 μm scale, composed of tightly bundled collagen fibrils, which are approximately 50 nm in diameter. Much of what we know about the use of GLUT to exogenously crosslink collagenous tissue is from Nimni *et al.* [8, 22, 7, 11, 4, 5, 6]. GLUT, which is an aldehyde-based crosslinker, aggressively

crosslinks free amines in proteins. This suppresses immunogenicity by crosslinking all cell membrane protein remnants but also forms polymeric networks (at the nm scale) which allow for long-range crosslinks to the nearby tissue microstructures. We previously found that exogenous crosslinking increases the bending stiffness of the matrix by four times the original stiffness [20]. We also tested the mechanical response of exogenously crosslinked BP before and after crosslinking and developed the first constitutive model for exogenously crosslinked soft tissue [32]. Interestingly, we also found that exogenously crosslinking does not increase the collagen fiber modulus, but significantly increases the interactions between collagen fibers [32], which is responsible for up to 30% of the stress in the fully loaded state.

The GLUT crosslinking process involves a Schiff-base reaction. Importantly, the molecular bonds formed from Schiff-base reactions are known to be unstable at room and temperatures [19, 9]. Thus, although GLUT is highly reactive and aggressively crosslinks extracellular matrix proteins, any resulting crosslinks will also readily undergo hydrolysis at body temperature [19]. As a result, under cyclic loading in-vivo, exogenous ECM crosslinks will constantly break and reform. This continual process will cause the reference configuration to evolve towards the current loaded state. *We thus hypothesize that this scission-healing behavior could be linked to the mechanisms that underlie how the BHV leaflet geometry evolves over time.*

This damageless change in the BHV geometry has many similarities to the permanent set (PS) mechanisms observed in elastomers. Permanent set is an irreversible deformation that remains after a structure or material has been subjected to external stresses and then released. It does not involve damage to the constituents of the material but instead changes the referential configuration. Although the outcomes may be similar, *this form of permanent set is not a plastic deformations*, as

they are entirely within the elastic regime. In particular, it has been used to model the scission-healing reactions of elastomers that occur when stretched, heated, cooled, then unloaded. This results in some of the materials to change in referential configuration to the loaded state. In this process, permanent set does not damage the polymeric fibers but is a result of the change in the configuration of the underlying polymeric fiber network. Some works on constitutive models of this process include the works of Rajagopal and Wineman [24], Andrews and Tobolsky [1], and Rottach *et al.* [26, 28, 27]. However, there are few known studies on the permanent set effect in soft tissues or soft tissue-derived exogenously crosslinked biomaterials.

Based on the above considerations, we hypothesize that the initial time evolving BHV geometry and mechanical response can be predicted by permanent set mechanisms. Rather than heating and cooling, we assume that permanent set in exogenously crosslinked tissue occurs continuously at body temperature due to the GLUT, allowing the reference configuration of the exogenously crosslinked matrix (EXL matrix) to evolve over time. As a result, the reference configuration of BHVs will change while not affecting the intrinsic material properties of their constituents such as collagen fibers and the EXL matrix. Since the BHVs deform into a new configuration (Fig. 4.1), there may develop regions of stress concentrations. The high stresses will increase the rate of structural damage and thus accelerate the rate of BHV failure. Thus, *by compensating for the permanent set effects, it may be possible to reduce the BHV leaflet stresses and thus reduce structural damage to BHVs during in vivo operation after implant.* Therefore, constitutive models that can predict the effects of permanent set are crucial for the simulation of BHVs.

4.1.5 Constitutive models for the permanent set effect for soft tissues

The only work in the simulation of the permanent set effect in native or exogenously crosslinked soft tissues is the pioneering study of Martin and Sun [18], who developed a time-dependent constitutive model for uniaxial cyclic loading of GLUT exogenously crosslinked BP strips using a damage analog. Briefly, to model the uncycled mechanical response, they used the Fung hyperelastic model for the strain energy density function, Ψ_0. The time-dependent stress softening was then described using a modification to the strain energy function as $\Psi_{\text{PS}} = (1 - D_s)\Psi_0 - \Psi_0(\mathbf{E}_{\text{PS}})$. Here the strain energy of the material after permanent set (Ψ_{PS}) is reduced from Ψ_0 in accordance with a scaled damage function D_s and the same strain energy function evaluated at the current amount of permanent set ($\mathbf{E}_{\text{PS}}$). Martin and Sun then measured the maximum permanent set deformation that occurs for each specimen and used that to set the maximum bound of $\mathbf{E}_{\text{PS}}$. Additionally, Martin and Sun used two parameters: a lower bound below which no permanent set occurs, and an upper bound above which the tissue fails. In the intermediate region, D_s and $\mathbf{E}_{\text{PS}}$ simply increase linearly with the number of cycles. The number of cycles needed to reach the maximum permanent set deformation was then described using an inverse exponential-like function of the maximum strain applied, which is analogous to the stress versus cycles (S–N) curve used to describe the fatigue behavior of traditional engineering materials. However, such approaches have the following limitations: 1) they are not predictive as there are no underlying mechanisms in the model. A damage-like model can mimic the results of permanent set but cannot explain nor predict the mechanisms responsible in exogenously crosslinked tissue, and 2) there is no way to extrapolate for predicting into unmeasured regimes using the Fung hyperelastic model. Therefore, there is a need for a more predictive constitutive model that

utilizes the underlying mechanisms.

4.1.6 A new approach for modeling the permanent set effect in exogenously crosslinked soft tissues

We utilize a structural constitutive modeling approach, which integrates information on tissue composition and structure for material characterization [30]. In principle, using structural models we only need to perform parameter estimation for the intrinsic material properties, such as collagen fiber modulus and EXL matrix modulus, to predict the mechanical response using the quantified tissue microstructure. This mechanism-based approach allows us to predict the mechanical response at strains outside of the strain range of the experimental data used for parameter estimation [45, 10]; a feat not possible using purely phenomenological approaches. In addition, by using a structural modeling approach coupled with the permanent set mechanism to predict the collagen fiber architecture after cyclic loading, we can also predict the mechanical response of the soft tissue at higher cycle numbers. Thus, we use 1) the structural model parameters obtained in the uncycled mechanical state and 2) the permanent set mechanisms to predict how the mechanical response of the exogenously crosslinked tissues evolves with cyclic loading. The key aspects of our approach include:

1. Model the change in mechanical response entirely as a kinematic change in the underlying microstructure; no actual change in mechanical properties (damage)

2. Predict the change in geometry from the loading history and the permanent set mechanism

3. Validate the permanent set mechanism under both strain and stress controlled loading conditions

4. Develop a time-dependent implementation with an evolving loaded configuration under stress control

4.2 Overall modeling approach

We hypothesize that permanent set and structural damage are two separate and largely sequential mechanisms that underlie the mechanical response of BHVs. Thus, the lifespan of BHVs can be separated into three stages: early (up to 2-5 years), intermediate (up to 10 years), and late stage (up to failure) (Fig. 4.2). In the early stage, permanent set induces significant changes in BHV geometry while structural damage does not play a detectable role. This leads to increased stress and structural damage in the intermediate term which leads to failure in the late term. Thus, by compensating for the effect of permanent set on the geometry, we hypothesize that we can extend the lifespan of BHVs. We focus our model on the early stage of cyclic loading and build a solid foundation for modeling and simulating the later stages.

We assume that permanent set is driven by the scission-healing behaviors of the GLUT polymer network in the non-fibrous EXL matrix, allowing for fractions of it to change in reference state (Fig. 4.3A). The formation of aldehyde bonds during crosslinking, as well as the occasional hydrolysis of the aldehyde bonds, follows *first order molecular kinetics* [19]. Since this process drives the scission-healing of GLUT polymers and thus permanent set, we hypothesize that permanent set also follows first order kinetics. In addition, we note that the length scale of crosslinks formed by GLUT polymers (nm) in the EXL matrix is several orders of magnitude smaller than that of the collagen fibers (μm). Thus, we assume that the collagen fiber architecture does *not* undergo scission-healing like the EXL matrix. Instead, the collagen fibers remain intact during cyclic loading. Rather, the collagen fiber architecture is con-

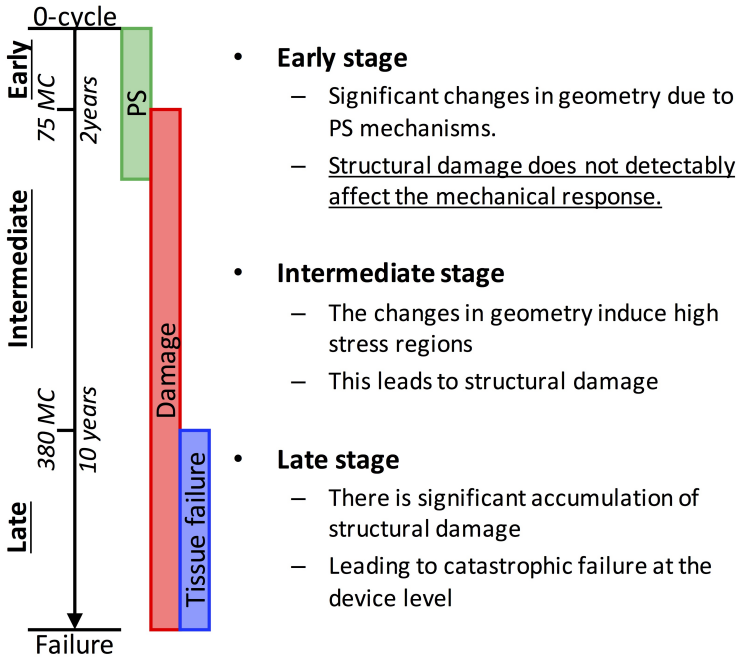

Figure 4.2: We speculate that the progression of structural damage and permanent set of BHV leaflets progress during long term cyclic loading can be separated into three stages: early, intermediate, and late.

vected by the changes in geometry that occurs with permanent set in the EXL matrix (Fig. 4.3B). *We refer to this mechanism as structural convection, which is defined as applying a permanent deformation (elongation and rotation of collagen fibers, Fig. 4.4) to the collagen fiber architecture based on the change in the reference configuration.* Previously, we have shown that dense collagenous tissues deform under affine kinematics [15]. Since deformations during cyclic loading are in the elastic regime and cyclic loading (second) is on a time scale much shorter than that of permanent set (weeks), the only change in collagen fiber architecture on a cycle to cycle period is also under affine kinematics. Therefore, we also assume that the convection of collagen fiber architecture due to permanent set is under affine kinematics as well. Thus, our approach is based on using the permanent set effect to model the evolving

properties of the EXL matrix, determine the change in reference configuration and convect collagen fiber architecture, which then allows us to determine the change in mechanical response of the collagen fibers using structural models.

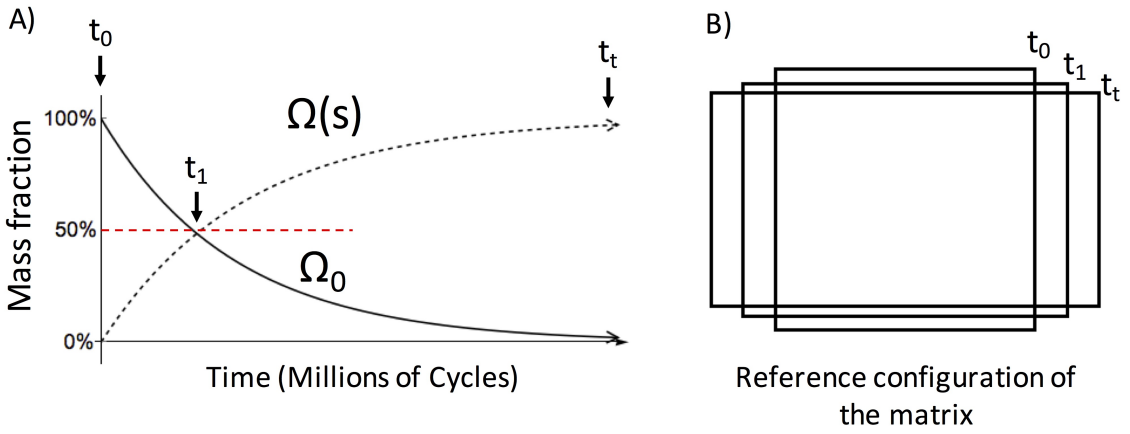

Figure 4.3: Illustration of the permanent set effect under cyclic uniaxial loading. A) There is a transfer of mass fraction of the EXL matrix to the loaded configuration $\Omega(s)$ from the original state Ω_0. B) This results in changes in the unloaded geometry of the tissue.

To develop the constitutive model form, we start by modeling the exogenously crosslinked tissue under cyclic loading as parts of a mixture of materials with the same properties but different evolving reference states. The reference state of each part of the EXL matrix is updated according to the strain history (Fig. 4.3A). The response of each part is then summed together for the bulk-level mechanical response of the EXL matrix. The new bulk level mechanical response is then used to determine the new unloaded state (Fig. 4.3B). The change in the EXL matrix from its uncycled state is then used to convect the collagen fiber architecture(Fig. 4.4). The new mechanical response of the EXL matrix is summed with the fiber ensemble interactions and collagen fiber response predicted from the new collagen fiber architecture to determine the full tissue-level mechanical response. Thus, how the *collagen fiber*

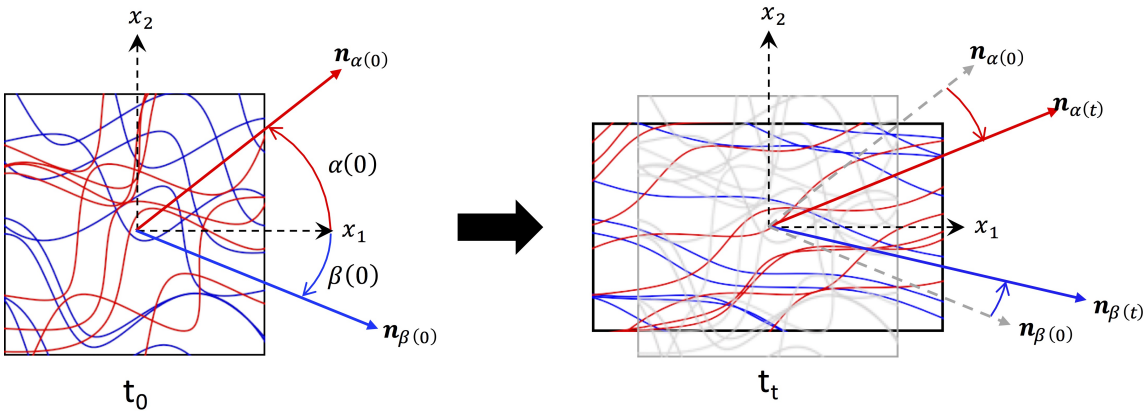

Figure 4.4: An illustration of how the collagen fiber architecture is convected by changes in the dimension of the bulk tissue. The left figure shows the origin geometry of the tissue at t_0 in figure 4.3 while the right figure shows the geometry of the tissue at t_t. Structural convection includes the rotation and straightening of the collagen fiber ensembles.

architecture (CFA) is convected by the EXL matrix is crucial to our model. We start developing our constitutive model by 1) modeling and parameter estimation for the native uncycled mechanical response of the exogenously crosslinked tissue. Then 2) develop the model form for the time evolving mechanical response based on the permanent set mechanism and cyclic loading data. The basic assumptions of our models are:

1. There is no structural damage to the collagen fibers or the EXL matrix
2. The crosslinking process that induces permanent set follows first-order kinetics
3. We are only modeling permanent set under physiological conditions and the process is thus isothermal
4. Permanent set occurs in the isotropic EXL matrix so that its rate constant is directionally independent

5. The permanent set rate constant is strain-level independent in the physiological range

6. Permanent set occurs over a time scale much longer than a single cardiac cycle

7. The tissue is functionally elastic, and thus viscoelastic effects are ignored

8. The convection of the collagen fiber architecture follows affine kinematics

9. collagen fibers do not bear load or interact until they are straightened [15]

4.3 Extant experimental data

We utilized data from the following two extant studies, which differ by their loading conditions and specimen orientations. In the study by Sun *et al.*[40], exogenously crosslinked BP patches were cycled along the preferred collagen fiber direction (PD) at a peak strain of 16% and maintained for up to 65 million cycles (Fig. 4.5A&B). The reference configurations of the exogenously crosslinked BP were tracked using fiducial markers attached to the center of the specimens[33]. The mechanical cycling was stopped at 30 and 65 million cycles for mechanical testing with multiple protocols and different loading paths. It was found that there were significant extensions in the direction of loading (7.1%), PD, and contractions in the cross direction (-7.7%). In addition, the collagen fiber crimp period increased from 40.6μm to 45.24μm which is consistent with the convection of the collagen fiber architecture that would occur as collagen fiber straighten (Fig. 4.4). The mechanical response also changed accordingly. The compliance in the PD decreased over time while the compliance in the cross direction of the tissue increased.

In the study by Sellaro *et al.*[35], the same exogenously crosslinked BP patches were cycled at 500kPa for up to 50 million cycles (Fig. 4.5C&D). In this case, the

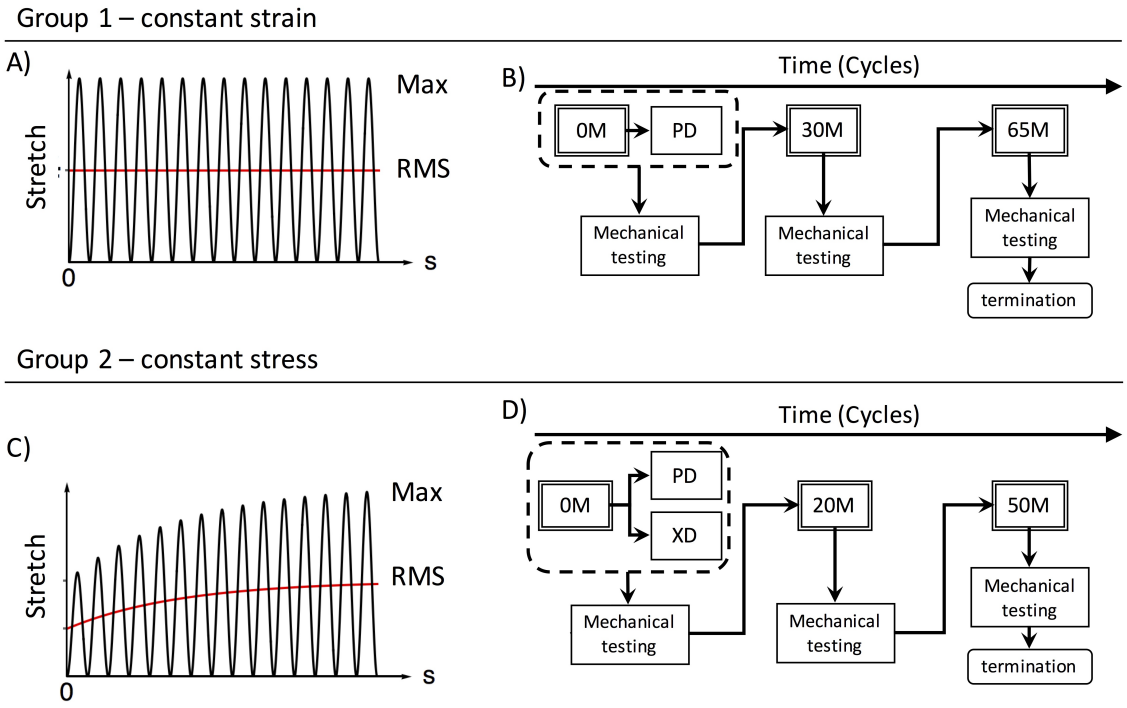

Figure 4.5: We utilize two extant databases in this study. The first is strain controlled, with A) constant strain level and is B) sorted for orientation along the preferred direction then put through cyclic loading and mechanical testing. The second is with C) constant strain but evolving strain level. The specimens are then D) sorted for orientation along both the preferred direction and cross-preferred direction, then put through cyclic loading and mechanical testing.

specimens were separated into two groups: with stress controlled loading along the 1) PD and 2) orthogonal to the PD (XD). Similarly, the reference states of the exogenously crosslinked BP specimens were tracked, with cycling stopped at 20 and 50 million cycles for mechanical testing. Analysis of the results showed interesting differences between the PD and XD cycled specimens. For both the PD and XD cycled specimens, we observed significant elongation in the direction of loading and contraction in the orthogonal direction with cycling. Additionally, the effective stiffness in the direction of loading increased over time, whereas the orthogonal direction decreased over time. In addition, we also studied how the collagen fiber architecture

of the tissue changed with cyclic loading. For the PD cycled specimens, it was observed that the collagen fiber orientation distribution became more aligned, and the collagen fiber crimp period increased from 24 μm to 28μm. On the other hand, for the XD cycled specimens, it was observed that the collagen fiber orientation distribution became more spread, and the collagen fiber crimp period remained unchanged. This findings on the structural changes with the direction of cyclic loading are consistent with the structural convection that we hypothesize with permanent set and lend further support to our model (Fig. 4.4).

4.4 Constitutive model for uncycled exogenously crosslinked tissue

4.4.1 Constitutive model for exogenous crosslinking

We have previously developed the first constitutive model for exogenously crosslinked collagenous tissues [32] and determined the following three contributors to the mechanical response: collagen fibers, EXL matrix, and fiber-fiber interactions, where the total strain energy density function is given by

$$\Psi = \phi_{\text{col}} \left[\Psi_{\text{col}} + \Psi_{\text{int}}\right] + \phi_m \Psi_m \tag{4.1}$$

In particular, we found the fiber ensemble interaction term ($\phi_{\text{col}}\Psi_{\text{int}}$) to be especially important in modeling exogenously crosslinked tissues, accounting for approximately 30% of the stress in the fully loaded state (Fig. 4.6A). To determine the model form of the interaction component, we used the remaining stress after subtracting the collagen fiber response and EXL matrix response from the mechanical response of the tissue after exogenous crosslinking (Fig. 4.6A). In that study, we consider three possible forms of interactions: intra-fiber ensemble (Fig. 4.6B) (an ensemble being a family of fibers sharing a common orientation), ensemble-ensemble rotations,

and ensemble-ensemble relative extensions (Fig. 4.6C&D). We found that intra-fiber ensemble and ensemble-ensemble rotations were not consistent with the experimental data, whereas ensemble-ensemble extensional interactions were able to explain all of the remaining stress.

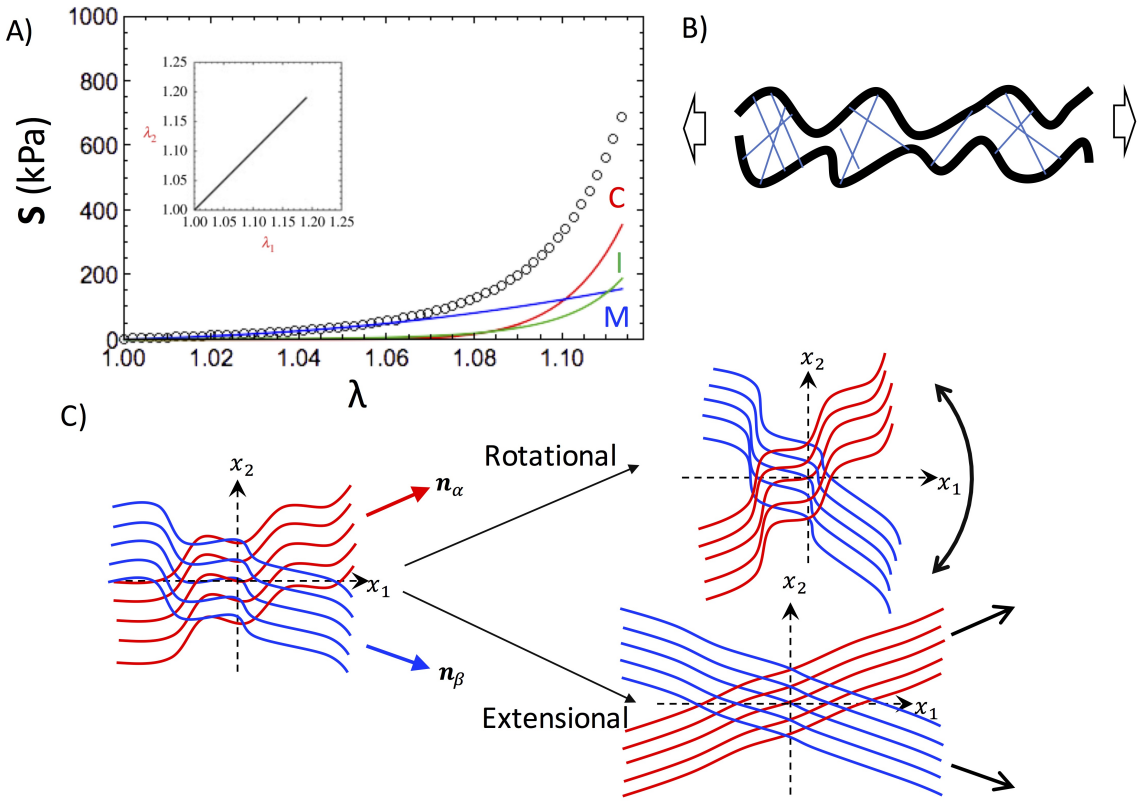

Figure 4.6: A) The mechanical response of exogenously crosslinked BP, which is composed of 3 parts: (C)ollagen in Red, (M)atrix in Blue, and the fiber ensemble (I)nteractions in Green. B) Illustration for intra-ensemble interactions due to crosslinking is shown. C) The inter-ensemble interactions could be separated into rotational effects and extensional effects.

The interaction model form, Ψ_{int}, was developed utilizing the pseudo invariant I_8, which is a function of the stretch and angle between two fiber ensembles oriented along the angle α and β directions in the tissue (Fig. 4.4), and then separated it into

its rotational and extensional components[32] (Fig. 4.6C&D),

$$\begin{aligned} I_8 &= \mathbf{n}_\alpha \cdot \mathbf{C} \cdot \mathbf{n}_\beta = \lambda_\alpha \lambda_\beta \cos(\alpha - \beta), \\ I_8^{\text{ext}} &= \lambda_\alpha \lambda_\beta, \qquad I_8^{\text{rot}} = \cos(\alpha - \beta) = \frac{I_8}{\lambda_\alpha \lambda_\beta}, \end{aligned} \tag{4.2}$$

where $\mathbf{n}_\alpha$ and $\mathbf{n}_\beta$ are vectors pointing along α and β, respectively, λ_α and λ_β are the stretches of the collagen fiber ensembles oriented along α and β, respectively , I_8^{ext} is the pseudo invariant for ensemble-ensemble extensions, and I_8^{rot} is the pseudo invariant for ensemble-ensemble rotations. From this, we established the model form for the interactions to be

$$\Psi_{\text{int}} = \frac{d_0}{4} \int_\alpha \int_\beta \Gamma(\alpha)\, \Gamma(\beta) \left[e^{d_1 (\lambda_\alpha \lambda_\beta - 1)^2} - 1 \right] \mathrm{d}\alpha\, \mathrm{d}\beta, \tag{4.3}$$

where Γ is the fiber orientation distribution (ODF), and d_0 and d_1 are material constants. However, this model form is still essentially phenomenological. Specifically, while it is sufficient to model the mechanical response in the range of the acquired experimental data, we have no method for predicting how it will change with changes in dimensions with cyclic loading. Thus, an extension to this model component is necessary.

4.4.2 Extension of the structural derivation of the fiber-fiber interactions term

The key to our approach in the constitutive model for the permanent set effect is to use the change in the collagen fiber architecture to predict the new mechanical response. Thus, having a full structural model, including a full structural derivation of the fiber-fiber interactions, is crucial. As in the previous model form [32], we will only keep the extensional component I_8^{ext}. In addition, since collagen fibers do not bear stress until fully straightened [38], we also assume that *collagen fibers do not play*

a role in the interactions of the fiber ensembles until they are straightened. Following the same approach common in structural models, we first define the stretch of the collagen fibers after it's straightened, which is also the true fiber stretch (λ_t) defined in Zhang et al. [45], to be $\lambda_t = \lambda_{\text{ens}}/\lambda_s$, where λ_{ens} is the stretch of the collagen fiber ensemble and λ_s is the slack stretch required to straighten the collagen fiber crimp. We assumed that interactions do not occur until the fibers are straightened, so the extensional invariant should be a function of the true stretch of the individual fibers, λ_t, rather than the stretch of the whole fiber ensembles as defined in equation 4.2,

$$I_8^{\text{ext}} = \frac{\lambda_\alpha \lambda_\beta}{{}_\alpha\lambda_s \, {}_\alpha\lambda_s}, \tag{4.4}$$

where ${}_\alpha\lambda_s$ and ${}_\beta\lambda_s$ are the slack stretches of the two ensembles oriented along α and β in the reference configuration, respectively. This invariant is then integrated only for fibers with $\lambda_t > 1$, i.e. fibers which are straightened. To develop the form for the interactions, we start from the strain energy. At the ensemble level, we integrate the invariant over the slack stretch (λ_s) of both the fiber ensembles orienting along α and β, weighted by the probability distribution function of the proportion of collagen fibers with that specific slack stretch $D(\lambda_s)$,

$$\Psi_{\text{int}}^{\text{ens}} = \frac{\eta_I}{2} \int_1^{\lambda_\alpha} \int_1^{\lambda_\beta} D\left(x_\alpha\right) D\left(x_\beta\right) \left(\frac{\lambda_\alpha \lambda_\beta}{x_\alpha x_\beta} - 1 \right)^2 \mathrm{d}x_\alpha \, \mathrm{d}x_\beta. \tag{4.5}$$

We refer to $D(\lambda_s)$ as the recruitment function, which is defined in Zhang et al. [45]. The ensemble-level model is then integrated with respect to the fiber ODF, Γ, for all possible pair of collagen fiber ensemble to give the tissue-level model

$$\Psi_{\text{int}} = \frac{\eta_I}{2} \int_\alpha \int_\beta \Gamma(\alpha)\Gamma(\beta) \int_1^{\lambda_\alpha} \int_1^{\lambda_\beta} D\left(x_\alpha\right) D\left(x_\beta\right) \left(\frac{\lambda_\alpha \lambda_\beta}{x_\alpha x_\beta} - 1 \right)^2 \mathrm{d}x_\alpha \, \mathrm{d}x_\beta \, \mathrm{d}\alpha \, \mathrm{d}\beta. \tag{4.6}$$

The second Piola Kirchhoff stress, using $\mathbf{S} = 2\frac{\partial \Psi}{\partial \mathbf{C}}$, is

$$\mathbf{S}_{\text{int}} = \eta_I \int_\alpha \int_\beta \Gamma(\alpha)\,\Gamma(\beta) \left[\left\{ \int_1^{\lambda_\alpha} \int_1^{\lambda_\beta} \frac{2\lambda_\beta D(x_\alpha) D(x_\beta)}{x_\alpha x_\beta} \left(\frac{\lambda_\alpha}{x_\alpha} \frac{\lambda_\beta}{x_\beta} - 1 \right) \mathrm{d}x_\alpha\, \mathrm{d}x_\beta + \int_1^{\lambda_\beta} D(x_\beta) \left(\frac{\lambda_\beta}{x_\beta} - 1 \right)^2 \mathrm{d}x_\beta \right\} \frac{\mathbf{n}_\alpha \otimes \mathbf{n}_\alpha}{\lambda_\alpha} + \left\{ \int_1^{\lambda_\alpha} \int_1^{\lambda_\alpha} \frac{2\lambda_\beta D(x_\alpha) D(x_\beta)}{x_\alpha x_\beta} \left(\frac{\lambda_\alpha}{x_\alpha} \frac{\lambda_\beta}{x_\beta} - 1 \right) \mathrm{d}x_\alpha\, \mathrm{d}x_\beta + \int_1^{\lambda_\alpha} D(x_\alpha) \left(\frac{\lambda_\alpha}{x_\alpha} - 1 \right)^2 \mathrm{d}x_\alpha \right\} \frac{\mathbf{n}_\beta \otimes \mathbf{n}_\beta}{\lambda_\beta} \right] \mathrm{d}\alpha\, \mathrm{d}\beta. \tag{4.7}$$

This model form has only one constant η_I to account for all interactions. The remaining mechanisms are all based on the collagen fiber architecture, which is determined through a convection using dimensional changes.

4.5 Permanent set model

4.5.1 Kinematics

For the bulk tissue-level mechanical response, consisting of the EXL matrix, the collagen fibers, and fiber ensemble interactions, we first consider the EXL matrix alone. Permanent set occurs in the EXL matrix and is the main driver for the evolving mechanical response and structural changes in the tissue. As such the permanent set model is our starting point (section 4.2), which then can be used to convect collagen fiber architecture and predict the remaining collagen fibers and fiber ensemble interactions components of the mechanical response. To model the EXL matrix under permanent set, many reference states need to be considered. Due to scission-healing,

the reference configuration of the EXL matrix is the configuration at its time of formation. For this we first introduce the following definition for the for the evolution of the configurations involved (Fig. 4.7):

1. The original unloaded configuration Ω_0

2. The evolving loaded configuration is $\Omega(s)$, where s is the current time.

3. We also make the distinction between $\hat{s}$, the intermediate time for which the EXL matrix is formed, and s. As the reference configuration of the EXL matrix evolves, there needs to be a distinction between the configuration for which the EXL matrix formed by the scission-healing reaction at time $\hat{s}$, referenced to $\Omega(\hat{s})$, and the current loaded configuration $\Omega(s)$. In this way, $\hat{s}$ is also suitable as a variable of integration.

4. The strain history, $\mathbf{A}(s)$, which is a deformation gradient tensor as a function of time s, that maps between the original configuration Ω_0 to the loaded configuration $\Omega(s)$ at which the EXL matrix is formed

5. We define $\tilde{\mathbf{B}}(s) = \mathbf{A}\mathbf{A}^{\mathsf{T}}$ to be left Cauchy Green tensor of the strain history $\mathbf{A}(s)$, which should not be confused with the left Cauchy Green tensor of the deformation applied to the tissue

6. We define the deformation gradient tensor from the intermediate loaded state $\Omega(\hat{s})$ to the current loaded state $\Omega(s)$ to be $\bar{\mathbf{F}}(\hat{s})$, where the following relation is assumed (Fig. 4.7)

$$\begin{aligned} \mathbf{F} &= \bar{\mathbf{F}}(\hat{s})\mathbf{A}(\hat{s}), \\ \bar{\mathbf{F}}(\hat{s}) &= \mathbf{F} \cdot \mathbf{A}(\hat{s})^{-1}. \end{aligned} \tag{4.8}$$

7. The evolving unloaded reference configuration after permanent set is $\Omega_{\text{PS}}(s)$ with $\mathbf{F}_{\text{PS}}(s)$ mapping from the original configuration Ω_0 to $\Omega_{\text{PS}}(s)$

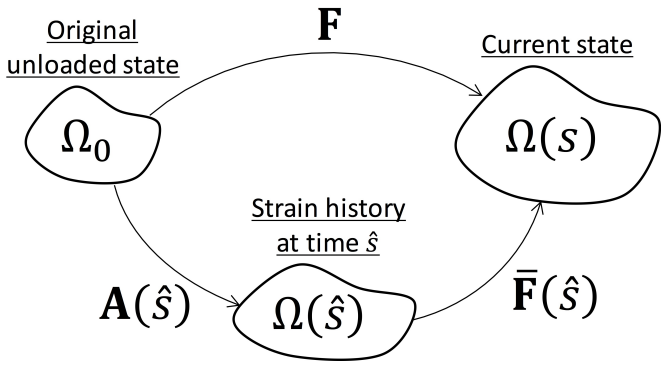

Figure 4.7: The relation between the reference configurations during cyclic loading.

We also note the following important considerations:

- The original reference configuration Ω_0 is important as it is the configuration for which the mechanical response of the original material and the collagen fiber architecture is referenced. Similarly, we track the loaded configuration ($\Omega(s)$) using $\mathbf{A}(s)$ and the unloaded configuration ($\Omega_{\text{PS}}(s)$) using $\mathbf{F}_{\text{PS}}$ from Ω_0.

- We also note that under cyclic loading, the exogenously crosslinked tissue is not held constant in the loaded configuration, it is put through a range of deformation each cycle. Because permanent set happens at a time scale much longer than a single cycle, we define the loaded configuration $\Omega(s)$ as the root mean squared configuration, which is the time-averaged deformation for a single loading cycle.

- We note that the tissue is never fully unloaded during cyclic loading. Thus, to simulate cyclic loading, the stresses are still referenced to the origin configu-

ration Ω_0. The unloaded geometry is determined *a posteriori* from $\Omega_{\mathrm{PS}}(s)$ for when cyclic loading is stopped for mechanical testing.

Thus the right Cauchy Green tensor when referenced to the strain history $\Omega(\hat{s})$ is given by $\bar{\mathbf{C}}(\hat{s}) = \bar{\mathbf{F}}(\hat{s})^{\mathsf{T}}\bar{\mathbf{F}}(\hat{s})$. This also has the following relation to the applied deformation $\mathbf{F}$,

$$\begin{aligned}\bar{\mathbf{C}}(\hat{s}) &= \left(\mathbf{F}\cdot\mathbf{A}(\hat{s})^{-1}\right)^{\mathsf{T}}\left(\mathbf{F}\cdot\mathbf{A}(\hat{s})^{-1}\right)\\ &= \mathbf{A}(\hat{s})^{-\mathsf{T}}\left(\mathbf{F}^{\mathsf{T}}\mathbf{F}\right)\mathbf{A}(\hat{s})^{-1}\\ &= \mathbf{A}(\hat{s})^{-\mathsf{T}}\cdot\mathbf{C}\cdot\mathbf{A}(\hat{s})^{-1}.\end{aligned} \tag{4.9}$$

Our material model for the EXL matrix is an isotropic model of $\Psi_m = \Psi_m(I_1)$, where I_1 is the first invariant of $\mathbf{C}$. For this, we can define the first invariant $\bar{I}_1(\hat{s})$ for the right Cauchy Green tensor $\bar{\mathbf{C}}(\hat{s})$ as

$$\bar{I}_1(\hat{s}) = \mathrm{Trace}(\bar{\mathbf{C}}(\hat{s})) = \mathrm{Trace}\left(\mathbf{A}^{-\mathsf{T}}(\hat{s})\cdot\mathbf{C}\cdot\mathbf{A}^{-1}(\hat{s})\right). \tag{4.10}$$

With this, the stress of the EXL matrix is given by

$$\bar{\mathbf{S}}_m = 2\frac{\partial\bar{\Psi}}{\partial\mathbf{C}} - p\mathbf{I} = 2\frac{\partial\bar{\Psi}}{\partial\bar{I}_1(\hat{s})}\frac{\partial\bar{I}_1(\hat{s})}{\partial\mathbf{C}} - p\mathbf{I}, \tag{4.11}$$

where p is the Lagrange multiplier enforcing incompressibility. The partial derivative of $\bar{I}_1(\hat{s})$ is

$$\frac{\partial\bar{I}_1}{\partial\mathbf{C}} = \frac{\partial\bar{I}_1}{\partial\bar{\mathbf{C}}(\hat{s})}\frac{\partial\bar{\mathbf{C}}(\hat{s})}{\partial\mathbf{C}} = \frac{\partial\mathbf{A}(\hat{s})^{-\mathsf{T}}\cdot\mathbf{C}\cdot\mathbf{A}(\hat{s})^{-1}}{\partial\mathbf{C}} = \mathbf{A}(\hat{s})^{-\mathsf{T}}\mathbf{A}(\hat{s})^{-1} = \tilde{\mathbf{B}}(\mathbf{A}(\hat{s}))^{-1}, \tag{4.12}$$

which is the inverse of the left Cauchy Green tensor of the strain history $\mathbf{A}(\mathbf{s})$.

4.5.1.1 Kinematics for updating the reference configuration

As the unloaded configuration changes due to permanent set, we need to be able to express the stresses with the new reference configuration. Since all configura-

tions are referenced to Ω_0, the deformation from the new reference configuration Ω_{PS} to the current loaded state $\Omega(s)$ is given by (Fig. 4.8)

$$\mathbf{F} = \bar{\mathbf{F}}(\hat{s}) \cdot \mathbf{A}(\hat{s}) \cdot \mathbf{F}_{\text{PS}}^{-1}. \tag{4.13}$$

Following the same derivation as equations 4.8–4.10, we have

$$\begin{aligned} \bar{\mathbf{F}}(\hat{s}) &= \mathbf{F} \cdot \mathbf{F}_{\text{PS}} \cdot \mathbf{A}(\hat{s})^{-1}, \\ \bar{\mathbf{C}}(\mathbf{F}_{\text{PS}}, \mathbf{A}(\hat{s})) &= \mathbf{A}(\hat{s})^{-\mathsf{T}} \cdot \mathbf{F}_{\text{PS}}^{\mathsf{T}} \cdot \mathbf{C} \cdot \mathbf{F}_{\text{PS}} \cdot \mathbf{A}(\hat{s})^{-1}, \\ \bar{I}_1\left(\mathbf{F}_{\text{PS}}, \mathbf{A}(s)\right) &= \text{Trace}\left(\mathbf{A}(\hat{s})^{-\mathsf{T}} \cdot \mathbf{F}_{\text{PS}}^{\mathsf{T}} \cdot \mathbf{C} \cdot \mathbf{F}_{\text{PS}} \cdot \mathbf{A}(\hat{s})^{-1}\right). \end{aligned} \tag{4.14}$$

and the new inverse of the left Cauchy Green tensor of the strain history is given by

$$\begin{aligned} \tilde{\mathbf{B}}(\mathbf{F}_{\text{PS}}, \mathbf{A}(\hat{s}))^{-1} &= \frac{\partial \bar{\mathbf{C}}(\mathbf{F}_{\text{PS}}, \mathbf{A}(\hat{s}))}{\partial \mathbf{C}} = \frac{\mathbf{A}(\hat{s})^{-\mathsf{T}} \cdot \mathbf{F}_{\text{PS}}^{\mathsf{T}} \cdot \mathbf{C} \cdot \mathbf{F}_{\text{PS}} \cdot \mathbf{A}(\hat{s})^{-1}}{\partial \mathbf{C}} \\ &= \mathbf{A}(\hat{s})^{-\mathsf{T}} \cdot \mathbf{F}_{\text{PS}}^{\mathsf{T}} \cdot \mathbf{F}_{\text{PS}} \cdot \mathbf{A}(\hat{s})^{-1}. \end{aligned} \tag{4.15}$$

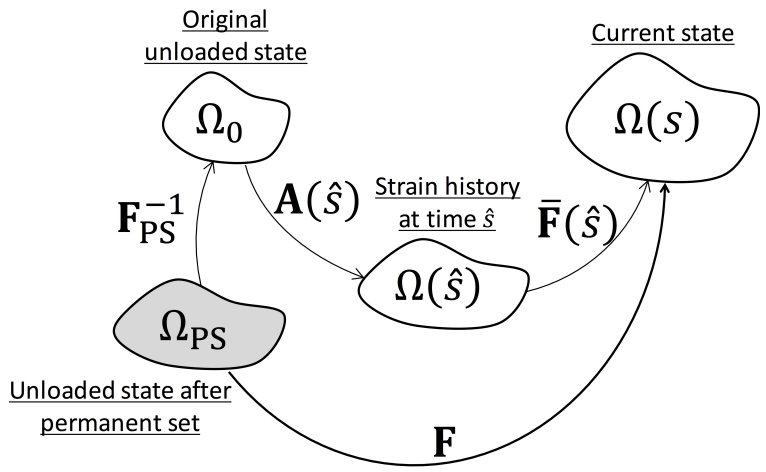

Figure 4.8: Modification of the relation between the different reference configurations when the unloaded configuration changes.

4.5.2 Extension to the EXL matrix model for changes in reference configuration

We start by extending the EXL matrix model from our previous model [32]. The strain energy is a modified form of the Yeoh model, which exhibits the following

stress-strain relation,

$$\begin{aligned}\Psi_m =& \frac{\eta_m}{2}\left(\frac{1}{\alpha}\left(I_1-3\right)^{\alpha}+\frac{r}{\beta}\left(I_1-3\right)^{\beta}\right),\\ &\text{with } 1<\alpha<\beta, \alpha\beta<2, 0\leq r.\end{aligned} \tag{4.16}$$

Here η_m is the EXL matrix modulus, α, β are the exponent and r is the relative weight between the two terms which is typically between 10 to 20. To modify the model form to reference the configuration at the time of formation $\Omega(\hat{s})$, we make the substitution for $\bar{I}_1(\mathbf{F}_{\mathrm{PS}}, \mathbf{A}(\hat{s}))$ (Eqn. 4.10),

$$\bar{\Psi}_m\left(\mathbf{C}, \mathbf{A}(\hat{s})\right) = \frac{\eta_m}{2}\left(\frac{1}{\alpha}\left(\bar{I}_1\left(\mathbf{F}_{\mathrm{PS}}, \mathbf{A}(s)\right)-3\right)^{\alpha}+\frac{r}{\beta}\left(\bar{I}_1\left(\mathbf{F}_{\mathrm{PS}}, \mathbf{A}(s)\right)-3\right)^{\beta}\right), \tag{4.17}$$

The derivative of the strain energy with respect to the invariant $\bar{I}_1$ is

$$\frac{\partial\bar{\Psi}}{\partial\bar{I}_1} = \frac{\eta_m}{2}\left(\left(\bar{I}_1\left(\mathbf{F}_{\mathrm{PS}}, \mathbf{A}(s)\right)-3\right)^{\alpha-1}+r\left(\bar{I}_1\left(\mathbf{F}_{\mathrm{PS}}, \mathbf{A}(s)\right)-3\right)^{\beta-1}\right). \tag{4.18}$$

After solving for the Lagrange multiplier p, with $\bar{S}_{m,33}=0$, we have

$$\begin{aligned}\bar{\mathbf{S}}_m\left(\mathbf{F}_{\mathrm{PS}}, \mathbf{A}(\hat{s}), \mathbf{C}\right) = \mu_m &\left(\left(\bar{I}_1\left(\mathbf{F}_{\mathrm{PS}}, \mathbf{A}(s)\right)-3\right)^{\alpha-1}+r\left(\bar{I}_1\left(\mathbf{F}_{\mathrm{PS}}, \mathbf{A}(s)\right)-3\right)^{\beta-1}\right)\\ &\times\left(\tilde{\mathbf{B}}(\mathbf{F}_{\mathrm{PS}}, \mathbf{A}(\hat{s}))^{-1}-\tilde{B}_{33}^{-1}(\mathbf{F}_{\mathrm{PS}}, \mathbf{A}(\hat{s}))C_{33}\mathbf{C}^{-1}\right).\end{aligned} \tag{4.19}$$

4.5.2.1 Extension of the EXL matrix for the permanent set effect

Next, we developed the model form for the EXL matrix after permanent set. This approach is based on the work by Rajagopal and Wineman [24], where we assume that the response of the full EXL matrix to be

$$\phi_m\mathbf{S}_m = b(s)\bar{\mathbf{S}}_m^{\text{existing}}+\int_0^s a(s,\hat{s})\bar{\mathbf{S}}_m^{\text{new}}\mathrm{d}\hat{s}, \tag{4.20}$$

where $b(s)$ is the remaining amount of the existing material, $a(s,\hat{s})$ is the remaining amount of the new material formed during the strain history ($\mathbf{A}(s)$) at time $\hat{s}$, $\bar{\mathbf{S}}_m^{\text{existing}}$

is the stress of the existing material and $\bar{\mathbf{S}}_m^{\text{new}}$ is the stress of the new material. Assuming first order kinetics with the permanent set rate constant k, we have for the material remaining (Fig. 4.9)

$$\frac{\partial b(s)}{\partial s} = -k \cdot b(s), \qquad \frac{\partial a(s,\hat{s})}{\partial s} = -k \cdot a(s,\hat{s}). \tag{4.21}$$

Given that the total amount of EXL matrix (ϕ_m) has not changed, $b(s)+\int_0^s a(s,\hat{s})\mathrm{d}\hat{s} = \phi_m$, and we have

$$b(s) = \phi_m \mathrm{Exp}\left[-k \cdot s\right], \qquad a(s,\hat{s}) = \phi_m k \mathrm{Exp}\left[-k(s-\hat{s})\right]. \tag{4.22}$$

Substitution into equation 4.20, we have the mechanical response of the EXL matrix after permanent set,

$$\begin{aligned}\phi_m \mathbf{S}_m =& \phi_m \Bigg[\mathrm{Exp}\left[-k \cdot s\right] \bar{\mathbf{S}}_m \left(\mathbf{F}_{\mathrm{PS}}, \mathbf{A}(0), \mathbf{C}\right) \\ &+ \int_0^s k \cdot \mathrm{Exp}\left[-k(s-\hat{s})\right] \bar{\mathbf{S}}_m \left(\mathbf{F}_{\mathrm{PS}}, \mathbf{A}(\hat{s}), \mathbf{C}\right) \mathrm{d}\hat{s} \Bigg].\end{aligned} \tag{4.23}$$

The final form for the EXL matrix component of the permanent set model is thus,

$$\begin{aligned}&\phi_m \mathbf{S}_m \left(\mathbf{F}_{\mathrm{PS}}, \mathbf{A}(\hat{s}), \mathbf{C}\right) \\ =&\phi_m \mu_m \Bigg[\mathrm{Exp}\left[-k \cdot s\right] \left(\left(\bar{I}_1(\mathbf{F}_{\mathrm{PS}}, \mathbf{A}(0)) - 3\right)^{\alpha-1} + r \left(\bar{I}_1(\mathbf{F}_{\mathrm{PS}}, \mathbf{A}(0)) - 3\right)^{\beta-1} \right) \\ &\times \left(\tilde{\mathbf{B}}(\mathbf{F}_{\mathrm{PS}}, \mathbf{A}(0))^{-1} - \tilde{B}_{33}(\mathbf{F}_{\mathrm{PS}}, \mathbf{A}(0))^{-1} C_{33} \mathbf{C}^{-1} \right) \\ &+ \int_0^s k \cdot \mathrm{Exp}\left[-k(s-\hat{s})\right] \left(\left(\bar{I}_1(\mathbf{F}_{\mathrm{PS}}, \mathbf{A}(\hat{s})) - 3\right)^{\alpha-1} + r \left(\bar{I}_1(\mathbf{F}_{\mathrm{PS}}, \mathbf{A}(\hat{s})) - 3\right)^{\beta-1} \right) \\ &\times \left(\tilde{\mathbf{B}}(\mathbf{F}_{\mathrm{PS}}, \mathbf{A}(\hat{s}))^{-1} - \tilde{B}_{33}(\mathbf{F}_{\mathrm{PS}}, \mathbf{A}(\hat{s}))^{-1} C_{33} \mathbf{C}^{-1} \right) \mathrm{d}\hat{s} \Bigg].\end{aligned} \tag{4.24}$$

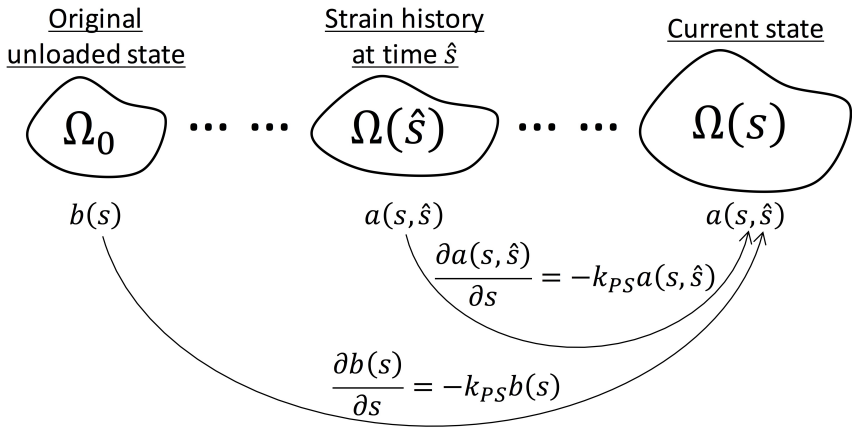

Figure 4.9: The mass fractions of the EXL matrix change over time, assuming first order kinetics.

4.5.3 Convection of the collagen fiber architecture

Now that the model form for the EXL matrix under permanent set is established, we need to consider how the collagen fiber architecture is convected by the change in reference configuration. The convection of the collagen fiber architecture is done through two parts: the ODF and the recruitment function. This is done by assuming that the collagen fiber architecture is convected under the affine assumption[15]. The form of the ODF and the recruitment distribution was previously described in Zhang *et al.* [45], and the operation used to convect the collagen fiber architecture is given in Sacks *et al.* [32]. Briefly, the convected ODF Γ_1 is determined from the ODF in the 0-cycle state Γ_0 and the deformation ${}^1_0\mathbf{F}$ by the conservation of the number of fiber $\Gamma(\theta_0)\mathrm{d}\theta_0 = \Gamma(\theta_1)\mathrm{d}\theta_1$ (Fig. 4.10A). This is given by

$$\begin{aligned} \Gamma_1\left({}^1_0\mathbf{F},\theta_1\right) &= \Gamma_0\left(\theta_0\left({}^1_0\mathbf{F},\theta_1\right)\right)\frac{{}^1_0\lambda(\theta_0)^2}{{}^1_0J_{2\mathrm{D}}}, \\ {}^1_0\lambda(\theta_0) &= \sqrt{\mathbf{n}_{\theta_0}\cdot{}^1_0\mathbf{F}^{\mathsf{T}}\,{}^1_0\mathbf{F}\cdot\mathbf{n}_{\theta_0}}, \qquad {}^1_0J_{2\mathrm{D}} = \det({}^1_0\mathbf{F}), \end{aligned} \tag{4.25}$$

where $\mathbf{n}_\theta$ is a unit vector for the orientation θ. The distribution of slack stretch needed to straighten collagen fiber crimp after convection, in other words the recruitment

distribution $D_1(\lambda_s)$ (Fig. 4.10B), is given by

$$D_1({}^1_0\mathbf{F}, \lambda_s) = \begin{cases} \frac{\mathrm{B}[\gamma_0,\gamma_1](y)}{{}_1\lambda_{\mathrm{ub}} - {}_1\lambda_{\mathrm{lb}}} & {}_1\lambda_{\mathrm{ub}} < y < {}_1\lambda_{\mathrm{lb}} \\ 0 & \text{else} \end{cases}, \qquad (4.26)$$
$$ {}_1\lambda_s = \frac{\lambda_s}{{}^1_0\lambda(\theta)}, \qquad y = \frac{{}_1\lambda_s - {}_1\lambda_{\mathrm{lb}}}{{}_1\lambda_{\mathrm{ub}} - {}_1\lambda_{\mathrm{lb}}}.$$

where ${}^1_0\lambda(\theta_0)$ is defined in equation 4.25, $({}_1\lambda_{\mathrm{lb}}, {}_1\lambda_{\mathrm{ub}})$ are the new bounds of the distribution after being convected, and (γ_0, γ_1) are the shape parameters of the beta distribution function B . The model form for collagen fibers in exogenously crosslinked BP after being convicted by a change in geometry is previously presented in Sacks et al. [32] and can also be used for the convection of the collagen fiber architecture due to the permanent set effect. The model form for the fiber ensemble interactions is given by equation 4.7, where equations 4.25 and 4.26 are substituted in for the ODF and recruitment distribution function for the mechanical response after permanent set.

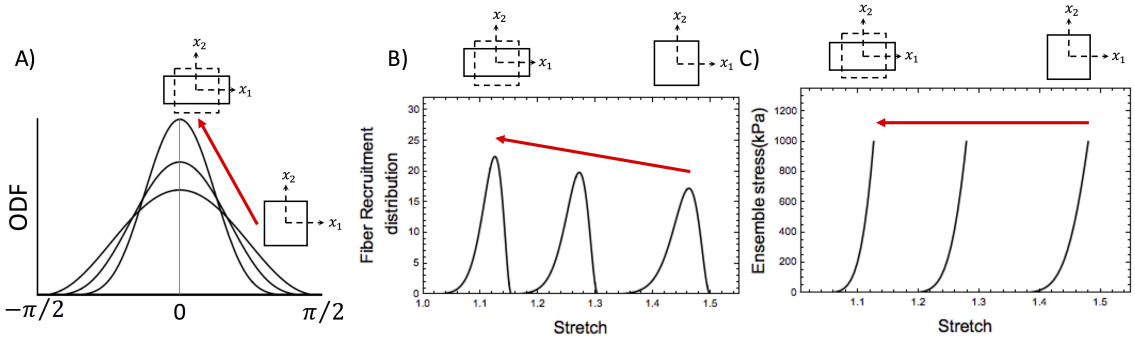

Figure 4.10: The effects of convecting the collagen fiber architecture show A) gradual alignment of collagen fibers, B) changes in the probability distribution of collagen fiber lack stretches and C) its effect on the mechanical response.

4.5.4 Further considerations of the permanent set mechanism.

In addition to the above considerations, we explored the following as a means to validate the mechanisms we proposed for permanent set. This was done by performing

an analysis on predicting the mechanical response after cyclic loading using only the convection of the collagen fiber architecture by the measured $\mathbf{F}_{PS}$. The analysis takes the following steps: 1) Material model parameter estimation for the 0-cycle data for the strain controlled data. This is done using the approach from Sacks *et al.*[32], with the constitutive model for collagen fibers and the EXL matrix from the same study, and the interaction model from equation 4.7. 2) Use equations 4.25 and 4.26 (Sec.4.5.3) to convect the collagen fiber architecture (Fig. 4.4 and Fig. 4.10). The deformation used to convect the collagen fiber architecture is determined from the fiducial markers. 3) We compare the new convected exogenously crosslinked mechanical response to the experimental data.

We used this approach to examine both the strain (n = 3) and stress controlled specimens (n = 5), and tested the hypothesis that *there is a significant difference between the mechanical response predicted from structural convection and the experimentally measure data*, in other words, our model is not sufficient to explain the change in mechanical response. We take the maximum stress of each specimen under equibiaxial strain and compared the difference between the model and the experimental data using student t-test. For the strain control specimens, we found that there is no statistically significant difference between the convected mechanical response and the experimental data, where the average p-value of the PD and XD for both after 30 million cycles and after 65 million cycles is $p = 0.37$ (minimum $p > 0.07$). Likewise, we also found no statistically significant differences between the convected response and the experimental data for the stress-controlled specimens, where the average p-value is 0.57 (Fig. 4.11). These results suggest that 1) the underlying collagen fiber architecture, including collagen fiber crimp and orientation, is convected affinely according to the permanent set in the EXL matrix. This indicates that our approach to

model permanent set is realistic, and the underlying mechanism for permanent set is likely to be correct. 2) Structural damage to the collagen fiber architecture was not detectable at this stage (up to 65 million cycles). These important results indicate that permanent set alone is sufficient to capture the response to cyclic loading up to 50-65 million cycles.

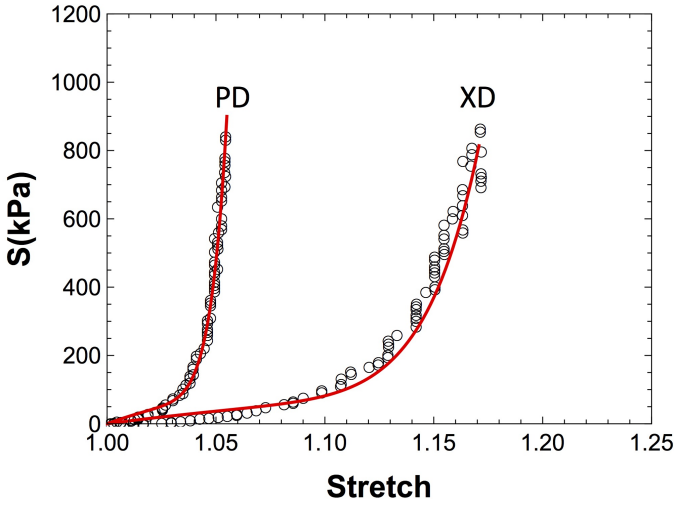

Figure 4.11: The equibiaxial mechanical response of an exogenously crosslinked BP specimen after 50 million cycles and the mechanical response determined from structural convection (Red) using the measured $\mathbf{F}_{PS}$

4.5.5 Full model form

Combining all three components, we have the final model form as a function of the permanent set rate constant k, the permanent set deformation $\mathbf{F}_{\mathrm{PS}}$, the strain history $\mathbf{A}(s)$, and the material parameters of the constitutive model in the uncycled state. The input of the model is the applied deformation $\mathbf{C}$ referenced to the current unloaded state Ω_{PS}, given by the deformation $\mathbf{F}_{\mathrm{PS}}$ from Ω_0. The full form is

$$\mathbf{S} = \mathbf{S}\left(k, \mathbf{F}_{\mathrm{PS}}, \mathbf{A}(\hat{s}), \mathbf{C}\right) = \phi_{\mathrm{col}}\left[\mathbf{S}_{\mathrm{col}} + \mathbf{S}_{\mathrm{int}}\right] + \phi_m \mathbf{S}_{\mathrm{m}}, \tag{4.27}$$

where the collagen contribution is

$$\begin{aligned}
&\phi_{\text{col}}\mathbf{S}_{\text{col}}\left(k, \mathbf{F}_{\text{PS}}, \mathbf{A}(\hat{s}), \mathbf{C}\right) \\
&\qquad = \phi_{\text{col}}\eta_C \int_{\theta} \Gamma_1(\mathbf{F}_{\text{PS}}, \theta) \left\{ \int_1^{\lambda_\theta} \frac{D_1\left(\mathbf{F}_{\text{PS}}, x\right)}{x} \left(\frac{1}{x} - \frac{1}{\lambda_\theta}\right) \mathrm{d}x \right\} \mathbf{n}_\theta \otimes \mathbf{n}_\theta \mathrm{d}\theta,
\end{aligned} \tag{4.28}$$

where $\lambda_\theta = \sqrt{\mathbf{n}_\theta \cdot \mathbf{C}\mathbf{n}_\theta}$ is the stretch of the fiber ensemble oriented along θ, the fiber ensemble interactions is

$$\begin{aligned}
&\phi_{\text{int}}\mathbf{S}_{\text{int}}\left(k, \mathbf{F}_{\text{PS}}, \mathbf{A}(\hat{s}), \mathbf{C}\right) \\
&\quad = \phi_{\text{col}}\eta_{\text{int}} \int_{\alpha} \int_{\beta} \Gamma_1\left(\mathbf{F}_{\text{PS}}, \alpha\right) \Gamma_1\left(\mathbf{F}_{\text{PS}}, \beta\right) \\
&\qquad \times \left[\left\{ \int_1^{\lambda_\alpha} \int_1^{\lambda_\beta} \frac{2\lambda_\beta D_1(\mathbf{F}_{\text{PS}}, x_\alpha) D_1(\mathbf{F}_{\text{PS}}, x_\beta)}{x_\alpha x_\beta} \left(\frac{\lambda_\alpha}{x_\alpha}\frac{\lambda_\beta}{x_\beta} - 1\right) \mathrm{d}x_\alpha \, \mathrm{d}x_\beta \right.\right. \\
&\qquad \left.\left. + \int_1^{\lambda_\beta} D_1(\mathbf{F}_{\text{PS}}, x_\beta) \left(\frac{\lambda_\beta}{x_\beta} - 1\right)^2 \mathrm{d}x_\beta \right\} \frac{\mathbf{n}_\alpha \otimes \mathbf{n}_\alpha}{\lambda_\alpha} \right. \\
&\qquad + \left\{ \int_1^{\lambda_\alpha} \int_1^{\lambda_\alpha} \frac{2\lambda_\beta D_1(\mathbf{F}_{\text{PS}}, x_\alpha) D_1(\mathbf{F}_{\text{PS}}, x_\beta)}{x_\alpha x_\beta} \left(\frac{\lambda_\alpha}{x_\alpha}\frac{\lambda_\beta}{x_\beta} - 1\right) \mathrm{d}x_\alpha \, \mathrm{d}x_\beta \right. \\
&\qquad \left. \left. + \int_1^{\lambda_\alpha} D_1(\mathbf{F}_{\text{PS}}, x_\alpha) \left(\frac{\lambda_\alpha}{x_\alpha} - 1\right)^2 \mathrm{d}x_\alpha \right\} \frac{\mathbf{n}_\beta \otimes \mathbf{n}_\beta}{\lambda_\beta} \right] \mathrm{d}\alpha \, \mathrm{d}\beta,
\end{aligned} \tag{4.29}$$

and the EXL matrix is

$$
\begin{aligned}
&\phi_m \mathbf{S}_{\mathrm{m}}\left(k, \mathbf{F}_{\mathrm{PS}}, \mathbf{A}(\hat{s}), \mathbf{C}\right) \\
&\quad = \phi_m \eta_m \Bigg[\operatorname{Exp}\left[-k \cdot s\right] \left(\left(\bar{I}_1(\mathbf{F}_{\mathrm{PS}}, \mathbf{A}(0)) - 3 \right)^{\alpha - 1} + r \left(\bar{I}_1(\mathbf{F}_{\mathrm{PS}}, \mathbf{A}(0)) - 3 \right)^{\beta - 1} \right) \\
&\quad \times \left(\tilde{\mathbf{B}}(\mathbf{F}_{\mathrm{PS}}, \mathbf{A}(0))^{-1} - \tilde{B}_{33}^{-1}(\mathbf{F}_{\mathrm{PS}}, \mathbf{A}(0)) C_{33} \mathbf{C}^{-1} \right) \\
&\quad + \int_0^s k \cdot \operatorname{Exp}\left[-k(s - \hat{s})\right] \left(\left(\bar{I}_1(\mathbf{F}_{\mathrm{PS}}, \mathbf{A}(\hat{s})) - 3 \right)^{\alpha - 1} + r \left(\bar{I}_1(\mathbf{F}_{\mathrm{PS}}, \mathbf{A}(\hat{s})) - 3 \right)^{\beta - 1} \right) \\
&\quad \times \left(\tilde{\mathbf{B}}(\mathbf{F}_{\mathrm{PS}}, \mathbf{A}(\hat{s}))^{-1} - \tilde{B}_{33}^{-1}(\mathbf{F}_{\mathrm{PS}}, \mathbf{A}(\hat{s})) C_{33} \mathbf{C}^{-1} \right) \mathrm{d}\hat{s} \Bigg] .
\end{aligned}
\tag{4.30}
$$

4.5.6 Determining permanent set deformation and loaded state

To solve for the permanent set deformation ($\mathbf{F}_{\mathrm{PS}}$), and for the deformation ($\mathbf{A}(s)$) to the new loaded state after permanent set ($\Omega(s)$) when under an applied stress of $\hat{\mathbf{S}}$, we need to use optimization as the permanent set constitutive model has no analytical inverse form. Specifically,

$$
\begin{aligned}
\mathbf{F}_{\mathrm{PS}} &= \arg\min_{\mathbf{F}} \left\| \mathbf{S}\left(k, \mathbf{I}, \mathbf{A}(\hat{s}), \mathbf{C} = \mathbf{F}^{\mathsf{T}}\mathbf{F}\right) - 0 \right\| , \\
\mathbf{A}(s) &= \arg\min_{\mathbf{F}} \left\| \mathbf{S}\left(k, \mathbf{I}, \mathbf{A}(\hat{s}), \mathbf{C} = \mathbf{F}^{\mathsf{T}}\mathbf{F}\right) - \hat{\mathbf{S}} \right\| .
\end{aligned}
\tag{4.31}
$$

4.5.7 Modeling approach and parameter estimation

4.5.7.1 Strain controlled cycling

Our goal using the strain controlled data is to validate the constitutive model form and perform parameter estimation. Since the loaded state never changes, the permanent set model can be simplified into a two-state model, with the loaded state ($\Omega(s)$) being the root mean square strain. Specifically, the EXL matrix can be sim-

plified to

$$\begin{aligned}\phi_m \mathbf{S}_m &= \phi_m \left[\operatorname{Exp}\left[-k \cdot s\right] \bar{\mathbf{S}}_m \left(\mathbf{F}_{\mathrm{PS}}, \mathbf{I}, \mathbf{C}\right) + \int_0^s k \cdot \operatorname{Exp}\left[-k(s-\hat{s})\right] \bar{\mathbf{S}}_m \left(\mathbf{F}_{\mathrm{PS}}, \mathbf{A}, \mathbf{C}\right) \mathrm{d}\hat{s} \right] \\ &= \phi_m \left[\operatorname{Exp}\left[-k \cdot s\right] \bar{\mathbf{S}}_m \left(\mathbf{F}_{\mathrm{PS}}, \mathbf{I}, \mathbf{C}\right) + \left(1 - \operatorname{Exp}\left[-k \cdot s\right]\right) \bar{\mathbf{S}}_m \left(\mathbf{F}_{\mathrm{PS}}, \mathbf{A}, \mathbf{C}\right) \right].\end{aligned} \tag{4.32}$$

Of the 3 time points (0, 30, and 65 million cycles), we fit the first two time points (0 and 30 million cycles) and use the results to predict the response to cycling at 65 million cycles as a way to validate our model (Fig. 4.12A). We note that the mounted configuration of the specimen for mechanical testing and cyclic loading are not the same, thus there is a small rigid body rotation of the specimen between the two testing configurations. We will compensate for this during the parameter estimation, which is done as followed

1. Determine the 0-cycled mechanical response using the methods of Sacks *et al.*[32]

2. Fit the permanent set deformation $\mathbf{F}_{\mathrm{PS}}$ and the mechanical response at the same time for the 30 million cycles time point

   (a) choose a k

   (b) choose a mounting direction θ_{mount}

   (c) compute $err_{\mathrm{PS}} = \mathbf{F}_{\mathrm{PS}} - \mathbf{F}_{\mathrm{PS}}^{\mathrm{data}}$ error at 30 million cycles

   (d) compute $err_{\mathbf{S}} = \mathbf{S}^{\max} - \mathbf{S}_{\mathrm{data}}^{\max}$

   (e) compute the weighted error $err_{\mathrm{PS}} + W_{\mathbf{S}} err_{\mathbf{S}}$, where the weight $W_{\mathbf{S}}$ =max strain in the direction of loading/$\mathbf{S}_{\mathrm{data}}^{\max}$

   (f) update k and θ_{mount} using the Quasi-Newton method [14]

3. Predict $\mathbf{F}_{\mathrm{PS}}$ and the mechanical response at 65 million cycles

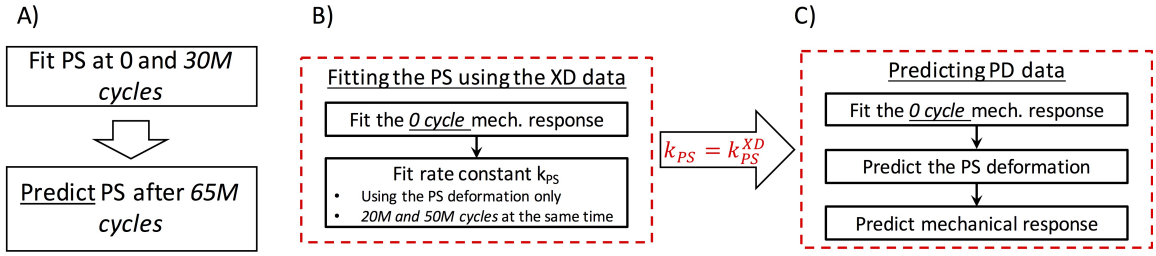

Figure 4.12: Our parameter estimation approach for the A) strain controlled cyclic loading data, B) stress controlled data cycled in the cross-preferred direction and C) in the preferred direction

4.5.7.2 Stress controlled cycling

The parameter estimation for the stress controlled specimens is more complicated than the strain controlled specimens as we do not know the strain history *a priori*. This becomes a dynamic simulation, and we need to use optimization to determine the strain history (Eqn. 4.31) at each time point. Thus, this data set is well suited to validate the full model using time dependent simulations. Since we have data for both PD-loading and XD-loading, we can fit the XD-loading data and used the resulting rate constant k to predict the PD-loading data. First, we discretized the problem as followed

$$\begin{aligned}\phi_m \mathbf{S}_m =& \phi_m \Bigg[\mathrm{Exp}\left[-k \cdot n \cdot \Delta s\right] \bar{\mathbf{S}}_m \left(\mathbf{F}_{\mathrm{PS}}, \mathbf{I}, \mathbf{C}\right) \\ &+ \sum_{i=1}^{n} (k\Delta s) \mathrm{Exp}\left[-k(n\Delta s - i\Delta s)\right] \bar{\mathbf{S}}_m \left(\mathbf{F}_{\mathrm{PS}}, \mathbf{A}(i\Delta s), \mathbf{C}\right) \Bigg] .\end{aligned} \tag{4.33}$$

After each time step Δs, we compute the new loaded state $\mathbf{A}(i\Delta s)$ using optimization(Eqn. 4.31, Fig. 4.13). Through preliminary trials, the most optimal resolution in time is $\Delta s = 1$ million cycles when considering both time to run the simulations

and accuracy of the results. We note that since an additional optimization is added to the parameter estimation process, we can no longer fit both the permanent set deformation $\mathbf{F}_{\text{PS}}$ and the mechanical data at the same time. Our attempts at fitting both at the same time were not able to converge. Thus, we choose to predict the mechanical data as a way to validate our results. The parameter estimation process for the XD-loading data is

1. Determine the 0-cycled mechanical response
2. Fit the permanent set deformation $\mathbf{F}_{\text{PS}}$
   (a) choose a k
   (b) choose a mounting direction $\theta^{20}_{\text{mount}}$ for cycling up to 20 million cycles
   (c) compute $err_{\text{PS}} = \mathbf{F}_{\text{PS}} - \mathbf{F}^{\text{data}}_{\text{PS}}$ error at 20 million cycles
   (d) choose a mounting direction $\theta^{50}_{\text{mount}}$ for cycling from 20 to 50 million cycles
   (e) compute $err_{\text{PS}} = \mathbf{F}_{\text{PS}} - \mathbf{F}^{\text{data}}_{\text{PS}}$ error at 50 million cycles
   (f) update k, $\theta^{20}_{\text{mount}}$, and $\theta^{50}_{\text{mount}}$ using Quasi-Newton
3. Predict the mechanical response

Next we, used k from the XD-loading data to predict the PD-loading data.

1. Determine the 0-cycled mechanical response
2. Compute Fit the permanent set deformation $\mathbf{F}_{\text{PS}}$
   (a) set k from XD-loading data
   (b) choose a mounting direction $\theta^{20}_{\text{mount}}$ for cycling up to 20 million cycles

(c) compute $err_{\mathrm{PS}} = \mathbf{F}_{\mathrm{PS}} - \mathbf{F}_{\mathrm{PS}}^{\mathrm{data}}$ error at 20 million cycles

(d) choose a mounting direction $\theta_{\mathrm{mount}}^{50}$ for cycling from 20 to 50 million cycles

(e) compute $err_{\mathrm{PS}} = \mathbf{F}_{\mathrm{PS}} - \mathbf{F}_{\mathrm{PS}}^{\mathrm{data}}$ error at 50 million cycles

(f) update $\theta_{\mathrm{mount}}^{20}$ and $\theta_{\mathrm{mount}}^{50}$ using Quasi-Newton

3. Predict the mechanical response

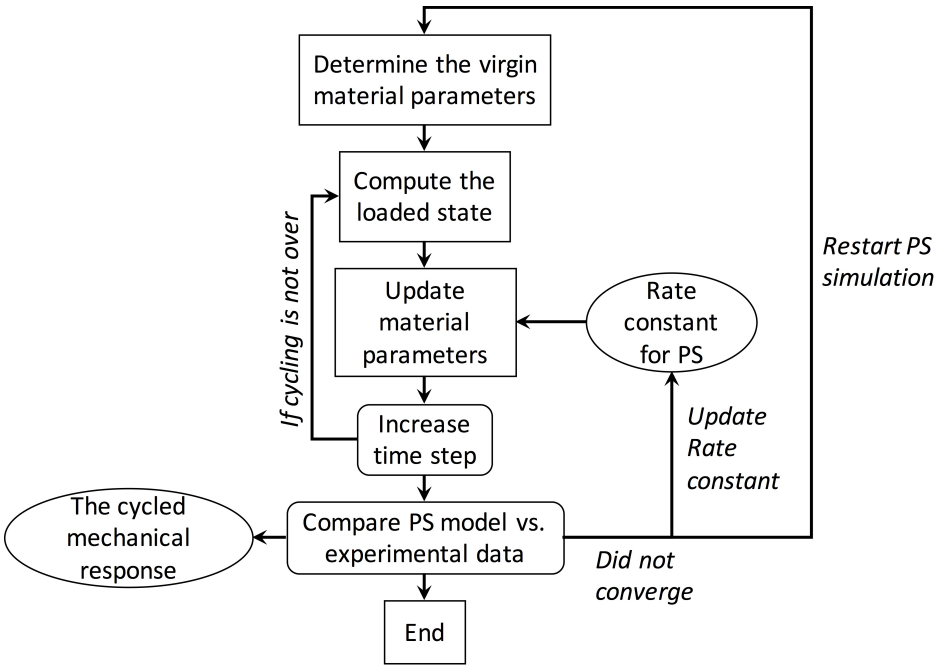

Figure 4.13: Implementation of the full model with updates in time.

4.5.8 Parametric studies

Next, we performed a parametric study using the stress-controlled PD data. The same material parameters and rate constant, k, from parameter estimation results above were used. We simulated one specimen by extending the cycle duration to 100 million cycles to examine how the changes in geometry due to permanent set respond to an extended cycling period.

4.6 Permanent set model results

4.6.1 Model fit and predictive capabilities

For the strain control specimens, we found that we were able to fit the permanent set deformations very well ($R^2 = 0.96$) (Fig. 4.14A). We were able to predict the mechanical response of the strain controlled specimens at 65 million cycles ($R^2 = 0.83$) (Fig. 4.14B&C). For the stress controlled specimens, we found we were able to fit the permanent set deformations for the XD specimens ($R^2 = 0.93$)(Fig. 4.15B), as well as predict the PD specimens very well ($R^2 = 0.97$) (Fig. 4.15C). The resulting rate constant from both data sets shown no statistical difference ($p > 0.98$)(Fig. 4.15A). The mechanical response for the stress-controlled XD specimens did not match as well in terms of the R^2 value($R^2 = 0.72$). However, given none of the mechanical data was involved in the parameter estimate this was nevertheless a very good prediction. For example, when comparing the model to the experimental data by extrapolating the loading path of the equibiaxial protocol and finding the peak strain at 1MPa, the R^2 value increases to 0.93. On the other hand, the predicted mechanical response for the PD controlled data was very good ($R^2 = 0.95$) (Fig. 4.16), suggesting that our model was able to capture the underlying mechanisms. These results agree with our hypothesis that the initial changes in the mechanical response (in the first 50 million cycles) can be predicted by the change in collagen fiber architecture alone, and that structural damage is low at this stage.

4.6.2 Parametric study results

By extending the cycling duration in the parametric study, we found that the permanent set deformation reaches an asymptote after approximately 70 million cycles when loading along the PD. This threshold slightly exceeds the lower bound

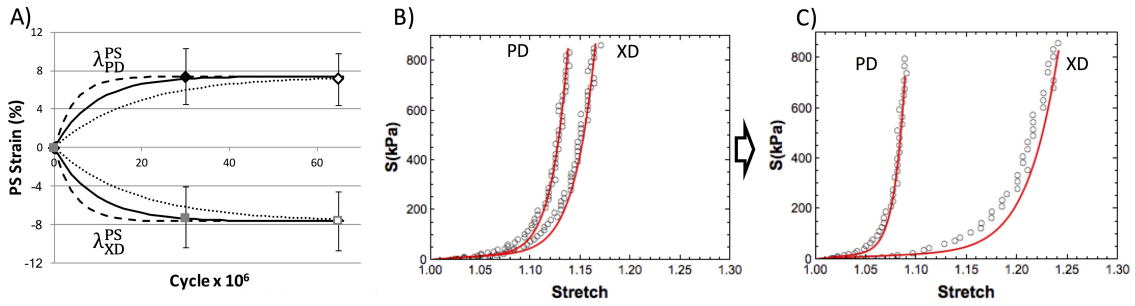

Figure 4.14: Results of the strain controlled cycling data, show how the A) model fits the permanent set deformation at 30 million cycles and predicts the 65 million cycles time point (hollow points). The dotted line shows the model prediction with $0.5k$ and the dashed line shows the model prediction with $2k$ and C) Shows how the model predicts the mechanical response at 65 million cycles using material parameters from the B) 0 cycle time point.

for collagen recruitment. We estimate that around 2.6% of collagen fiber is recruited when the permanent set deformation reaches this threshold (Fig. 4.17). This suggests that collagen fibers are limiting the maximum change in geometry that can occur, and that the lower bound of the collagen fiber recruitment can serve as an estimated bound for the changes in geometry due to the permanent set effect in BHVs. Once this bound is exceeded, some collagen fibers can exist perennially in an extended state. This could be a potential mechanism in exacerbating the rate of damage to the collagen fiber architecture. This can have significant implications in optimizing BHV design. By optimizing the BHV geometry for the post permanent set state, we can minimize the stresses in for the BHV for the majority of the BHV lifespan, minimizing structural damage and potentially increasing BHV durability.

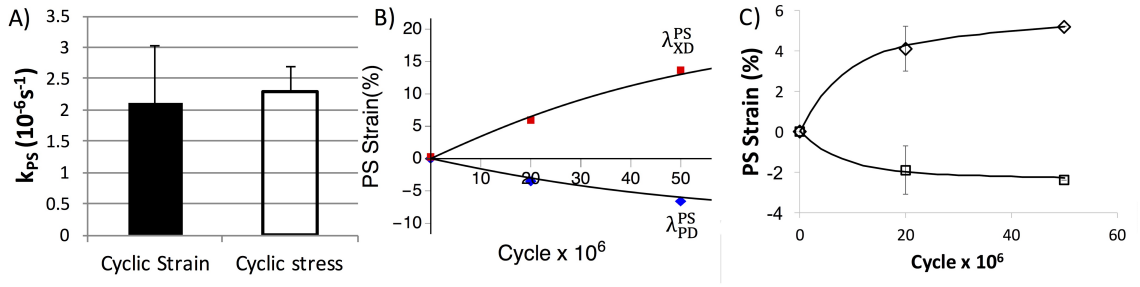

Figure 4.15:) Comparison of the permanent set rate constant between the strain controlled and stress controlled specimens. B) The model fit for the permanent set deformation at both 20 and 50 million cycles for the stress controlled XD cycled specimens. C) The predicted permanent set deformation for the PD cycled specimens using the rate constant from fitting the XD cycled specimens.

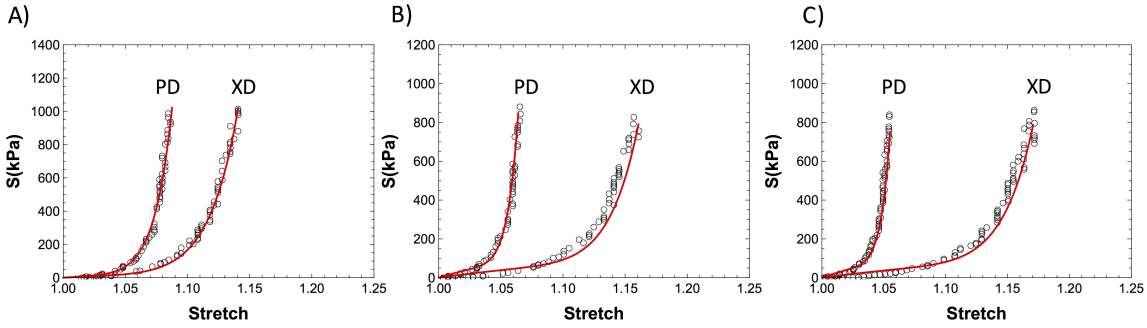

Figure 4.16: A) Best fit of the mechanical response at 0 cycle for the material parameters ($r^2 = 0.98$). The predicted mechanical response for the representative PD cycled specimen at B) 20 ($r^2 = 0.87$) and C) 50 million cycles. ($r^2 = 0.82$)

4.7 Discussion

4.7.1 Permanent set is sufficient to describe early stages of BHV cycling

The most important result from this study is that a permanent set mechanism in the EXL matrix alone is sufficient to explain the responses due to cyclic loading in the range of 0 to 65 million cycles. This further suggests that there is no detectable damage to the collagen fiber architecture and that the overall collagen fiber architecture stays intact and convected under affine kinematics. This is not unexpected, as we previously found dense collagenous tissues to behave affinely when deforming in

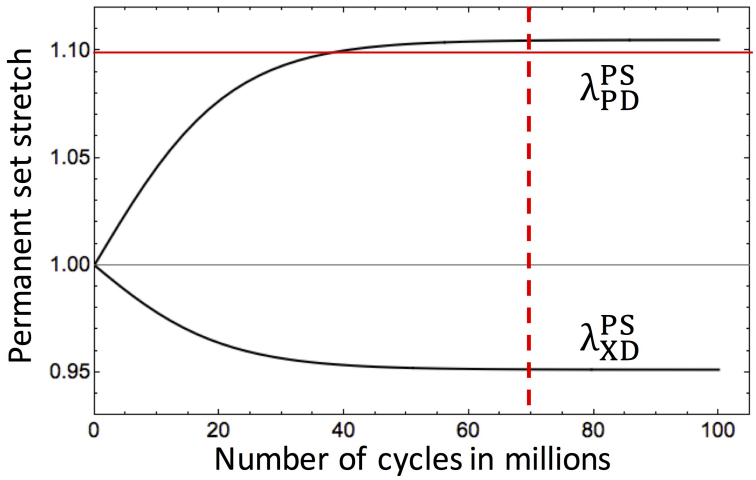

Figure 4.17: The results of the parametric study. The red solid line shows the lower bound for the collagen fiber slack stretches and the red dashed line show the approximate cycle when the permanent set stretches reach an assymptote.

the physiological range [15]. Although the permanent set effect is very noticeable in the early stages of the cyclic loading, it still takes millions of cycles; in other words, years. Due to the time scale difference between the opening and closing of heart valves versus permanent set, BHVs always deforms quasi-statically, which means it always follows affine kinematics. It follows that any structural changes in the collagen fiber architecture are affine as well. This is all extremely important, as this allows us to completely separate permanent set from other cyclic loading effects and independently determine the permanent set rate constant just from the cyclic loading data in the early stage.

4.7.2 Lack of detectable structural damage

We have observed that there are molecular conformation changes in the collagen fiber during this early stage [40, 35]. This suggests that while effects of collagen fiber damage are not detectable at the bulk level, it remains an ongoing but much

slower process in comparison to permanent set. Significant tearing and delamination have been observed after 500 million cycles [31], but this corresponds to the late stage (Fig. 4.2), for which we do not have extant mechanical data. There are no other existing experimental data quantifying the intrinsic structural damage in BHVs during cyclic loading. This is not surprising as actual structural damage is difficult to distinguish from other processes such as permanent set. The relation between molecular changes and mechanical response is not well understood. The most promising way of quantifying structural damage is through constitutive modeling and simulations. Structural models can separate structural damage and permanent set, but we do not have sufficient data at high cycle numbers where structural damage is detectable. This remains an important extension for the model in the future.

4.7.3 Permanent set is driven by the scission-healing of the EXL matrix

One important assumption in our model is that permanent set only occurs in the EXL matrix due to scission-healing. Based on our theory for permanent set, the process is driven entirely by the first order kinetics of the crosslinking reactions of GLUT leading to scission-healing, as well as the kinematics involved in the reference state evolution. Our results indicate that these mechanisms and permanent set can indeed explain the response to cyclic loading. This highlights the importance of understanding the effects of GLUT crosslinks and their role in the cyclic loading response of BHVs. The use of GLUT was originally intended for suppressing immunogenicity by crosslinking antigen within BP xenographs, but also has the fortunate consequence of stiffening the mechanical response of the BHV. Unfortunately, the scission-healing behavior of GLUT also plays a major role in the cyclic loading of BHVs. By severely changing the geometry of the BHV in the first 1-2 years, it strongly influences the cyclic loading response of BHVs at latter stages. It may be possible to design BHVs

to accommodate permanent set deformations caused by GLUT's scission-healing. Alternative exogenous crosslinking chemistry [41, 42] may be an important area for technological advancement of BHVs. Protecting the optimal mechanical response of the BHVs by reducing the impact of permanent set can significantly limit the peak stress on BHVs and protect the underlying tissue microstructure.

4.7.4 Collagen fiber recruitment can limit the maximum change in geometry due to permanent set

One of the most important findings from our permanent set model is that collagen fibers may play a significant role in limiting the changes in BHV geometry due to the permanent set effect. Our parametric study results show that the permanent set deformation eventually reaches a threshold asymptotically (Fig. 4.17). This is due to the different parts of the EXL matrix as well as the collagen fibers separating into different reference configurations due to the permanent set effect. Although the bulk tissue as a whole is at a stress-free equilibrium, there exists some internal stress between the different parts of the EXL matrix and the collagen fibers as a result of the different reference states. If the changes in geometry are sufficiently large, some collagen fibers will be recruited and exert compressive stress on the EXL matrix. However, since the stiffness of collagen fibers is over three magnitudes higher than the EXL matrix, the deformation of collagen fibers due to the internal stress is insignificant. As such, the recruitment of collagen fibers can resist further changes in the geometry of the tissue due to permanent set. In addition, we generally found significant collagen fiber structural reserve in collagenous tissue [45]. From the parametric study, no more than 2-4% of collagen fibers are straightened under physiological loading levels (up to 1 MPa) due to permanent set. Coupled with the exponentially increased cumulative stiffness of the collagen fibers with strain, significant structural reserved implies that

loading stresses several orders of magnitudes higher than the physiological loading level is necessary to further deform the collagen fibers. Also, taking into account the rapid recruitment of native collagen fibers (collagen fibers do not extend by more than 5-8% strain before breaking [3]), the collagen fiber architecture serves as a barrier in limiting the changes in geometry due to permanent set. This potentially gives us a way of predicting the final stress-free BHV geometry after permanent set has largely ceased. This can have a significant impact on the design BHVs as we can optimize the BHV geometry based on these results to minimize the leaflet stresses. Since the permanent effect is most significant during the first 40 to 50 million cycles (Fig. 4.17), which approximates to the first 8-9 month after implant, BHVs will operate in the post permanent set geometry during the majority of its lifespan (Fig. 4.2, when structural damage the accumulation of structural damage is most significant. Thus predicting the post permanent set geometry can have significant implications on the durability of BHV designs.

4.7.5 Effects on the durability of BHVs

Our findings suggest that this that the permanent set mechanism has great potential in predicting the non-biological driven changes in the BHVs in the first 2-5 years. As such, the permanent set mechanism can greatly aid the use of computational simulations in exploring BHV designs and the impact of permanent set at the valve level. Specifically, computational models can be used to adjust the initial geometry to tailor for optimal stress distribution in the valve leaflets after permanent set. Thus, the permanent set mechanism can help us explain why stress concentrations develop, which will accelerate structural damage, and help to create designs which can mitigate this effect. High-stress regions have been linked to regions with high structural damage which has a significant impact on the long-term behavior of BHVs. By

quantifying factors such as how the peak stress and stress distribution change due to permanent, we can predict the increased likelihood of structural damage in the leaflet due to permanent set and how it impacts BHV durability.

4.7.6 Limitations

Our available cyclic loading data for exogenously crosslinked BP is limited in terms of cycled duration, strain levels, the rate of cyclic loading and number of specimens. However, it is important to note that our goal was to develop the constitutive model form for exogenously crosslinked tissue under cyclic loading, not to obtain a population of material parameters for statistical testing and simulations. The extant experimental data we used for parameter estimation was sufficient for this purpose, which has specimens under both constant strain level and time-evolving strain level, and with loading along the preferred collagen fiber direction and more rigorous loading orthogonal to preferred collagen fiber direction. We note that some modification may be necessary, such as extending the model for the rate constant as a function of strain level and rate of cycling. However, the permanent set mechanism described was able to explain the effects of cyclic loading in the early stage. The lack of cyclic loading data beyond 65 million cycles, especially up to 100 or 200 million cycles, means that we are not able to incorporate structural damage into our constitutive model at this point. Although, based on what we observed, structural damage does not appear to play an observable 65 million cycles.

4.8 Summary and Future Directions

We have developed the first structural-based constitutive model for the time evolving properties of exogenously crosslinked collagenous soft tissues under cyclic

loading. We focused on permanent set as the mechanism for the geometry changes in the early stage of cycling and developed our constitutive model based on the underlying scission-healing reaction of the GLUT crosslinked matrix. Permanent set allows the reference configuration of the exogenously crosslinked matrix to evolve over time and convect the collagen fiber architecture through the change in geometry. The results show that permanent set alone is sufficient to explain all changes in the early stage of BHV cycling, and more importantly predict how the shape and reference configuration evolve during this stage. Moreover, structural damage does not play a detectable role up to 65 million cycles. Our model also indicates that the collagen fiber architecture can play a role in limiting the permanent set effect, where the straightening of collagen fibers prevents further changes in geometry. Thus, accounting for the permanent set effect is especially important in the design of BHVs to better improve their performance and durability.

In addition to the exogenously crosslinked tissue applications addressed herein, we have observed permanent set like phenomenon in mitral valve tissue during pregnancy [25]. In that study, our results suggested that much of the growth and remodeling in the MV leaflet does not begin immediately, but rather undergoes mostly passive leaflet enlargement until these parameters reach a critically low level, at which point growth and remodeling are triggered. This initial tissue distension process is very similar in behavior to the permanent set mechanism outlined in the present work. Thus, the current approach could be applied to these types of the early phases of soft tissue remodeling, where non-failure mechanisms occur before the onset of growth of tissue growth and remodeling. In addition, although the permanent set model we described only include the remodeling of the matrix due to scission-healing, the same concept can be extended by separating the rate constant into growth and resorp-

tion to simulate growth and remodeling of the matrix. Furthermore, the framework outlined in section 5 can also be extended for the remodeling of the collagen fiber architecture, given further studies on mechanisms for how the collagen fiber architecture grows once the critical level observed in Rego *et al* [25] is exceeded. This is the advantage for the structural-based approach to modeling permanent set, which allows us to describe the mechanical response based on real physically measure-able quantities. We can further extend the more toward effects such as structural damage are the fiber-level, proteolytic degradation, and growth based on how these effects affect the components of the permanent set model laid out herein.

Nomenclature

Key Terms

Matrix Non-fibrous part of the extracellular matrix

EXL Exogenously crosslinked

PS Permanent set, an irreversible deformation that remains in a structure or material after it has been subjected to stress.

Damage Loss of mechanical properties

Fatigue Weakening of a material caused by repeated loading

Plastic deformation Deformation of a material undergoing irreversible change in shape in response to applied forces

Structural convection A permanent deformation of the collagen fiber architecture based on the change in the reference configuration

BP Bovine pericardium

CFA Collagen fiber architecture

BHV Bioprosthetic heart valve

AWT Accelerated wear testing

GLUT Glutaraldehyde

TVI Transcatheter aortic intervention

PD Preferred direction

XD Cross-preferred direction

ODF Orientation distribution function

Recruitment Probability distribution function describing the strain at which a collagen fiber's crimp is straightened

Fiber ensemble A group of fibers which share a common orientation

Symbols

Ψ Strain energy

$\Psi_{\text{col}}, \Psi_{\text{int}}, \Psi_m$ Strain energy of the collagen fiber, ensemble-ensemble interactons, and matrix components respectively

D Collagen fiber recruitment distribution function

λ_s The slack stretch, the stretch needed to straighten the collagen fiber crimp

Γ Collagen fiber orientation distribution function

ϕ Mass fraction

η_C, η_m, η_I The modulus of collagen, EXL matrix and fiber-fiber interactions

$\mathbf{I}$ Identity tensor

$\mathbf{F}$ An arbitrary deformation gradient tensor applied to the tissue, referenced to the original uncycled stress free state

$\mathbf{C}$ Right Cauchy-Green strain tensor, referenced to the original uncycled stress free state

$\mathbf{E}$ Green Lagrange strain, referenced to the original uncycled stress free state

λ Stretch

$\mathbf{n}_\alpha$ A vector pointing at the angle α

$\lambda_\alpha = \sqrt{\mathbf{n}_\alpha \cdot \mathbf{C}\mathbf{n}_\alpha}$ The applied stretch at the fiber ensemble-level in the direction α

${}_\alpha\lambda_s$ The slack stretch of a collagen fiber oriented with the angle α

$\mathbf{S}$ Second Piola Kirchhoff tensor, referenced to the original uncycled stress free state

I_1 First invariant

I_8 Eighth pseudo invariant

I_8^{rot} The rotational component of I_8

I_8^{ext} The extensional component of I_8

k Rate constant for permanent set

s The current time in seconds

$\hat{s}$ The intermediate time when the EXL matrix is formed by the scission-healing process

Ω_0 The original unloaded configuration of the tissue before any cyclic loading

$\Omega(s)$ The current loaded configuration of the tissue during cyclic loading

$\mathbf{A}(s)$ Strain history, which is the root mean square strain of each cycle as a function of time

$\tilde{\mathbf{B}}(s) = \mathbf{A}\mathbf{A}^\mathsf{T}$ Left Cauchy Green tensor of the strain history

$\bar{\mathbf{F}}(\hat{s})$ Deformation gradient tensor applied to the tissue, referenced to the strain history $\mathbf{A}(\hat{s})$ at time $\hat{s}$

$\bar{\mathbf{C}}(\hat{s})$ The right Cauchy Green strain tensor applied to the tissue, referenced to the strain history $\mathbf{A}(\hat{s})$ at time $\hat{s}$

$\bar{I}_1$ Modified first invariant, referenced to the strain history $\mathbf{A}(\hat{s})$ at time $\hat{s}$

$\bar{\mathbf{\Psi}}_m$ Strain energy of the matrix as function of $\bar{I}_1$

$\bar{\mathbf{S}}_m$ Stress of the matrix as function of $\bar{I}_1$

$\Omega_{\mathrm{PS}}(s)$ The current unloaded configuration due to changes in geometry caused by permanent set

$\mathbf{F}_{\mathrm{PS}}(s)$ The deformation from Ω_0 to the current unloaded configuration (Ω_{PS}) due to permanent set

$b(s)$ The proportion of the existing amount of material remaining

$a(s, \hat{s})$ The proportion of the material newly formed at time $\hat{s}$ remaining

${}^1_0\mathbf{F}$ The deformation gradient from Ω_0 to some arbitrary state Ω_1, most commonly $\Omega_1 = \Omega_{\mathrm{PS}}$

${}^1_0\lambda(\theta_0)$ The stretch of an ensemble oriented along θ_0 in Ω_0 deformed from Ω_0 to some arbitrary state Ω_1

D_1 The collagen fiber recruitment distribution function convected from Ω_0 to to some arbitrary state Ω_1

Γ_1 The collagen fiber orientation distribution function convected from Ω_0 to to some arbitrary state Ω_1

$\hat{\mathbf{S}}$ The applied stress during cyclic loading

Chapter Bibliography

[1] R. D. Andrews, A. V. Tobolsky, and E. E. Hanson. The theory of permanent set at elevated temperatures in natural and synthetic rubber vulcanizates. *Journal of Applied Physics*, 17(5):352–361, may 1946. doi: 10.1063/1.1707724.

[2] Robert O. Bonow, Blase A. Carabello, Kanu Chatterjee, Antonio C. de Leon, David P. Faxon, Michael D. Freed, William H. Gaasch, Bruce Whitney Lytle, Rick A. Nishimura, Patrick T. O'Gara, Robert A. O'Rourke, Catherine M. Otto, Pravin M. Shah, Jack S. Shanewise, Sidney C. Smith, Alice K. Jacobs, Cynthia D. Adams, Jeffrey L. Anderson, Elliott M. Antman, David P. Faxon, Valentin Fuster, Jonathan L. Halperin, Loren F. Hiratzka, Sharon A. Hunt, Bruce W. Lytle, Rick Nishimura, Richard L. Page, and Barbara Riegel. ACC/AHA 2006 guidelines for the management of patients with valvular heart disease. *Journal of the American College of Cardiology*, 48(3):e1–e148, aug 2006. ISSN 1558-3597 (Electronic) 0735-1097 (Linking). doi: 10.1016/j.jacc.2006.05.021. URL `http://www.ncbi.nlm.nih.gov/entrez/query.fcgi?cmd=Retrieve&db=PubMed&dopt=Citation&list_uids=16875962`.

[3] Markus J. Buehler. Atomistic and continuum modeling of mechanical properties of collagen: elasticity, fracture, and self-assembly. *Journal of Materials Research*, 21(08):1947–1961, aug 2006. ISSN 2044-5326. doi: 10.1557/jmr.2006.0236. URL `http://dx.doi.org/10.1557/jmr.2006.0236`.

[4] D T Cheung, P DiCesare, P D Benya, E Libaw, and M E Nimni. The presence of intermolecular disulfide cross-links in type III collagen. *The Journal of biological chemistry*, 258(12):7774–7778, June 1983. ISSN 0021-9258.

[5] David T. Cheung and Marcel E. Nimni. Mechanism of crosslinking of proteins by glutaraldehyde I: reaction with model compounds. *Connective Tissue Research*, 10(2):187–199, jan 1982. doi: 10.3109/03008208209034418.

[6] David T. Cheung and Marcel E. Nimni. Mechanism of crosslinking of proteins by glutaraldehyde II.: reaction with monomeric and polymeric collagen. *Connective Tissue Research*, 10(2):201–216, jan 1982. doi: 10.3109/03008208209034419.

[7] David T. Cheung, Natasha Perelman, Ellen C. Ko, and Marcel e. Nimni. Mechanism of crosslinking of proteins by glutaraldehyde III: reaction with collagen in tissues. *Connective Tissue Research*, 13(2):109–115, jan 1985. doi: 10.3109/03008208509152389.

[8] David T. Cheung, Deborah Tong, Natasha Perelman, Delia Ertl, and Marcel E. Nimni. Mechanism of crosslinking of proteins by glutaraldehyde IV: in vitro and in vivo stability of a crosslinked collagen matrix. *Connective Tissue Research*, 25(1):27–34, jan 1990. doi: 10.3109/03008209009009810.

[9] L. H. H. Olde Damink, P. J. Dijkstra, M. J. A. Van Luyn, P. B. Van Wachem, P. Nieuwenhuis, and J. Feijen. Glutaraldehyde as a crosslinking agent for collagen-based biomaterials. *Journal of Materials Science: Materials in Medicine*, 6(8):460–472, aug 1995. doi: 10.1007/bf00123371.

[10] Bahar Fata, Will Zhang, Rouzbeh Amini, and Michael S. Sacks. Insights into regional adaptations in the growing pulmonary artery using a meso-scale structural model: effects of ascending aorta impingement. *Journal of Biomechanical Engineering*, 136(2):021009–021009–13, feb 2014. ISSN 0148-0731. doi: 10.1115/1.4026457. URL `http://dx.doi.org/10.1115/1.4026457`.

[11] E. Gendler, S. Gendler, and M. E. Nimni. Toxic reactions evoked by glutaraldehyde-fixed pericardium and cardiac valve tissue bioprosthesis. *Journal of Biomedical Materials Research*, 18(7):727–736, sep 1984. ISSN 1097-4636. doi: 10.1002/jbm.820180703. URL http://dx.doi.org/10.1002/jbm.820180703.

[12] Robert Guidoin, Yvan Douville, Marie-Annick Clavel, Ze Zhang, Mark Nutley, Philippe Pîbarot, and Guy Dionne. The marvel of percutaneous cardiovascular devices in the elderly. *Annals of the New York Academy of Sciences*, 1197(1):188–199, June 2010. ISSN 1749-6632 (Electronic) 0077-8923 (Linking). doi: 10.1111/j.1749-6632.2010.05517.x. URL http://www.ncbi.nlm.nih.gov/entrez/query.fcgi?cmd=Retrieve&db=PubMed&dopt=Citation&list_uids=20536849.

[13] Jason C. Isenburg, Dan T. Simionescu, and Naren R. Vyavahare. Tannic acid treatment enhances biostability and reduces calcification of glutaraldehyde fixed aortic wall. *Biomaterials*, 26(11):1237–1245, April 2005. ISSN 0142-9612 (Print). doi: 10.1016/j.biomaterials.2004.04.034. URL http://www.ncbi.nlm.nih.gov/entrez/query.fcgi?cmd=Retrieve&db=PubMed&dopt=Citation&list_uids=15475053.

[14] Davis E. King. Dlib-ml: a machine learning toolkit. *Journal of Machine Learning Research*, 10:1755–1758, 2009.

[15] Chung-Hao Lee, Will Zhang, Jun Liao, Christopher A. Carruthers, Jacob I. Sacks, and Michael S. Sacks. On the presence of affine fibril and fiber kinematics in the mitral valve anterior leaflet. *Biophysical Journal*, 108(8):2074–2087, April 2015. ISSN 1542-0086 (Electronic) 0006-3495 (Linking). doi: 10.1016/j.bpj.2015.03.019. URL http://www.ncbi.nlm.nih.gov/pubmed/25902446.

[16] Raj R. Makkar, Gregory P. Fontana, Hasan Jilaihawi, Samir Kapadia, Augusto D. Pichard, Pamela S. Douglas, Vinod H. Thourani, Vasilis C. Babaliaros, John G. Webb, Howard C. Herrmann, Joseph E. Bavaria, Susheel Kodali, David L. Brown, Bruce Bowers, Todd M. Dewey, Lars G. Svensson, Murat Tuzcu, Jeffrey W. Moses, Matthew R. Williams, Robert J. Siegel, Jodi J. Akin, William N. Anderson, Stuart Pocock, Craig R. Smith, and Martin B. Leon. Transcatheter aortic-valve replacement for inoperable severe aortic stenosis. *New England Journal of Medicine*, 366(18):1696–1704, may 2012. doi: 10.1056/nejmoa1202277. URL `http://www.nejm.org/doi/full/10.1056/NEJMoa1202277`.

[17] Rizwan A Manji, Alan H Menkis, Burcin Ekser, and David KC Cooper. The future of bioprosthetic heart valves. *The Indian journal of medical research*, 135 (2):150, 2012. ISSN 0971-5916.

[18] Caitlin Martin and Wei Sun. Modeling of long-term fatigue damage of soft tissue with stress softening and permanent set effects. *Biomechanics and Modeling in Mechanobiology*, 12(4):645–655, sep 2012. ISSN 1617-7940. doi: 10.1007/s10237-012-0431-6. URL `http://dx.doi.org/10.1007/s10237-012-0431-6`.

[19] Isabelle Migneault, Catherine Dartiguenave, Michel J. Bertrand, and Karen C. Waldron. Glutaraldehyde: behavior in aqueous solution, reaction with proteins, and application to enzyme crosslinking. *Biotechniques*, 37(5):790–802, nov 2004. doi: 10.2144/04375rv01.

[20] Ali Mirnajafi, Brett Zubiate, and Michael S. Sacks. Effects of cyclic flexural fatigue on porcine bioprosthetic heart valve heterograft biomaterials. *Journal of Biomedical Materials Research Part A*, 94A(1):205–213, feb

2010. ISSN 1552-4965 (Electronic) 1549-3296 (Linking). doi: 10.1002/jbm.a.32659. URL http://www.ncbi.nlm.nih.gov/entrez/query.fcgi?cmd=Retrieve&db=PubMed&dopt=Citation&list_uids=20166221.

[21] Dariush Mozaffarian, Emelia J. Benjamin, Alan S. Go, Donna K. Arnett, Michael J. Blaha, Mary Cushman, Sandeep R. Das, Sarah de Ferranti, Jean-Pierre Després, Heather J. Fullerton, Virginia J. Howard, Mark D. Huffman, Carmen R. Isasi, Monik C. Jiménez, Suzanne E. Judd, Brett M. Kissela, Judith H. Lichtman, Lynda D. Lisabeth, Simin Liu, Rachel H. Mackey, David J. Magid, Darren K. McGuire, Emile R. Mohler, Claudia S. Moy, Paul Muntner, Michael E. Mussolino, Khurram Nasir, Robert W. Neumar, Graham Nichol, Latha Palaniappan, Dilip K. Pandey, Mathew J. Reeves, Carlos J. Rodriguez, Wayne Rosamond, Paul D. Sorlie, Joel Stein, Amytis Towfighi, Tanya N. Turan, Salim S. Virani, Daniel Woo, Robert W. Yeh, and Melanie B. Turner. Heart disease and stroke statistics-2016 update: a report from the american heart association. *Circulation*, 133(4):e38–e360, dec 2015. ISSN 1524-4539 (Electronic) 0009-7322 (Linking). doi: 10.1161/cir.0000000000000350. URL http://www.ncbi.nlm.nih.gov/pubmed/26673558.

[22] M. E. Nimni, D. Cheung, B. Strates, M. Kodama, and K. Sheikh. Chemically modified collagen : a natural biomaterial for tissue replacement. *Journal of Biomedical Materials Research*, 21(6):741–771, jun 1987. doi: 10.1002/jbm.820210606.

[23] Ki Dong Park, Won Kyu Lee, Ju Young Yun, Dong Keun Han, Soo hyun Kim, Young Ha Kim, Hyoung Mook Kim, and Kwang Taek Kim. Novel anti-calcification treatment of biological tissues by grafting of sulphonated

poly(ethylene oxide). *Biomaterials*, 18(1):47–51, jan 1997. ISSN 0142-9612. doi: http://dx.doi.org/10.1016/S0142-9612(96)00096-8. URL http://www.sciencedirect.com/science/article/pii/S0142961296000968.

[24] K. R. Rajagopal and A. S. Wineman. A constitutive equation for nonlinear solids which undergo deformation induced microstructural changes. *International Journal of Plasticity*, 8(4):385–395, jan 1992. doi: 10.1016/0749-6419(92)90056-i.

[25] Bruno V. Rego, Sarah M. Wells, Chung-Hao Lee, and Michael S. Sacks. Mitral valve leaflet remodelling during pregnancy: insights into cell-mediated recovery of tissue homeostasis. *Journal of The Royal Society Interface*, 13(125):20160709, dec 2016. ISSN 1742-5689. doi: 10.1098/rsif.2016.0709. URL http://rsif.royalsocietypublishing.org/content/13/125/20160709.

[26] Dana R. Rottach, John G. Curro, Gary S. Grest, and Aidan P. Thompson. Effect of strain history on stress and permanent set in cross-linking networks: a molecular dynamics study. *Macromolecules*, 37(14):5468–5473, jul 2004. doi: 10.1021/ma049723j. URL http://dx.doi.org/10.1021/ma049723j.

[27] Dana R. Rottach, John G. Curro, Joanne Budzien, Gary S. Grest, Carsten Svaneborg, and Ralf Everaers. Permanent set of cross-linking networks: comparison of theory with molecular dynamics simulations. *Macromolecules*, 39(16):5521–5530, aug 2006. doi: 10.1021/ma060767x. URL http://dx.doi.org/10.1021/ma060767x.

[28] Dana R. Rottach, John G. Curro, Joanne Budzien, Gary S. Grest, Carsten Svaneborg, and Ralf Everaers. Molecular dynamics simulations of polymer networks undergoing sequential cross-linking and scission reactions. *Macro-*

molecules, 40(1):131–139, jan 2007. doi: 10.1021/ma062139l. URL http://dx.doi.org/10.1021/ma062139l.

[29] M. S. Sacks and F. J. Schoen. Collagen fiber disruption occurs independent of calcification in clinically explanted bioprosthetic heart valves. *J Biomed Mater Res*, 62(3):359–71, December 2002. doi: 10.1002/jbm.10293. URL http://www.ncbi.nlm.nih.gov/entrez/query.fcgi?cmd=Retrieve&db=PubMed&dopt=Citation&list_uids=12209921.

[30] Michael S. Sacks. A structural constitutive model for chemically treated planar tissues under biaxial loading. *Computational Mechanics*, 26(3):243–249, sep 2000. doi: 10.1007/s004660000175.

[31] Michael S. Sacks and David B. Smith. Effects of accelerated testing on porcine bioprosthetic heart valve fiber architecture. *Biomaterials*, 19(11-12):1027–1036, jun 1998. doi: 10.1016/s0142-9612(98)00002-7.

[32] Michael S. Sacks, Will Zhang, and Silvia Wognum. A novel fibre-ensemble level constitutive model for exogenous cross-linked collagenous tissues. *Interface Focus*, 6(1):20150090, dec 2015. doi: 10.1098/rsfs.2015.0090. URL http://rsfs.royalsocietypublishing.org/royfocus/6/1/20150090.full.pdf.

[33] MS Sacks. Biaxial mechanical evaluation of planar biological materials. *J Elasticity*, 61:199–246, 2000.

[34] Frederick J. Schoen and Robert J. Levy. Calcification of tissue heart valve substitutes: progress toward understanding and prevention. *The Annals of Thoracic Surgery*, 79(3):1072–1080, March 2005. doi: 10.1016/j.athoracsur.2004.06.033. URL http://www.ncbi.nlm.nih.gov/entrez/query.fcgi?cmd=Retrieve&db=PubMed&dopt=Citation&list_uids=15734452.

[35] Tiffany L. Sellaro, Daniel Hildebrand, Qijin Lu, Naren Vyavahare, Michael Scott, and Michael S. Sacks. Effects of collagen fiber orientation on the response of biologically derived soft tissue biomaterials to cyclic loading. *Journal of Biomedical Materials Research Part A*, 80A(1):194–205, January 2007. ISSN 1549-3296 (Print). doi: 10.1002/jbm.a.30871. URL `http://www.ncbi.nlm.nih.gov/entrez/query.fcgi?cmd=Retrieve&db=PubMed&dopt=Citation&list_uids=17041913`.

[36] D. B. Smith, M. S. Sacks, P. M. Pattany, and R. Schroeder. High-resolution magnetic resonance imaging to characterize the geometry of fatigued porcine bioprosthetic heart valves. *The Journal of heart valve disease*, 6(4):424–432, July 1997. ISSN 0966-8519.

[37] D. B. Smith, M. S. Sacks, P. M. Pattany, and R. Schroeder. Fatigue-induced changes in bioprosthetic heart valve three-dimensional geometry and the relation to tissue damage. *The Journal of heart valve disease*, 8(1):25–33, January 1999. ISSN 0966-8519.

[38] Joao S. Soares, Kristen R. Feaver, Will Zhang, David Kamensky, Ankush Aggarwal, and Michael S. Sacks. Biomechanical behavior of bioprosthetic heart valve heterograft tissues: characterization, simulation, and performance. *Cardiovascular Engineering and Technology*, 7(4):309–351, aug 2016. ISSN 1869-4098. doi: 10.1007/s13239-016-0276-8. URL `http://dx.doi.org/10.1007/s13239-016-0276-8`.

[39] Albert Starr. The artificial heart valve. *Nature Medicine*, 13(10):1160–1164, oct 2007. doi: 10.1038/nm1644.

[40] Wei Sun, Michael Sacks, Gregory Fulchiero, Joshua Lovekamp, Naren Vyavahare, and Michael Scott. Response of heterograft heart valve biomaterials to moderate cyclic loading. *Journal of Biomedical Materials Research*, 69A(4):658–669, June 2004. doi: 10.1002/jbm.a.30031. URL `http://www.ncbi.nlm.nih.gov/entrez/query.fcgi?cmd=Retrieve&db=PubMed&dopt=Citation&list_uids=15162408`.

[41] H. Tam, W. Zhang, D. Infante, N. Parchment, M.S. Sacks, and N. Vyavahare. Fixation of bovine pericardium-based tissue biomaterial with irreversible chemistry improves biochemical and biomechanical properties. *Journal of Cardiovascular Translational Research*, 10(2):194–205, feb 2017. doi: 10.1007/s12265-017-9733-5.

[42] Hobey Tam, Will Zhang, Kristen R. Feaver, Nathaniel Parchment, Michael S. Sacks, and Naren Vyavahare. A novel crosslinking method for improved tear resistance and biocompatibility of tissue based biomaterials. *Biomaterials*, 66:83–91, October 2015. ISSN 1878-5905 (Electronic) 0142-9612 (Linking). doi: 10.1016/j.biomaterials.2015.07.011. URL `http://www.ncbi.nlm.nih.gov/pubmed/26196535`.

[43] N. Vyavahare, D. Hirsch, E. Lerner, J. Z. Baskin, F. J. Schoen, R. Bianco, H. S. Kruth, R. Zand, and R. J. Levy. Prevention of bioprosthetic heart valve calcification by ethanol preincubation. Efficacy and mechanisms. *Circulation*, 95(2):479–488, jan 1997. doi: 10.1161/01.cir.95.2.479. URL `http://www.ncbi.nlm.nih.gov/htbin-post/Entrez/query?db=m&form=6&dopt=r&uid=0009008467`.

[44] Sarah M. Wells, Tiffany Sellaro, and Michael S. Sacks. Cyclic loading response of bioprosthetic heart valves: effects of fixation stress

state on the collagen fiber architecture. *Biomaterials*, 26(15):2611–2619, May 2005. doi: 10.1016/j.biomaterials.2004.06.046. URL http://www.ncbi.nlm.nih.gov/entrez/query.fcgi?cmd=Retrieve&db=PubMed&dopt=Citation&list_uids=15585264.

[45] Will Zhang, Salma Ayoub, Jun Liao, and Michael S. Sacks. A meso-scale layer-specific structural constitutive model of the mitral heart valve leaflets. *Acta Biomaterialia*, 32:238–255, March 2016. ISSN 1878-7568 (Electronic) 1742-7061 (Linking). doi: 10.1016/j.actbio.2015.12.001. URL http://www.ncbi.nlm.nih.gov/pubmed/26712602.

Chapter 5

Effective model representation of structural and multi-scale models using effective constitutive models for facilitating numerical simulations[1]

Preface

One of the most crucial aspects of biomechanical simulations of organs and systems that seek to predict the outcomes of disease, injury, and surgical interventions is the underlying constitutive model. Current soft tissue constitutive modeling approaches have become increasingly complex, often utilizing meso- and multi-scale methods for greater predictive capability and linking to the underlying mechanisms. However, such modeling approaches are associated with substantial computational costs. One solution is to use effective constitutive models, which only reproduces the essential responses but not the underlying mechanisms. Effective constitutive models can be implemented in place of meso- and multi-scale models in numerical simulations, but derive their responses by homogenizing the responses of the underlying meso- or multi-scale models. A robust effective constitutive model can thus drastically increase the speed of simulations for a wide range of meso- and multi-scale models. However, there is no general consensus on how to develop a single effective

[1]**The work contained in this chapter was submitted for publication as**: Zhang, W., Zakerzadeh, Z., Zhang, W. & Sacks, M. S. A Material Modeling Approach for the Effective Response of Planar Soft Tissues for Efficient Computational Simulations. Journal of the mechanical behavior of biomedical materials. In review.
The author contributed to: performing the research, model development, data analysis, coding development, and writing the manuscript.

constitutive model for a wide range of soft tissue responses. In the present study, we developed an effective constitutive model, which can fully reproduce the response of a wide range of planar soft tissue responses, along with methods for fast-convergent parameter estimation. We evaluated this approach and demonstrated that it is able to handle materials of widely varying degrees of anisotropy, such as exogenously cross-linked bovine pericardium and aortic valve leaflet. This effective constitutive model approach has shown significant potential for improving the computational efficiency and numerical robustness of multi-scale and meso-scale modeling approaches, facilitating the application of inverse modeling and simulations of growth and remodeling of soft tissues and organs.

5.1 Introduction

Computational studies of organs and bioprosthetic devices have become increasingly popular for predicting the outcomes of diseases, injuries, and surgical interventions. Such applications include the simulation of aneurysm growth [45, 43, 22, 54], blood flow [38, 40, 41, 39, 6], and natural or bioprosthetic heart valves [57, 49, 26, 4, 36, 12]. One of the most important components of predictive simulations is an accurate constitutive model that can predict the mechanical behavior of the soft tissues and biomaterials involved. Such tissues have highly nonlinear anisotropic behaviors, often resulting in specific forms for different tissue types. In addition, these constitutive models are often extended to model growth, remodeling, pathology, fatigue, trauma and other time evolving processes. As such, constitutive models are often developed to take advantage of the structure to function relationship to predict how the response of the materials will evolve, utilizing physical models, multi-scale approaches, and/or molecular dynamics. Not surprisingly, constitutive models are becoming exceeding complex, and the computational costs are becoming a hindrance to more complex numerical simulations.

Examples of such approaches are meso-scale structural approaches for soft tissue modeling [29]. This class of soft tissue models homogenizes the tissue response at the meso-scale, where the simplified models of the mechanical response of collagen, elastin and other fibers are integrated with tissue microstructure [27]. This type of constitutive model has been shown to be able to accurately represent the mechanical behaviors of many soft tissues including valvular tissues [59, 44], pericardium [58], myocardium [5], and elastomeric scaffolds [14]. Recently, we have extended these models to include interaction terms [58, 5], which require multiple integrals to accurately compute the strain energy of fiber interactions.

In a broader context, multi-scale approaches utilize fundamental mechanisms at the micro-scale to derive the response of materials at the macro-scale. Often, multi-scale modeling begins at the molecular level, where the molecular structure of the constituents and the physical laws governing their interactions are well known and well-studied in chemistry and physics. At this level, molecular dynamics can be used to determine the mechanical response of constituent proteins. This can be upscaled to quaternary protein structures using coarse grain methods. This response is then integrated with higher level structures of the tissue to determine the response at even larger scales. Homogenization is thus critical in multi-scale modeling to simplify the response of the downscale models to improve the efficiency of simulations at higher scales. This process is repeated until the macro- or tissue-level. Examples using this approach are the modeling of collagenous tissues by Buehler *et al.* [10, 11] and intermediate filaments of cells by Qin *et al.* [42].

However, numerical simulations using these approaches are also quite costly. They can only be used for simulating the response of the materials, but cannot be easily incorporated into inverse modeling and time-dependent frameworks. Even the computational cost of meso-scale structural approaches is five magnitudes higher than conventional phenomenological approaches. For more detailed cell or molecular level information, which is important for better understanding cellular environments and growth and remodeling, the exceedingly high computational cost of multi-scale approaches makes it difficult for them to be directly implemented in computational simulations. As such, the multi-scale models used in simulations need to be simplified.

It is for this reason that many types of phenomenological models with computationally efficient forms, such as the generalized Fung type [18], Holzapfel-Gasser-

Ogden [24], generalized Ogden [37], generalized Rivlin [46], and Humphrey models [35], are popular for numerical simulations. These models utilize constitutive modeling approaches which do not take into account the underlying mechanisms, thus can only reproduce the mechanical response in the limited range of the experimental data utilized for parameter estimation. Furthermore, the mechanical data used and parameter estimation are not done in an optimal manner. This makes finding the optimal parameters inconsistent due to the high covariance between parameters. This is demonstrated in Sun and Sacks [51] for modeling pericardium under high in-plane shear. Here, it was shown that fitting only a subset of the loading paths acquired from biaxial mechanical testing cannot predict the remaining unfitted loading paths. Yet for *in vivo* simulations, these constitutive models are often derived from incomplete data while being asked to predict the mechanical response under non-physiological and often unpredictable ranges of deformations. As the parameters of such models have no physical meaning, it is often difficult to extend them for time-dependent processes such as growth and remodeling or to average and produce a population representative. As such, accurate simulations often still require detailed mechanism-based models.

To address these problems, an approach which can take advantage of mechanisms and predictive capabilities of micro-models (meso-scale, multi-scale, or other complex constitutive models) and the numerical efficiency of phenomenological approaches for simulations at the macro-scale is very beneficial. An effective constitutive model, based on phenomenological approaches, can be used to accurately reproduce the responses of a wide range of tissues using the same form, acting as an intermediate step between micro-models for material behavior and organ-level numerical simulations (Fig. 5.1A). For each iteration of the simulation, whether forward, inverse, or

time-evolving, the effective constitutive model is first fit to the micro-model(s) to determine the model parameters, then it is used to perform the actual numerical simulation. Subsequent updates to the evolving material properties, geometry, and boundary conditions are then performed (Fig. 5.1B). This makes the effective constitutive models especially useful for the final upscaling step of multi-scale models, increasing their efficiency. However, developing a generalized effective constitutive model is not straightforward. In addition to the issues described above, no specific constitutive model has yet been developed that is able to capture the material response of a wide range of soft tissue responses. Typically, a different constitutive model is used for each soft tissue type. These issues remain to be reconciled if effective constitutive models are to be used to fully reproduce the response of micro-models in computational simulations.

Thus, we hereby develop an effective constitutive model for planar soft tissues and a parameter estimation approach for rapidly determining the model parameters from the micro-model. Planar constitutive models are a good starting point, which are applicable to a wide range of soft tissues such as arteries, skin, heart valve, cells, vocal folds, bladder wall, synovial membrane, cornea, and cranial membrane. For the form of the effective constitutive model, we require the following characteristics:

1. Widely applicable in that it is able to faithfully reproduce a wide range of tissue responses

2. Computationally efficient and numerically robust

3. Allows for fast and accurate convergence during parameter estimation for upscaling micro-models, thus having the minimal number of and minimally covariant model parameters

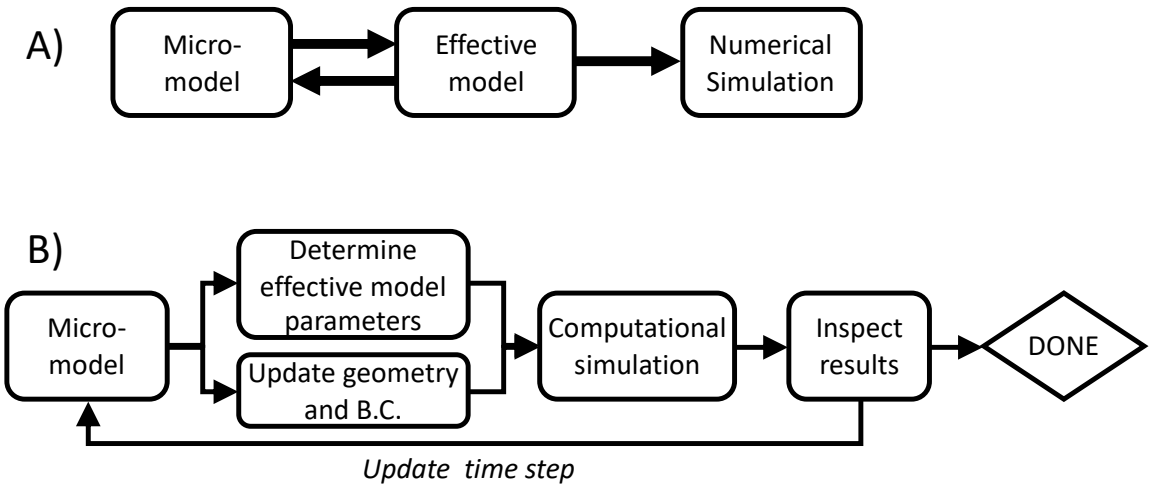

Figure 5.1: Proposed framework for using an effective constitutive model to improve the efficiency of using complex meso- or multi-scale models (micro-models) in numerical simulations. Here, A) effective constitutive models act as an intermediate step between micro-models and numerical simulations, where micro-models inform the changes to the effective constitutive model while the effective constitutive model for the simulation. B) An example of how this may be implemented for time-evolving is shown.

4. Easy to implement, no integrations or functions without closed-form expressions

Using meso-scale structural models as an example, we will examine the ability of the effective constitutive model to fit the mechanical response of micro-models for a wide range of deformations, examine the speed and convergence of parameter estimation, and demonstrate the use of the effective constitutive model to facilitate the simulation of heart valves with a wide range of material properties.

5.2 Effective constitutive model formulation

5.2.1 Kinematic considerations

The choice of kinematic basis is the first step to formulate constitutive models. Very often, it is useful to limit the choice of kinematic basis based on the available

mechanical data or how well each basis matches the response of the soft tissues, thus simplifying the form of the constitutive model and reducing parameter covariance during parameter estimation. However, for our approach, our aim is a highly generalized constitutive model that can match a wide range of possible micro-model responses using the same form, not restricting itself to the response and physics of specific soft tissue types. There is also no limitations to having sufficient mechanical data for parameter estimation, as this will be generated from the micro-models. As such, our considerations for choosing the kinematic basis are mainly:

1. Most generalized form for reproducing a wide range of mechanical responses
2. Simplest form for implementation and computational cost in numerical simulations
3. Minimal number of parameters
4. Minimal parameter covariance for parameter estimation

The smallest set of kinematic variables that can describe a wide range of soft tissues and deformations using the same simple form is ideal.

The invariants and pseudo-invariants of the right or left Cauchy Green tensor is very popular for the constitutive models of soft tissues. Indeed, we use them often with our structural models [16, 59, 5, 48, 58]. There is a large number of invariants, each describes a facet of deformation: isotropic, volumetric strain, anisotropic, or interactions between them. The breadth of choices allows for more freedom in selecting the best combination when modeling specific soft tissues. However, there are simply too many invariants and many of which are highly covariant. This does not lend itself

for minimizing the number of parameters and the parameter covariance in a single fully generalized form.

It's here that using the components of the strain tensors is more practical for our approach. Although all strains are equivalent for constitutive modeling because they can be expressed with respect to each other, different strain tensors can have different effects when used directly in place of each other in the same form. For us, with the purpose of keeping the constitutive model form simple for implementation, the Green Lagrange strains are the most practical. Based on preliminary testing (Appendix A.1), the Green Lagrange strains result in the simplest 2nd Piola Kirchhoff stress and elasticity tensor forms and have behaviors that closely resemble the response of collagen fibers in soft tissues when under compression. We examined these aspects more closely in Appendix A.1.

It is also convenient to express the Green Lagrange strain tensor with respect to the material axis (Fig. 5.2), $\mathbf{m}_0$, where

$$E_m = \mathbf{m}_0 \cdot \mathbf{E}\mathbf{m}_0, \quad E_n = \mathbf{n}_0 \cdot \mathbf{E}\mathbf{n}_0, \quad E_\phi = \mathbf{m}_0 \cdot \mathbf{E}\mathbf{n}_0, \tag{5.1}$$

and $\mathbf{n}_0$ is the direction orthogonal to $\mathbf{m}_0$ (Fig. 5.2). This symmetry is helpful for further reducing the constitutive model form.

5.2.2 Effective constitutive model form

5.2.2.1 Possible family of forms for the effective constitutive model

Using phenomenological approaches is necessary for minimal computational cost. The form of phenomenogical models for soft tissues generally falls into three families. The first family is composed of a summation of polynomials,

$$\Psi = \sum_i \sum_j \sum_k c_{ijk} E_m^i E_n^j E_\phi^k. \tag{5.2}$$

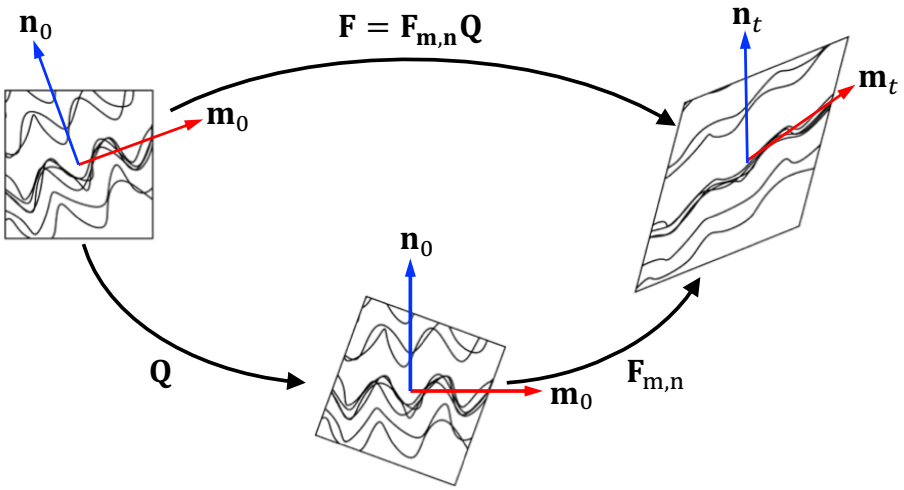

Figure 5.2: By taking the right polar decomposition of the deformation gradient tensor, we can express the components of the Green Lagrange strain tensor with respect to the material axis. This creates symmetry for the shear component of the Green Lagrange strain tensor, allowing us to further simplify the model form.

We will refer to this family as the polynomial series approach. The second family is composed of separated exponential functions of individual or combinations of invariants or strains used, for example by Vito *et al.* [53],

$$\Psi = \sum_i \sum_j \sum_k c_{ijk} e^{b_{ijk} E_m^i E_n^j E_\phi^k}. \tag{5.3}$$

We will refer to this family as the separated exponential approach. The final family is exponential models composed of a single exponential function of the sum of polynomials,

$$\begin{aligned} \Psi &= c_0 \left(e^Q - 1 \right) \\ Q &= \sum_i \sum_j \sum_k b_{ijk} E_m^i E_n^j E_\phi^k. \end{aligned} \tag{5.4}$$

This was first introduced by Fung [19] and we will refer to this family as the single exponential approach.

5.2.2.2 Generalized effective constitutive model form determination

Each approach (Eqn. 5.2-5.4) has its own advantages and disadvantages. The polynomial series approach has the most flexibility. With a sufficient number of terms, it can it reproduce the response in a similar manner to Taylor series expansions. In pilot testing, the polynomial series approach requires a significant number of terms than other choices, at least 27 terms in preliminary testing. 21 of the 27 terms are coupling terms. As a result, constraints needed for convexity are both complex and difficult to enforce. In the most general form, convexity cannot be enforced globally or only at the boundaries. It needs to be enforced at separate points within the domain or by integration. These constraints do not only have computational costs that vastly exceed the cost of the model itself, but will also significantly impacts convergence during parameter estimation. The constraints are not convex, with many local minima, often failing to converge even after 200,000 iterations. In additional, extrapolation using this approach is extremely unreliable. This makes constrained optimization often intractable to implement within a simulation framework such as the one proposed (Fig. 5.1).

The separated exponential approach generally suffers from the same issues as the polynomial series. This model form behaves like polynomial series with variable exponents, i.e. $c_1 e^{b_1 E_m} = c_1 y^{b_1}$, where $y = e^{E_m}$. The advantage of this family of models is that similar and highly covariant terms such as $c_1 E_m + c_2 E_m^2 + c_3 E_m^3 ...$ can be avoided, reducing the number of parameters needed. However, like the polynomial series family, coupling terms such as $c_4 e^{b_4 E_m E_n}$ are not convex or elliptical functions, resulting in the same issues for parameter estimation and enforcing convexity. The number of parameters required to fully reproduce the mechanical response is still quite large. Moreover, for the same number of parameters, the separated exponential

form is woefully insufficient at reproducing the mechanical response of soft tissues in comparison to the single exponential approach. As such, the advantages gained for parameter covariance by separating the terms are actually quite minimal.

The single exponential approach has substantial parameter covariance, but is extremely effective at reproducing the response of soft tissues using a small number of parameters, is computationally efficient, and is easy to enforce convexity for. Because the exponential function is monotonically increasing, enforcing convexity and ellipticity only requires the polynomial Q to be convex and elliptical. This is the best balance for our goals, and is thus our choice for the effective constitutive model. The first step is of course to examine the generalized Fung model [19]

$$\begin{aligned} \Psi &= c_0 \left(e^Q - 1 \right) \\ Q &= \sum_i \sum_j \sum_k \sum_l b_{ijkl} E_{ij} E_{kl}. \end{aligned} \tag{5.5}$$

We find that the generalized Fung model is not able to fully reproduce the mechanical response of pericardium and aortic valve tissues, it can only do so in a limited range. Although this is enough for most numerical simulations, where the deformations are generally limited to the physiologic range, it is not always sufficient for predicting the mechanical response when organs undergo significant changes in geometry, causing the deformations to change drastically. The easiest way to visualize this is through contour plots of the strain energy function (Fig. 5.3). The mechanical response of soft tissues general has hyperelliptical contours (Fig. 5.3A), whereas the generalized Fung model always has precisely elliptical contours (Fig. 5.3B). This attribute of the generalized Fung model makes it easy to enforce ellipticity and convexity, and its elasticity tensor and behavior at small strains are easy to derive. However, when the range of deformation is sufficiently large, the generalized Fung model is essentially limited to stretching and rotating its contours to match that of the soft tissue (Fig.

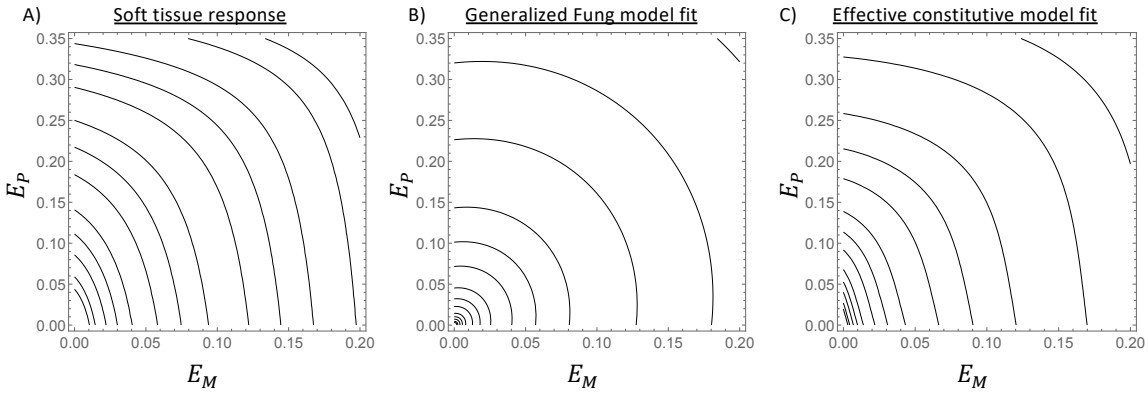

Figure 5.3: The contour plots of strain energy (kPa) of A) a bovine pericardial specimen using a meso-scale structural model [58], B) best fit using the generalized Fung model (Eqn. A.6), and C) best fit using the effective constitutive model we develop from herein showing the necessity of extending existence phenomenological model form.

5.3B), but cannot fully reproduce the resulting tissue responses. It can only serve as an approximation.

5.2.2.3 Final effective material model form

Thus, for the effective constitutive model, we extended the polynomial Q one step further, allowing the strain energy density function to be hyperelliptic (Fig. 5.3C). For the additional terms to include, we move up to the next even powers, up to the quartic terms (exponents $i+j+k \leq 4$) (Eqn. 5.4), as odd powers alone do not yield elliptical functions. There are a total of 34 possible terms in Q. Not all terms are required or even admissible. Specifically, the following constraints are enforced on the model:

Constraint 1: The stress must be zero in the reference configuration. Given that the stress is the gradient of Ψ, where is $\Psi' = c_0 Q' e^Q$, all terms in Q' must be zero at zero strain. This corresponds to all $i+j+k=1$ terms being removed, leaving 31 terms remaining.

Constraint 2: The response must be elliptic. That is the shortest line inscribed on the strain energy function surface joining any two points must have a positive curvature. Keeping in mind that the generalized Fung model (Eqn. 5.4) is already close to being sufficient at reproducing the response of many soft tissues we tested. We only want to extend this to be able to reproduce a wider range of soft tissue responses. Furthermore, in considerations of limiting the number of parameters, reducing parameter correlation, improving the conditioning of the constrained objective function surface, and that the non-elliptical terms must be small, we choose to forgo all $i + j + k = 3$ terms, leaving 21 terms remaining.

Constraint 3: Response must be independent of the direction of shear. Since we decompose the Green-Lagrange strain relative to the material axis, this creates a plane of symmetry in the soft tissue response for the direction of shear. Thus, the value of E_ϕ can only have even powers, $k = 2, 4$. The following terms are thus necessarily zero: $E_m^3 E_\phi$, $E_m^2 E_n E_\phi$, $E_m E_n^2 E_\phi$, $E_n^3 E_\phi$, $E_m E_\phi^3$, $E_n E_\phi^3$, $E_m E_\phi$, and $E_n E_\phi$.

The final form of the effective constitutive model is thus

$$\begin{aligned}\Psi =& c_0 \left(e^Q - 1\right)\\ Q =& b_1 E_m^2 + b_2 E_n^2 + b_3 E_\phi^2 + b_4 E_m E_n + b_5 E_m^4 + b_6 E_n^4 + b_7 E_m^3 E_n + b_8 E_m^2 E_n^2 + b_9 E_m E_n^3\\ &+ b_{10} E_\phi^4 + b_{11} E_m^2 E_\phi^2 + b_{12} E_n^2 E_\phi^2 + b_{13} E_m E_n E_\phi^2.\end{aligned} \tag{5.6}$$

5.2.2.4 Enforcing convexity and ellipticity

Perhaps the biggest advantage of the single exponential approach models is the convenience for enforcing ellipticity and convexity. Because ellipticity and convexity are preserved by monotonically increase functions, such as e^x, we only have to enforce ellipticity and convexity of Q (Eqn. 5.6). For strong ellipticity, the following must be

satisfied,

$$\frac{\partial^2 \Psi}{\partial F_{ij} \partial F_{kl}} \lambda_i \lambda_k \mu_j \mu_l > 0 \equiv \frac{\partial^2 Q}{\partial F_{ij} \partial F_{kl}} \lambda_i \lambda_k \mu_j \mu_l > 0, \tag{5.7}$$

where F is any tensor, and λ and μ are arbitrary non-zero vectors. *This condition is also equivalent of strict convexity [7]*, so both conditions will be satisfied. Satisfying this constraint requires that the elasticity tensor $C_{ijkl} = \dfrac{\partial^2 \Psi}{\partial E_{ij} \partial E_{kl}}$ is positive definite, or rather $\dfrac{\partial^2 Q}{\partial E_{ij} \partial E_{kl}}$ is positive definite, satisfying Drucker stability for numerical purposes. Sylvester's criterion [20], is the most convenient in this scenario, which is given by

$$\begin{gathered} \frac{\partial^2 Q}{\partial E_m^2} \geq 0, \quad \det \begin{bmatrix} \dfrac{\partial^2 Q}{\partial E_m^2} & \dfrac{\partial^2 Q}{\partial E_m \partial E_n} \\ \dfrac{\partial^2 Q}{\partial E_m \partial E_n} & \dfrac{\partial^2 Q}{\partial E_n^2} \end{bmatrix} \geq 0, \\ \det \begin{bmatrix} \dfrac{\partial^2 Q}{\partial E_m^2} & \dfrac{\partial^2 Q}{\partial E_m \partial E_n} & \dfrac{\partial^2 Q}{\partial E_m \partial E_\phi} \\ \dfrac{\partial^2 Q}{\partial E_m \partial E_n} & \dfrac{\partial^2 Q}{\partial E_n^2} & \dfrac{\partial^2 Q}{\partial E_n \partial E_\phi} \\ \dfrac{\partial^2 Q}{\partial E_m \partial E_\phi} & \dfrac{\partial^2 Q}{\partial E_n \partial E_\phi} & \dfrac{\partial^2 Q}{\partial E_\phi^2} \end{bmatrix} \geq 0. \end{gathered} \tag{5.8}$$

For the generalized Fung model (Eqn. A.6), $b_1 > 0$, $b_1 b_2 - b_4 > 0$, and $b_3(b_1 b_2 - b_4^2) - b_5(b_2 b_5 - b_4 b_6) - b_6(b_1 b_6 - b_4 b5) > 0$ will enforce convexity everywhere. For equation 5.6, this is slightly more complex. The non-convex region starts from a point along the respective axis for each component E_m, E_n, and E_ϕ, then spreads out in the shape of a fan as the strain increases depending on which specific coupling terms, such as $E_m^3 E_n$ and $E_m E_n^3$ are present (Fig. 5.4). As long as the effective constitutive model is convex on the largest value along the E_m, E_n, and E_ϕ axis respectively, then the effective constitutive model is convex over the entire range. For example, the effective constitutive model is convex if the maximum point on the E_m-axis is convex for $E_m^3 E_n$ (Fig. 5.4A) or if the maximum point on the E_n-axis is convex for

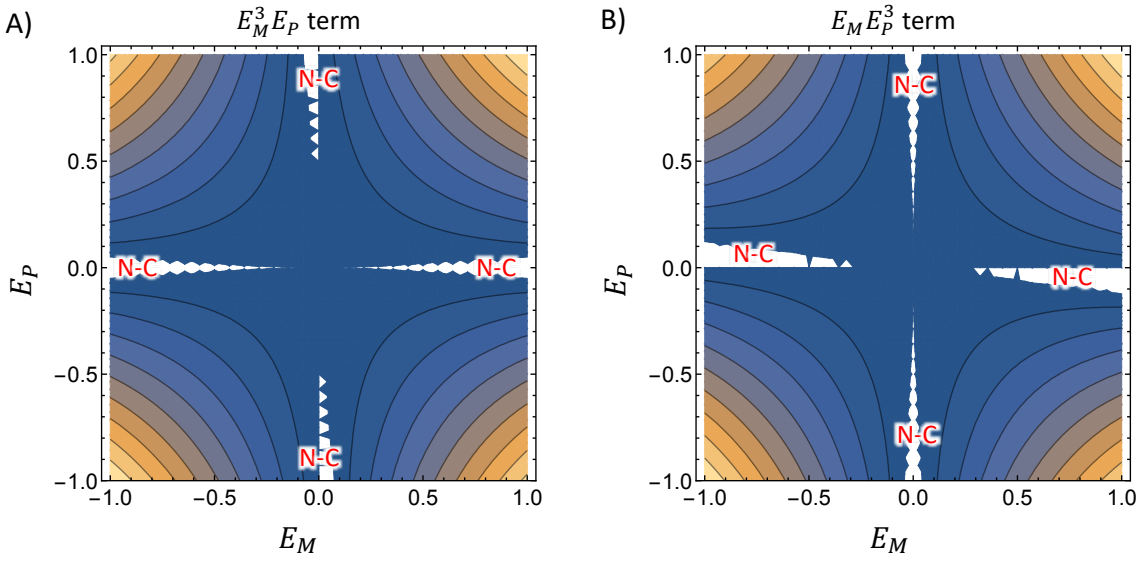

Figure 5.4: The criteria for ellipticity (Eqn. 5.8) plotted against the components of the Green-Lagrange strain for A) when including the $E_m^3 E_n$ term and B) $E_m E_n^3$ term. The white regions are not convex (N-C), which start at a point along the axes and spreads out as the strain increases.

$E_m E_n^3$ (Fig. 5.4B). Thus, assuming an upper limit of $E_m < 1$, $E_n < 1$, and $E_\phi < 1$, the following constraints on the parameters are sufficient to guarantee convexity and ellipticity,

$$\begin{aligned} b_1, b_2, b_3, b_5, b_6, b_{10} &\geq 0 \\ 4(b_1 + 6b_5)(b_2 + b_8) - (b_4 + 3b_7)^2 &\geq 0 \\ 4(b_2 + 6b_6)(b_1 + b_8) - (b_4 + 3b_9)^2 &\geq 0 \\ 4(b_1 + b_{11})(b_2 + b_{12}) - (b_{13} + b_4)^2 &\geq 0 \\ b_3 + b_{11} &\geq 0 \\ b_3 + b_{12} &\geq 0. \end{aligned} \tag{5.9}$$

5.2.3 Model scaling method to improve parameters correlation for parameter estimation

5.2.3.1 Parameter correlation for exponential type models

One challenging problem with model parameter determination is covariance between the parameters during parameter estimation. Covariance explains how two parameters influence the response of the model and how they will be updated during parameter estimation. High parameter covariance results in both slow convergence and poor reliability and reproducibility of the material parameters. When scaled by the variance, this becomes the correlation between the parameters, with an absolute value between 0 and 1. Correlation equal to 1 implies that two parameters have the exact same effect on the model response, and are thus indistinguishable during parameter estimation. The covariance issue for constitutive models with an exponential function is well described by Aggarwal [2, 1]. These constitutive models with exponential functions have a long valley-like region in the objective function space. Inside this valley, significantly different parameters produce similar objective function values. This presents several problems. 1) It's difficult to compare model parameters between different specimens because drastically different parameters can produce similar responses. As such, the average or representative specimen has little real meaning, and each specimen needs to be fitted individually for simulations. 2) The convergence of gradient-based optimization algorithms becomes excruciatingly slow due to the small gradients while trapped within this valley. 3) The covariance between parameters being extremely large decreases the accuracy or in other word increases the confidence interval of parameters obtained.

Aggarwal *et al.* suggested two improvements to alleviate this problem [1]. These improvements are 1) modifying the modulus parameter A to e^a, straightening the shape of the valley, and 2) introducing the log-norm for the objective function,

improving the gradient along the valley. These modifications have been shown to be effective. However, this is not always ideal. The suggested logarithmic norm faces some issues when used to fit stresses or strains, which may be negative and thus becomes undefined. Although this may be alleviated by forgoing data points with negative strains or stresses, the model may still produce negative values during parameter estimation. Other methods can be used to discard negative values or to take the norm of such values, but these approaches create discontinuities in the gradient of the objective function, causing convergence problems during parameter estimation. Clearly, additional improvements can still be made.

5.2.3.2 Model scaling method

We begin by examining the fundamental reason for the high parameter covariance. For this, we will use the 1-D case as an example,

$$\begin{aligned} \Psi &= A\left(e^{B\epsilon} - 1\right) \\ \mathcal{F} &= \sum_i \left(\Psi(\epsilon_i) - \Psi_i\right)^2, \end{aligned} \tag{5.10}$$

where Ψ is the strain energy of our model, ϵ is some invariant that is a function of the strain, ϵ_i and Ψ_i are simulated data, and $\mathcal{F}$ is our objective function for parameter estimation. The parameters A and B have different purposes: A is like a modulus, linearly increasing the stiffness of the material, while B modifies the shape of the response, controlling the nonlinearity of the material. However, practically, the two parameters have nearly the same effect on the mechanical response, increasing A increases the stiffness (Fig. 5.5A) and increasing B also increases the stiffness (Fig. 5.5B). This is the reason for the high correlation between the parameters (Fig. 5.5), 0.9979.

To address this problem, we introduce a scaling term to normalize the expo-

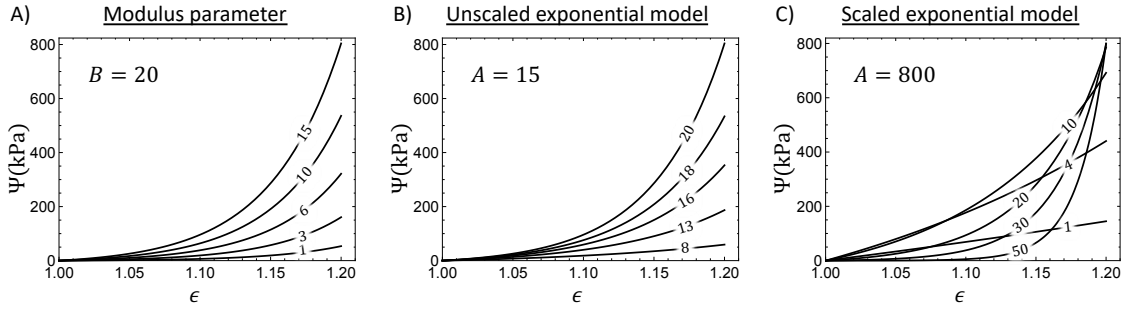

Figure 5.5: A)The effect of increasing the values of the modulus A on exponential type models. B) The effect of increasing the values of exponent B on exponential type models, which is nearly indistinguishable from the modulus A. C) The effect of increasing the values of the parameter B after applying the proposed scaling, increasing the values of the parameter A remains the same as in A).

nential part of the model. This prevents increasing B from increasing the value of the strain energy as a whole, allowing it to only control the curvature. For this, we will use a value ϵ_{max}, which represents the data point with the maximum strain energy value used for parameter estimation, which is also the point where the strain energy stays constant with changes in B. The scaled form is thus given by

$$\Psi = \Psi_s = \bar{A}\left[e^{-B\epsilon_{max}}\left(e^{B\epsilon} - 1\right)\right], \tag{5.11}$$

where $\bar{A}$ is the scaled version of the modulus A. This scaling keeps the exponential part of the model, $e^{-B\epsilon_{max}}(e^{B\epsilon} - 1)$, at approximately 1.0 at $\epsilon = \epsilon_{max}$, regardless of the changes in the value of the parameter B (Fig. 5.5C). This effect is not exact when the value of B is small due to the -1 needed to set the strain energy to 0 in the referential configuration but is nonetheless sufficient for our goal: decoupling the modulus increasing effect of the parameter A from the curvature increasing effect of the parameter B. Indeed, we found this approach to be successful. We examined the contour plot of the objective function with respect to each of the 4 cases in Aggarwal's work [1], with the standard objective function, with $A = e^a$, with log-norm, and with

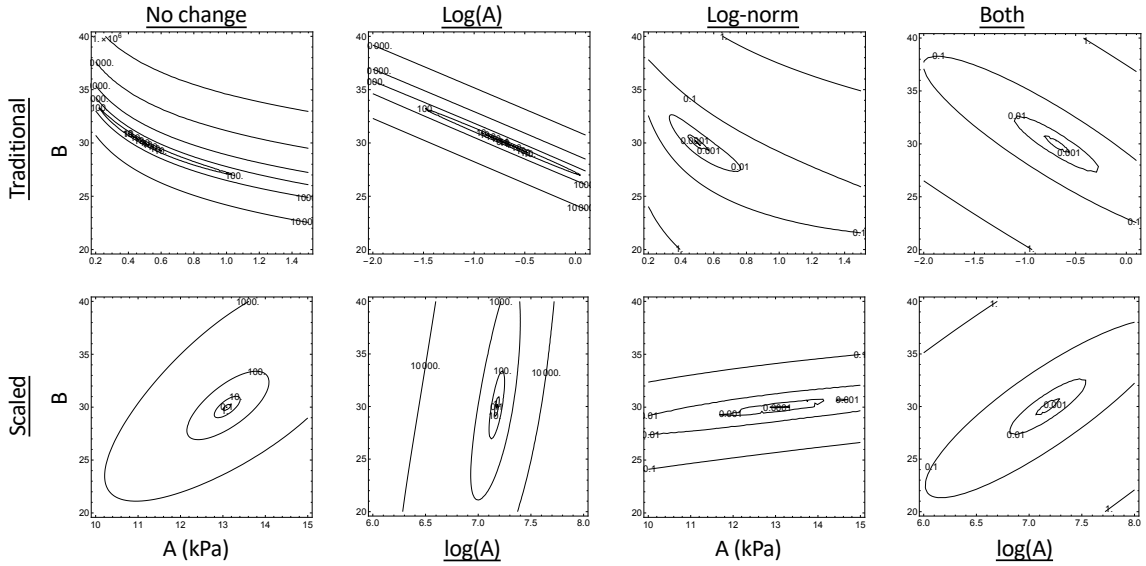

Figure 5.6: (Top) The objective function surface for the traditional unscaled exponential models and (Bottom) objective function surface after scaling. From Left to Right are: the unchanged surface, the surface after changing A to e^a, using the log-norm for the objective function, and applying both changes. The scaled form with no other changes behaves the best.

$A = e^a$ and the log-norm, for both without scaling and with scaling (Fig. 5.6). First, the correlation between the parameters does not change with $A = e^a$. The log-norm improves the correlation from 0.9979 to 0.9063 (Table 5.1), which significantly improves the objective function surface (Fig. 5.6). On the other hand, our scaling method improves the correlation from 0.9979 to 0.6186, more significant than using the log-norm. Interestingly, combining scaling and the log-norm has the adverse effect, increasing the correlation back from 0.6186 to 0.8592. This is a result of essentially linearizing the relation between A and B, i.e. from $Ae^{B\epsilon}$ to $Log(A) + B\epsilon$, causing the relationship between A and B to go from modulus and nonlinearity to baseline and modulus. Clearly, *the most optimal parameter estimation approach is to use scaling method with no other modifications.*

Table 5.1: The correlation between model parameter when using Hencky strains

	No change	log(A)	log-norm	Both
Traditional	-0.9979	-0.9979	-0.9063	-0.9063
Scaled	0.6186	0.6186	0.8592	0.8592

By design, the value of the exponential parameter B does not change by using the scaling method. Since the scaling term does not depend on the input strain, it acts as a modification to the modulus A while keeping the exponential term the same. This also implies that the relationship between the unscaled modulus A and the scaled modulus $\bar{A}$ is

$$A = \bar{A}e^{-B\epsilon_{max}}, \tag{5.12}$$

which makes finding the actual unscaled parameters a simple task. One other benefit of this scaling approach is that the value of $\bar{A}$ is extremely straight forward and intuitive, it is the strain energy of the model at ϵ_{max}. As a result, the value of $\bar{A}$ can be determined *a priori*, or at the very least it is easy to make an initial guess for $\bar{A}$. This will in turn also help to make parameter estimation faster and more accurate, leaving only the parameter B to be determined.

5.2.3.3 Extension to multiple variables

Extending this method to multiple variables is very simple. For Ψ_{eff} (Eqn. 5.6), the input variables become $\epsilon = \{E_m, E_n, E_\phi\}$, and $\epsilon_{max} = \{E_m^{max}, E_n^{max}, E_\phi^{max}\}$. Determining the values for ϵ_{max} depends on the form of the objective function. Using the most common case as the example, which is the sum of the squares of the differences in the 2nd Piola Kirchhoff stress,

$$\mathcal{F} = \sum_i \left(S_{11}(\epsilon_i) - \hat{S}_{11}^i\right)^2 + \left(S_{12}(\epsilon_i) - \hat{S}_{12}^i\right)^2 + \left(S_{22}(\epsilon_i) - \hat{S}_{22}^i\right)^2, \tag{5.13}$$

ϵ_{max} is the data point ϵ_i which maximizes $\left(\hat{S}^i_{11}\right)^2 + \left(\hat{S}^i_{12}\right)^2 + \left(\hat{S}^i_{22}\right)^2$. Thus, we also introduce a Q_{max} such that,

$$\begin{aligned}
\Psi_{eff} =& c_0 \left(e^Q - 1\right) = c_0' e^{-Q_{max}} \left(e^Q - 1\right) \\
Q =& b_1 E_m^2 + b_2 E_n^2 + b_3 E_\phi^2 + b_4 E_m E_n + b_5 E_m^4 + b_6 E_n^4 + b_7 E_m^3 E_n + b_8 E_m^2 E_n^2 \\
& + b_9 E_m E_n^3 + b_{10} E_\phi^4 + b_{11} E_m^2 E_\phi^2 + b_{12} E_n^2 E_\phi^2 + b_{13} E_m E_n E_\phi^2 \\
Q =& b_1 (E_m^{max})^2 + b_2 (E_n^{max})^2 + b_3 (E_\phi^{max})^2 + b_4 (E_m^{max})(E_n^{max}) + b_5 (E_m^{max})^4 \\
& + b_6 (E_n^{max})^4 + b_7 (E_m^{max})^3 (E_n^{max}) + b_8 (E_m^{max})^2 (E_n^{max})^2 + b_9 (E_m^{max})(E_n^{max})^3 \\
& + b_{10} (E_\phi^{max})^4 + b_{11} (E_m^{max})^2 (E_\phi^{max})^2 + b_{12} (E_n^{max})^2 (E_\phi^{max})^2 \\
& + b_{13} (E_m^{max})(E_n^{max})(E_\phi^{max})^2,
\end{aligned} \tag{5.14}$$

where parameter estimation will be done for c_0' instead of c_0. Computing the response functions and the stresses, or even the elasticity tensor remains very simple, only requiring multiplying each term by $e^{-Q_{max}}$. Thus, this scaling method is a very simple and easy to implement method of improving the speed and convergence for the parameter estimation of exponential type models.

5.2.4 Optimal *in silico* loading paths for parameter estimation

Another technique for improving the parameter estimation process for determining Ψ_{eff} from respective micro-models is establishing optimal loading paths. An example is the work of Avazmohammadi [5], where optimal experimental design is used to 1) minimize the amount of data necessary and 2) improve model parameter covariance for parameter estimation. Just like one of the most important question to ask before performing any mechanical testing is how much and what kind of data is necessary, we should also be selective with our choice of sampling points for parameter estimation. The theory for optimal design of experiment is well-studied and docu-

mented [30, 60]. Vast majority of the methods for optimal design uses D-optimality as the design variable,

$$D = \det(\boldsymbol{\mathcal{I}}), \quad \boldsymbol{\mathcal{I}} = \mathbf{J}^{\mathsf{T}}\mathbf{J} \quad \text{or} \quad \boldsymbol{\mathcal{I}} = \boldsymbol{\mathcal{H}}, \\ \text{where } J_{ij} = \frac{\partial f_i}{\partial \xi_j}, \quad \mathcal{H}_{ij} = \frac{\partial^2 \mathcal{F}}{\partial \xi_i \partial \xi_j}, \tag{5.15}$$

where ξ is a vector of model parameters and $\boldsymbol{\mathcal{I}}$ is the information matrix. $\boldsymbol{\mathcal{I}}$ can be computed from the derivatives of the objective function $\mathcal{F}$, where f is the model evaluated at each data point, or it can be computed from the Hessian of the objective function, $\boldsymbol{\mathcal{H}}$ (Appendix A.3). D-optimality is the determinant of the information or the Hessian matrix at the best fit value. It offers the best representation of both parameter accuracy (parameter covariance or correlation) and precision (parameter variance) at the same time.

The first and foremost step is to establish the parameterization for loading paths so they can be optimized. This is not a straightforward choice, as the number of loading path required is not yet established. Another issue is that the number of data points is discrete, thus the gradient of the D-optimality with respect to the control parameters is not smooth. For the sake of time spent for optimization, the number of data points should be kept as small as possible, thus exacerbating the issue of differentiability. Even worse is perhaps that the objective function is essentially flat when not near the optimum, making gradient algorithms not practical. Monte Carlo, random search or divide and conquer strategies are needed, which are much more time-consuming. The search space also increases exponentially with the number of loading paths, making a fully exhaustive search difficult to implement. Thus, a simple parameterization for loading paths is ideal.

We define loading paths based on the following conditions:

1. The number of loading paths is as small as possible

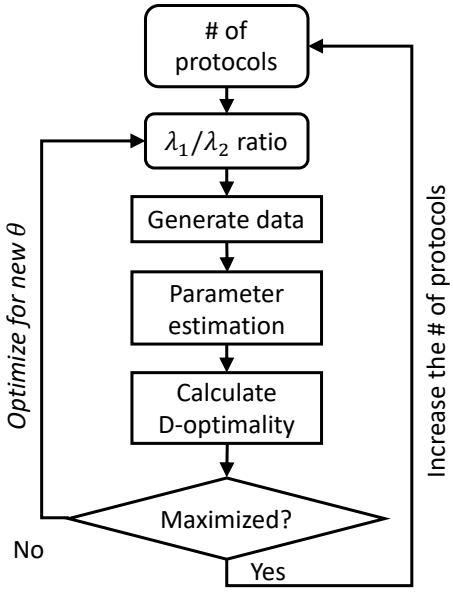

Figure 5.7: Our approach for optimizing for the optimal loading paths for parameter estimation.

2. The number of variables needed to define a loading path is as small as possible

3. Possible application to mechanical testing of tissues.

Starting with planar extensions only, we chose a loading path as data points which shares the same stretch ratio, λ_1/λ_2, which is typically the same definition used for biaxial mechanical testing. This only requires one constant to be defined for each loading path and the resulting fan shape covers the largest range of deformation with the least number of data points. To determine the optimal loading paths, 1) the total number of loading paths was set, then 2) each combination of the stretch ratios was evaluated for the highest D-optimality (Fig. 5.7). For a total number of loading paths ranging from 1 to 6, we found the point when the D-optimality stops increasing significantly, and choose this as the optimal set. Next, the shear component, κ_1, is added. For this study, we constrained the shear to be $0 < \kappa_1 < 0.2$. Only the positive

values of κ_1 are allowed due to the material symmetry. Furthermore, the optimal planar extensions loading paths are always included as a part of the data set.

5.2.5 Example application for planar soft tissues

The exogenously cross-linked structural model presented in Zhang and Sacks [58] is used to test our approach (Fig. 5.1) and see if Ψ_{eff} (Eqn. 5.14) can completely reproduce its response. This meso-scale structural model is computationally expensive due to integration over the collagen fiber architecture but have been shown to be able to accurately reproduce the mechanical response of a variety of soft tissues, such as mitral valve leaflets [59], ovine pulmonary artery [16], myocardium [5], and exogenously cross-linked bovine pericaridium [48]. To briefly summarize, this model is composed of 3 components: collagen, Ψ_{col}, matrix, Ψ_{mat}, and interactions, Ψ_{int}.

$$\Psi = \Psi_{\text{col}} + \Psi_{\text{mat}} + \Psi_{\text{int}} \tag{5.16}$$

The matrix term, Ψ_{mat}, is a modified version of the Yeoh model that is more linear when expressed in 2nd Piola Kirchhoff stress versus stretch,

$$\begin{aligned} \Psi_{\text{mat}} =& \frac{\eta_M}{2}\left[\frac{1}{a}\left(I_1-3\right)^a + \frac{r}{b}\left(I_1-3\right)^b\right], \\ & \text{with } 1 < a < b, ab < 2, 0 \leq r. \end{aligned} \tag{5.17}$$

This model contains four parameters: η_M is the modulus parameter corresponding to the same parameter in the Neo Hookean model, a, b, and r are the shape parameters, where a and b control the shape of the two terms, while r is the weight between the two terms. In general, $a \approx 1$, $b \approx 1.87$ and $r \approx 15$ can be treated as constants.

The response of collagen fibers is given by the integration over the collagen fibers architecture, their orientation and crimp. The fiber orientations is described by a beta distribution function and fiber crimp is described by another beta distribution

function of the stretches needed to straighten the fibers, the slack stretch λ_s. These are referred to as the orientation distribution function (ODF), Γ, and the recruitment distribution function (RDF), D, respectively, with the forms given in Zhang and Sacks [59, 58, 48]. The form of the strain energy function is

$$\Psi_{\text{col}} = \phi_{\text{col}} \eta_C \int_{\theta} \Gamma(\theta) \int_{1}^{\lambda_\theta} D\left(\lambda_s\right) \left(\frac{\lambda_\theta}{\lambda_s} - 1 \right)^2 \mathrm{d}\lambda_s \mathrm{d}\theta, \tag{5.18}$$

where η_C is the modulus of the collagen fibers, $\lambda_\theta = \sqrt{\mathbf{n}_\theta \cdot \mathbf{C}\mathbf{n}_\theta}$ is the stretch of the ensemble of collagen fiber with the same orientation, and $\lambda_\theta / \lambda_s$ is the true stretch of the collagen fibers after they are straightened [59]. Similarly, the response of the interaction term is given by integration over pairs of fibers based on their orientation and crimp, which contains a quadruple integral.

$$\Psi_{\text{int}} = \frac{\eta_I}{2} \int_{\alpha} \int_{\beta} \Gamma(\alpha) \Gamma(\beta) \int_{1}^{\lambda_\alpha} \int_{1}^{\lambda_\beta} D\left(x_\alpha\right) D\left(x_\beta\right) \left(\frac{\lambda_\alpha \lambda_\beta}{x_\alpha x_\beta} - 1 \right)^2 \mathrm{d}x_\alpha \, \mathrm{d}x_\beta \, \mathrm{d}\alpha \, \mathrm{d}\beta. \tag{5.19}$$

For clarity of presentation, the slack stretches, λ_s, are replaced by x_α and x_β for fiber oriented along the angle α and β respectively. Only one parameter, the modulus η_I, is used to account for all interactions, with the same Γ and D already given above.

The second Piola Kirchhoff stress, $\mathbf{S} = 2\frac{\partial \Psi}{\partial \mathbf{C}}$, is

$$
\begin{aligned}
\mathbf{S} =& \phi_{\text{col}}\eta_C \int_\theta \Gamma(\theta) \left\{ \int_1^{\lambda_\theta} \frac{D\left(x\right)}{x} \left(\frac{1}{x} - \frac{1}{\lambda_\theta} \right) \mathrm{d}x \right\} \mathbf{n}_\theta \otimes \mathbf{n}_\theta \mathrm{d}\theta \\
&+ \phi_{\text{col}}\eta_I \int_\alpha \int_\beta \Gamma\left(\alpha\right) \Gamma\left(\beta\right) \\
&\quad \times \Bigg[\left\{ \int_1^{\lambda_\alpha} \int_1^{\lambda_\beta} \frac{2\lambda_\beta D(x_\alpha) D(x_\beta)}{x_\alpha x_\beta} \left(\frac{\lambda_\alpha}{x_\alpha} \frac{\lambda_\beta}{x_\beta} - 1 \right) \mathrm{d}x_\alpha \, \mathrm{d}x_\beta \right. \\
&\qquad \left. + \int_1^{\lambda_\beta} D(x_\beta) \left(\frac{\lambda_\beta}{x_\beta} - 1 \right)^2 \mathrm{d}x_\beta \right\} \frac{\mathbf{n}_\alpha \otimes \mathbf{n}_\alpha}{\lambda_\alpha} \\
&\quad + \left\{ \int_1^{\lambda_\alpha} \int_1^{\lambda_\beta} \frac{2\lambda_\alpha D(x_\alpha) D(x_\beta)}{x_\alpha x_\beta} \left(\frac{\lambda_\alpha}{x_\alpha} \frac{\lambda_\beta}{x_\beta} - 1 \right) \mathrm{d}x_\alpha \, \mathrm{d}x_\beta \right. \\
&\qquad \left. + \int_1^{\lambda_\alpha} D(x_\alpha) \left(\frac{\lambda_\alpha}{x_\alpha} - 1 \right)^2 \mathrm{d}x_\alpha \right\} \frac{\mathbf{n}_\beta \otimes \mathbf{n}_\beta}{\lambda_\beta} \Bigg] \mathrm{d}\alpha \, \mathrm{d}\beta \\
&+ \phi_{\text{mat}}\eta_M \left[\left(\left(I_1 - 3\right)^{a-1} + r\left(I_1 - 3\right)^{b-1} \right) \left(\mathbf{I} - C_{33}\mathbf{C}^{-1} \right) \right],
\end{aligned}
\tag{5.20}
$$

where ϕ_{col} and ϕ_{mat} are the mass fraction of collagen and matrix respectively.

Although this model is very accurate and predictive, it is also computationally expensive. Moreover, numerical integration results in a significant decrease in numerical precision when the number of quadrature point is insufficient. This can create a number of issues for convergence during parameter optimization. Thus, the implementation of this model is complicated by a constant balance between computational cost and numerical robustness during optimization. Using Ψ_{eff} to reproduce its response is a solution to these issues.

5.2.6 Parameter estimation

The objective function we use is

$$
\begin{aligned}
S_m &= \frac{\partial \Psi}{\partial E_m} = \mathbf{m}_0 \cdot \mathbf{S}\mathbf{m}_0,\ S_n = \frac{\partial \Psi}{\partial E_n} = \mathbf{n}_0 \cdot \mathbf{S}\mathbf{n}_0,\ S_\phi = \frac{\partial \Psi}{\partial E_\phi} = 2\mathbf{m}_0 \cdot \mathbf{S}\mathbf{n}_0 \\
\mathcal{F} &= \sum_i^n \left(S_m(\hat{E}_M^i, \hat{E}_S^i, \hat{E}_\phi^i) - \hat{S}_M^i \right)^2 + \left(S_n(\hat{E}_M^i, \hat{E}_S^i, \hat{E}_\phi^i) - \hat{S}_S^i \right)^2 \\
&\quad + \left(S_\phi(\hat{E}_M^i, \hat{E}_S^i, \hat{E}_\phi^i) - \hat{S}_\phi^i \right)^2
\end{aligned}
\tag{5.21}
$$

This removes rigid body rotation and puts the stresses along the material axes, giving the response functions and minimizes covariance between the parameters during optimization. Other possible options include the log of the L2-norm, the log-norm presented by Aggarwal [1], and L2-norm of the strain energy and other stresses.

For optimal speed, gradient methods are ideal. Because we require some nonlinear constraints to enforce convexity, we utilized the interior point algorithm provided by the IPOPT library [55]. The initial guess is easily derived for the model scaling method, with the parameter c_0 being the maximum strain energy in the available data. The exponent parameters b_i are generally very consistent in value, with the quadratic parameters being $b_1 \approx 10$, $b_2 \approx 10$, and $b_4 \approx -10$, the quartic parameters being $b_5 \approx 2000$, $b_6 \approx 500$, $b_9 \approx 200$, $b_{10} \approx 200$, $b_{11} \approx 200$, $b_{12} \approx 200$. We find this setup to work extremely well, and no further modifications are necessary.

5.2.7 Reproducing the response of soft tissues using the effective constitutive model and optimal loading paths

For our approach (Fig. 5.1), we need to overcome the limitation of common phenomenological approaches in predicting the mechanical response of micro-models outside of the data set used for parameter estimation [51]. To verify this, we will first reproduced the results of Sun *et al.* [51] using the generalized Fung model, then repeat

the process using Ψ_{eff} (Eqn. 5.14) with optimal loading paths. We will focus on glutaraldehyde cross-linked bovine pericardium as the tissue. Bovine pericardium is the most common material used to fabricate bioprosthetic heart valves. It is extremely dense in collagenous fibers, having broad fiber splays with approximately 30 deg in standard deviation. The resulting mechanical behavior has strong coupling between the axial stretches. Thus, the mechanical response of some bovine pericardium specimens was fitted to the structural model (Eqn. 5.20). The structural model is then used to generate stress-strain data along loading paths with stress ratios (S_{11}/S_{22}) of 0.1 : 1, 0.5 : 1, 0.75 : 1, 1 : 1, 1 : 0.75, 1 : 0.5, and 1 : 0.1. Following Sun *et al.* [51], the generalized Fung model (Eqn. A.6a) was fitted to the five loading paths in the physiologic range (0.5 : 1, 0.75 : 1, 1 : 1, 1 : 0.75, 1 : 0.5), then the remaining two loading paths were predicted and compared to the data. Next, the reverse scenario was done, where the generalized Fung model was fitted to the non-physiologic loading paths (0.1 : 1 and 1 : 0.1), while the remaining five loading paths were predicted. Following the same step, Ψ_{eff} was fitted to the three optimal loading paths (0.1 : 1, 1 : 1, and 1 : 0.1) while the remaining loading paths were predicted.

We also considered some alternative loading paths. In the original paper by Fung et al. on the constitutive modeling of arteries [19], they discussed the use of 'physiologic protocols' as the optimal data set for parameter estimation. These 'physiologic protocols' are loading paths that cover a range past some predetermined lower bounds for E_{11} and E_{22}. Conceptually, this is meant to correspond to the range after accounting for the strain between the zero stress configuration and the *in vivo* unloaded (not stress-free) configuration. For clarity, to distinguish between this and the physiologic range (the range where the physiologic loading path is likely to reside) in Sun *et al.*, we will refer to this as the prestrained range. We reproduced

the prestrained protocols in figure 5 of Fung *et al.* [19], and compared the results to those with optimal loading paths.

5.3 Results

5.3.1 Optimal *in silico* loading paths for parameter estimation

The optimal loading paths for reproducing the response of dense collagenous soft tissues such as bovine pericardium and porcine aortic valve consist of 8 loading paths (Fig. 5.8C): 5 loading paths consisting of only inplane extensions (Fig. 5.8D), and 3 with the addition of the shear component. The increase in D-optimality is significantly less after three loading paths for the in-plane extensions (Fig. 5.8A). Same is true for the loading paths with shear. These three loading paths are the equibiaxial stress (Fig. 5.8B, Blue), and two uniaxial loading paths (Black, Green). The type of stress is consistent with the stress used for parameter estimation. The loading paths with shear simply iterate on these three loading paths by adding the shear component, we specified the maximum strain to be applied to be 0.2. We consider this to be the minimal number of loading paths necessary for parameter estimation. In practice, it's better to add the intermediate inplane tension loading paths (Red, Orange) as a precaution, forming the full set of 8 loading paths (Fig. 5.8C).

The equibiaxial stress loading path is the most important loading path. The D-optimality is 10^{-17} for the equibiaxial loading path versus less than 10^{-300} (using *Mathematica*'s extended precision) for other loading paths. The set of optimal loading paths will always contain the equibiaxial stress loading path if the total number is odd, whereas it will always contain two loading paths just beside the equibiaxial loading paths if it is even. The other loading paths complement the equibiaxial loading path

by spanning the range being searched. More details on the optimal loading path results are presented in appendix A.4.

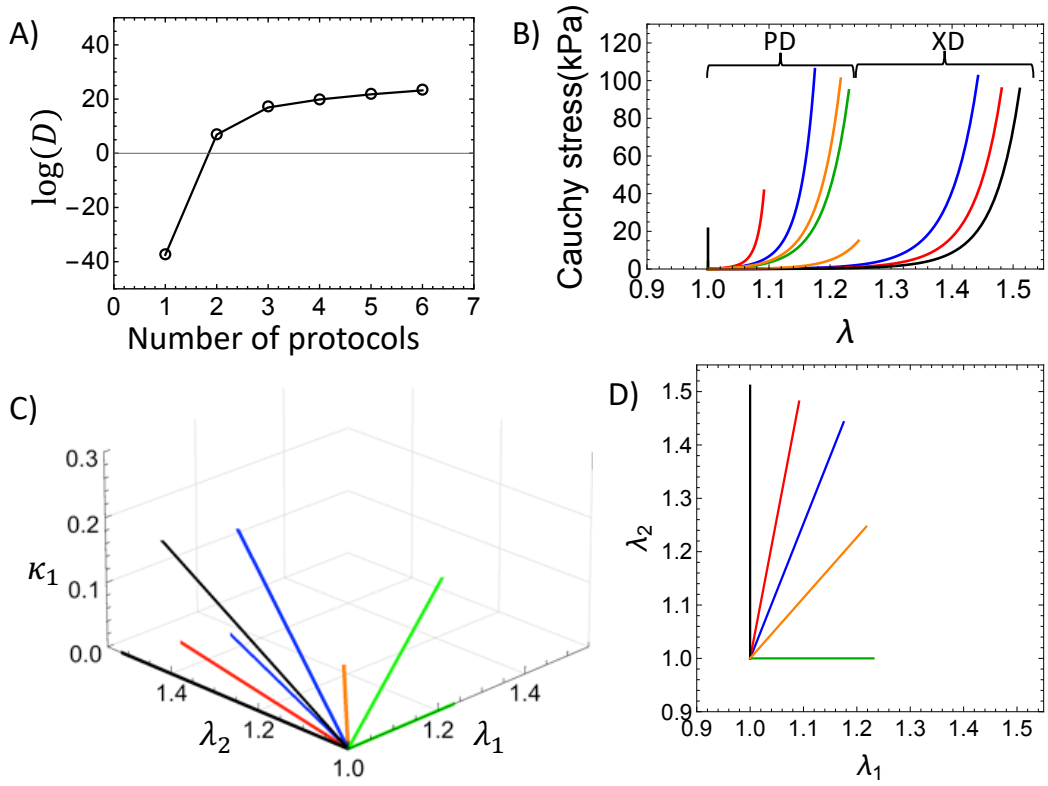

Figure 5.8: A) The best D-optimality value for a given number of loading paths used to generate the data, which stops increasing significantly after three. B) The stress-strain curve of the optimal set of five loading paths with no shear. C) The full set of optimal loading paths including the shear component are shown. The same colored loading paths are built upon the corresponding D) planar stretch loading paths by adding a shear component.

5.3.2 Parameter estimation and the quality of fit

The time taken for parameter estimation (5-10 seconds) is significantly lower in comparison to meso-scale structural approaches, such for the mitral valve [59] (10-40 minutes) and exogenously crosslinked tissues [58](30 min - 4 hours). In addition, we found that the model scaling method significantly improves the consistency of

convergence. Parameters converge in approximately 40-60 iterations regardless of starting point, whereas it can vary between 40-120 iterations without using scaling. The additional iterations occur within the valley like region in the objective function surface (Fig. 5.6), where the gradient and thus the step size is very small. Of course, we found both methods to be essentially equivalent with a sufficiently good initial guess. We note that the model scaling method does not improve the correlations between the exponent parameters $b_1 - b_{13}$ in Q. With that being said, the correlations between the exponent parameters $b_1 - b_{13}$ are significantly better than the correlations between these exponents and modulus c_0 (Fig. A.2 and Appendix A.3 Table A.2 & A.3 vs. Table 5.1), which is not much of a problem for parameter estimation. It is difficult to further improve the parameter correlation of Q without changing the form of the model, but, for our purpose, this is already sufficient.

Qualitatively, Ψ_{eff} (Eqn. 5.14) matches the response of collagenous soft tissues reproduced using the structural model (Eqn. 5.20). It is able to follow all the characteristics of the response function (derivatives of the strain energy density function), including the symmetry with respect to shear (Fig. 5.9). The average R^2 is 0.958 (n = 6) for the bovine pericardium specimens tested. We found similar values for porcine aortic valve leaflets. The main improvements are in the uniaxial strain regions.

For a more detailed comparison, we replicated the result of Sun *et al.* [51]. Similarly, we found that the generalized Fung model (Eqn. A.6a) fitted the five loading paths in the physiologic range very well (Fig. 5.10), but predicted the remaining unfitted loading paths poorly (Fig. 5.11). When the non-physiologic loading paths are fit ((Fig. 5.10)), the remaining protocols are still predicted poorly. However, we do note here that the generalized Fung model cannot fit the non-physiologic proto-

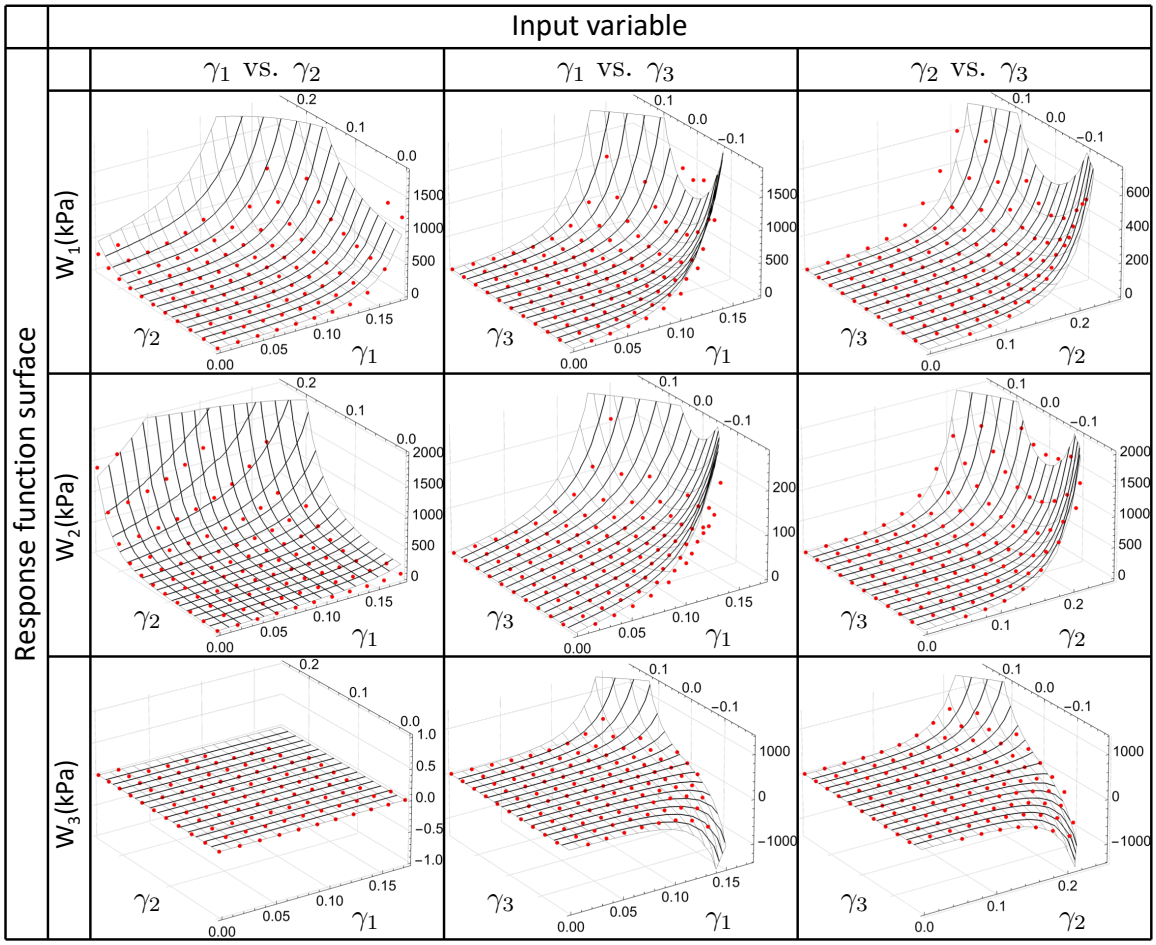

Figure 5.9: Parameter estimation results showing that Ψ_{eff} is able to replicate the response function of the structural model (Eqn. 5.21) (Top) $S_m = \partial\Psi / \mathrm{d}E_m$, (Middle) $S_n = \partial\Psi / \mathrm{d}E_n$, and (Bottom) $S_\phi = \partial\Psi / \mathrm{d}E_\phi$ for each pair of Green Lagrange strain components.

cols very well, illustrating the limitation of the generalized Fung model at fitting the response of soft tissue in a wide range of deformations (Section 5.2.2.2).

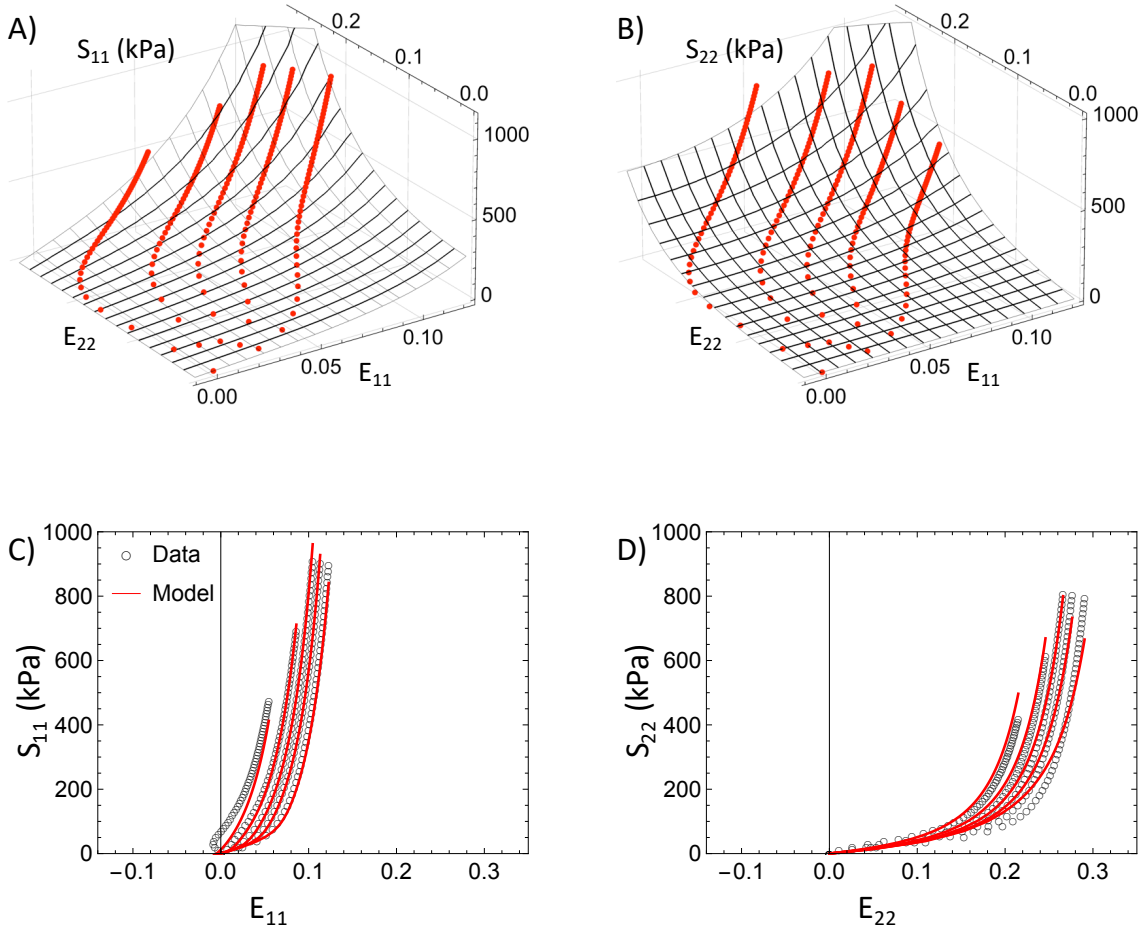

Figure 5.10: Reproducing the results of Sun *et al.* [51] showing that the generalized Fung model is able to fit the loading paths in the physiologic range very well. A) The S_{11} surface fitted to the data points. B) The S_{22} surface fitted to the data points. C) The best fit of the S_{11} component of the loading paths. D) The best fit of the S_{22} component of the loading paths.

Using Ψ_{eff} (Eqn. 5.14) (Fig. 5.14) improves these results, but using non-optimal loading paths, such as based on Fung *et al.*'s prestrained protocols [19], lead to poor predictions for other loading paths (Fig. 5.15). Although not obvious at first, Ψ_{eff} severely underestimates the response of the material in the low-stress region.

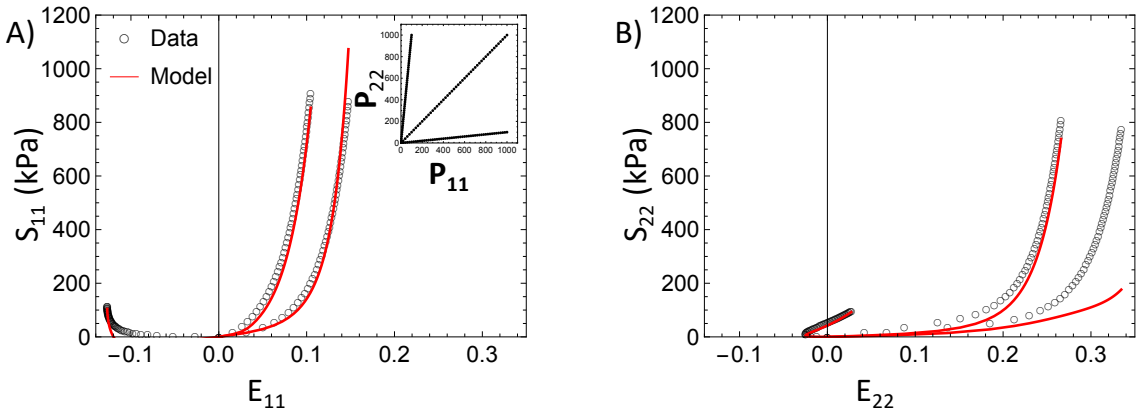

Figure 5.11: Reproducing the results of Sun *et al.* [51] showing the A) S_{11} component and B) S_{22} component of the remaining unfitted loading paths are predicted poorly from fit (Fig. 5.10). The inset in A shows the corresponding loading paths.

The D-optimality with two protocols in this prestrained range is only 1.35, which improves to 1.98×10^4 with six protocols. This pales in comparison to 9.7×10^2 for the two optimal protocols and 2.2×10^7 with three optimal protocols. When both Ψ_{eff} and three optimal loading paths are utilized, we found that the loading paths are both fitted (Fig. 5.16) and predicted very well (Fig. 5.17). We also tested other non-optimal loading paths with modifications to the form of Ψ_{eff} (Appendix A.5). To briefly summarize these results, with an optimal set of loading paths, Ψ_{eff} is able to fully reproduce the response of collagenous soft tissue for a wide range of deformation. However, without optimal loading paths, the form of Ψ_{eff} can have an unpredictable impact on the predicted response, even though the quality of fit is very similar.

5.4 Discussion

5.4.1 Using the effective constitutive model for homogenization in numerical simulations

The most fundamental issues with using phenomenological models for soft tissue and organ numerical simulations are that they 1) cannot simulate deformation

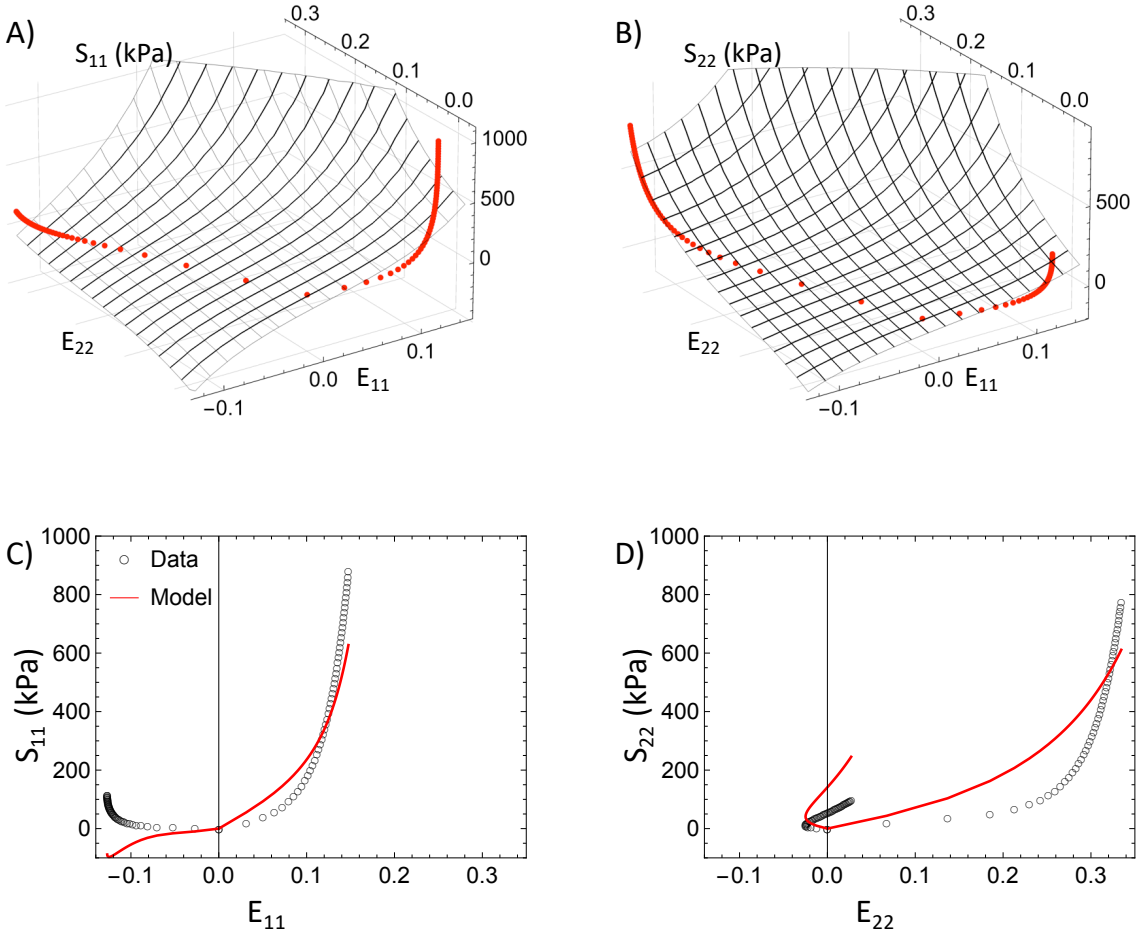

Figure 5.12: Reproducing the results of Sun *et al.* [51] showing the best fit of the generalized Fung model to the loading paths in the non-physiologic range is poor. A) The S_{11} surface fitted to the data points. B) The S_{22} surface fitted to the data points. C) The best fit of the S_{11} component of the loading paths. D) The best fit of the S_{22} component of the loading paths.

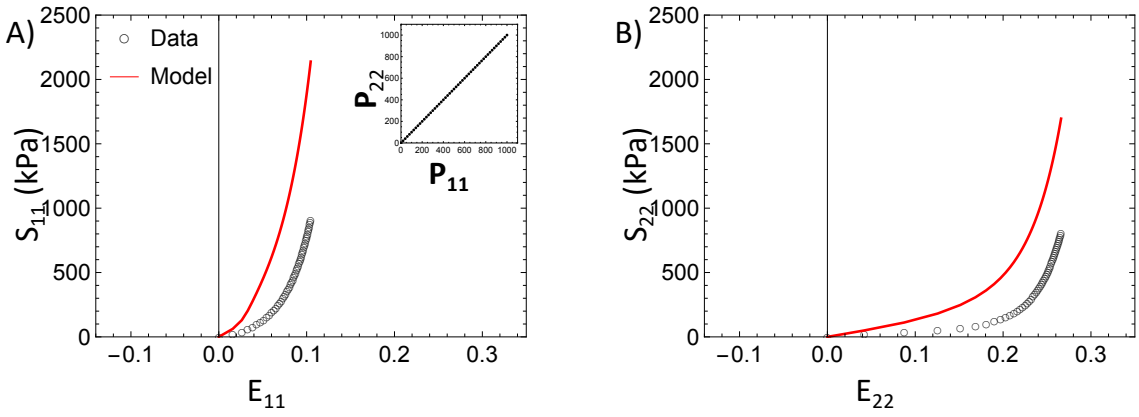

Figure 5.13: Reproducing the results of Sun *et al.* [51] showing the A) S_{11} component and B) S_{22} component of the equi-biaxial stress loading path are predicted poorly from fit (Fig. 5.12). The inset in A shows the corresponding loading paths.

beyond the range of data used for parameter estimation, and 2) cannot be widely used for tissues other than the ones they are specifically formulated for. Without being able to fully reproduce the response of micro-models, the resulting response may become inconsistent with the mechanisms of these micro-models, impacting their ability to simulate soft tissue responses, particular when modeling time-dependent processes. In the present work we found that using Ψ_{eff} (Eqn. 5.14) along with optimally selected loading paths reconciles this issue. Ψ_{eff} demonstrates much better capabilities at fitting the mechanical response of soft tissues in general. Admittedly, this may not be especially important for simulations of soft tissues in the normal physiological range as most models can fit the response of tissues if the range of deformation is small, as demonstrated with the generalized Fung model. However, for simulating abnormal conditions such as those that will drastically alter the deformation of the tissue, using Ψ_{eff} will be much more accurate.

The second and equally important part is the need for optimal data to determine the model parameters. Admittedly, the amount of data needed is not necessarily

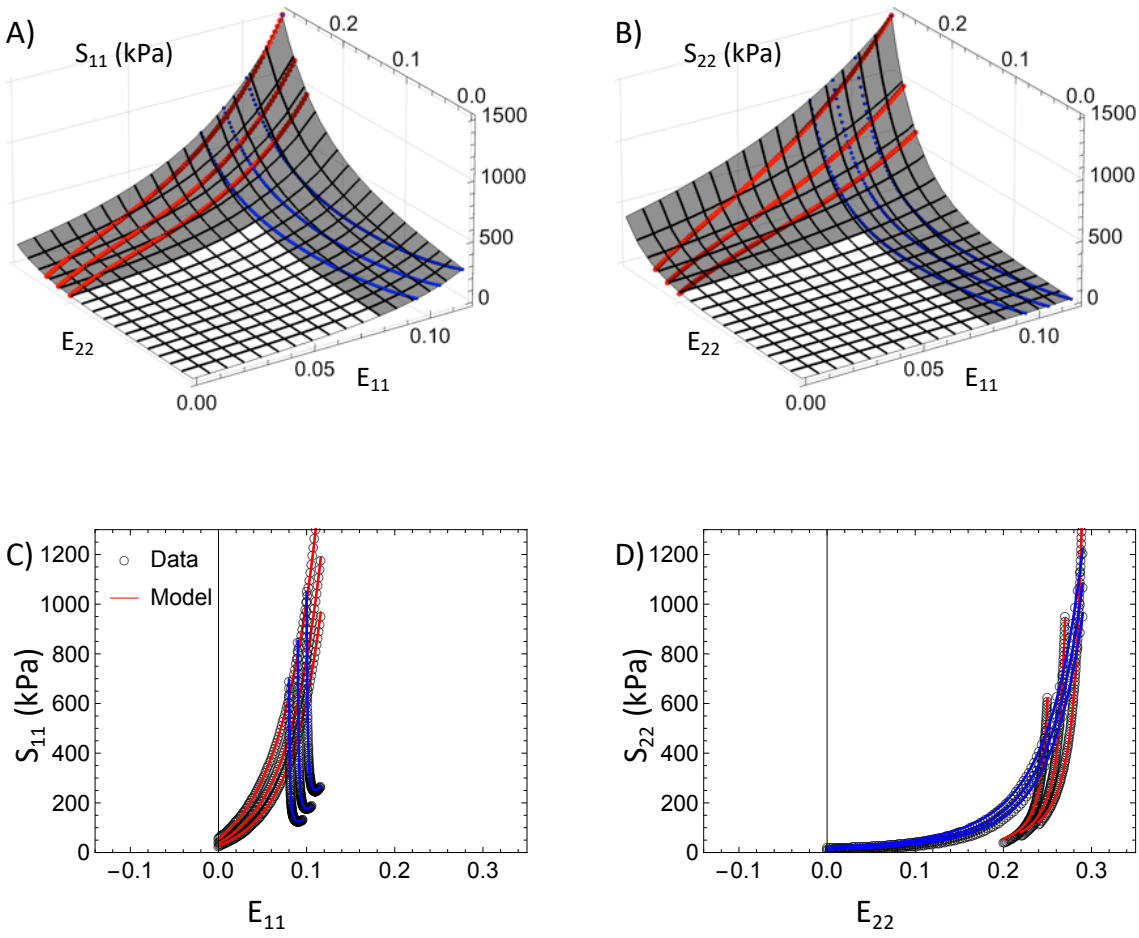

Figure 5.14: The fit of Ψ_{eff} to the prestrained loading paths is very good. A) The S_{11} surface fitted to the data points. B) The S_{22} surface fitted to the data points. C) The best fit of the S_{11} component of the loading paths. D) The best fit of the S_{22} component of the loading paths.

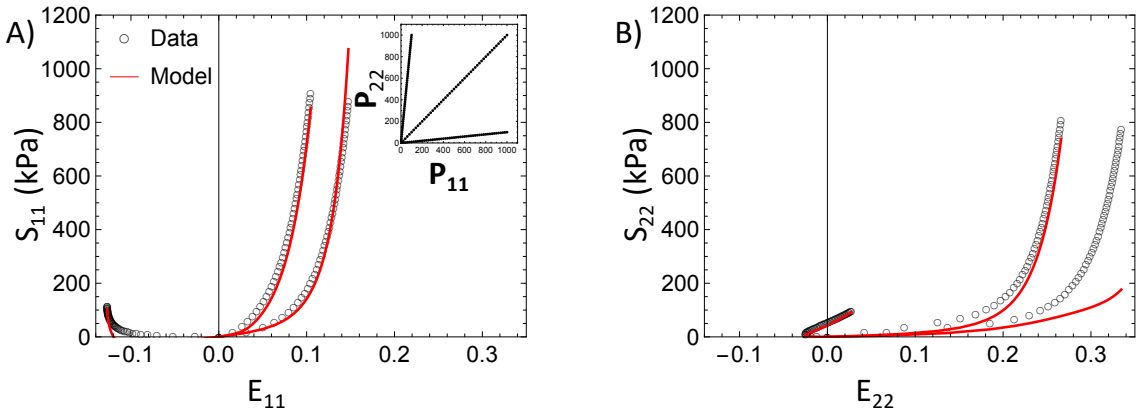

Figure 5.15: Ψ_{eff} predicts the A) S_{11} component and B) S_{22} component of the unfitted loading paths very poorly even though the fit to the prestrained range is very good (Fig. 5.14). The inset in A shows the corresponding loading paths.

extensive. For example, we have shown that just three carefully selected loading paths can greatly improve the predictive capability of Ψ_{eff} over the entire range of deformations. However, when the loading paths are selected poorly, Ψ_{eff} still has some issue when predicting protocol beyond the range used to fit the model. Examples of this are when only using a single protocol under equibiaxial stress (Appendix A.5, Fig. A.9D), or only using protocols in the prestrained range (Fig. 5.15). Mechanisms are still the major factor limiting the predictive capability in these cases. However, the intended role of Ψ_{eff} is only to homogenize the response of mechanisms-based micro-models, not to help to better understand soft tissue function. The loading paths can be simulated by choice, thus should not be a major factor affecting Ψ_{eff} in numerical simulations.

As we have shown, Ψ_{eff} is able to handle a wide range of soft tissue behavior with no change in model form. This greatly simplifies the need of implementing a different constitutive model for every tissue type, especially when the Jacobian or the elasticity tensor must be implemented separately for computational efficiency,

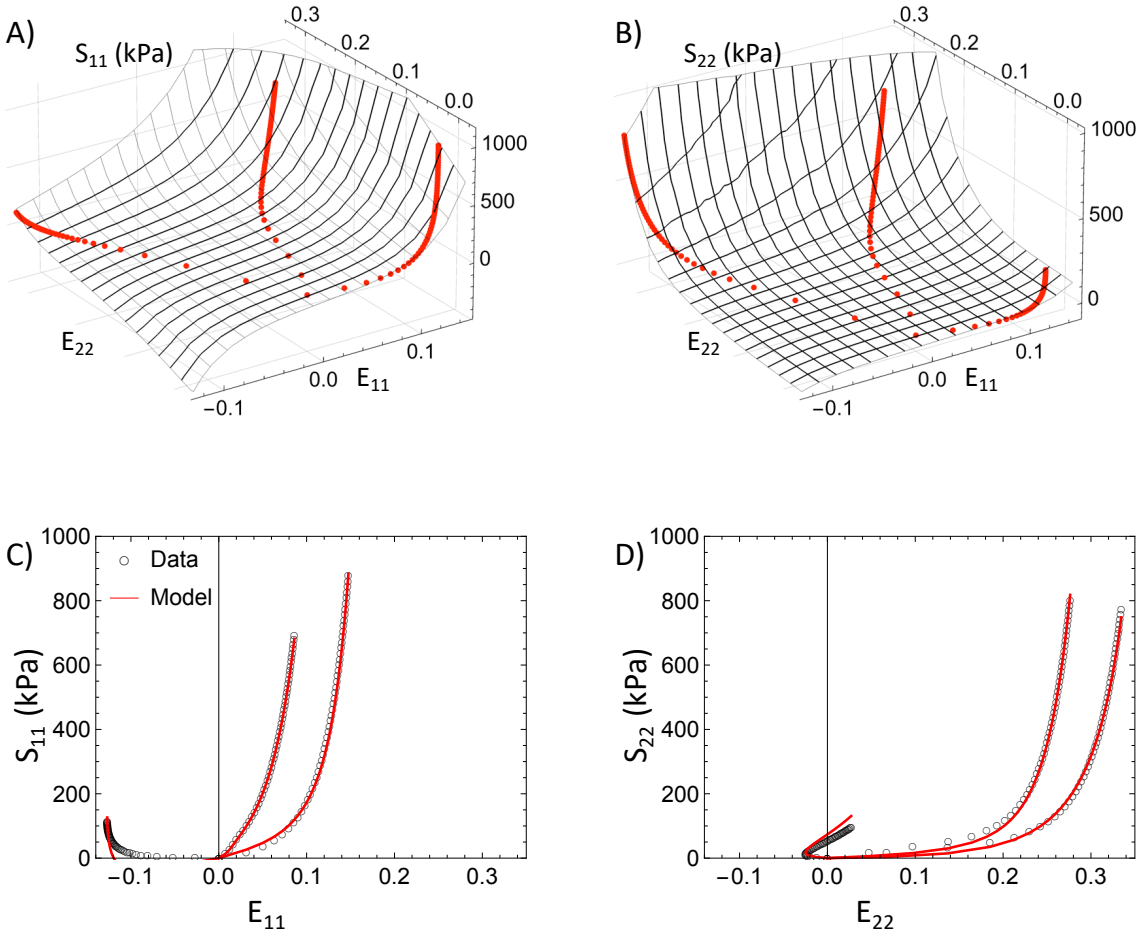

Figure 5.16: Ψ_{eff} fit optimal loading paths very well. A) The S_{11} surface fitted to the data points. B) The S_{22} surface fitted to the data points. C) Best fit of the S_{11} component of the loading paths. D) Best fit of the S_{22} component of the loading paths.

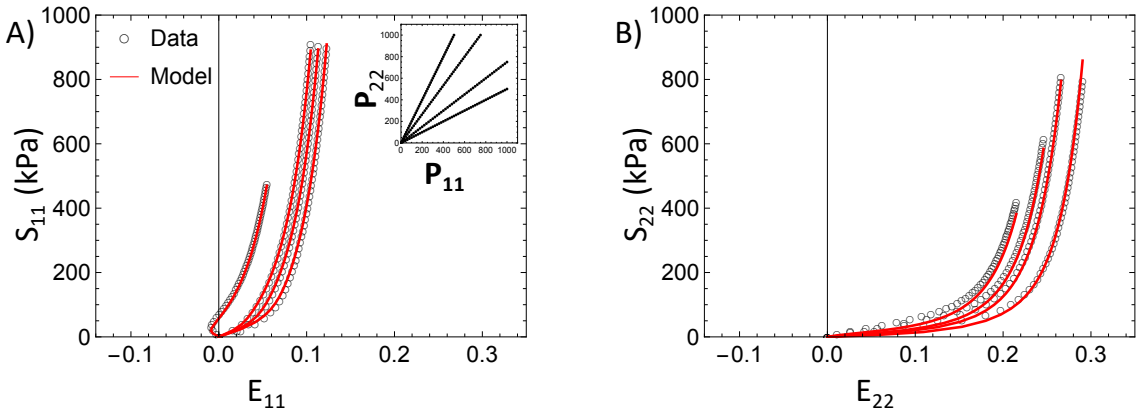

Figure 5.17: Combining Ψ_{eff} with optimal loading paths to predicts the A) S_{11} component and B) S_{22} component of the remaining unfitted loading paths very well from fit (Fig. 5.16). The inset in B shows the corresponding loading predicted paths.

which can be quite complex, i.e. in ABAQUS UMAT. Ψ_{eff} alone is capable of fully reproducing their mechanical response for simulations without significant loss of accuracy. Thus, the use of effective constitutive models can greatly facilitate in not only the computation speed of numerical simulations but also the speed of implementing constitutive models of different soft tissue for simulations. In these cases, only the parameters of Ψ_{eff} and organ geometry needs to be changed. Ψ_{eff} is smooth, easily differentiable, and easy to implement. With optimal loading path and model scaling, the process of converting the micro-model response to Ψ_{eff} (Eqn. 5.14) should take not more than a few seconds while saving a significant amount of time during numerical simulations.

On the other hand, micro-models are very useful for reproducing the response of tissue to which the full microstructure is known. This avoids the need for extensive mechanical data and parameter estimation, saving a time-consuming step for evaluating different material designs. Some structural and geometry information may also be measurable *in vivo* due to advances in techniques such as 3D ultrasound

[50, 56, 17] and DT-MRI [9, 8], and can be directly incorporated into meso-scale structural models. However, these techniques are not yet sufficient to determine the mechanical properties of tissues. As such, micro-models are still a necessary and important part of any predictive simulation. Not surprisingly, even most traditional invariant based models, such as the Holzapfel-Gasser-Ogden model [24], are being extended to incorporate the microstructures of the tissue [23].

5.4.2 Effective constitutive model applications

One application of effective constitutive models is for simulating time-dependent processes, such as growth and remodeling. Growth and remodeling have been a long-time interest of the biomechanics community and has an important role in predictive simulations. Theories for growth and remodeling have been well studied, from Rodriguez in 1994 to Lanir and others in the current time [31, 21, 47, 25, 13, 52]. The general theories for growth and remodeling involve the mechanisms for the changes in the reference configurations and a constrained mixture model involving the combined response of old original materials and newly generated materials. This again multiplies the computational cost of the material models and the summation of many individual responses can significantly reduce numerical precision. Here homogenization using Ψ_{eff} (Eqn. 5.14) can be useful.

Another important application is for inverse modeling, which is important for patient-specific modeling. Outside of *in vitro* studies, performing the experiments necessary to determine the mechanical response of soft tissues is extremely difficult. Here, inverse modeling approaches are a solution to this problem [32, 2, 3, 28, 34]. In inverse modeling, the model parameters and the errors between the simulated and measured strains are simultaneously optimized. However, the available data that can

be obtained *in vivo* is limited and is not always sufficient to accurately determine the model parameters. In these cases, the tissue microstructure can be used along with meso- and multi-scale models to narrow down the range of possible parameters. However, this multiplies the already hefty costs of these constitutive models. Here, the approach we proposed (Fig. 5.1B) can be used to reduce computational cost.

5.4.3 Model scaling method in other applications

Although not introduced as such, the model scaling method, or a similar technique to this, was briefly described by Fung *et al.* in their original work on the mathematical modeling of arteries [19]. The paper introduced the strain energy density function as

$$\rho_0 W^{(2)} = \frac{C'}{2} \exp\left[\alpha_1 \left(E_{\theta\theta}^2 - E_{\theta\theta}^{*2}\right) + \alpha_2 \left(E_{zz}^2 - E_{zz}^{*2}\right) + \alpha_4 \left(E_{\theta\theta} E_{zz} - E_{\theta\theta}^* E_{zz}^*\right)\right] \quad (5.22)$$

in equation 2 of the said work (C is changed to C' to consistency in notation with the present work). $E_{\theta\theta}^*$ and E_{zz}^* are introduced as strains corresponding to some fixed stresses of $S_{\theta\theta}^*$ and S_{zz}^*, usually taken in the physiologic range. Similarly, this "scaling" can be absorbed into the parameter C' like in the present work. This idea was not greatly expanded upon, but *Fung et al.* notes that:

> "But in practice it is very helpful to introduce $E_{\theta\theta}^*$ and E_{zz}^*. Not only are the values corresponding to $S_{\theta\theta}^*$ and S_{zz}^* very important information, but also their use makes the constants $[C']$, α_1, α_2, and α_4 much more stable for each set of specimen." [19]

and that

> "$[E_{\theta\theta}^*$ and $E_{zz}^*]$ are indexes of compliance of the vessel. Using $E_{\theta\theta}^*$ and E_{zz}^*, the variations of the constants C, α_1, α_2, and α_4, which determines

the shape of the stress-strain curve, are greatly reduced. The assignment of $S^*_{\theta\theta}$ and S^*_{zz} is arbitrary, but hopefully standard values will be adopted by the biomechanics community." [19]

In truth, we did not find that the model scaling method necessarily makes α_1, α_2, and α_4 more consistent, but rather that they are exactly the same values with or without this method, assuming parameter estimation was not trapped in some local minimum. The model scaling method does make reaching the values of these parameters more consistent. The biggest benefit remains the significant improvement in the correlation between the parameters C' and α_1, α_2, and α_4, improving the conditioning of the objective function surface during parameter estimation. It also imparts some physical meaning to the value of C', or for A_s and c'_0 in present work. For Fung *et al.*, this is some arbitrary physiologic stresses, for us, this is exactly 'maximum' (with respect to the objective function) value of strain energy within the data used for parameter estimation. This does bestow some consistency to the value of C', as it is exactly the total strain energy density at the stresses of $S^*_{\theta\theta}$ and S^*_{zz}, which will likely be similar between specimens taken from the same arteries from healthy subjects. However, the choice of $E^*_{\theta\theta}$ and E^*_{zz}, or $E^{\max}_m$, $E^{\max}_n$, and $E^{\max}_\phi$ for Ψ_{eff} (Eqn. 5.14), should not be arbitrary. The model scaling method works due to altering the functional effect of c_0 and b_i, or C and α. $E^{\max}_m$, $E^{\max}_n$, and $E^{\max}_\phi$ should be chosen deliberately so that area under the constitutive model, based on the objective function, remains approximately the same, thus decoupling changes in modulus and changes in curvature from the exponential parameters.

Perhaps, the biggest advantage of the model scaling method is that it is applicable to nearly any constitutive model with an exponential function, such as models like the Holzapfel-Gasser-Ogden, Humphrey, Vito, or even the meso-scale structural

model with simplified ensemble response such as in Fan and Sacks [15], Lee *et al.* [33], and Aggarwal and Sacks [2]. Even polynomial model forms with a power law, $\Psi = A\epsilon^B$, such as the generalized Ogden model, or the elastin model for the mitral valve in Zhang et al. [59] can see benefits from the model scaling method. In this case, the scaling term becomes $A = \bar{A}e^{-B\log(\epsilon_{max})}$. In summary, this model scaling method should have significant implications in improving the speed and consistency of parameter estimation for any model with an exponential-like form.

5.4.4 The equibiaxial stress protocol in optimal loading paths

One highlight from the optimal loading path study is that the equibiaxial stress loading path is extremely important. The equibiaxial stress loading path is always the one shown in figures for most paper, as it gives most intuitively understandable information on the mechanical properties of the tissue. It gives insights into the general form, anisotropy, and stiffness of the material at a glance, and is not surprisingly also the best loading path for parameter estimation. However, it is surprising just how little the equibiaxial stress loading path can provide alone. The difference in magnitude between the D-optimality values for one vs. two loading paths is almost 20. The equibiaxial stress alone simply is not enough to determine the material parameters using phenomenological approaches. However, the addition of only one or two more protocols, even if they are along similar loading paths, can significantly improve the predictive capabilities. However, this may be partially overcome by meso-scale structural approaches, given the information on the microstructure of the tissue.

5.4.5 Alternative options for optimal *in silico* loading paths

The limitation on predicting outside of the loading paths used for parameter estimation can be somewhat remedied by densely sampling the response of the micro-

model over a larger range of deformations. However, this is not entirely ideal for computational speed during parameter estimation, and choosing the sampling points for parameter estimation is not a trivial task itself. Points with high stresses tend to weight heavily during parameter estimation. Thus, proper care needs to be taken to capture both the high stress and low-stress response. Given that the number of data points scales cubically with the distance between data points, this approach is still limited.

Having said this, our investigation of optimal loading paths is restricted to constant strain ratios or constant stress ratios. In reality, there are many ways to define loading paths, some can be quite creative. We do not deny the possibility of other forms of loading paths that are more optimal. However, the current approach with three, or at most five protocols, is already sufficient. We did test some alternative loading paths, such as Fung *et al.*'s prestrained loading paths [19]. They cover much of the physiological range but are still insufficient for parameter estimation. Increasing the number of loading paths, in this case, has minor improvements, but pales in comparison to just picking better types of loading paths. The poor predictive capabilities for the low-stress region can have significant impacts on underestimating the mechanical properties of matrix and elastin, and their properties can be important to the functions of micro-models. For example, the mechanical properties of the matrix have significant implications for simulating the process of permanent set in exogenously cross-linked soft tissues [58]. Failing to properly reproduce this response, can affect the predictive capabilities of the associated micro-models, causing the whole framework of using Ψ_{eff} to facilitate numerical simulations (Fig. 5.1B) to fall apart.

5.5 Limitations

One major limitation of Ψ_{eff} (Eqn. 5.14) is the large number of parameters, 14 in the fully generalized form. This is not very favorable, as the time complexity for most optimization algorithms scales nonlinearly with the number of parameters. However, Ψ_{eff} has very low computational cost and reasonably low parameter covariance, thus this should not be a major problem. Alternatives are also less favorable, as they either require more parameters or cannot sufficiently capture the response of soft tissues in a wide range or reproduce the response of multiple tissue types.

Another limitation, which also applies to all phenomenological models, is that Ψ_{eff} has no intrinsic mechanisms built in. Without sufficient mechanical data to derive the model parameters, phenomenological models have limited predictive capabilities. Specifically, the phenomenological models perform poorly when extrapolating outside of the range of available data. This also means that phenomenological models can only provide limited information on how the tissue functions. It can reproduce the mechanical response of soft tissues very well, but it is also harder to infer more about the structure and function of the tissue. This is not a major concern for us. For the mechanisms or the structure to function relationship of soft tissues, micro-models already fulfills the need. Ψ_{eff} is intended as a fit all model for fulfilling the gap between predictive micro-models and computationally efficient simulations. With carefully selected of loading paths for parameter estimation (Section 5.2.4), Ψ_{eff} can accurately reproduce the mechanical response of soft tissue within the expected range. In other words, Ψ_{eff} does not have to be able to predict the mechanical response of soft tissues under unmeasured and extrapolated deformations, it only has to be able to fully reproduce the entire range of responses predicted by the micro-models, which is its main purpose.

5.6 Conclusion and Future Directions

In this work, we developed a constitutive model form for the effective response of planar soft tissues. This effective constitutive model (Eqn. 5.14) is applicable to a wide range of soft tissue responses while being as computationally efficient as most common phenomenological approaches, such as Holzapfel-Gasser-Ogden or the generalized Fung model. This model utilizes the modeling scaling method for minimizing covariance between parameter, which shows significant improvements in the speed and accuracy of parameter estimation. We have shown that our effective constitutive model along with optimal loading paths is able to fully replicate the response of complex meso-scale structural models for the entire range of deformations, whereas most phenomenological models have difficulties when predicting unfitted loading paths. The effective constitutive model is robust enough to be able to handle a wide range of soft tissue behaviors and anisotropy for accurate numerical simulations, such as in simulations of heart valves. Thus, the effective constitutive model can play an important role in the upscaling and homogenization of the response of complex micro-models for improving the efficiency of organ-level simulations.

One nature extension to this effective modeling approach is for 3-dimensional soft tissues. The extension to 3 dimensions doubles the number of inputs in comparison to planar models, with the additional inputs being E_{13}, E_{23}, and E_{33}. This means that the initial most generalized form for the 3-D soft tissue models (Eqn. 5.4) has 209 terms before reduction. This is unmanageable for establishing the initial approach, where using a planar soft tissue model is more suitable. However, applying the same restrictions to the model form (section 5.2.2.3) reduces this to 48 terms. This is possible due to symmetry by expressing the components of the Green-Lagrange strain tensor with respect to the material axis (Eqn. 5.1). This is not so easy to do in 3-

dimensions, requiring a third vector corresponding to the direction of least stiffness, which in turn requires the 3-dimensional fiber orientation distribution.

Nomenclature

Key Terms

Phenomenological model Constitutive models that reproduces the mechanical response of materials without taking into considerations any underlying structure or mechanisms

Micro-models Constitutive models utilizing structures and mechanism at a lower scale to predict the mechanical response at a higher scale

Structural model Constitutive models that utilize the meso-scale microstructures to predict the mechanical response of soft tissues

Effective constitutive model A computationally phenomenological model used to reproduce the response of micro material models in numerical simulations

Polynomial series family Effective model forms composed primarily of sums of polynomial functions

Separated exponential family Effective model forms composed primarily of sums of exponential functions

Single exponential family Effective model forms composed primarily of a single exponential function of sums of polynomial functions

ODF Orientation distribution function

RDF Recruitment distribution function, the distribution of stretched needed to straighten the collagen fibers

Physiologic range The range of deformations most likely to contain the physiologic loading path

Symbols

s Scalar variables

$\mathbf{v}$ Vector variables, bold lower case

$\mathbf{M}$ Matrix variables, bold upper case

$\hat{\Psi}, \hat{S}, \hat{f}$ Data

$\mathbf{I}$ Identity tensor

J The Jacobian for volume change due to deformation

$\mathbf{F}$ The deformation gradient tensor

$\mathbf{f}$ The upper triangular decomposition of the deformation gradient tensor

$\mathbf{C}$ Right Cauchy-Green strain tensor

$\mathbf{B}$ Left Cauchy-Green strain tensor

$\mathbf{E}$ Green Lagrange strain

$\mathbf{U}$ Right stretch tensor

$\mathbf{T}$ The Cauchy stress tensor

$\mathbf{S}$ Second Piola Kirchhoff tensor

I_1 First invariant of the right Cauchy strain tensor

I_2 Second invariant of the right Cauchy strain tensor

I_3 Third invariant of the right Cauchy strain tensor

I_4 Fourth pseudo-invariant of the right Cauchy strain tensor describing the stretch along an axis

I_8 Eighth pseudo invariant, describing the relative stretch along two axes

I_8^{ext} The extensional component of I_8

$\mathbf{m}_0$ The material axis in the reference configuration

$\mathbf{n}_0$ The perpendicular axis to the material axis in the reference configuration

$\mathbf{m}_t$ The material axis in the deformed configuration

$\mathbf{n}_t$ The perpendicular axis to the material axis in the deformed configuration

λ_m The stretch along the material axis

λ_n The stretch perpendicular to the material axis

ϕ The shear angle between $\mathbf{m}_0$ and $\mathbf{n}_0$

E_m, E_n, E_ϕ The Green Lagrange strain along the respective axes and to shearing

S_m, S_n, S_ϕ The 2nd Piola Kirchhoff stress along the respective axes and to shearing, which are also response functions, gradients of the strain energy

$\gamma_1, \gamma_2, \gamma_3$ The Hencky strains

Ψ The strain energy

$\Psi_{\text{col}}, \Psi_{\text{int}}, \Psi_{\text{mat}}$ Strain energy of the collagen fiber, ensemble-ensemble interactions, and matrix components respectively

η_C, η_M, η_I The modulus of collagen, matrix and fiber-fiber interactions

ϕ_{col}, ϕ_{mat}, ϕ_{int} The mass fractions of collagen, matrix and fiber-fiber interactions

D	Collagen fiber recruitment distribution function
Γ	Collagen fiber orientation distribution function
λ	Stretch
λ_s	The slack stretch, the stretch needed to straighten the collagen fiber crimp
$\mathcal{F}$	Objective function for parameter estimation
$\boldsymbol{\mathcal{I}}$	The information matrix
$\mathbf{J}$	The Jacobian of the objective function
$\boldsymbol{\mathcal{H}}$	The Hessian of the objective function
ξ	Vector of material parameters

Chapter Bibliography

[1] Ankush Aggarwal. An improved parameter estimation and comparison for soft tissue constitutive models containing an exponential function. *Biomechanics and Modeling in Mechanobiology*, 16(4):1309–1327, mar 2017. doi: 10.1007/s10237-017-0889-3.

[2] Ankush Aggarwal and Michael S. Sacks. An inverse modeling approach for semilunar heart valve leaflet mechanics: exploitation of tissue structure. *Biomechanics and Modeling in Mechanobiology*, 15(4):909–932, oct 2015. ISSN 1617-7959. doi: 10.1007/s10237-015-0732-7.

[3] Ankush Aggarwal, Vanessa S. Aguilar, Chung-Hao Lee, Giovanni Ferrari, Joseph H. Gorman, Rober C. Gorman, and Michael S. Sacks. Patient-specific modeling of heart valves: from image to simulation. In *Functional Imaging and Modeling of the Heart*, pages 141–149. Springer Berlin Heidelberg, 2013. ISBN 3-642-38898-1. doi: 10.1007/978-3-642-38899-6_17.

[4] Ankush Aggarwal, Alison M. Pouch, Eric Lai, John Lesicko, Paul A. Yushkevich, Joseph H. Gorman III, Robert C. Gorman, and Michael S. Sacks. In-vivo heterogeneous functional and residual strains in human aortic valve leaflets. *Journal of Biomechanics*, 49(12):2481–2490, aug 2016. ISSN 0021-9290. doi: 10.1016/j.jbiomech.2016.04.038.

[5] Reza Avazmohammadi, Michael R. Hill, Marc A. Simon, Will Zhang, and Michael S. Sacks. A novel constitutive model for passive right ventricular myocardium: evidence for myofiber-collagen fiber mechanical coupling. *Biomechanics and Modeling in Mechanobiology*, 16(2):561–581, oct 2016. ISSN 1617-7940. doi: 10.1007/s10237-016-0837-7.

[6] Prosenjit Bagchi. Mesoscale simulation of blood flow in small vessels. *Biophysical Journal*, 92(6):1858–1877, mar 2007. doi: 10.1529/biophysj.106.095042.

[7] J. M. Ball. Strict convexity, strong ellipticity, and regularity in the calculus of variations. *Mathematical Proceedings of the Cambridge Philosophical Society*, 87 (03):501–513, may 1980. doi: 10.1017/s0305004100056930.

[8] Peter J. Basser and Carlo Pierpaoli. Microstructural and physiological features of tissues elucidated by quantitative-diffusion-tensor MRI. *Journal of Magnetic Resonance*, 213(2):560–570, dec 2011. doi: 10.1016/j.jmr.2011.09.022.

[9] Peter J. Basser, Sinisa Pajevic, Carlo Pierpaoli, Jeffrey Duda, and Akram Aldroubi. In vivo fiber tractography using DT-MRI data. *Magnetic Resonance in Medicine*, 44(4):625–632, 2000. doi: 10.1002/1522-2594(200010)44:4⟨625::aid-mrm17⟩3.0.co;2-o.

[10] Markus J. Buehler. Atomistic and continuum modeling of mechanical properties of collagen: elasticity, fracture, and self-assembly. *Journal of Materials Research*, 21(08):1947–1961, aug 2006. ISSN 2044-5326. doi: 10.1557/jmr.2006.0236. URL `http://dx.doi.org/10.1557/jmr.2006.0236`.

[11] Markus J. Buehler. Nanomechanics of collagen fibrils under varying cross-link densities: atomistic and continuum studies. *Journal of the Mechanical Behavior of Biomedical Materials*, 1(1):59–67, jan 2008. doi: 10.1016/j.jmbbm.2007.04.001.

[12] Rui Cheng, Yong G. Lai, and Krishnan B. Chandran. Three-dimensional fluid-structure interaction simulation of bileaflet mechanical heart valve flow dynamics. *Annals of Biomedical Engineering*, 32(11):1471–1483,

nov 2004. ISSN 0090-6964 (Print). doi: 10.1114/b:abme.0000049032.51742.10. URL http://www.ncbi.nlm.nih.gov/entrez/query.fcgi?cmd=Retrieve&db=PubMed&dopt=Citation&list_uids=15636108.

[13] Stephen C. Cowin. Tissue growth and remodeling. *Annual Review of Biomedical Engineering*, 6(1):77–107, aug 2004. ISSN 1523-9829 (Print). doi: 10.1146/annurev.bioeng.6.040803.140250. URL http://www.ncbi.nlm.nih.gov/entrez/query.fcgi?cmd=Retrieve&db=PubMed&dopt=Citation&list_uids=15255763.

[14] Antonio D'Amore, Joao S. Soares, John A. Stella, Will Zhang, Nicholas J. Amoroso, John E. Mayer, William R. Wagner, and Michael S. Sacks. Large strain stimulation promotes extracellular matrix production and stiffness in an elastomeric scaffold model. *Journal of the Mechanical Behavior of Biomedical Materials*, 62:619–635, sep 2016. ISSN 1878-0180 (Electronic) 1878-0180 (Linking). doi: 10.1016/j.jmbbm.2016.05.005. URL https://www.ncbi.nlm.nih.gov/pubmed/27344402.

[15] Rong Fan and Michael S. Sacks. Simulation of planar soft tissues using a structural constitutive model: finite element implementation and validation. *Journal of Biomechanics*, 47(9):2043–2054, jun 2014. doi: 10.1016/j.jbiomech.2014.03.014.

[16] Bahar Fata, Will Zhang, Rouzbeh Amini, and Michael S. Sacks. Insights into regional adaptations in the growing pulmonary artery using a meso-scale structural model: effects of ascending aorta impingement. *Journal of Biomechanical Engineering*, 136(2):021009–021009–13, feb 2014. ISSN 0148-0731. doi: 10.1115/1.4026457. URL http://dx.doi.org/10.1115/1.4026457.

[17] Aaron Fenster and Donnal B. Downey. 3-D ultrasound imaging: a review. *IEEE Engineering in Medicine and Biology Magazine*, 15(6):41–51, 1996. doi: 10.1109/51.544511.

[18] Y. C. Fung. *Biomechanics: Mechanical Properties of Living Tissues*. Springer Verlag, New York, 2nd edition, 1993.

[19] Y. C. Fung, K. Fronek, and P. Patitucci. Pseudoelasticity of arteries and the choice of its mathematical expression. *American Journal of Physiology-Heart and Circulatory Physiology*, 237(5):H620–H631, nov 1979. doi: 10.1152/ajpheart.1979.237.5.h620.

[20] George T. Gilbert. Positive definite matrices and Sylvester's criterion. *The American Mathematical Monthly*, 98(1):44, jan 1991. doi: 10.2307/2324036.

[21] R.L. Gleason and J.D. Humphrey. A mixture model of arterial growth and remodeling in hypertension: altered muscle tone and tissue turnover. *Journal of Vascular Research*, 41(4):352–363, July 2004. doi: 10.1159/000080699. URL `http://www.ncbi.nlm.nih.gov/entrez/query.fcgi?cmd=Retrieve&db=PubMed&dopt=Citation&list_uids=15353893`.

[22] Yiemeng Hoi, Hui Meng, Scott H. Woodward, Bernard R. Bendok, Ricardo A. Hanel, Lee R. Guterman, and L. Nelson Hopkins. Effects of arterial geometry on aneurysm growth: three-dimensional computational fluid dynamics study. *Journal of Neurosurgery*, 101(4):676–681, oct 2004. doi: 10.3171/jns.2004.101.4.0676.

[23] G. A. Holzapfel, J. A. Niestrawska, R. W. Ogden, A. J. Reinisch, and A. J. Schriefl. Modelling non-symmetric collagen fibre dispersion in arterial

walls. *Journal of The Royal Society Interface*, 12(106):20150188–20150188, apr 2015. ISSN 1742-5689. doi: 10.1098/rsif.2015.0188. URL http://rsif.royalsocietypublishing.org/content/12/106/20150188.

[24] Gerhard A. Holzapfel, Thomas C. Gasser, and Ray W. Ogden. A new constitutive framework for arterial wall mechanics and a comparative study of material models. *Journal of Elasticity*, 61(1/3):1–48, 2000. doi: 10.1023/a:1010835316564.

[25] J.D. Humphrey and K.R. Rajagopal. A constrained mixture model for growth and remodeling of soft tissues. *Mathematical models and methods in applied sciences*, 12(3):407–430, 2002. doi: 10.1142/s0218202502001714.

[26] David Kamensky, Ming-Chen Hsu, Dominik Schillinger, John A. Evans, Ankush Aggarwal, Yuri Bazilevs, Michael S. Sacks, and Thomas J.R. Hughes. An immersogeometric variational framework for fluid-structure interaction: application to bioprosthetic heart valves. *Computer Methods in Applied Mechanics and Engineering*, 284:1005–1053, February 2015. ISSN 0045-7825 (Print) 0045-7825 (Linking). doi: 10.1016/j.cma.2014.10.040. URL http://www.ncbi.nlm.nih.gov/pubmed/25541566.

[27] Ghassan S. Kassab and Michael S. Sacks, editors. *Structure-Based Mechanics of Tissues and Organs*. Springer US, 2016. doi: 10.1007/978-1-4899-7630-7.

[28] Wangdo Kim, Derek C. Tretheway, and Sean S. Kohles. An inverse method for predicting tissue-level mechanics from cellular mechanical input. *Journal of Biomechanics*, 42(3):395–399, feb 2009. doi: 10.1016/j.jbiomech.2008.11.014.

[29] Y. Lanir. Constitutive equations for fibrous connective tissues. *Journal of Biomechanics*, 16(1):1–12, jan 1983. doi: 10.1016/0021-9290(83)90041-6.

[30] Y. Lanir, O. Lichtenstein, and O. Imanuel. Optimal design of biaxial tests for structural material characterization of flat tissues. *Journal of Biomechanical Engineering*, 118(1):41, February 1996. ISSN 0148-0731 (Print) 0148-0731 (Linking). doi: 10.1115/1.2795944. URL `http://www.ncbi.nlm.nih.gov/entrez/query.fcgi?cmd=Retrieve&db=PubMed&dopt=Citation&list_uids=8833073`.

[31] Yoram Lanir. Mechanistic micro-structural theory of soft tissues growth and remodeling: tissues with unidirectional fibers. *Biomechanics and Modeling in Mechanobiology*, 14(2):245–266, jun 2014. ISSN 1617-7959. doi: 10.1007/s10237-014-0600-x.

[32] Chung-Hao Lee, Rouzbeh Amini, Robert C. Gorman, Joseph H. Gorman, and Michael S. Sacks. An inverse modeling approach for stress estimation in mitral valve anterior leaflet valvuloplasty for in-vivo valvular biomaterial assessment. *Journal of Biomechanics*, 47(9):2055–2063, June 2014. ISSN 1873-2380 (Electronic) 0021-9290 (Linking). doi: 10.1016/j.jbiomech.2013.10.058. URL `http://www.ncbi.nlm.nih.gov/pubmed/24275434`.

[33] Chung-Hao Lee, Jean-Pierre Rabbah, Ajit P. Yoganathan, Robert C. Gorman, Joseph H. Gorman, and Michael S. Sacks. On the effects of leaflet microstructure and constitutive model on the closing behavior of the mitral valve. *Biomechanics and Modeling in Mechanobiology*, 14(6):1281–1302, May 2015. ISSN 1617-7940 (Electronic) 1617-7940 (Linking). doi: 10.1007/s10237-015-0674-0. URL `http://www.ncbi.nlm.nih.gov/pubmed/25947879`.

[34] Hongbin Liu, Kiattisak Sangpradit, Min Li, Prokar Dasgupta, Kaspar Althoefer, and Lakmal D. Seneviratne. Inverse finite-element modeling for tissue parameter

identification using a rolling indentation probe. *Medical & Biological Engineering & Computing*, 52(1):17–28, sep 2013. doi: 10.1007/s11517-013-1118-6.

[35] K. May-Newman and F. C. Yin. A constitutive law for mitral valve tissue. *Journal of Biomechanical Engineering*, 120(1):38–47, 1998. doi: 10.1115/1.2834305. URL `http://www.ncbi.nlm.nih.gov/htbin-post/Entrez/query?db=m&form=6&dopt=r&uid=0009675679`.

[36] Matteo Nobili, Umberto Morbiducci, Raffaele Ponzini, Costantino Del Gaudio, Antonio Balducci, Mauro Grigioni, Franco Maria Montevecchi, and Alberto Redaelli. Numerical simulation of the dynamics of a bileaflet prosthetic heart valve using a fluid–structure interaction approach. *Journal of Biomechanics*, 41 (11):2539–2550, aug 2008. doi: 10.1016/j.jbiomech.2008.05.004.

[37] R. W. Ogden. Large deformation isotropic elasticity - on the correlation of theory and experiment for incompressible rubberlike solids. *Proceedings of the Royal Society A: Mathematical, Physical and Engineering Sciences*, 326(1567): 565–584, feb 1972. doi: 10.1098/rspa.1972.0026.

[38] Mette S. Olufsen, Charles S. Peskin, Won Yong Kim, Erik M. Pedersen, Ali Nadim, and Jesper Larsen. Numerical simulation and experimental validation of blood flow in arteries with structured-tree outflow conditions. *Annals of Biomedical Engineering*, 28(11):1281–1299, nov 2000. doi: 10.1114/1.1326031.

[39] Marie Oshima, Ryo Torii, Toshio Kobayashi, Nobuyuki Taniguchi, and Kiyoshi Takagi. Finite element simulation of blood flow in the cerebral artery. *Computer Methods in Applied Mechanics and Engineering*, 191(6-7):661–671, dec 2001. doi: 10.1016/s0045-7825(01)00307-3.

[40] Karl Perktold and Gerhard Rappitsch. Computer simulation of local blood flow and vessel mechanics in a compliant carotid artery bifurcation model. *Journal of Biomechanics*, 28(7):845–856, jul 1995. doi: 10.1016/0021-9290(95)95273-8.

[41] A. R. Pries, T. W. Secomb, P. Gaehtgens, and J. F. Gross. Blood flow in microvascular networks. experiments and simulation. *Circulation Research*, 67 (4):826–834, oct 1990. doi: 10.1161/01.res.67.4.826.

[42] Zhao Qin, Markus J. Buehler, and Laurent Kreplak. A multi-scale approach to understand the mechanobiology of intermediate filaments. *Journal of Biomechanics*, 43(1):15–22, January 2010. doi: 10.1016/j.jbiomech.2009.09.004.

[43] C. Ramault, A. Makris, D. Van Hemelrijck, E. Lamkanfi, and W. Van Paepegem. Comparison of different techniques for strain monitoring of a biaxially loaded cruciform specimen. *Strain*, 47:210–217, jun 2010. ISSN 1475-1305. doi: 10.1111/j.1475-1305.2010.00760.x. URL `http://dx.doi.org/10.1111/j.1475-1305.2010.00760.x`.

[44] Bruno V. Rego, Sarah M. Wells, Chung-Hao Lee, and Michael S. Sacks. Mitral valve leaflet remodelling during pregnancy: insights into cell-mediated recovery of tissue homeostasis. *Journal of The Royal Society Interface*, 13(125):20160709, dec 2016. ISSN 1742-5689. doi: 10.1098/rsif.2016.0709. URL `http://rsif.royalsocietypublishing.org/content/13/125/20160709`.

[45] Peter Rissland, Yared Alemu, Shmuel Einav, John Ricotta, and Danny Bluestein. Abdominal aortic aneurysm risk of rupture: patient-specific FSI simulations using anisotropic model. *Journal of Biomechanical Engineering*, 131(3):031001, 2009. doi: 10.1115/1.3005200.

[46] R. S. Rivlin and D. W. Saunders. Large elastic deformations of isotropic materials 7: experiments on the deformation of rubber. *Philosophical Transactions of the Royal Society A: Mathematical, Physical and Engineering Sciences*, 243(865): 251–288, apr 1951. doi: 10.1098/rsta.1951.0004. URL `://A1951UU63300001`.

[47] Edward K. Rodriguez, Anne Hoger, and Andrew D. McCulloch. Stress-dependent finite growth in soft elastic tissues. *Journal of Biomechanics*, 27(4):455–467, April 1994. doi: 10.1016/0021-9290(94)90021-3. URL `http://www.ncbi.nlm.nih.gov/entrez/query.fcgi?cmd=Retrieve&db=PubMed&dopt=Citation&list_uids=8188726`.

[48] Michael S. Sacks, Will Zhang, and Silvia Wognum. A novel fibre-ensemble level constitutive model for exogenous cross-linked collagenous tissues. *Interface Focus*, 6(1):20150090, dec 2015. doi: 10.1098/rsfs.2015.0090. URL `http://rsfs.royalsocietypublishing.org/royfocus/6/1/20150090.full.pdf`.

[49] Joao S. Soares, Kristen R. Feaver, Will Zhang, David Kamensky, Ankush Aggarwal, and Michael S. Sacks. Biomechanical behavior of bioprosthetic heart valve heterograft tissues: characterization, simulation, and performance. *Cardiovascular Engineering and Technology*, 7(4):309–351, aug 2016. ISSN 1869-4098. doi: 10.1007/s13239-016-0276-8. URL `http://dx.doi.org/10.1007/s13239-016-0276-8`.

[50] Horst Steiner, Alf Staudach, Dietmar Spitzer, and Heinz Schaffer. Diagnostic techniques: three-dimensional ultrasound in obstetrics and gynaecology: technique, possibilities and limitations. *Human Reproduction*, 9(9):1773–1778, sep 1994. doi: 10.1093/oxfordjournals.humrep.a138793.

[51] W. Sun, M.S. Sacks, T.L. Sellaro, W.S. Slaughter, and M.J. Scott. Biaxial mechanical response of bioprosthetic heart valve biomaterials to high in-plane shear. *Journal of Biomechanical Engineering*, 125(3):372–380, jun 2003. doi: 10.1115/1.1572518.

[52] Larry A. Taber. Biomechanics of growth, remodeling, and morphogenesis. *Applied Mechanics Reviews*, 48(8):487–545, 1995. doi: 10.1115/1.3005109.

[53] Raymond P. Vito and James Hickey. The mechanical properties of soft tissues–II: the elastic response of arterial segments. *Journal of Biomechanics*, 13(11):951–957, jan 1980. doi: 10.1016/0021-9290(80)90166-9. URL `http://www.ncbi.nlm.nih.gov/htbin-post/Entrez/query?db=m&form=6&dopt=r&uid=0007276003`.

[54] K.Y. Volokh and D.A. Vorp. A model of growth and rupture of abdominal aortic aneurysm. *Journal of Biomechanics*, 41(5):1015–1021, 2008. doi: 10.1016/j.jbiomech.2007.12.014.

[55] Andreas Wächter and Lorenz T. Biegler. On the implementation of an interior-point filter line-search algorithm for large-scale nonlinear programming. *Mathematical Programming*, 106(1):25–57, apr 2005. doi: 10.1007/s10107-004-0559-y.

[56] Lin Yang, Bogdan Georgescu, Yefeng Zheng, Peter Meer, and Dorin Comaniciu. 3d ultrasound tracking of the left ventricle using one-step forward prediction and data fusion of collaborative trackers. In *2008 IEEE Conference on Computer Vision and Pattern Recognition*, pages 1–8. IEEE, June 2008. doi: 10.1109/cvpr.2008.4587518.

[57] Rana Zakerzadeh, Ming-Chen Hsu, and Michael S. Sacks. Computational methods for the aortic heart valve and its replacements. *Expert Review of Medical*

Devices, 14(11):849–866, oct 2017. ISSN 1745-2422. doi: 10.1080/17434440.2017.1389274.

[58] Will Zhang and Michael S. Sacks. Modeling the response of exogenously crosslinked tissue to cyclic loading: The effects of permanent set. *Journal of the Mechanical Behavior of Biomedical Materials*, 75:336–350, November 2017. ISSN 1878-0180. doi: 10.1016/j.jmbbm.2017.07.013.

[59] Will Zhang, Salma Ayoub, Jun Liao, and Michael S. Sacks. A meso-scale layer-specific structural constitutive model of the mitral heart valve leaflets. *Acta Biomaterialia*, 32:238–255, March 2016. ISSN 1878-7568 (Electronic) 1742-7061 (Linking). doi: 10.1016/j.actbio.2015.12.001. URL `http://www.ncbi.nlm.nih.gov/pubmed/26712602`.

[60] Li Zhu, Tirthankar Dasgupta, and Qiang Huang. A D-optimal design for estimation of parameters of an exponential-linear growth curve of nanostructures. *Technometrics*, 56(4):432–442, oct 2014. doi: 10.1080/00401706.2013.866600.

Chapter 6

Quasi-static and time-evolving simulation of intact bioprosthetic heart valves using the effective model approach

Preface

AWT is currently the only way to evaluate BHV durability in a feasible amount of time (months instead of years). However, the loading conditions and environment during AWT are not physiological and the only durability information currently used is the presence of visible damage. Only the clinical evaluation stage can provide true indications of the *in vivo* performance of BHV designs. However, this is the final, most difficult, most expensive and most time-consuming stage. Clearly, current methods of evaluating BHV designs are not feasible for advancing the BHV technology in a timely manner. In this chapter, we implement our constitutive model for the permanent set of BHVs developed in a previous chapter in a time-evolving numerical simulation framework using the effective constitutive model approach, and attempt to predict the geometric and structural change that occurs with the onset of permanent set.

6.1 Introduction

6.1.1 Background

The most popular replacement heart valves continue to be bioprosthetic heart valves (BHV) fabricated from xenograft biomaterials, for both established surgical and more novel percutaneous valve designs [14, 16, 15, 17, 13]. While these devices have provided great benefits for many patients, device failure continues to be the result of leaflet structural deterioration mediated by fatigue and/or tissue mineralization [21, 11]. As a result, the lifespan of BHVs remains limited to 10–15 years and the mechanisms that underlie such failures remain poorly understood. Thus, improved durability remains an important clinical goal and represents a unique cardiovascular engineering challenge resulting from the extreme valvular mechanical demands. Yet, current BHV assessments rely exclusively on device-level evaluations, which are confounded by simultaneous and highly coupled biomaterial mechanical fatigue, valve design, hemodynamics, and calcification. Thus, despite decades of clinical BHV usage and growing popularity, there exists no acceptable method for simulating BHV durability in any design context. While efforts to mitigate tissue mineralization have progressed well, efforts to minimize structural degradation remain limited. For example, in vitro accelerated wear tests (AWT) are used only for the most basic device-level durability evaluations. Yet no systematic attempt has been made to glean important durability information from these required tests to inform mechanisms and means to simulate BHV durability. There is thus a profound need for the development of novel simulation technologies for the prediction of the changes in the properties of BHVs to long-term cyclic loading.

6.1.2 Mechanisms of BHV failure

The causes of BHV failure can be divided into two broad categories, mineralization, and structural damage, with both processes occurring in parallel or independently [11]. Mineralization is the accumulation of mineral deposits, mainly calcium phosphate, within the BHV leaflets [17]. This disrupts the underlying microstructure preventing the proper mechanical function of BHVs, increasing the likelihood of tearing, and reducing flexibility (preventing normal opening and closing motions, and induce valve stenosis). The causes of calcification and associated anti-calcification treatments are extensively studied in literature [9, 5, 22]. On the other hand, structural damage includes the collagen fiber damage and breakdown of the non-fibrous part of the extracellular matrix (ECM), *which we will refer to as simply the matrix*. Fourier transform infrared spectroscopy(FTIR) results have shown changes in the collagen fiber molecular structure after 50 million cycles [20], which suggests that some collagen fiber damage has occurred during this period. However, its effect on the mechanical response of BHVs was not detectable. Nevertheless, it is important to maintain the structural integrity of the BHV, as this will help to improve BHV durability.

6.1.3 Constitutive model of BHV biomaterial under permanent set

In previous chapters, we developed a constitutive model for the underlying mechanical properties of collagenous soft tissues used to fabricate BHVs (Chapter 2, 3) as well as the extensions for the evolution of the material properties in response to permanent set (Chapter 4). The constitutive model utilizes the mechanisms at the meso-scale (i.e. at the level of the fiber, 10-100 μm in length scale), takes into account the layered structure of these tissue and the contributions from the distinct collagen

and elastin fiber networks within each tissue layer to predict the mechanical response at the tissue scale. This approach was further extended for the effect of crosslinking on the fiber matrix interactions to simulate exogenously crosslinked materials. Requisite collagen and elastin fibrous structural information can be obtained using microscopy and conventional histology, and the approach was validated using a novel fibril-level (0.1 to 1 μm) approach to compare the predicted collagen fiber/fibril mechanical behavior with extant MV small angle X-ray scattering data.

Permanent set is the significant changes in the geometry of BHVs observed in experimental studies [19][18] with in vivo operation. This can lead to stress concentrations that can have a significant impact on structural damage. Structural damage was not detected in the time frame when permanent set is the most dominant. We hypothesize that the scission-healing reaction of glutaraldehyde is the underlying mechanism responsible for permanent set in exogenously crosslinked soft tissues. The continuous scission-healing process of glutaraldehyde allows a portion of the exogenously crosslinked matrix, which is considered to be the non-fibrous part of the extracellular matrix, to be re-crosslinked in the loaded state. We model the permanent set effect in chapter 4 by assuming that the exogenously crosslinked matrix undergoes changes in reference configurations over time. The changes in the collagen fiber architecture due to dimensional changes allow us to predict subsequent changes in mechanical response. A key finding we have is that the collagen fiber architecture has a limiting effect on the maximum changes in geometry that the permanent set effect can induce. This is due to the recruitment of collagen fibers as the changes in geometry due to permanent set increase. This means we can potentially optimize the BHV geometry based on the predicted the final BHV geometry after permanent set has largely ceased.

6.1.4 Numerical simulation framework

However, numerical simulations using our constitutive model for permanent set is quite costly. Due to the incorporation of the quadruple integral to calculate fiber interactions, the resulting computational cost is five magnitudes higher than conventional phenomenological approaches. It is for this reason that we developed an effective constitutive model for planar soft tissues and a parameter estimation approach for rapidly determining the model parameters from the micro-model. This approach takes advantage of the computationally efficient forms of phenomenological models and the mechanisms and predictive capabilities of micro-models (meso-scale, multi-scale, or other complex constitutive models) (Fig. 5.1A). For each iteration of the simulation, whether forward, inverse, or time-evolving, the effective constitutive model is first fit to the micro-model(s) to determine the model parameters, then it is used to perform the actual numerical simulation. Subsequent updates to the evolving material properties, geometry, and boundary conditions are then performed (Fig. 5.1B). This approach can greatly improve the computational efficiency of numerical simulations and make it possible for a finite element implementation of the permanent set simulation (Chapter 4). In this chapter, we develop and numerical simulation framework for the time evolving properties of BHVs in response to permanent set, and attempt to predict the geometric and structural change that occurs with long-term cyclic loading.

6.2 Methods

6.2.1 Overall framework

To implement the permanent set model (chapter 4) for numerical simulations, we will utilize the effective constitutive model approach (chapter 5). This imple-

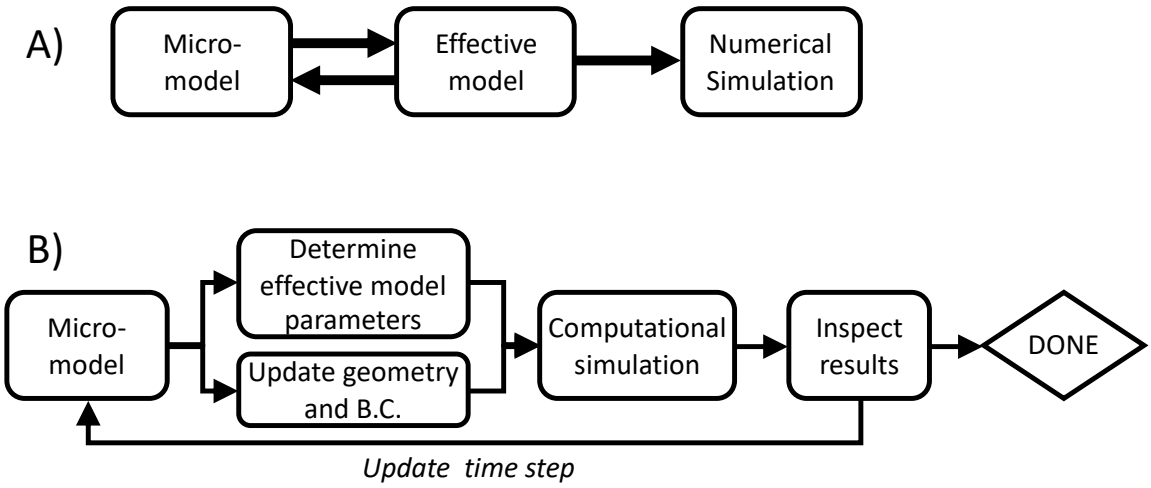

Figure 6.1: Proposed framework for using an effective constitutive model to improve the efficiency of using complex meso- or multi-scale models (micro-models) in numerical simulations. Here, A) effective constitutive models act as an intermediate step between micro-models and numerical simulations, where micro-models inform the changes to the effective constitutive model while the effective constitutive model for the simulation. B) An example of how this may be implemented for time-evolving is shown.

mentation has 4 main components (Fig. 6.2): 1) initial state model, 2) quasistatic simulation, 3) updates to the material properties in response to permanent set and 4) updates to the finite element model geometry in response to permanent set.

6.2.2 Initial state model

In this part, the initial parameters of the simulation are established. The 3 main components are: 1) finite element mesh for BHV geometry, 2) leaflet material properties, and 3) mapped collagen fiber architecture. For the BHV geometry, our group developed a pipeline using micro-CT to measure the 3-dimensional geometry of the BHV and fitting the atrial surface points to a NURBS mesh using the grasshopper plugin in Rhino (Copyright Robert McNeel & Associates) (Fig. 6.3). We also previously developed an approach for mapping the collagen fiber architecture to the finite element mesh [2, 1]. However, due to the lack of available experimental data, we used the Edwards valve geometry from [1], bovine pericardium material properties from [12], and circumferential aligned collagen fiber orientation distributions.

6.2.3 Quasistatic simulation of bioprosthetic heart valves

For the quasistatic simulation, which is necessary to determine the current loaded state, we will utilize the effective model approach (Fig. 6.1) established in chapter 5. For finite element model, we utilized the custom finite element simulation software developed by Hsu *et al.* [4, 6, 7, 23]. Briefly, the finite element code was developed for isogeometric fluid-solid dynamics simulation of heart valves, focusing mostly on the tri-leaflet atrioventricular valves. The tri-leaflet geometry is based on the commonly used Edwards Pericardial Heart Valve with Kirchhoff-Love shells for the leaflets [7] and finite element solver developed in by Kamensky *et al.* [6]. We utilized this code to simulate leaflet deformation under physiological quasi-static

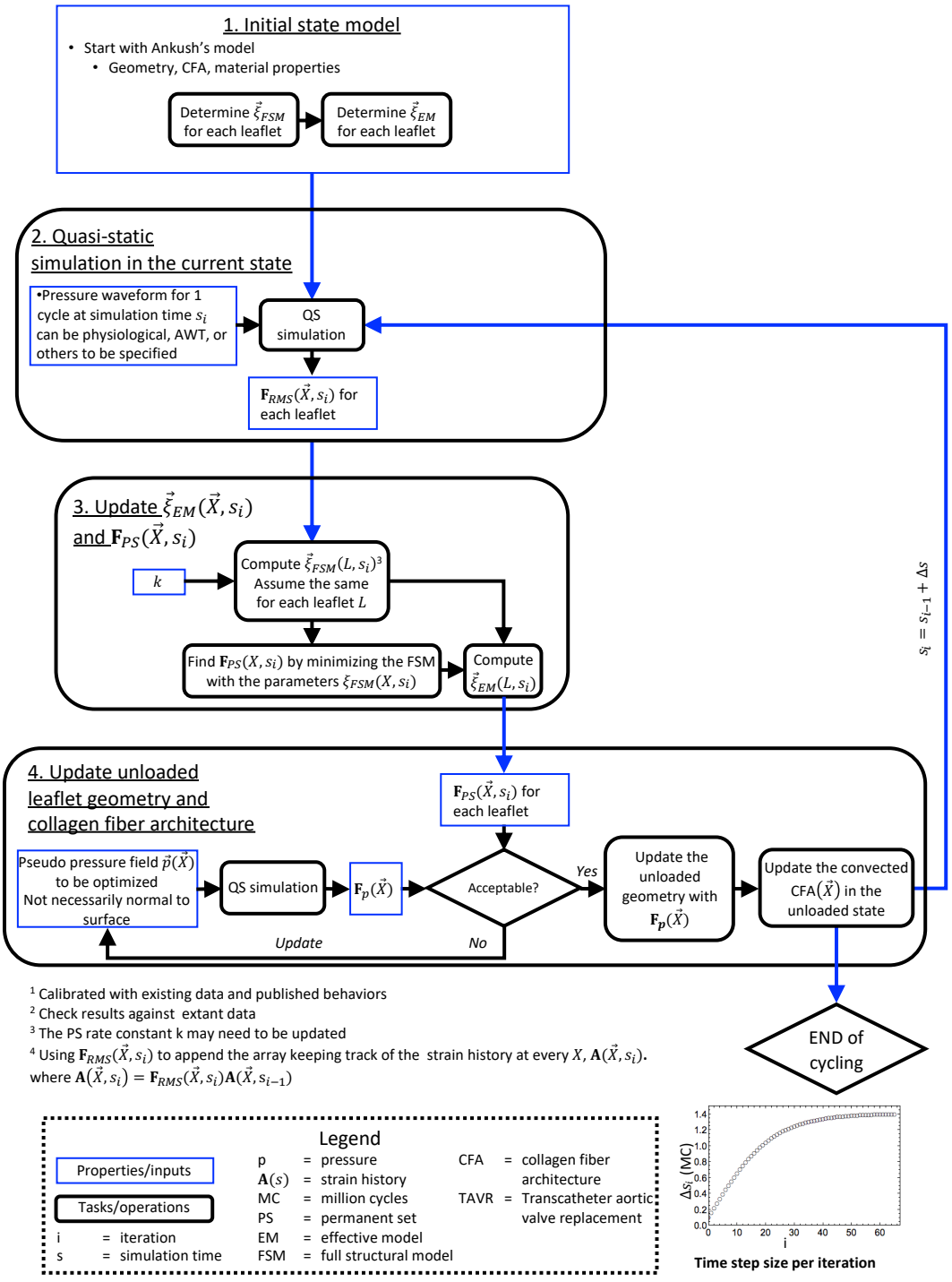

Figure 6.2: Proposed framework for simulation the evolving properties of BHVs in response to permanent set.

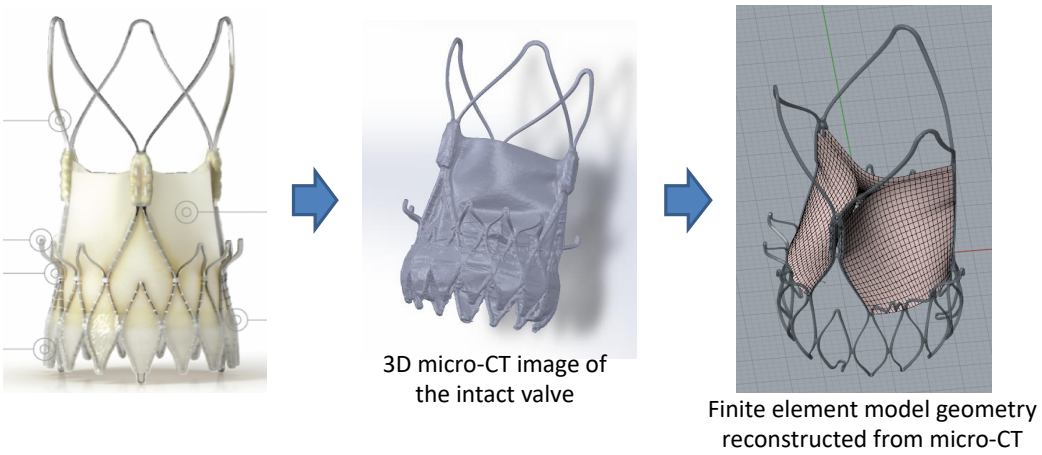

Figure 6.3: Pipeline for converting micro-CT data for each reference and loading states to finite element meshes and geometry.

transvalvular pressure. A total was 484 Bézier elements was used for each leaflet, with a leaflet density of 1.0 g/cm^3 and a uniform leaflet thickness of 0.386mm thick [4]. Contact between leaflets is handled by a penalty-based approach and imposed at quadrature points of the shell structure, and clamped boundary condition is applied to the leaflet attachment edge. For simplicity and consistency, the collagen fiber direction was assumed to be aligned to the circumferential direction of each leaflet. No root, atrial chamber or the surrounding artery was used. The bioprosthetic heart valve stent was made rigid and undeformable, serving a stationary reference for the leaflets. A similar validation process to the one presented by Wu *et al.* [23] to verify the implementation.

For the constitutive model for the leaflet material, we used the effective ma-

terial model (chapter 5)

$$
\begin{aligned}
\Psi_{eff} =& c_0 \left(e^Q - 1\right) = c_0' e^{-Q_{max}} \left(e^Q - 1\right) \\
Q =& b_1 E_m^2 + b_2 E_n^2 + b_3 E_\phi^2 + b_4 E_m E_n + b_5 E_m^4 + b_6 E_n^4 + b_7 E_m^3 E_n + b_8 E_m^2 E_n^2 \\
& + b_9 E_m E_n^3 + b_{10} E_\phi^4 + b_{11} E_m^2 E_\phi^2 + b_{12} E_n^2 E_\phi^2 + b_{13} E_m E_n E_\phi^2 \\
Q =& b_1 (E_m^{max})^2 + b_2 (E_n^{max})^2 + b_3 (E_\phi^{max})^2 + b_4 (E_m^{max})(E_n^{max}) + b_5 (E_m^{max})^4 \\
& + b_6 (E_n^{max})^4 + b_7 (E_m^{max})^3 (E_n^{max}) + b_8 (E_m^{max})^2 (E_n^{max})^2 + b_9 (E_m^{max})(E_n^{max})^3 \\
& + b_{10} (E_\phi^{max})^4 + b_{11} (E_m^{max})^2 (E_\phi^{max})^2 + b_{12} (E_n^{max})^2 (E_\phi^{max})^2 \\
& + b_{13} (E_m^{max})(E_n^{max})(E_\phi^{max})^2,
\end{aligned}
\tag{6.1}
$$

to homogenize the mechanical response of the permanent set model. The resulting elasticity tensor can be found in Appendix A.2, Eqn. A.11). To test the finite element implementation, and the effective constitutive model approaches, we performed several quasi-static simulations of BHVs with different leaflet materials properties. The main properties considered are bovine pericardium (most commonly used for bioprosthetic heart valve leaflets), porcine aortic valve (highly anisotropy response), and bovine pericardium with a uniform fiber ODF (isotropic). We replicated the response of these tissues using the static part of the permanent set constitutive model for collagenous soft tissues (Eqn. 6.4) based on their microstructure. We then fit Ψ_{eff} (Eqn. 6.1) their response by sampling along optimal loading paths. Next, we evaluated the computational cost and numerical robustness of Ψ_{eff} and its ability to handle a wide range of material properties and the complex *in vivo* deformations in numerical simulations.

6.2.4 Constitutive model for the evolving material properties under permanent set

The detailed theory for the constitutive model for permanent set is presented in chapter 4. Briefly, the constitutive model consists of three parts: collagen, matrix, and interactions,

$$\Psi = \Psi_{\text{col}} + \Psi_{\text{mat}} + \Psi_{\text{int}}. \tag{6.2}$$

The time evolving mechanism is based on the work by Rajagopal and Wineman [10], where we assume that the response of the EXL matrix is a constrained mixture model consisting of the origin fraction being continuously converted to new fractions with a reference state in the current loaded configuration.

$$\phi_m \mathbf{S}_m = b(s)\bar{\mathbf{S}}_m^{\text{existing}} + \int_0^s a(s,\hat{s})\bar{\mathbf{S}}_m^{\text{new}} \mathrm{d}\hat{s}, \tag{6.3}$$

The final model form as a function of the permanent set rate constant k, the permanent set deformation $\mathbf{F}_{\text{PS}}$, the strain history $\mathbf{A}(s)$, and the material parameters of the constitutive model in the uncycled state. The input of the model is the applied deformation $\mathbf{C}$ referenced to the current unloaded state Ω_{PS}, given by the deformation $\mathbf{F}_{\text{PS}}$ from Ω_0. The full form is

$$\mathbf{S} = \mathbf{S}\left(k, \mathbf{F}_{\text{PS}}, \mathbf{A}(\hat{s}), \mathbf{C}\right) = \phi_{\text{col}}\left[\mathbf{S}_{\text{col}} + \mathbf{S}_{\text{int}}\right] + \phi_m \mathbf{S}_{\text{m}}, \tag{6.4}$$

where the collagen contribution is

$$\begin{aligned}
&\phi_{\text{col}}\mathbf{S}_{\text{col}}\left(k, \mathbf{F}_{\text{PS}}, \mathbf{A}(\hat{s}), \mathbf{C}\right) \\
&\qquad = \phi_{\text{col}}\eta_C \int_\theta \Gamma_1(\mathbf{F}_{\text{PS}}, \theta) \left\{ \int_1^{\lambda_\theta} \frac{D_1\left(\mathbf{F}_{\text{PS}}, x\right)}{x} \left(\frac{1}{x} - \frac{1}{\lambda_\theta}\right) \mathrm{d}x \right\} \mathbf{n}_\theta \otimes \mathbf{n}_\theta \mathrm{d}\theta,
\end{aligned} \tag{6.5}$$

where $\lambda_\theta = \sqrt{\mathbf{n}_\theta \cdot \mathbf{C}\mathbf{n}_\theta}$ is the stretch of the fiber ensemble oriented along θ, the fiber

ensemble interactions is

$$
\begin{aligned}
&\phi_{\text{int}}\mathbf{S}_{\text{int}}\left(k,\mathbf{F}_{\text{PS}},\mathbf{A}(\hat{s}),\mathbf{C}\right)\\
&\quad=\phi_{\text{col}}\eta_{\text{int}}\int_{\alpha}\int_{\beta}\Gamma_1\left(\mathbf{F}_{\text{PS}},\alpha\right)\Gamma_1\left(\mathbf{F}_{\text{PS}},\beta\right)\\
&\qquad\times\Bigg[\Bigg\{\int_1^{\lambda_\alpha}\int_1^{\lambda_\beta}\frac{2\lambda_\beta D_1(\mathbf{F}_{\text{PS}},x_\alpha)D_1(\mathbf{F}_{\text{PS}},x_\beta)}{x_\alpha x_\beta}\left(\frac{\lambda_\alpha}{x_\alpha}\frac{\lambda_\beta}{x_\beta}-1\right)\mathrm{d}x_\alpha\,\mathrm{d}x_\beta\\
&\qquad+\int_1^{\lambda_\beta}D_1(\mathbf{F}_{\text{PS}},x_\beta)\left(\frac{\lambda_\beta}{x_\beta}-1\right)^2\mathrm{d}x_\beta\Bigg\}\frac{\mathbf{n}_\alpha\otimes\mathbf{n}_\alpha}{\lambda_\alpha}\\
&\qquad+\Bigg\{\int_1^{\lambda_\alpha}\int_1^{\lambda_\alpha}\frac{2\lambda_\beta D_1(\mathbf{F}_{\text{PS}},x_\alpha)D_1(\mathbf{F}_{\text{PS}},x_\beta)}{x_\alpha x_\beta}\left(\frac{\lambda_\alpha}{x_\alpha}\frac{\lambda_\beta}{x_\beta}-1\right)\mathrm{d}x_\alpha\,\mathrm{d}x_\beta\\
&\qquad+\int_1^{\lambda_\alpha}D_1(\mathbf{F}_{\text{PS}},x_\alpha)\left(\frac{\lambda_\alpha}{x_\alpha}-1\right)^2\mathrm{d}x_\alpha\Bigg\}\frac{\mathbf{n}_\beta\otimes\mathbf{n}_\beta}{\lambda_\beta}\Bigg]\mathrm{d}\alpha\,\mathrm{d}\beta,
\end{aligned}
\tag{6.6}
$$

and the EXL matrix is

$$
\begin{aligned}
&\phi_m\mathbf{S}_{\text{m}}\left(k,\mathbf{F}_{\text{PS}},\mathbf{A}(\hat{s}),\mathbf{C}\right)\\
&\quad=\phi_m\eta_m\Bigg[\text{Exp}\left[-k\cdot s\right]\left(\left(\bar{I}_1(\mathbf{F}_{\text{PS}},\mathbf{A}(0))-3\right)^{\alpha-1}+r\left(\bar{I}_1(\mathbf{F}_{\text{PS}},\mathbf{A}(0))-3\right)^{\beta-1}\right)\\
&\quad\times\left(\tilde{\mathbf{B}}(\mathbf{F}_{\text{PS}},\mathbf{A}(0))^{-1}-\tilde{B}_{33}^{-1}(\mathbf{F}_{\text{PS}},\mathbf{A}(0))C_{33}\mathbf{C}^{-1}\right)\\
&\quad+\int_0^s k\cdot\text{Exp}\left[-k(s-\hat{s})\right]\left(\left(\bar{I}_1(\mathbf{F}_{\text{PS}},\mathbf{A}(\hat{s}))-3\right)^{\alpha-1}+r\left(\bar{I}_1(\mathbf{F}_{\text{PS}},\mathbf{A}(\hat{s}))-3\right)^{\beta-1}\right)\\
&\quad\times\left(\tilde{\mathbf{B}}(\mathbf{F}_{\text{PS}},\mathbf{A}(\hat{s}))^{-1}-\tilde{B}_{33}^{-1}(\mathbf{F}_{\text{PS}},\mathbf{A}(\hat{s}))C_{33}\mathbf{C}^{-1}\right)\mathrm{d}\hat{s}\Bigg].
\end{aligned}
\tag{6.7}
$$

6.2.5 Geometry update in response to permanent set

Although the permanent set model can find the local change in reference geometry, ($\mathbf{F}_{\mathrm{PS}}$), can be determined from equation 6.7 using

$$\mathbf{F}_{\mathrm{PS}} = \arg\min_{\mathbf{F}} \left\| \mathbf{S}\left(k, \mathbf{I}, \mathbf{A}(\hat{s}), \mathbf{C} = \mathbf{F}^{\mathsf{T}}\mathbf{F}\right) - 0 \right\|. \tag{6.8}$$

This is only local and will not be sufficient for generating a compatible mesh. To generate the updated reference configuration, we will do this by simulation. First the local change in geometry is found (Eqn. 6.8). Next, we will compute an equivalent stress using equation 6.4, by

$$\mathbf{S}_{\mathrm{PS}} = \mathbf{S}(\mathbf{F}_{\mathrm{PS}}). \tag{6.9}$$

This permanent set stress, $\mathbf{S}_{\mathrm{PS}}$, is equivalent of a growth stress, which is then added to the weak form presented in equation 1 of Wu et al. [23] as

$$\begin{aligned} \int_{\Gamma_0} \mathbf{w} \cdot \rho h_{th} \left.\frac{\partial^2 y}{\partial t^2}\right|_{\mathbf{X}} \mathrm{d}\Gamma + \int_{\Gamma_0} \int_{-h_{th}/2}^{h_{th}/2} \delta\mathbf{E} : (\mathbf{S} + \mathbf{S}_{\mathrm{PS}})\, \mathrm{d}\xi^3\, \mathrm{d}\Gamma \\ - \int_{\gamma_0} \mathbf{w} \cdot \rho h_{th} \mathbf{f}\, \mathrm{d}\Gamma - \int_{\Gamma_t} \mathbf{w} \cdot \mathbf{h}\, \mathrm{d}\Gamma = 0 \end{aligned} \tag{6.10}$$

The resulting control point displacements are then added to the finite element mesh from the previous time step to generate the new mesh in the new reference configuration.

6.2.6 Complete implementations with Python wrapper

The complete implementation of the time evolving simulation is done using a Python3 wrapper (Fig. 6.4) of the different components:

A Quasi-static (QS) simulation code to obtain the NURBS control point displacement data for different loading conditions

B A post processor for translate displacement data to strain data at each gauss point

C The constitutive model for determining the change in material properties due to permanent set gauss point

D Parameter estimation code for determining the effective model parameters at each time step and gauss point

E Python code for updating the NURBS finite element mesh after each time step

F Python code for updating the collagen fiber orientation after each time step

To start, we will use the Edwards valve geometry from [1], bovine pericardium material properties from [12], and circumferential aligned collagen fiber orientation distributions. Next, the following process is iterated:

1. Perform QS simulation using the finite element code to determine the loading state

2. Using the post processor to convert control point displacement data to local strain data, $\mathbf{A}(\hat{s})$, at the current time $\hat{s}$

3. Append the strain in the loaded configuration, $\mathbf{A}(\hat{s})$, to the full strain history $\mathbf{A}(s)$

4. Update the permanent set constitutive model (Eqn. 6.4)

5. Use equation 6.4 to compute the local $\mathbf{F}_{\text{PS}}$, $\mathbf{S}_{\text{PS}}$, and mechanical data along optimal loading paths (chapter 5.2.4)

6. Use the local permanent set deformation to convect the collagen fiber orientation distribution Γ_i in the current state to Γ_{i+1} in the post permanent set state using

$$\Gamma_{i+1}[\mu_\Gamma, \sigma_\Gamma, \theta_{i+1}] = \Gamma_i[\mu_\Gamma, \sigma_\Gamma, \theta_i({}^{i+1}_{i}\mathbf{F}, \theta_{1+1}) \frac{{}^{i+1}_{i}\lambda^2_{\theta_i}}{{}^{i+1}_{i}J_{\text{2D}}}]. \tag{6.11}$$

Note that the angle θ_1 of a fibre originally oriented at θ_0 can be determined using

$$\theta_{i+1}({}^{i+1}_{0i}\mathbf{F}, \theta_i) = \tan^{-1}\left(\frac{{}^{i+1}_{i}F_{21}\cos\theta_i + {}^{i+1}_{i}F_{22}\sin\theta_i}{{}^{i+1}_{i}F_{11}\cos\theta_i + {}^{i+1}_{i}F_{12}\sin\theta_i}\right) \tag{6.12}$$

7a Perform QS simulation using the finite element code with $\mathbf{S}_{\text{PS}}$ as the loading condition

7b Added the control point displacement data to the current mesh geometry

8 Determine the new effective constitutive model parameters by performing parameter estimation on the optimal loading path data using equation 6.1

9 Go to step 1 and rerun the QS simulation using the new mesh geometry, effective constitutive model parameters, and collagen fiber architecture

This loop is run for the desired number of cycles.

6.3 Results and Discussion

6.3.1 Numerical simulation of bioprosthetic heart valve deformation

Planar biaxial test simulations were conducted to ensure that Ψ_{eff} (Eqn. 6.1) and the elasticity tensor (Appendix A.2, Eqn. A.11) were properly implemented in the finite element simulation framework. We compared the computation time for both Ψ_{eff} and Holzapfel-Gasser-Ogden model for biaxial simulation of bioprosthetic heart valve tissues and expectedly found no significant increase in computational cost.

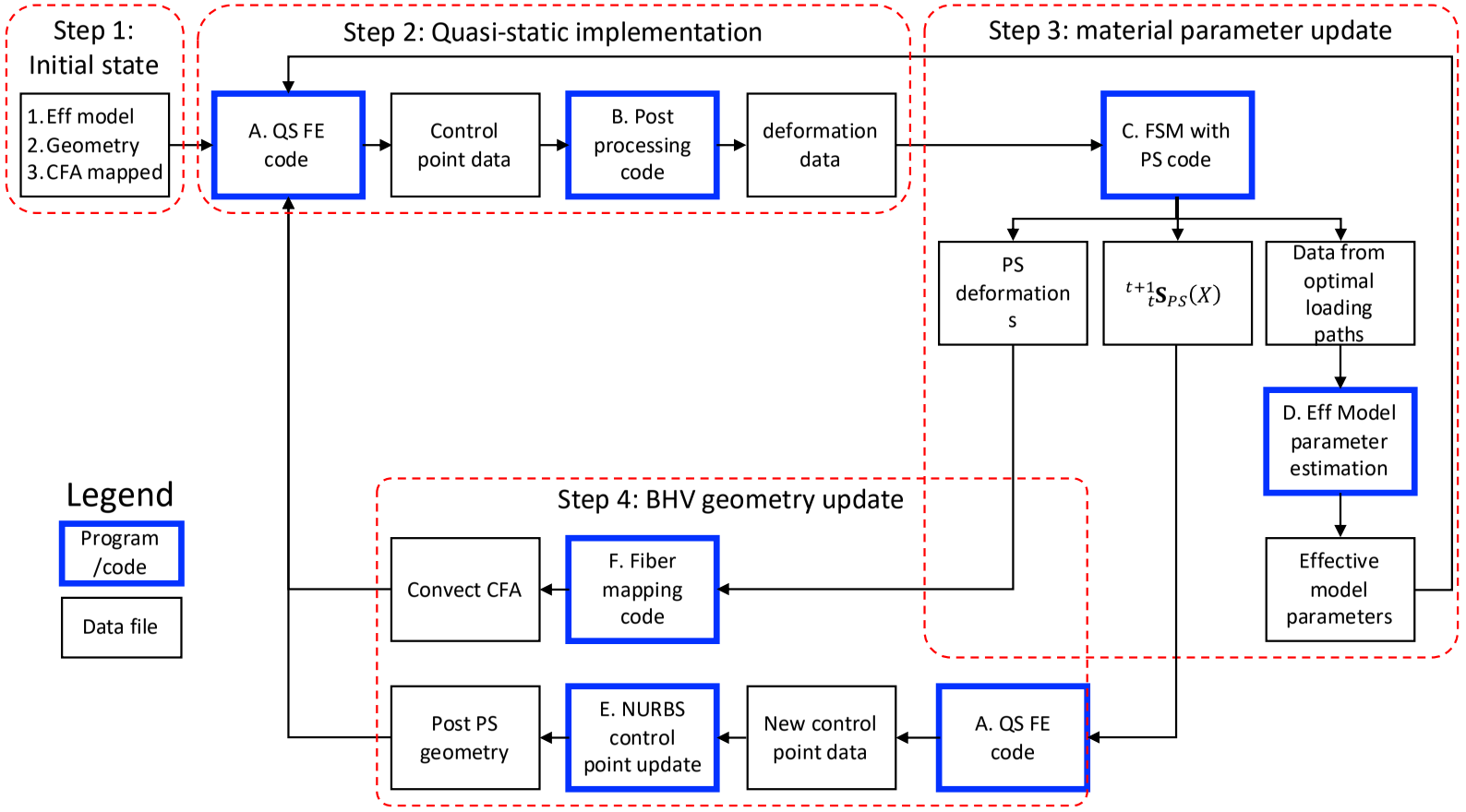

Figure 6.4: The python wrapper for communicating and execution of the different component of the time dependent simulation framework.

The total elapsed time for Ψ_{eff} is 7.58 seconds in comparison to 6.40 seconds for the Holzapfel-Gasser-Ogden model, much faster than any micro-models can achieve.

Next, we simulated tri-leaflet valves with model parameters derived from bovine pericardium, porcine aortic valve leaflet, and an idealized isotropic case. This is a simple demonstration of the use of the Ψ_{eff} for the upscaling and homogenizing of micro-models. The model parameters for the bovine pericardium case were derived from the simplified structural model and model parameter of Aggarwal and Sacks [1], and the resulting response matched very well qualitatively. Due to a lack of fiber mapping in the quasi-static simulation software used, some minor differences are still expected. We found no difficulty when simulating the pericardium, aortic, or isotropic valves. Suggesting that Ψ_{eff} is quite robust numerically.

The material properties have significant effects on the mechanical behaviors of the leaflets (Fig. 6.5). The strain distributions within the leaflets were obtained for the pressure-loaded, fully-closed configurations of the valve, and then plotted with the maximum in-plane Green-Lagrange strain (MIPE). When comparing the three different material, we can see that the native aortic valve properties result in significant heterogeneities in the deformation of the leaflets (Fig. 6.5C). Specifically, the belly region of the leaflets significantly protrudes out, increasing the load in the surrounding regions, especially near the commissures. This results in some stress concentrations that are not conducive to heart valve durability and health in general. The bovine pericardium valve (Fig. 6.5B) and the isotropic valve (Fig. 6.5A) on the other hand have significantly more homogeneous leaflet deformations, especially from the top-down view. Both of these undergo approximately the same deformation of 0.2 in MIPE. The largest difference between the two is near the commissure regions of the valve. Where the isotropic case is under significantly higher strain. Functionally,

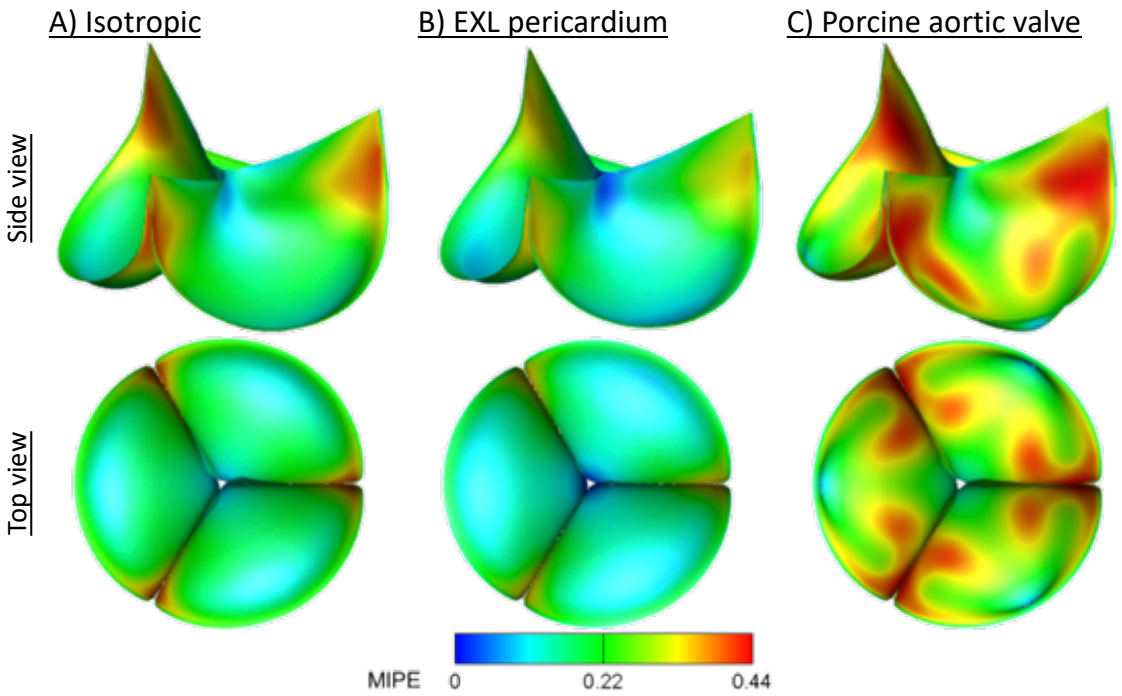

Figure 6.5: Simulations of intact tri-leaflet valves using A) the porcine aortic valve properties with a uniform fiber orientation distribution, B) exogenously cross-linked bovine pericardium properties with the most homogenous stress distribution, and C) the porcine aortic valve properties which results in a very heterogeneous stress distribution and the belly region caving in. The top row shows the side view of the valves at 80 mmHg and the bottom row shows the top-down view of the valves at the same transvalvular pressure.

the material properties of the exogenously cross-linked bovine pericardium are the most suitable for heart valve leaflets, which distributes the stresses more evenly.

Much of the reasons behind these differences are likely to be due to the differences between the apparent mechanical properties *in vivo* and the measured mechanical response in the laboratory setting. This is especially true for the aortic valve, which is extremely anisotropic with very high compliance in the radial direction of the leaflets. This difference is most likely due to the mismatch of referential configuration between the two states. Residual strain or residual stress has significant impacts on the functional properties of the leaflets, specifically the apparent anisotropy and stiffness. Collagen fiber directions and varying regional properties can also have a significant impact on the functional properties of the leaflets, and thus the results of the simulation. The valve leaflet shape, root geometry and properties, the arterial or ventricular geometry and loading conditions, can all be significant factors affecting the functions and stress distribution of the valve leaflets. Furthermore, how these factors affect the fluid dynamics of the valves is also an interesting question, suitable for further study. All in all, this is meant to be a demonstration and proof of concept for using Ψ_{eff} to handle a wide range of soft tissue behaviors and anisotropy for the simulation of biological organs, in this case, heart valves. Further and more detailed studies will be reserved for the future.

6.3.2 Permanent set simulation of bioprosthetic heart valve

This initial was done with 1) homogenous material parameters similar to bovine pericardium from Sacks and Zhang [12], 2) the Edward valve geometry from [1], and collagen fiber distributions aligned with the circumference direction and a standard deviation of 30°. The key result is that permanent set slow done after

around 20 million cycles and nearly completely seizes after 30 million cycles (Fig. 6.6 &6.7). This effect is closely linked to the microstructural of the collagen fiber network. The gradual slow down is correlated with the straightening and recruitment of collagen fibers. This was predicted from the constitutive model (Eqn. 6.4) (Fig. 4.17). This is an important structural response, which allows us to predict the final reference geometry of the BHV. Since 30 million cycles correspond to only 1 year after being surgically implanted, the BHV will remain in this configuration for the rest of its 9-14 year lifespan. By optimizing the initial BHV design so that the peak stress is minimal in the configuration after permanent set has seized, we can potentially improve the durability of BHVs by minimizing the load on the collagen fibers. Because collagen fibers have high rates of failure after being extended by 7-8% [8][3], more evenly distributing the stresses can reduce this mode of failure.

Here we also note that the regions that undergo most permanent set are: the belly region, the center of the free edge, and the regions near the commissures, where the leaflets initial make contact (Fig. 6.6). These regions are also the most common regions of failure in BHVs. Due to the change in reference configuration, the collagen fibers in these regions recruit more quickly and may even be held in a constant extended state. This can have dramatic consequences on the likelihood of failure of these collagen fibers due to their low extensibility and could be a major mechanism for the fiber level damage in BHVs.

We have also shown that we can predict the change in the collagen fiber architecture (Fig. 6.7). Here we plotted the normalized orientation index (NOI)

$$NOI = \frac{\sigma_i so - \sigma(s)}{\sigma_i so}, \tag{6.13}$$

which is based on how spread apart (standard deviation σ) is collagen fiber orientation is. Here, $NOI = 1$ indicate fully aligned distributions (delta distributions), which

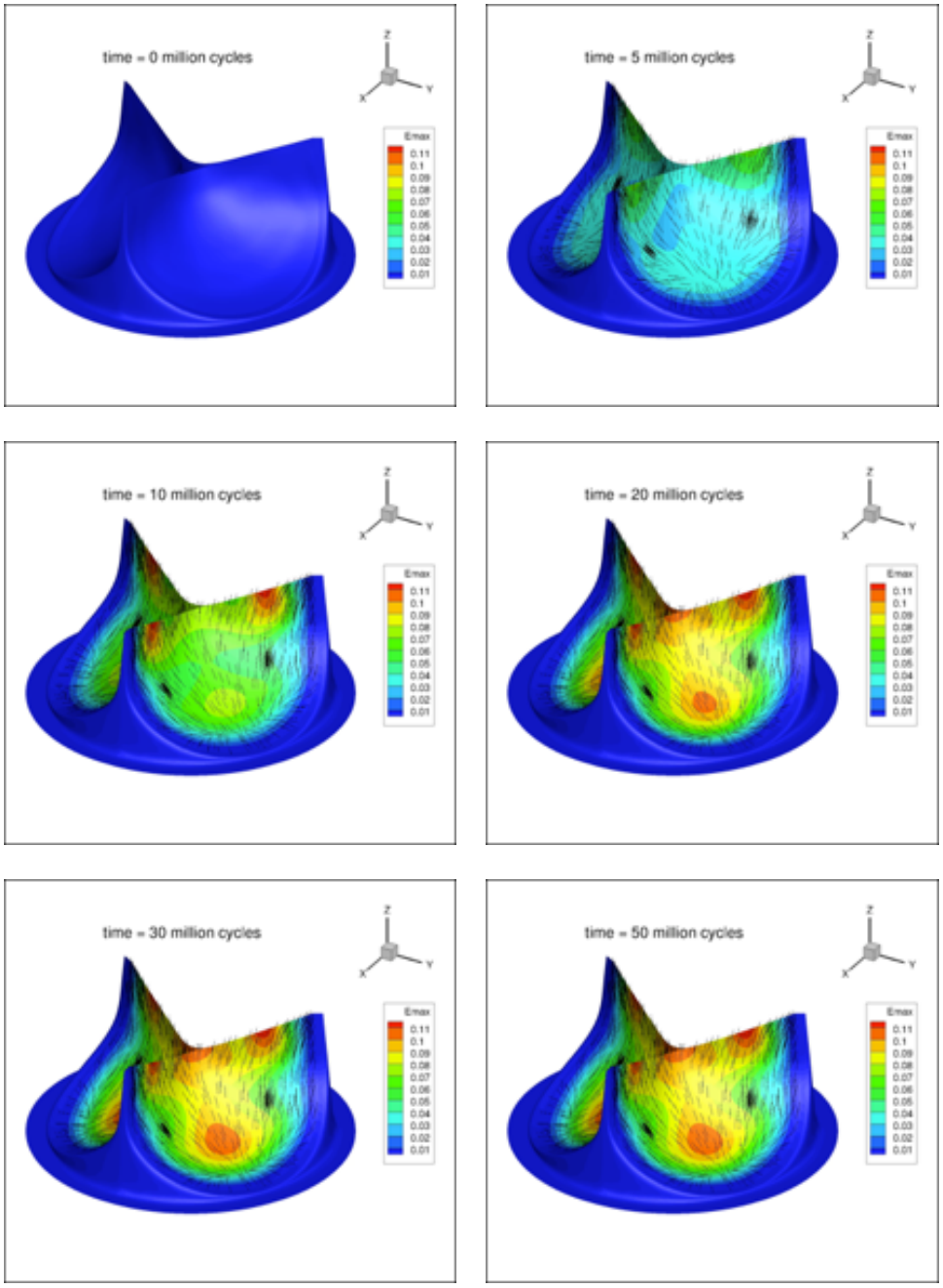

Figure 6.6: The simulation of the evolution of the referential configuration with the maximum principal in-plane Green-Lagrange strain (MIPE) overlayed on top at different cycle levels. Colors indicate the magnitude of MIPE, and the lines indicate the principal direction of the permanent set deformation.

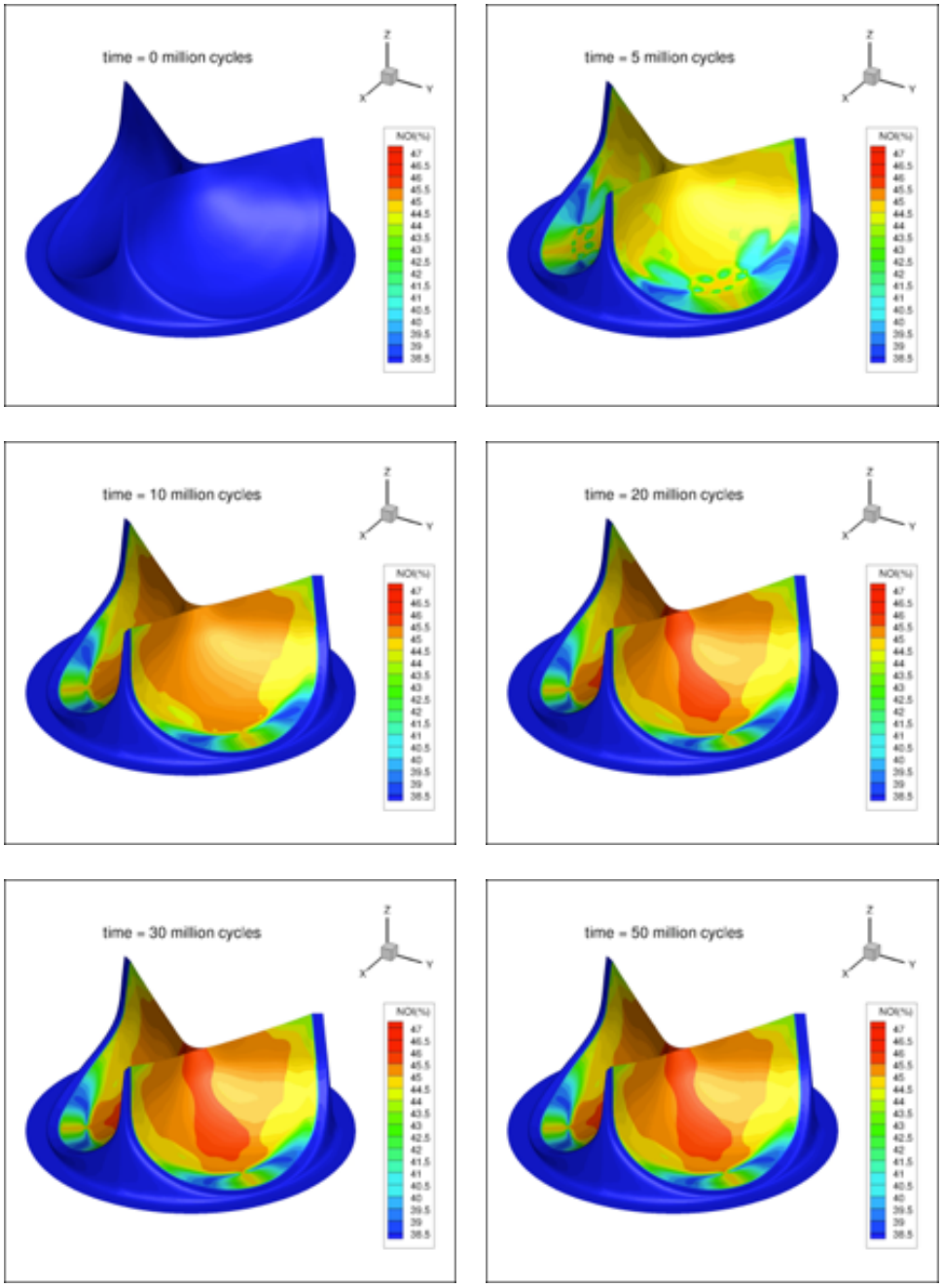

Figure 6.7: The simulation of the evolution of the referential configuration with the normalized orientation index (NOI) overlayed, showing the changes in the degree of alignment of collagen fibers at different cycle levels. Higher NOI indicate higher aligned fiber orientation distributions.

$NOI = 0$ indication that the fiber distribution is an uniform distribution. We can see that the belly region and the free edge undergoes the greatest degree of realignment. This is most likely due to the fact that these two regions receive the least amount of support from the neighboring leaflets. The most important aspect of being able to predict the structural changes is that we can use it to compute the degree of recruitment of collagen fibers in a similar method to chapter 2.3.3. This allows us to compute the distribution of collagen fiber by their stretches after being straightened. This mechanism can be used to potentially develop a strain-level dependent model for the likelihood of collagen fiber damage in a future extension.

6.4 Conclusions

We have developed a complete time-dependent framework for the simulation of BHVs under long-term cyclic loading. This simulation utilizes the predictive mechanism based constitutive model for the permanent set effect in exogenously crosslinked soft tissues that we previously developed. We have shown that we can use this simulation to predict the evolving geometry, microstructural and material property changes. These results can then be used to predict regions of increasing likelihood of structural damage and can be used to optimize the initial design of BHVs based on these factors. Most important of these effects is that the collagen fiber architecture can play a role in limiting the permanent set effect, where the straightening of collagen fibers prevents further changes in geometry. Thus, accounting for the permanent set effect is especially important in the design of BHVs to better improve their performance and durability.

Chapter Bibliography

[1] Ankush Aggarwal and Michael S. Sacks. An inverse modeling approach for semilunar heart valve leaflet mechanics: exploitation of tissue structure. *Biomechanics and Modeling in Mechanobiology*, 15(4):909–932, oct 2015. ISSN 1617-7959. doi: 10.1007/s10237-015-0732-7.

[2] Ankush Aggarwal, Vanessa S. Aguilar, Chung-Hao Lee, Giovanni Ferrari, Joseph H. Gorman, Rober C. Gorman, and Michael S. Sacks. Patient-specific modeling of heart valves: from image to simulation. In *Functional Imaging and Modeling of the Heart*, pages 141–149. Springer Berlin Heidelberg, 2013. ISBN 3-642-38898-1. doi: 10.1007/978-3-642-38899-6_17.

[3] Markus J. Buehler. Atomistic and continuum modeling of mechanical properties of collagen: elasticity, fracture, and self-assembly. *Journal of Materials Research*, 21(08):1947–1961, aug 2006. ISSN 2044-5326. doi: 10.1557/jmr.2006.0236. URL `http://dx.doi.org/10.1557/jmr.2006.0236`.

[4] Ming-Chen Hsu, David Kamensky, Fei Xu, Josef Kiendl, Chenglong Wang, Michael C. H. Wu, Joshua Mineroff, Alessandro Reali, Yuri Bazilevs, and Michael S. Sacks. Dynamic and fluid-structure interaction simulations of bioprosthetic heart valves using parametric design with T-splines and Fung-type material models. *Computational Mechanics*, 55(6):1211–1225, may 2015. ISSN 0178-7675. doi: 10.1007/s00466-015-1166-x.

[5] Jason C. Isenburg, Dan T. Simionescu, and Naren R. Vyavahare. Tannic acid treatment enhances biostability and reduces calcification of glutaraldehyde fixed aortic wall. *Biomaterials*, 26(11):1237–1245, April 2005. ISSN 0142-9612 (Print). doi: 10.1016/j.biomaterials.2004.

04.034. URL http://www.ncbi.nlm.nih.gov/entrez/query.fcgi?cmd=Retrieve&db=PubMed&dopt=Citation&list_uids=15475053.

[6] David Kamensky, Ming-Chen Hsu, Dominik Schillinger, John A. Evans, Ankush Aggarwal, Yuri Bazilevs, Michael S. Sacks, and Thomas J.R. Hughes. An immersogeometric variational framework for fluid-structure interaction: application to bioprosthetic heart valves. *Computer Methods in Applied Mechanics and Engineering*, 284:1005–1053, February 2015. ISSN 0045-7825 (Print) 0045-7825 (Linking). doi: 10.1016/j.cma.2014.10.040. URL http://www.ncbi.nlm.nih.gov/pubmed/25541566.

[7] Josef Kiendl, Ming-Chen Hsu, Michael C.H. Wu, and Alessandro Reali. Isogeometric Kirchhoff-Love shell formulations for general hyperelastic materials. *Computer Methods in Applied Mechanics and Engineering*, 291(0):280–303, jul 2015. ISSN 0045-7825. doi: 10.1016/j.cma.2015.03.010. URL http://dx.doi.org/10.1016/j.cma.2015.03.010.

[8] Y. Lanir. A structural theory for the homogeneous biaxial stress-strain relationships in flat collagenous tissues. *Journal of Biomechanics*, 12(6):423–436, jan 1979. doi: 10.1016/0021-9290(79)90027-7.

[9] Ki Dong Park, Won Kyu Lee, Ju Young Yun, Dong Keun Han, Soo hyun Kim, Young Ha Kim, Hyoung Mook Kim, and Kwang Taek Kim. Novel anti-calcification treatment of biological tissues by grafting of sulphonated poly(ethylene oxide). *Biomaterials*, 18(1):47–51, jan 1997. ISSN 0142-9612. doi: http://dx.doi.org/10.1016/S0142-9612(96)00096-8. URL http://www.sciencedirect.com/science/article/pii/S0142961296000968.

[10] K. R. Rajagopal and A. S. Wineman. A constitutive equation for nonlinear solids which undergo deformation induced microstructural changes. *International Journal of Plasticity*, 8(4):385–395, jan 1992. doi: 10.1016/0749-6419(92)90056-i.

[11] M. S. Sacks and F. J. Schoen. Collagen fiber disruption occurs independent of calcification in clinically explanted bioprosthetic heart valves. *J Biomed Mater Res*, 62(3):359–71, December 2002. doi: 10.1002/jbm.10293. URL `http://www.ncbi.nlm.nih.gov/entrez/query.fcgi?cmd=Retrieve&db=PubMed&dopt=Citation&list_uids=12209921`.

[12] Michael S. Sacks, Will Zhang, and Silvia Wognum. A novel fibre-ensemble level constitutive model for exogenous cross-linked collagenous tissues. *Interface Focus*, 6(1):20150090, dec 2015. doi: 10.1098/rsfs.2015.0090. URL `http://rsfs.royalsocietypublishing.org/royfocus/6/1/20150090.full.pdf`.

[13] F. J. Schoen. Pathology of heart valve substitution with mechanical and tissue prostheses. In M.D. Silver, A.I. Gotlieb, and F. J. Schoen, editors, *Cardiovascular Pathology*, volume 3. Livingstone, New York, 2001.

[14] F. J. Schoen. Evolving concepts of cardiac valve dynamics: the continuum of development, functional structure, pathobiology, and tissue engineering. *Circulation*, 118(18):1864–1880, October 2008. ISSN 1524-4539 (Electronic). doi: 10.1161/circulationaha.108.805911. URL `http://www.ncbi.nlm.nih.gov/entrez/query.fcgi?cmd=Retrieve&db=PubMed&dopt=Citation&list_uids=18955677`.

[15] Frederick J. Schoen. Cardiac valves and valvular pathology: update on function, disease, repair, and replacement. *Cardiovascular Pathology*, 14 (4):189–194, July 2005. ISSN 1054-8807 (Print). doi: 10.1016/j.carpath.

2005.03.005. URL http://www.ncbi.nlm.nih.gov/entrez/query.fcgi?cmd=Retrieve&db=PubMed&dopt=Citation&list_uids=16009317.

[16] Frederick J. Schoen. New frontiers in the pathology and therapy of heart valve disease: 2006 society for cardiovascular pathology, distinguished achievement award lecture, united states-canadian academy of pathology, Atlanta, GA, february 12, 2006. *Cardiovascular Pathology*, 15(5):271–279, September 2006. ISSN 1054-8807 (Print). doi: 10.1016/j.carpath.2006.05.001. URL http://www.ncbi.nlm.nih.gov/entrez/query.fcgi?cmd=Retrieve&db=PubMed&dopt=Citation&list_uids=16979034.

[17] Frederick J. Schoen and Robert J. Levy. Calcification of tissue heart valve substitutes: progress toward understanding and prevention. *The Annals of Thoracic Surgery*, 79(3):1072–1080, March 2005. doi: 10.1016/j.athoracsur.2004.06.033. URL http://www.ncbi.nlm.nih.gov/entrez/query.fcgi?cmd=Retrieve&db=PubMed&dopt=Citation&list_uids=15734452.

[18] D. B. Smith, M. S. Sacks, P. M. Pattany, and R. Schroeder. High-resolution magnetic resonance imaging to characterize the geometry of fatigued porcine bioprosthetic heart valves. *The Journal of heart valve disease*, 6(4):424–432, July 1997. ISSN 0966-8519.

[19] D. B. Smith, M. S. Sacks, P. M. Pattany, and R. Schroeder. Fatigue-induced changes in bioprosthetic heart valve three-dimensional geometry and the relation to tissue damage. *The Journal of heart valve disease*, 8(1):25–33, January 1999. ISSN 0966-8519.

[20] Wei Sun, Michael Sacks, Gregory Fulchiero, Joshua Lovekamp, Naren Vyavahare, and Michael Scott. Response of heterograft heart valve bio-

materials to moderate cyclic loading. *Journal of Biomedical Materials Research*, 69A(4):658–669, June 2004. doi: 10.1002/jbm.a.30031. URL http://www.ncbi.nlm.nih.gov/entrez/query.fcgi?cmd=Retrieve&db=PubMed&dopt=Citation&list_uids=15162408.

[21] I. Vesely, J. E. Barber, and N. B. Ratliff. Tissue damage and calcification may be independent mechanisms of bioprosthetic heart valve failure. *The Journal of heart valve disease*, 10(4):471–477, July 2001. ISSN 0966-8519. URL http://www.ncbi.nlm.nih.gov/entrez/query.fcgi?cmd=Retrieve&db=PubMed&dopt=Citation&list_uids=11499593.

[22] N. Vyavahare, D. Hirsch, E. Lerner, J. Z. Baskin, F. J. Schoen, R. Bianco, H. S. Kruth, R. Zand, and R. J. Levy. Prevention of bioprosthetic heart valve calcification by ethanol preincubation. Efficacy and mechanisms. *Circulation*, 95(2):479–488, jan 1997. doi: 10.1161/01.cir.95.2.479. URL http://www.ncbi.nlm.nih.gov/htbin-post/Entrez/query?db=m&form=6&dopt=r&uid=0009008467.

[23] Michael C.H. Wu, Rana Zakerzadeh, David Kamensky, Josef Kiendl, Michael S. Sacks, and Ming-Chen Hsu. An anisotropic constitutive model for immersogeometric fluid–structure interaction analysis of bioprosthetic heart valves. *Journal of Biomechanics*, 74:23–31, jun 2018. doi: 10.1016/j.jbiomech.2018.04.012.

Chapter 7

Conclusions, and future directions

7.1 Summary

Soft-tissue-derived exogenously cross-linked (EXL) biomaterials continue to play an important role in the fabrications of bioprosthetic heart valves (BHV), by having advantages in immunogenic and mechanical behaviors [6]. Despite ongoing research, our understanding of these materials and of the mechanisms leading to their failure remains at an empirical level. A significant challenge prohibiting accurate and predictive simulations of BHVs is a lack of understanding of the mechanism of BHV failure. One significant mechanical change in response to cyclic loading is the change in geometry of the BHV leaflets. This process is induced by permanent set, which changes the referential configuration of the leaflet material and thus how they deform in response to transvalvular loading. The further analysis has shown that significant structural damage occurred within the same region that undergoes significantly permanent set [5]. Permanent set occurs only within the early stages after surgical implantation. Although no structural damage occurs, this has important implications in geometrical change and durability of BHVs. Using permanent set we can predict change in geometry and optimal the initial design of BHVs for increase durability. To develop the constitutive model and framework for numerical simulation, we have taken the following steps:

1. We developed a meso-scale structural constitutive model for soft tissues. Constitutive models are fundamental to developing a deeper understanding of and pre-

dicting soft tissue function and pathology. To develop this constitutive model, we utilized the MV leaflets as an example. This model takes into account the layered structure of these tissues and the contributions from the distinct collagen and elastin fiber networks within each tissue layer. The requisite collagen and elastin fibrous structural information for each layer was quantified using second harmonic generation microscopy and conventional histology. A comprehensive mechanical data set was also used to guide the model formulation and parameter estimation. Furthermore, novel to tissue-level structural constitutive modeling approaches, we allowed the collagen fiber recruitment function to vary with orientation. Finally, a novel fibril-level (0.1 to 1 μm) validation approach was used to compare the predicted collagen fiber/fibril mechanical behavior with extant MV small angle X-ray scattering data. Results demonstrated excellent agreement, indicating that the MSSCM fully captures the tissue-level function. Future utilization of the MSSCM in computational models of the MV will aid in producing highly accurate simulations in non-physiological loading states that can occur in repair situations, as well as guide the form of simplified models for real-time simulation tools.

2. We extended the meso-scale structural modeling approach for the effect of exogenous crosslinking, which is a crucial part of the fabrication of BHVs to suppress immunogenicity. Despite decades of research, development and clinical use, no such model previously existed. In this study, we develop the first rigorous full structural model (i.e. explicitly incorporating various features of the collagen fiber architecture) for exogenously cross-linked soft tissues. This was made possible, in part, with the use of native to cross-linked matched experimental data sets and an extension to the collagenous structural constitutive model so that

the uncross-linked collagen fiber responses could be mapped to the cross-linked configuration. This allowed us to separate the effects of cross-linking from kinematic changes induced in the cross-linking process, which in turn allowed the non-fibrous tissue matrix component and the interaction effects to be identified. The most novel findings of this study were that: (i) the effective collagen fiber modulus was unaffected by cross-linking and (ii) fiber-ensemble interactions played a large role in stress development, often dominating the total tissue response (depending on the stress component and loading path considered).

3. We extended this constitutive model further for time-dependent effects like permanent set. Permanent set is an effect which causes BHVs to undergo significant changes in geometry with in vivo operation, which leads to stress concentrations that can have a significant impact on structural damage. These changes do not appear to be due to plastic deformation, as the leaflets only deform in the elastic regime. Moreover, structural damage was not detected by the 65 million cycle time point. We hypothesize that the scission-healing reaction of glutaraldehyde is the underlying mechanism responsible for permanent set in exogenously crosslinked soft tissues. The continuous scission-healing process of glutaraldehyde allows a portion of the exogenously crosslinked matrix, which is considered to be the non-fibrous part of the extracellular matrix, to be re-crosslinked in the loaded state. To model the permanent set effect, we assume that the exogenously crosslinked matrix undergoes changes in reference configurations over time. The changes in the collagen fiber architecture due to dimensional changes allow us to predict subsequent changes in mechanical response. Results show that permanent set alone can explain and, more importantly, predict how the mechanical response of the biomaterial change with time. An important find-

ing we have is that the collagen fiber architecture has a limiting effect on the maximum changes in geometry that the permanent set effect can induce. This is due to the recruitment of collagen fibers as the changes in geometry due to permanent set increase. This means we can potentially optimize the BHV geometry based on the predicted the final BHV geometry after permanent set has largely ceased.

4. We developed a framework for the use of effective constitutive models to homogenize and facilitate numerical simulations. Effective which only reproduces the essential responses of soft tissue but not the underlying mechanisms. Current soft tissue constitutive modeling approaches have become increasingly complex, often utilizing meso- and multi-scale methods for greater predictive capability and linking to the underlying mechanisms. However, such modeling approaches are associated with substantial computational costs, making the use of effective constitutive model approaches an important part of efficient numerical simulations. We evaluated this approach and demonstrated that it is able to handle materials of widely varying degrees of anisotropy, such as exogenously crosslinked bovine pericardium and aortic valve leaflet. This effective constitutive model approach has shown significant potential for improving the computational efficiency and numerical robustness of multi-scale and meso-scale modeling approaches, facilitating the application of inverse modeling and simulations of growth and remodeling of soft tissues and organs.

5. Finally, we completed this process by developing a Python-based framework for the implementation and simulation of permanent set. This simulation utilizes the predictive mechanism based constitutive model for the permanent set effect in exogenously crosslinked soft tissues that we previously developed. We

have shown that we can use this simulation to predict the evolving geometry, microstructural and material property changes. These results can then be used to predict regions of increasing likelihood of structural damage and can be used to optimize the initial design of BHVs based on these factors. Most important of these effects is that the collagen fiber architecture can play a role in limiting the permanent set effect, where the straightening of collagen fibers prevents further changes in geometry. Thus, accounting for the permanent set effect is especially important in the design of BHVs to better improve their performance and durability.

7.2 Conclusions

In conclusion, we have developed a novel predictive and mechanism-based constitutive modeling and numerical simulation framework for the time-dependent simulation of bioprosthetic heart valves. This work has important implication for predicting BHV durability. By being able to predict the evolving geometry of BHVs, we can utilize this approach for optimizing the initial design of BHVs for more homogeneous distributed loading to the constitutive collagen fibers as well as better fluid dynamics. With future extensions to this model and framework, this can open the door to improving the process for BHV design and thus more durable BHVs.

7.3 Future directions

The next sequential step for this work is the inclusion of structural damage to the constitutive model. Part of the reason preventing the inclusion of structural damage to this current work is the lack of sufficient experimental data. Structural damage is difficult to quantify as it only gradually accumulates over long periods of

time. Due to the exponential nature and large structural reserves of soft tissues, small decreases in the number or modulus of collagen fiber is very difficult to detect. This is also complicated by the fact that strain is difficult to quantify in the first place. In accelerated wear testing or other similar environments, this process is further complicated by the heterogeneity of the resulting response. However, by simulation and removing of the permanent set effect on the change in geometry, we can more accurately determine the remaining changes due to structural damage. This opens the doors to the development of mechanism-based structural damage models which is lacking in literature.

Another part of this ongoing project is the simulation of the fluid dynamics of the BHVs in response to the complex environment surrounding tissues. Fluid-solid interactions (FSI) have long been a popular field of study [2][1][7][3]. However, this permanent set framework opens the doors to evaluating how the fluid dynamics change over time in response to cyclic loading. The FSI finite element soft is directive included in the permanent set simulations to facilitate this extension, and more parametric studies to evaluated and optimize BHV design designs. This also lends itself to help us better understand the results of accelerated wear testing environments, which as FDA required but drastically differs from the in vivo environments. This will provide a better analysis of fatigue testing results, better prepare these designs for clinical trials and surgical implantation.

Growth and remodeling is a similar important future area, as this has important implications in the prediction of the outcomes of diseases, injuries, and surgical interventions. The permanent set model and simulation framework developed herein is a simplification of the growth and remodeling framework by removing the growth component. This can have important potential implications are devices such

as tissue engineered valves which have the possibility of growing and adaption to the surrounding environment if seeded with interstitial cells. In addition to the exogenously crosslinked tissue applications addressed herein, we have observed permanent set like phenomenon in mitral valve tissue during pregnancy [4]. In that study, our results suggested that much of the growth and remodeling in the MV leaflet does not begin immediately, but rather undergoes mostly passive leaflet enlargement until these parameters reach a critically low level, at which point growth and remodeling are triggered. This initial tissue distension process is very similar in behavior to the permanent set mechanism outlined in the present work. Thus, the current approach could be applied to the early phases of soft tissue remodeling, where non-failure mechanisms occur before the onset of growth of tissue growth and remodeling. This is the advantage for the structural-based approach to modeling permanent set, which allows us to describe the mechanical response based on real physically measure-able quantities.

Chapter Bibliography

[1] Ming-Chen Hsu, David Kamensky, Fei Xu, Josef Kiendl, Chenglong Wang, Michael C. H. Wu, Joshua Mineroff, Alessandro Reali, Yuri Bazilevs, and Michael S. Sacks. Dynamic and fluid-structure interaction simulations of bioprosthetic heart valves using parametric design with T-splines and Fung-type material models. *Computational Mechanics*, 55(6):1211–1225, may 2015. ISSN 0178-7675. doi: 10.1007/s00466-015-1166-x.

[2] David Kamensky, Ming-Chen Hsu, Dominik Schillinger, John A. Evans, Ankush Aggarwal, Yuri Bazilevs, Michael S. Sacks, and Thomas J.R. Hughes. An immersogeometric variational framework for fluid-structure interaction: application to bioprosthetic heart valves. *Computer Methods in Applied Mechanics and Engineering*, 284:1005–1053, February 2015. ISSN 0045-7825 (Print) 0045-7825 (Linking). doi: 10.1016/j.cma.2014.10.040. URL `http://www.ncbi.nlm.nih.gov/pubmed/25541566`.

[3] Josef Kiendl, Ming-Chen Hsu, Michael C.H. Wu, and Alessandro Reali. Isogeometric Kirchhoff-Love shell formulations for general hyperelastic materials. *Computer Methods in Applied Mechanics and Engineering*, 291(0):280–303, jul 2015. ISSN 0045-7825. doi: 10.1016/j.cma.2015.03.010. URL `http://dx.doi.org/10.1016/j.cma.2015.03.010`.

[4] Bruno V. Rego, Sarah M. Wells, Chung-Hao Lee, and Michael S. Sacks. Mitral valve leaflet remodelling during pregnancy: insights into cell-mediated recovery of tissue homeostasis. *Journal of The Royal Society Interface*, 13(125):20160709, dec 2016. ISSN 1742-5689. doi: 10.1098/rsif.2016.0709. URL `http://rsif.royalsocietypublishing.org/content/13/125/20160709`.

[5] D. B. Smith, M. S. Sacks, P. M. Pattany, and R. Schroeder. Fatigue-induced changes in bioprosthetic heart valve three-dimensional geometry and the relation to tissue damage. *The Journal of heart valve disease*, 8(1):25–33, January 1999. ISSN 0966-8519.

[6] Albert Starr. The artificial heart valve. *Nature Medicine*, 13(10):1160–1164, oct 2007. doi: 10.1038/nm1644.

[7] Michael C.H. Wu, Rana Zakerzadeh, David Kamensky, Josef Kiendl, Michael S. Sacks, and Ming-Chen Hsu. An anisotropic constitutive model for immersogeometric fluid–structure interaction analysis of bioprosthetic heart valves. *Journal of Biomechanics*, 74:23–31, jun 2018. doi: 10.1016/j.jbiomech.2018.04.012.

Appendices

Appendix A

More on effective constitutive modeling of soft tissues, kinematics, parameter correlation, and form.[1]

Preface

In this appendix, we cover some of the loose ends for the effective constitutive models (chapter 5) we developed and as well as some of the considerations and tests we have done that were not included in the main text. First, we will look at the choice of kinematic variable and how they affect the constitutive model. Next, we will look at how this choice will affect the parameter correlations, stress and elasticity tensor forms, and thus how we arrived at the choice of Green-Lagrange strain for our effective constitutive model. We will also go into more detail about the optimal loading paths, how they develop as you are additional loading paths. Finally, we will go into a deeper look at the effect of changing the effective model form and loading paths of the ability of the model to fit and predict mechanical responses.

[1] **The work contained in this appendix was submitted for publication in the appendix of**: Zhang, W., Zakerzadeh, Z., Zhang, W. & Sacks, M. S. A Material Modeling Approach for the Effective Response of Planar Soft Tissues for Efficient Computational Simulations. Journal of the mechanical behavior of biomedical materials. In review.
The author contributed to: performing the research, model development, data analysis, coding development, and writing the manuscript.

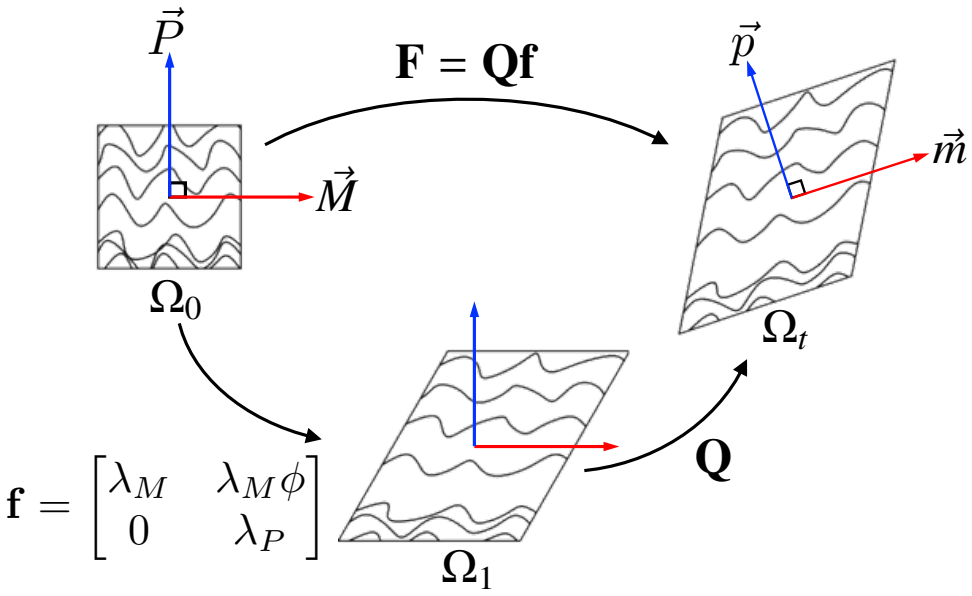

Figure A.1: The upper triangular decomposition of the deformation gradient tensor with respect the preferred material axis of soft tissues, whose components are used to define the Hencky strains.

A.1 Effective constitutive model formulation

One additional strain basis we have considered is the Hencky strains, which is the logarithmic strain calculated from the upper triangular decomposition of the deformation gradient tensor with respect to the material axis as described in Criscione *et al.* [5] and then further expanded on by Srinivasa [7] and Freed [3, 4, 2]. This has the following number of advantages: (1) The decomposed strains are easy to interpret physically, (2) it results in an extremely simple mathematical form the Cauchy stress, (3) the logarithmic strains are beneficial when dealing with experimental errors in reference configurations, and (4) It is expected to be slightly less correlated in comparison to the Green Lagrange strains. The Hencky strains different from the Green-Lagrange strains, and are thus a good choice for comparing the strain bases.

The Hencky strains can be formulated as followed. Briefly, the upper triangular

decomposition, $\mathbf{f}$, when expressed with respect to the material axis of the tissue is given by

$$[\mathbf{f}]_{\mathbf{m}_0,\mathbf{n}_0} = \begin{bmatrix} \lambda_m & \lambda_m\phi \\ 0 & \lambda_n \end{bmatrix}. \tag{A.1}$$

Here, $\mathbf{m}_0$ is the material axis in the referential configuration, which is generally the preferred direction of the fibers embedded in the tissue, $\mathbf{n}_0$ is the direction perpendicular to $\mathbf{m}_0$, $\mathbf{m}_t$ is the material axis in the deformed configuration, $\mathbf{n}_t$ is the direction perpendicular to $\mathbf{m}_t$, λ_m and λ_n are the stretches along these axes respectively, and ϕ is the angle of shear between $\mathbf{m}_0$ and $\mathbf{n}_0$. The corresponding deformation gradient tensor can thus be expressed as

$$\mathbf{F} = \lambda_m \mathbf{m}_t \otimes \mathbf{m}_0 + \lambda_m \phi \mathbf{m}_t \otimes \mathbf{n}_0 + \lambda_n \mathbf{n}_t \otimes \mathbf{n}_0. \tag{A.2}$$

The Hencky strains $(\gamma_1, \gamma_2, \gamma_3)$, which are functions of the components of $\mathbf{f}$, can be determined using,

$$\gamma_1 = \log(\lambda_m), \qquad \gamma_2 = \log(\lambda_n), \qquad \gamma_3 = \phi \tag{A.3a}$$

$$\lambda_m = \mathbf{m}_t \cdot \mathbf{F}\mathbf{m}_0, \qquad \lambda_n = \mathbf{n}_t \cdot \mathbf{F}\mathbf{n}_0, \qquad \phi = (\mathbf{m}_t \cdot \mathbf{F}\mathbf{m}_0)^{-1}\, \mathbf{m}_t \cdot \mathbf{F}\mathbf{n}_0. \tag{A.3b}$$

We are most interested in the difference between Green-Lagrange and the Hencky strains for the formulation of the effective constitutive model (Summary Table A.1). Firstly, as stated above , Hencky strains lead to a very convenient form for the Cauchy stresses,

$$\mathbf{T} = \frac{1}{J}\frac{\partial \Psi}{\partial \gamma_1}\, \mathbf{m}_t \otimes \mathbf{m}_t + \frac{1}{J}\frac{\partial \Psi}{\partial \gamma_2}\, \mathbf{n}_t \otimes \mathbf{n}_t + \frac{\lambda_n}{J\lambda_m}\frac{\partial \Psi}{\partial \gamma_3}\left(\mathbf{m}_t \otimes \mathbf{n}_t + \mathbf{n}_t \otimes \mathbf{m}_t\right). \tag{A.4}$$

where Ψ is the strain energy density function. In comparison, the 2nd Piola Kirchhoff stress with Green-Lagrange strains is,

$$\mathbf{S} = \frac{\partial \Psi}{\partial E_m}\, \mathbf{m}_0 \otimes \mathbf{m}_0 + \frac{\partial \Psi}{\partial E_n}\, \mathbf{n}_0 \otimes \mathbf{n}_0 + \frac{1}{2}\frac{\partial \Psi}{\partial E_\phi}\left(\mathbf{m}_0 \otimes \mathbf{n}_0 + \mathbf{n}_0 \otimes \mathbf{m}_0\right), \tag{A.5}$$

with the Cauchy stress obtained from push forward, $\mathbf{T} = (1/J)\mathbf{F}\mathbf{S}\mathbf{F}^{\mathsf{T}}$. Expressing the Green-Lagrange strain with respect to the material axis, E_m, E_n, E_ϕ, is preferred, so that the model parameters are invariant with respect to rigid body motion and changes in the reference coordinate system. There isn't a significant advantage to either strain measure here. However, we do note that the partial derivative of Green-Lagrange strain, $\frac{\partial \mathbf{E}}{\partial \mathbf{C}}$ (Eqn. A.9), is much simpler than that of the Hencky strains, $\frac{\partial \gamma}{\partial \mathbf{C}}$ (Eqn. A.17). As a result, the elasticity tensor, $\mathbb{C} = C_{ijkl}$, for the Hencky strain is much more complex (see Appendix A.2).

One other aspect is the difference in correlation between model parameters when using Green-Lagrange strain, $\{E_m, E_n, E_\phi\}$ vs. using Hencky strains $\{\gamma_1, \gamma_2, \gamma_3\}$. For example, using the for form of the generalized Fung model,

$$\Psi = c_0 \left(e^Q - 1 \right),$$

$$\text{with} \qquad Q = b_1 E_m^2 + b_2 E_n^2 + b_3 E_\phi^2 + 2b_4 E_m E_n + 2b_5 E_m E_\phi + 2b_6 E_n E_\phi \tag{A.6a}$$

$$\text{or} \qquad Q = b_1 \gamma_1^2 + b_2 \gamma_2^2 + b_3 \gamma_3^2 + 2b_4 \gamma_1 \gamma_2 + 2b_5 \gamma_1 \gamma_3 + 2b_6 \gamma_2 \gamma_3 \tag{A.6b}$$

we compared these two strain basis by computing the correlation matrix between the parameters b_1 to b_6 for the mechanical data acquired from an exogenously cross-linked bovine pericardium specimen [9] (Appendix A.3). The only difference is that we replaced Green Lagrange strain, E_m, E_n, E_ϕ (Eqn. A.6a), with the corresponding Hencky strains γ_1, γ_2, γ_3 (Eqn. A.6b) in the model. The correlation between the parameters are mostly similar in both cases, but the Hencky strains come on top with slightly lower correlations, and the determinant of the correlation matrix is higher, 9.38×10^{-3}, in comparison to using the Green Lagrange strains, 7.13×10^{-3}, (Fig. A.2, Appendix A.3 Table A.2 & A.3).

The last and most important difference between Green-Lagrange and Hencky strains is that they handle compression very differently. With the same model form,

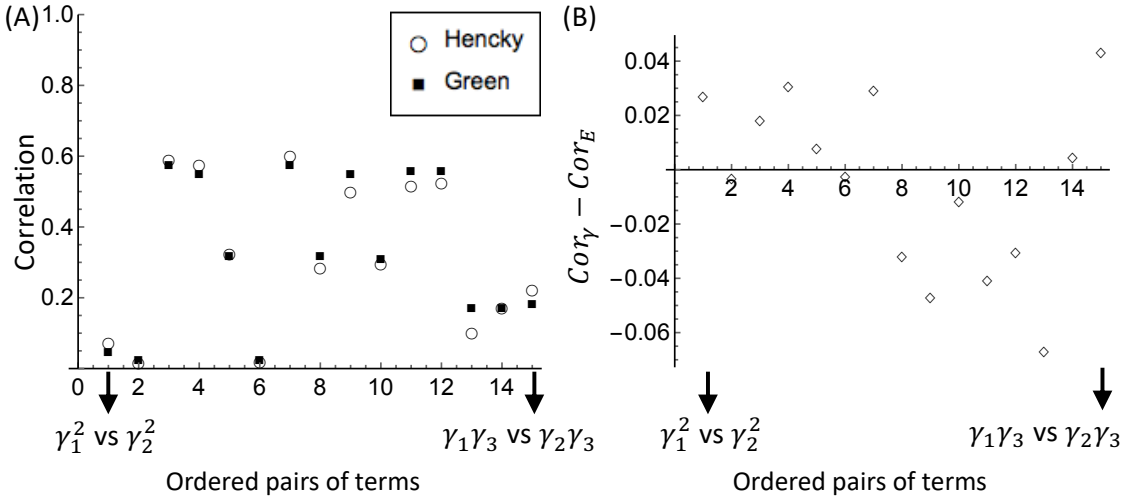

Figure A.2: (A) The correlation between parameters pairs in the generalized Fung model when using Green-Lagrange vs Hencky strains. (B) The difference in correlation between each pair of parameters, which is very small but with the Hencky strains being lower overall.

stresses increase exponentially under compression with Hencky strains, but only mildly with Green-Lagrange strains. We illustrated this again using the generalized Fung model (Eqn. A.6) in the physiologically relevant range, with Green-Lagrange or Hencky strain as the input variable (Fig. A.3). The reason for this is actually fairly simple, Green-Lagrange strain maps deformations from $\mathbf{E} : [0, \infty] \rightarrow [-1/2, \infty]$, while Hencky strains maps deformations from $\gamma : [0, \infty] \rightarrow [-\infty, \infty]$, drastically increasing the magnitude of the same strain value under compression. This behavior very convenient for modeling collageneous tissues, where collagen fibers crimps unload compression but do not increase the stress [6]. Due to all factors considered (Table A.1), we proceed to use the Green-Lagrange strain tensor as the best kinematic basis to formulate the effective constitutive model.

Table A.1: The difference between using the Green-Lagrange strain tensor versus the Hencky strains to formulate constitutive models. **Bold** text indicates key advantages and *Italic* text indicate key disadvantages.

Attributes	**Green-Lagrange strain**	**Hencky strain**
General	Most commonly used in modeling	**Easy to interpret physically**
Stress	Even simpler form for the 2nd Piola Kirchhoff stress $\mathbf{S} = \frac{\partial \Psi}{\partial E_m}\,\mathbf{m}_0 \otimes \mathbf{m}_0 + \frac{\partial \Psi}{\partial E_n}\,\mathbf{n}_0 \otimes \mathbf{n}_0 + \frac{1}{2}\,\frac{\partial \Psi}{\partial E_\phi}\,(\mathbf{m}_0 \otimes \mathbf{n}_0 + \mathbf{n}_0 \otimes \mathbf{m}_0)$	Simple form for the Cauchy stress $\mathbf{T} = \frac{\partial \Psi}{\partial \gamma_1}\,\mathbf{m}_t \otimes \mathbf{m}_t + \frac{\partial \Psi}{\partial \gamma_2}\,\mathbf{n}_t \otimes \mathbf{n}_t + \frac{\lambda_n}{\lambda_m}\,\frac{\partial \Psi}{\partial \gamma_3}\,(\mathbf{m}_t \otimes \mathbf{n}_t + \mathbf{n}_t \otimes \mathbf{m}_t)$
Elasticity tensor	**Much simpler form for the elasticity tensor**	*The equations for the elasticity tensor is extremely long*
Parameter covariance		**Modestly less correlation between parameters**
Response under compression	**Modest changes in stress under compression, behaves much more similar to soft tissues due to collagen fiber crimp**	*Behaves badly under large compression* • Log scaling cause the strain energy to increase exponentially with compression

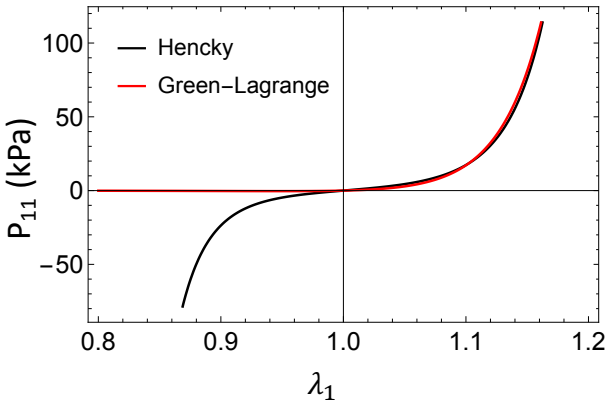

Figure A.3: The response of a generalized Fung model when using Green-Lagrange (Black) vs Hencky strains(Red). Both models are able to match extensional response nearly perfectly with respect to each other, but drastically differ under compression.

A.2 Elasticity tensor

An analytical form for the elasticity tensor is extremely important for fast and convergent numerical simulations. A constitutive model without a smooth, continuous, and convex elasticity tensor can pose significant problems for simulation of nonlinear materials to converge quickly, or even to converge at all. The strain basis used for the model can have significant impact on the form of the elasticity tensor. Here, we derived the generalized form of the elasticity tensor for using the Green-Lagrange basis (Eqn. 5.1) and the Hencky strain basis (Eqn. A.3). Note that this is the generalized form, which does not depend on the explicit form of the constitutive model, it is only a function of the strain basis and the response functions (derivatives of the strain energy function), whose form doesn't not have to be explicitly stated. The 9 response functions are:

$$\frac{\partial \Psi}{\partial E_m}, \quad \frac{\partial \Psi}{\partial E_n}, \quad \frac{\partial \Psi}{\partial E_\phi}, \quad \frac{\partial^2 \Psi}{\partial E_m^2}, \quad \frac{\partial^2 \Psi}{\partial E_n^2}, \quad \frac{\partial^2 \Psi}{\partial E_\phi^2}, \quad \frac{\partial^2 \Psi}{\partial E_m \partial E_n}, \quad \frac{\partial^2 \Psi}{\partial E_m \partial E_\phi}, \quad \frac{\partial^2 \Psi}{\partial E_n \partial E_\phi}. \tag{A.7}$$

A.2.1 Derivation with Green-Lagrange strain

The elasticity tensor is given by the second derivative of the strain energy function with respect to the right Cauchy strain. Using the chain rules, fully expanding all terms, and enforcing symmetry of partial derivatives, $\frac{\partial^2 \Psi}{\partial E_m \partial E_n} = \frac{\partial^2 \Psi}{\partial E_n \partial E_m}$, the generalized form for the elasticity tensor is given by

$$\begin{aligned}
\frac{\mathrm{d}^2\Psi}{\mathrm{d}\mathbf{C}^2} = & \frac{\partial \Psi}{\partial E_m} \frac{\mathrm{d}^2 E_m}{\mathrm{d}\mathbf{C}^2} + \frac{\partial \Psi}{\partial E_n} \frac{\mathrm{d}^2 E_n}{\mathrm{d}\mathbf{C}^2} + \frac{\partial \Psi}{\partial E_\phi} \frac{\mathrm{d}^2 E_\phi}{\mathrm{d}\mathbf{C}^2} \\
& + \frac{\partial^2 \Psi}{\partial E_m^2} \frac{\mathrm{d}E_m}{\mathrm{d}\mathbf{C}} \frac{\mathrm{d}E_m}{\mathrm{d}\mathbf{C}} + \frac{\partial^2 \Psi}{\partial E_n^2} \frac{\mathrm{d}E_n}{\mathrm{d}\mathbf{C}} \frac{\mathrm{d}E_n}{\mathrm{d}\mathbf{C}} + \frac{\partial \Psi}{\partial E_\phi} \frac{\mathrm{d}E_\phi}{\mathrm{d}\mathbf{C}} \frac{\mathrm{d}E_\phi}{\mathrm{d}\mathbf{C}} \\
& + \frac{\partial^2 \Psi}{\partial E_m \partial E_n} \left(\frac{\mathrm{d}E_n}{\mathrm{d}\mathbf{C}} \frac{\mathrm{d}E_m}{\mathrm{d}\mathbf{C}} + \frac{\mathrm{d}E_m}{\mathrm{d}\mathbf{C}} \frac{\mathrm{d}E_n}{\mathrm{d}\mathbf{C}} \right) \\
& + \frac{\partial^2 \Psi}{\partial E_m \partial E_\phi} \left(\frac{\mathrm{d}E_\phi}{\mathrm{d}\mathbf{C}} \frac{\mathrm{d}E_m}{\mathrm{d}\mathbf{C}} + \frac{\mathrm{d}E_m}{\mathrm{d}\mathbf{C}} \frac{\mathrm{d}E_\phi}{\mathrm{d}\mathbf{C}} \right) \\
& + \frac{\partial^2 \Psi}{\partial E_n \partial E_\phi} \left(\frac{\mathrm{d}E_n}{\mathrm{d}\mathbf{C}} \frac{\mathrm{d}E_\phi}{\mathrm{d}\mathbf{C}} + \frac{\mathrm{d}E_\phi}{\mathrm{d}\mathbf{C}} \frac{\mathrm{d}E_n}{\mathrm{d}\mathbf{C}} \right).
\end{aligned} \tag{A.8}$$

To break this down, we begin with the derivatives of the Green-Lagrange strains, which are given by,

$$\begin{aligned}
\frac{\mathrm{d}E_m}{\mathrm{d}\mathbf{C}} &= \frac{1}{2} \mathbf{m} \otimes \mathbf{m} \\
\frac{\mathrm{d}E_n}{\mathrm{d}\mathbf{C}} &= \frac{1}{2} \mathbf{n} \otimes \mathbf{n} \\
\frac{\mathrm{d}E_\phi}{\mathrm{d}\mathbf{C}} &= \frac{1}{4} \left(\mathbf{m} \otimes \mathbf{n} + \mathbf{n} \otimes \mathbf{m} \right),
\end{aligned} \tag{A.9}$$

and

$$\frac{\mathrm{d}^2 E_m}{\mathrm{d}\mathbf{C}^2} = \frac{\mathrm{d}^2 E_n}{\mathrm{d}\mathbf{C}^2} = \frac{\mathrm{d}^2 E_\phi}{\mathrm{d}\mathbf{C}^2} = \mathbf{0}. \tag{A.10}$$

Right away, the Green-Lagrange strains have the benefit of the second derivatives being zero, reducing the elasticity tensor (Eqn. A.8) from 9 to 6 terms. Substituting

with the partial derivatives (Eqn. A.9) gives

$$\begin{aligned}\frac{\mathrm{d}^2\Psi}{\mathrm{d}\mathbf{C}^2} =& \frac{1}{4}\frac{\partial^2\Psi}{\partial E_m^2}\,\mathbf{m}\otimes\mathbf{m}\otimes\mathbf{m}\otimes\mathbf{m} \\ &+ \frac{1}{8}\frac{\partial^2\Psi}{\partial E_m\partial E_\phi}\,(\mathbf{m}\otimes\mathbf{m}\otimes\mathbf{m}\otimes\mathbf{n}+\mathbf{m}\otimes\mathbf{m}\otimes\mathbf{n}\otimes\mathbf{m} \\ &\quad+\mathbf{m}\otimes\mathbf{n}\otimes\mathbf{m}\otimes\mathbf{m}+\mathbf{n}\otimes\mathbf{m}\otimes\mathbf{m}\otimes\mathbf{m}) \\ &+ \frac{1}{4}\frac{\partial^2\Psi}{\partial E_m\partial E_n}\,(\mathbf{m}\otimes\mathbf{m}\otimes\mathbf{n}\otimes\mathbf{n}+\mathbf{n}\otimes\mathbf{n}\otimes\mathbf{m}\otimes\mathbf{m}) \\ &+ \frac{1}{16}\frac{\partial^2\Psi}{\partial E_\phi^2}\,(\mathbf{m}\otimes\mathbf{n}\otimes\mathbf{m}\otimes\mathbf{n}+\mathbf{m}\otimes\mathbf{n}\otimes\mathbf{n}\otimes\mathbf{m} \\ &\quad+\mathbf{n}\otimes\mathbf{m}\otimes\mathbf{m}\otimes\mathbf{n}+\mathbf{n}\otimes\mathbf{m}\otimes\mathbf{n}\otimes\mathbf{m}) \\ &+ \frac{1}{8}\frac{\partial^2\Psi}{\partial E_n\partial E_\phi}\,(\mathbf{m}\otimes\mathbf{n}\otimes\mathbf{n}\otimes\mathbf{n}+\mathbf{n}\otimes\mathbf{m}\otimes\mathbf{n}\otimes\mathbf{n} \\ &\quad+\mathbf{n}\otimes\mathbf{n}\otimes\mathbf{m}\otimes\mathbf{n}+\mathbf{n}\otimes\mathbf{n}\otimes\mathbf{n}\otimes\mathbf{m}) \\ &+ \frac{1}{4}\frac{\partial^2\Psi}{\partial E_n^2}\,\mathbf{n}\otimes\mathbf{n}\otimes\mathbf{n}\otimes\mathbf{n}\end{aligned} \tag{A.11}$$

A.2.2 Derivation with Hencky strains

The elasticity tensor when using the Hencky strains is much more complex. For start, the second derivatives of the Hencky strains are non-zero. The derivatives themselves are complex both in form and conceptually. The derivation of the derivatives is not straight forward. To make this simpler, we start with an alternative definition for the Hencky strains, which relates the 4 variables, γ_1, γ_2, γ_3, and $\mathbf{C}$.

$$\begin{aligned}\gamma_1 &= \ln(\lambda_m), \quad \lambda_m^2 = \mathbf{m}\cdot\mathbf{C}\mathbf{m} \\ \gamma_2 &= \ln(\lambda_n), \quad \lambda_n^2 = \mathbf{n}\cdot\mathbf{C}\mathbf{n} - \lambda_m^2\phi^2 \\ \gamma_3 &= \phi, \qquad\qquad \phi = (\lambda_m)^{-2}\,\mathbf{m}\cdot\mathbf{C}\mathbf{n}.\end{aligned} \tag{A.12}$$

It is important here that with this definition, the vector basis, $\mathbf{m}$ and $\mathbf{n}$, are defined on the reference coordinate system, which does not change with deformation. By

chain rule, the first derivatives are as followed,

$$\frac{\mathrm{d}\gamma_1}{\mathrm{d}\mathbf{C}} = \frac{\partial\gamma_1}{\partial\lambda_m}\frac{\mathrm{d}\lambda_m}{\mathrm{d}\mathbf{C}}, \qquad \frac{\mathrm{d}\lambda_m^2}{\mathrm{d}\mathbf{C}} = \frac{\partial\lambda_m^2}{\partial\mathbf{C}} : \frac{\mathrm{d}\mathbf{C}}{\mathrm{d}\mathbf{C}} + \frac{\partial\lambda_m^2}{\partial\lambda_n}\frac{\mathrm{d}\lambda_n}{\mathrm{d}\mathbf{C}} + \frac{\partial\lambda_m^2}{\partial\phi}\frac{\mathrm{d}\phi}{\mathrm{d}\mathbf{C}} \tag{A.13a}$$

$$\frac{\mathrm{d}\gamma_2}{\mathrm{d}\mathbf{C}} = \frac{\partial\gamma_2}{\partial\lambda_n}\frac{\mathrm{d}\lambda_n}{\mathrm{d}\mathbf{C}}, \qquad \frac{\mathrm{d}\lambda_n^2}{\mathrm{d}\mathbf{C}} = \frac{\partial\lambda_n^2}{\partial\mathbf{C}} : \frac{\mathrm{d}\mathbf{C}}{\mathrm{d}\mathbf{C}} + \frac{\partial\lambda_n^2}{\partial\lambda_m}\frac{\mathrm{d}\lambda_m}{\mathrm{d}\mathbf{C}} + \frac{\partial\lambda_n^2}{\partial\phi}\frac{\mathrm{d}\phi}{\mathrm{d}\mathbf{C}} \tag{A.13b}$$

$$\frac{\mathrm{d}\gamma_3}{\mathrm{d}\mathbf{C}} = \frac{\mathrm{d}\phi}{\mathrm{d}\mathbf{C}}, \qquad \frac{\mathrm{d}\phi}{\mathrm{d}\mathbf{C}} = \frac{\partial\phi}{\partial\mathbf{C}} : \frac{\mathrm{d}\mathbf{C}}{\mathrm{d}\mathbf{C}} + \frac{\partial\phi}{\partial\lambda_m}\frac{\mathrm{d}\lambda_m}{\mathrm{d}\mathbf{C}} + \frac{\partial\phi}{\partial\lambda_n}\frac{\mathrm{d}\lambda_n}{\mathrm{d}\mathbf{C}}. \tag{A.13c}$$

First, note that all the partial derivatives are functions of each other. This is indeed problematic, but also note from equation A.12 that λ_m does not depend on λ_n and ϕ, and ϕ does not depend on λ_n. This means that the following partial derivatives are zero,

$$\frac{\partial\lambda_m}{\partial\lambda_n} = \frac{\partial\lambda_m}{\partial\phi} = \frac{\partial\phi}{\partial\lambda_n} = 0, \tag{A.14}$$

allowing the equations to be solved.

For the second derivatives, note from the definition we have above, the Hencky strains are only linear function of $\mathbf{C}$, thus their 2nd *partial derivatives* are zero with respect to $\mathbf{C}$ only,

$$\frac{\partial}{\partial\mathbf{C}}\left(\frac{\mathrm{d}\gamma_1}{\mathrm{d}\mathbf{C}}\right) = \frac{\partial}{\partial\mathbf{C}}\left(\frac{\mathrm{d}\gamma_2}{\mathrm{d}\mathbf{C}}\right) = \frac{\partial}{\partial\mathbf{C}}\left(\frac{\mathrm{d}\gamma_3}{\mathrm{d}\mathbf{C}}\right) = 0. \tag{A.15}$$

The second derivatives are thus defined to be,

$$\frac{\mathrm{d}}{\mathrm{d}\mathbf{C}}\left(\frac{\mathrm{d}\gamma_1}{\mathrm{d}\mathbf{C}}\right) = \frac{\partial}{\partial\lambda_m}\left(\frac{\mathrm{d}\gamma_1}{\mathrm{d}\mathbf{C}}\right)\frac{\mathrm{d}\lambda_m}{\mathrm{d}\mathbf{C}} + \frac{\partial}{\partial\lambda_n}\left(\frac{\mathrm{d}\gamma_1}{\mathrm{d}\mathbf{C}}\right)\frac{\mathrm{d}\lambda_n}{\mathrm{d}\mathbf{C}} + \frac{\partial}{\partial\phi}\left(\frac{\mathrm{d}\gamma_1}{\mathrm{d}\mathbf{C}}\right)\frac{\mathrm{d}\phi}{\mathrm{d}\mathbf{C}} \tag{A.16a}$$

$$\frac{\mathrm{d}}{\mathrm{d}\mathbf{C}}\left(\frac{\mathrm{d}\gamma_2}{\mathrm{d}\mathbf{C}}\right) = \frac{\partial}{\partial\lambda_m}\left(\frac{\mathrm{d}\gamma_2}{\mathrm{d}\mathbf{C}}\right)\frac{\mathrm{d}\lambda_m}{\mathrm{d}\mathbf{C}} + \frac{\partial}{\partial\lambda_n}\left(\frac{\mathrm{d}\gamma_2}{\mathrm{d}\mathbf{C}}\right)\frac{\mathrm{d}\lambda_n}{\mathrm{d}\mathbf{C}} + \frac{\partial}{\partial\phi}\left(\frac{\mathrm{d}\gamma_2}{\mathrm{d}\mathbf{C}}\right)\frac{\mathrm{d}\phi}{\mathrm{d}\mathbf{C}} \tag{A.16b}$$

$$\frac{\mathrm{d}}{\mathrm{d}\mathbf{C}}\left(\frac{\mathrm{d}\phi}{\mathrm{d}\mathbf{C}}\right) = \frac{\partial}{\partial\lambda_m}\left(\frac{\mathrm{d}\phi}{\mathrm{d}\mathbf{C}}\right)\frac{\mathrm{d}\lambda_m}{\mathrm{d}\mathbf{C}} + \frac{\partial}{\partial\lambda_n}\left(\frac{\mathrm{d}\phi}{\mathrm{d}\mathbf{C}}\right)\frac{\mathrm{d}\lambda_n}{\mathrm{d}\mathbf{C}} + \frac{\partial}{\partial\phi}\left(\frac{\mathrm{d}\phi}{\mathrm{d}\mathbf{C}}\right)\frac{\mathrm{d}\phi}{\mathrm{d}\mathbf{C}} \tag{A.16c}$$

Taking advantage of equation A.14, the first and second derivatives of the Hencky

strains are presented as followed:

$$\frac{\mathrm{d}\gamma_1}{\mathrm{d}\mathbf{C}} = \frac{1}{2\lambda_m^2}\mathbf{m}\otimes\mathbf{m} \tag{A.17a}$$

$$\frac{\mathrm{d}\gamma_2}{\mathrm{d}\mathbf{C}} = \frac{1}{2\lambda_n^2}\left(\mathbf{n}\otimes\mathbf{n} - \phi\left(\mathbf{m}\otimes\mathbf{n}+\mathbf{n}\otimes\mathbf{m}\right) + \phi^2\mathbf{m}\otimes\mathbf{m}\right) \tag{A.17b}$$

$$\frac{\mathrm{d}\gamma_3}{\mathrm{d}\mathbf{C}} = \frac{1}{2\lambda_m^2}\left(\mathbf{m}\otimes\mathbf{n}+\mathbf{n}\otimes\mathbf{m} - 2\phi\mathbf{m}\otimes\mathbf{m}\right) \tag{A.17c}$$

$$\frac{\mathrm{d}^2\gamma_1}{\mathrm{d}\mathbf{C}^2} = -\frac{1}{2}\frac{1}{\lambda_m^4}\mathbf{m}\otimes\mathbf{m}\otimes\mathbf{m}\otimes\mathbf{m} \tag{A.17d}$$

$$\begin{aligned}\frac{\mathrm{d}^2\gamma_2}{\mathrm{d}\mathbf{C}^2} =& -\frac{1}{2}\frac{1}{\lambda_n^4}\left[\mathbf{n}\otimes\mathbf{n}\otimes\mathbf{n}\otimes\mathbf{n} - \phi\mathbf{m}\otimes\mathbf{n}\otimes\mathbf{n}\otimes\mathbf{n} - \phi\mathbf{n}\otimes\mathbf{m}\otimes\mathbf{n}\otimes\mathbf{n}\right.\\ &-\phi\mathbf{n}\otimes\mathbf{n}\otimes\mathbf{m}\otimes\mathbf{n} - \phi\mathbf{n}\otimes\mathbf{n}\otimes\mathbf{n}\otimes\mathbf{m} + \phi^2\mathbf{m}\otimes\mathbf{m}\otimes\mathbf{n}\otimes\mathbf{n}\\ &\left.+\phi^2\mathbf{n}\otimes\mathbf{n}\otimes\mathbf{m}\otimes\mathbf{m}\right]\\ &-\left(\frac{1}{4}\frac{1}{\lambda_m^2\lambda_n^2}+\frac{1}{2}\phi^2\frac{1}{\lambda_n^4}\right)\left[\mathbf{m}\otimes\mathbf{n}\otimes\mathbf{m}\otimes\mathbf{n}+\mathbf{m}\otimes\mathbf{n}\otimes\mathbf{n}\otimes\mathbf{m}\right.\\ &\left.+\mathbf{n}\otimes\mathbf{m}\otimes\mathbf{m}\otimes\mathbf{n}+\mathbf{n}\otimes\mathbf{m}\otimes\mathbf{n}\otimes\mathbf{m}\right]\\ &+\left(\frac{1}{2}\phi\frac{1}{\lambda_m^2\lambda_n^2}+\frac{1}{2}\phi^3\frac{1}{\lambda_n^4}\right)\left[\mathbf{m}\otimes\mathbf{m}\otimes\mathbf{m}\otimes\mathbf{n}+\mathbf{m}\otimes\mathbf{m}\otimes\mathbf{n}\otimes\mathbf{m}\right.\\ &\left.+\mathbf{m}\otimes\mathbf{n}\otimes\mathbf{m}\otimes\mathbf{m}+\mathbf{n}\otimes\mathbf{m}\otimes\mathbf{m}\otimes\mathbf{m}\right]\\ &-\left(\phi^2\frac{1}{\lambda_m^2\lambda_n^2}+\frac{1}{2}\phi^4\frac{1}{\lambda_n^4}\right)\left[\mathbf{m}\otimes\mathbf{m}\otimes\mathbf{m}\otimes\mathbf{m}\right]\end{aligned} \tag{A.17e}$$

$$\begin{aligned}\frac{\mathrm{d}^2\gamma_3}{\mathrm{d}\mathbf{C}^2} =& -\frac{1}{2}\frac{1}{\lambda_m^4}\times\left(\mathbf{n}\otimes\mathbf{m}\otimes\mathbf{m}\otimes\mathbf{m}+\mathbf{m}\otimes\mathbf{n}\otimes\mathbf{m}\otimes\mathbf{m}\right.\\ &\left.+\mathbf{m}\otimes\mathbf{m}\otimes\mathbf{n}\otimes\mathbf{m}+\mathbf{m}\otimes\mathbf{m}\otimes\mathbf{m}\otimes\mathbf{n}-4\phi\mathbf{m}\otimes\mathbf{m}\otimes\mathbf{m}\otimes\mathbf{m}\right)\end{aligned} \tag{A.17f}$$

Saving everyone from the algebra, without further ado, the most elegant form

of the elasticity tensor for constitutive models based on the Hencky strains is,

$$\begin{aligned}\frac{\mathrm{d}^2\Psi}{\mathrm{d}\mathbf{C}^2} =&\psi_1\mathbf{m}\otimes\mathbf{m}\otimes\mathbf{m}\otimes\mathbf{m}\\ &+\psi_2\left(\mathbf{m}\otimes\mathbf{m}\otimes\mathbf{m}\otimes\mathbf{n}+\mathbf{m}\otimes\mathbf{m}\otimes\mathbf{n}\otimes\mathbf{m}\right.\\ &\quad\left.+\,\mathbf{m}\otimes\mathbf{n}\otimes\mathbf{m}\otimes\mathbf{m}+\mathbf{n}\otimes\mathbf{m}\otimes\mathbf{m}\otimes\mathbf{m}\right)\\ &+\psi_3\left(\mathbf{m}\otimes\mathbf{m}\otimes\mathbf{n}\otimes\mathbf{n}+\mathbf{n}\otimes\mathbf{n}\otimes\mathbf{m}\otimes\mathbf{m}\right)\\ &+\psi_4\left(\mathbf{m}\otimes\mathbf{n}\otimes\mathbf{m}\otimes\mathbf{n}+\mathbf{m}\otimes\mathbf{n}\otimes\mathbf{n}\otimes\mathbf{m}\right.\\ &\quad\left.+\,\mathbf{n}\otimes\mathbf{m}\otimes\mathbf{m}\otimes\mathbf{n}+\mathbf{n}\otimes\mathbf{m}\otimes\mathbf{n}\otimes\mathbf{m}\right)\\ &+\psi_5\left(\mathbf{m}\otimes\mathbf{n}\otimes\mathbf{n}\otimes\mathbf{n}+\mathbf{n}\otimes\mathbf{m}\otimes\mathbf{n}\otimes\mathbf{n}+\mathbf{n}\otimes\mathbf{n}\otimes\mathbf{m}\otimes\mathbf{n}+\mathbf{n}\otimes\mathbf{n}\otimes\mathbf{n}\otimes\mathbf{m}\right)\\ &+\psi_6\mathbf{n}\otimes\mathbf{n}\otimes\mathbf{n}\otimes\mathbf{n}\end{aligned} \tag{A.18a}$$

$$\begin{aligned}\psi_1 =&-\frac{1}{2}\frac{1}{\lambda_m^4}W^{(1)}-\left(\frac{\phi^2}{\lambda_m^2\lambda_n^2}+\frac{1}{2}\frac{\phi^4}{\lambda_n^4}\right)W^{(2)}+2\frac{\phi}{\lambda_m^4}W^{(3)}+\frac{1}{4}\frac{1}{\lambda_m^4}W^{(11)}\\ &+\frac{1}{4}\frac{\phi^4}{\lambda_n^4}W^{(22)}+\frac{\phi^2}{\lambda_m^4}W^{(33)}+\frac{1}{2}\frac{\phi^2}{\lambda_m^2\lambda_n^2}W^{(12)}-\frac{\phi}{\lambda_m^4}W^{(13)}-\frac{\phi^3}{\lambda_m^2\lambda_n^2}W^{(23)}\end{aligned} \tag{A.18b}$$

$$\begin{aligned}\psi_2 =&\frac{1}{2}\left(\frac{\phi}{\lambda_m^2\lambda_n^2}+\frac{\phi^3}{\lambda_n^4}\right)W^{(2)}-\frac{1}{2}\frac{1}{\lambda_m^4}W^{(3)}-\frac{1}{4}\frac{\phi^3}{\lambda_n^4}W^{(22)}-\frac{1}{2}\frac{\phi}{\lambda_m^4}W^{(33)}\\ &-\frac{1}{4}\frac{\phi}{\lambda_m^2\lambda_n^2}W^{(12)}+\frac{1}{4}\frac{1}{\lambda_m^4}W^{(13)}+\frac{3}{4}\frac{\phi^2}{\lambda_m^2\lambda_n^2}W^{(23)}\end{aligned} \tag{A.18c}$$

$$\psi_3 =-\frac{1}{2}\frac{\phi^2}{\lambda_n^4}W^{(2)}+\frac{1}{4}\frac{\phi^2}{\lambda_n^4}W^{(22)}+\frac{1}{4}\frac{1}{\lambda_m^2\lambda_n^2}W^{(12)}-\frac{1}{2}\frac{\phi}{\lambda_m^2\lambda_n^2}W^{(23)} \tag{A.18d}$$

$$\psi_4 =-\left(\frac{1}{4}\frac{1}{\lambda_m^2\lambda_n^2}+\frac{1}{2}\frac{\phi^2}{\lambda_n^4}\right)W^{(2)}+\frac{1}{4}\frac{\phi^2}{\lambda_n^4}W^{(22)}+\frac{1}{4}\frac{1}{\lambda_m^4}W^{(33)}-\frac{1}{2}\frac{\phi}{\lambda_m^2\lambda_n^2}W^{(23)} \tag{A.18e}$$

$$\psi_5 =\frac{1}{2}\frac{\phi}{\lambda_n^4}W^{(2)}-\frac{1}{4}\frac{\phi}{\lambda_n^4}W^{(22)}+\frac{1}{4}\frac{1}{\lambda_m^2\lambda_n^2}W^{(23)} \tag{A.18f}$$

$$\psi_6 =-\frac{1}{2}\frac{1}{\lambda_n^4}W^{(2)}+\frac{1}{4}\frac{1}{\lambda_n^4}W^{(22)} \tag{A.18g}$$

where $W^{ij}=\frac{\partial^2\Psi}{\partial\gamma_i\partial\gamma_j}$.

Some final remarks The elasticity tensor for the Hencky strains (Eqn. A.18) are somewhat complicated, but most terms are weighted by γ_3, which is the shear angle ϕ. Under no shear, the form for the elasticity tensor reduces significantly, to similar in form to the Green-Lagrange strains (Eqn. A.11). The shear angle is typically a small value as well, making most terms in the elasticity tensor small as well. However, they are still necessary to accurately compute the elasticity tensor and are representative of the coupling between the strains components.

More interesting is perhaps that the Hencky strains overall leads to less covariance in model parameters overall, despite there being many more coupling terms than the Green-Lagrange strain. This is indicative of the covariance within the model form and of the tissue, which in turn is necessary to reproduce soft tissue responses. Due to this natural covariance of the tissues themselves, truly non-covariant models are not feasibly attainable. The level of covariance demonstrated by Ψ_{eff} (Eqn. 5.14) within are likely close to optimal without sacrificing for addition model complexity.

A.3 Parameter correlation

The Fisher's information matrix for a maximum likelihood problem described by a multivariate normally distributed statistical model is defined to be the negative of the second partial derivatives of the log-likelihood function with respect to the parameters, ξ_i, evaluated at the maximum likelihood estimates. When converting to least squares minimization, which is equivalent of a negative log-likelihood minimization, the information matrix is defined to be

$$\mathcal{I}_{jk} = \frac{\partial^2 \mathcal{F}}{\partial \xi_j \partial \xi_k} = \mathcal{H}_{jk}, \tag{A.19}$$

which is also exactly the Hessian matrix, $\boldsymbol{\mathcal{H}}$, at the best fit value. The D-optimality is the determinant of this information matrix, whereas other optimality measures are

mostly similar functions of this information matrix. The main reason is because, for a maximum likelihood problem governed by a normally distributed statistical model, the covariance matrix is exactly proportional to the inverse of the information matrix,

$$\mathbf{Cov} = \sigma^2 \boldsymbol{\mathcal{I}}^{-1}, \tag{A.20}$$

where σ^2 is the scalar variance of the statistical model, and can be estimated by the mean squared error weighted by the degree of freedom. Maximizing the D-optimality is equivalent of minimizing the variance of each parameter along with minimizing the covariance between parameters. Defining the objective function as

$$\mathcal{F} = \sum_i \big(f(x_i) - f_i\big)^2, \tag{A.21}$$

where $f(x_i)$ is the model and f_i are date points, the information matrix, or Hessian matrix, is given by

$$\begin{aligned} \frac{\partial \mathcal{F}}{\partial \xi_j} &= \sum_i 2\left(f(x_i) - f_i\right) \frac{\partial f(x_i)}{\partial \xi_j} \\ \mathcal{H}_{jk} = \frac{\partial^2 \mathcal{F}}{\partial \xi_j \partial \xi_k} &= \sum_i 2\,\frac{\partial f(x_i)}{\partial \xi_k}\,\frac{\partial f(x_i)}{\partial \xi_j} + 2\left(f(x_i) - f_i\right) \frac{\partial^2 f(x_i)}{\partial \xi_j \partial \xi_k} \end{aligned} \tag{A.22}$$

Note here that $\mathcal{J}_{ij} = \dfrac{\partial f(x_i)}{\partial \xi_j}$ is the Jacobian matrix for the non-linear least squares problem, and when the errors are small, i.e. when the model fits the data, in other words such that $\big(f(x_i) - f_i\big)$ is small or approximately 0, then the information matrix can by approximated by

$$\mathcal{I}_{jk} \approx \mathcal{J}_{ji}\mathcal{J}_{ik} \quad \text{or} \quad \boldsymbol{\mathcal{I}} \approx \boldsymbol{\mathcal{J}}^{\mathsf{T}}\boldsymbol{\mathcal{J}}, \tag{A.23}$$

a form much more familiar to most doing nonlinear least squares parameter estimation.

For Ψ_{eff} (Eqn. 5.14), let $f = c_0 Q' e^Q$ be the stress, where Q' is one of $\frac{\partial Q}{\partial E_m}$, $\frac{\partial Q}{\partial E_n}$, or $\frac{\partial Q}{\partial E_\phi}$. The Jacobian matrix is thus,

$$\mathcal{J}_{ij} = Q' e^Q \delta_{0j} + c_0 e^Q \frac{\partial Q'}{\partial \xi_j} + c_0 Q' e^Q \frac{\partial Q}{\partial \xi_j} \tag{A.24}$$

Note that since Q is a sum of polynomials, the second partial derivatives of Q and Q' with respect to ξ is precisely 0,

$$\frac{\partial^2 Q}{\partial \xi_j \partial \xi_k} = \frac{\partial^2 Q'}{\partial \xi_j \partial \xi_k} = 0. \tag{A.25}$$

Thus,

$$\begin{aligned}\frac{\partial^2 f}{\partial \xi_j \partial \xi_k} =& e^Q \delta_{0j} \frac{\partial Q'}{\partial \xi_k} + Q' e^Q \delta_{0j} \frac{\partial Q}{\partial \xi_k} + e^Q \frac{\partial Q'}{\partial \xi_j} \delta_{0k} + c_0 e^Q \frac{\partial Q'}{\partial \xi_j} \frac{\partial Q}{\partial \xi_k} + Q' e^Q \frac{\partial Q}{\partial \xi_j} \delta_{0k} \\ &+ c_0 e^Q \frac{\partial Q}{\partial \xi_j} \frac{\partial Q'}{\partial \xi_k} + c_0 Q' e^Q \frac{\partial Q}{\partial \xi_j} \frac{\partial Q}{\partial \xi_k}\end{aligned} \tag{A.26}$$

and the Hessian matrix is given by

$$\begin{aligned}\mathcal{H}_{jk} = 2 \sum_i \Bigg[& (Q' e^Q)^2 \delta_{0j} \delta_{0k} + c_0 Q' e^{2Q} \left(\delta_{0j} \frac{\partial Q'}{\partial \xi_k} + \frac{\partial Q'}{\partial \xi_j} \delta_{0k} \right) \\ & + c_0 (Q' e^Q)^2 \left(\delta_{0j} \frac{\partial Q}{\partial \xi_k} + \frac{\partial Q}{\partial \xi_j} \delta_{0k} \right) + (c_0 e^Q)^2 \frac{\partial Q'}{\partial \xi_j} \frac{\partial Q'}{\partial \xi_k} \\ & + (c_0 e^Q)^2 Q' \left(\frac{\partial Q'}{\partial \xi_j} \frac{\partial Q}{\partial \xi_k} + \frac{\partial Q}{\partial \xi_j} \frac{\partial Q'}{\partial \xi_k} \right) + (c_0 Q' e^Q)^2 \frac{\partial Q}{\partial \xi_j} \frac{\partial Q}{\partial \xi_k} \\ & + (c_0 Q' e^Q - f_i) \Bigg[e^Q \left(\delta_{0j} \frac{\partial Q'}{\partial \xi_k} + \frac{\partial Q'}{\partial \xi_j} \delta_{0k} \right) + Q' e^Q \left(\delta_{0j} \frac{\partial Q}{\partial \xi_k} + \frac{\partial Q}{\partial \xi_j} \delta_{0k} \right) \\ & + c_0 e^Q \left(\frac{\partial Q'}{\partial \xi_j} \frac{\partial Q}{\partial \xi_k} + \frac{\partial Q}{\partial \xi_j} \frac{\partial Q'}{\partial \xi_k} \right) + c_0 Q' e^Q \frac{\partial Q}{\partial \xi_j} \frac{\partial Q}{\partial \xi_k} \Bigg] \Bigg].\end{aligned} \tag{A.27}$$

Here, the summation is over each data point i and then sums for each component of stress S_m, S_n, and S_ϕ for $Q' = \frac{\partial Q}{\partial E_m}$, $\frac{\partial Q}{\partial E_n}$ and $\frac{\partial Q}{\partial E_\phi}$ respectively.

Using this approach, we compared the covariance of the model parameters for with Green-Lagrange strains and with Hencky strains for the Fung model (Table A.2&A.3, Fig. A.2), Ψ_{eff} (Eqn. 5.14) (Fig. A.4), and the polynomial series type model with $i, j, k \leq 6$ (Fig. A.5). The Hencky strains have lower parameter correlation as shown, but this appears to be minimal for Ψ_{eff}. The main benefits are seen with higher order coupling terms, and may still be beneficial for other constitutive models forms.

Table A.2: The correlation between model parameter when using Green Lagrange strains

	b_1	b_2	b_3	b_4	b_5	b_6
b_1	1.	0.0439916	0.0195981	-0.571707	-0.545413	0.314503
b_2	0.0439916	1.	0.0195981	-0.571707	0.314503	-0.545413
b_3	0.0195981	0.0195981	1.	0.306268	-0.555437	-0.555437
b_4	-0.571707	-0.571707	0.306268	1.	-0.167068	-0.167068
b_5	-0.545413	0.314503	-0.555437	-0.167068	1.	-0.179471
b_6	0.314503	-0.545413	-0.555437	-0.167068	-0.179471	1.

Table A.3: The correlation between model parameter when using Hencky strains

	b_1	b_2	b_3	b_4	b_5	b_6
b_1	1.	0.0709169	0.016636	-0.590101	-0.576084	0.322457
b_2	0.0709169	1.	-0.0173651	-0.601126	0.282699	-0.49857
b_3	0.016636	-0.0173651	1.	0.294546	-0.514879	-0.524943
b_4	-0.590101	-0.601126	0.294546	1.	-0.100413	-0.171661
b_5	-0.576084	0.282699	-0.514879	-0.100413	1.	-0.222942
b_6	0.322457	-0.49857	-0.524943	-0.171661	-0.222942	1.

A.4 Optimal *in silico* loading paths

The most optimal loading path is the equibiaxial stress loading paths. This is not surprising as the equibiaxial stress response generally given very intuitive in-

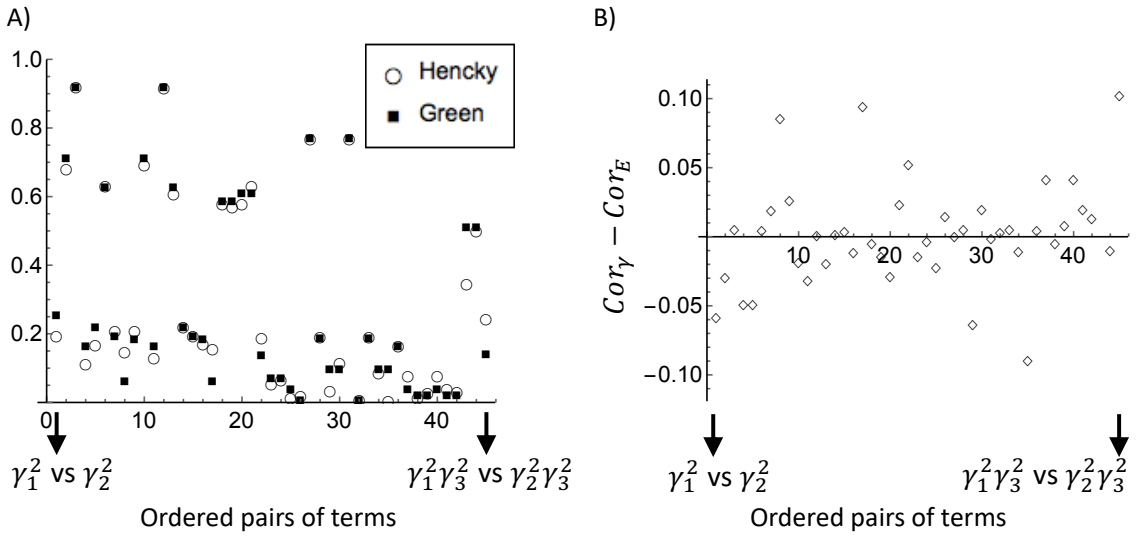

Figure A.4: (A) The correlation between parameters pairs in Ψ_{eff} (Eqn. 5.14) when using Green-Lagrange vs Hencky strains. (B) The difference in correlation between each pair of parameters is minimal.

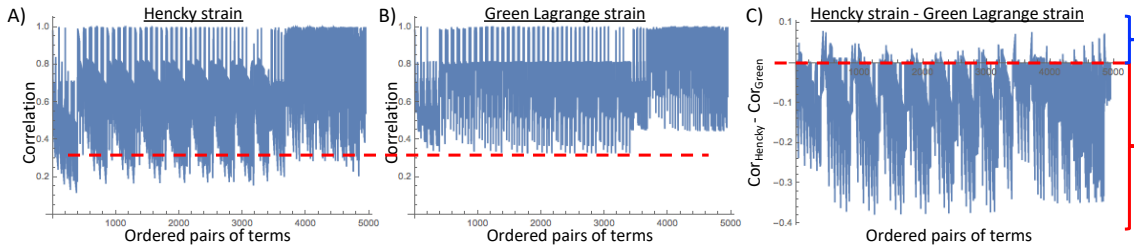

Figure A.5: (A) The correlation between parameters pairs in a polynomial series type model with powers up to 6 when using Green-Lagrange vs (B) Hencky strains. (C) The difference in correlation between each pair of parameters. The red bracketed terms are benefited from using Hencky strains whereas the significantly fewer blue bracketed terms has better correlations with Green-Lagrange strain.

formation on the mechanical response of soft tissues. Any odd number of loading paths will include the equibiaxial stress loading paths (Fig. A.6). Even when the number is even, we can observe that at least a few protocols are nearly equibiaxial in stress (Fig. A.7). For this reason, using an odd number of loading paths is highly recommended, as they will always include the minimal necessary set of loading paths, with the rest being average ratios in between (Fig. A.6). Even number of loading paths are generally very inconsistent and change slightly with each additional pairs of loading paths.

A.5 Additional results for other tissue types and effective constitutive model forms

Bovine pericardium is a good soft tissue to start with due high axes stretch coupling from their broad fiber splays. However, soft tissue behavior is drastically different with greater degree and anisotropy. For example, aortic valve leaflets have larger elastin content resulting in larger toe region and extremely narrow ODFs, which can cause contraction along the material axis under equibiaxial tension [1]. This behavior is hard for most constitutive models to replicate. However, Ψ_{eff} (Eqn. 5.14) has no problem replicating this behavior (Fig. A.8).

Based on D-optimality, we determined the optimal loading paths and shown its importance for model predictability. The equibiaxial stress loading path (near equibiaxial) came out as especially important, as it is included in all sets of optimal loading paths except for two and four (Fig. A.6&A.7). Commonly, when reproducing results from older publication, only the equibiaxial stress loading path may be included in the figures as it is the most informative. Indeed, using the equibiaxial stress loading paths simply results in much higher D-optimality than other choices.

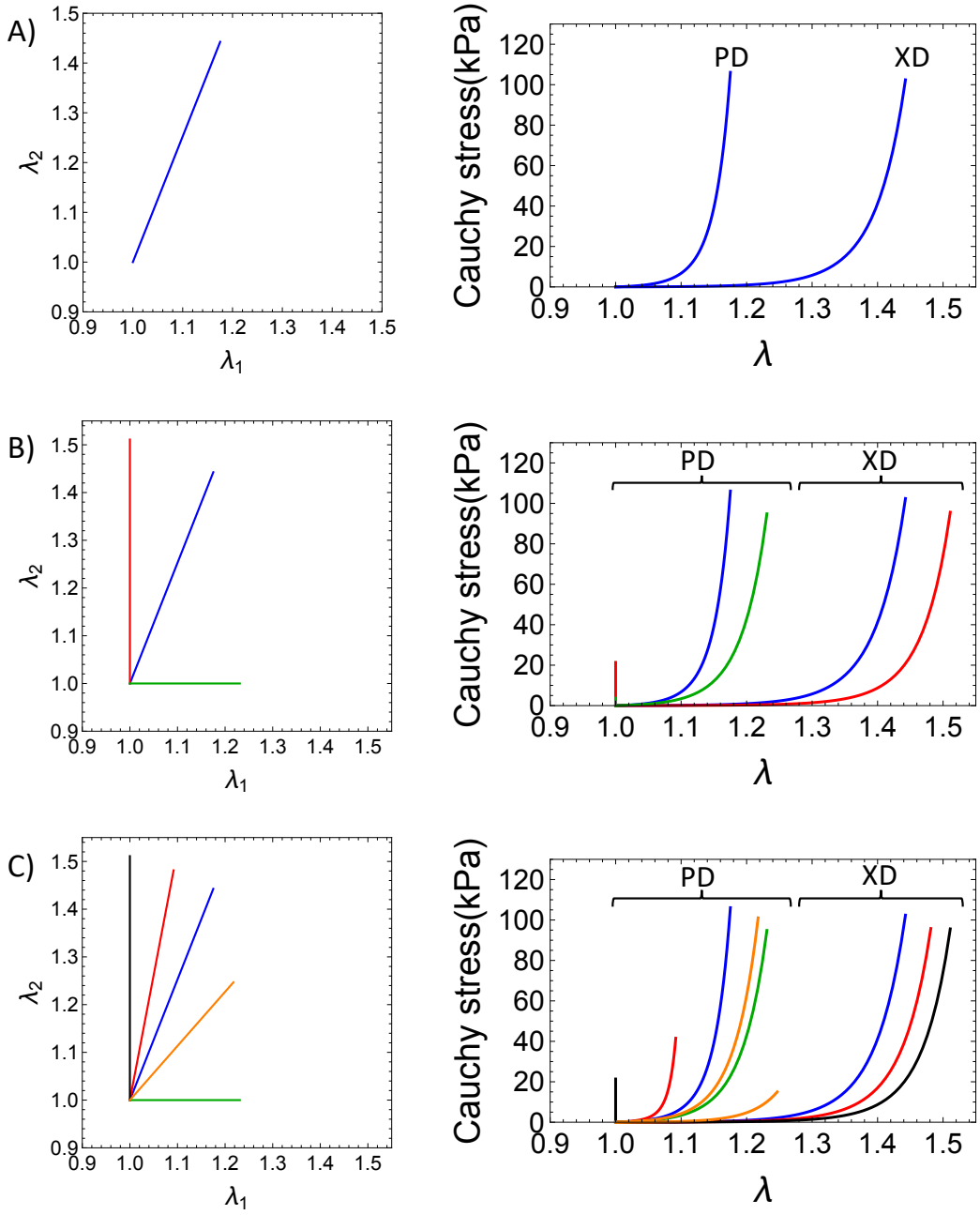

Figure A.6: The optimal loading paths for generating data for a given total odd number of paths as well as the associated mechanical response, which is consistently containing the equibiaxial stress loading path and the loading paths at the boundary.

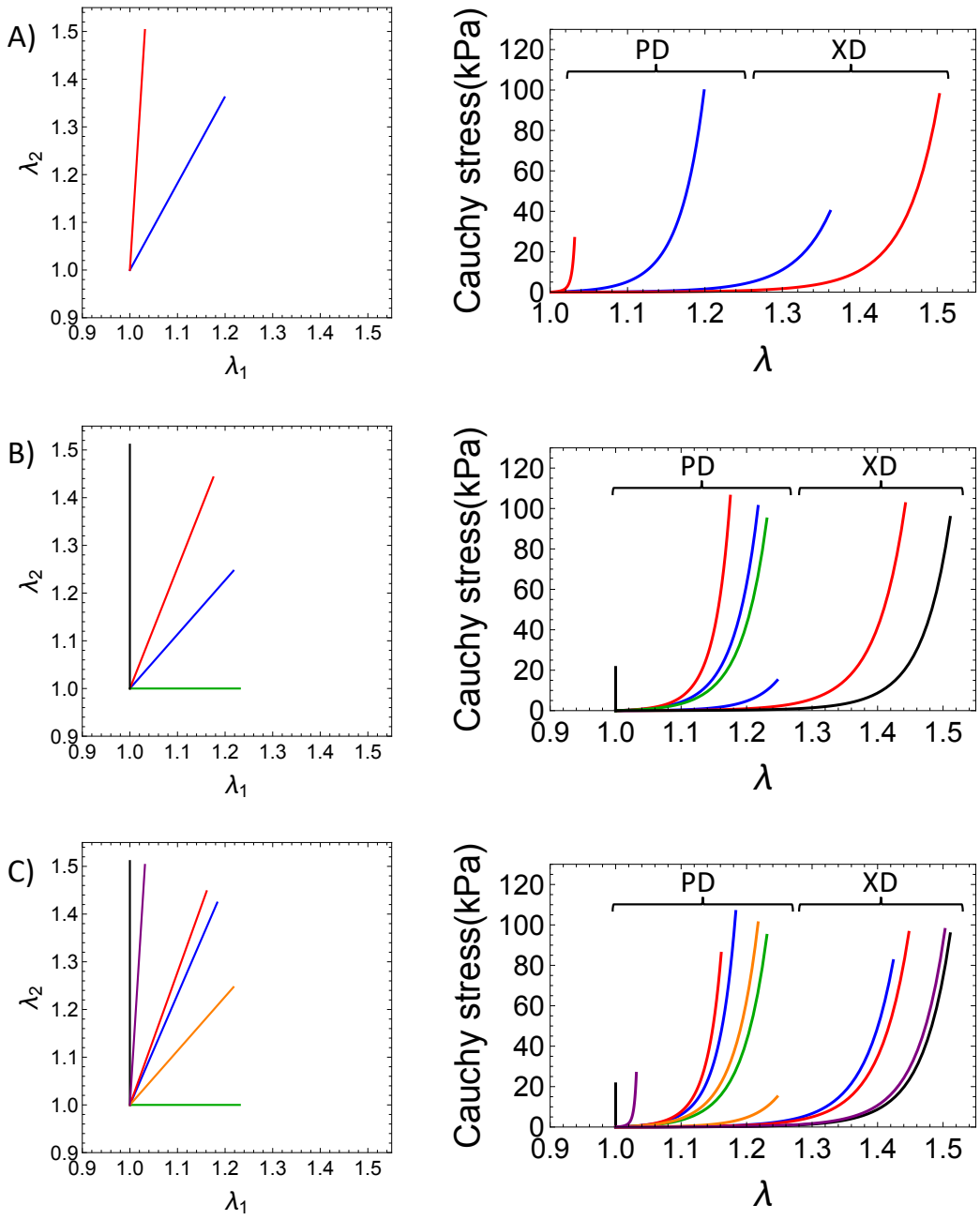

Figure A.7: The optimal loading paths for generating data for a given even total number as well as the associated mechanical response, which is much more unpredictable than the odd (Fig. A.6) but gravitates towards the boundaries and the equibiaxial loading paths as the number increases.

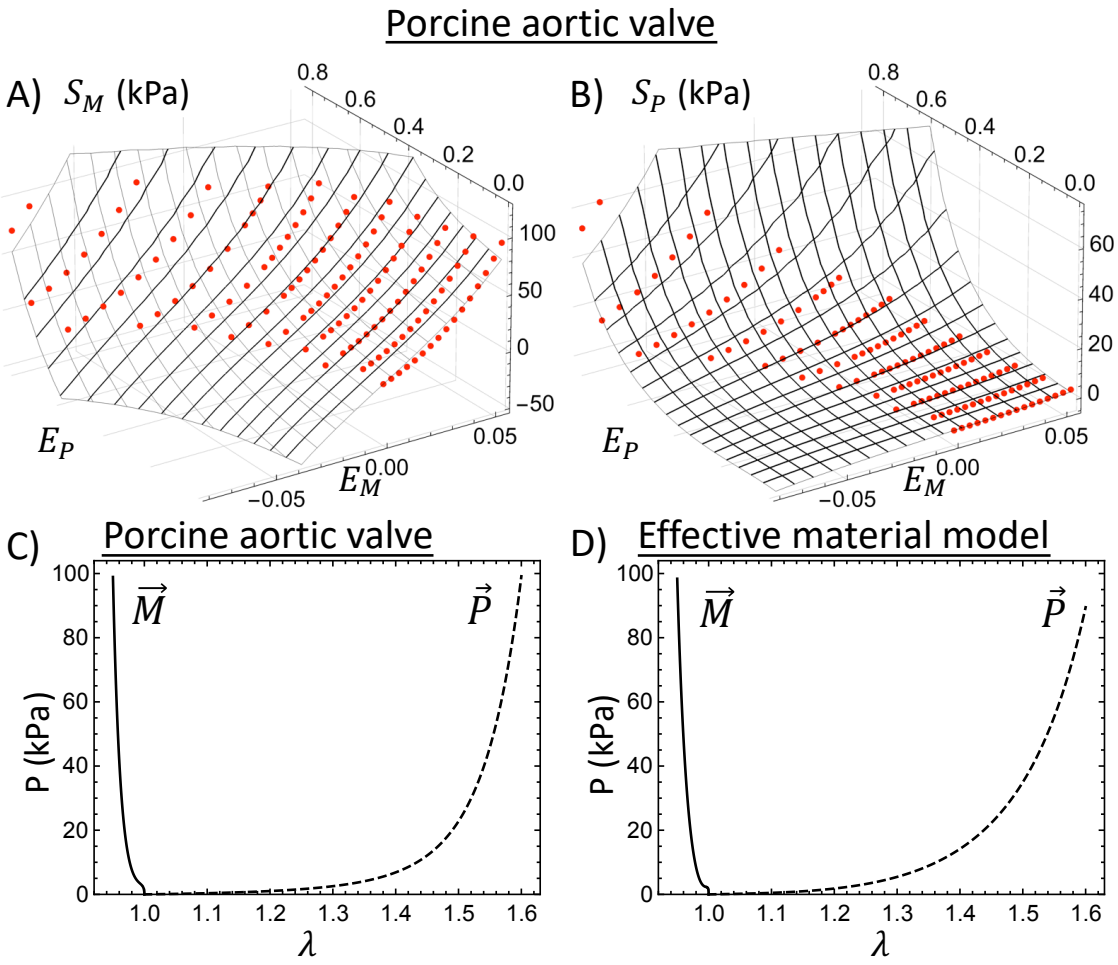

Figure A.8: Parameter estimation results for porcine aortic valve specimen with highly align collagen fibers, $\sigma_{ODF} = 10\,\text{deg}$. The response function A) S_m and b) S_n are shown. C) This specimen contracts in the preferred fiber direction under equi-biaxial tension, a trait of soft tissues with highly aligned collagen fibers. D) Ψ_{eff} (Eqn. 5.14) is able to reproduce this effect.

However, using this loading path alone is not sufficient for parameter estimation. Although the quality of fit is very good (Fig. A.9A&B), it cannot predict other loading paths (Fig. A.9C&D)

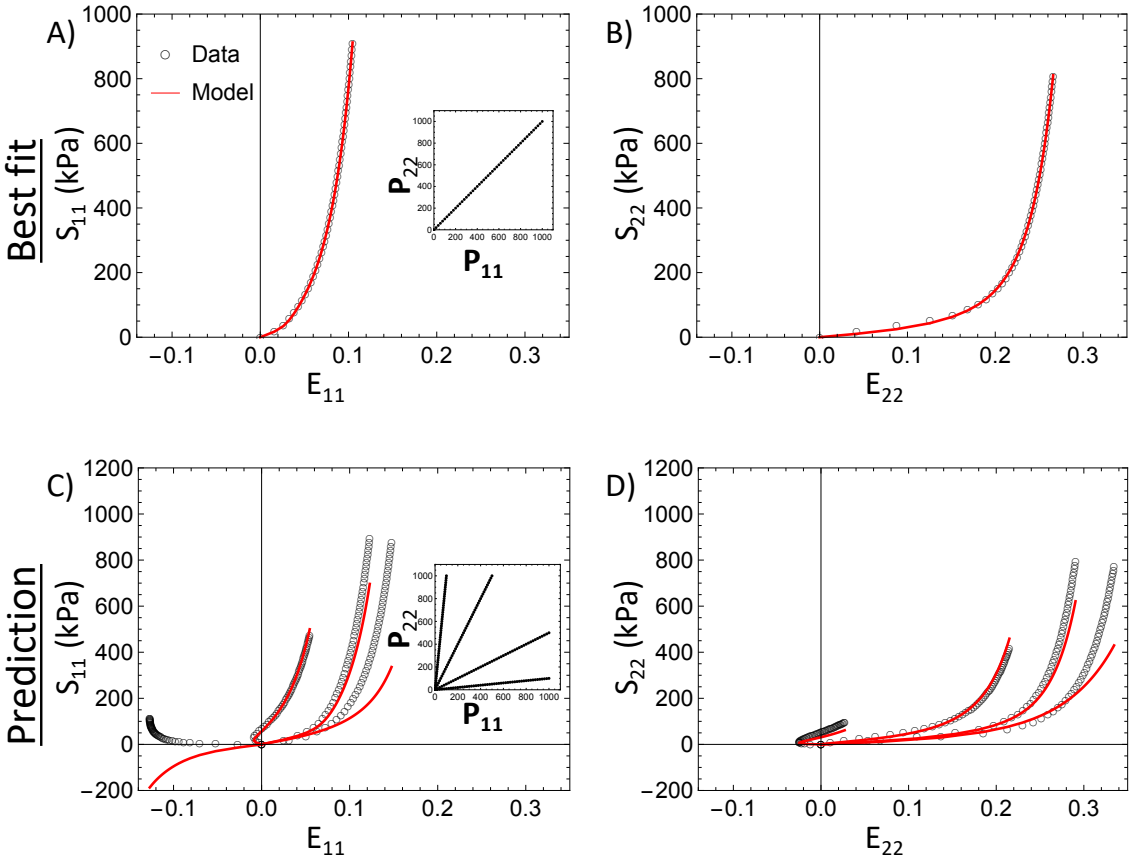

Figure A.9: Ψ_{eff} fitting to a single equi-biaxial loading path, showing the A) S_{11} and B) S_{22} component. The prediction for the C) S_{11} component and D) S_{22} component of the unfitted loading paths are poor. The inset in C shows the corresponding loading paths.

With the addition of other loading paths, even non-optimal, this can significantly improve the predictive capabilities (Fig. A.11A&B). However, we can clearly see that because the loading paths are not optimal, the 0.1/1 loading path is not predicted very well (Fig. A.11B). We tested to see if this can be improved through

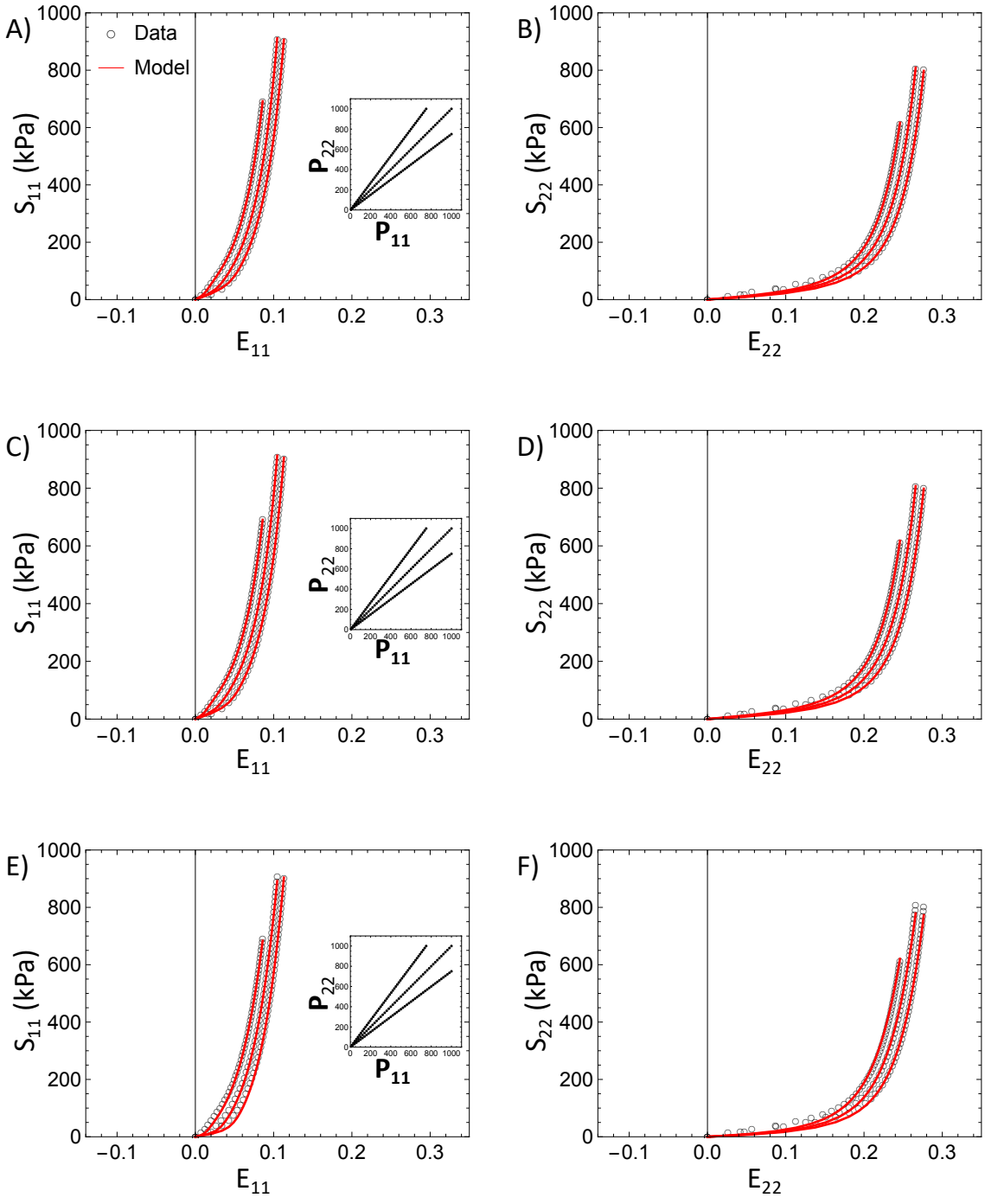

Figure A.10: All three models, A&B) Ψ_{eff} (Eqn. 5.14), C&D) extended Fung (Sun et al. [8] Eqn. 4), and E&F) the Sun model (A.28), can fit the data equally as well.

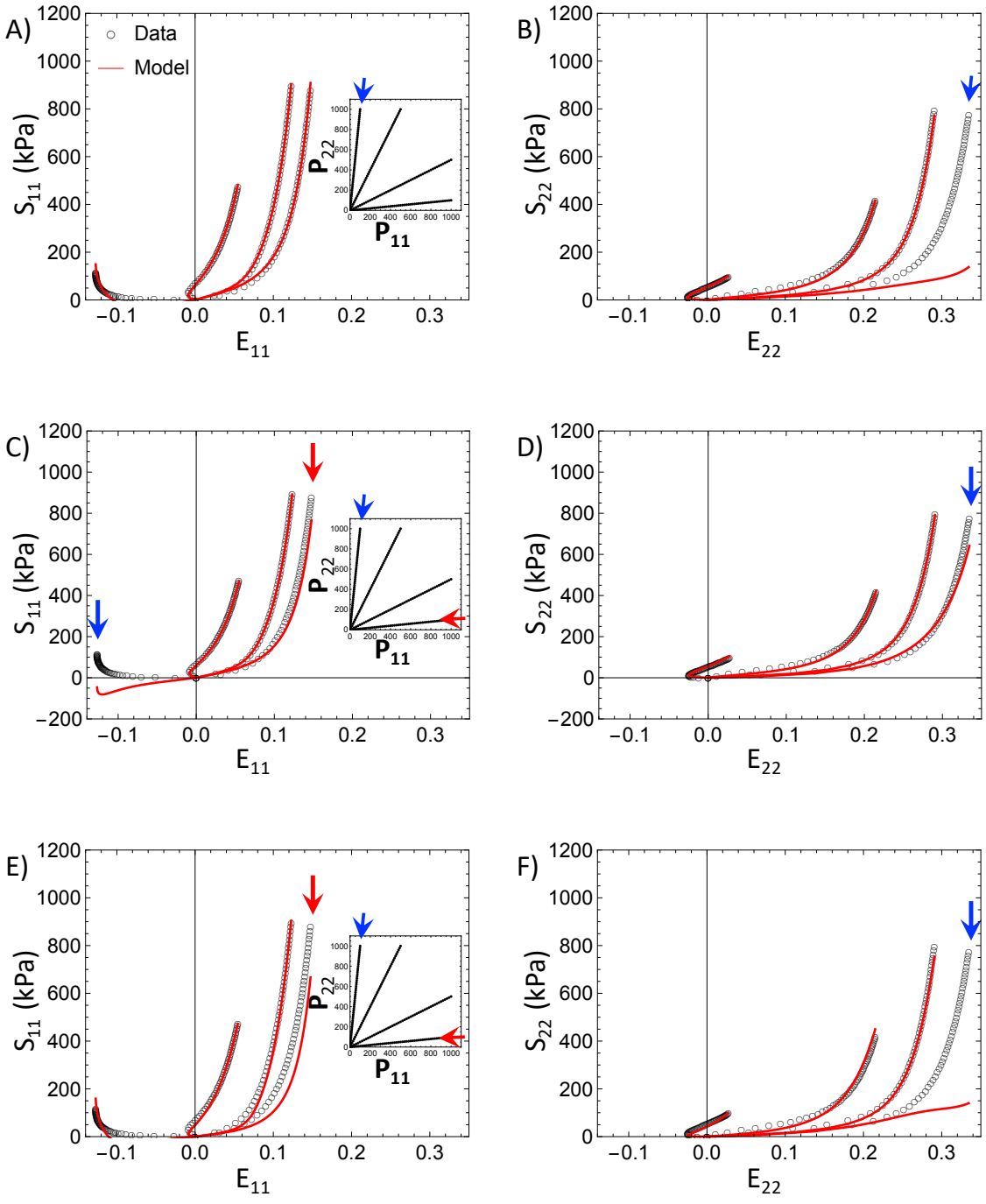

Figure A.11: The predictions for the unfitted loading paths from Fig. A.10. The blue and red arrows point out the poorly predicted paths, and which path they are on the inset figures.

more specific forms of Ψ_{eff} (Eqn. 5.14). For this, we looked at an extension of the generalized Fung model to quadratic terms presented by Sun *et al.* [8] to better fit the response of the glutaraldehyde cross-linked bovine pericardium. The additional terms are only of cubic and quartic powers, $B_{ijkl}E_{ij}^2E_{kl}^2$. In comparison to Ψ_{eff}, this is only missing $E_m^3E_n$ and $E_m^3E_n$,

$$\begin{aligned}\Psi =& c_0\left(e^Q-1\right)\\ Q =& A_1E_{11}^2+A_2E_{22}^2+2A_3E_{11}E_{22}+A_4E_{12}^2+2A_5E_{12}E_{11}\\ &+2A_6E_{12}E_{22}+B_1E_{11}^4+B_2E_{22}^4+2B_3E_{11}^2E_{22}^2+B_4E_{12}^4\\ &+2B_5E_{12}^2E_{11}^2+2B_6E_{12}^2E_{22}^2\end{aligned} \qquad \text{(Sun et al. [8] Eqn. 4)}$$

We will call this the extended Fung model. In addition, Sun *et al.* [8] also recommended a more minimalistic form, where only the coupling term $2B_3E_{11}^2E_{22}^2$ is added as ,

$$\begin{aligned}\Psi =& c_0\left(e^Q-1\right)\\ Q =& A_1E_{11}^2+A_2E_{22}^2+2A_3E_{11}E_{22}+A_4E_{12}^2+2A_5E_{12}E_{11}\\ &+2A_6E_{12}E_{22}+2B_3E_{11}^2E_{22}^2+B_4E_{12}^4.\end{aligned} \qquad \text{(A.28)}$$

We shall call this the Sun model.

Although the equality of fit are all equally as good A.10, the extended Fung model (Eqn. Sun et al. [8] Eqn. 4) predicts S_{22} component of the 0.1/1 loading path much better, but predicts the wrong sign for S_{11} for the same loading path, as well as predicting the 1/0.1 loading path worse (Fig. A.11C&D). The Sun model (Eqn. A.28) on the other hand is similar to Ψ_{eff} but worse at predicting S_{11} of the 1/0.1 loading path (Fig. A.11E&F). It's hard to predict how these constitutive models will behave when the loading paths are not optimal. This is especially true when only a single protocol is used, where predictions for all other protocols can be very poor (Fig. A.9). However, as little as three loading paths are needed to fully reproduce the

mechanical response of soft tissue over the entire range of deformations (Fig. 5.17).

Chapter Bibliography

[1] Kristen L. Billiar and Michael S. Sacks. Biaxial mechanical properties of the native and glutaraldehyde-treated aortic valve cusp: part II a structural constitutive model. *Journal of Biomechanical Engineering*, 122(4):327–35, August 2000. ISSN 0148-0731 (Print) 0148-0731 (Linking). doi: 10.1115/1.1287158. URL `http://www.ncbi.nlm.nih.gov/pubmed/11036555`.

[2] Veysel Erel and Alan D. Freed. Stress/strain basis pairs for anisotropic materials. *Composites Part B: Engineering*, 120:152–158, jul 2017. doi: 10.1016/j.compositesb.2017.03.065.

[3] A. D. Freed and A. R. Srinivasa. Logarithmic strain and its material derivative for a QR decomposition of the deformation gradient. *Acta Mechanica*, 226(8): 2645–2670, apr 2015. doi: 10.1007/s00707-015-1344-0.

[4] Alan Freed, Veysel Erel, and Michael Moreno. Conjugate stress/strain base pairs for planar analysis of biological tissues. *Journal of Mechanics of Materials and Structures*, 12(2):219–247, jan 2017. doi: 10.2140/jomms.2017.12.219.

[5] Michael S. Sacks. Experimentally tractable, pseudo-elastic constitutive law for biomembranes: I theory. *Journal of Biomechanical Engineering*, 125(1):94–99, feb 2003. doi: 10.1115/1.1530770.

[6] João S Soares, Will Zhang, and Michael S Sacks. A mathematical model for the determination of forming tissue moduli in needled-nonwoven scaffolds. *Acta Biomaterialia*, 51:220–236, March 2017. ISSN 1878-7568. doi: 10.1016/j.actbio.2016.12.038.

[7] A.R. Srinivasa. On the use of the upper triangular (or QR) decomposition for developing constitutive equations for Green-elastic materials. *International Journal of Engineering Science*, 60:1–12, nov 2012. doi: 10.1016/j.ijengsci.2012.05.003.

[8] W. Sun, M.S. Sacks, T.L. Sellaro, W.S. Slaughter, and M.J. Scott. Biaxial mechanical response of bioprosthetic heart valve biomaterials to high in-plane shear. *Journal of Biomechanical Engineering*, 125(3):372–380, jun 2003. doi: 10.1115/1.1572518.

[9] Wei Sun, Michael Sacks, Gregory Fulchiero, Joshua Lovekamp, Naren Vyavahare, and Michael Scott. Response of heterograft heart valve biomaterials to moderate cyclic loading. *Journal of Biomedical Materials Research*, 69A(4):658–669, June 2004. doi: 10.1002/jbm.a.30031. URL `http://www.ncbi.nlm.nih.gov/entrez/query.fcgi?cmd=Retrieve&db=PubMed&dopt=Citation&list_uids=15162408`.

Bibliography

[1] Margaret M. Adamczyk and Ivan Vesely. Characteristics of compressive strains in porcine aortic valves cusps. *The Journal of heart valve disease*, 11(1):75–83, January 2002. ISSN 0966-8519. URL `http://www.ncbi.nlm.nih.gov/entrez/query.fcgi?cmd=Retrieve&db=PubMed&dopt=Citation&list_uids=11843509`.

[2] Ankush Aggarwal. An improved parameter estimation and comparison for soft tissue constitutive models containing an exponential function. *Biomechanics and Modeling in Mechanobiology*, 16(4):1309–1327, mar 2017. doi: 10.1007/s10237-017-0889-3.

[3] Ankush Aggarwal and Michael S. Sacks. A framework for determination of heart valves' mechanical properties using inverse-modeling approach. In *Functional Imaging and Modeling of the Heart*, volume 9126, pages 285–294. Springer International Publishing, 2015. doi: 10.1007/978-3-319-20309-6_33.

[4] Ankush Aggarwal and Michael S. Sacks. An inverse modeling approach for semilunar heart valve leaflet mechanics: exploitation of tissue structure. *Biomechanics and Modeling in Mechanobiology*, 15(4):909–932, oct 2015. ISSN 1617-7959. doi: 10.1007/s10237-015-0732-7.

[5] Ankush Aggarwal, Vanessa S. Aguilar, Chung-Hao Lee, Giovanni Ferrari, Joseph H. Gorman, Rober C. Gorman, and Michael S. Sacks. Patient-specific modeling of heart valves: from image to simulation. In *Functional Imaging and Modeling of the Heart*, pages 141–149. Springer Berlin Heidelberg, 2013. ISBN 3-642-38898-1. doi: 10.1007/978-3-642-38899-6_17.

[6] Ankush Aggarwal, Alison M. Pouch, Eric Lai, John Lesicko, Paul A. Yushkevich, Joseph H. Gorman III, Robert C. Gorman, and Michael S. Sacks. In-vivo heterogeneous functional and residual strains in human aortic valve leaflets. *Journal of Biomechanics*, 49(12):2481–2490, aug 2016. ISSN 0021-9290. doi: 10.1016/j.jbiomech.2016.04.038.

[7] E. Aikawa and C. M. Otto. Look more closely at the valve: imaging calcific aortic valve disease. *Circulation*, 125(1):9–11, nov 2011. ISSN 0009-7322. doi: 10.1161/circulationaha.111.073452. URL `http://circ.ahajournals.org/content/125/1/9.full.pdf`.

[8] Ivan Alferiev, Stanley J. Stachelek, Zhibin Lu, Angela L. Fu, Tiffany L. Sellaro, Jeanne M. Connolly, Richard W. Bianco, Michael S. Sacks, and Robert J. Levy. Prevention of polyurethane valve cusp calcification with covalently attached bisphosphonate diethylamino moieties. *Journal of Biomedical Materials Research*, 66A(2):385–395, jul 2003. doi: 10.1002/jbm.a.10896. URL `http://www.ncbi.nlm.nih.gov/entrez/query.fcgi?cmd=Retrieve&db=PubMed&dopt=Citation&list_uids=12889009`.

[9] Rouzbeh Amini, Chad E. Eckert, Kevin Koomalsingh, Jeremy McGarvey, Masahito Minakawa, Joseph H. Gorman, Robert C. Gorman, and Michael S. Sacks. On the in vivo deformation of the mitral valve anterior leaflet: effects of annular geometry and referential configuration. *Annals of Biomedical Engineering*, 40(7):1455–1467, feb 2012. ISSN 1573-9686 (Electronic) 0090-6964 (Linking). doi: 10.1007/s10439-012-0524-5. URL `http://www.ncbi.nlm.nih.gov/pubmed/22327292`.

[10] R. D. Andrews, A. V. Tobolsky, and E. E. Hanson. The theory of permanent set

at elevated temperatures in natural and synthetic rubber vulcanizates. *Journal of Applied Physics*, 17(5):352–361, may 1946. doi: 10.1063/1.1707724.

[11] Reza Avazmohammadi, Michael R. Hill, Marc A. Simon, Will Zhang, and Michael S. Sacks. A novel constitutive model for passive right ventricular myocardium: evidence for myofiber-collagen fiber mechanical coupling. *Biomechanics and Modeling in Mechanobiology*, 16(2):561–581, oct 2016. ISSN 1617-7940. doi: 10.1007/s10237-016-0837-7.

[12] Salma Ayoub, Giovanni Ferrari, Robert C. Gorman, Joseph H. Gorman, Frederick J. Schoen, and Michael S. Sacks. *Heart Valve Biomechanics and Underlying Mechanobiology*, pages 1743–1780. American Cancer Society, 2016. ISBN 9780470650714. doi: 10.1002/cphy.c150048. URL `https://onlinelibrary.wiley.com/doi/abs/10.1002/cphy.c150048`.

[13] Ali N. Azadani, Sam Chitsaz, Peter B. Matthews, Nicolas Jaussaud, James Leung, Tonia Tsinman, Liang Ge, and Elaine E. Tseng. Comparison of mechanical properties of human ascending aorta and aortic sinuses. *The Annals of Thoracic Surgery*, 93(1):87–94, jan 2012. ISSN 0003-4975. doi: 10.1016/j.athoracsur.2011.08.002. URL `http://www.sciencedirect.com/science/article/pii/S0003497511019205`.

[14] Prosenjit Bagchi. Mesoscale simulation of blood flow in small vessels. *Biophysical Journal*, 92(6):1858–1877, mar 2007. doi: 10.1529/biophysj.106.095042.

[15] J. M. Ball. Strict convexity, strong ellipticity, and regularity in the calculus of variations. *Mathematical Proceedings of the Cambridge Philosophical Society*, 87(03):501–513, may 1980. doi: 10.1017/s0305004100056930.

[16] J. E. Barber, N. Ratliff, and I. Vesely. Mechanics of explanted bioprosthetic heart valves. *Biomedical Sciences Instrumentation*, 35:29–32, 1999. ISSN 0067-8856. URL http://www.ncbi.nlm.nih.gov/entrez/query.fcgi?cmd=Retrieve&db=PubMed&dopt=Citation&list_uids=11143364.

[17] Peter J. Basser and Carlo Pierpaoli. Microstructural and physiological features of tissues elucidated by quantitative-diffusion-tensor MRI. *Journal of Magnetic Resonance*, 213(2):560–570, dec 2011. doi: 10.1016/j.jmr.2011.09.022.

[18] Peter J. Basser, Sinisa Pajevic, Carlo Pierpaoli, Jeffrey Duda, and Akram Aldroubi. In vivo fiber tractography using DT-MRI data. *Magnetic Resonance in Medicine*, 44(4):625–632, 2000. doi: 10.1002/1522-2594(200010)44:4⟨625::aid-mrm17⟩3.0.co;2-o.

[19] Erik Beckmann, Juan B Grau, Rachana Sainger, Paolo Poggio, and Giovanni Ferrari. Insights into the use of biomarkers in calcific aortic valve disease. *The Journal of heart valve disease*, 19(4):441–452, July 2010. ISSN 0966-8519. URL http://www.ncbi.nlm.nih.gov/pmc/articles/PMC2941903/pdf/nihms214883.pdf.

[20] Chiara Bellini, Paul Glass, Metin Sitti, and Elena S. Di Martino. Biaxial mechanical modeling of the small intestine. *Journal of the Mechanical Behavior of Biomedical Materials*, 4(8):1727–1740, nov 2011. ISSN 1751-6161. doi: 10.1016/j.jmbbm.2011.05.030. URL http://www.sciencedirect.com/science/article/pii/S175161611100138X.

[21] J. A. Benton, H. B. Kern, L. A. Leinwand, P. D. Mariner, and K. S. Anseth. Statins block calcific nodule formation of valvular interstitial cells by inhibiting smooth muscle actin expression. *Arteriosclerosis, Thrombosis,*

and Vascular Biology, 29(11):1950–1957, aug 2009. ISSN 1079-5642. doi: 10.1161/atvbaha.109.195271. URL http://atvb.ahajournals.org/content/29/11/1950.full.pdf.

[22] K. L. Billiar and M. S. Sacks. Biaxial mechanical properties of the natural and glutaraldehyde treated aortic valve cusp: part I experimental results. *Journal of Biomechanical Engineering*, 122(1):23–30, February 2000. ISSN 0148-0731 (Print) 0148-0731 (Linking). doi: 10.1115/1.429624. URL http://www.ncbi.nlm.nih.gov/pubmed/10790826.

[23] Kristen Billiar, Jim Murray, Damien Laude, Ginger Abraham, and Nathaniel Bachrach. Effects of carbodiimide crosslinking conditions on the physical properties of laminated intestinal submucosa. *Journal of Biomedical Materials Research*, 56(1):101–108, July 2001. doi: 10.1002/1097-4636(200107)56:1⟨101::aid-jbm1074⟩3.0.co;2-6. URL http://www.ncbi.nlm.nih.gov/entrez/query.fcgi?cmd=Retrieve&db=PubMed&dopt=Citation&list_uids=11309796.

[24] Kristen L. Billiar and Michael S. Sacks. Biaxial mechanical properties of the native and glutaraldehyde-treated aortic valve cusp: part II a structural constitutive model. *Journal of Biomechanical Engineering*, 122(4):327–35, August 2000. ISSN 0148-0731 (Print) 0148-0731 (Linking). doi: 10.1115/1.1287158. URL http://www.ncbi.nlm.nih.gov/pubmed/11036555.

[25] A. Bini, K. G. Mann, B. J. Kudryk, and F. J. Schoen. Noncollagenous bone matrix proteins, calcification, and thrombosis in carotid artery atherosclerosis. *Arteriosclerosis, Thrombosis, and Vascular Biology*, 19(8):1852–1861, aug 1999. doi: 10.1161/01.atv.19.8.1852. URL

http://www.ncbi.nlm.nih.gov/htbin-post/Entrez/query?db=m&form=6&dopt=r&uid=0010446063http://www.atvbaha.org/cgi/content/full/19/8/1852http://www.atvbaha.org/cgi/content/abstract/19/8/1852.

[26] M.M. Black, I.C. Howard, X. Huang, and E.A. Patterson. A three-dimensional analysis of a bioprosthetic heart valve. *Journal of Biomechanics*, 24(9): 793–801, jan 1991. ISSN 0021-9290 (Print) 0021-9290 (Linking). doi: 10.1016/0021-9290(91)90304-6. URL http://www.ncbi.nlm.nih.gov/pubmed/1752863.

[27] Robert O. Bonow, Blase A. Carabello, Kanu Chatterjee, Antonio C. de Leon, David P. Faxon, Michael D. Freed, William H. Gaasch, Bruce Whitney Lytle, Rick A. Nishimura, Patrick T. O'Gara, Robert A. O'Rourke, Catherine M. Otto, Pravin M. Shah, Jack S. Shanewise, Sidney C. Smith, Alice K. Jacobs, Cynthia D. Adams, Jeffrey L. Anderson, Elliott M. Antman, David P. Faxon, Valentin Fuster, Jonathan L. Halperin, Loren F. Hiratzka, Sharon A. Hunt, Bruce W. Lytle, Rick Nishimura, Richard L. Page, and Barbara Riegel. ACC/AHA 2006 guidelines for the management of patients with valvular heart disease. *Journal of the American College of Cardiology*, 48(3):e1–e148, aug 2006. ISSN 1558-3597 (Electronic) 0735-1097 (Linking). doi: 10.1016/j.jacc.2006.05.021. URL http://www.ncbi.nlm.nih.gov/entrez/query.fcgi?cmd=Retrieve&db=PubMed&dopt=Citation&list_uids=16875962.

[28] N. S. Braunwald, T. Cooper, and A. G. Morrow. Complete replacement of the mitral valve. Successful clinical application of a flexible polyurethane prosthesis. *The Journal of thoracic and cardiovascular surgery*, 40:1–11, July 1960. ISSN 0022-5223.

[29] Rachel M. Buchanan and Michael S. Sacks. Interlayer micromechanics of the aortic heart valve leaflet. *Biomechanics and Modeling in Mechanobiology*, 13(4):813–826, nov 2013. ISSN 1617-7940 (Electronic) 1617-7940 (Linking). doi: 10.1007/s10237-013-0536-6. URL `http://www.ncbi.nlm.nih.gov/pubmed/24292631`.

[30] Markus J. Buehler. Atomistic and continuum modeling of mechanical properties of collagen: elasticity, fracture, and self-assembly. *Journal of Materials Research*, 21(08):1947–1961, aug 2006. ISSN 2044-5326. doi: 10.1557/jmr.2006.0236. URL `http://dx.doi.org/10.1557/jmr.2006.0236`.

[31] Markus J. Buehler. Nanomechanics of collagen fibrils under varying cross-link densities: atomistic and continuum studies. *Journal of the Mechanical Behavior of Biomedical Materials*, 1(1):59–67, jan 2008. doi: 10.1016/j.jmbbm.2007.04.001.

[32] F. Cacho, P.J. Elbischger, J.F. Rodriguez, M. Doblare, and G.A. Holzapfel. A constitutive model for fibrous tissues considering collagen fiber crimp. *International Journal of Non-Linear Mechanics*, 42(2):391–402, mar 2007. ISSN 0020-7462. doi: 10.1016/j.ijnonlinmec.2007.02.002. URL `http://www.sciencedirect.com/science/article/pii/S0020746207000558`.

[33] Christopher A. Carruthers, Christina M. Alfieri, Erinn M. Joyce, Simon C. Watkins, Katherine E. Yutzey, and Michael S. Sacks. Gene expression and collagen fiber micromechanical interactions of the semilunar heart valve interstitial cell. *Cellular and Molecular Bioengineering*, 5(3):254–265, may 2012. doi: 10.1007/s12195-012-0230-2.

[34] Christopher A. Carruthers, Bryan Good, Antonio D'Amore, Jun Liao, Rouzbeh Amini, Simon C. Watkins, and Michael S. Sacks. Alterations in the microstructure of the anterior mitral valve leaflet under physiological stress. In *ASME 2012 Summer Bioengineering Conference, Parts A and B*, pages 227–228. American Society of Mechanical Engineers, jun 2012. doi: 10.1115/sbc2012-80820.

[35] Francisco S. A. Cavalcante, Satoru Ito, Kelly Brewer, Hiroaki Sakai, Adriano M. Alencar, Murilo P. Almeida, José S. Andrade, Arnab Majumdar, Edward P. Ingenito, and Béla Suki. Mechanical interactions between collagen and proteoglycans: implications for the stability of lung tissue. *Journal of Applied Physiology*, 98(2):672–679, feb 2005. doi: 10.1152/japplphysiol.00619.2004. URL `http://www.ncbi.nlm.nih.gov/entrez/query.fcgi?cmd=Retrieve&db=PubMed&dopt=Citation&list_uids=15448123`.

[36] John A. Chapman and David J. S. Hulmes. Electron microscopy of the collagen fibril. In A. Ruggeri and P. M. Motto, editors, *Ultrastructure of the Connective Tissue Matrix*, pages 1–33. Springer US, Boston, 1984. doi: 10.1007/978-1-4613-2831-5_1.

[37] Huan Chen, Yi Liu, Xuefeng Zhao, Yoram Lanir, and Ghassan S. Kassab. A micromechanics finite-strain constitutive model of fibrous tissue. *Journal of the Mechanics and Physics of Solids*, 59(9):1823–1837, sep 2011. ISSN 0022-5096 (Electronic) 0022-5096 (Linking). doi: 10.1016/j.jmps.2011.05.012. URL `http://www.ncbi.nlm.nih.gov/pubmed/21927506`.

[38] Rui Cheng, Yong G. Lai, and Krishnan B. Chandran. Three-dimensional fluid-structure interaction simulation of bileaflet mechanical heart valve flow dynamics. *Annals of Biomedical Engineering*, 32(11):1471–1483,

nov 2004. ISSN 0090-6964 (Print). doi: 10.1114/b:abme.0000049032.51742.10. URL http://www.ncbi.nlm.nih.gov/entrez/query.fcgi?cmd=Retrieve&db=PubMed&dopt=Citation&list_uids=15636108.

[39] D T Cheung, P DiCesare, P D Benya, E Libaw, and M E Nimni. The presence of intermolecular disulfide cross-links in type III collagen. *The Journal of biological chemistry*, 258(12):7774–7778, June 1983. ISSN 0021-9258.

[40] David T. Cheung and Marcel E. Nimni. Mechanism of crosslinking of proteins by glutaraldehyde I: reaction with model compounds. *Connective Tissue Research*, 10(2):187–199, jan 1982. doi: 10.3109/03008208209034418.

[41] David T. Cheung and Marcel E. Nimni. Mechanism of crosslinking of proteins by glutaraldehyde II.: reaction with monomeric and polymeric collagen. *Connective Tissue Research*, 10(2):201–216, jan 1982. doi: 10.3109/03008208209034419.

[42] David T. Cheung, Natasha Perelman, Ellen C. Ko, and Marcel e. Nimni. Mechanism of crosslinking of proteins by glutaraldehyde III: reaction with collagen in tissues. *Connective Tissue Research*, 13(2):109–115, jan 1985. doi: 10.3109/03008208509152389.

[43] David T. Cheung, Deborah Tong, Natasha Perelman, Delia Ertl, and Marcel E. Nimni. Mechanism of crosslinking of proteins by glutaraldehyde IV: in vitro and in vivo stability of a crosslinked collagen matrix. *Connective Tissue Research*, 25(1):27–34, jan 1990. doi: 10.3109/03008209009009810.

[44] Grant W. Christie and Brian G. Barratt-Boyes. Age-dependent changes in the radial stretch of human aortic valve leaflets determined by biaxial testing. *The*

Annals of Thoracic Surgery, 60(2 Suppl):S156–S159, aug 1995. doi: 10.1016/0003-4975(95)00219-b.

[45] M. F. Coughlin, B. Suki, and D. Stamenovic. Dynamic behavior of lung parenchyma in shear. *Journal of Applied Physiology*, 80 (6):1880–1890, jun 1996. doi: 10.1152/jappl.1996.80.6.1880. URL http://www.ncbi.nlm.nih.gov/entrez/query.fcgi?cmd=Retrieve&db=PubMed&dopt=Citation&list_uids=8806890.

[46] T. Courtney, M. S. Sacks, J. Stankus, J. Guan, and W. R. Wagner. Design and analysis of tissue engineering scaffolds that mimic soft tissue mechanical anisotropy. *Biomaterials*, 27(19):3631–8, July 2006. ISSN 0142-9612 (Print). URL http://www.ncbi.nlm.nih.gov/entrez/query.fcgi?cmd=Retrieve&db=PubMed&dopt=Citation&list_uids=16545867.

[47] S. Joanna Cowell, David E. Newby, Robin J. Prescott, Peter Bloomfield, John Reid, David B. Northridge, and Nicholas A. Boon. A randomized trial of intensive lipid-lowering therapy in calcific aortic stenosis. *New England Journal of Medicine*, 352(23):2389–2397, jun 2005. ISSN 0028-4793. doi: 10.1056/nejmoa043876. URL http://www.nejm.org/doi/pdf/10.1056/NEJMoa043876.

[48] Stephen C. Cowin. Tissue growth and remodeling. *Annual Review of Biomedical Engineering*, 6(1):77–107, aug 2004. ISSN 1523-9829 (Print). doi: 10.1146/annurev.bioeng.6.040803.140250. URL http://www.ncbi.nlm.nih.gov/entrez/query.fcgi?cmd=Retrieve&db=PubMed&dopt=Citation&list_uids=15255763.

[49] L. H. H. Olde Damink, P. J. Dijkstra, M. J. A. Van Luyn, P. B. Van Wachem, P. Nieuwenhuis, and J. Feijen. Glutaraldehyde as a crosslinking agent for collagen-based biomaterials. *Journal of Materials Science: Materials in Medicine*, 6(8):460–472, aug 1995. doi: 10.1007/bf00123371.

[50] Antonio D'Amore, Joao S. Soares, John A. Stella, Will Zhang, Nicholas J. Amoroso, John E. Mayer, William R. Wagner, and Michael S. Sacks. Large strain stimulation promotes extracellular matrix production and stiffness in an elastomeric scaffold model. *Journal of the Mechanical Behavior of Biomedical Materials*, 62:619–635, sep 2016. ISSN 1878-0180 (Electronic) 1878-0180 (Linking). doi: 10.1016/j.jmbbm.2016.05.005. URL `https://www.ncbi.nlm.nih.gov/pubmed/27344402`.

[51] L. Debelle and A.M. Tamburro. Elastin: molecular description and function. *The International Journal of Biochemistry & Cell Biology*, 31(2):261–272, feb 1999. doi: 10.1016/s1357-2725(98)00098-3. URL `http://www.ncbi.nlm.nih.gov/htbin-post/Entrez/query?db=m&form=6&dopt=r&uid=10216959`.

[52] Laurent Debelle and Alain J.P. Alix. The structures of elastins and their function. *Biochimie*, 81(10):981 – 994, 1999. ISSN 0300-9084. doi: https://doi.org/10.1016/S0300-9084(99)00221-7. URL `http://www.sciencedirect.com/science/article/pii/S0300908499002217`.

[53] Niels J. B. Driessen, Carlijn V. C. Bouten, and Frank P. T. Baaijens. A structural constitutive model for collagenous cardiovascular tissues incorporating the angular fiber distribution. *Journal of Biomechanical Engineering*, 127(3):494–503, June 2005. ISSN 0148-0731 (Print). doi: 10.1115/

1.1894373. URL http://www.ncbi.nlm.nih.gov/entrez/query.fcgi?cmd=Retrieve&db=PubMed&dopt=Citation&list_uids=16060356.

[54] Chad E. Eckert, Brett Zubiate, Mathieu Vergnat, Joseph H. Gorman, Robert C. Gorman, and Michael S. Sacks. In vivo dynamic deformation of the mitral valve annulus. *Annals of Biomedical Engineering*, 37 (9):1757–1771, jul 2009. ISSN 1521-6047 (Electronic). doi: 10.1007/s10439-009-9749-3. URL http://www.ncbi.nlm.nih.gov/entrez/query.fcgi?cmd=Retrieve&db=PubMed&dopt=Citation&list_uids=19585241.

[55] Chad E. Eckert, Rong Fan, Brandon Mikulis, Mathew Barron, Christopher A. Carruthers, Vincent M. Friebe, Naren R. Vyavahare, and Michael S. Sacks. On the biomechanical role of glycosaminoglycans in the aortic heart valve leaflet. *Acta Biomaterialia*, 9(1):4653–4660, jan 2013. ISSN 1878-7568 (Electronic) 1742-7061 (Linking). doi: 10.1016/j.actbio.2012.09.031. URL http://www.ncbi.nlm.nih.gov/pubmed/23036945.

[56] S.J Eppell, B.N Smith, H Kahn, and R Ballarini. Nano measurements with micro-devices: mechanical properties of hydrated collagen fibrils. *Journal of The Royal Society Interface*, 3(6):117–121, feb 2006. doi: 10.1098/rsif.2005.0100. URL http://rsif.royalsocietypublishing.org/content/3/6/117.abstract.

[57] Veysel Erel and Alan D. Freed. Stress/strain basis pairs for anisotropic materials. *Composites Part B: Engineering*, 120:152–158, jul 2017. doi: 10.1016/j.compositesb.2017.03.065.

[58] Rong Fan and Michael S. Sacks. Simulation of planar soft tissues using a structural constitutive model: finite element implementation and validation.

Journal of Biomechanics, 47(9):2043–2054, jun 2014. doi: 10.1016/j.jbiomech.2014.03.014.

[59] Bahar Fata, Will Zhang, Rouzbeh Amini, and Michael S. Sacks. Insights into regional adaptations in the growing pulmonary artery using a meso-scale structural model: effects of ascending aorta impingement. *Journal of Biomechanical Engineering*, 136(2):021009–021009–13, feb 2014. ISSN 0148-0731. doi: 10.1115/1.4026457. URL http://dx.doi.org/10.1115/1.4026457.

[60] Aaron Fenster and Donnal B. Downey. 3-D ultrasound imaging: a review. *IEEE Engineering in Medicine and Biology Magazine*, 15(6):41–51, 1996. doi: 10.1109/51.544511.

[61] W. Flameng, P. Herijgers, and K. Bogaerts. Recurrence of mitral valve regurgitation after mitral valve repair in degenerative valve disease. *ACC Current Journal Review*, 12(4):85, jul 2003. doi: 10.1016/s1062-1458(03)00323-4. URL http://www.ncbi.nlm.nih.gov/entrez/query.fcgi?cmd=Retrieve&db=PubMed&dopt=Citation&list_uids=12668494.

[62] Willem Flameng, Bart Meuris, Paul Herijgers, and Marie-Christine Herregods. Durability of mitral valve repair in Barlow disease versus fibroelastic deficiency. *The Journal of Thoracic and Cardiovascular Surgery*, 135(2):274–282, feb 2008. ISSN 0022-5223. doi: 10.1016/j.jtcvs.2007.06.040.

[63] Gregory M. Fomovsky and Jeffrey W. Holmes. Evolution of scar structure, mechanics, and ventricular function after myocardial infarction in the rat. *American Journal of Physiology-Heart and Circulatory Physiology*, 298(1):H221–H228, jan 2010. doi: 10.1152/ajpheart.00495.2009. URL http://europepmc.org/abstract/MED/19897714.

[64] A. D. Freed and A. R. Srinivasa. Logarithmic strain and its material derivative for a QR decomposition of the deformation gradient. *Acta Mechanica*, 226(8): 2645–2670, apr 2015. doi: 10.1007/s00707-015-1344-0.

[65] Alan Freed, Veysel Erel, and Michael Moreno. Conjugate stress/strain base pairs for planar analysis of biological tissues. *Journal of Mechanics of Materials and Structures*, 12(2):219–247, jan 2017. doi: 10.2140/jomms.2017.12.219.

[66] Alan D. Freed, Daniel R. Einstein, and Michael S. Sacks. Hypoelastic soft tissues: part II: in-plane biaxial experiments. *Acta Mechanica*, 213(1-2):205–222, jul 2010. ISSN 1619-6937 (Electronic). doi: 10.1007/s00707-010-0357-y. URL `http://www.ncbi.nlm.nih.gov/pubmed/21394222`.

[67] R. V. Freeman. Spectrum of calcific aortic valve disease: pathogenesis, disease progression, and treatment strategies. *Circulation*, 111(24):3316–3326, jun 2005. ISSN 0009-7322. doi: 10.1161/circulationaha.104.486738. URL `http://circ.ahajournals.org/content/111/24/3316.full.pdf`.

[68] R. V. Freeman and C. M. Otto. Management of asymptomatic valvular aortic stenosis. *Indian Heart Journal*, 54(1):31–8, January 2002. ISSN 0019-4832 (Print) 0019-4832.

[69] Y. C. Fung. *Biomechanics: Mechanical Properties of Living Tissues*. Springer Verlag, New York, 2nd edition, 1993.

[70] Y. C. Fung, K. Fronek, and P. Patitucci. Pseudoelasticity of arteries and the choice of its mathematical expression. *American Journal of Physiology-Heart and Circulatory Physiology*, 237(5):H620–H631, nov 1979. doi: 10.1152/ajpheart.1979.237.5.h620.

[71] K. Garikipati, S. Göktepe, and C. Miehe. Elastica-based strain energy functions for soft biological tissue. *Journal of the Mechanics and Physics of Solids*, 56(4):1693–1713, April 2008. ISSN 0022-5096. doi: 10.1016/j.jmps.2007.07.005. URL http://www.sciencedirect.com/science/article/pii/S0022509607001597.

[72] K. Gelse, E. Poschl, and T. Aigner. Collagens–structure, function, and biosynthesis. *Advanced Drug Delivery Reviews*, 55(12):1531–1546, nov 2003. ISSN 0169-409X (Print). doi: 10.1016/j.addr.2003.08.002. URL http://www.ncbi.nlm.nih.gov/entrez/query.fcgi?cmd=Retrieve&db=PubMed&dopt=Citation&list_uids=14623400.

[73] E. Gendler, S. Gendler, and M. E. Nimni. Toxic reactions evoked by glutaraldehyde-fixed pericardium and cardiac valve tissue bioprosthesis. *Journal of Biomedical Materials Research*, 18(7):727–736, sep 1984. ISSN 1097-4636. doi: 10.1002/jbm.820180703. URL http://dx.doi.org/10.1002/jbm.820180703.

[74] Eileen Gentleman, Andrea N. Lay, Darryl A. Dickerson, Eric A. Nauman, Glen A. Livesay, and Kay C. Dee. Mechanical characterization of collagen fibers and scaffolds for tissue engineering. *Biomaterials*, 24(21):3805–3813, sep 2003. ISSN 0142-9612. doi: 10.1016/s0142-9612(03)00206-0. URL http://www.sciencedirect.com/science/article/pii/S0142961203002060.

[75] S. Michael Gharacholou, Barry L. Karon, Clarence Shub, and Patricia A. Pellikka. Aortic valve sclerosis and clinical outcomes: moving toward a definition. *The American Journal of Medicine*, 124(2):103–110, feb 2011. ISSN 0002-9343.

doi: 10.1016/j.amjmed.2010.10.012. URL http://www.amjmed.com/article/S0002-9343(10)00913-7/abstract.

[76] George T. Gilbert. Positive definite matrices and Sylvester's criterion. *The American Mathematical Monthly*, 98(1):44, jan 1991. doi: 10.2307/2324036.

[77] R.L. Gleason and J.D. Humphrey. A mixture model of arterial growth and remodeling in hypertension: altered muscle tone and tissue turnover. *Journal of Vascular Research*, 41(4):352–363, July 2004. doi: 10.1159/000080699. URL http://www.ncbi.nlm.nih.gov/entrez/query.fcgi?cmd=Retrieve&db=PubMed&dopt=Citation&list_uids=15353893.

[78] A. S. Go, D. Mozaffarian, V. L. Roger, E. J. Benjamin, J. D. Berry, M. J. Blaha, S. Dai, E. S. Ford, C. S. Fox, S. Franco, H. J. Fullerton, C. Gillespie, S. M. Hailpern, J. A. Heit, V. J. Howard, M. D. Huffman, S. E. Judd, B. M. Kissela, S. J. Kittner, D. T. Lackland, J. H. Lichtman, L. D. Lisabeth, R. H. Mackey, D. J. Magid, G. M. Marcus, A. Marelli, D. B. Matchar, D. K. McGuire, E. R. Mohler, C. S. Moy, M. E. Mussolino, R. W. Neumar, G. Nichol, D. K. Pandey, N. P. Paynter, M. J. Reeves, P. D. Sorlie, J. Stein, A. Towfighi, T. N. Turan, S. S. Virani, N. D. Wong, D. Woo, and M. B. Turner and. Heart disease and stroke statistics–2014 update: a report from the American Heart Association. *Circulation*, 129(3):e28–e292, dec 2013. ISSN 0009-7322. doi: 10.1161/01.cir.0000441139.02102.80. URL http://graphics.tx.ovid.com/ovftpdfs/FPDDNCGCFADEAN00/fs046/ovft/live/gv025/00003017/00003017-201401210-00019.pdf.

[79] G. Golomb, F. J. Schoen, M. S. Smith, J. Linden, M. Dixon, and R. J. Levy. The role of glutaraldehyde-induced cross-links in calcification of bovine pericardium

used in cardiac valve bioprostheses. *The American journal of pathology*, 127(1): 122–130, April 1987. ISSN 0002-9440. URL http://www.ncbi.nlm.nih.gov/htbin-post/Entrez/query?db=m&form=6&dopt=r&uid=0003105321.

[80] Joseph H. Gorman, Krishanu B. Gupta, James T. Streicher, Robert C. Gorman, Benjamin M. Jackson, Mark B. Ratcliffe, Daniel K. Bogen, and L.Henry Edmunds. Dynamic three-dimensional imaging of the mitral valve and left ventricle by rapid sonomicrometry array localization. *The Journal of Thoracic and Cardiovascular Surgery*, 112(3):712–724, sep 1996. doi: 10.1016/s0022-5223(96)70056-9. URL http://www.ncbi.nlm.nih.gov/entrez/query.fcgi?cmd=Retrieve&db=PubMed&dopt=Citation&list_uids=8800160.

[81] Joseph H Gorman, Benjamin M Jackson, Yoshiharu Enomoto, and Robert C Gorman. The effect of regional ischemia on mitral valve annular saddle shape. *The Annals of Thoracic Surgery*, 77(2):544–548, feb 2004. doi: 10.1016/s0003-4975(03)01354-7. URL http://www.ncbi.nlm.nih.gov/entrez/query.fcgi?cmd=Retrieve&db=PubMed&dopt=Citation&list_uids=14759435.

[82] Jonathan S. Grashow, Michael S. Sacks, Jun Liao, and Ajit P. Yoganathan. Planar biaxial creep and stress relaxation of the mitral valve anterior leaflet. *Annals of Biomedical Engineering*, 34(10): 1509–1518, October 2006. ISSN 0090-6964 (Print). doi: 10.1007/s10439-006-9183-8. URL http://www.ncbi.nlm.nih.gov/entrez/query.fcgi?cmd=Retrieve&db=PubMed&dopt=Citation&list_uids=17016761.

[83] Jonathan S. Grashow, Ajit P. Yoganathan, and Michael S. Sacks. Biaxial stress-stretch behavior of the mitral valve anterior leaflet at physiologic strain rates. *Annals of Biomedical Engineering*, 34(2):315–325, feb 2006. doi: 10.1007/

s10439-005-9027-y. URL http://www.ncbi.nlm.nih.gov/entrez/query.fcgi?cmd=Retrieve&db=PubMed&dopt=Citation&list_uids=16450193.

[84] Juan B. Grau, Paolo Poggio, Rachana Sainger, William J. Vernick, William F. Seefried, Emanuela Branchetti, Benjamin C. Field, Joseph E. Bavaria, Michael A. Acker, and Giovanni Ferrari. Analysis of osteopontin levels for the identification of asymptomatic patients with calcific aortic valve disease. *The Annals of Thoracic Surgery*, 93(1):79–86, January 2012. ISSN 0003-4975. doi: 10.1016/j.athoracsur.2011.08.036. URL http://www.annalsthoracicsurgery.org/article/S0003-4975(11)02049-2/pdf.

[85] Diane E. Gregory and Jack P. Callaghan. A comparison of uniaxial and biaxial mechanical properties of the annulus fibrosus: a porcine model. *Journal of Biomechanical Engineering*, 133(2):024503, 2011. ISSN 0148-0731. doi: 10.1115/1.4003327. URL http://dx.doi.org/10.1115/1.4003327.

[86] Rafael Grytz and Günther Meschke. Constitutive modeling of crimped collagen fibrils in soft tissues. *Journal of the Mechanical Behavior of Biomedical Materials*, 2(5):522–533, October 2009. ISSN 1751-6161. doi: 10.1016/j.jmbbm.2008.12.009. URL http://www.sciencedirect.com/science/article/pii/S1751616108001227.

[87] Robert Guidoin, Yvan Douville, Marie-Annick Clavel, Ze Zhang, Mark Nutley, Philippe Pîbarot, and Guy Dionne. The marvel of percutaneous cardiovascular devices in the elderly. *Annals of the New York Academy of Sciences*, 1197(1):188–199, June 2010. ISSN 1749-6632 (Electronic) 0077-8923 (Linking). doi: 10.1111/j.1749-6632.2010.

05517.x. URL http://www.ncbi.nlm.nih.gov/entrez/query.fcgi?cmd=Retrieve&db=PubMed&dopt=Citation&list_uids=20536849.

[88] Yasuhiro Hanabusa, Hideo Takizawa, and Toshihiko Kuwabara. Numerical verification of a biaxial tensile test method using a cruciform specimen. *Journal of Materials Processing Technology*, 213(6):961–970, jun 2013. ISSN 0924-0136. doi: 10.1016/j.jmatprotec.2012.12.007. URL http://www.sciencedirect.com/science/article/pii/S0924013612003780.

[89] Kristi A. Hansen, Jeffrey A. Weiss, and Jennifer K. Barton. Recruitment of tendon crimp with applied tensile strain. *Journal of Biomechanical Engineering*, 124(1):72–7, February 2002. doi: 10.1115/1.1427698. URL http://www.ncbi.nlm.nih.gov/entrez/query.fcgi?cmd=Retrieve&db=PubMed&dopt=Citation&list_uids=11871607.

[90] Stephen L. Hilbert, Victor J. Ferrans, and W. Milton Swanson. Optical methods for the nondestructive evaluation of collagen morphology in bioprosthetic heart valves. *Journal of Biomedical Materials Research*, 20(9):1411–1421, nov 1986. doi: 10.1002/jbm.820200914.

[91] Stephen L. Hilbert, Mary K. Barrick, and Victor J. Ferrans. Porcine aortic valve bioprostheses: a morphologic comparison of the effects of fixation pressure. *Journal of Biomedical Materials Research*, 24(6):773–787, jun 1990. doi: 10.1002/jbm.820240611.

[92] Michael R. Hill, Xinjie Duan, Gregory A. Gibson, Simon Watkins, and Anne M. Robertson. A theoretical and non-destructive experimental approach for direct inclusion of measured collagen orientation and recruitment into mechanical models of the artery wall. *Journal of Biomechanics*, 45(5):762–771, March 2012.

ISSN 1873-2380 (Electronic) 0021-9290 (Linking). doi: 10.1016/j.jbiomech.2011.11.016. URL http://www.ncbi.nlm.nih.gov/pubmed/22305290.

[93] A.J. Hodge and J.A. Petruska. Recent studies with the electron microscope on ordered aggregates of the tropocollagen molecules. *Aspects of protein structure*, pages 289–300, 1963. URL https://ci.nii.ac.jp/naid/10027103318/en/.

[94] Yiemeng Hoi, Hui Meng, Scott H. Woodward, Bernard R. Bendok, Ricardo A. Hanel, Lee R. Guterman, and L. Nelson Hopkins. Effects of arterial geometry on aneurysm growth: three-dimensional computational fluid dynamics study. *Journal of Neurosurgery*, 101(4):676–681, oct 2004. doi: 10.3171/jns.2004.101.4.0676.

[95] Yaniv Hollander, David Durban, Xiao Lu, Ghassan S. Kassab, and Yoram Lanir. Constitutive modeling of coronary arterial media–comparison of three model classes. *Journal of Biomechanical Engineering*, 133(6):061008, June 2011. ISSN 1528-8951 (Electronic) 0148-0731 (Linking). doi: 10.1115/1.4004249. URL http://www.ncbi.nlm.nih.gov/pubmed/21744928.

[96] G. A. Holzapfel, J. A. Niestrawska, R. W. Ogden, A. J. Reinisch, and A. J. Schriefl. Modelling non-symmetric collagen fibre dispersion in arterial walls. *Journal of The Royal Society Interface*, 12(106):20150188–20150188, apr 2015. ISSN 1742-5689. doi: 10.1098/rsif.2015.0188. URL http://rsif.royalsocietypublishing.org/content/12/106/20150188.

[97] Gerhard A. Holzapfel. *Nonlinear Solid Mechanics: A Continuum Approach for Engineering*. John Wiley & Sons, Ltd., Chichester, 2000. ISBN 0471823198. URL https://www.ebook.de/de/product/3056011/gerhard_a_holzapfel_nonlinear_solid_mechanics.html.

[98] Gerhard A. Holzapfel, Thomas C. Gasser, and Ray W. Ogden. A new constitutive framework for arterial wall mechanics and a comparative study of material models. *Journal of Elasticity*, 61(1/3):1–48, 2000. doi: 10.1023/a:1010835316564.

[99] Ming-Chen Hsu, David Kamensky, Fei Xu, Josef Kiendl, Chenglong Wang, Michael C. H. Wu, Joshua Mineroff, Alessandro Reali, Yuri Bazilevs, and Michael S. Sacks. Dynamic and fluid-structure interaction simulations of bioprosthetic heart valves using parametric design with T-splines and Fung-type material models. *Computational Mechanics*, 55(6):1211–1225, may 2015. ISSN 0178-7675. doi: 10.1007/s00466-015-1166-x.

[100] J.-J. Hu, G.-W. Chen, Y.-C. Liu, and S.-S. Hsu. Influence of specimen geometry on the estimation of the planar biaxial mechanical properties of cruciform specimens. *Experimental Mechanics*, 54(4):615–631, April 2013. ISSN 0014-4851. doi: 10.1007/s11340-013-9826-2. URL `http://dx.doi.org/10.1007/s11340-013-9826-2`.

[101] X. Huang, M. M. Black, I. C. Howard, and E. A. Patterson. A two-dimensional finite element analysis of a bioprosthetic heart valve. *Journal of Biomechanics*, 23(8):753–762, jan 1990. ISSN 0021-9290 (Print) 0021-9290 (Linking). doi: 10.1016/0021-9290(90)90022-u. URL `http://www.ncbi.nlm.nih.gov/pubmed/2384487`.

[102] JD Humphrey and M Epstein. Cardiovascular solid mechanics: cells, tissues, and organs. *Applied Mechanics Reviews*, 55(5):B103, 2002. doi: 10.1115/1.1497492.

[103] J.D. Humphrey and K.R. Rajagopal. A constrained mixture model for growth and remodeling of soft tissues. *Mathematical models and methods in applied sciences*, 12(3):407–430, 2002. doi: 10.1142/s0218202502001714.

[104] Jason C. Isenburg, Dan T. Simionescu, and Naren R. Vyavahare. Tannic acid treatment enhances biostability and reduces calcification of glutaraldehyde fixed aortic wall. *Biomaterials*, 26(11):1237–1245, April 2005. ISSN 0142-9612 (Print). doi: 10.1016/j.biomaterials.2004.04.034. URL `http://www.ncbi.nlm.nih.gov/entrez/query.fcgi?cmd=Retrieve&db=PubMed&dopt=Citation&list_uids=15475053`.

[105] W. R. Eric Jamieson, Hilton Ling, Lawrence H Burr, Guy J Fradet, Robert T Miyagishima, Michael T Janusz, and Samuel V. Lichtenstein. Carpentier-Edwards supraannular porcine bioprosthesis evaluation over 15 years. *The Annals of Thoracic Surgery*, 66(6):S49–S52, dec 1998. doi: 10.1016/s0003-4975(98)01127-8.

[106] A. Jayakrishnan and S. R. Jameela. Glutaraldehyde as a fixative in bioprostheses and drug delivery matrices. *Biomaterials*, 17(5):471–484, jan 1996. doi: 10.1016/0142-9612(96)82721-9.

[107] Jorge H. Jimenez, Shasan W. Liou, Muralidhar Padala, Zhaoming He, Michael Sacks, Robert C. Gorman, Joseph H. Gorman, and Ajit P. Yoganathan. A saddle-shaped annulus reduces systolic strain on the central region of the mitral valve anterior leaflet. *The Journal of Thoracic and Cardiovascular Surgery*, 134(6):1562–1568, dec 2007. ISSN 1097-685X (Electronic) 0022-5223 (Linking). doi: 10.1016/j.jtcvs.2007.08.037. URL `http://www.ncbi.nlm.nih.gov/pubmed/18023684`.

[108] Jessica W. Y. Jor, Martyn P. Nash, Poul M. F. Nielsen, and Peter J. Hunter. Estimating material parameters of a structurally based constitutive relation for skin mechanics. *Biomechanics and Modeling in Mechanobiology*, 10(5):767–778, nov 2010. ISSN 1617-7940 (Electronic) 1617-7940 (Linking). doi: 10.1007/s10237-010-0272-0. URL http://www.ncbi.nlm.nih.gov/pubmed/21107636.

[109] Erinn M. Joyce, Jun Liao, Frederick J. Schoen, John E. Mayer, and Michael S. Sacks. Functional collagen fiber architecture of the pulmonary heart valve cusp. *The Annals of Thoracic Surgery*, 87(4):1240–1249, April 2009. ISSN 1552-6259 (Electronic). doi: 10.1016/j.athoracsur.2008.12.049. URL http://www.ncbi.nlm.nih.gov/entrez/query.fcgi?cmd=Retrieve&db=PubMed&dopt=Citation&list_uids=19324159.

[110] Alexey V. Kamenskiy, Iraklis I. Pipinos, Yuris A. Dzenis, Carol S. Lomneth, Syed A. Jaffar Kazmi, Nicholas Y. Phillips, and Jason N. MacTaggart. Passive biaxial mechanical properties and in vivo axial pre-stretch of the diseased human femoropopliteal and tibial arteries. *Acta Biomaterialia*, 10(3):1301–1313, March 2014. ISSN 1742-7061. doi: 10.1016/j.actbio.2013.12.027. URL http://www.sciencedirect.com/science/article/pii/S1742706113006296.

[111] David Kamensky, Ming-Chen Hsu, Dominik Schillinger, John A. Evans, Ankush Aggarwal, Yuri Bazilevs, Michael S. Sacks, and Thomas J.R. Hughes. An immersogeometric variational framework for fluid-structure interaction: application to bioprosthetic heart valves. *Computer Methods in Applied Mechanics and Engineering*, 284:1005–1053, February 2015. ISSN 0045-7825 (Print) 0045-7825 (Linking). doi: 10.1016/j.cma.2014.10.040. URL http://www.ncbi.nlm.nih.gov/pubmed/25541566.

[112] Tsuyoshi Kaneko and Lawrence H Cohn. Mitral valve repair. *Circulation Journal*, 78(3):560–566, 2014. ISSN 1346-9843. doi: 10.1253/circj.cj-14-0069.

[113] Ghassan S. Kassab and Michael S. Sacks, editors. *Structure-Based Mechanics of Tissues and Organs*. Springer US, 2016. doi: 10.1007/978-1-4899-7630-7.

[114] J. Kastelic, I. Palley, and E. Baer. A structural mechanical model for tendon crimping. *Journal of Biomechanics*, 13(10):887–893, jan 1980. ISSN 0021-9290 (Print). doi: 10.1016/0021-9290(80)90177-3. URL `http://www.ncbi.nlm.nih.gov/entrez/query.fcgi?cmd=Retrieve&db=PubMed&dopt=Citation&list_uids=7462263`.

[115] Paul D. Kemp, John F. Cavallaro, and Deborah N. Hastings. Effects of carbodiimide crosslinking and load environment on teh remodeling of collagen scaffolds. *Tissue Engineering*, 1(1):71–79, mar 1995. doi: 10.1089/ten.1995.1.71.

[116] Eugene Khor. Methods for the treatment of collagenous tissues for bioprostheses. *Biomaterials*, 18(2):95–105, January 1997. doi: 10.1016/s0142-9612(96)00106-8. URL `http://www.ncbi.nlm.nih.gov/entrez/query.fcgi?cmd=Retrieve&db=PubMed&dopt=Citation&list_uids=9022956`.

[117] Josef Kiendl, Ming-Chen Hsu, Michael C.H. Wu, and Alessandro Reali. Isogeometric Kirchhoff-Love shell formulations for general hyperelastic materials. *Computer Methods in Applied Mechanics and Engineering*, 291(0):280–303, jul 2015. ISSN 0045-7825. doi: 10.1016/j.cma.2015.03.010. URL `http://dx.doi.org/10.1016/j.cma.2015.03.010`.

[118] Wangdo Kim, Derek C. Tretheway, and Sean S. Kohles. An inverse method for predicting tissue-level mechanics from cellular mechanical input. *Journal of Biomechanics*, 42(3):395–399, feb 2009. doi: 10.1016/j.jbiomech.2008.11.014.

[119] Davis E. King. Dlib-ml: a machine learning toolkit. *Journal of Machine Learning Research*, 10:1755–1758, 2009.

[120] Susheel K. Kodali, Mathew R. Williams, Craig R. Smith, Lars G. Svensson, John G. Webb, Raj R. Makkar, Gregory P. Fontana, Todd M. Dewey, Vinod H. Thourani, Augusto D. Pichard, Michael Fischbein, Wilson Y. Szeto, Scott Lim, Kevin L. Greason, Paul S. Teirstein, S. Chris Malaisrie, Pamela S. Douglas, Rebecca T. Hahn, Brian Whisenant, Alan Zajarias, Duolao Wang, Jodi J. Akin, William N. Anderson, and Martin B. Leon. Two-year outcomes after transcatheter or surgical aortic-valve replacement. *New England Journal of Medicine*, 366(18):1686–1695, may 2012. doi: 10.1056/nejmoa1200384. URL `http://www.nejm.org/doi/full/10.1056/NEJMoa1200384`.

[121] M Kojic, S Mijailovic, and N Zdravkovic. A numerical algorithm for stress integration of a fiber-fiber kinetics model with Coulomb friction for connective tissue. *Computational Mechanics*, 21(2):189–198, mar 1998. doi: 10.1007/s004660050294.

[122] Gaurav Krishnamurthy, Daniel B. Ennis, Akinobu Itoh, Wolfgang Bothe, Julia C. Swanson, Matts Karlsson, Ellen Kuhl, D. Craig Miller, and Neil B. Ingels. Material properties of the ovine mitral valve anterior leaflet in vivo from inverse finite element analysis. *American Journal of Physiology-Heart and Circulatory Physiology*, 295(3):H1141–H1149, September 2008. ISSN 0363-6135 (Print) 0363-6135 (Linking). doi: 10.1152/ajpheart.00284.2008. URL `http://www.ncbi.nlm.nih.gov/pubmed/18621858`.

[123] Christopher E. Kurtz and Catherine M. Otto. Aortic stenosis: clinical aspects of diagnosis and management, with 10 illustrative case reports from a 25-year

experience. *Medicine*, 89(6):349–379, November 2010. ISSN 0025-7974. doi: 10.1097/md.0b013e3181fe5648.

[124] Y. Lanir. A structural theory for the homogeneous biaxial stress-strain relationships in flat collagenous tissues. *Journal of Biomechanics*, 12(6):423–436, jan 1979. doi: 10.1016/0021-9290(79)90027-7.

[125] Y. Lanir. Constitutive equations for fibrous connective tissues. *Journal of Biomechanics*, 16(1):1–12, jan 1983. doi: 10.1016/0021-9290(83)90041-6.

[126] Y. Lanir. Plausibility of structural constitutive equations for isotropic soft tissues in finite static deformations. *Journal of Applied Mechanics*, 61(3):695–702, September 1994. doi: 10.1115/1.2901516.

[127] Y. Lanir and Y.C. Fung. Two-dimensional mechanical properties of rabbit skin. I. Experimental system. *Journal of Biomechanics*, 7(1):29–34, jan 1974. doi: 10.1016/0021-9290(74)90067-0.

[128] Y. Lanir, O. Lichtenstein, and O. Imanuel. Optimal design of biaxial tests for structural material characterization of flat tissues. *Journal of Biomechanical Engineering*, 118(1):41, February 1996. ISSN 0148-0731 (Print) 0148-0731 (Linking). doi: 10.1115/1.2795944. URL `http://www.ncbi.nlm.nih.gov/entrez/query.fcgi?cmd=Retrieve&db=PubMed&dopt=Citation&list_uids=8833073`.

[129] Yoram Lanir. Mechanistic micro-structural theory of soft tissues growth and remodeling: tissues with unidirectional fibers. *Biomechanics and Modeling in Mechanobiology*, 14(2):245–266, jun 2014. ISSN 1617-7959. doi: 10.1007/s10237-014-0600-x.

[130] Chung-Hao Lee, Rouzbeh Amini, Robert C. Gorman, Joseph H. Gorman, and Michael S. Sacks. An inverse modeling approach for stress estimation in mitral valve anterior leaflet valvuloplasty for in-vivo valvular biomaterial assessment. *Journal of Biomechanics*, 47(9):2055–2063, June 2014. ISSN 1873-2380 (Electronic) 0021-9290 (Linking). doi: 10.1016/j.jbiomech.2013.10.058. URL `http://www.ncbi.nlm.nih.gov/pubmed/24275434`.

[131] Chung-Hao Lee, Rouzbeh Amini, Yusuke Sakamoto, Christopher A. Carruthers, Ankush Aggarwal, Robert C. Gorman, Joseph H. Gorman, and Michael S. Sacks. Mitral valves: a computational framework. In *Multiscale Modeling in Biomechanics and Mechanobiology*, pages 223–255. Springer London, oct 2014. ISBN 1-4471-6598-5. doi: 10.1007/978-1-4471-6599-6_10.

[132] Chung-Hao Lee, Christopher A. Carruthers, Salma Ayoub, Robert C. Gorman, Joseph H. Gorman, and Michael S. Sacks. Quantification and simulation of layer-specific mitral valve interstitial cells deformation under physiological loading. *Journal of Theoretical Biology*, 373:26–39, may 2015. doi: 10.1016/j.jtbi.2015.03.004.

[133] Chung-Hao Lee, Jean-Pierre Rabbah, Ajit P. Yoganathan, Robert C. Gorman, Joseph H. Gorman, and Michael S. Sacks. On the effects of leaflet microstructure and constitutive model on the closing behavior of the mitral valve. *Biomechanics and Modeling in Mechanobiology*, 14(6):1281–1302, May 2015. ISSN 1617-7940 (Electronic) 1617-7940 (Linking). doi: 10.1007/s10237-015-0674-0. URL `http://www.ncbi.nlm.nih.gov/pubmed/25947879`.

[134] Chung-Hao Lee, Will Zhang, Jun Liao, Christopher A. Carruthers, Jacob I. Sacks, and Michael S. Sacks. On the presence of affine fibril and fiber kinematics

in the mitral valve anterior leaflet. *Biophysical Journal*, 108(8):2074–2087, April 2015. ISSN 1542-0086 (Electronic) 0006-3495 (Linking). doi: 10.1016/j.bpj.2015.03.019. URL `http://www.ncbi.nlm.nih.gov/pubmed/25902446`.

[135] J. Michael Lee, Ralph Corrente, and Sean A. Haberer. The bovine pericardial xenograft: II. Effect of tethering or pressurization during fixation on the tensile viscoelastic properties of bovine pericardium. *Journal of Biomedical Materials Research*, 23(5):477–489, may 1989. doi: 10.1002/jbm.820230503.

[136] J. Michael Lee, Sean A. Haberer, and Derek R. Boughner. The bovine pericardial xenograft: I. Effect of fixation in aldehydes without constraint on the tensile viscoelastic properties of bovine pericardium. *Journal of Biomedical Materials Research*, 23(5):457–475, may 1989. doi: 10.1002/jbm.820230502.

[137] J. Michael Lee, Michael Ku, and Sean A. Haberer. The bovine pericardial xenograft: III. Effect of uniaxial and sequential biaxial stress during fixation on the tensile viscoelastic properties of bovine pericardium. *Journal of Biomedical Materials Research*, 23(5):491–506, may 1989. doi: 10.1002/jbm.820230504.

[138] JM Lee, SA Haberer, CA Pereira, WA Naimark, DW Courtman, and GJ Wilson. High strain rate testing and structural analysis of pericardial bioprosthetic materials. In HE Kambic and AT Yokobori, editors, *Biomaterials' Mechanical Properties*, volume STP 1173, pages 19–19–24. ASTM International, Philadelphia, 1994. doi: 10.1520/stp18091s.

[139] Tse Chung Lee, Ronald J Midura, Vincent C Hascall, and Ivan Vesely. The effect of elastin damage on the mechanics of the aortic valve. *Journal of Biomechanics*, 34(2):203–210, feb 2001. doi: 10.1016/s0021-9290(00)

00187-1. URL http://www.ncbi.nlm.nih.gov/htbin-post/Entrez/query?db=m&form=6&dopt=r&uid=11165284.

[140] S. Leikin, V. A. Parsegian, W.-H. Yang, and G. E. Walrafen. Raman spectral evidence for hydration forces between collagen triple helices. *Proceedings of the National Academy of Sciences*, 94(21):11312–11317, October 1997. doi: 10.1073/pnas.94.21.11312. URL http://www.pnas.org/content/94/21/11312.abstract.

[141] Jun Liao and Ivan Vesely. Relationship between collagen fibrils, glycosaminoglycans, and stress relaxation in mitral valve chordae tendineae. *Annals of Biomedical Engineering*, 32(7):977–983, July 2004. doi: 10.1023/b:abme.0000032460.97278.e9. URL http://www.ncbi.nlm.nih.gov/entrez/query.fcgi?cmd=Retrieve&db=PubMed&dopt=Citation&list_uids=15298435.

[142] Jun Liao, Lin Yang, Jonathan Grashow, and Michael S. Sacks. The relation between collagen fibril kinematics and mechanical properties in the mitral valve anterior leaflet. *Journal of Biomechanical Engineering*, 129(1):78–87, 2007. ISSN 0148-0731 (Print). doi: 10.1115/1.2401186. URL http://www.ncbi.nlm.nih.gov/entrez/query.fcgi?cmd=Retrieve&db=PubMed&dopt=Citation&list_uids=17227101.

[143] Y. Lis, M. C. Burleigh, D. J. Parker, A. H. Child, J. Hogg, and M. J. Davies. Biochemical characterization of individual normal, floppy and rheumatic human mitral valves. *Biochemical Journal*, 244(3):597–603, jun 1987. doi: 10.1042/bj2440597. URL http://www.ncbi.nlm.nih.gov/entrez/query.fcgi?cmd=Retrieve&db=PubMed&dopt=Citation&list_uids=3446179.

[144] Hongbin Liu, Kiattisak Sangpradit, Min Li, Prokar Dasgupta, Kaspar Althoefer, and Lakmal D. Seneviratne. Inverse finite-element modeling for tissue parameter identification using a rolling indentation probe. *Medical & Biological Engineering & Computing*, 52(1):17–28, sep 2013. doi: 10.1007/s11517-013-1118-6.

[145] Joshua J. Lovekamp, Dan T. Simionescu, Jeremy J. Mercuri, Brett Zubiate, Michael S. Sacks, and Narendra R. Vyavahare. Stability and function of glycosaminoglycans in porcine bioprosthetic heart valves. *Biomaterials.*, 27(8):1507–1518, March 2006. ISSN 0142-9612. doi: 10.1016/j.biomaterials.2005.08.003. URL `http://www.sciencedirect.com/science/article/pii/S0142961205007702`.

[146] Feroze Mahmood, Balachundhar Subramaniam, Joseph H. Gorman, Robert M. Levine, Robert C. Gorman, Andrew Maslow, Peter J. Panzica, Robert M. Hagberg, Swaminathan Karthik, and Kamal R. Khabbaz. Three-dimensional echocardiographic assessment of changes in mitral valve geometry after valve repair. *The Annals of Thoracic Surgery*, 88(6):1838–1844, dec 2009. ISSN 1552-6259 (Electronic) 0003-4975 (Linking). doi: 10.1016/j.athoracsur.2009.07.007. URL `http://www.ncbi.nlm.nih.gov/pubmed/19932245`.

[147] Raj R. Makkar, Gregory P. Fontana, Hasan Jilaihawi, Samir Kapadia, Augusto D. Pichard, Pamela S. Douglas, Vinod H. Thourani, Vasilis C. Babaliaros, John G. Webb, Howard C. Herrmann, Joseph E. Bavaria, Susheel Kodali, David L. Brown, Bruce Bowers, Todd M. Dewey, Lars G. Svensson, Murat Tuzcu, Jeffrey W. Moses, Matthew R. Williams, Robert J. Siegel, Jodi J. Akin, William N. Anderson, Stuart Pocock, Craig R. Smith, and

Martin B. Leon. Transcatheter aortic-valve replacement for inoperable severe aortic stenosis. *New England Journal of Medicine*, 366(18):1696–1704, may 2012. doi: 10.1056/nejmoa1202277. URL http://www.nejm.org/doi/full/10.1056/NEJMoa1202277.

[148] A. Makris, T. Vandenbergh, C. Ramault, D. Van Hemelrijck, E. Lamkanfi, and W. Van Paepegem. Shape optimisation of a biaxially loaded cruciform specimen. *Polymer Testing*, 29(2):216–223, apr 2010. ISSN 0142-9418. doi: 10.1016/j.polymertesting.2009.11.004. URL http://www.sciencedirect.com/science/article/pii/S0142941809001846.

[149] Rizwan A Manji, Alan H Menkis, Burcin Ekser, and David KC Cooper. The future of bioprosthetic heart valves. *The Indian journal of medical research*, 135(2):150, 2012. ISSN 0971-5916.

[150] Caitlin Martin and Wei Sun. Modeling of long-term fatigue damage of soft tissue with stress softening and permanent set effects. *Biomechanics and Modeling in Mechanobiology*, 12(4):645–655, sep 2012. ISSN 1617-7940. doi: 10.1007/s10237-012-0431-6. URL http://dx.doi.org/10.1007/s10237-012-0431-6.

[151] K. May-Newman and F. C. Yin. Biaxial mechanical behavior of excised porcine mitral valve leaflets. *American Journal of Physiology-Heart and Circulatory Physiology*, 269(4):H1319–H1327, oct 1995. doi: 10.1152/ajpheart.1995.269.4.h1319. URL http://www.ncbi.nlm.nih.gov/htbin-post/Entrez/query?db=m&form=6&dopt=r&uid=0007485564.

[152] K. May-Newman and F. C. Yin. A constitutive law for mitral valve tissue. *Journal of Biomechanical Engineering*, 120(1):38–47, 1998. doi: 10.1115/1.

2834305. URL http://www.ncbi.nlm.nih.gov/htbin-post/Entrez/query?db=m&form=6&dopt=r&uid=0009675679.

[153] J. Merodio and R. W. Ogden. The influence of the invariant I-8 on the stress-deformation and ellipticity characteristics of doubly fiber-reinforced non-linearly elastic solids. *International Journal of Non-Linear Mechanics*, 41(4):556–563, May 2006. ISSN 0020-7462. doi: 10.1016/j.ijnonlinmec.2006.02.001. URL ://WOS:000237905700008.

[154] W. David Merryman, Inchan Youn, Howard D. Lukoff, Paula M. Krueger, Farshid Guilak, Richard A. Hopkins, and Michael S. Sacks. Correlation between heart valve interstitial cell stiffness and transvalvular pressure: implications for collagen biosynthesis. *American Journal of Physiology-Heart and Circulatory Physiology*, 290(1):H224–H231, January 2006. doi: 10.1152/ajpheart.00521.2005. URL http://www.ncbi.nlm.nih.gov/entrez/query.fcgi?cmd=Retrieve&db=PubMed&dopt=Citation&list_uids=16126816.

[155] Isabelle Migneault, Catherine Dartiguenave, Michel J. Bertrand, and Karen C. Waldron. Glutaraldehyde: behavior in aqueous solution, reaction with proteins, and application to enzyme crosslinking. *Biotechniques*, 37(5):790–802, nov 2004. doi: 10.2144/04375rv01.

[156] A. Mirnajafi, J. Raymer, M. J. Scott, and M. S. Sacks. The effects of collagen fiber orientation on the flexural properties of pericardial heterograft biomaterials. *Biomaterials*, 26(7):795–804, March 2005. doi: 10.1016/j.biomaterials.2004.03.004. URL http://www.ncbi.nlm.nih.gov/entrez/query.fcgi?cmd=Retrieve&db=PubMed&dopt=Citation&list_uids=15350785.

[157] Ali Mirnajafi, Brett Zubiate, and Michael S. Sacks. Effects of cyclic flexural fatigue on porcine bioprosthetic heart valve heterograft biomaterials. *Journal of Biomedical Materials Research Part A*, 94A(1):205–213, feb 2010. ISSN 1552-4965 (Electronic) 1549-3296 (Linking). doi: 10.1002/jbm.a.32659. URL http://www.ncbi.nlm.nih.gov/entrez/query.fcgi?cmd=Retrieve&db=PubMed&dopt=Citation&list_uids=20166221.

[158] Luis M. Moura, Sandra F. Ramos, José L. Zamorano, Isabel M. Barros, Luis F. Azevedo, Francisco Rocha-Gonçalves, and Nalini M. Rajamannan. Rosuvastatin affecting aortic valve endothelium to slow the progression of aortic stenosis. *Journal of the American College of Cardiology*, 49(5):554–561, February 2007. ISSN 0735-1097. doi: 10.1016/j.jacc.2006.07.072. URL http://ac.els-cdn.com/S0735109706028579/1-s2.0-S0735109706028579-main.pdf?_tid=05961d66-3e08-11e4-b55e-00000aab0f26&acdnat=1410916670_d5494ce195923cac55e850293f0e130a.

[159] Dariush Mozaffarian, Emelia J. Benjamin, Alan S. Go, Donna K. Arnett, Michael J. Blaha, Mary Cushman, Sandeep R. Das, Sarah de Ferranti, Jean-Pierre Després, Heather J. Fullerton, Virginia J. Howard, Mark D. Huffman, Carmen R. Isasi, Monik C. Jiménez, Suzanne E. Judd, Brett M. Kissela, Judith H. Lichtman, Lynda D. Lisabeth, Simin Liu, Rachel H. Mackey, David J. Magid, Darren K. McGuire, Emile R. Mohler, Claudia S. Moy, Paul Muntner, Michael E. Mussolino, Khurram Nasir, Robert W. Neumar, Graham Nichol, Latha Palaniappan, Dilip K. Pandey, Mathew J. Reeves, Carlos J. Rodriguez, Wayne Rosamond, Paul D. Sorlie, Joel Stein, Amytis Towfighi, Tanya N. Turan, Salim S. Virani, Daniel Woo, Robert W. Yeh, and Melanie B. Turner. Heart disease and stroke statistics-2016 update: a report from the american

heart association. *Circulation*, 133(4):e38–e360, dec 2015. ISSN 1524-4539 (Electronic) 0009-7322 (Linking). doi: 10.1161/cir.0000000000000350. URL http://www.ncbi.nlm.nih.gov/pubmed/26673558.

[160] W.A. Naimark, J.M. Lee, H. Limeback, and D. Cheung. Correlation of structure and viscoelastic properties in the pericardia of four mammalian species. *American Journal of Physiology-Heart and Circulatory Physiology*, 263(4):H1095–H1106, oct 1992. doi: 10.1152/ajpheart.1992.263.4.h1095.

[161] Stephanie Nemir and Jennifer L. West. Synthetic materials in the study of cell response to substrate rigidity. *Annals of Biomedical Engineering*, 38(1):2–20, oct 2009. doi: 10.1007/s10439-009-9811-1.

[162] M. E. Nimni, D. Cheung, B. Strates, M. Kodama, and K. Sheikh. Chemically modified collagen : a natural biomaterial for tissue replacement. *Journal of Biomedical Materials Research*, 21(6):741–771, jun 1987. doi: 10.1002/jbm.820210606.

[163] Marcel E Nimni. *Collagen: volume II: biochemistry and biomechanics*. CRC Press, 2018.

[164] Matteo Nobili, Umberto Morbiducci, Raffaele Ponzini, Costantino Del Gaudio, Antonio Balducci, Mauro Grigioni, Franco Maria Montevecchi, and Alberto Redaelli. Numerical simulation of the dynamics of a bileaflet prosthetic heart valve using a fluid–structure interaction approach. *Journal of Biomechanics*, 41 (11):2539–2550, aug 2008. doi: 10.1016/j.jbiomech.2008.05.004.

[165] K. D. O'Brien. Pathogenesis of calcific aortic valve disease: a disease process comes of age (and a good deal more). *Arteriosclerosis, Thrombosis, and Vascu-*

lar Biology, 26(8):1721–1728, aug 2006. doi: 10.1161/01.atv.0000227513.13697.ac.

[166] Grace D. O'Connell, Sounok Sen, and Dawn M. Elliott. Human annulus fibrosus material properties from biaxial testing and constitutive modeling are altered with degeneration. *Biomechanics and Modeling in Mechanobiology*, 11(3-4): 493–503, jul 2011. ISSN 1617-7959. doi: 10.1007/s10237-011-0328-9. URL `http://dx.doi.org/10.1007/s10237-011-0328-9`.

[167] R. W. Ogden. Large deformation isotropic elasticity - on the correlation of theory and experiment for incompressible rubberlike solids. *Proceedings of the Royal Society A: Mathematical, Physical and Engineering Sciences*, 326(1567): 565–584, feb 1972. doi: 10.1098/rspa.1972.0026.

[168] Mette S. Olufsen, Charles S. Peskin, Won Yong Kim, Erik M. Pedersen, Ali Nadim, and Jesper Larsen. Numerical simulation and experimental validation of blood flow in arteries with structured-tree outflow conditions. *Annals of Biomedical Engineering*, 28(11):1281–1299, nov 2000. doi: 10.1114/1.1326031.

[169] Marie Oshima, Ryo Torii, Toshio Kobayashi, Nobuyuki Taniguchi, and Kiyoshi Takagi. Finite element simulation of blood flow in the cerebral artery. *Computer Methods in Applied Mechanics and Engineering*, 191(6-7):661–671, dec 2001. doi: 10.1016/s0045-7825(01)00307-3.

[170] Catherine M. Otto. Calcific aortic valve disease: new concepts. *Seminars in Thoracic and Cardiovascular Surgery*, 22(4):276–284, dec 2010. ISSN 1043-0679. doi: 10.1053/j.semtcvs.2011.01.009.

[171] Muralidhar Padala, Ross A. Hutchison, Laura R. Croft, Jorge H. Jimenez, Robert C. Gorman, Joseph H. Gorman, Michael S. Sacks, and

Ajit P. Yoganathan. Saddle shape of the mitral annulus reduces systolic strains on the P2 segment of the posterior mitral leaflet. *The Annals of Thoracic Surgery*, 88(5):1499–1504, nov 2009. ISSN 1552-6259 (Electronic) 0003-4975 (Linking). doi: 10.1016/j.athoracsur.2009.06.042. URL http://www.ncbi.nlm.nih.gov/entrez/query.fcgi?cmd=Retrieve&db=PubMed&dopt=Citation&list_uids=19853100.

[172] Ki Dong Park, Won Kyu Lee, Ju Young Yun, Dong Keun Han, Soo hyun Kim, Young Ha Kim, Hyoung Mook Kim, and Kwang Taek Kim. Novel anti-calcification treatment of biological tissues by grafting of sulphonated poly(ethylene oxide). *Biomaterials*, 18(1):47–51, jan 1997. ISSN 0142-9612. doi: http://dx.doi.org/10.1016/S0142-9612(96)00096-8. URL http://www.sciencedirect.com/science/article/pii/S0142961296000968.

[173] A. Parolari, E. Tremoli, L. Cavallotti, M. Trezzi, S. Kassem, C. Loardi, F. Veglia, G. Ferrari, D. Pacini, and F. Alamanni. Do statins improve outcomes and delay the progression of non-rheumatic calcific aortic stenosis? *Heart*, 97 (7):523–529, jan 2011. ISSN 1355-6037. doi: 10.1136/hrt.2010.215046. URL http://heart.bmj.com/content/97/7/523.full.pdf.

[174] David A.D. Parry. The molecular and fibrillar structure of collagen and its relationship to the mechanical properties of connective tissue. *Biophysical Chemistry*, 29(1-2):195–209, feb 1988. doi: 10.1016/0301-4622(88)87039-x. URL http://www.ncbi.nlm.nih.gov/entrez/query.fcgi?cmd=Retrieve&db=PubMed&dopt=Citation&list_uids=3282560.

[175] E. A. Patterson, I. C. Howard, and M. A. Thornton. A comparative study of linear and nonlinear simulations of the leaflets in a bioprosthetic heart valve during

the cardiac cycle. *Journal of Medical Engineering & Technology*, 20(3):95–108, jan 1996. doi: 10.3109/03091909609008387. URL http://www.ncbi.nlm.nih.gov/htbin-post/Entrez/query?db=m&form=6&dopt=r&uid=0008877750.

[176] Karl Perktold and Gerhard Rappitsch. Computer simulation of local blood flow and vessel mechanics in a compliant carotid artery bifurcation model. *Journal of Biomechanics*, 28(7):845–856, jul 1995. doi: 10.1016/0021-9290(95)95273-8.

[177] John A. Petruska and Alan J. Hodge. A subunit model for the tropocollagen macromolecule. *Proceedings of the National Academy of Sciences*, 51(5): 871–876, May 1964. doi: 10.1073/pnas.51.5.871. URL http://www.pnas.org/content/51/5/871.short.

[178] Tobias Pflederer and Stephan Achenbach. Aortic valve stenosis: CT contributions to diagnosis and therapy. *Journal of Cardiovascular Computed Tomography*, 4(6):355–364, November 2010. ISSN 1876-861x. doi: 10.1016/j.jcct.2010.09.008. URL http://www.journalofcardiovascularct.com/article/S1934-5925(10)00542-3/abstract.

[179] Paolo Poggio, Rachana Sainger, Emanuela Branchetti, Juan B. Grau, Eric K. Lai, Robert C. Gorman, Michael S. Sacks, Alessandro Parolari, Joseph E. Bavaria, and Giovanni Ferrari. Noggin attenuates the osteogenic activation of human valve interstitial cells in aortic valve sclerosis. *Cardiovascular Research*, 98(3):402–410, mar 2013. ISSN 1755-3245 (Electronic) 0008-6363 (Linking). doi: 10.1093/cvr/cvt055. URL http://www.ncbi.nlm.nih.gov/pubmed/23483047.

[180] A. R. Pries, T. W. Secomb, P. Gaehtgens, and J. F. Gross. Blood flow in microvascular networks. experiments and simulation. *Circulation Research*, 67 (4):826–834, oct 1990. doi: 10.1161/01.res.67.4.826.

[181] Zhao Qin, Markus J. Buehler, and Laurent Kreplak. A multi-scale approach to understand the mechanobiology of intermediate filaments. *Journal of Biomechanics*, 43(1):15–22, January 2010. doi: 10.1016/j.jbiomech.2009.09.004.

[182] K. R. Rajagopal and A. S. Wineman. A constitutive equation for nonlinear solids which undergo deformation induced microstructural changes. *International Journal of Plasticity*, 8(4):385–395, jan 1992. doi: 10.1016/0749-6419(92)90056-i.

[183] C. Ramault, A. Makris, D. Van Hemelrijck, E. Lamkanfi, and W. Van Paepegem. Comparison of different techniques for strain monitoring of a biaxially loaded cruciform specimen. *Strain*, 47:210–217, jun 2010. ISSN 1475-1305. doi: 10.1111/j.1475-1305.2010.00760.x. URL `http://dx.doi.org/10.1111/j.1475-1305.2010.00760.x`.

[184] Manuel K. Rausch, Wolfgang Bothe, John-Peder Escobar Kvitting, Serdar Göktepe, D. Craig Miller, and Ellen Kuhl. In vivo dynamic strains of the ovine anterior mitral valve leaflet. *Journal of Biomechanics*, 44(6):1149–1157, apr 2011. ISSN 1873-2380 (Electronic) 0021-9290 (Linking). doi: 10.1016/j.jbiomech.2011.01.020. URL `http://www.ncbi.nlm.nih.gov/pubmed/21306716`.

[185] Bruno V. Rego, Sarah M. Wells, Chung-Hao Lee, and Michael S. Sacks. Mitral valve leaflet remodelling during pregnancy: insights into cell-mediated recovery of tissue homeostasis. *Journal of The Royal Society Interface*, 13(125):20160709, dec 2016. ISSN 1742-5689. doi: 10.1098/rsif.2016.0709. URL `http://rsif.royalsocietypublishing.org/content/13/125/20160709`.

[186] Peter Rissland, Yared Alemu, Shmuel Einav, John Ricotta, and Danny Bluestein. Abdominal aortic aneurysm risk of rupture: patient-specific FSI simulations using anisotropic model. *Journal of Biomechanical Engineering*, 131(3):031001, 2009. doi: 10.1115/1.3005200.

[187] R. S. Rivlin and D. W. Saunders. Large elastic deformations of isotropic materials 7: experiments on the deformation of rubber. *Philosophical Transactions of the Royal Society A: Mathematical, Physical and Engineering Sciences*, 243(865):251–288, apr 1951. doi: 10.1098/rsta.1951.0004. URL : `//A1951UU63300001`.

[188] Edward K. Rodriguez, Anne Hoger, and Andrew D. McCulloch. Stress-dependent finite growth in soft elastic tissues. *Journal of Biomechanics*, 27(4):455–467, April 1994. doi: 10.1016/0021-9290(94)90021-3. URL `http://www.ncbi.nlm.nih.gov/entrez/query.fcgi?cmd=Retrieve&db=PubMed&dopt=Citation&list_uids=8188726`.

[189] DonaldN. Ross. Replacement of aortic and mitral valves with a pulmonary autograft. *The Lancet*, 290(7523):956–958, November 1967. doi: 10.1016/s0140-6736(67)90794-5. URL `http://www.ncbi.nlm.nih.gov/entrez/query.fcgi?cmd=Retrieve&db=PubMed&dopt=Citation&list_uids=4167516`.

[190] Anne B. Rossebø, Terje R. Pedersen, Kurt Boman, Philippe Brudi, John B. Chambers, Kenneth Egstrup, Eva Gerdts, Christa Gohlke-Bärwolf, Ingar Holme, Y. Antero Kesäniemi, William Malbecq, Christoph A. Nienaber, Simon Ray, Terje Skjærpe, Kristian Wachtell, and Ronnie Willenheimer. Intensive lipid lowering with simvastatin and ezetimibe in aortic stenosis. *New*

England Journal of Medicine, 359(13):1343–1356, September 2008. ISSN 0028-4793. doi: 10.1056/nejmoa0804602. URL http://www.nejm.org/doi/pdf/10.1056/NEJMoa0804602.

[191] Dana R. Rottach, John G. Curro, Gary S. Grest, and Aidan P. Thompson. Effect of strain history on stress and permanent set in cross-linking networks: a molecular dynamics study. *Macromolecules*, 37(14):5468–5473, jul 2004. doi: 10.1021/ma049723j. URL http://dx.doi.org/10.1021/ma049723j.

[192] Dana R. Rottach, John G. Curro, Joanne Budzien, Gary S. Grest, Carsten Svaneborg, and Ralf Everaers. Permanent set of cross-linking networks: comparison of theory with molecular dynamics simulations. *Macromolecules*, 39 (16):5521–5530, aug 2006. doi: 10.1021/ma060767x. URL http://dx.doi.org/10.1021/ma060767x.

[193] Dana R. Rottach, John G. Curro, Joanne Budzien, Gary S. Grest, Carsten Svaneborg, and Ralf Everaers. Molecular dynamics simulations of polymer networks undergoing sequential cross-linking and scission reactions. *Macromolecules*, 40(1):131–139, jan 2007. doi: 10.1021/ma062139l. URL http://dx.doi.org/10.1021/ma062139l.

[194] M. S. Sacks. A method for planar biaxial mechanical testing that includes in-plane shear. *Journal of Biomechanical Engineering*, 121(5):551–5, 1999. doi: 10.1115/1.2835086.

[195] M. S. Sacks and F. J. Schoen. Collagen fiber disruption occurs independent of calcification in clinically explanted bioprosthetic heart valves. *J Biomed Mater Res*, 62(3):359–71, December 2002. doi: 10.1002/

jbm.10293. URL http://www.ncbi.nlm.nih.gov/entrez/query.fcgi?cmd=Retrieve&db=PubMed&dopt=Citation&list_uids=12209921.

[196] M. S. Sacks, Z. He, L. Baijens, S. Wanant, P. Shah, H. Sugimoto, and A. P. Yoganathan. Surface strains in the anterior leaflet of the functioning mitral valve. *Annals of Biomedical Engineering*, 30(10):1281–1290, November 2002. doi: 10.1114/1.1529194. URL http://www.ncbi.nlm.nih.gov/entrez/query.fcgi?cmd=Retrieve&db=PubMed&dopt=Citation&list_uids=12540204.

[197] M. S. Sacks, T. V. Lam, and J. E. Mayer, Jr. A structural constitutive model for the native pulmonary valve. In *The 26th Annual International Conference of the IEEE Engineering in Medicine and Biology Society*, volume 5, pages 3734–6. IEEE, 2004. doi: 10.1109/iembs.2004.1404048. URL http://www.ncbi.nlm.nih.gov/entrez/query.fcgi?cmd=Retrieve&db=PubMed&dopt=Citation&list_uids=17271106.

[198] Michael S. Sacks. A structural constitutive model for chemically treated planar tissues under biaxial loading. *Computational Mechanics*, 26(3):243–249, sep 2000. doi: 10.1007/s004660000175.

[199] Michael S. Sacks. Experimentally tractable, pseudo-elastic constitutive law for biomembranes: I theory. *Journal of Biomechanical Engineering*, 125(1):94–99, feb 2003. doi: 10.1115/1.1530770.

[200] Michael S. Sacks. Incorporation of experimentally-derived fiber orientation into a structural constitutive model for planar collagenous tissues. *Journal of Biomechanical Engineering*, 125(2):280–7, April 2003. doi: 10.1115/1.1544508. URL http://www.ncbi.nlm.nih.gov/entrez/query.fcgi?cmd=Retrieve&db=PubMed&dopt=Citation&list_uids=12751291.

[201] Michael S. Sacks and C. J. Chuong. Orthotropic mechanical properties of chemically treated bovine pericardium. *Annals of Biomedical Engineering*, 26(5): 892–902, sep 1998. doi: 10.1114/1.135.

[202] Michael S. Sacks and David B. Smith. Effects of accelerated testing on porcine bioprosthetic heart valve fiber architecture. *Biomaterials*, 19(11-12):1027–1036, jun 1998. doi: 10.1016/s0142-9612(98)00002-7.

[203] Michael S. Sacks and Wei Sun. Multiaxial mechanical behavior of biological materials. *Annual Review of Biomedical Engineering*, 5(1): 251–284, aug 2003. doi: 10.1146/annurev.bioeng.5.011303.120714. URL `http://www.ncbi.nlm.nih.gov/entrez/query.fcgi?cmd=Retrieve&db=PubMed&dopt=Citation&list_uids=12730082`.

[204] Michael S. Sacks, David B. Smith, and Erik D. Hiester. A small angle light scattering device for planar connective tissue microstructural analysis. *Annals of Biomedical Engineering*, 25(4):678–689, jul 1997. ISSN 1573-9686. doi: 10.1007/bf02684845. URL `https://doi.org/10.1007/BF02684845`.

[205] Michael S. Sacks, David B. Smith, and Erik D. Hiester. The aortic valve microstructure: effects of transvalvular pressure. *Journal of Biomedical Materials Research*, 41(1):131–141, jul 1998. doi: 10.1002/(sici)1097-4636(199807)41:1⟨131::aid-jbm16⟩3.0.co;2-q.

[206] Michael S. Sacks, Yoshiharu Enomoto, Jeffrey R. Graybill, W. David Merryman, Ahmad Zeeshan, Ajit P. Yoganathan, Robert J. Levy, Robert C. Gorman, and Joseph H. Gorman. In-vivo dynamic deformation of the mitral valve anterior leaflet. *The Annals of Thoracic Surgery*, 82(4):1369–1377, oct 2006. ISSN 1552-6259 (Electronic). doi: 10.1016/j.athoracsur.

2006.03.117. URL http://www.ncbi.nlm.nih.gov/entrez/query.fcgi?cmd=Retrieve&db=PubMed&dopt=Citation&list_uids=16996935.

[207] Michael S Sacks, Ali Mirnajafi, Wei Sun, and Paul Schmidt. Bioprosthetic heart valve heterograft biomaterials: structure, mechanical behavior and computational simulation. *Expert Review of Medical Devices*, 3(6):817–834, November 2006. ISSN 1743-4440 (Print). doi: 10.1586/17434440.3.6.817. URL http://www.ncbi.nlm.nih.gov/entrez/query.fcgi?cmd=Retrieve&db=PubMed&dopt=Citation&list_uids=17280546.

[208] Michael S. Sacks, Hirotsugu Hamamoto, Jeanne M. Connolly, Robert C. Gorman, Joseph H. Gorman, and Robert J. Levy. In vivo biomechanical assessment of triglycidylamine crosslinked pericardium. *Biomaterials*, 28(35):5390–5398, dec 2007. ISSN 0142-9612 (Print). doi: 10.1016/j.biomaterials.2007.08.021. URL http://www.ncbi.nlm.nih.gov/entrez/query.fcgi?cmd=Retrieve&db=PubMed&dopt=Citation&list_uids=17822757.

[209] Michael S. Sacks, W. David Merryman, and David E. Schmidt. On the biomechanics of heart valve function. *Journal of Biomechanics*, 42(12):1804–1824, aug 2009. ISSN 1873-2380 (Electronic). doi: 10.1016/j.jbiomech.2009.05.015. URL http://www.ncbi.nlm.nih.gov/entrez/query.fcgi?cmd=Retrieve&db=PubMed&dopt=Citation&list_uids=19540499.

[210] Michael S. Sacks, Will Zhang, and Silvia Wognum. A novel fibre-ensemble level constitutive model for exogenous cross-linked collagenous tissues. *Interface Focus*, 6(1):20150090, dec 2015. doi: 10.1098/rsfs.2015.0090. URL http://rsfs.royalsocietypublishing.org/royfocus/6/1/20150090.full.pdf.

[211] MS Sacks. Biaxial mechanical evaluation of planar biological materials. *J Elasticity*, 61:199–246, 2000.

[212] I. S. Salgo, J. H. Gorman, R. C. Gorman, B. M. Jackson, F. W. Bowen, T. Plappert, M. G. S. J. Sutton, and L. H. Edmunds. Effect of annular shape on leaflet curvature in reducing mitral leaflet stress. *Circulation*, 106(6):711–717, jul 2002. ISSN 0009-7322. doi: 10.1161/01.Cir.0000025426.39426.83. URL ://WOS:000177401700015.

[213] Naoki Sasaki and Shingo Odajima. Elongation mechanism of collagen fibrils and force-strain relations of tendon at each level of structural hierarchy. *Journal of Biomechanics*, 29(9):1131–1136, sep 1996. doi: 10.1016/0021-9290(96)00024-3.

[214] Naoki Sasaki and Singo Odajima. Stress-strain curve and Young's modulus of a collagen molecule as determined by the X-ray diffraction technique. *Journal of Biomechanics*, 29(5):655–658, may 1996. doi: 10.1016/0021-9290(95)00110-7.

[215] F. J. Schoen. Pathology of heart valve substitution with mechanical and tissue prostheses. In M.D. Silver, A.I. Gotlieb, and F. J. Schoen, editors, *Cardiovascular Pathology*, volume 3. Livingstone, New York, 2001.

[216] F. J. Schoen. Valvular heart disease: changing concepts in disease management. *Circulation*, 118(18):1864–1880, oct 2008. doi: 10.1161/circulationaha.108.805911.

[217] F. J. Schoen. Evolving concepts of cardiac valve dynamics: the continuum of development, functional structure, pathobiology, and tissue engineering. *Circulation*, 118(18):1864–1880, October 2008. ISSN 1524-4539 (Electronic). doi: 10.1161/circulationaha.108.805911. URL

http://www.ncbi.nlm.nih.gov/entrez/query.fcgi?cmd=Retrieve&db=PubMed&dopt=Citation&list_uids=18955677.

[218] F J Schoen and R J Levy. Pathology of substitute heart valves: new concepts and developments. *Journal of cardiac surgery*, 9:222–227, March 1994. ISSN 0886-0440.

[219] F. J. Schoen and R. J. Levy. Founder's award, 25th annual meeting of the society for biomaterials, perspectives. providence, RI, april 28-may 2, 1999. Tissue heart valves: current challenges and future research perspectives. *Journal of biomedical materials research*, 47(4):439–465, December 1999. ISSN 0021-9304. URL http://www.ncbi.nlm.nih.gov/htbin-post/Entrez/query?db=m&form=6&dopt=r&uid=0010497280.

[220] Frederick J. Schoen. Cardiac valves and valvular pathology: update on function, disease, repair, and replacement. *Cardiovascular Pathology*, 14 (4):189–194, July 2005. ISSN 1054-8807 (Print). doi: 10.1016/j.carpath.2005.03.005. URL http://www.ncbi.nlm.nih.gov/entrez/query.fcgi?cmd=Retrieve&db=PubMed&dopt=Citation&list_uids=16009317.

[221] Frederick J. Schoen. New frontiers in the pathology and therapy of heart valve disease: 2006 society for cardiovascular pathology, distinguished achievement award lecture, united states-canadian academy of pathology, Atlanta, GA, february 12, 2006. *Cardiovascular Pathology*, 15(5):271–279, September 2006. ISSN 1054-8807 (Print). doi: 10.1016/j.carpath.2006.05.001. URL http://www.ncbi.nlm.nih.gov/entrez/query.fcgi?cmd=Retrieve&db=PubMed&dopt=Citation&list_uids=16979034.

[222] Frederick J. Schoen and Charles E. Hobson. Anatomic analysis of removed prosthetic heart valves: causes of failure of 33 mechanical valves and 58 bioprostheses, 1980 to 1983. *Human Pathology*, 16(6):549–559, jun 1985. doi: 10.1016/s0046-8177(85)80103-9.

[223] Frederick J. Schoen and Robert J. Levy. Tissue heart valves: current challenges and future research perspectives. *Journal of Biomedical Materials Research*, 47(4):439–465, dec 1999. doi: 10.1002/(sici)1097-4636(19991215)47:4⟨439::aid-jbm1⟩3.0.co;2-o.

[224] Frederick J. Schoen and Robert J. Levy. Calcification of tissue heart valve substitutes: progress toward understanding and prevention. *The Annals of Thoracic Surgery*, 79(3):1072–1080, March 2005. doi: 10.1016/j.athoracsur.2004.06.033. URL `http://www.ncbi.nlm.nih.gov/entrez/query.fcgi?cmd=Retrieve&db=PubMed&dopt=Citation&list_uids=15734452`.

[225] Michael Scott and Ivan Vesely. Aortic valve cusp microstructure: the role of elastin. *The Annals of Thoracic Surgery*, 60:S391–S394, aug 1995. doi: 10.1016/0003-4975(95)00263-k.

[226] Tiffany L. Sellaro, Daniel Hildebrand, Qijin Lu, Naren Vyavahare, Michael Scott, and Michael S. Sacks. Effects of collagen fiber orientation on the response of biologically derived soft tissue biomaterials to cyclic loading. *Journal of Biomedical Materials Research Part A*, 80A(1):194–205, January 2007. ISSN 1549-3296 (Print). doi: 10.1002/jbm.a.30871. URL `http://www.ncbi.nlm.nih.gov/entrez/query.fcgi?cmd=Retrieve&db=PubMed&dopt=Citation&list_uids=17041913`.

[227] Zhilei L. Shen, Mohammad Reza Dodge, Harold Kahn, Roberto Ballarini, and Steven J. Eppell. Stress-strain experiments on individual collagen fibrils. *Biophysical Journal*, 95(8):3956–3963, oct 2008. ISSN 0006-3495. doi: 10.1529/biophysj.107.124602. URL `http://www.sciencedirect.com/science/article/pii/S0006349508785345`.

[228] Raheela Fareed Siddiqui, Johnathan Rajiv Abraham, and Jagdish Butany. Bioprosthetic heart valves: modes of failure. *Histopathology*, 55(2):135–144, aug 2009. doi: 10.1111/j.1365-2559.2008.03190.x.

[229] Raquel Simón-Allué, Alberto Cordero, and Estefanía Peña. Unraveling the effect of boundary conditions and strain monitoring on estimation of the constitutive parameters of elastic membranes by biaxial tests. *Mechanics Research Communications*, 57(0):82–89, apr 2014. ISSN 0093-6413. doi: 10.1016/j.mechrescom.2014.01.009. URL `http://www.sciencedirect.com/science/article/pii/S0093641314000226`.

[230] D. B. Smith, M. S. Sacks, P. M. Pattany, and R. Schroeder. High-resolution magnetic resonance imaging to characterize the geometry of fatigued porcine bioprosthetic heart valves. *The Journal of heart valve disease*, 6(4):424–432, July 1997. ISSN 0966-8519.

[231] D. B. Smith, M. S. Sacks, P. M. Pattany, and R. Schroeder. Fatigue-induced changes in bioprosthetic heart valve three-dimensional geometry and the relation to tissue damage. *The Journal of heart valve disease*, 8(1):25–33, January 1999. ISSN 0966-8519.

[232] Joao S. Soares, Kristen R. Feaver, Will Zhang, David Kamensky, Ankush Aggarwal, and Michael S. Sacks. Biomechanical behavior of bioprosthetic heart

valve heterograft tissues: characterization, simulation, and performance. *Cardiovascular Engineering and Technology*, 7(4):309–351, aug 2016. ISSN 1869-4098. doi: 10.1007/s13239-016-0276-8. URL http://dx.doi.org/10.1007/s13239-016-0276-8.

[233] João S Soares, Will Zhang, and Michael S Sacks. A mathematical model for the determination of forming tissue moduli in needled-nonwoven scaffolds. *Acta Biomaterialia*, 51:220–236, March 2017. ISSN 1878-7568. doi: 10.1016/j.actbio.2016.12.038.

[234] Gerhard Sommer, Maximilian Eder, Laszlo Kovacs, Heramb Pathak, Lars Bonitz, Christoph Mueller, Peter Regitnig, and Gerhard A. Holzapfel. Multiaxial mechanical properties and constitutive modeling of human adipose tissue: A basis for preoperative simulations in plastic and reconstructive surgery. *Acta Biomaterialia*, 9(11):9036–9048, nov 2013. ISSN 1742-7061. doi: 10.1016/j.actbio.2013.06.011. URL http://www.sciencedirect.com/science/article/pii/S174270611300295X.

[235] A.R. Srinivasa. On the use of the upper triangular (or QR) decomposition for developing constitutive equations for Green-elastic materials. *International Journal of Engineering Science*, 60:1–12, nov 2012. doi: 10.1016/j.ijengsci.2012.05.003.

[236] Albert Starr. The artificial heart valve. *Nature Medicine*, 13(10):1160–1164, oct 2007. doi: 10.1038/nm1644.

[237] Horst Steiner, Alf Staudach, Dietmar Spitzer, and Heinz Schaffer. Diagnostic techniques: three-dimensional ultrasound in obstetrics and gynaecology: tech-

nique, possibilities and limitations. *Human Reproduction*, 9(9):1773–1778, sep 1994. doi: 10.1093/oxfordjournals.humrep.a138793.

[238] John A. Stella and Michael S. Sacks. On the biaxial mechanical properties of the layers of the aortic valve leaflet. *Journal of Biomechanical Engineering*, 129(5):757–66, 2007. ISSN 0148-0731 (Print) 0148-0731 (Linking). doi: 10.1115/1.2768111. URL `http://www.ncbi.nlm.nih.gov/entrez/query.fcgi?cmd=Retrieve&db=PubMed&dopt=Citation&list_uids=17887902`.

[239] John A. Stella, Jun Liao, and Michael S. Sacks. Time-dependent biaxial mechanical behavior of the aortic heart valve leaflet. *Journal of Biomechanics*, 40(14):3169–3177, jan 2007. ISSN 0021-9290 (Print) 0021-9290 (Linking). doi: 10.1016/j.jbiomech.2007.04.001. URL `http://www.ncbi.nlm.nih.gov/entrez/query.fcgi?cmd=Retrieve&db=PubMed&dopt=Citation&list_uids=17570376`.

[240] W. Sun, M.S. Sacks, T.L. Sellaro, W.S. Slaughter, and M.J. Scott. Biaxial mechanical response of bioprosthetic heart valve biomaterials to high in-plane shear. *Journal of Biomechanical Engineering*, 125(3):372–380, jun 2003. doi: 10.1115/1.1572518.

[241] W. Sun, A. Abad, and M.S. Sacks. Simulated bioprosthetic heart valve deformation under quasi-static loading. *Journal of Biomechanical Engineering*, 127(6):905–914, jul 2005. doi: 10.1115/1.2049337.

[242] Wei Sun and Michael S. Sacks. Finite element implementation of a generalized Fung-elastic constitutive model for planar soft tissues. *Biomechanics and Modeling in Mechanobiology*, 4(2-3):190–199, August 2005. doi: 10.1007/

s10237-005-0075-x. URL http://www.ncbi.nlm.nih.gov/entrez/query.fcgi?cmd=Retrieve&db=PubMed&dopt=Citation&list_uids=16075264.

[243] Wei Sun, Michael S Sacks, and Michael J Scott. Numerical simulations of the planar biaxial mechanical behavior of biological materials. *ASME Summer Bioengineering, Miami, FL*, 2003.

[244] Wei Sun, Michael Sacks, Gregory Fulchiero, Joshua Lovekamp, Naren Vyavahare, and Michael Scott. Response of heterograft heart valve biomaterials to moderate cyclic loading. *Journal of Biomedical Materials Research*, 69A(4):658–669, June 2004. doi: 10.1002/jbm.a.30031. URL http://www.ncbi.nlm.nih.gov/entrez/query.fcgi?cmd=Retrieve&db=PubMed&dopt=Citation&list_uids=15162408.

[245] Wei Sun, Michael S. Sacks, and Michael J. Scott. Effects of boundry conditions on the estimation of the planar biaxial mechanical properties of soft tissues. *Journal of Biomechanical Engineering*, 127(4):709–715, August 2005. ISSN 0148-0731. doi: 10.1115/1.1933931. URL ://WOS:000231034400019.

[246] Hsing-Wen Sung, Wen-Hisang Chang, Chiun-Yuang Ma, and Meng-Horng Lee. Crosslinking of biological tissues using genipin and/or carbodiimide. *Journal of Biomedical Materials Research*, 64A(3):427–438, feb 2003. doi: 10.1002/jbm.a.10346.

[247] Larry A. Taber. Biomechanics of growth, remodeling, and morphogenesis. *Applied Mechanics Reviews*, 48(8):487–545, 1995. doi: 10.1115/1.3005109.

[248] H. Tam, W. Zhang, D. Infante, N. Parchment, M.S. Sacks, and N. Vyavahare. Fixation of bovine pericardium-based tissue biomaterial with irre-

versible chemistry improves biochemical and biomechanical properties. *Journal of Cardiovascular Translational Research*, 10(2):194–205, feb 2017. doi: 10.1007/s12265-017-9733-5.

[249] Hobey Tam, Will Zhang, Kristen R. Feaver, Nathaniel Parchment, Michael S. Sacks, and Naren Vyavahare. A novel crosslinking method for improved tear resistance and biocompatibility of tissue based biomaterials. *Biomaterials*, 66:83–91, October 2015. ISSN 1878-5905 (Electronic) 0142-9612 (Linking). doi: 10.1016/j.biomaterials.2015.07.011. URL `http://www.ncbi.nlm.nih.gov/pubmed/26196535`.

[250] Ge Tao, James D. Kotick, and Joy Lincoln. Heart valve development, maintenance, and disease. In *Current Topics in Developmental Biology*, pages 203–232. Elsevier, 2012. doi: 10.1016/b978-0-12-387786-4.00006-3.

[251] M Thubrikar. *The aortic valve*. CRC, Boca Raton, 1990.

[252] D. A. Towler. Molecular and cellular aspects of calcific aortic valve disease. *Circulation Research*, 113(2):198–208, July 2013. ISSN 0009-7330. doi: 10.1161/circresaha.113.300155. URL `http://circres.ahajournals.org/content/113/2/198.full.pdf`.

[253] G. I. Tseretely and O. I. Smirnova. DSC study of melting and glass transition in gelatins. *Journal of Thermal Analysis*, 38(5):1189–1201, may 1992. doi: 10.1007/bf01979179. URL `http://dx.doi.org/10.1007/BF01979179`.

[254] I. Vesely and W. J. Mako. Comparison of the compressive buckling of porcine aortic valve cusps and bovine pericardium. *The Journal of heart valve disease*, 7(1):34–39, January 1998. ISSN

0966-8519. URL http://www.ncbi.nlm.nih.gov/entrez/query.fcgi?cmd=Retrieve&db=PubMed&dopt=Citation&list_uids=9502137.

[255] I. Vesely, J. E. Barber, and N. B. Ratliff. Tissue damage and calcification may be independent mechanisms of bioprosthetic heart valve failure. *The Journal of heart valve disease*, 10(4):471–477, July 2001. ISSN 0966-8519. URL http://www.ncbi.nlm.nih.gov/entrez/query.fcgi?cmd=Retrieve&db=PubMed&dopt=Citation&list_uids=11499593.

[256] Ivan Vesely. The role of elastin in aortic valve mechanics. *Journal of Biomechanics*, 31(2):115–123, may 1997. doi: 10.1016/s0021-9290(97)00122-x.

[257] Ivan Vesely and Ronald Noseworthy. Micromechanics of the fibrosa and the ventricularis in aortic valve leaflets. *Journal of Biomechanics*, 25(1):101–113, jan 1992. doi: 10.1016/0021-9290(92)90249-z.

[258] Raymond P. Vito and James Hickey. The mechanical properties of soft tissues–II: the elastic response of arterial segments. *Journal of Biomechanics*, 13(11):951–957, jan 1980. doi: 10.1016/0021-9290(80)90166-9. URL http://www.ncbi.nlm.nih.gov/htbin-post/Entrez/query?db=m&form=6&dopt=r&uid=0007276003.

[259] K.Y. Volokh and D.A. Vorp. A model of growth and rupture of abdominal aortic aneurysm. *Journal of Biomechanics*, 41(5):1015–1021, 2008. doi: 10.1016/j.jbiomech.2007.12.014.

[260] N. Vyavahare, D. Hirsch, E. Lerner, J. Z. Baskin, F. J. Schoen, R. Bianco, H. S. Kruth, R. Zand, and R. J. Levy. Prevention of bioprosthetic

heart valve calcification by ethanol preincubation. Efficacy and mechanisms. *Circulation*, 95(2):479–488, jan 1997. doi: 10.1161/01.cir.95.2.479. URL http://www.ncbi.nlm.nih.gov/htbin-post/Entrez/query?db=m&form=6&dopt=r&uid=0009008467.

[261] Narendra Vyavahare, Matthew Ogle, Frederick J. Schoen, Robert Zand, D. Claire Gloeckner, Michael Sacks, and Robert J. Levy. Mechanisms of bioprosthetic heart valve failure: fatigue causes collagen denaturation and glycosaminoglycan loss. *Journal of Biomedical Materials Research*, 46(1):44–50, July 1999. ISSN 0021-9304 (Print) 0021-9304 (Linking). doi: 10.1002/(sici)1097-4636(199907)46:1⟨44::aid-jbm5⟩3.0.co;2-d. URL http://www.ncbi.nlm.nih.gov/pubmed/10357134.

[262] S. M. Wells and M. S. Sacks. Effects of fixation pressure on the biaxial mechanical behavior of porcine bioprosthetic heart valves with long-term cyclic loading. *Biomaterials*, 23(11):2389–2399, June 2002. doi: 10.1016/s0142-9612(01)00375-1. URL http://www.ncbi.nlm.nih.gov/entrez/query.fcgi?cmd=Retrieve&db=PubMed&dopt=Citation&list_uids=12013187.

[263] S. M. Wells, S. L. Adamson, B. L. Langille, and J. M. Lee. Thermomechanical analysis of collagen crosslinking in the developing ovine thoracic aorta. *Biorheology*, 35(6):399–414, November 1998. doi: 10.1016/s0006-355x(99)80019-5. URL http://www.ncbi.nlm.nih.gov/entrez/query.fcgi?cmd=Retrieve&db=PubMed&dopt=Citation&list_uids=10656049.

[264] Sarah M. Wells, Tiffany Sellaro, and Michael S. Sacks. Cyclic loading response of bioprosthetic heart valves: effects of fixation stress

state on the collagen fiber architecture. *Biomaterials*, 26(15):2611–2619, May 2005. doi: 10.1016/j.biomaterials.2004.06.046. URL http://www.ncbi.nlm.nih.gov/entrez/query.fcgi?cmd=Retrieve&db=PubMed&dopt=Citation&list_uids=15585264.

[265] Sarah M. Wells, Caitlin M. Pierlot, and Andrew D. Moeller. Physiological remodeling of the mitral valve during pregnancy. *American Journal of Physiology-Heart and Circulatory Physiology*, 303(7):H878–H892, oct 2012. ISSN 1522-1539 (Electronic) 0363-6135 (Linking). doi: 10.1152/ajpheart.00845.2011. URL http://www.ncbi.nlm.nih.gov/pubmed/22886410.

[266] SM Wells and MS Sacks. Effects of stress-state during fixation on the fatigue properties of bioprosthetic heart valve tissue. In *Transactions of the Sixth World Biomaterials Congress, Kamuela, HI, May*, pages 15–20, 2000.

[267] Marco P.E. Wenger, Laurent Bozec, Michael A. Horton, and Patrick Mesquida. Mechanical properties of collagen fibrils. *Biophysical Journal*, 93(4):1255–1263, August 2007. ISSN 0006-3495. doi: 10.1529/biophysj.106.103192. URL http://www.sciencedirect.com/science/article/pii/S0006349507713838http://www.ncbi.nlm.nih.gov/pmc/articles/PMC1929027/pdf/1255.pdf.

[268] Dena Wiltz, C. Alexander, Liezl R., Alicia A. Blancas, Matthew C., Xing Zhang, and K. Jane. Extracellular matrix organization, structure, and function. In *Calcific Aortic Valve Disease*. InTech, jun 2013. doi: 10.5772/52842.

[269] Michael C.H. Wu, Rana Zakerzadeh, David Kamensky, Josef Kiendl, Michael S. Sacks, and Ming-Chen Hsu. An anisotropic constitutive model for immersogeometric fluid–structure interaction analysis of bioprosthetic heart valves. *Journal of Biomechanics*, 74:23–31, jun 2018. doi: 10.1016/j.jbiomech.2018.04.012.

[270] Andreas Wächter and Lorenz T. Biegler. On the implementation of an interior-point filter line-search algorithm for large-scale nonlinear programming. *Mathematical Programming*, 106(1):25–57, apr 2005. doi: 10.1007/s10107-004-0559-y.

[271] Fei Xu, Simone Morganti, Rana Zakerzadeh, David Kamensky, Ferdinando Auricchio, Alessandro Reali, Thomas J. R. Hughes, Michael S. Sacks, and Ming-Chen Hsu. A framework for designing patient-specific bioprosthetic heart valves using immersogeometric fluid-structure interaction analysis. *International Journal for Numerical Methods in Biomedical Engineering*, 34(4):e2938, jan 2018. doi: 10.1002/cnm.2938.

[272] Lanti Yang, Kees O. van der Werf, Bart F.J.M. Koopman, Vinod Subramaniam, Martin L. Bennink, Pieter J. Dijkstra, and Jan Feijen. Micromechanical bending of single collagen fibrils using atomic force microscopy. *Journal of Biomedical Materials Research Part A*, 82A(1):160–168, 2007. ISSN 1552-4965. doi: 10.1002/jbm.a.31127. URL `http://dx.doi.org/10.1002/jbm.a.31127http://onlinelibrary.wiley.com/doi/10.1002/jbm.a.31127/abstract`.

[273] Lanti Yang, Carel F.C. Fitié, Kees O. van der Werf, Martin L. Bennink, Pieter J. Dijkstra, and Jan Feijen. Mechanical properties of single electrospun collagen type i fibers. *Biomaterials*, 29(8):955–962, mar 2008. doi: 10.1016/j.biomaterials.2007.10.058.

[274] Lin Yang, Bogdan Georgescu, Yefeng Zheng, Peter Meer, and Dorin Comaniciu. 3d ultrasound tracking of the left ventricle using one-step forward prediction and data fusion of collaborative trackers. In *2008 IEEE Conference on Computer Vision and Pattern Recognition*, pages 1–8. IEEE, June 2008. doi: 10.1109/cvpr.2008.4587518.

[275] Rana Zakerzadeh, Ming-Chen Hsu, and Michael S. Sacks. Computational methods for the aortic heart valve and its replacements. *Expert Review of Medical Devices*, 14(11):849–866, oct 2017. ISSN 1745-2422. doi: 10.1080/17434440.2017.1389274.

[276] Will Zhang and Michael S. Sacks. Modeling the response of exogenously crosslinked tissue to cyclic loading: The effects of permanent set. *Journal of the Mechanical Behavior of Biomedical Materials*, 75:336–350, November 2017. ISSN 1878-0180. doi: 10.1016/j.jmbbm.2017.07.013.

[277] Will Zhang, Yuan Feng, Chung-Hao Lee, Kristen L. Billiar, and Michael S. Sacks. A generalized method for the analysis of planar biaxial mechanical data using tethered testing configurations. *Journal of Biomechanical Engineering*, 137(6):064501, apr 2015. ISSN 1528-8951 (Electronic) 0148-0731 (Linking). doi: 10.1115/1.4029266. URL `http://www.ncbi.nlm.nih.gov/pubmed/25429606`.

[278] Will Zhang, Salma Ayoub, Jun Liao, and Michael S. Sacks. A meso-scale layer-specific structural constitutive model of the mitral heart valve leaflets. *Acta Biomaterialia*, 32:238–255, March 2016. ISSN 1878-7568 (Electronic) 1742-7061 (Linking). doi: 10.1016/j.actbio.2015.12.001. URL `http://www.ncbi.nlm.nih.gov/pubmed/26712602`.

[279] X. Zhao, Z. C. Berwick, J. F. Krieger, H. Chen, S. Chambers, and G. S. Kassab. Novel design of cruciform specimens for planar biaxial testing of soft materials. *Experimental Mechanics*, 54(3):343–356, sep 2013. ISSN 0014-4851. doi: 10.1007/s11340-013-9808-4. URL `http://dx.doi.org/10.1007/s11340-013-9808-4`.

[280] Li Zhu, Tirthankar Dasgupta, and Qiang Huang. A D-optimal design for estimation of parameters of an exponential-linear growth curve of nanostructures. *Technometrics*, 56(4):432–442, oct 2014. doi: 10.1080/00401706.2013.866600.